THE DEVELOPMENT OF A BINDER SYSTEM AND PROCESS FOR THE MANUFACTURE OF LARGE DIAMETER TUNGSTEN CARBIDE DRILL BLANKS

by

BENJAMIN LUKE BLACKHAM

A thesis submitted to

The University of Birmingham

Engineering Doctorate in Formulation Engineering

School of Chemical Engineering,

The University of Birmingham,

Edgbaston,

B15 2TT

February 2015

ABSTRACT

A novel extrusion binder system was developed to enable the manufacture of tungsten carbide drill blanks greater than 14 mm in sintered cross-sectional diameter at Sandvik Hard Materials Coventry. The binder system comprised primarily of methyl cellulose and water, which was capable of being removed from the extrudate with no adverse effects on extrudate quality or increases in drying and de-binding times. The tungsten carbide feedstock was prepared by z-blade mixing on laboratory, pilot and production plant scales. Extrudates were manufactured either as solid cylindrical rods or as rods formed with internal coolant channels following a helical rotation up to 20 mm sintered diameter. Extrusion tooling was modified to aid the forming process and maintain the desired tolerances of internal properties of the drill blanks. Such properties included coolant hole diameter, coolant hole relative concentricity and the distance between the coolant hole centres (pitch circle diameter).

Controlled stress rheometry and oscillatory rheometry techniques were used in the selection of the methyl cellulose and water based binder for further analysis. Controlled stress and oscillatory rheological techniques were also used to determine how modifications to the binder systems could be used to improve the extrusion feedstock behaviour. Controlling the concentration of methyl cellulose in the binder system and the solids loading of feedstocks enabled the desired rheological paste properties to be obtained. It was shown that increasing the binder concentration gave increased elastic behaviour which lead to the formulation of stiffer extrusion pastes. Stiffer extrusion pastes were shown to give greater extrusion flow stability whilst maintaining the ability to dry large diameter parts under the Sandvik Hard Materials standardised drying conditions. Similarly, increasing the tungsten carbide solids loading was also shown to increase the stiffness of the extrusion feedstock.

The Benbow Bridgwater model was used extensively during this work in order to predict paste parameters across a range of extrusion pressures and velocities with the aim of characterising the different materials. Extrusion tooling and process development also benefitted from the application of the Benbow Bridgwater analysis as the optimum pressures and extrudate velocity for given feedstocks were subsequently determined.

Scanning electron microscopy and optical light microscopy were used to determine the tungsten carbide grain size and cobalt distribution of sintered samples. Cobalt magnetic techniques were also used to non-destructively measure the cobalt content of sintered samples. Finally the mechanical

properties such as transverse rupture strength and Vickers hardness were determined as a measure of quality control.

Acknowledgments

The author gratefully acknowledges Professor Stuart Blackburn for his guidance and encouragement during the completion of this thesis. Without his continued support, reading and highly influential advice it would not have been possible. Similarly, thanks go to Doctor Richard Greenwood for his incredible commitment to the EngD set up and rapid reading of this work, not to mention his ability to pull such a large group of students together. Thanks also go to Professor Neil Rowson for his support, particularly for providing Sandvik Hard Materials with excellent support and student projects and to Doctor Ihsan Al-Dawery for always endeavouring to assist, guide and supervise in the best way possible. The author would also like to express thanks to the EPSRC for the continued funding throughout this work and also the IRC for the heavy use of mixing and extrusion equipment.

A special thank you must go out to Sandvik Hard Materials for the use of pilot and production scale mixing and extrusion equipment. The accommodating nature of all operators in both the mixing and extrusion areas was much appreciated and alleviated the added pressures of running large scale test procedures. The completion of such trials, testing and exciting engineering activities would also not have been possible without the advice and commitment of Engineers Tom Bendrey, Adam Dixon and tool designer Karl Rowbotham. All three engineers have provided great support for this large scale project over the years as well as a togetherness that was essential for keeping the atmosphere strong. Due to the scale of the project, many R & D engineers and technicians present at Sandvik Hard Materials have been involved in some way with the work that has been completed. Therefore, further thanks must go to the R & D team; Christopher Thompson for his unwavering support and unofficial mentoring, Alexander Hirsch and Milena Mech for their incredible German efficiency and expertise in sintering, Ludwig Schneider for his knowledge of pressing and Meek Humpage for her continued practical support in just about every area.

Furthermore I would like to thank Elise Ravet for continuing to stand by me during the most challenging and grumpy spells, which was probably even more difficult than writing this thesis. Similarly, a mention must go to my parents for putting up with me over the last few years of my academic career, it is probably a good job that I lived away from home throughout the project.

Table of Contents

List of Figures

List of Tables

Chapter 1

1.0 Introduction

Historically, hard metals have been produced by methods such as pressing and extrusion with a large expansion in the market commencing in the first two decades after the Second World War. Expansion in the market was due to the fabrication of pressed inserts used in cutting applications and the introduction of new grades of WC-Co with nickel additives used for grain refinement. Sandvik Hard Materials (SHM) Coventry seeks to develop existing technologies around pressing whilst pushing the boundaries of extrusion. Pre-formulated ready to press powders are used in pressing, however, extrusion requires the preparation of a paste-like feedstock. Tungsten carbide wear parts can be prepared via either method although pressing demands are reducing due to a requirement for continuous or semi-continuous production. The largest volume application within SHM is rotary drill blanks and extrusion offers a semi-continuous production route. A complete range of products is required from extrusion production processes in a bid to have less of a reliance on pressing which is a solely batch process with limitations on geometry. Pressing larger diameter products in economic quantities becomes more difficult with increasing diameter and demands cannot be matched. Extrusion offers faster production rates and smaller machinery, with one extruder much more suitable for producing multiple geometries than an equivalent press. The greatest limitation with pressing is the production of drill blanks containing coolant holes of the desired diameter and length. It is a requirement of the tool itself that coolant holes run through the length of the blank following a helical pattern so that flutes can be machined in after forming. The pressing of a geometry that is complex results in dimensional inaccuracies and added processing stages to remove an internal core put in place to provide the coolant holes. Tungsten carbide extrusion feedstocks comprise tungsten carbide powder with metallic cobalt binder (WC-Co) and an organic binder forming aid. The binder system used for the extrusion feedstocks plays an important role in determining the capability of the final product. As there are many geometries produced by extrusion there is not one binder which fits all. This EngD project focuses specifically on large diameter products. Therefore this thesis aims to develop a novel binder formulation to enable the forming of complex large diameter geometries containing helical patterned coolant holes. Currently SHM Coventry does not have the capability to manufacture WC-Co drill blanks greater than 14 mm in sintered diameter. There is a large market share available in this sector and providing the larger diameter drills also offers an opportunity for SHM to be the sole supplier for its target customers and existing customers. The EngD project therefore aims to support the development of the capability to

produce the larger diameter products at large scales. Currently Sandvik supplies drill blanks to an internal customer, which then sells the products on to an external market. Further into the future, the aim is to sell drill blanks externally although presently the market focus is internal sales. The current market potential has been analysed based on the consumption of large diameter parts. These parts are bought in from external companies and the consumption is a conservative estimate based on the figures from 2012, given in table 1.

Table 1 Product cost per piece

Product	Pieces Consumed	Cost per Piece (£)	Total Cost
14 mm	6300	80	504000
16 mm	8035	100	803500
18 mm	3562	130	463060
20 mm	1902	152	289104

The above diameter range totals a cost of £2.06 million per year which has the potential to grow substantially given that there are ranges of products within each diameter that are currently outside the scope of this work. Preliminary studies involved rheological analysis of six appropriate binder systems to determine which had promising performance. Initial rheology measurements of currently used binder and dough systems showed what basic properties were required. Properties derived from viscosity and oscillatory studies on new binder systems have been correlated with desirable material characteristics for large product formulation. Following the initial studies, extrusion feedstocks were prepared using z-blade mixers from which further rheological measurements could be made based on torque, density and solids loading as a form of mixer torque rheometry. Mixer torque rheometry has been used to determine the critical solids loading for each of the given feedstocks. Extensive extrusion work and capillary rheometry tests coupled with the aforementioned rheological techniques has indicated that the optimum formulation for large diameter extrusion with complex geometries to be based on a methyl cellulose binder system. This binder system allowed for the extrusion of precise geometries whilst maintaining the ability to successfully dry and sinter large parts with the correct metallurgical and physical qualities.

Chapter 2

2.0 Literature Review

2.1 Cemented Carbide

In cemented carbides, the carbide particles are bonded by a binder metal which is liquid at the sintering temperature [1]. Many forms of cemented carbide are described collectively as tungsten carbide (WC) because WC is the major component. Consequently, the first commercially available cemented carbide was known as WC which consisted of fine angular particles of tungsten carbide bonded with metallic cobalt (WC-Co) [1]. It is still believed that this original composition has one of the greatest resistances to abrasive wear and hence its popularity in industry [1]. Cemented carbides can include titanium carbo-nitride, titanium carbide, tantalum carbide and other carbides together with WC in a nickel or cobalt based matrices.

2.1.1 Tungsten Carbide (WC-Co)

Cemented WC-Co is a metal matrix composite whereby cobalt is present as the binder matrix. The potential of WC-Co was first realised in the early 20^{th} century when the discovery of hard carbide particles present in high-speeds steels was made [1]. Many of the properties of tungsten carbide as with other sintered hard metals depend strongly on the microstructure. According to Brookes, the microstructure of WC-Co can be broken down into the following categories [1]:

- Compositions of hard and matrix phases.
- Size, shape and distribution of carbide particles.
- Relative proportions of hard and matrix phases.
- Carbon balance; often varied with sintering parameters.
- Variations in composition and structure caused by diffusion, precipitation or segregation.
- Production methods such as milling, carburising (a heat treatment process to liberate carbon) and sintering.
- Raw materials.
- Post sintering processing.
- Coatings or diffusion layers.

Obtaining the correct balance of each of category determines the desired properties of the final product. As well as the microstructure, the organic processing aid (binder) used with WC-Co is highly influential during processing and manufacturing. It is often the binder which is modified to vary the

structure and properties of the final product so that the powder matrix can be kept at a fixed composition in terms of cobalt and WC-Co. The WC and metallic binder composition define the powder grade. The crystal structure of the tungsten carbide to be used for a given application must also be considered. Typically, there are two forms of crystal structure that are used, hexagonal and cubic.

2.1.1.1 Hexagonal Tungsten Carbide

Hexagonal tungsten carbide, figure 1 is the most commonly used tungsten carbide due to its high stability over a large temperature range (represented by β in the phase diagram, figure 3). It is the hexagonal tungsten carbide that is used in this work.

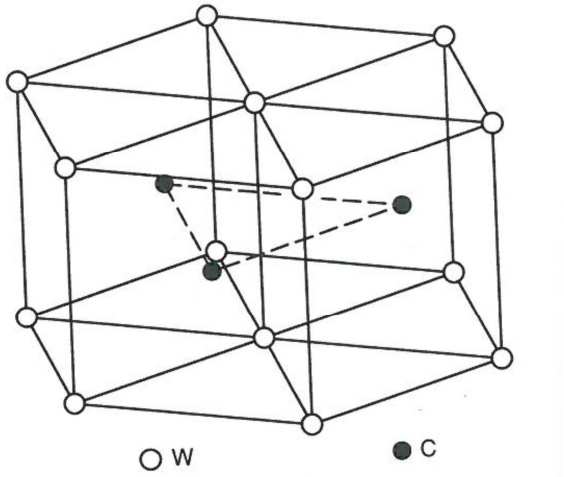

Figure 1 Hexagonal tungsten carbide [2]

The hexagonal structure is not observed for the pure metal and results from the introduction of planes of carbon atoms [3]. Additionally, the segregation of carbon atoms during the manufacture of W_2C converts the simple hexagonal structure to the close packed hexagonal structure.

2.1.1.2 Cubic Tungsten Carbide

Cubic tungsten carbide is less commonly used than hexagonal tungsten carbide and the unit cell takes the form of the face centred cubic structure, figure 2.

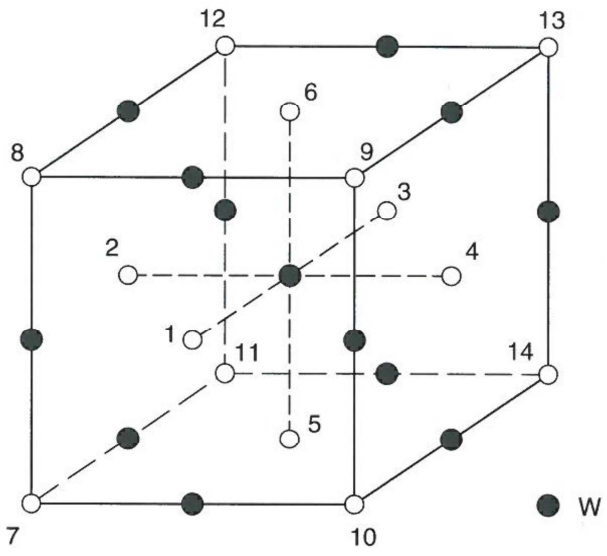

Figure 2 Cubic tungsten carbide [2]

The cubic tungsten carbide is less commonly used because it is only stable when prepared at temperatures greater than 2525 °C which can be observed in the phase diagram in figure 3 (δ). To retain the cubic structure, rapid quenching is required.

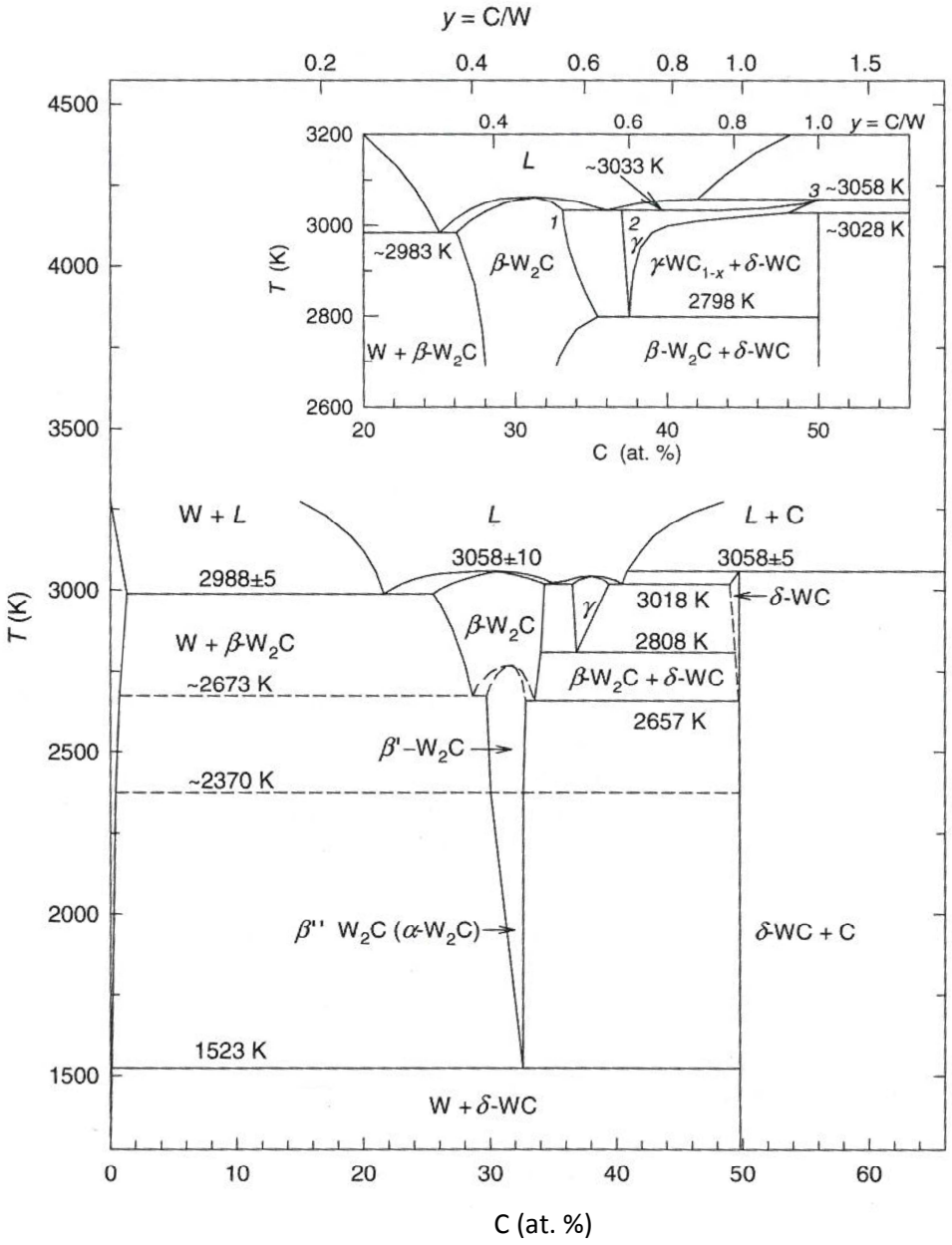

Figure 3 tungsten carbide phase diagram [2]

The crystal structure of tungsten carbide and variant chosen are highly significant when considering the applications of the material.

2.1.1.3 Non-metal Cutting Applications of Tungsten Carbide

Classical applications of tungsten carbide are in the machining of metals such as cutting tools and metal forming tools, rock drilling and cutting, wear applications and specialised structural components. The aforementioned applications are common due to the properties of WC such as high hardness, toughness, wear resistance and corrosion resistance and also high elastic modulus and such properties are crucial to this work. Lesser known applications however include the respective fields of

ammunition, nuclear, sports, surgical and jewellery. In terms of ammunition, tungsten carbide is often used in armour piercing bullets. Where steel bullets fail to penetrate ceramic faced armour, tungsten carbide core bullets are capable of penetration due to a high hardness. Armour piercing bullets are traditionally manufactured from a WC-Co core placed in an aluminium casing which itself is encased in a Cu-Zn jacket [4]. Encasing the carbide core in a material of greater ductility aids aerodynamic performance whilst the high hardness core is for penetration performance [5]. Tungsten carbide is also used in the ammunitions field for the manufacture of gun barrels due to high wear resistance and consequently prolonged life [6]. As well as acting to pierce armour, tungsten carbides have also been used in industry for protective purposes. In the nuclear industry, tungsten carbide is used for protection due to its high radiation absorbance, corrosion and wear resistance and neutron reflection capabilities. A high wear resistance also makes tungsten carbide suitable for sporting applications such as skiing and trekking. Top end athletes are known to use tungsten carbide tipped trekking poles and ski poles due to constant impacts occurring with hard surfaces. Similarly, high wear resistance, hardness and toughness give rise to surgical applications. In any surgical application, cleanliness and hygiene are of paramount importance. In order for surgical implements such as scissors and forceps to remain free from dirt and bacteria, they must remain smooth and easy to clean after extensive use. Combining medical and cutting industries, tungsten carbide is likewise used in dentistry for drills and burs. Dental burs are used to cut and grind through teeth. In order for patient discomfort to be minimised, highly accurate tolerances are required so that the burs can rotate at extremely high velocities without vibration. Tolerances are more easily achieved with WC than for alternative materials such as steel combined with diamond. It has previously been shown that a better cutting efficiency over diamond for dental burs can be achieved with tungsten carbide. The greater efficiency is regardless of applied torque and an additional benefit is that lower tool temperatures are developed due to shorter cutting times [7]. An ability to be easy to clean, highly polished and easily formed also makes tungsten carbide an attractive option for jewellery makers and customers. A high hardness and lower cost when compared to diamond provides impressive scratch resistance against high value jewellery items and hence its recent popularity for wedding rings. Each of the various applications mentioned comes in some way or form from the same starting raw materials. Differences in processing methods and additive components are what provide the desired properties for the given application.

2.2 Raw Materials

The ores of tungsten are sheelite and wolframite, Ammoniumparatungstate (APT) is a derivative of sheelite and wolframite and is the starting point for many WC-Co industries [8].

2.3 Manufacture

The production of WC-Co is shown in Figure 4.

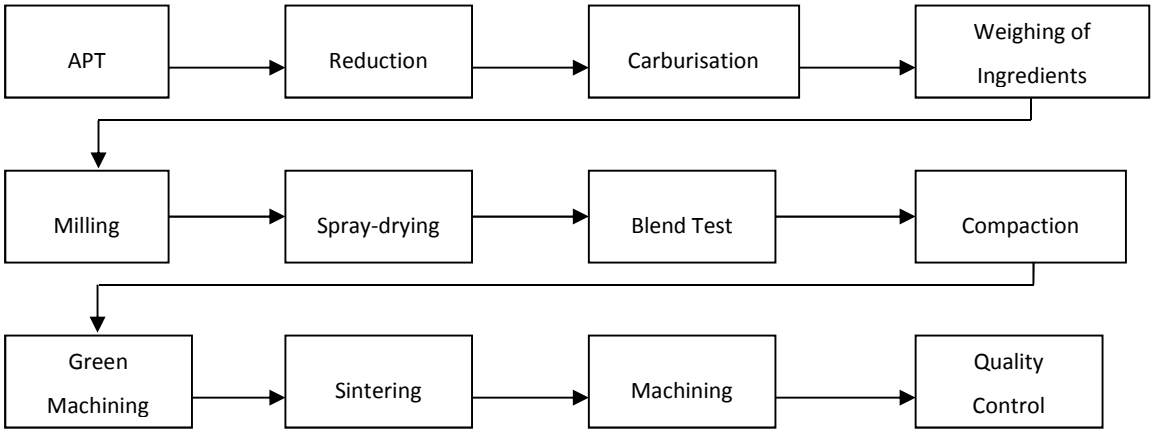

Figure 4 SHM WC-Co production [8]

APT first has to be produced from minerals such as sheelite and wolframite. Thermal decomposition of APT ($(NH_4)_{10}[H_2W_{12}O_{42}]\bullet 4H_20$) at 380 °C [3],[4] forms tungsten trioxide (WO_3) which can also be used in high temperature applications and catalysis [11] [12]. WO_3 is reduced by hydrogen to give the metal [13]. The addition of cobalt during the reduction stage increases the rate of reduction towards the metallic phases, whilst increasing particle size; this also increases the relative density of the material [14]. Cobalt is a catalyst during the reduction process, however it can also cause the undesirable effect of agglomeration of the metal powder and so the correct balance has to be achieved [14]. Cobalt is present primarily to bind the grains of carbide whilst providing a degree of ductility and is described in more detail in section 2.8.2. The carburisation step of the manufacturing process converts tungsten oxides into micron scale WC-Co powders. More recent developments in spray conversion and chemical co-precipitation have led to the production of nanostructured powders [14]. Nanostructured powders give the advantage of higher quality sintered WC-Co parts, with future developments in catalyst technology [14],[15]. This is due to WC-Co showing similar catalytic activity to that of platinum [16].

WC-Co is produced via the carburisation of tungsten powder by carbon black [15]. The reaction takes place in fixed bed tubular reactors under flowing hydrogen at temperatures above 1400°C [15]. By combining the correct tungsten particle size and reaction temperature, WC with a wide particle size range can be produced [15]. Zeiler noted that a particle size range from 55 µm down to 0.15 µm can be produced [17]. There are three well defined steps for the carburisation of tungsten to tungsten carbide powder which occur over the temperature range of 800-850 °C.

1. Adsorption of carbon atoms at the surface of the tungsten particles.

2. Diffusion of carbon atoms in the tungsten lattice.
3. Nucleation and growth of the carbide phases [15].

The first step depends on the contact area between the tungsten particles and carbon black. Good dispersion of carbon black and high specific surface area increase the contact area. Carburisation rate depends on the rate of each reaction step and the step with the lowest rate controls the overall reaction rate. Carburisation of WC powder can also be achieved by using methane; giving shorter reaction times at lower temperatures. Methane also increases the contact allowing more carbon atoms to be absorbed. Effective carburisation has been carried out at 800°C [15] and following carburisation, WC is mixed with cobalt by extensive milling to obtain WC-Co powder. Cobalt content determines many of the properties of the product. Traditional cemented WC-Co contains 3-30 wt% cobalt binder phase [18]. The WC-Co used throughout this work contains 10% cobalt. The carbide grains are embedded in the cobalt and due to grain size, the degree of milling can determine toughness and hardness of the product. Decreasing the cobalt concentration also increases hardness whilst decreasing rupture strength and fracture toughness [18]. Figure 5 shows properties of functionally graded WC-Co. Hardness decreases with increasing cobalt content and increasing grain size.

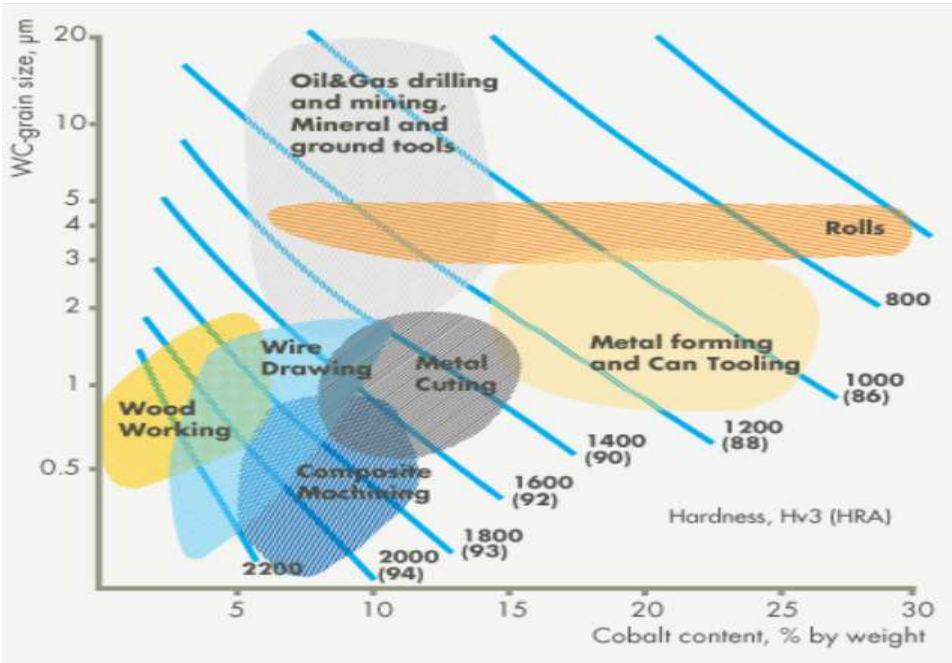

Figure 5 WC-Co products, Cobalt content vs hardness [8]

Optimising the milling procedure achieves a finer-grained microstructure with a homogenous grain size distribution. A common milling procedure is ball milling in which the powder matrix is milled using hard balls rotating and tumbling in a cylindrical container. Finer grained microstructure tends to

increase hardness, toughness and abrasion resistance [18]. Ball milling is the preferred milling technique as well controlled size distributions can be achieved whilst the PEG binders are also well mixed. Ball milling achieves a good cobalt distribution and therefore low porosity and the presence of ethanol and water aids cooling and lubrication whilst minimising oxidation. Other procedures in the manufacture also result in a degree of grain refinement such as co-precipitation. During ball milling contamination from mill media can occur and hence ball mill materials require careful consideration [19]. Contamination is prevented by using cemented carbide milling materials. Such materials also prevent excessive mill wear. Processes involved in ball milling are those of repeated deformation, fracture and cold welding which are caused by continuous impacts taking place within the mill barrel [19]. Figure 6 represents samples of WC-Co before and after ball milling respectively.

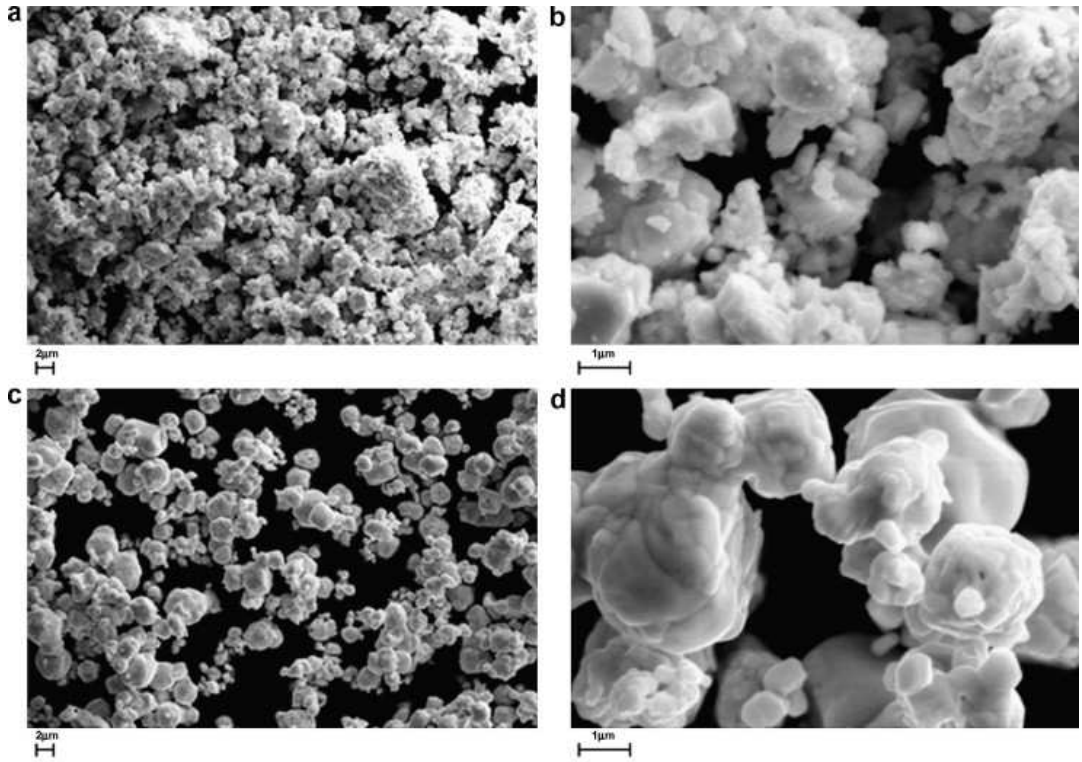

Figure 6 WC-Co (a before milling, b after milling at room temperature, c before milling, d after milling at -30° C) [20]

The work of Hewitt, Laoui and Kibble [20] show that the milling temperature of WC-Co is also significant. Material milled at -30°C gave a PSD of 26 nm, increased deformation and less irregularity whereas room temperature milling gave a PSD of 21 nm and a higher relative density. Milling at -30°C also gave a 0.8 GPa harder product after sintering.

Following milling in an ethanol and water mixture, the powder matrix is spray-dried. For pressing processes spray drying is required to allow for bulk free flowing powder. The principle of spray drying is the atomisation of the liquid phase which leads to the formation of droplets and large loose spheres

by a process of granulation [21]. Droplets can be dispersed into the hot gas stream to increase surface area and reduce drying time [21]. Five factors influence the properties of a spray-dried powder [22]:

- Suspension composition
- Type of atomiser
- Feeding rate
- Drying temperature
- Atomising pressure [23],[24]

As each of the above factors have an effect on the quality of the spray dried powder, each factor consequently has an effect on the final product. Due to the fact that the final product quality can be affected, it is essential that the spray-drying process is fully optimised. With focus on suspension composition, there are several parameters which require careful control. Such parameters range from slurry viscosity and yield stress through to slurry pH, zeta potential and sedimentation height.

pH, viscosity and yield stress are interlinked properties as pH has a direct influence on the flocculation or de-flocculation of the slurry. Generally, increased pH towards the iso-electric point causes electrostatic de-stabilisation and increased yield stress [25]. The iso-electric point of a slurry is the point at which the zeta potential is zero and corresponds to a pH value at which the eletro-kinetic surface charge of the particles is zero [26]. Slurry pH is also closely linked to sedimentation height and zeta potential. A zeta potential of zero generally leads to the formation of a flocculated slurry. This is because at zero zeta potential, there is no electro-static repulsion between particles. When electrostatic repulsion exits then particles can behave more as individuals rather than as one unit and this occurs in a pH zone far from the iso-electric point of the slurry [27], [28]. Additionally, the yield stress of a given slurry is important for particle mobility. In low yield stress slurries, ceramic particles can easily move and migrate towards the surface during the drying process (as the solvent, in this case ethanol, is removed). As the binder in this instance is soluble in ethanol, it is able to migrate to the surface at the same time. This migration leaves behind a hole or void and in the industry this is a process known as dohnutting. Subsequent migration leads to the formation of a dense outer shell and a hollow centre. Conversely, if the yield stress of the slurry is high, particles cannot move towards the surface during drying and therefore the outer shell and voids do not form [29]. It is also true that a well flocculated slurry corresponds to a slurry with a high relative sedimentation height. Therefore, it can be concluded that a slurry with a pH close to the iso-electric point (low inter-particle repulsion), a high yield stress and viscosity (low mobility) and a high sedimentation height, is well flocculated and therefore preferred. Such slurries are preferred as the formation of voids is avoided thus giving solid spray dried spheres that are free-flowing.

Following Spray drying, particle size distribution and flowability are measured to ensure that all of the cavities in the press tool will be filled uniformly assuming that pressing is the method of manufacture [8]. Once powder quality is confirmed as being within specification it can then be compacted. Different methods of compaction give different properties. In electric-discharge compaction, powders are fed into an insulating tube in which a high voltage and high density current is pulsed. This applies external pressure and therefore leads to compaction. Short discharge times due to high rates of heating and cooling limit cobalt migration [31]. Cobalt migration is caused by differences in WC grain size and cobalt content per unit area and finer grains give less cobalt migration during sintering [30], [31]. With the correct powder properties further processing such as ram extrusion (section 2.3.1.2), screw extrusion and pressing (Appendix A) is necessary to form products.

2.3.1 Extrusion

Extrusion is a forming process used to manufacture products of constant cross-sections. Many extrusion processes exist and typically hard metal feedstocks are either ram extruded or screw extruded (Appendix A) [1]. In ceramic extrusion, a ceramic powder is mixed with organic processing aids before being extruded through a die at the end of the extruder.

2.3.1.1 Ram Extrusion

Ram extrusion is a batch process and can only be operated in a semi-continuous manner as barrel filling is required [32]. A large volume of feedstock paste is compressed into a plug or billet inside an extrusion barrel. Compressive forces are developed by the reaction of the billet with the barrel surface [33]. Further compression forces the billet through a reduced orifice (die or nozzle). The internal die surface and size of the die determines the shape and size of the product. Many complex products are formed from ram extrusion processes such as bricks, catalysts, tiles, fertilisers, pharmaceutics and in relevance to this work drill blanks and cutting tools [34]. The correct liquid content in a ram extrusion feedstock is vital; a low liquid content can give excessive pressure drop leading to geometry rupture, whilst high liquid content leads to a loss of product structural integrity [34]. Paste rheological parameters are dependent on the liquid content of extrusion feedstocks and hence are described in detail in section 2.5.3. Tooling is designed with material rheology in mind as the two aspects work together to insure product quality. Solid shapes such as rods are formed purely via volume reduction from the extrusion barrel size to the die size required. Complex geometries require intricate tooling; Figure 7 shows an extrusion set up including a mandrel and spider. A spider holds the mandrel in place whilst allowing material to flow through the holes around its edge. The mandrel is used to form shapes in the centre of the extrudate such as coolant holes in the case of making drill blanks from WC and is often described as a core pin.

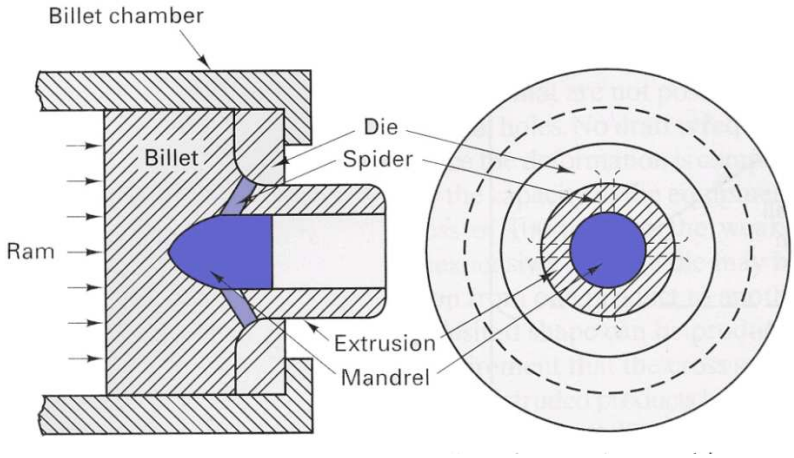

Figure 7 Extrusion tooling, mandrel/spider [35]

During ram extrusion, the feedstock consisting of liquid and solid phases is subjected to stresses. A pressure gradient exists due to the stress applied to the liquid component which causes liquid motion in the feedstock [34]. Uneven distribution of the liquid from this pressure gradient as a result of material instability and phase migration can cause issues with green strength and variability in the sintered product. Liquid phase migration is an inherent problem with aqueous based extrusion feedstocks and is described by Rough et al. [36]. Rough reports that the porosity of a compacted body decreases with an increasing applied shear stress. Therefore, extrusion at slower velocities encourages a greater amount of liquid phase migration. The liquid phase can travel more easily through a porous body, thus encouraging phase migration. Yaras et al. [37] reports that flow instabilities resulting from severe liquid phase migration have been observed in highly loaded suspensions. It is therefore important that the optimum extrusion velocity is obtained for aqueous feedstocks in order to minimise the effects of liquid phase migration. The work of Fielden et al. [38] indicates that the majority of phase migration occurs in the compaction stage of the extrusion process. There are a number of mechanisms taking place during ram extrusion and the typical extrusion process is described by three stages (below).

1. The Billet (material plug) is moved and pressure rises rapidly to a yield maximum.
2. Pressure decreases and reaches steady state.
3. Pressure reaches minimum value followed by a sharp rise as the material is compacted [33].

   The sharp rise in pressure at the end of stage 3 is normally not observed as extrusion is not pushed to this limit for safety reasons. Figure 8 indicates the 3 stages of extrusion with milled and un-milled alumina pastes without the sharp rise in pressure after stage 3 has commenced [39].

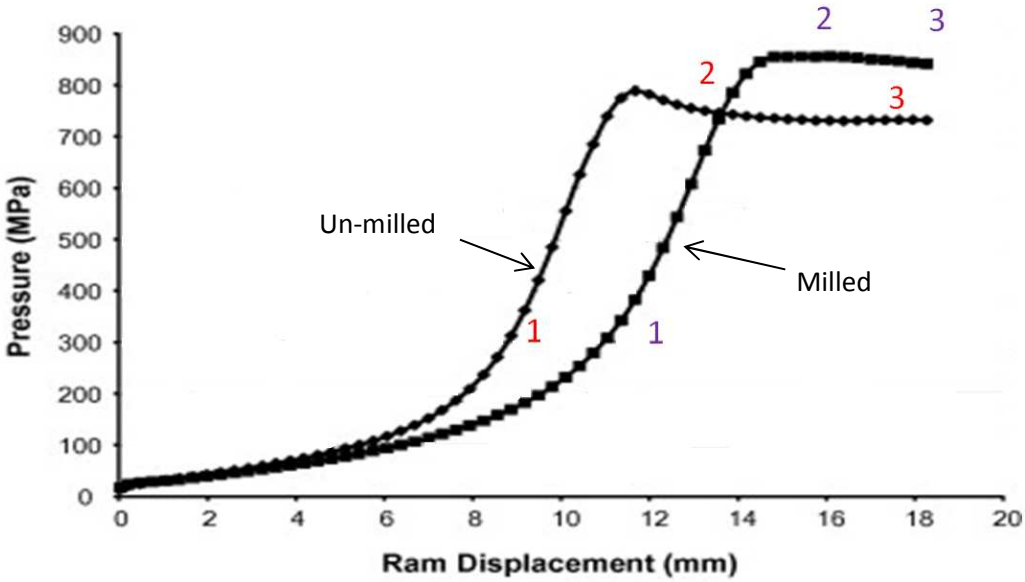

Figure 8 Milled and un-milled alumina pastes, extrusion stages [39]

Paste flow has been modelled extensively and is described in this work in section 2.5.3. Figure 9 shows the ram extrusion tooling used at SHM.

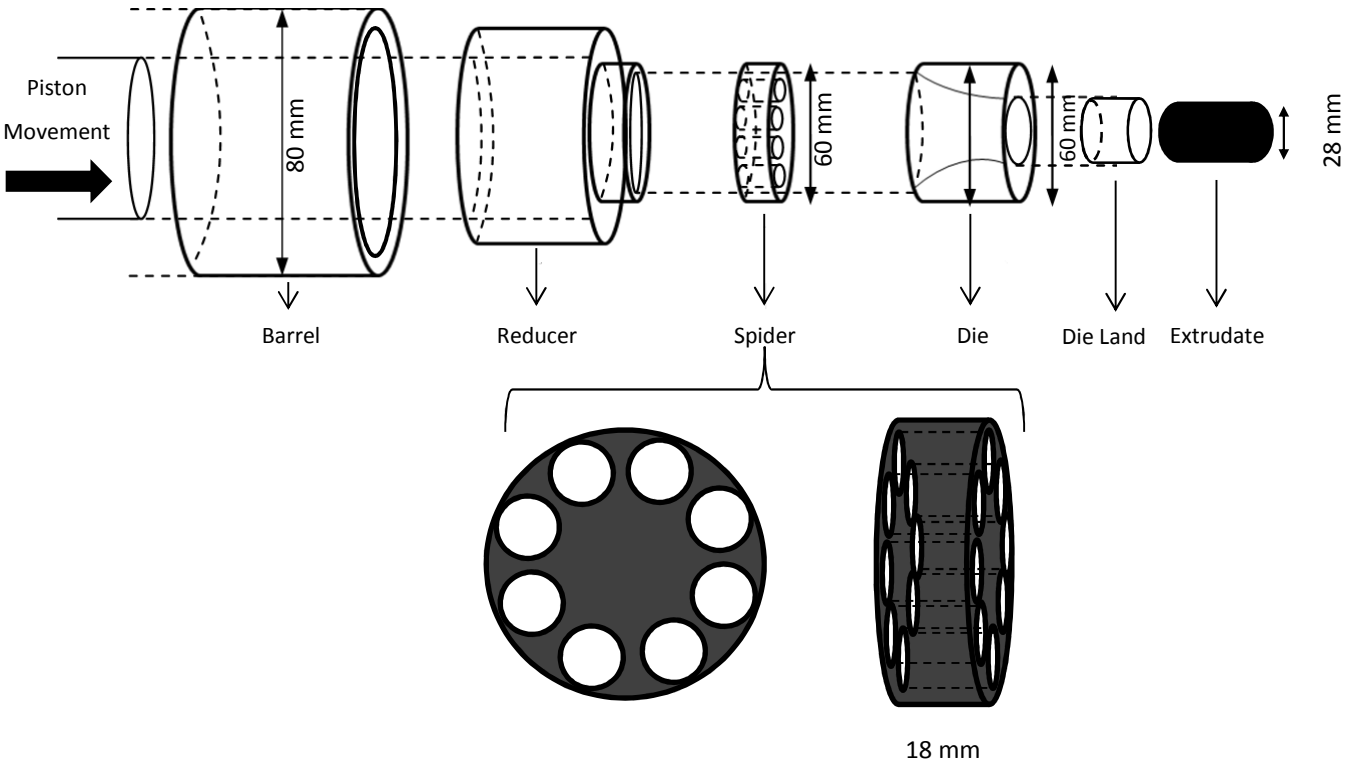

Figure 9 Sandvik Hard Materials ram extrusion tooling setup

Highly loaded WC-Co feedstock is fed into the extrusion barrel and compacted under vacuum to remove voidage and air entrapment. Typically extrusion set-ups consist of a reducer both to aid compaction and support the main tooling. The reducer ensures a reduction in diameter so that the

spider can be aligned properly. Tooling can be broken down into key geometry forming components including the spider, die and die land (Figure 9). The spider is in place to hold a core pin in order to form extrudates of complex geometry or tubular products. The core-pin is often referred to as a mandrel when tubular products are being formed. The core-pin is not shown in figure 9 as there are several variants as described later in section 3.12.1. The spider is also known to promote better extrudate quality due to enhanced shear during extrusion and its design can vary accordingly. Material flows through sections of reducing cross-sectional area giving regions of increasing pressure building up to the die land. Extrusion of WC-Co powder requires the addition of organic processing aids.

2.3.2 Organic Extrusion Processing Aids

Known binder systems for WC-Co processing are summarised in Table 2. Binder systems used in ceramic extrusion have also been included as the processing environment is similar.

Table 2 Binder system survey

Particulate (powder feedstock)	Binder used	Process	Reference
WC-Co (8 wt% cobalt)	Paraffin wax Steric acid Finely dispersed polymers	Screw extrusion	[29]
WC-5TiC-10Co	Paraffin wax Vegetable oil Low density polyethylene Steric acid	Injection moulding	[30]
WC-Co (10 wt% cobalt)	Alcohols Dissolved polymer	Ram Extrusion	[31]
WC-Co (12 wt% cobalt)	Methyl cellulose Water	Compaction/pressing	[32]
WC-Co (6 wt% cobalt)	1. Paraffin wax 2. Polyethylene wax 3. Amide wax 4. Canauba wax 5. Montan wax	Injection moulding	[33]
SiC cordierite	Methyl cellulose Water	Screw extrusion	[34]
Alumina	Boehmite Nitric acid Water	Ram extrusion	[35]
Alumina	Bentonite Starch Water	Ram extrusion	[36]
Alumina	PEG Vegetable fat	Injection moulding	[37]
Alumina	Hydroxypropyl methyl cellulose water	Ram extrusion	[38]
Tungsten Titania Clays Glass fibres	PEG Methyl hydroxyethyl cellulose Water	Screw extrusion	[39]
Alumina	Methyl cellulose Water	Slurry preparation	[40]
H-ZSM-5 zeolite	Methyl cellulose Water	Twin screw extrusion	[41]
Ceramic (general)	Methyl cellulose Carbohydrates Water	Ram and screw extrusion	[42]
Titania Alumina Silica	Methyl cellulose Water Clay Stearic acid	Screw extrusion and pressing	[43]

Many binders are incompatible with a WC-Co matrix as they are capable of leaching the cobalt from the system whilst agglomeration can also be common. Binders are combined with lubricants and stabilisers to aid the extrusion process. Table 2 shows that there is a bias towards methyl cellulose in the extrusion industry. In the case of WC-Co extrusion it is also common for paraffin wax to be used as a major binder constituent. The binder system currently used at SHM is described in section 2.3.2.1. Details of other binder systems have also been expanded on in sections 2.3.2.2 to 2.3.2.6.

2.3.2.1 Sandvik Hard Materials Current Binder System

The SHM binder system has not been included in Table 2 as it was designed specifically for production processes at Sandvik Hard Materials and is not in the public domain. It does however provide a bench mark of quality for new binder development. The current SHM system contains polyethylene glycol (PEG) as the major binder component. The PEG major binder is additional to any PEG earned in the powder from spray-drying and combined with proportions of monopropylene glycol (MPG), triethanolamine and oleic acid. A large number of waxes and waxy materials have been used for similar applications. Many derivatives of PEG have been used in pharmaceutical extrusion applications. WC-Co powder containing PEG from spray-drying is used as a feedstock as it does not become airborne and present hazardous conditions. Spray-dried WC-Co is a powder matrix prepared for pressing processes as well as extrusion and is well understood by SHM. PEG is present in a range of chain lengths to improve rheological behaviour during extrusion and stability during de-binding. MPG is used as a plasticiser in binder systems [55], however in this binder system MPG acts as a solvent for PEG and also as a lubricant. Oleic acid is added to the binder system to wet out the WC-Co powder by acting as a surfactant compatible with both WC and PEG.

2.3.2.2 Alumina Extrusion Binder Systems

PEG has also been used in the extrusion of alumina-bohemite pastes with comparisons drawn against Hydroxypropyl-methyl cellulose binders (HPMC) [46]. Ananthakumar et al. showed that alumina-bohemite pastes gave higher die exit pressures than alumina-HPMC pastes under similar conditions [46]. Additions of polyvinylacrylate lowered extrusion pressures in this case whilst similar effects were noted with the addition of glycerin [46]. PEG is known to improve wetting of powders, whilst glycerine has certain water retention properties. External lubrication is poor and die land pressures can be high with the glycerine additive system when combined with alumina [47]. Although low extrusion pressures aid tooling life, higher extrusion pressures generated by highly viscous pastes result in better extrudate quality. Greater paste compaction (higher pressure) results in better dimensional accuracy and die filling. Whilst stiff pastes give high extrusion pressures, ram speeds can be increased to obtain increased extrusion pressures for softer paste formulations. Compaction is referring to the removal of

pores in the extrudate, rather than reduction in powder-binder voids. The removal of pores is also aided by extruding under vacuum.

2.3.2.3 Methyl Cellulose Binder Systems

Methyl cellulose is commonly used in the extrusion industry due to its versatility in extrusion and its drying properties. It has been used to extrude a variety of complex geometries ranging from rods to honeycombs [46]. Methyl cellulose binders are often combined with water as the dispersion medium and mixes containing poly vinyl alcohol have also been utilised [47]. Cellulose is insoluble in water although suitable reactions yielding methyl side groups enable water solubility [45]. Rheological characteristics of extrusion feedstock have shown to be dependent on the rheological properties of the methyl cellulose binder itself [45]. Methyl cellulose forms a stable rigid gel above gelation temperature [45]. Gelation was first explained by Heymann who concluded that at high temperatures methyl cellulose chains dehydrated causing gelation [56]. Haque witnessed that at lower temperatures crystalline structures were formed in methyl cellulose, that subsequently melt out during heating, allowing for the formation of different structures [57]. Similarly, relating to structure, Sarkar observed that at lower temperatures the water in the cellulose binder forms ice-like structures around hydrophobic groups. When increasing the temperature the ice-like structure, thought to be caused by methyl substitution, breaks down. This break down causes an increase in entropy allowing for hydrophobic groups to interact and cause gelation [58]. Upon cooling, a sol like material can be formed meaning that the gelation process is thermo-reversible [59]. Ceramic pastes prepared with methyl cellulose binders show shear thinning behaviour as a result of the polymer coils aligning with the direction of extrusion flow [70]. Green strength is also required and so modifiers are often used in combination with methyl cellulose.

2.3.2.4 Methyl Cellulose Binder System with additives

Various grades of methyl cellulose are often used in conjunction with viscosity modifiers in industrial applications to enhance performance. Grades of methyl cellulose include hydroxypropyl methyl cellulose (HPMC), microcrystalline cellulose and carboxy-methyl cellulose. A common additive to each grade is polyacrylamide. Polyacrylamide acts as a thickener in water based systems as it has good solvent absorbing properties [61]. The work of Dey et al. [62] and Das et al. [63] has shown that polyacrylamide (PAM) can be grafted to HPMC causing an increase in the hydrogel viscosity. The thermal stability of the PAM doped HPMC hydrogel was also shown to increase in their work. It was shown that water diffused into the space between the cellulose backbone which hydrated the grafted PAM chains. Further diffusion pushed the grafted chains away from each other and increased swelling of the hydrogel. Increasing PAM content and therefore grafting efficiency however caused a greater

entanglement between PAM chains. Increased entanglement provided resistance against the pushing away from the cellulose backbone, thus limiting the swelling. The increased entanglement resulted in a form of cross-linking to yield an insoluble network facilitating swelling [62]. Controlled swelling with increased entanglement of PAM chains enabled a highly viscous hydrogel to be formed. Increased thermal stability was indicated by an additional zone of weight loss in thermal gravimetric analysis work. The work of Dey and Das has shown that polyacrylamide can be added to cellulose based gels in order to increase gel viscosity and thermal stability. Such properties are useful properties for extrusion flow and extrudate drying respectively. As well as PAM, glycerol has also been used as a binder modifier in methyl cellulose systems. Glycerol, having an affinity to water removes water from the gel. This increases the cellulose concentration thus increasing gel strength [49]. Whilst various properties were improved by adding polyacrylamide to hydrogels, the bio-degradability also increased. This is an undesirable property when considering the shelf-life of the hydrogel. Whilst different grades of cellulose play a role in defining different properties such as viscosity in an extrusion formulation, different functional groups also have significant effects.

2.3.2.5 Ethyl Cellulose Binder Systems

Ethyl cellulose has been used as a binder system in the pharmaceutical industry for the manufacture of dosage forms [64]. As ethyl cellulose is insoluble in water, binders are often prepared with ethanol. Ethyl cellulose binders have also been used in the extrusion of superconducting wire [65]. The work of Kim et al. showed that an extrusion binder could be prepared from ethyl cellulose and ethanol with glycerol as a lubricant and steric acid as a dispersant. In his work it was reported that low viscosity binders tended to form micro cracks in the as dried extrudate surface. Alternatively, hydroxy-ethyl cellulose has been used with water as a binder for the preparation of extrudable alumina pastes with shear thinning results [66]. Ethyl cellulose has also been used in conjunction with methyl cellulose as a coating in the extrusion process [67].

2.3.2.6 Other Pharmaceutical Binders

PEG derived components have been developed specifically for the extrusion of pharmaceutical pellets by Gatefosse, France. Such binders use the trade name Gelucire 5013 and are described in detail in section 3.3.6. Variants of Gelucire materials have also been used in conjunction with ethyl cellulose and methyl cellulose in extrusion processes [68]. Mehuys et al. have shown that an ethyl cellulose pipe can be extruded with an HPMC-Gelucire core in a monolith type structure. Complex structures were formed using both ethyl cellulose and Gelucire substances showing both compatibility and suitability in extrusion processing.

2.3.2.7 *Aqueous vs non-Aqueous Binder Systems*

From table 2, it is clear that for hard metal processing, many of the binders discussed in the literature are non-aqueous. Of the non-aqueous binders, several are wax based and as a result require different processing techniques to those that are available at Sandvik Hard Materials Coventry. However, the current PEG based binder system used by SHM is also non-aqueous and has several advantages over aqueous based binder systems. There are advantages and disadvantages for both aqueous and non-aqueous binders. The key factors are given in table 3:

Table 3 Aqueous vs non-aqueous binder systems

	Advantages	**Disadvantages**
Aqueous Binder	Ease of feedstock preparation	Phase migration (extrusion instability)
	Preparation time	Shelf life
	Ease of drying (removal of water)	Sensitivity to seasonal changes (humidity in particular)
	Ease of binder burnout in short times (cellulose)	Handling difficulties (moisture driven off by sample levitation on air cushion)
	Environmentally friendly (disposal of waste and burnout components)	
	Low drying temperatures	
	Relatively low cost, simple procedure	
	Adapted to z-blade mixing	
Non-Aqueous binder	Flow stability (higher yield stress and viscosity attainable)	Binder burnout procedure can be complex
	Longer shelf life achievable	Flow instability due to viscous heating (thermo plastic binders)
	Can be processed over a range of temperatures	Feedstock preparation
	Less sensitive to seasonal changes	Un-environmentally friendly
	Organics can be added in the powder milling stage	Long burn out/de-binding times
		Requires temperature control
		Not often suited to ram extrusion
		Requires feedstock granulation

In the case of this work, the primary advantage of using aqueous binders is that they are more suited to the drying and de-binding operations that are currently used. As there is little scope for change in this regard it would be difficult to produce high quality large diameter parts without completely modifying the drying and de-binding procedures. Similarly, many of the non-aqueous binders, wax based in particular, require elevated temperatures and increased shear during the extrusion process. As the current production methods are by ram extrusion, elevated temperatures would be costly to implement and difficult to control. The majority of non-aqueous binder systems are more suited to screw extrusion as a result. The major disadvantages from a production scale standpoint for the aqueous binders are the shelf life and likelihood of phase migration of the binder phase.

2.3.2.8 Binder Mixing

Binder pre-mixes are often prepared prior to mixing an extrusion feedstock due to the complexity of feedstock systems. Mixing frequently takes place at elevated temperatures, particularly if waxy binders are used. Demands on the material depending on the application are related to binding, lubrication, green strength, binder removal, elasticity and stiffness. Binding defines the physical binding of the carrying fluid material to WC-Co powder which is related strongly to wettability. In certain cases binder materials may not have the correct make up to bind to WC-Co which could be a result of binder shear viscosity and agglomeration. Physical properties of extrusion feedstocks are strongly linked to lubrication. Lubrication properties often refer to lubrication at the wall during extrusion although inter-particle lubrication is also present. Green strength, an important property in any extrudate refers to the transverse rupture strength of extruded products after drying when many binder components have been removed. Elasticity is a property of binder materials that is more useful when considering the extrudate prior to drying as it can affect flow properties significantly. The mixing process of binder materials has significant effects on the extrusion feedstock. Mixing binder systems at elevated temperatures causes the evaporation of key components whilst in other binder systems gelation may occur at higher temperatures. Generally mixing of organic extrusion binders requires elevated temperatures for dissolution. This is noticeable in methyl cellulose based binders or for homogenous mixing of multi-component materials in the case of waxy binders. Aqueous systems that form gel like structures can are prepared using simple planetary mixers whilst they are in the liquid state. However, wax and PEG based binder systems need either higher shear forces and or higher temperatures to form fully dispersed materials due to their high room temperature viscosity. High temperature mixing of waxes allows for low shear mixing equipment such as mechanical stirrers to be used, as waxy materials have a low viscosity at temperatures above 70 °C [69]. Using high temperatures also allows for reduced mixing times providing that the dispersion remains homogenous upon cooling. Planetary mixers are useful as there are no dead zones as the whole material volume is

swept equally [70] (Figure 11). Mixing via this method is also inexpensive and quick if high shear forces are not required. A typical planetary mixing attachment is shown in Figure 10 and follows the mixing path shown in Figure 11 allowing for efficient mixing [71].

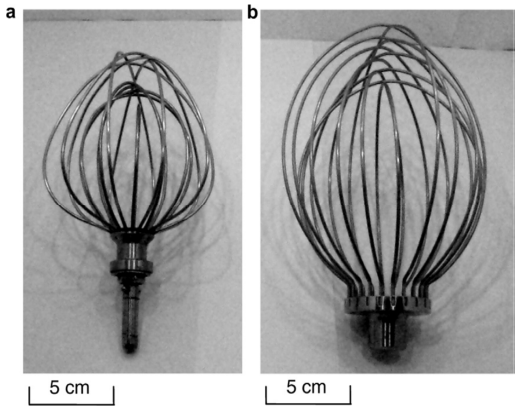

Figure 10 Planetary mixer attachments [71]

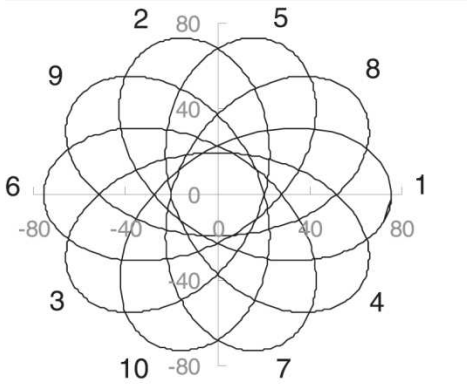

Figure 11 Planetary mixing attachment motion pattern [71]

2.3.2.9 Extrusion Feedstock Preparation

The preparation of highly loaded extrusion feedstocks in an industrial environment is dominated by high shear mixing. High shear mixing processes are ubiquitous to both extrusion and injection moulding. High shear mixing takes many forms such as twin roll mill, twin screw and z-blade mixing. Twin roll mixing offers geometrical simplicity insuring that high shear stresses can be evaluated and controlled. A schematic of the twin roll mill is shown in Figure 12 where H_0 is half the minimum gap between the rolls and v is the mean roller surface speed. Knowledge of apparent viscosity, roller geometry and velocity allows for the calculation of maximum shear stress applied to the material travelling between the rollers.

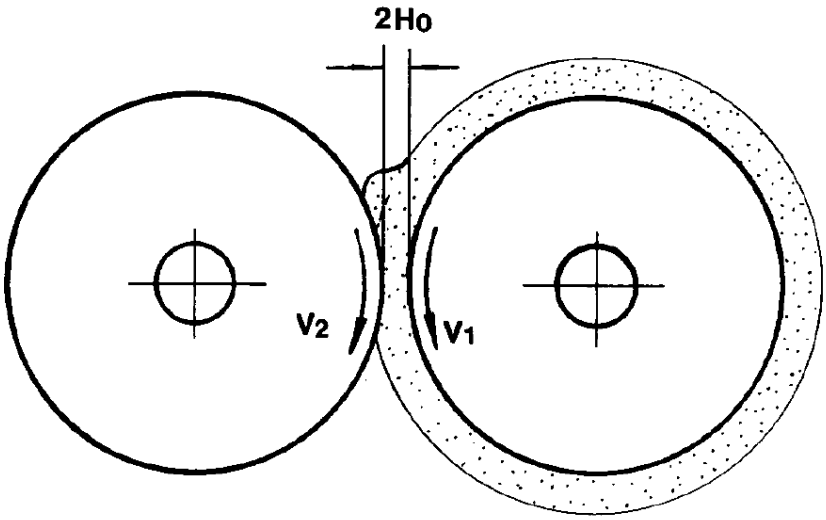

Figure 12 Twin roll mill schematic

Shear rate ($\dot{\gamma}$) can be calculated using the relationship first developed by Cogswell and Mckelvey given by equation 2-1.

$$\dot{\gamma} = \frac{v_2 - v_1}{2H_0} \qquad 2\text{-}1$$

Twin roll mixing was used by Grida and Evans for the preparation of zirconia in a waxy binder to be free formed using extrusion [72], they determined that inhomogeneous regions were produced. Song et al. have utilised twin roll milling followed by ultrasonic mixing of ceramic ink slurries [73]. The twin roll mill has limitations, particularly with the feed mechanism and handling after mixing. Twin screw extruders offer a more convenient process of mixing and exist in three principle forms, co-rotating, counter rotating and intermeshing [74]. Continuous feeding of powder and binder materials allow for continuous mixing using a twin screw extruder or kneader. Co-rotating screws are used for high efficiency mixing of highly viscous fluids as counter rotating screws have proved to be inefficient [75]. Three types of elements are used for twin screw extruders; conveying, kneading and distributive (Figure 13 left to right respectively). Conveying elements transport material whilst kneading elements are used to break up and homogenise material. Distributive elements are used for mixing and impart minimal energy into the material [75].

Figure 13 Screw extruder elements designs (conveying, kneading and distributive) [75]

Z-blade mixers are similar in design to counter rotating non-intermeshing twin screw extruders. Z-blade mixers are appropriate for all scales of high shear mixing, hence their popularity in the carbide industry. Figure 14 shows the blade design of a common laboratory scale Z-blade mixer.

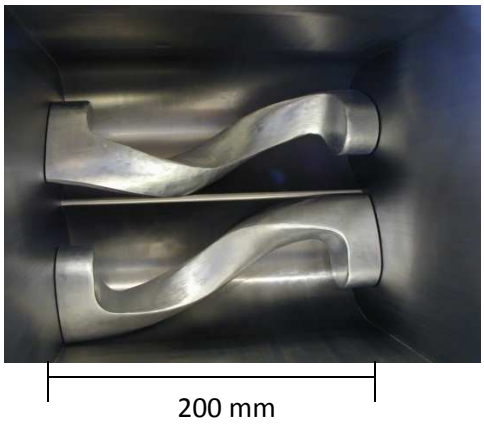

Figure 14 Z-blade mixer blades [76]

A high torque is required due to high paste apparent shear viscosity with a kneading and folding action and few dead zones. Z-blade mixing is also convenient for the application of a vacuum during mixing. However, when mixing high viscosity multi-component suspensions diffusion and turbulence are difficult to achieve [77]. Turbulent mixing is not practical as turbulence would only occur at a high Reynolds number requiring high mixing velocities. As a result high shear mixing equipment is designed to use a slower mixing velocity. Tight clearance tolerances between moving and stationary parts such as mixer blades and bowl surface are therefore required for high shear forces [77]. The tighter the tolerance, the greater the shear forces applied to the mix thus reducing agglomeration. Viscous pastes such as WC-Co dough have a high resistance to motion meaning that appreciable force is required to promote mixing. Lindley [77] claims that mixing occurs from cutting the material into smaller elements whilst redistributing them. Haraszi however observed that Z-blade mixers work with more of a kneading and folding mechanism whereby material is squeezed between the blades and bowl rather than broken up [78]. It is therefore more dependent on the material properties than the mixer as to

how the feedstock is distributed. For example, if a thermoplastic binder is used, higher temperatures will cause softening and melting of the feedstock. This will reduce cutting and promote a kneading action. Conversely, thermosetting binders would be more prone to breakage at elevated temperatures due to brittle behaviour. As material that is not easily moved is not easily mixed, it is desirable to have a mixing flow pattern that moves material into all zones of the mixing equipment readily [66]. Zones of slow movement are often found when mixing viscous feedstocks as viscous drag removes kinetic energy applied to the fluid [77]. Böhm and Blackburn [79] claim that pockets of dry powder develop in the corners of the mixer bowl (dead zones) whilst Matchett et al. claim that it is in fact areas of high moisture content that collect in the dead zones of the mixer bowl [80]. It is possible for either finding to be correct depending on the nature and solids loading of the pastes. Highly loaded pastes are prone to dry behaviour and incomplete wetting by the binder phase. This leads to deposits of powder forming in dead zones. Due to tight mixer tolerances the binder phase in this instance is squeezed out to the mixer dead zones and consequently is not re-distributed. Blackburn and Böhm have shown that higher solids loading pastes gave a better dispersion [79]. Their work also indicates that more highly loaded extrusion pastes require a higher extrusion pressure and therefore higher mixing torques. Pores, voids, micro-cracks, increased grain size and uneven sintering were observed for pastes mixed with a high moisture content due to the formation of agglomerates [79]. Other processing techniques do exist such as slurry filtration although mechanical mixing is often preferred. Prabhakaran has shown that extrudable alumina pastes can be prepared via pressure filtration of concentrated alumina slurries [81]. In this case, excess electrolyte was added to dilute suspensions of alumina to cause flocculation and aid pressure filtration and subsequent consolidation.

2.3.2.10 Pre-Extrusion Feedstock Analysis

The majority of extrusion feedstock analysis methods are a form of destructive testing. Whilst other methods used such as density measurements may be non-destructive. Previous work suggests that for density measurements to be accurate, measured samples must be free from air [82]. This can be difficult to achieve with highly loaded pastes without high quality vacuum pumps and sealing. Poor sealing can also result in liquid loss for pastes of high moisture content. True density measurements of extrusion feedstock are made using helium pycnometry and is defined as the ratio of the measured mass to the volume (occupied by the measured mass) [83]. Helium pycnometry is required because often internal pores are present in powder processed materials that would not be detected by volume displacement methods. Helium is often the preferred gas because it has a small atom size able to penetrate the smallest of pores whilst being an inert gas [83]. Increasing densities coincide with increasing solids loadings and falling densities coincide with porosity. Density is therefore used as a non-destructive quality measure. Mixer torque rheometry combined with density provides an

indication of how well mixed feedstocks are. Density and torque measurements can be used to determine if air entrapment has occurred and if the critical solids loading for a given material has been reached respectively. The critical solids loading represents the maximum volume of powder in a fluid that yields a coherent stiff paste that does not break [84]. For example, when examining solids loading a rise in torque is a function of increasing binder concentration whilst a subsequent drop in torque represents over wetting (Figure 15) [85]. Feedstocks 1 and 2 were prepared using PEG 20000 and PEG 3000 binders respectively.

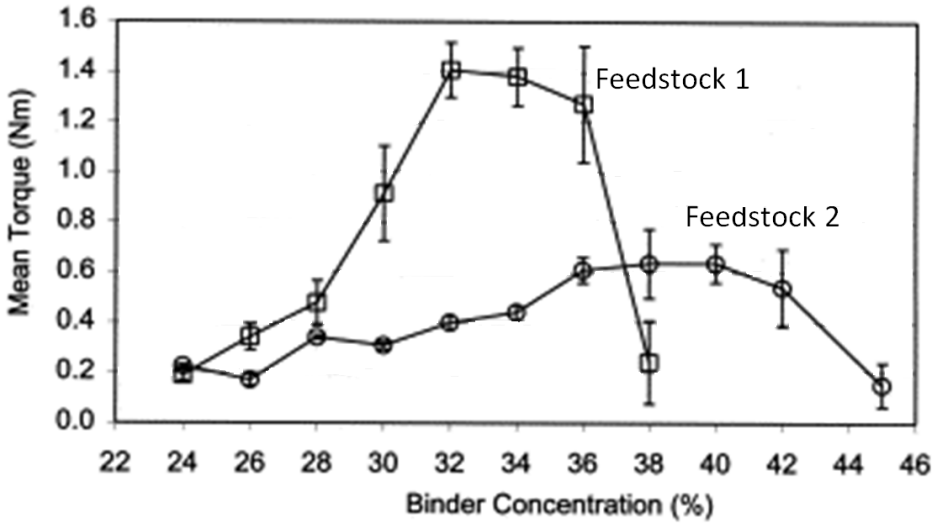

Figure 15 Effects of binder concentration on mixer torque [85]

Low torque is also indicative of weak substrate/binder interactions. The rising torque is attributed to a growing cohesiveness of powder particles with increasing liquid content [86]. The measurement of torque required to shear a wet mass therefore equates to rheological characteristics of the system [87]. Knowing that the torque measurements also correlate to liquid content and that liquid content can be used as a measure of solids loading then optimum loadings can be evaluated using this method. If torque for a given system is known to give optimum parameters then this can also be used as a measure of quality for a feedstock mix and it also holds that torque can be used as a measure of stability. A stable torque implies that the mix is homogenous and torque increases with mixing time from the onset of mixing before plateauing, thus showing stability [88]. An example of plateauing torque for feedstocks prepared from blends of Cellulose acetate (CA), glycerol triacetate (GTA), glycerol di-acetate (GDA) and ethylene glycol di-acetate (EGDA) is given in figure 16.

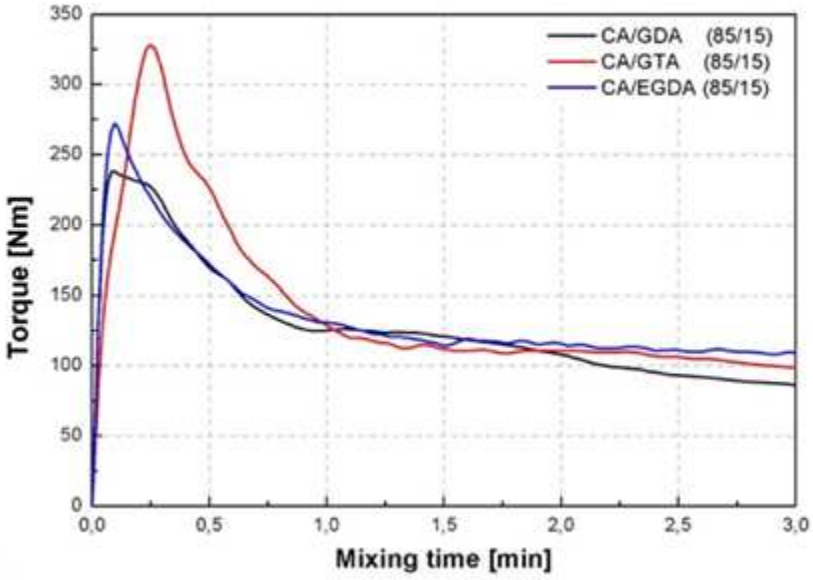

Figure 16 Plateau of measured mixer torque with time [89]

2.4 Paste Flow

A paste is a material consisting of liquid and solid components with each phase contributing to the behaviour of the whole material. Often, the presence of gas can lead to problems in extrusion [90] such as porosity and a sudden release of pressure. The work of many authors has contributed to the theory of paste flow. Benbow and Bridgewater contributed much in terms of the practical analysis of pastes. Their methods are often used when work is combined with industrial scale applications. Similarities are drawn between the Herschel Bulkley equation (2-10) and the Benbow Bridgwater equation. The Benbow Bridgwater model, however, assumes wall slip whereas the Herschel Bulkley model assumes no wall slip. The limitations of the Benbow Bridgwater approach have been well documented (section 2.5.3). In terms of tooling design and extrusion process conditions, the model still proves to be useful. Paste flow behaviour has also been predicted by Aydin et al. [91] Their work used numerical modelling based on a finite element analysis to predict the flow of paste materials through conical dies using ram extrusion. Paste flow was described by an elasto-viscoplastic constitutive model and used the Herschel Bulkley model to describe shear stress. Finite element analysis and computational modelling was also used by Horrobin [92]. Horrobin developed flow models based on assumed material flow properties in order to understand paste flow. Improvements on existing technologies have been trialled by Martin [93] in order to model radial flow extruders. Many of the models and theories in the literature are based on axisymmetric flow through square

entry die sets with materials such as play doh and plasticine. It becomes more difficult to model real pastes for practical applications due to the complexity of material and often a simplified model such as the Benbow Bridgwater approach is more easily applied. Highly loaded pastes are required for the manufacture of high strength parts. For highly loaded pastes, sufficient lubrication is needed to aid the formulation process. Lubricating agents are normally contained within the binder system such as oleic or stearic acid as well as other binder components. The lubricants cause extrusion feedstocks to plastically deform increasing the shear thinning behaviour giving rise to a better flowability [90]. High green strength and low feedstock apparent viscosities are needed for ease of handling and processing respectively. For low viscosity feedstock the solids loading should be greater than 1-2 volume % below the maximum solids loading (maximum powder content that can be sufficiently wetted by the binder system). This is the region in which pastes are likely to have a high apparent yield stress and a highly shear thinning behaviour which also serves to give a small drying shrinkage and dense extrudate bodies [90].

2.5 Materials Characterisation

Controlled stress rheometry can be used to determine binder viscosity based on shear rate and shear stress providing there is no slip at the wall of the geometry. The essential components of a controlled stress rheometer are shown in Figure 19 and Figure 20. These geometries can also be used for oscillatory rheometry. However for the extrusion feedstock capillary rheometry is used (section 2.5.3) as higher stresses are required to enable high viscosity material flow.

2.5.1 Binder Material Classification and Models

Extrusion binders are typically shear thinning fluids. A shear thinning fluid is defined as having a decreasing apparent viscosity with increasing shear rate [94]. If an extrusion binder did not exhibit shear thinning behaviour, extruding at increased velocities (and therefore shear rates) would not be practical. For industrial purposes, faster extrusion rates are more desirable for rapid production. Many binder materials exhibit properties of a Bingham plastic type material which begins to flow (with shear thinning behaviour) after a certain yield stress has been overcome. Shear thinning fluids are described by many names and models, historically, as pseudoplastic. Other forms of shear thinning materials are thixotropic, which are time-dependant shear thinning materials [95]. Many equations and models have been developed to describe the shape of flow curves for given materials. Some common fluid types are shown in Figure 17 and represented by Equations 2-2 to 2-10. The linear viscosity period is indicated for the Sisko fluid as it is difficult to differentiate between the Casson and Herschel Bulkley fluids without using a log/log scale plot.

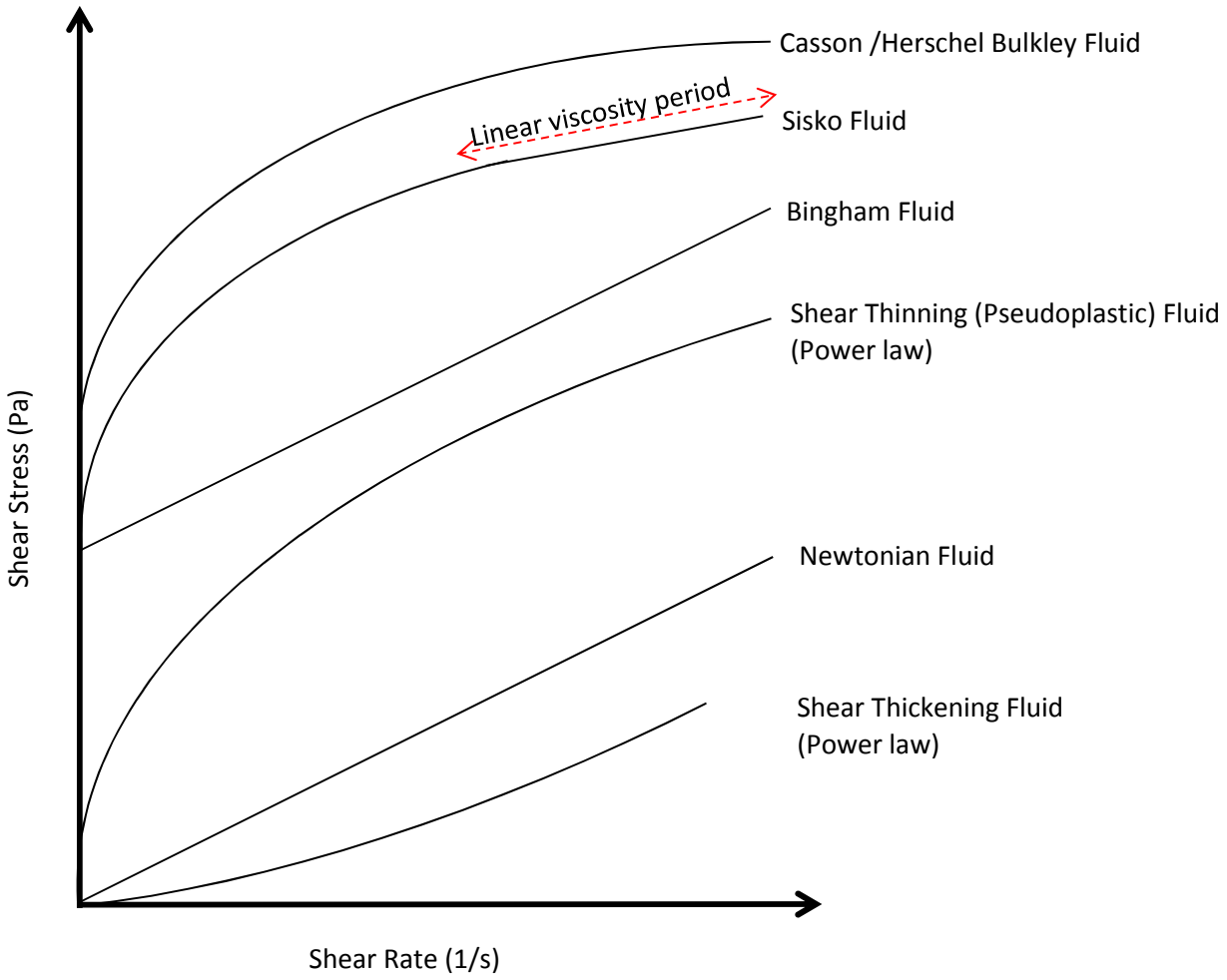

Figure 17 Common fluid type flow behavior

The material types shown in figure 17 are also indicated in figure 18 whereby viscosity is plotted against shear rate. In figure 18, the Sisko fluid is not indicated as it would more or less overlap the Casson/Herschel-Bulkley curve.

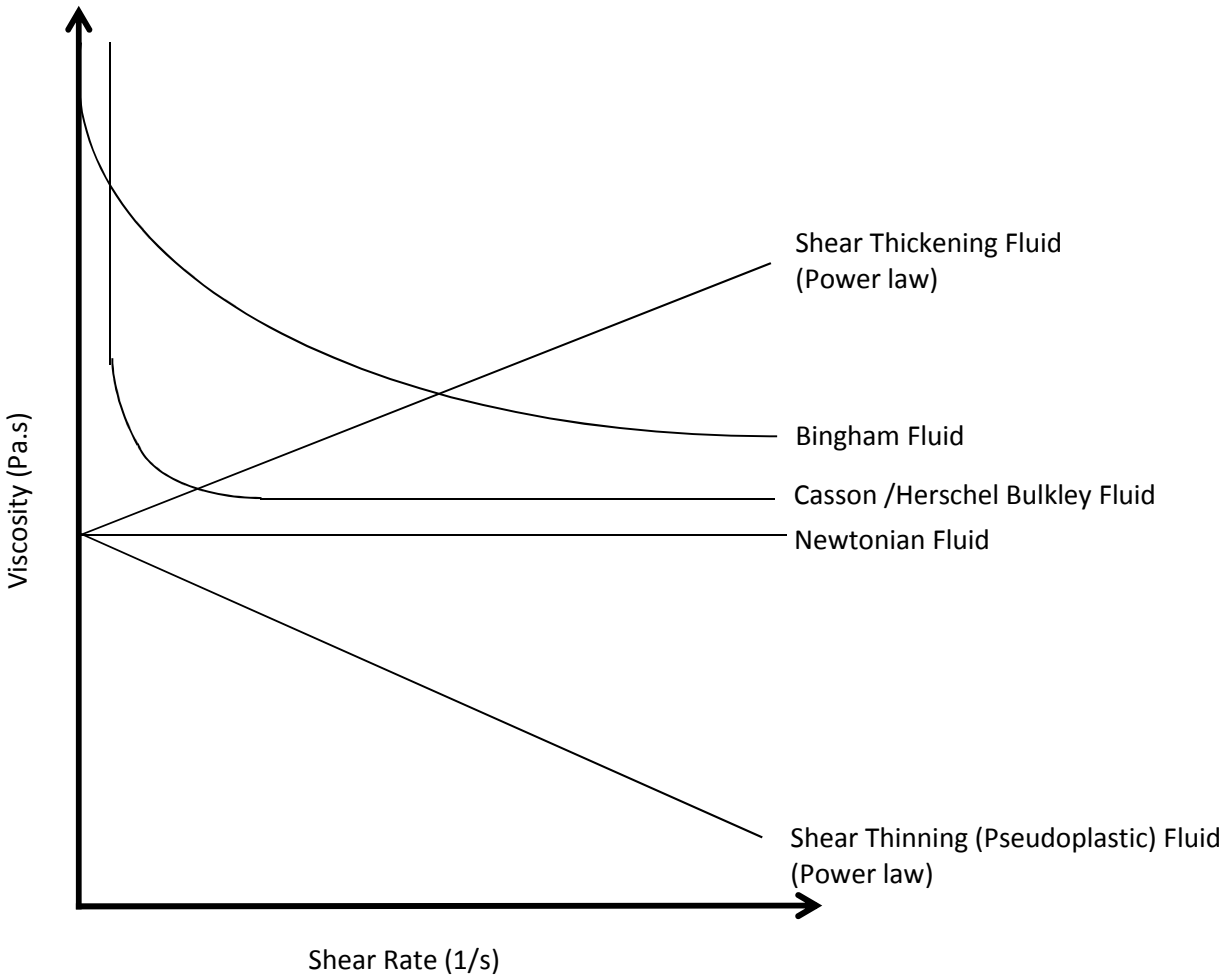

Figure 18 Common fluid type flow behaviour (viscosity)

Figure 18 shows shear thinning and shear thickening fluids, both of which are non-Newtonian and time dependent. Shear thinning is often described as thixotropy and relates to a decrease in viscosity under prolonged shear. Shear thinning occurs due to a break down in the structure of material under shear whereas shear thickening is often related to the building of structure within a material with increased shear. In the case of polymer solutions, shear thinning can be explained by the deformation of individual molecules. Under shear, macromolecules change their shape resulting in a decrease in their resistance to flow due to stream lining at higher rates of shear [96]. At lower shear rates, often the structure of a material is not broken down fully and the flow can be described by the sliding of thin molecular sized layers in between elements of a solid phase. The resistance to such sliding is high and consequently at low shear rates the viscosity is high [96]. Shear thinning can also be explained in terms of both agglomeration and particle shape. Agglomerates in a suspension contribute to shear thinning behaviour due to their ability to retain solvents (liquid phase). Once shear is applied, the agglomerates can break up, thus releasing the liquid phase which can reduce viscosity by dilution. With regards to

particle shape, asymmetric particles are randomly oriented at low rates of shear. When the shear rate is increased, however, the particles can align with one another which consequently reduce the resistance to flow and therefore the viscosity. Shear thickening materials are much less understood than shear thinning materials, due in part to a lack of industrial applications. Shear thickening (dilatancy) is often described as rheopecty or rheopexy which is a time dependent property of non-Newtonian fluids whereby viscosity increases under prolonged shear. Shear thickening is commonly found in highly concentrated dispersed suspensions. The most popular theories for the mechanism of shear thickening are based on the existence of a three dimensional network. The network exists between the particles and acts in resistance against flow. In polymer solutions, the three dimensional network consists of particles bridged by flexible polymer coils. Such suspensions are prone to shear thinning behaviour at low rates of shear due to a breakdown of floc structure and shear thickening at high rates of shear due to the existence of networks [97]. An example of a shear thickening suspension in action is trying to move to escape the grasp of quick sand. As shear is increased (increased movement), the quick sand becomes more viscous as the three dimensional network is more constrained. If movement is reduced, the three dimensional network is allowed to expand and thus relieve stress which allows material flow. Few industrial materials exhibit such behaviour as there is generally a requirement for shear thinning flow in some capacity. A large proportion of materials in practical applications exhibit Bingham flow. Bingham flow in a sense is shear thinning; only a critical stress has to be overcome before flow occurs (yield stress). Bingham flow is dependent on both solvent content and particle packing and as a general rule of thumb, a greater proportion of coarse, non-spherical particles results in a greater level of plastic deformation. The flow curves in figure 17 and 18 have been generated from the models given in equation 2-2 through to 2-10.

An early model for pseudoplasticity is the Cross model shown as equation 2-2. Cross states that a high degree of pseudoplasticity is undesirable for material flow, as there is an implication of poor flow at low rates of shear [98]. The Cross relationship is:

$$\frac{\eta_0 - \eta}{\eta - \eta_\infty} = (K\dot{\gamma})^m \qquad 2\text{-}2$$

where η_0 and η_∞ are very low and high shear rate viscosities. K is a constant with time, m is a dimensionless constant and $\dot{\gamma}$ is shear rate [84]. A common reduction of the Cross model is shown as equation 2-3. The reduction is possible with the assumption that $\eta \ll \eta_\infty$ and $\eta \gg \eta_0$ which is the case for many material's [95].

$$\eta = \frac{\eta_0}{(K\dot{\gamma})^m} \qquad 2\text{-}3$$

Equation 2-3 simplifies to the power law model shown in equation 2-4 [95].

$$\eta = K_2\dot{\gamma}^{n-1} \quad \text{2-4}$$

where n is the power law index and K_2 is the consistency, power law fluids are shear thinning with no yield stress. For the power law equation if $\eta \ll \eta_\infty$ it can be re-written in the form of the Sisko equation: [95].

$$\eta = \eta_\infty + K_2\dot{\gamma}^{n-1} \quad \text{2-5}$$

The Sisko model is used at higher shear rates, where the power law model fails as n approaches 1. With a zero power law index equation 2-5 simplifies to equation 2-6 [95].

$$\eta = \eta_\infty + \frac{K_2}{\dot{\gamma}} \quad \text{2-6}$$

Re-defining equation 2-6 leads to the Bingham model given in 2-7 [95].

$$\sigma = \sigma_y + \eta_p\dot{\gamma} \quad \text{2-7}$$

where σ_y is the yield stress and η_p is the plastic viscosity. The Bingham model represents flow in which the Bingham viscosity is constant after yield stress has been overcome. A similarly used alternative to the Cross model is the Carreau model shown by equation 2-8 [95].

$$\frac{\eta_0 - \eta}{\eta - \eta_\infty} = \frac{1}{(1 + (K_1\dot{\gamma})^{2^{m_1/2}}} \quad \text{2-8}$$

The Bingham model has been generalised to form the Herschel Bulkley model expressed in equation 2-10 which itself stems from the Casson model given in 2-9 when $\dot{\gamma} \geq 0$ [95].

$$\sqrt{\tau} = \sqrt{\tau_y} + \sqrt{K\,\dot{\gamma}} \quad \text{2-9}$$

$$\tau = \tau_y + K_H\dot{\gamma}^n \quad \text{2-10}$$

where τ shear stress, τ_y is yield stress, K is Casson viscosity and K_H is consistency, the Herschel Bulkley model represents materials that are shear thinning after overcoming yield stress. The Herschel Bulkley model is more often used for the characterisation in pastes to give paste parameters in a similar style to the model employed by Benbow and Bridgwater [48] (section 2.6.3). Modern controlled stress rheometers measure stress and shear strain rate and fit a suitable model (similar to

those represented by equation 2-2 through to equation 2-10) to the data measured using internal software in order to generate flow curves. The Herschel Bulkley model is similar to the Bingham model although above the yield stress, the model is no longer linear which is a behavioural attribute of many industrial materials [100].

2.5.2 Controlled Stress Rheometry

Controlled stress rheometers are used to measure a materials resistance to the torque applied by a rotating spindle. Geometries such as cone and plate, parallel plate, bob and cup and vane geometries exist. Torque or stress applied can be varied precisely and the materials resistance to that torque gives an indication as to how the material flows. Cone and plate geometries are commonly used and are suitable for applications presented in this work where the gap is pre-set based on the truncation. The cone tip is positioned to be just in contact with the base although it is removed by design to reduce errors caused by extra friction (Figure 19). Figure 20 shows the parallel plate type geometry.

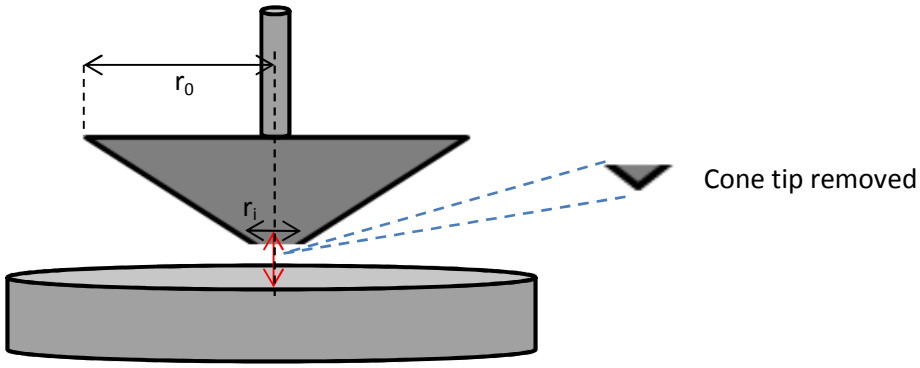

Figure 19 Controlled stress rheometer geometry gap pre-set by truncation

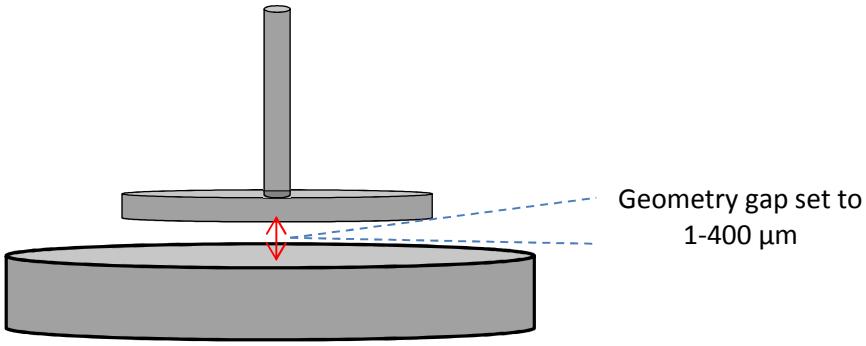

Figure 20 controlled stress rheometer, parallel plate geometry

Controlled stress rheometry measurements can be classed broadly as either static or dynamic. Static testing requires the application of stress in a series of step changes or ramps. In observing the response over time, material properties such as viscosity can be measured. Dynamic tests however

involve the application of a strain varying at a certain frequency in order to measure properties such as thixotropy [95]. Either static or dynamic measurements require careful selection of the correct geometry for which mathematical models have been developed. For parallel plate and cone and plate type geometries, equations are noted for evaluating the viscosity.

2.5.2.1 Parallel Plate

For torsional flow between parallel plates the shear rate at the rim (r=a) is given by :[95].

$$\dot{\gamma}_a = \frac{a\Omega}{h} \qquad 2\text{-}11$$

where Ω is rotational speed (s^{-1}), a is the geometry radius (m) and h is the gap size (m) [95]. The viscosity is given by:

$$\eta = \frac{3Ch}{2\pi a^4 \Omega}\left[1 + \frac{1}{3}\frac{d\ln C}{d\ln \Omega}\right] \qquad 2\text{-}12$$

where C is the couple on one of the plates measured above the material measured in Nm and corresponds to a pair of forces that are equal in magnitude but opposite in direction, thus giving a resultant moment but no resultant force. a is the radius of the geometry, Ω is rotational speed and h is the gap size [95]. For power law fluids 2-12 can be further modified to give: [95].

$$\eta = \frac{3Ch}{2\pi a^4 \Omega 1}\left[1 + \frac{n}{3}\right] \qquad 2\text{-}13$$

The rim shear rate is adjusted by changing the speed and the distance between the plates [95]. It is important to maintain the correct gap size, as for every 10 μm of error in axial separation, there is a 1% error in the value given for shear rate for geometries of 50 mm radius [95].

2.5.2.2 Cone and Plate

The shear rate for a cone and plate geometry is given by:

$$\gamma = \frac{r_o \Omega}{r_o - r_i} \qquad 2\text{-}14$$

where r_o is the outer radius, r_i is the inner radius (figure 19) and Ω is the angular velocity as before. The shear stress is given by: [95].

$$\sigma = \frac{C}{2\pi r_0^2 L} \qquad 2\text{-}15$$

From Equation 2-14 and 2-15 the viscosity can be calculated using 2-16 [23].

$$\eta = \frac{C(r_o - r_i)}{2\pi r_0^3 \Omega L} \qquad 2\text{-}16$$

where L is the effective immersed length of the fluid being sheared in between the geometry and the base plate [23]. It is the effective immersed length rather than the actual immersed length of fluid due to the existence of end effects. End effects occur due to different shearing conditions at the geometry edge. All of the geometries rotate against a fixed plate or cylinder which results in the shearing of material. The torque required to give a certain angular velocity gives a measure of the viscosity of the material. Cone and plate geometries are advantageous over parallel plate because the strain rate is independent of the position in the gap providing that the angle between the cone and plate is sufficiently small. This implies that elements of a sample have the same shear history which is important for time dependant behaviour [100]. The cone shape takes into account the change in shear rate with the radius of the plate that exits for the parallel plate type geometries. As there is an increase in tangential velocity with radius, for the applied shear rate to remain constant throughout the sample, the geometry height must also reduce [90]. If particles are present in the system to be measured then a cone and plate cannot be used. Particles would interfere with the small gap associated with cones and give misleading results although particles less than 5 µm in diameter are acceptable.

2.5.2.3 Oscillatory Rheometry and Visco-elastic Behaviour

Oscillatory measurements of binder systems can be used to describe the visco-elastic properties of a given sample. The complexity of many binder systems due to multiple components often results in non-Newtonian, shear thinning behaviour with an apparent yield stress. Oscillatory rheometry is a dynamic measurement in which the sample is subjected to a sinusoidally varying stress [101]. Oscillatory rheometry theory is derived from material behaviour within the linear viscoelastic region which is determined by the application of a strain sweep. A strain sweep is applied to the sample determining a ratio between Hookean and Newtonian behaviour (elastic and viscous). Elastic behaviour (Hookean solid) is defined by a materials ability to store energy whilst the Newtonian liquid or viscous component is defined by a loss modulus. The linear viscoelastic region (LVER) is a region in which both the storage and loss moduli are independent of strain. Running tests in the LVER ensures that the material microstructure has not been broken down. The elastic modulus *G'* is referred to as

the storage modulus whilst the viscous modulus G'' is referred to as the loss modulus. Figure 21 shows that in applying a sinusoidally varying stress to a material, information relating to its viscous and elastic components can be gathered by measuring the strain response [102].

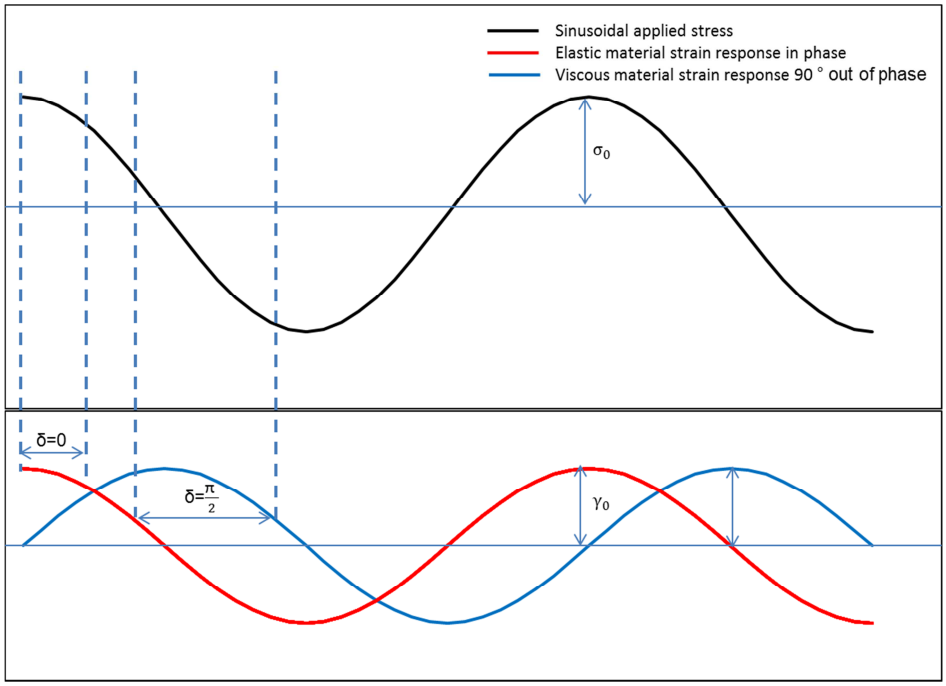

Figure 21 Strain response to oscillatory shear (in and out of phase)

From figure 21, the sinusoidally varying applied stress can be represented by equation 2-17:

$$\sigma = \sigma_0 \sin \omega t \qquad 2\text{-}17$$

Where σ_0 is peak stress, ω is angular frequency and t is time and consequently, the strain response is represented as:

$$\gamma = \gamma_0 \sin(\omega t + \delta) \qquad 2\text{-}18$$

Where γ_0 is peak strain and δ is the phase lag shown in figure 21. The viscous and elastic moduli can therefore be resolved by observing the phase angle δ and amplitude of the resultant strain response [88] using figure 22.

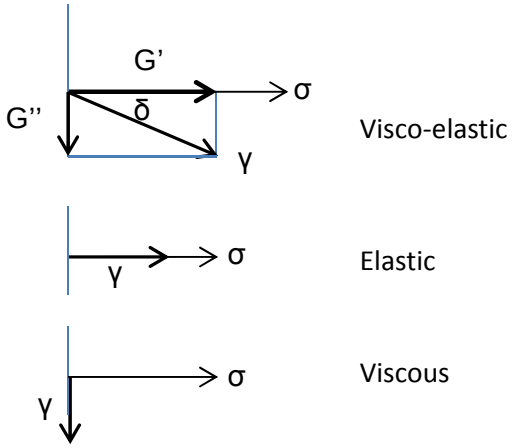

Figure 22 Resolving the viscous and elastic moduli

The complex modulus is the ratio of peak stress over peak strain (σ/γ) and can also be defined as equation 2-19 [103]. From figure 22, equation 2-22 can also be defined.

$$G^* = G' + iG'' \qquad 2\text{-}19$$

From figure 22, equations y and z can also be derived:

$$G' = G^* \cos\delta \qquad 2\text{-}20$$

$$G'' = G^* \sin\delta \qquad 2\text{-}21$$

$$tan\ \delta = \frac{G''}{G'} \qquad 2\text{-}22$$

where δ is the angular displacement or phase lag between the applied stress and strain response [101]. For Elastic materials, Hookean solids, the strain response is exactly in phase with the applied stress and $G'' \ll G'$ (figure 21) and the phase lag is zero. For Newtonian fluids however, $G'' \gg G'$ and the strain response is 90° out of phase with the applied stress and the phase lag is δ. Any material having a strain response between 0 and 90° out of phase with the applied stress is said to be visco-elastic. The dynamic viscosity can also be derived in a similar way, in complex form. Dynamic (or in this form complex) viscosity is a useful material parameter as it is analogous to shear viscosity [103].

$$\eta^* = \frac{G^*}{i\omega} \qquad 2\text{-}23$$

where ω is the applied angular oscillation and i is the imaginary part ($\sqrt{-1}$), imaginary only in a mathematical sense and is associated with the out of phase components of stress and strain rate [104]. 2-23 can be expressed in real terms as: [103].

$$\eta' = \frac{G''}{\omega} \qquad 2\text{-}24$$

Visco-elastic materials possess both viscous and elastic properties and hence have viscous and elastic moduli. In plotting *G'* and G'' against angular frequency the viscoelastic properties of a material can be observed. The work of Lin suggests that methyl cellulose variants have a decreasing complex viscosity with increasing frequency within the LVER indicating non-Newtonian behaviour and pseudoplasticity [105]. Similarly, ethyl cellulose is known to have a decreasing complex viscosity with increasing frequency at 150 °C and the same result holds when blended with various quantities and molecular weights of PEG [106]. Blends of ethyl cellulose prepared with PEG showed significant decreases in complex viscosity in this instance.

2.5.3 Capillary Rheometry

Capillary rheometry is a method of ram extrusion making it suited to analysing the processes in this work. It can be used to evaluate paste flow properties with methods such as those developed by Benbow and Bridgwater. In order to well define the Benbow and Bridgwater equations it is useful to consider the apparatus used for their practical work (Figure 23).

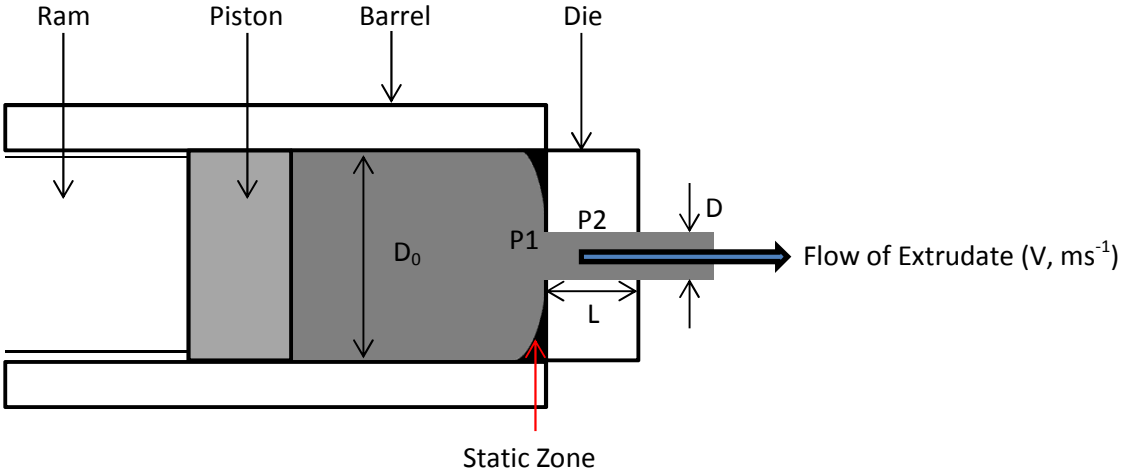

Figure 23 Configuration for Benbow Bridgwater experiments

Their work began from derivations used in metals extrusion such as equation 2-25. Equation 2-25 represents die entry pressure (ΔP1) and is only applicable for materials showing no change in ΔP1 with changes in velocity [93]**.** Equation 2-26 also represents die entry pressure (P1) and is derived from semi-empirical relationships.

$$\Delta P1 = \sigma \ln\left(\frac{A0}{A}\right) \quad 2\text{-}25$$

where ΔP1 is die entrance pressure drop (MPa), σ is the uniaxial yield stress (Pa), A0 is the barrel cross-sectional area (m^2) and A is the cross-sectional area of the die (m^2). Pressure data is obtained using a capillary die set and parameters are extrapolated to determine flow properties of a given material. Capillary rheometry can be carried out either using dedicated equipment, or by using a load frame in the correct configuration. Benbow and Bridgwater used capillary rheometry to obtain pressure data and extrusion parameters from equations 2-26 to 2-31:

$$\Delta P1 = (\sigma_0 + \alpha V)\ln\left(\frac{A0}{A}\right) \quad 2\text{-}26$$

$$\tau = \tau_0 + \beta V \quad 2\text{-}27$$

$$\Delta P2 = (\tau_0 + \beta V)L\left(\frac{C}{A}\right) \quad 2\text{-}28$$

where ΔP2 is die land pressure (Pa), σ_0 is bulk yield stress extrapolated to zero velocity (Pa), A0 is cross-sectional area of barrel (m^2), A is cross-sectional area of the die land (m^2), α is a velocity factor, V is paste velocity in the die (ms^{-1}), τ is shear stress (MPa), τ_0 is die wall shear stress (MPa), β is a factor indicating a change in wall shear stress with velocity, L is die land length (m) and C is the perimeter length of the die (m).

Knowing that the total pressure drop is equal to the sum of the pressure drop at the die entrance and the pressure drop across the die land, equation 2-29 can be generated.

$$\Delta P = (\sigma_0 + \alpha V)\ln\left(\frac{A0}{A}\right) + (\tau_0 + \beta V)L\left(\frac{C}{A}\right) \quad 2\text{-}29$$

There are limitations as with any predictive equation that is subsequently used for extrapolation. The limitation that has caused much controversy over the years tends to be the assumption of 100% wall slip. Due to this assumption the second term is often replaced by the Herschel Bulkley relationship to compensate. It is known, however, that the fluid phase shows a power law relationship whereby the velocity dependence is better represented by equation 2-30.

$$\Delta P = (\sigma_0 + \alpha V^m)\ln\left(\frac{A0}{A}\right) + (\tau_0 + \beta V^n)L\left(\frac{C}{A}\right) \quad 2\text{-}30$$

Equation 2-26 is often re-written for systems with a circular die to give 2-31.

$$\Delta P = 2(\sigma_0 + \alpha V^m)\ln\left(\frac{D0}{D}\right) + 4(\tau_0 + \beta V^n)\left(\frac{L}{D}\right) \quad 2\text{-}31$$

The work of Martin [93] and Zheng et al. [107] has shown that extrusion pressure is not only dependent on extrudate velocity. Zheng et al. used numerical simulations of paste extrusion to show that extrusion pressure is dependent on the ratio of extrudate velocity to die diameter. Nevertheless pastes can still be modelled and characterised using the Benbow and Bridgwater approach for design applications in an industrial environment in order to make predictions of paste flow. Using a load frame, the force required to push or extrude material through a die can be obtained. The extrusion is carried out over at least three different length dies typically over five ram speeds; the extrudate speed is then calculated from this using the ram area and extrudate area. Using this extrudate speed with the length/diameter properties for each die, extrudate pressures can be extrapolated for a length/diameter ratio equal to zero. This eliminates the pressure in the die land which can be re-evaluated once other terms are determined. The Benbow Bridgwater experiment has been used by many to evaluate the pressure drop during extrusion for hard metal pastes [55]. The technique has been used to analyse flow with changes in temperature for a hard metal paste formed with an alcohol binder with dissolved biopolymer. With increased temperature, the Benbow Bridgwater parameters decreased, as expected with a thermo-softening extrusion binder [55]. When using dedicated capillary rheometry equipment as described in section 3.7 it is necessary to correct the data as a result of die entrance effects. In capillary rheometry, there is an extra pressure drop associated with the contraction flow at the capillary entrance [107]. The extra pressure drop is caused by the stretching of fluid elements in the formulation and such effects are decreased with increasing L/D ratios. However, longer dies also impart other more significant errors due to viscous heating which reduces paste viscosity and therefore large L/D ratio capillaries should be avoided. Die entrance effects are corrected by the Bagley correction. The shear stress at the wall is given by:

$$\tau_\omega = \frac{(\Delta P - \Delta P_0)D}{4L} \quad 2\text{-}32$$

where ΔP is total pressure drop, ΔP_0 is die entrance pressure drop, D is die diameter and L is the die length. By extruding material over a range of velocities and die lengths at fixed die diameter, the pressure at L/D = zero can be calculated. This is a useful parameter because it removes the pressure drop effect caused by the stretching of fluids. Such pressure drop effects can be large as shown in chapter 5 in this work due to a relatively high paste fluid content and therefore need to be accounted for. If the entrance effects are not accounted for then pressure measurements can be inaccurate. Similar procedures can be used with similar results such as extrusion through an orifice die. An orifice

effectively has no die land and Hatzikiriakos et al concluded that using the Bagley correction and an orifice die method yielded comparable results [108]. The Bagley correction process is also effectively carried out for the Benbow Bridgwater analysis described in 2.5.3. Figure 24 shows how ΔP_0 is obtained and each blue marker represents dies of 4 mm diameter and length 4 mm, 16 mm and 24 mm [110].

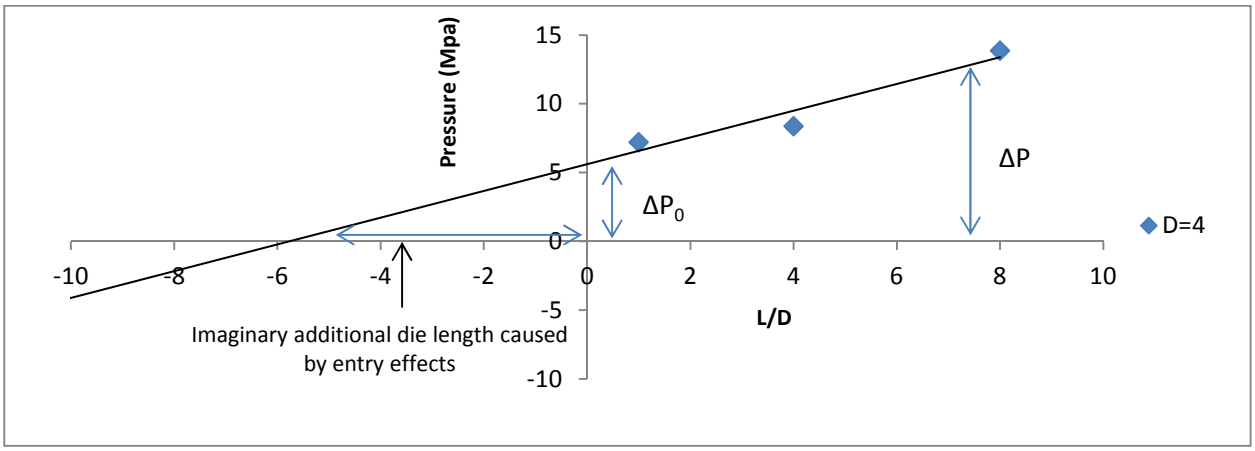

Figure 24 Obtaining ΔP_0 for use in Bagley correction

Alternatively, a twin barrel system is often used in which a paste is extruded simultaneously through a long and short die. The pressure is measured near to the die entry point in each barrel allowing for extrapolation back to P_0. This is the same procedure as used to generate figure 24 although requires only one extrusion run and is therefore a more efficient way to obtain the pressure at zero die length. However for the purposes of quality control as long as extrusion tests are repeated accurately the Bagley correction is not necessary as pressure data will be comparable if not correct.

In order to obtain the actual dough viscosity, a shear rate at the wall can be calculated using the Rabinowitsch-Mooney correction given by: [110].

$$\dot{\gamma}_w = \left(\frac{3n' + 1}{4n'}\right)\frac{8\bar{V}}{D} \qquad 2\text{-}33$$

where n is the slope of ln(τ) verses ln($\dot{\gamma}$ app), and V is bulk velocity determined from volumetric flow-rate. The true viscosity of feedstocks can then be calculated based on die entrance corrections using:

$$\mu = \frac{\tau_w}{\dot{\gamma}_w} \qquad 2\text{-}34$$

2.6 Drying

There are many types of drying that can be applied to WC-Co extrudate, particularly when polar binder systems are used. Principally, drying is the removal of low molecular weight components from the extruded part before de-binding of other higher molecular weight components can begin. In most cases, heat is transferred to the wet surface of the solid and through to the interior, giving a temperature gradient. However, in more elaborate processes such as di-electric, radio frequency or microwave freeze drying, energy is supplied to generate heat internally and then flow outwards towards the surface [114].

2.6.1 Thermal Drying

Thermal drying is a precursory step to de-binding and sintering used at Sandvik Hard Materials. It is the most basic and well defined form of drying and utilises the application of uniform temperature distribution to drive low molecular weight components out of extruded parts. The stages of drying are defined as the initial condition, the constant rate period (CRP) and the falling rate period. The majority of shrinkage occurs in the CRP and consequently this is where stresses are at their highest [111]. In the CRP the rate of evaporation per unit area of the drying surface is independent of time. At the end of the CRP shrinkage has virtually stopped and the falling rate period begins. Parts drying in the constant rate period are in the funicular state where the binder materials are continuously flowing liquids. In the falling rate period, the rate of evaporation decreases and the surface temperature increases above the wet bulb temperature. However, most evaporation still occurs at the exterior surface and therefore the surface remains below ambient temperature [111]. Liquid is now only removed by diffusion of its vapour where evaporation occurs inside the body and this is known as the pendular state (isolated pockets of liquid) [112]. Tension in the liquid is greatest near the surface of the part resulting in greater stresses at this point which is often where drying cracks are initially formed. Due to stresses being greater at the surface, differential shrinkage occurs causing cracking. The probability of cracking due to drying processes is linked to the size of the part, the rate of evaporation and the strength of the network formed in the body by the binder system. During both the drying and de-binding processes, liquid is forced through a porous body in response to a pressure gradient [111]. The pressure gradient causes deformation of the part and expansion of pores allowing the liquid to be transported. Drying of extrudates removes low molecular weight components from the product. Drying is a slow and delicate process carried out in drying ovens designed as a precursor to de-binding which is carried out in the sintering furnace. In many extruded or injection moulded parts binder materials can be categorised as major and minor binders. The minor binder is used to form passages to allow for the removal of the major binder at higher temperatures [113]. Minor binders have high melt viscosities whilst major binders have low melt viscosities. Other methods of extrudate drying

such as microwave and di-electric drying involve significantly different theories and procedures to thermal drying (section 2.6.2).

2.6.2 Microwave and Di-electric Drying

Microwave and Di-electric terminology are often confused with one another as the processes are very similar and essentially the heating mechanisms are the same. However, microwave heating occurs in the range of 300 MHz to 300 GHz whereas di-electric heating occurs at a lower frequency range of 1-100 MHz. Microwaves and di-electrics are not forms of heat, but are forms of energy that manifests itself as heat via interactions with the material. The primary mechanisms of energy conversion used in microwave and di-electric drying are ionic conduction and dipole rotation [114].

2.6.2.1 Ionic Conduction

Due to the fact that ions carry charge, they are accelerated in the application of an electric field. As the ions move they are caused to collide with un-ionised molecules and therefore give up kinetic energy. Subsequently, this causes the un-ionised molecules to accelerate and collide with other un-ioinized molecules which has a knock on effect [114]. Changing the polarity, by opposing the electric field causes movement of the charged ions in the opposite direction. As this can happen at millions of times per second, the number of collisions of ions and un-ionised molecules is large giving in turn, a large transfer of energy and therefore heat. In summary, there are two clear stages.

1. The application of an electric field to the material in question.
2. The conversion of electric field energy into kinetic energy which then is manifested as heat energy.

2.6.2.2 Dipolar Rotation

Many molecules such as water are dipolar in nature and normally have a disorientated random structure. The application of an electric field attempts to align polar molecules in the direction of the electric field. As the electric field is applied and decayed, the alignment of the dipole is reduced to its random state. The rapid application and decay of the electric field (millions of times per second) causes rapid alignment and randomisation of the dipole which imparts energy into the material which can then again manifest itself as heat. Similarly to ionic conduction, electric field energy is converted to stored potential energy and then random kinetic or thermal energy in the material. The advantages and disadvantages of the discussed drying types are summarised in table 4:

Table 4 Advantages and disadvantages of drying techniques

Process	Advantages	Disadvantages
Microwave and di-electric drying	Can be rapid If required due to bulk heating	Not suitable for many materials
	Uniform heating, avoiding large temperature gradients	Cost
	Efficiency of energy conversion	Scorching of products
	Small floor space requirement	
Thermal Drying	Cost	Inefficient
	Simplicity	Large floor space requirement
	Easy of control	Slow for large cross-section parts
	Suitable for vast majority of products	

2.7 De-Binding

During de-binding, extrusion aids such as organic binders are removed from the bulk material. De-binding has been described as the process in which the volume occupied by the binder system gradually becomes the pore network [115]. Often de-binding is referred to as de-waxing because paraffin wax is a common organic binder material. Thermal de-binding is commonly employed due to cost and simplicity. However, when extruding at increased diameters thermal de-binding can be too time consuming, but a shorter de-binding cycle may result in product rupture. Alternative methods include solvent de-binding and catalytic de-binding and combinations of the two. De-binding processes are used in other formulation techniques such as injection moulding and pressing, both of which require organic binder removal before sintering. De-binding is measured as a mass percentage of binder removed as in Figure 25.

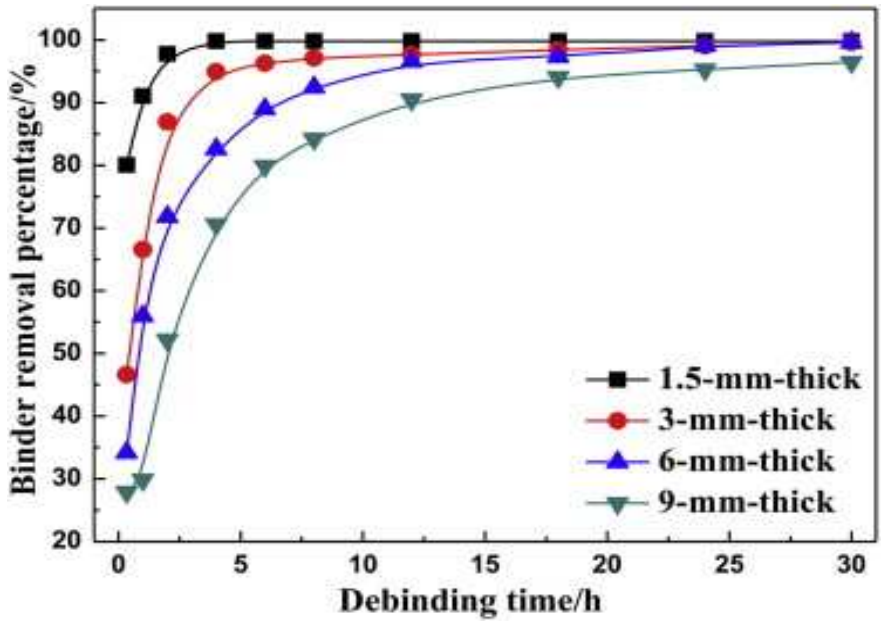

Figure 25 De-binding curve for injection moulded parts at 60 °C [117]

Figure 25 shows that initial rates of binder removal are rapid followed by a decrease in rate and a plateau nearing 100% binder removal. In the initial stages of figure 25, mass transport occurs by diffusion as binder liquid and gas flow cannot occur at lower temperatures. Low molecular weight components diffuse through the high molecular weight components to the surface meaning that the initial stage is limited by diffusion. The initial rapid rise of figure 25 can be explained by Fick's law of diffusion, which states that flow (in this case binder removal) is proportional to the concentration gradient.

$$J = -D_e\left(\frac{\delta M}{\delta x}\right) \qquad 2\text{-}35$$

where J is the diffusion flux ($molm^{-2}s^{-1}$) which is a measure of how much material will flow through a given area, D_e is the diffusion coefficient (m^2s^{-1}) and x is length (m). Initially, as the concentration gradient is very high, the removal rate or flow of material is rapid. As the concentration gradient reduces with material removal from the part (by diffusion), the rate of removal also decreases which is explained by Fick's second law.

$$\frac{\delta C}{\delta t} = D_e\left(\frac{\delta^2 C}{\delta x^2}\right) \qquad 2\text{-}36$$

where C is concentration, and t is time, it is shown that diffusion causes the concentration gradient to change with time [118].The diffusion of the low molecular weight components opens up porosity in

the compact. Porosity allows the molten binders to then flow through the part to the surface at higher temperatures, allowing degradation and subsequent vaporisation of the remaining binder. During the later stages of figure 25, the binder removal rate is limited by both convection of and diffusion of vapour. Flatter curves for thicker parts indicate that binder removal rates are slower for higher binder volumes. Chen et al. [117] also showed that the total mass of binder removed is lower for thicker parts in an equivalent de-binding time. Models for de-binding have been developed to predict de-binding time in relation to sample thickness. Cima and Calvert have derived two cases of binder burnout. Case one involves the retreating of a sharp interface into the green body as polymer (binder) is removed. Case two however, involves the formation of fine porosity which permeates the green body allowing for gas phase diffusion [116]. The two cases are known as series and parallel models respectively and were developed experimentally. The polymeric binder used in the study was poly(methyl methacrylate) (PMMA). Models developed were based on large flat sheets of green ceramic bodies. The steady state burnout model first developed considered a sheet of ceramic and binder of thickness twice the sample length. PMMA decomposed to create Methyl methacrylate (MMA) which was gas at the burnout temperature and soluble in the polymer. Assuming that no porosity was developed (series model) and that MMA was produced at a rate of R, g/mL.s and diffused at a rate of D (cm^{2-s}) then the concentration at some distance x from the centreline (x=0) was given by:

$$C = \left(\frac{R}{2D}\right)(l^2 - x^2) + C_i \qquad 2\text{-}37$$

which stems from Cranks planar solution to Fick's second law, where $C_i$is the concentration of monomer in the liquid at the surface. Equation 2-35 is based on steady state Fickian diffusion from a constant source that is uniformly distributed within the thickness of the ceramic. This equation allowed for the calculation of burnout concentration based on the type of reaction rate, first order for example. This assumed that no bubbling was taking place, whereas the parallel model takes porosity into account as diffusivity of the binder increases with fractional porosity thus affecting the burnout rate. The early formation of porosity needs to be considered in the development of burnout models because it allows a path for rapid gas phase diffusion and hence the burnout time is reduced. The parallel model developed by Cima and Calvert describes two parallel diffusion paths for the monomer to follow, as liquid through the solid and as vapour through the voids developed as porosity [116]. The parallel model is given as:

$$D = D_l(1 - v) + D_g vK \qquad 2\text{-}38$$

where D is the diffusivity of the whole medium, v is the volume fraction of porosity, $D_l$and $D_g$are the diffusion coefficients of monomer in liquid and gas and K is the gas/liquid partition coefficient. K is a measure of how much of the monomer is liquid or gas, if K is 1 then the monomer is 100% gas and if K is 0 the monomer is 100% liquid. The diffusivity was related to volume fraction of polymer and particles for which the polymer volume fraction was assumed to be 0.35. Conclusions drawn from their work suggested that samples greater than 3 mm in thickness required several days of drying and de-binding combined. It was also concluded that de-binding can be vastly improved by the early development of porosity [116].

2.7.1 Vacuum De-binding

Vacuum de-binding was the first process to allow the de-binding and sintering of hard-metals in one furnace [119]. The vacuum is used to lower the vapour pressure of binders, enabling lower temperatures to be used. [119]. Kennedy observed that de-binding at lower pressures increased the binder removal rate (Figure 26) [120]. His work focussed on removing paraffin wax from metal injection moulded parts in a combined de-binding and sintering process (Figure 27). The majority of the cycle was carried out below atmospheric pressure (750 torr).

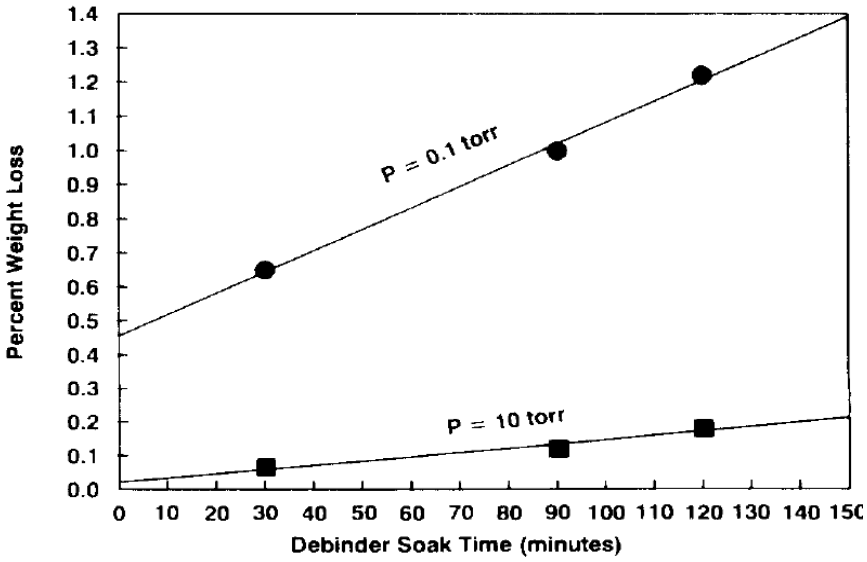

Figure 26 Pressure influence on extrusion binder removal rate [120]

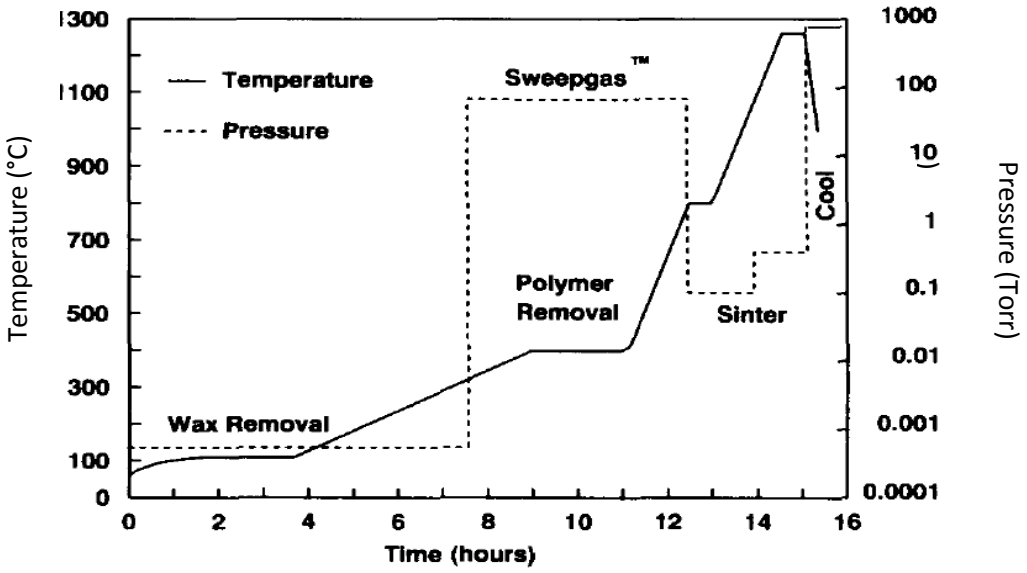

Figure 27 Typical vacuum de-bind and sinter cycle for extruded parts [120]

Pressure was always kept below the vapour pressure of the paraffin wax allowing for the diffusing wax to move freely through the porous matrix and through the surface of the part to be collected by the sweep gas [120]. A disadvantage of de-waxing in vacuum is that the wax can eventually infiltrate furnace linings which can again cause cracking and caking. Removal of the de-bound wax was aided by using an inert carrier gas (sweep gas)[119]. Due to the added gas load less vacuum can be used, making the process longer, but overall quicker due to shorter cleaning times [119]. Sweep gas technology also helps to prolong the life of the hot zone due to less wax build up. More care has to be taken with the removal of lubricants from WC in a positive pressure environment because carbon content has to be controlled. Thermal de-binding is the most attractive option for the mass production of products provided that the correct carbon content can be achieved. This is because of an ability to handle large furnace loads with simple operation [121]. In a WC compact it is known that carbon leaves in the form of methane as a result of the reaction between hydrogen in the furnace atmosphere and carbon in the component [121]. It can also leave in the form of carbon dioxide due to the carbothermic reduction of tungsten oxides with a small amount leaving as carbon monoxide [121]. From Figure 27 it can also be seen that there are two clear stages in vacuum de-binding, wax removal and polymer removal. This is true in most thermal de-binding processes as reported by Shengjie et al. [122]. In the first stage of thermal de-binding porosity is not opened up meaning that binder and liquid gas flow cannot occur. Mass transport therefore occurs by diffusion of low molecular weight components through the high molecular weight components to the surface. The high molecular weight components are in a melted state during this stage. If degradation products of the melt stage high molecular weight components have a higher than ambient vapour pressure then a bubble can form and grow. This is often where defects are formed and why solvent de-binding is preferred over the first thermal de-binding stage in many cases [122]. Defect formation from bubble growth can be

reduced by increasing the de-bind time for this initial stage. The second stage of thermal de-binding is the removal of high molecular weight components or residual polymers. As porosity has been opened up by this stage by removal of the low molecular weight components, mass transport is not via diffusion alone. Shengjie [122] found that in the second stage of thermal de-binding that three main processes occurred. The first process was liquid polymer travelling from the internal surface to the exterior surface. The second process was the degradation of the polymer to vapour, which then flowed from the internal surface to the exterior surface via convection and diffusion. The vapour could then be carried away by the flow of a sweep gas. The third process was the flow of vapour that had dissolved in the liquid polymer from the internal to outer surface. Thermal de-binding is versatile and as a result, PEG, wax and cellulose based binder systems can all be removed in similar processes providing that atmospheres can be controlled. In the case of methyl cellulose based binder systems, a thermo-reversible gelation is witnessed at 40-70 °C whereby the binder stiffens and green strength increases forming a hard clear film [45].

2.7.2 Solvent De-binding

Solvent de-binding is advantageous in systems with major and minor binders due to the high solubility of low molecular weight components in the major binder [58]. Extracting binder components creates porosity in the green component. This allows the minor binder components to diffuse through to the surface. As a result of the extraction and diffusion, thermal removal of the insoluble binder components can occur more quickly without damaging the sample structure. Solvent de-binding often involves solvent evaporation-condensation, solvent immersion and supercritical extraction [69]. Where paraffin wax was used, the rate controlling step in these processes was found to be the diffusion of paraffin wax. Following solvent de-binding, vacuum drying is necessary to evaporate the remaining solvent so that a constant weight sample can be obtained [69]. In the solvent de-binding of PEG, water is the solvent and diffuses into the PEG binder causing dissolution of the PEG. Hydrated PEG then diffuses out of the part through a network of pores. PEG removal is initially quick given that diffusion distances are small and slows towards the end of PEG removal [123]. Water solvent de-binding cannot be used in the case of methyl cellulose binders because they are insoluble in water. In many cases thermal de-binding is employed to remove what is left of the PEG after diffusion has ceased. A summary of the main thermal de-binding processes are given in Table 53, and Table 55 in Appendix C.

2.8 Sintering

Sintering is a densification process under the application of high temperatures with or without the application of external pressure [124].

Particulates are formed into a coherent body over three common stages:

1. Particle rearrangement
2. Liquid phase sintering
3. Grain Growth

Strength is gained in sintering through lower temperature inter-particle bonding represented by neck growth and densification at higher temperatures [125]. Thermal softening can reduce the compact's strength at higher temperatures. Strength during the process is therefore determined by a combination of the three effects [125]. At the sintering stage, all of the organic materials used in processing have been removed in the drying and de-binding stages. For PEG bound WC-Co, the initial stages of de-binding occur over 250-600 °C under vacuum heating in a hydrogen atmosphere. During vacuum heating, oxide reduction occurs and solid state sintering begins at approximately 1250 °C. This allows for partial pore closure and grain growth in the WC agglomerate. Oxides of tungsten, titanium and chromium are reduced during vacuum heating. Such oxides are introduced from the raw materials, milling processes and the aging of raw powder. Liquid state sintering begins at 1350 °C as the cobalt binder melts. Further growth of WC grains occurs and the cobalt binder re-distributes itself. Pore closure also occurs at this stage as the process is under pressure (sinter HIP). Extruded products are sintered in a sinter HIP (hot isostatic press) furnace in order to remove porosity left behind by organic binder removal. If there is a natural resistance to high temperatures by a material then it can be difficult to achieve full density without the application of an external pressure. Ordinarily, the driving force for sintering comes from the surface energy associated with small particles. An external pressure increases the driving force which allows for faster densification rates. A sintering stress acts on particles, effectively pulling them together during the sintering process. The application of an external pressure supplements this stress and encourages the pulling of particles together further. In the early stages of sintering, such a stress is amplified at the particle contacts, which enhances the internal sintering stress [126]. When the pressure is applied, particles flatten at the contacts which can give vast improvements in densification due to plastic flow. Plastic flow occurs because the small particle contacts amplify the applied stress beyond the yield stress of the material. High pressures are required at low temperatures to encourage plastic flow because yield stresses are generally very high. The external pressure also serves to reduce residual porosity, thus improving densification further still. Pressed parts do not require the sinter HIP process as there is less organic binder present. As well as removing porosity, cobalt lakes are also less common. Cobalt lakes are regions of cobalt greater than 10 μm depending on tolerances. Generally cobalt can be squeezed into a macro pore during liquid state sintering. There is also the risk that pores can be hidden in the form of cobalt lakes. If a pore in the microstructure is large enough, cobalt can be squeezed into the pore during the sinter HIP process.

The advantages and disadvantages of sinter HIP processing compared to vacuum sintering are shown in Table 5.

Table 5 Sinter HIP advantages and disadvantages

Advantages	Disadvantages
Removes majority of pores	Can mask defects as cobalt formation
Reduces defect formation	High running costs
Fewer cobalt lakes	High equipment costs
	High maintenance costs

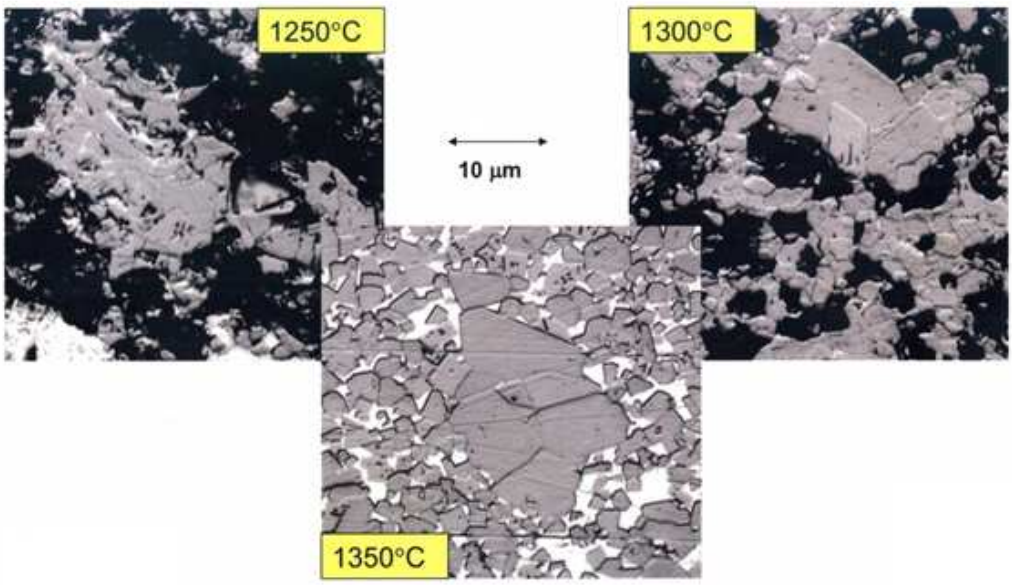

Figure 28 Solid state sintering of WC-Co

Interrupted sintering cycles have been run at SHM in order to determine the grain growth during solid and liquid state sintering. Optical micrographs of the stages were generated and are shown in Figure 28 (solid state) and Figure 29 (liquid state) In Figure 28 the cobalt is shown as black up to 1300°C as it has not yet melted. At temperatures greater than 1300 °C the cobalt appears lighter than the WC grains as it is more reflective. Figure 29 therefore indicates that at 1350 °C the cobalt is entirely in the liquid state.

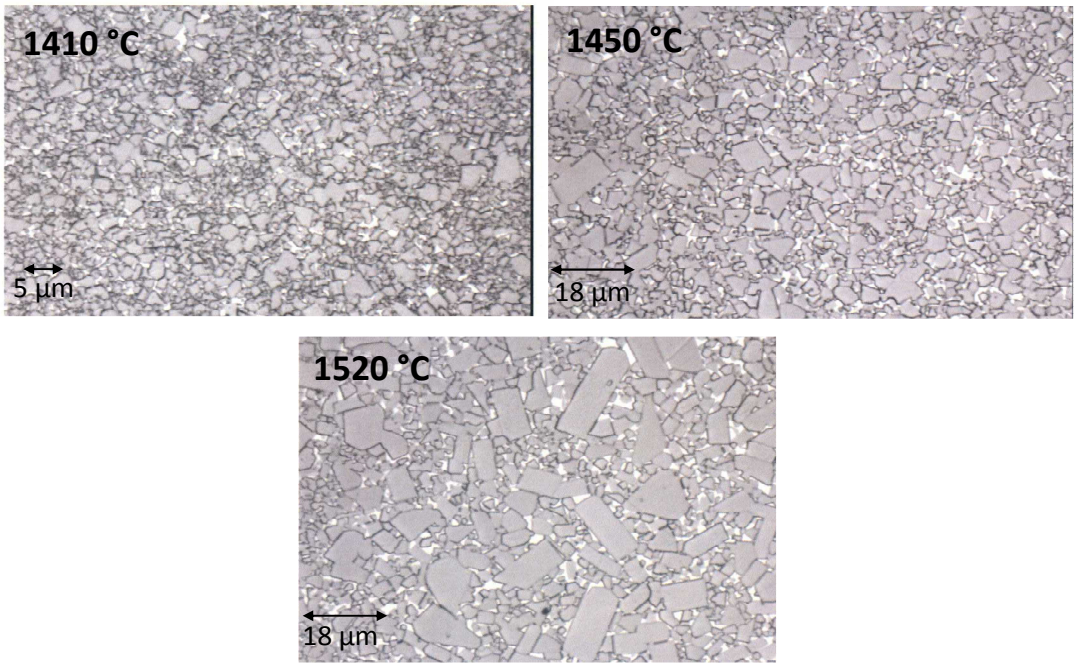

Figure 29 Liquid state sintering of WC-Co

The liquid state sintering stages shown in Figure 29 indicate grain growth with increased temperature. Cobalt binder re-distribution has also been evaluated using the interrupted sintering technique and is shown in Figure 30. Figure 30 shows that cobalt is more evenly distributed with increased temperature as it can surround the WC grains more easily and uniformly. An even cobalt distribution is also encouraged by grain boundary infiltration which breaks up WC agglomerates.

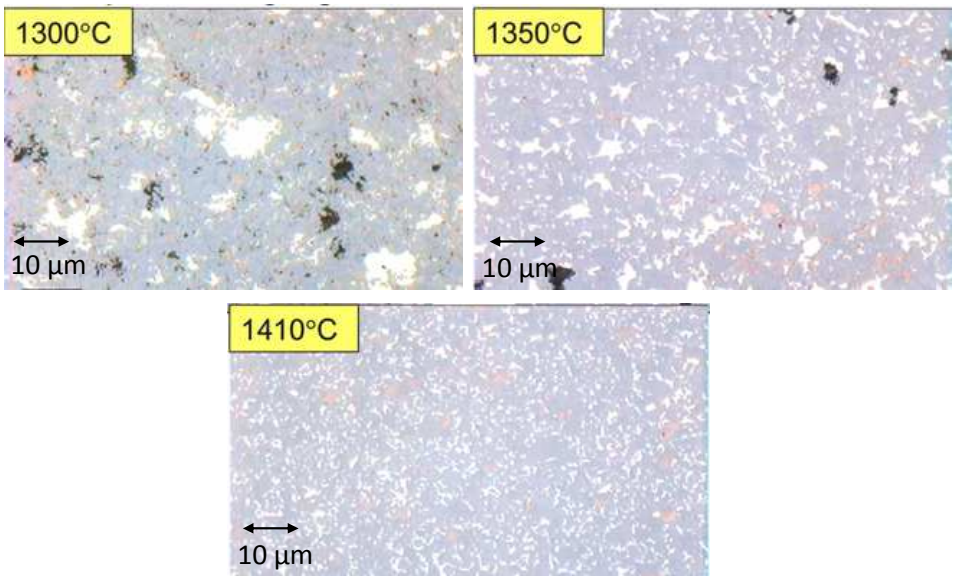

Figure 30 Cobalt binder re-distribution during sintering

Solid and liquid state sintering is described in sections 2.8.1 and 2.8.2 respectively although new compaction techniques for sintering have also been developed. Such techniques include high

temperature induction heating [127], ultra high pressure rapid hot consolidation, microwave sintering [128] and spark plasma sintering [129]. The sinter HIP process is used by SHM on all extruded carbide products. There are several stages in the sinter HIP process, de-binding, detailed in section 2.7 is followed by vacuum heating, solid state sintering and liquid state sintering. The principle driving force for the sinter reaction is a minimisation of surface energy in order to achieve a minima in total free enthalpy. In the early stages of sinter HIP processes (solid state) a change of pore shape with little change in pore volume occurs due to a reduction of surface energy [124].

2.8.1 Solid State Sintering

During the sinter HIP process for WC-Co products solid state sintering is carried out at lower temperatures after de-binding (700 - 900 °C) and before liquid state sintering. Liquid state sintering begins beyond 1300 °C [130]. In some cases solid state sintering is used as a pre-sintering method to avoid the use of an external collapsible can. In other cases, a collapsible can surrounds the product to provide strength for the next stages of sintering. [131]. During solid state sintering there are three critical stages known as the initial stage, the intermediate stage and the final stage [131].

2.8.1.1 Initial Stage of Solid State Sintering

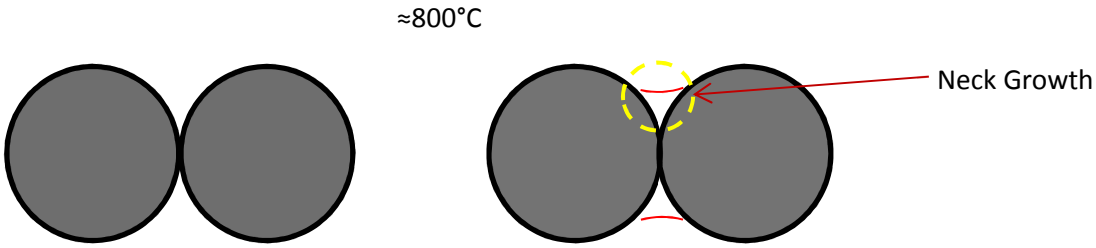

Figure 31a Onset of initial stage **Figure 31b End of initial stage**

The initial stage consists of rapid inter-particle neck growth caused by diffusion, vapour transport and plastic flow [131]. The neck growth at the onset and end of the initial stage is represented by Figure 31 a and b showing inter-particle bonding at lower temperatures of solid state sintering. Once the pores in between particles have reached an equilibrium shape based on surface tension, the intermediate stage of solid state sintering begins.

2.8.1.2 Intermediate Stage of Solid State Sintering

Grain boundaries dictate the equilibrium shape of the pores because forces are balanced at the point whereby the pore surfaces are surrounded by grain boundaries [131]. The forces are represented by the tension in the interface (solid-vapour) and the tension in the grain boundary. Densification occurs

in the intermediate stage as a result of pore size reduction leading to the breaking away of pores into isolation, leading to the final stage.

2.8.1.3 Final Stage of Solid State Sintering

An indication of the final stage of solid state sintering is once the pores have broken off and become isolated at the grain corners. The pores continue to shrink and in some case are removed completely, giving rise to a relative density of ≈0.9 or greater. Typically densities range from 0.65-0.9 through the stages of solid state sintering [131].

2.8.2 Liquid State Sintering

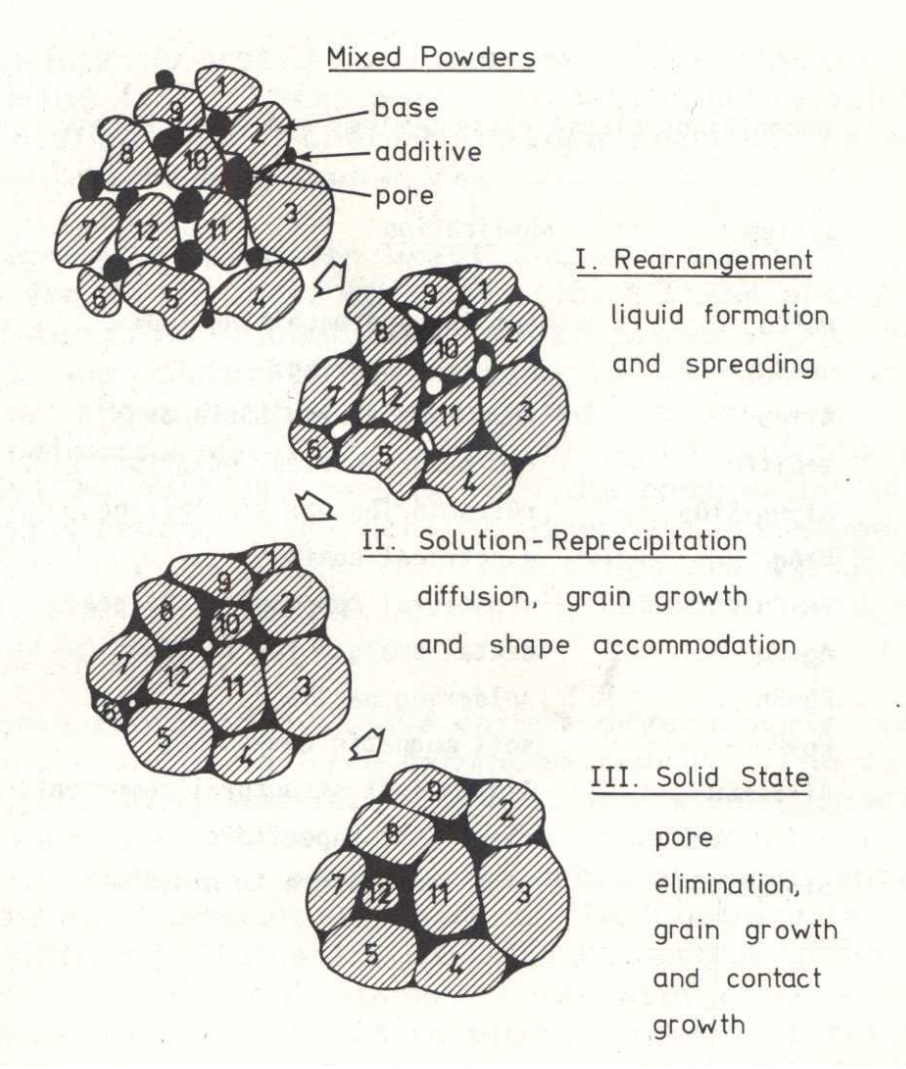

Figure 32 Stages of liquid state sintering [132]

The stages of liquid state sintering are illustrated in Figure 32. For WC-Co, the base and additive are WC and cobalt respectively. In liquid state sintering of WC-Co, liquid metal cobalt wets out and has solubility for the WC at higher temperatures. Due to solubility, cobalt eliminates any porosity that may remain following the solid state sintering whilst interfacial energy is reduced [132]. The classic stages

include rearrangement; solution-reprecipitation and solid state controlled sintering. Although termed solid state sintering, the latter stages of the liquid state sintering process involve the formation of a solid skeleton rather than solid grains. Rearrangement occurs as liquid cobalt is formed at temperatures above 1100 °C [133]. Further increases in temperature lead to the solution-precipitation stage in which diffusion, grain growth and shape accommodation occur [132]. Microstructural coarsening occurs in this stage of liquid state sintering due to grain size distribution. Smaller or finer WC grains have a greater surface area and thus dissolve more quickly in the surrounding cobalt than the larger grains giving a concentration gradient in the liquid cobalt [12]. The existing concentration gradient is the driving force for diffusion to occur and hence material transportation exists and is termed coarsening or Ostwald ripening [132]. Ostwald ripening causes progressive growth of larger grains in the solution-reprecipitation stage contributing to fewer grains, grain coarsening and densification [132]. The driving force for densification is the reduction of the liquid-vapour interfacial area [131]. A reduction in interfacial area is caused by the dissolution of sharp edges giving smoother particle surfaces aiding rearrangement [131]. Grain shape accommodation also occurs due to diffusion, eliminating porosity as the grain surfaces become flatter so grains can be closer to one another. Grain shape is determined by the interfacial energies between the solid and liquid. The final stage of liquid state sintering (solid state controlled sintering) is where pore elimination, grain growth and contact growth occur [132]. In the final stage, a solid skeleton is formed inhibiting rearrangement. Pore changes can occur in this stage if the pores contain gas which subsequently expands causing swelling. Grain contacts, however, can encourage solid state sintering and longer final stages can cause material deterioration in liquid phase sintering [132]. The liquid state sintering stage in the sinter HIP is carried out under gas pressure to remove unwanted pores. In processes other than extrusion such as pressing, pressure in sintering is not always needed as pore formation in the product is not common. However, low cobalt content or coarse grained powders require sinter HIP due to a low sintering activity. To give an indication of liquid state sintering, an optical micrograph of liquid phase sintered WC-Co is shown in Figure 33. The WC-Co was sintered in hydrogen.

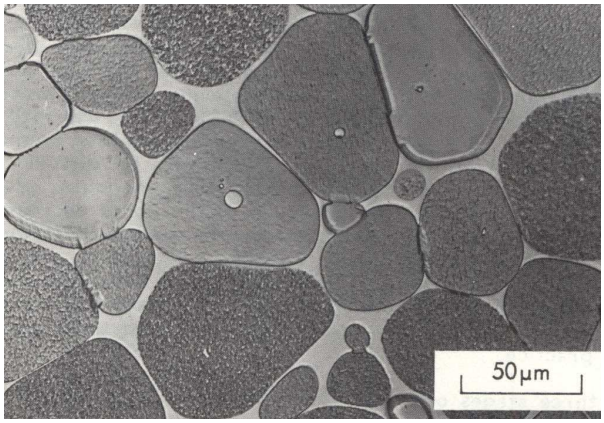

Figure 33 Liquid phase sintered WC-Co [111]

2.8.3 Alternative forms of Sintering

Vacuum and sinter HIP processes are common in the ceramics industry, however, there are other less conventional processes emerging that offer significant advantages.

2.8.3.1 High Temperature Induction Sintering

High temperature induction sintering is a process involving the application of an induced current to a sample under pressure. Typically, ultra-fine powders are placed in a graphite die, which is introduced into high frequency induction heating sintering apparatus. The sample is first evacuated and then pressed high pressure (60 MPa) before applying the induced current until densification is negligible. The induced current results in initial thermal expansion followed by shrinkage due to consolidation [133]. The advantage of this process is that it allows very quick densification to near theoretical densities whilst prohibiting grain growth. Sintering can occur in a time as little as 2 minutes and relative densities of over 98 % can be achieved. Whilst a very rapid process, it is often only of use for ultra-fine and binderless materials.

2.8.3.2 Microwave Sintering

Microwave heating is fundamentally different to conventional heating methods. Microwaves are a form of electromagnetic radiation with short wavelengths (1 mm to 1 m) and high frequencies (300 Ghz to 300 MHz) [134]. In the case of WC-Co, the source of heating is from oscillations of free electrons at high frequency in cobalt and free carbon and in the ions of WC. Consequently, volumetric heating is initiated throughout the green body rather than from the surface inwards in conventional sintering. It is often the mechanism of thermal conduction from heating elements through the oven wall and vessel to the sample surface through to the sample centre that consumes processing time. However, as the heating mechanism is almost instantaneous with microwave sintering, the advantages are clearly of reduced processing time and energy consumption which has been shown across many different applications. The significantly reduced processing time over conventional

methods owes much to the removal of various complicated burn out stages [135]. It would be possible to use microwave sintering equipment to carry out the drying, de-binding and sintering stages in a fraction of the time currently used at SHM with improved material properties. A reduced sintering time also provides the added benefit of reduced grain growth, thus enabling a finer microstructure to be produced, giving better mechanical properties [136]. Other advantages of microwave sintering stem from an ability to control the temperature increase rates with better accuracy as well as at a much greater rate. A comparison of microwave sintering against conventional sintering is given in table 6:

Table 6 Microwave vs conventional sintering

Parameter	Microwave Heating	Conventional Sintering
Sintering temperature (°C)	1300	1450
Total cycle time	90 minutes	12-24 hours
Sintering time	10	60
Density (% of theoretical density)	99.8	99.7
Average grain size (µm)	0.6	2
Bending strength (MPa)	1800	1700
Hardness (Rockwell A)	93	91

The major disadvantages of microwave sintering however are high capital costs and a lack of flexibility where product shape is concerned.

2.8.3.3 Spark Plasma Sintering

Spark plasma sintering (SPS) has been used to sinter tungsten carbide for approximately 80 years [137]. SPS utilises a different heating mechanism to conventional sintering and microwave sintering. Heat for sintering is generated from high power, pulsed DC current which can be accurately controlled. As WC is conductive, the current generates heat within the bulk of the sample internally which is key to rapid rises in temperature. In the case of WC, powder is loaded into a graphite die which serves as a heating element when current is passed through. The die has a small thermal mass which enables heating rates up to 1000 degrees per minute. The current is supplied to the die and sample under high pressure which reduces required sintered temperatures and aids powder compaction. Fast heating and short sinter temperature hold times are unique to SPS and aid in grain growth and sintering control [137] .Although SPS has been used for sintering WC for a long time, there is little information in the literature available. The lack of information is due in part to the limited number of applications of SPS on an industrial scale. The limitations arise not only from high cost but

also from the size of part that can be produced via this method. Similarly the application is limited due to the fact that it is typically only used for near binderless tungsten carbide. Binderless WC has a very fine microstructure, a high hardness, wear resistance and corrosion resistance and consequently it is inherently brittle. The brittleness limits its use to where toughness is not vital such as in water jet cutting nozzles. The fine microstructure stems from the starting powder grain size which is normally submicron and also the fact that grain growth can be easily restricted with such rapid sintering. Whilst SPS offers many benefits, it is not a suitable process for extruded parts of the scale discussed in this work. Added to the issues associated with sample size, SPS would not be easily adapted to use with WC containing cobalt as it would be challenging to retain the binder phase due to its relatively low point of evaporation.

2.8.4 Machining

2.8.4.1 Green Machining

Precise machining of extruded parts is required before sintering in order to save on the wear of expensive cutting tools. Green machining is carried out after drying and before sintering. Green machining of the extrusion blanks after extrusion consists of end slitting. End slitting is carried out to allow the drill to fit into the tool holder and align with coolant holes when used in its application. Diamond wheels and blades are used for the green machining of WC-Co tool blanks.

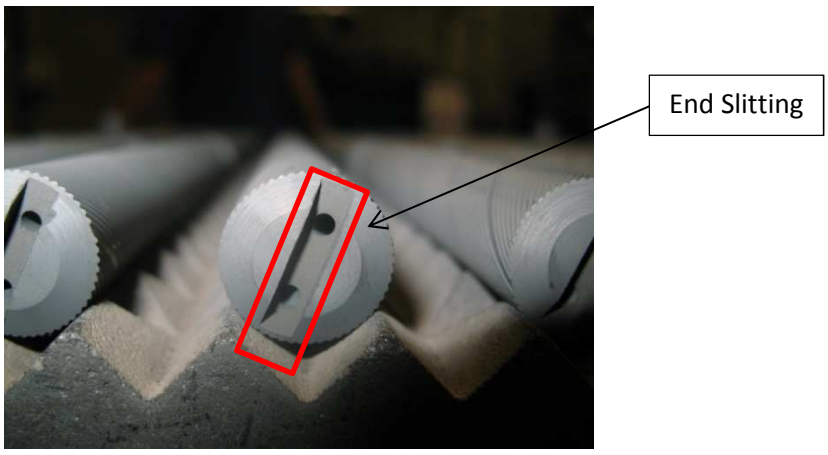

Figure 34 Green Machined WC-Co Extruded Rod

2.8.4.2 Hard Machining

Hard machining refers to machining of sintered products. Complex geometries are extruded with rifles on the outer diameter surface. The rifles are not needed in the sintered product and hence are ground away using centre-less grinding. Following grinding, polishing is also necessary for a high surface finish. High surface finish standards are set to minimise rod breakage due to surface defects, thus improving the transverse rupture strength.

Chapter 3

3.0 Materials and Methods

3.1 Raw Materials

Extrusion binders are made up of shear thinning pre-mixed pastes of solid and liquid components in which liquids and solids act as lubricants and thickeners respectively. Rheology modifiers such as polyacrylamide have been used to fine tune formulations to give the desired extrusion properties. Polyethylene glycol (PEG) and PEG derivatives as well as combinations of methyl cellulose and water or ethyl cellulose and ethanol were investigated in this work. The raw powder material provided by SHM was a spray dried powder in which PEG was used as the binding agent. The powder consisted of 90 mass% WC-Co and 10 mass% cobalt metallic binder bound by PEG with a range of molecular weights. The spray-dried WC-Co was originally developed for pressing and has since been used in extrusion processes. A requirement of this project was that binders developed were to be compatible with the WC-Co pressing feedstock and the ram extrusion process. Using spray dried powder was not ideal for the purposes of binder development and extrusion. PEG from the spray-drying process interacts with solvents (water in particular as it is hygroscopic). Spray-dried powders are also not necessary for extrusion as the spherical particles are broken up in the mixing process. However, non-spray dried powder can become air born and is therefore hazardous. Spray-dried powder is safer to handle and is manufactured in large quantities for pressing. This allowed for constant supply for extrusion testing and any future expansion of production.

3.1.1 WC-Co

WC-Co powder is manufactured in house following the procedure detailed in section 2.3. Initially, WC and cobalt powders were wet ball milled in ethanol with the PEG formulation to give the desired particle size distribution. The slurry was spray-dried to give a free-flowing granular powder with the typical morphology given in Figure 35.

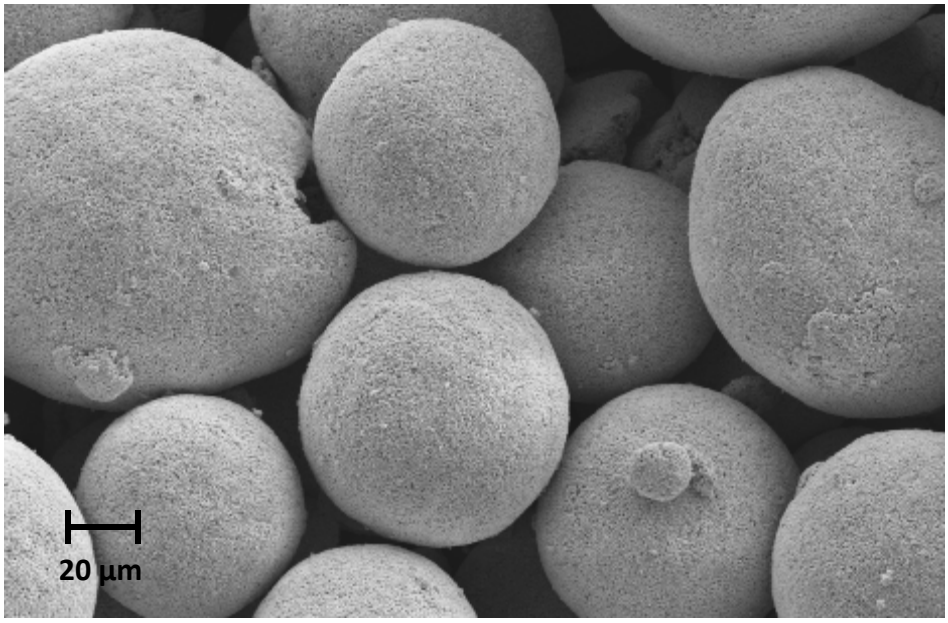

Figure 35 PEG Spray-dried particles of WC-Co

The powder density was measured against a standard of 11300 Kgm^{-3} and powder flow was checked using Hall flow meters. Hall flow meters measure the time taken for a powder to flow through a standardised orifice under gravity. A poorly flowing powder is indicative of errors in the spray-drying process or poor storage conditions, as wet or moist powders do not flow freely. The powders were pressed into test pieces (Sandvik standard test bar of 20 x 5 x 5 mm) and provided that specifications were met, samples were sintered. Sintered density was measured using a density balance. Tungsten content in the binder phase and carbon content in the sintered substrate were also measured using magnetic techniques. Magnetic saturation is measured using a magnetic balance. The SHM term for this test is cobalt-magnetic which is abbreviated to Com. The ratio between Com and cobalt weight % in the sample is termed Com/Co. This ratio is a measurement of the tungsten content in the binder phase but also of the carbon content in the grade. Typically, low ratios mean low carbon content and high tungsten content. This is significant as low carbon contents can form the eta-phase which is a brittle form of carbide. Conversely, high carbon contents can form free graphite which is also undesirable. Free carbon in the polished and sintered sample of WC-Co shown in Figure 36, is a form of carbon porosity and can result in component failure.

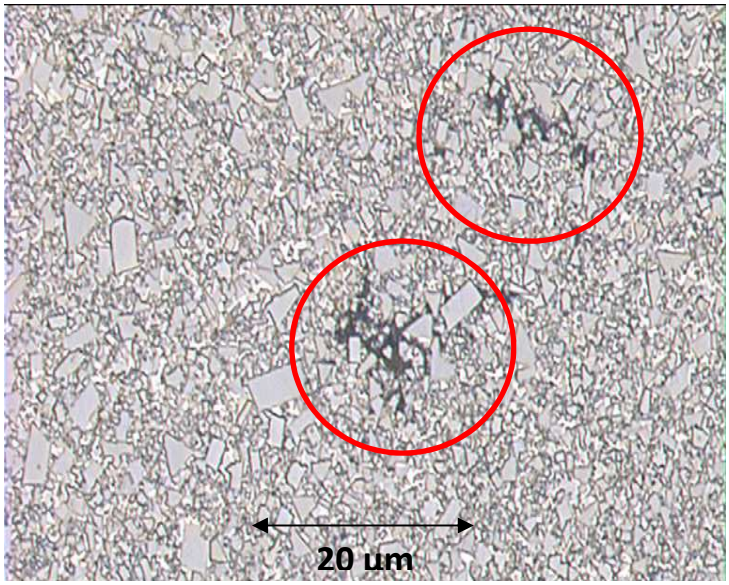

Figure 36 Free carbon in sintered WC-Co sample

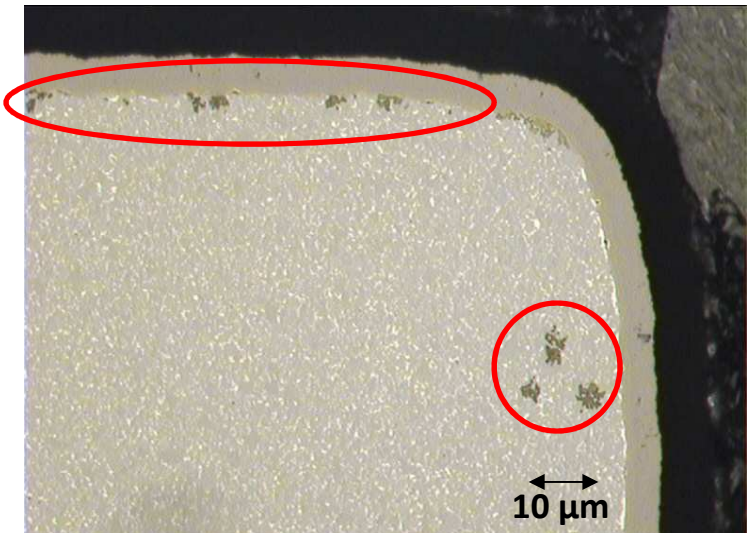

Figure 37 Eta-phase in sintered WC-Co sample

Figure 37 shows the formation of eta-phase which causes excessive brittleness in the specimen. In the Com measurement, the sample is magnetised in an electromagnetic field up to the point of magnetic saturation. The sample is then removed from the coil and magnetic field which generates a current according to Faraday's law. The instrument is then able to re-calculate the signal required to obtain magnetic saturation divided by the mass of the sample. This provides a weight specific magnetic saturation known as com% or cobalt magnetic %. As well as measuring cobalt magnetic % a coercivity measurement is carried out on sintered samples. Coercivity is used to indirectly and non-destructively measure the WC grain size. This is used in conjunction with the Com test because samples can have the same cobalt content, but different grain sizes and as a result different hardness and toughness. The coercivity is abbreviated to Hc. Hc is the size of a reversed magnetic

field that is needed to de-magnetize a fully magnetized sample. Hc is related to grain size because a fine-grained sample has magnetic domains in the Cobalt binder phase that are more difficult to reverse. This implies that a fine-grained sample has a higher Hc value measured in kA/m. A finer grain size generally gives higher sample hardness and therefore high Hc values imply high hardness. As cobalt % is used in Hc calculations, Hc values cannot be directly compared if samples have different cobalt content. A measure of cobalt and carbon content is required to check that the furnace has been controlled appropriately. If the carbon balance was correct, samples were evaluated for hardness (Hv30) and microstructure. Microstructural examination checked for porosity and the correct carbon phases. Each powder batch prepared was measured under these guidelines to insure powder and product quality.

3.2 Organic Binder Materials selection

In order to make the correct selection of binder materials, the requirements of the project and therefore binder systems were defined.

3.2.1 Binder requirements

A requirement of the project was to produce drill blanks of a quality equalling or bettering that of current extruded material supplied by SHM greater than 12 mm sintered diameter. It was also desirable where possible to employ the processing equipment already in place for manufacture. The primary criteria to be fulfilled based on the binder requirements are represented by Figure 38.

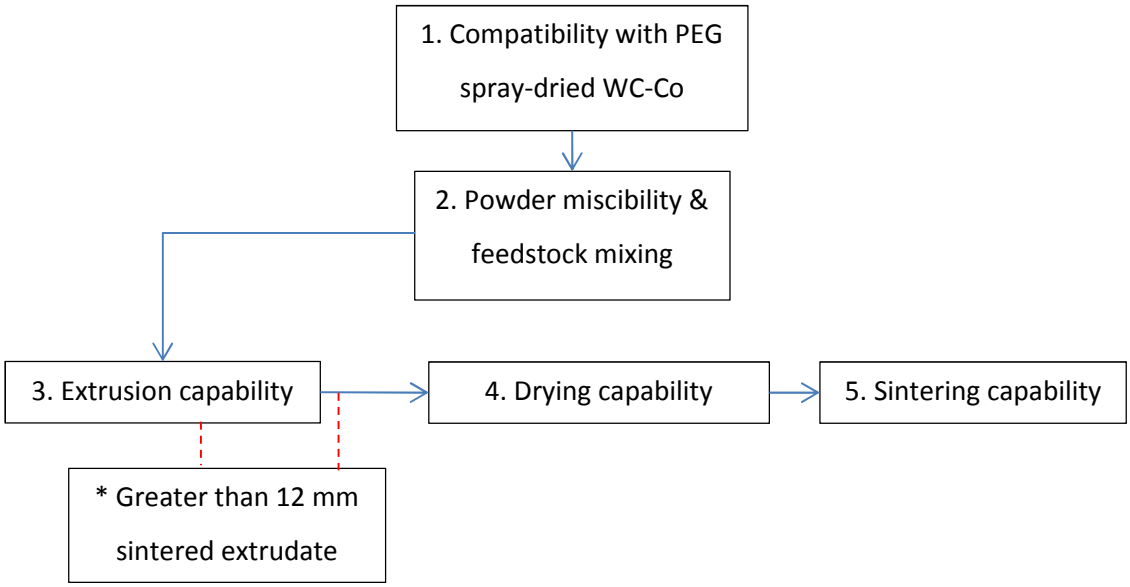

Figure 38 Binder system criteria to be fulfilled. Greater than 12 mm sintered diameter is the major priority of this work; although smaller diameter samples were investigated in the early part of the study.

Table 2 in section 2.3.2 shows binders used in the extrusion of WC-Co and other ceramic materials. From the literature it was clear that an overriding bias towards using methyl cellulose in extrusion binder systems was present regardless of the particulate being processed. Cellulose based binders are also used in catalyst production with large cross-sections and flow stability respectively. Ideally binders should have high shear viscosity. High shear viscosities help to resist phase migration and preferential flow of the liquid phase from the paste which results in flow instability and poor quality [139]. The current binder system used by Sandvik has a high shear viscosity and exhibits good flow properties in terms of stability. Components in the Sandvik binder are of different molecular weights insuring that burn out occurs over a range of temperatures. The extrudate was brittle however, making handling and burnout difficult. Brittleness is thought to result from high molecular weight binder components combined with a high WC-Co solids loading. The mono propylene glycol is also highly volatile causing material loss during mixing at temperatures above 40 °C. Whilst higher dough apparent shear viscosity results in extrudate stability, it also contributes to dough brittleness in this case. A degree of flexibility would aid binder removal by allowing for parts to move during drying and sintering without cracking and failing. High density and brittle extrudate has a tendency to fail under its own weight during drying and sintering. A shortlist of candidate binders was created based on Table 2 and the experience of the Sandvik extrusion department. Historical testing at Sandvik has shown that aqueous binder systems were compatible with WC-Co powder. PEG based materials are also already used by Sandvik with WC-Co and so fulfil the first criterion outlined in Figure 38. The literature study in this work has shown that methyl cellulose based binders were a good starting point for development. Other celluloses are also used in the pharmaceutical, extrusion and spheronisation field. The binder systems detailed in Table 2 were systematically reduced to those in Table 7 based on the criteria given in Figure 38 and initial testing. Initial testing included z-blade mixing with the powder matrix and laboratory scale extrusion, drying and sintering. Laboratory scale extrusion did not test for larger diameters, but gave an indication of extrusion capability and product quality. From the extrusion team at Sandvik there was an interest in ethyl cellulose binder systems due to compatibility with ethanol and their current extrusion processes. There was also a clear interest in developing a binder system derived from PEG using Gelucire 5013 due to process and equipment compatibility. Binder systems selected for initial trials together with the SHM existing binder systems are shown in Table 7.

Table 7 Reduced short list of binder materials based on initial criteria and testing

	Criteria (from figure 38)					
Binder	**1.**	**2.**	**3.**	**4.**	**5.**	*****
SHM	✓	✓	✓	✓	✓	×
Methyl cellulose and water	✓ initial testing	✓ initial testing	✓ for simple geometry	✓ for simple geometry	✓ for simple geometry	✓From catalysis literature
Methyl cellulose, water, PAM	✓ initial testing	✓ initial testing	✓ for simple geometry	✓ for simple geometry	✓ for simple geometry	Unknown
Ethyl cellulose, Ethanol, PVB	✓ initial testing	✓ initial testing	✓ for simple geometry	✓ for simple geometry	✓ for simple geometry	Unknown
Gelucire 5013, MPG	✓ initial testing	✓ initial testing	✓ for simple geometry	✓ for simple geometry	✓ for simple geometry	Unknown

Table 7 was then expanded to Table 10 (a summary of the binders studied in this thesis) based on initial experiments and as a result of fine tuning to optimise the material.

3.3 Organic Binder Materials Preparation

Oleic acid was used in every new formulation due to its compatibility with WC-Co powder and lubricating properties.

3.3.1 Oleic Acid

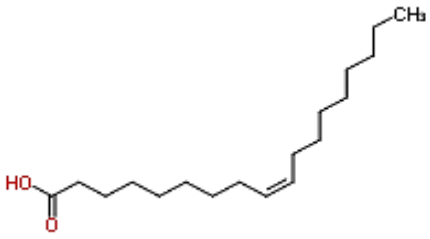

Figure 39 Oleic Acid Chemical Structure [140]

Oleic acid (Figure 39) provides WC powder particles with a polymer coating allowing for effective particle dispersion in organic media. Stabilisation stems from the non-saturated bond (kink in chain in Figure 39) resulting in steric stabilisation via bonding of oleic acid to the surface of dispersed particles [141]. Bonding occurs by adsorption or grafting of the macromolecule head group to the WC-Co surfaces whilst the tail has an affinity to the binder medium (Figure 40). This provides a

protective polymer layer around the WC-Co particles thus preventing particle aggregation via van der Waals forces of attraction [142].

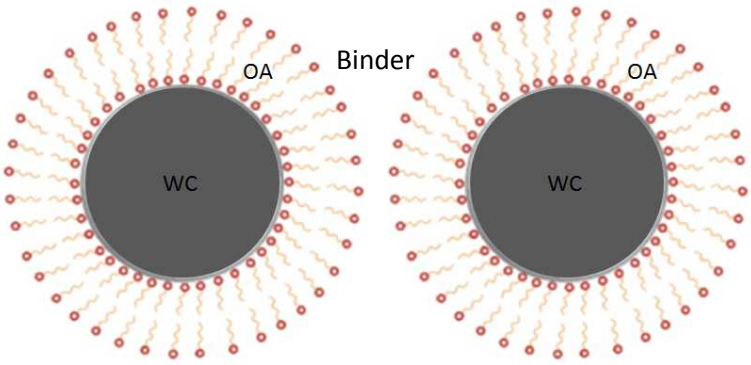

Figure 40 Oleic acid stabilisation schematic [144]

Oleic acid additions results in a homogenous distribution of binder materials in moulded compacts giving a more uniform particle packing [143]. Uniform particle packing is critical in providing a homogenous sintered microstructure in ceramic products [144]. Oleic acid is a mono saturated fatty acid and is the main constituent of olive oil [149]. Lubrication and particle coating allowed for higher solids loadings of WC-Co to be achieved. This enabled a stiffer, more compacted paste with better dimensional accuracy and flow stability to be formed. The quantity of oleic acid used in the existing PEG based formulation at Sandvik was 0.42 mass % of the WC-Co content which was also used in newly developed feedstocks.

3.3.2 Commercial Sandvik Hard Materials (SHM) Organic Binder System

The PEG based binder system used in extrusion by SHM consists of three grades of PEG of increasing molecular weights, mixed with monopropylene glycol (MPG). PEG (Figure 41) is a waxy polymer of ethylene oxide with increasing melting points with molecular weight.

Figure 41 PEG Chemical Structure [140]

PEG and monopropylene glycol properties are given in Table 8.

Table 8 PEG properties

PEG Type	Melting Point (°C)	Viscosity (Pa.s) (100°C)	Flash Point (°C)	Average MW	Density (g/cm^3)
Monopropylene glycol (MPG)	-59	0.056 (20°C)	99	76.1	1.04 (20°C)
PEG 300	-11	5.8	218	285-315	1.12 (20°C)
PEG 1500	42-46	26.5	246	1305-1505	1.09 (60°C)
PEG 3400	53-57	90.8	246	3015-3685	1.09 (60°C)

PEG provides a strong backbone for binder systems, giving high green strength and the MPG provides lubrication. Higher molecular weight PEG molecules provide high yield stress and high flow stability [146]. On a pilot scale a pre-mix was prepared by heating the PEG grades to melting temperature. The melted pre-mix was stirred until a homogenous mixture was formed. MPG was added upon cooling (so not to evaporate) and stirred into the molten mix. MPG is a clear, odourless viscous liquid with a vapour point of 40°C. It is used for lubrication and has the chemical structure shown in Figure 42 [147], [140].

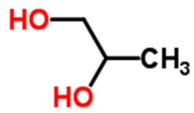

Figure 42 Chemical Structure of MPG [140]

When PEG and MPG were mixed to form the pre-mix, a white odourless waxy material was formed with a low yield stress.

3.3.3 Methyl Cellulose and Water Binder

The methyl cellulose used had a viscosity of 0.4 Pa.s in 2 % water solution (Sigma-Aldrich). Methyl cellulose is a white powder under ambient conditions. When dissolved in water at 80 °C it forms a clear and homogenous gel-like material. Methyl cellulose has the chemical structure shown in Figure 43.

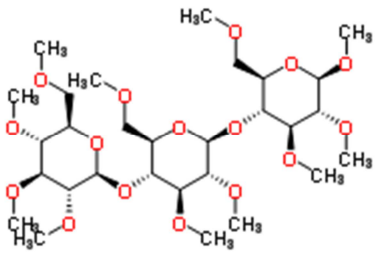

Figure 43 Methyl cellulose chemical structure [140]

In the preparation of the binder system, varying mass ratios of methyl cellulose to water were investigated to provide binders with a range of viscosities in the form of stable gels. The binders were mixed in a Kenwood planetary mixer at approximately 2000 R.P.M with hot distilled water. 2000 R.P.M refers to the rotation of the mixer head which was measured using strobe lighting. The rotation of the mixing arm around the mixer bowl was unknown. Mixing was carried out until homogeneity was achieved. For each batch, cooling was accelerated and the solution was stirred to prevent separation. After 60 minutes a translucent low viscosity gel was formed. This was then left for 24 hours at 5°C to allow for complete dissolution and clear gel formation. Longer chain lengths of methyl cellulose were also investigated to form pre-mixes with higher molecular weight using the same approach.

3.3.4 Methyl Cellulose and Water Binder with Polyacrylamide Additions

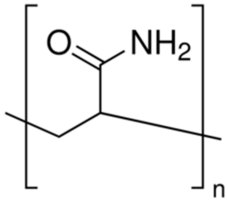

Figure 44 Polyacrylamide Chemical Structure [140]

Polyacrylamide (Sigma-Aldrich) was added to the methyl cellulose binder system detailed in section 3.3.3 to increase binder viscosity. Polyacrylamide is a cross-linked polymer with a molecular weight of 10-20 million g/mol (5-6 thousand times that of PEG 3400) [148]. High molecular weight ensures that binder shear viscosity is increased significantly when PAM is added in small quantities. Due to the swelling of PAM on introduction to water, it can be used to thicken aqueous binders. PAM has the chemical structure shown in Figure 44 [149]. It has the physical appearance of a coarse powder and was added to the methyl cellulose and water system slowly during mixing until fully dissolved.

3.3.5 Ethyl Cellulose and Ethanol Binder

Ethyl cellulose (Sigma-Aldrich) has the chemical structure in Figure 45.

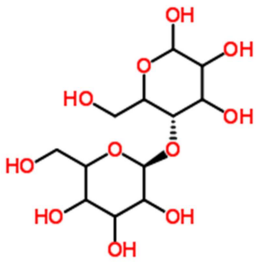

Figure 45 Ethyl Cellulose Chemical Structure [140]

Ethyl cellulose is insoluble in water although is soluble in alcohol, as shown by Larrson [150]. Ethanol is used in the ball milling process at Sandvik, and was hence a practical solvent to use. Ethyl cellulose was added to ethanol gradually in a planetary mixer. Due to increased viscosity over the methyl cellulose binder, stiffer mixing blades (Figure 46) were required rather than the whisk shown in Figure 10 which deformed under load.

Figure 46 Mixing attachment for ethyl cellulose binder preparation

Ethyl cellulose was added at 23 mass % to ethanol, a higher mass % resulted in incomplete dissolution of cellulose. 20 mass % ethyl cellulose and 80 mass % ethanol was used to insure that incomplete dissolution could not occur. Polyvinyl butyral (PVB) plasticiser was added at a later stage to prevent the formation of a brittle binder system [151]. The final binder formulation consisted of 20 % ethyl cellulose, 65% ethanol and 15% PVB by mass.

3.3.6 Gelucire 50/13 Waxy Binder System

Gelucire 50/13 is a trade name for Stearoyl Macrogolglyceride and is used in the pharmaceuticals industry as a waxy polymer binder in extrusion processes. It is derived from esters of PEG with a molecular weight of 32 and Glyceryl.

PEG-32 esters have the chemical formula:

$H\text{-}[CH_2\text{-}(CH_2)_n\text{-}CO]i\text{-}(O\text{-}CH_2\text{-}CH_2\text{-})32[O\text{-}CO\text{-}(CH_2)n\text{-}CH_2]j\text{-}H$

where n is 10 to 18, I and j are 0 or 1 [126].

Glyceryl esters have the chemical formula:

$C_3\ H_5\ O_3\ [-\ CO\ -\ (CH_2)_n\ -\ CH_3]_h$

where h can be one, two or three [152]. Figure 47 shows the chemical structure of glyceryl esters.

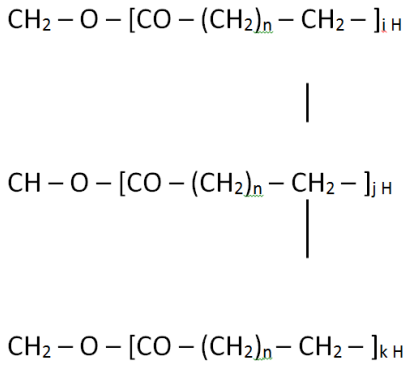

Figure 47 Glyceryl ester chemical structure

where n ranges from 10 to 18 and I, j and k can be 0 or 1 [152].

3.3.7 Methyl cellulose based binder containing PEG

Binder systems were prepared containing the equivalent mass of PEG used in the spray dry process as the presence of that PEG would alter the binder performance. Commercial constraints led to the use of PEG spray-dried powder due to additive free powder being hazardous and not readily available. PEG however, is a plasticiser for methyl cellulose which aids fluidity in extrusion processes [153]. Methyl cellulose-PEG based binders were prepared in the same manner as methyl cellulose based binders only PEG 300, 1500 and 3400 were added. Dough batches containing WC-Co, had 2 mass % PEG (of the WC-Co powder) added for spray-drying WC-Co. Therefore an equivalent mass of PEG was added to the methyl cellulose pre-mix in order to analyse true binder properties. As an example, in a 6 Kg powder mix, 12 g of PEG 300 and PEG 1500 were added with 96 g of PEG 3400. Variants of this binder system were also prepared for increased WC-Co loadings with increased PEG content.

Table 9 Methyl cellulose plus PEG binder composition

Binder Component	Mass (%)
Methyl cellulose	0.51
Water	5.91
Potential WC-Co	91.74
PEG 300	0.18
PEG 1500	0.18
PEG 3400	1.47

3.3.8 Binder System Summary

Table 10 summarises the binder systems prepared. Binder variants titled MC x% (PEGy) refer to the masses of methyl cellulose (x) and PEG (y). The methyl cellulose mass % is related to the mass of

methyl cellulose in the binder only and stems from originally prepared formulations. For example MC8 % (PEG42) implies that if the binder was prepared alone then it would consist of 8 mass % methyl cellulose and 92 mass % water. PEG42 implies that when made into a dough, 42 volume % of WC-Co would be added. However, the addition of WC-Co would include a set amount of PEG from spray drying. Therefore the binder has been made up to include the set amount of PEG. The mass% values in Table 10 are for the total material in the binder.

Table 10 Binder Summary (methyl cellulose based binder formulations)

Binder Code	Material	Mass %	Grade (Product code)	Supplier
SHM	PEG 300	18.78		Lehnkering GmbH, Mannhein
	PEG 1500	18.78		Lehnkering GmbH, Mannhein
	PEG 3400	22.07		Lehnkering GmbH, Mannhein
	PEG 8000	10.01		Lehnkering GmbH, Mannhein
	triethanolamine	1.23		
	Propylene glycol	29.11		Firmin Coates Ltd, Byley, UK
MC 8% (no PEG)	Methyl cellulose	8.00	M0262	Sigma-Aldrich (MW 41000)
	Distilled water	92.00	-	SHM
MC 25% (no PEG)	Methyl cellulose	25.00	M0262	Sigma-Aldrich (MW 41000)
	Distilled water	75.00	-	SHM
MC 8% (PEG42)	Methyl cellulose	6.22	M0262	Sigma-Aldrich (MW 41000)
*PEG 42 is the equivalent	Distilled water	71.56	-	SHM
PEG content in a dough	PEG 300	2.22		Lehnkering GmbH, Mannhein
batch with WC-Co 42%	PEG 1500	2.22		Lehnkering GmbH, Mannhein
solids loading	PEG 3400	17.78		Lehnkering GmbH, Mannhein
MC 16% (PEG42)	Methyl cellulose	12.69	M0262	Sigma-Aldrich (MW 41000)
*PEG 42 is the equivalent	Distilled water	66.62	-	SHM
PEG content in a dough	PEG 300	2.07		Lehnkering GmbH, Mannhein
batch with WC-Co 42%	PEG 1500	2.07		Lehnkering GmbH, Mannhein
solids loading	PEG 3400	16.55		Lehnkering GmbH, Mannhein
MC 8% (PEG44)	Methyl cellulose	6.03	M0262	Sigma-Aldrich (MW 41000)
*PEG 44 is the equivalent	Distilled water	69.39	-	SHM
PEG content in a dough	PEG 300	2.46		Lehnkering GmbH, Mannhein
batch with WC-Co 44%	PEG 1500	2.46		Lehnkering GmbH, Mannhein
solids loading	PEG 3400	19.66		Lehnkering GmbH, Mannhein
MC 10 % (PEG40)	Methyl cellulose	7.93	M0262	Sigma-Aldrich (MW 41000)
*PEG 40 is the equivalent	Distilled water	71.38	-	SHM
PEG content in a dough	PEG 300	2.07		Lehnkering GmbH, Mannhein
batch with WC-Co 40%	PEG 1500	2.07		Lehnkering GmbH, Mannhein
solids loading	PEG 3400	16.55		Lehnkering GmbH, Mannhein
MC 10% (PEG44)	Methyl cellulose	7.55	M0262	Sigma-Aldrich (MW 41000)
*PEG 44 is the equivalent	Distilled water	67.97	-	SHM
PEG content in a dough	PEG 300	2.45		Lehnkering GmbH, Mannhein
batch with WC-Co 44%	PEG 1500	2.45		Lehnkering GmbH, Mannhein
solids loading	PEG 3400	19.58		Lehnkering GmbH, Mannhein
MCPAM	Methyl cellulose	17.64	M0262	Sigma-Aldrich (MW 41000)
	Distilled water	78.68	-	SHM
	Polyacrylamide	3.68		Sigma-Aldrich
MC medium chain length (MCM)	Methyl cellulose	8.00	M0362	Sigma-Aldrich (MW 63000)
	Distilled water	92.00	-	SHM
MC long chain length (MCL)	Methyl cellulose	8.00	M0512	Sigma-Aldrich (MW 88000)
	Distilled water	92.00	-	SHM
MCGLY1	Methyl cellulose	9.14	M0262	Sigma-Aldrich (MW 41000)
	Distilled water	84.60	-	SHM
	Glycerol	6.26		Sigma-Aldrich
MCGLY5	Methyl cellulose	7.14	M0262	Sigma-Aldrich (MW 41000)
	Distilled water	41.07	-	SHM
	Glycerol	51.79		Sigma-Aldrich
MCMPG	Methyl cellulose	6.61	M0262	Sigma-Aldrich (MW 41000)
	Distilled water	76.06	-	SHM
	Propylene glycol	17.33		Firmin Coates Ltd, Byley, UK

Binders not included in Table 10 are MC8PEG44, MC10PEG42, MC12PEG42, MC15PEG42 and variants in between MC8% through to MC25% with increments of 1 mass % cellulose. Table 11 describes the suppliers and quantities of materials not made up from methyl cellulose.

Table 11 Binder summary (not containing methyl cellulose)

Binder Code	Material	Mass %	Grade (Product code)	Supplier
ECETHPVB	Ethyl cellulose	19.69	200689	Sigma-Aldrich
	Ethanol	64.98	-	SHM
	Polyvinyl butyral	15.33	418439	Sigma-Aldrich
GCMPG	Gelucire 5013	50.00	-	Gatefosse, France
	Propylene glycol	50.00	-	Firmin Coates Ltd, Byley, UK

3.4 Rotational Rheometer Apparatus

Rotational rheometry theory has been discussed in section 2.5.1. A TA instruments AR500 rheometer was used to analyse the extrusion binder materials. The primary set up used was a cone and plate type geometry. The bottom plate was a fixed peltier capable of heating to 180 °C and the geometries rotated on an air cushioned spindle.

3.5 Binder Rheological Techniques

Apparent viscosity measurements were carried out using shear stress and shear rate sweep tests. Viscoelastic properties were tested using oscillatory shear. The results for each binder system have been modelled using either a power law or Herschel Bulkley curve fit. Each binder rheological test was carried out at 22°C unless stated otherwise as SHM extrusion labs and production rooms are kept at 22°C. Solvent traps were used where appropriate to prevent evaporation and cone geometries of 20 mm diameter were used where possible.

3.5.1 Shear Stress Sweeps

A shear stress sweep was applied to each binder system to observe flow behaviour. This was a comparative test in order to rate binder performance in relation to the current binder system used by SHM. A shear stress range was determined prior to running the test to prevent geometry spin out at higher shear stresses. Shear stress was ramped up for each binder test and a shear rate response was recorded. Shear stress data and shear rate response data was plotted in SigmaPlot software. Using SigmaPlot allowed for models to be written in code and fitted to the data so that binder parameters could be calculated. Herschel Bulkley parameters were used to compare binder paste properties (section 4.1). Exporting data into Sigma-plot allowed for easier data analysis and a greater accuracy of fit.

3.5.2 Strain Sweeps

Strain sweeps were used to find the linear visco-elastic region (LVER) of each binder. Strain sweeps were carried out across a range in which the values of elastic and viscous moduli began to drop. The drop in viscous and elastic moduli indicated that the LVER had been passed. Determining the LVER allowed for accurate further testing with no interference or disrupted microstructure. Strain values were taken in the centre of the LVER for frequency sweep testing.

3.5.3 Frequency Sweeps

Frequency sweeps of each binder system were run in the LVER and where possible a full range of frequency was used which was 0-273 rads/s for the TA instruments AR500 equipment. Frequency was ramped up across the range over 40 minutes. The viscous and elastic properties were plotted against frequency on a log plot. The phase angle delta was also recorded to compare each binder system without overcrowding the plot with excessive data.

3.5.4 Aging tests (aqueous binder)

Aging effects were observed with aqueous binder materials and dough formulations that were selected for production scale extrusion. Capillary rheometry was used to test the aging effects of aqueous dough systems. Age related changes to dough were predicted to be a result of changes in binder rheology. In order to verify this, binder rheological testing was required under the same conditions as the capillary rheology work. The capillary rheometer was controlled using pre-determined shear rate values. The binders that required testing in this manner were of low shear viscosity and could not be tested with the same geometry (3 mm die) as the dough feedstock. The weight of the ram and piston alone applied sufficient force to extrude the binder system and so a smaller capillary was required. Die diameters of 0.5 and 1 mm provided a greater resistance to material flow although the binder systems could not withstand the higher pressure and tended to separate. Due to this behaviour, rotational rheometry was the most practical procedure to determine aging effects on binder viscosity. The shear rate sweep was carried out from 0-300 s^{-1} as this range compared well with the conditions of the dough rheology test. Controlled shear rate sweeps and strain/frequency sweep tests were run to observe apparent viscosity and visco-elastic binder property changes with time. Strain sweeps were run under conditions described in section 3.5.2 in order to observe changes in the LVER. Frequency sweeps were then run in the LVER with increased time intervals. For comparisons with mixing and extrusion testing, the binders were tested on day one (day of mixing), day two (day of extrusion) and day 7 (one week after day of binder pre-mix preparation). In the aqueous binder materials, water is lost with time from the formulation. This was thought to be the largest contributor to the aging effect.

3.6 Dough Materials and Preparation

Dough materials were prepared in a Winkworth MZ2 2 litre Z-blade mixer for the majority of experiments. A Werner and Pfleiderer (LDDK05KSPV) Z-blade mixer was also used in mixer torque rheometry experiments. The optimum solids loadings for each of the feedstock was determined with mixer torque and density measurements. The theoretical maximum solids loading was determined using extrusion data.

3.6.1 SHM PEG based dough

On a pilot scale (6 Kg), SHM feedstock was prepared at a temperature of 40 °C at 45 R.P.M until a dough had been formed from the powder and binder materials. Higher temperatures aided the distribution of PEG around the powder matrix and promoted homogenous formulations. A visually smooth dough typically formed within 45 minutes, after which the mixer was cooled to 10 °C and the dough was granulated in the mixer for 10 minutes. In the production environment crushers were designed specifically for this purpose. Pre-mixed dough was vibratory fed into a rotary crusher device in which a baffled cylinder rotated clockwise and counter-clockwise in oscillatory motion up against a 5 mm square wire mesh.

3.6.2 Methyl cellulose, water based dough

Methyl cellulose dough was prepared at colder temperatures. Oleic acid was first added to the WC-Co powder and mixed at 45 revolutions per minute (RPM) for 10 minutes. This was to insure that the surfactant was fully distributed in the powder matrix. The methyl cellulose pre-mix was then added and mixed for 25 minutes at the same blade speed. Mix temperature was restricted by cooling to not exceed 20 °C. In the last 5 minutes of mixing, the vacuum was turned on to remove air to reduce pore formation in the dough. The methyl cellulose based dough was less viscous than SHM dough, owing in part to a lower solids loading. The dough was stored at 5 °C to prevent further moisture loss.

3.6.3 Methyl Cellulose, Water, Polyacrylamide Additions

The polyacrylamide additions were made in the pre-mix stage as described in section 3.3.4. All other techniques in dough preparation remained the same as the materials described in section 3.6.2.

3.6.4 Methyl cellulose, water, MPG

Methyl cellulose and water pre-mix was mixed with WC-Co by the same method as described in section 3.6.2. The proportions of methyl cellulose pre-mix were reduced to account for the MPG addition later in the mixing process. MPG was added at a later stage to avoid evaporation during the mixing process.

3.6.5 Methyl cellulose, water, glycerol

This dough formulation was prepared in the same manner as the dough in section 3.6.4, although MPG was replaced with glycerol.

3.6.6 Ethyl Cellulose, Ethanol

Ethyl cellulose and ethanol pre-mix was added to the WC-Co and oleic acid mix. The mix was prepared at lower temperatures to avoid the evaporation of ethanol. Ethanol evaporated despite lower mixing temperatures due to increased vapour pressure when under vacuum. Mixing times were shorter as homogeneity was reached in a shorter time due to increased WC-Co wettability by this system.

3.6.7 Ethyl cellulose, ethanol, polyvinyl butyral

Ethyl cellulose and ethanol dough with PVB was prepared under the same conditions as the dough in section 3.6.6. The WC-Co solids loading was adjusted to account for the PVB plasticiser which was added after initial dough formation. Smoother dough surfaces were observed in the mixer than those seen in the standard ethyl cellulose and ethanol dough.

3.6.8 Gelucire 50/13-MPG waxy binder

Due to its PEG-like structure the Gelucire 50/13–MPG dough was prepared in a same way as the SHM standard dough (section 3.6.1). The Gelucire 5013-MPG binder has a lower melting point than the PEG binder and for a given liquid volume addition and temperature a lower viscosity dough was observed during mixing. Smoother more paste-like dough was formed with a shorter mixing time than the SHM dough. Higher solids loadings were also achievable. On first inspection, this dough formulation gave the optimum mixing results.

3.7 Dough Rheological Techniques and Analysis

The dough formulations were rheologically evaluated using a Rosand RH7 capillary rheometer, an Instron load frame adapted for capillary analysis and by mixer torque rheometry. The dough formulations reported in sections 3.6.4, 3.6.5, 3.6.7, were not analysed in such detail as no benefits to the base line formulations were observed in terms of extrusion quality. Density measurements of the doughs were also made using helium pycnometry (section 2.3.4.9).

3.7.1 Capillary Rheometry

Capillary rheometry was used to measure the apparent viscosity of the dough formulations described in sections 3.6.1, 3.6.2, 3.6.3, 3.6.6 and 3.6.8. From the pressure traces recorded in these experiments it is possible to comment on the stability of the paste. Once stable flow is established a

good paste would show a gradual and smooth reduction in the required pressure with time. Deviations can imply phase migration or inhomogeneity. In capillary rheometry, flow effects at the die entrance and exit (Figure 48) must be accounted for. The barrel and die sets used with the Instron load frame were manufactured from WC-Co to minimise wear.

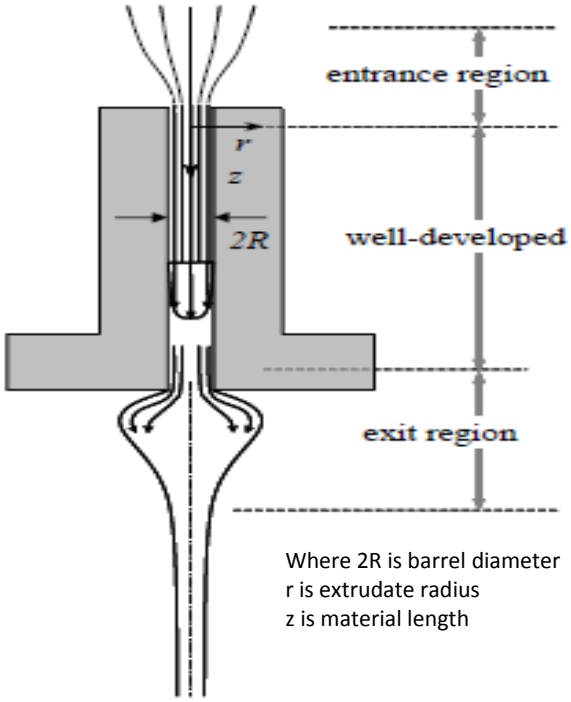

Figure 48 Extrusion die entrance effects (Bagley correction) [154]

The die exit effects in Figure 48 are exaggerated for illustrative purposes. Such exit effects are more common in polymer melts such as polyethylene and concentrated suspensions [155] rather than in WC-Co dough. The die exit effects in figure 48 are commonly referred to as die swelling. Die swell is a phenomena that occurs in many material types and of particular interest in literature is the die swell of Newtonian and viscoelastic extrusion feedstocks. It is known that for visco-elastic materials, the swelling ratio of the material increases significantly with shear rate, whilst for Newtonian fluids this is not the case [156]. In fact, for high levels of Reynolds number (high shear rates), a Newtonian fluid extrudate exhibits decreased swelling. For viscoelastic fluids, die swelling is related to the elastic recoil of molecules which generally dominates over viscous effects. The elastic recoil of the molecules exists due to the absence of rigid walls (the die) and thus the material swells. For Newtonian fluids however, viscous effects dominate and there is little to no recoil effect.

A 3 mm diameter die 10 mm in length was used for the measurements being fed from a 23 mm diameter barrel. The extrusion barrel was filled to capacity and compacted until the point of extrusion. Following the first compaction, the barrel was refilled and compacted until the point of extrusion again. This procedure was repeated until the barrel was at full capacity. As there was no opportunity to apply vacuum equipment to the capillary rheometer, this was the optimum method to achieve a compacted plug of material. A blanking plate over the die exit was also evaluated to give a fully compacted paste. The barrel strength for the rheometer, however, was not known and such high pressures were not desirable for safety reasons. High pressures and blanking plates were also not advisable with the aqueous systems as it could encourage preferential flow of the liquid phase through gaps in the equipment.

3.7.1.1 Shear Rate Step Changes

Shear rate step changes were applied to dough materials to observe material behaviour over a range of ram speeds. Shear rates of 0-500 s^{-1} were used as this was the maximum range of the equipment and pressure was measured using a pressure transducer placed just before the die entrance. This allowed for the calculation of a shear stress response as shear rate was changing under stable conditions. From the shear rate and shear stress data, apparent viscosity was calculated by the equipment software and tabulated in excel. This data was corrected for die entrance effects using the Bagley correction (section 2.5.3).

3.7.1.2 Increased MC Concentration Evaluation

Binders containing 8, 10, 15 and 16 mass % cellulose were used to form doughs. Binders exceeding 16% by mass of cellulose were not used in dough extrusion experiments. The feedstock was dry at any reasonable solids loading and was therefore not extrudable. The test described in section 3.7.1.1 was used for each variation in dough formulation.

3.7.1.3 Increased WC-Co Concentration Evaluation

In this set of experiments the methyl cellulose binder concentration was kept constant in the dough formulation at 8 mass %. WC-Co content was offset at 40.6, 41.6 and 42.6 volume % of the total formulation. Each material batch was extruded as described in section 3.7.1.1. Higher solids loadings were not achievable for this binder system whilst lower solids loadings were too soft to retain shape.

3.7.2 Benbow Bridgwater Analysis

Benbow Bridgwater analysis was used, allowing paste parameters to be assigned to dough types described in sections 3.6.2, 3.6.3, 3.6.6 and 3.6.8 as well as the standard SHM dough. A bespoke WC-

Co barrel 23 mm in diameter and stainless steel piston with brass tip were designed to be used with an Instron load frame for this extrusion process (Figure 49).

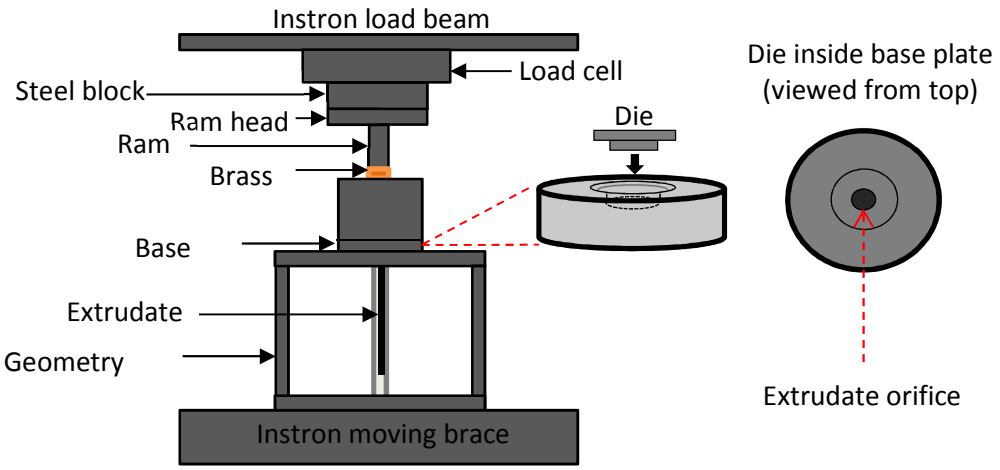

Figure 49 Instron load frame extrusion schematic

The WC-Co barrel was designed for high pressures and the barrel entry was chamfered to allow for tooling misalignment. A brass tip was used for sacrificial wear and cost effective replacement. WC-Co dies were also prepared and extrusion polished for a smooth surface finish. The Benbow Bridgwater model was resolved using Sigmaplot so that a 6-parameter equation could be fitted to the various data sets. The software used non-linear regression to fit the model to experimental data. Extrusion data was generated by extruding dough at 0.125, 0.25, 0.5, 1, 2 and 4 mms^{-1}. Extrusion was repeated through dies with a length over diameter (L/D) ratio of 1, 4 and 8. Ram speeds were controlled by the Instron equipment Bluehill software. A 4 mms^{-1} stage was included at the start and end of the procedure to check for flow stability. Force was measured using a 100 kN load cell which was converted to pressure based on geometry. Pressure data was then plotted against die L/D and extrudate velocity in a three dimensional plot. This experiment was carried out over three dies of 4, 6 and 8 mm diameter, the 4 mm die being used for the model fitting. Bagley plots were generated to show pressure drop against the length-diameter ratio, thus allowing extrapolation to L/D =0 as described in section 2.5.3. Comparisons could then be made between the back calculated pressures and the pressure generated experimentally. The data generated could also be used for the calculation of pressure drop in other geometries (Chapter 6).

3.7.3 Density Measurements

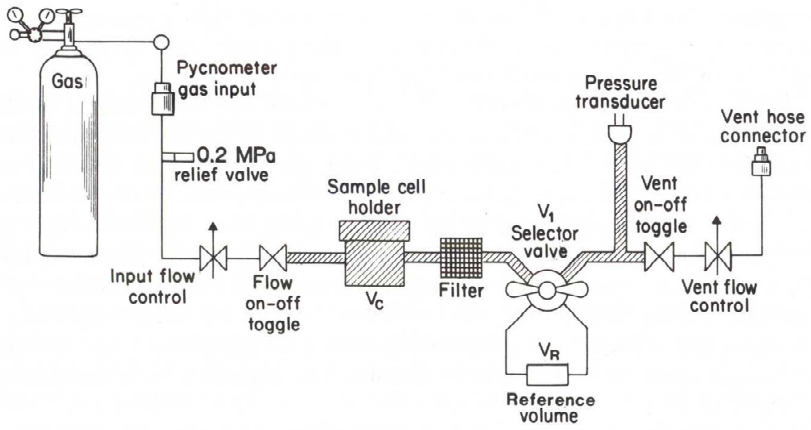

Figure 50 Helium pycnometry schematic [83]

Dough density measurements were made using a Micromeritics AccuPyc II 1340 helium pycnometer (section 2.3.4.9), a schematic of which is shown in Figure 50 [83]. A sample of known mass was purged with helium over 10 cycles. The powder volume was calculated from the volume of the sample cell and the volume of a reference cell based on pressure differences. The sample and reference volumes were purged with helium to reach ambient pressure. The sample cell pressure was then increased to P_2. Valve V1 was opened, dropping the pressure to P_1 [83]. Powder volume was calculated from the pycnometer software based on Equations 3-1 and 3-2.

$$V_p = V_C + \left(\frac{V_R}{1 - P_2/P_1}\right) \quad 3\text{-}1$$

where V_C is the sample cell volume, V_R is the reference volume. The reference volume was calculated using:

$$V_R = \frac{V_{cal}}{\left[\frac{1}{(p_2/p_1 - 1)} - \frac{1}{p'_2/p_{,1} - 1)}\right]} \quad 3\text{-}2$$

where V_{cal} was the volume of a calibrated blank and $p'1$ and $p'2$ are similar to p_2 and p_1 only measured when the calibrated blank was in place. Density measurements were used in conjunction with mixer torque to determine the critical solids loadings of various feedstocks.

3.7.4 Mixer Torque Rheometry and Viscous Heating

Dough materials were prepared using Z-blade mixers by combining the powder with the selected binder systems. Torque measurements were made with a Winkworth MZ2 2 litre Z-blade mixer. A 1 litre Werner and Pfleiderer Z-blade LDDK05KSPV mixer was also used for comparison of dough

quality based on density measurements. Differences in mixing were expected due to differing mixing conditions as a result of both maintenance and advancing mixing technology. The WP mixer was awaiting refurbishment whilst the Winkworth mixer was newly set up with optimum clearances. Materials were added in the same manner for each mixer. Firstly the stabilisers and WC-Co powder were mixed for 10 minutes followed by the addition of a binder pre-mix. The mixer temperature was maintained between 10 and 20°C during mixing for each dough system. Due to the differences in dough stiffness different levels of cooling were required as a result of friction and work. The different levels of cooling required for different materials can also be explained in part by viscous heating. Cendrowicz amongst others [110] has reported that the average temperature rise of a fluid is dependent on material properties such as heat capacity and density as well as the work applied by external processing equipment. The average temperature rise (ΔT_{av}) is given by:

$$\Delta T_{av} = \frac{\Delta P}{\rho C} \qquad 3\text{-}3$$

where ΔP is pressure difference, ρ is material density and C is heat capacity. Equation 3-3 shows that average fluid temperature increases with increased work (in this case pressure) for continuous throughput. Increased work from mixing equipment could be applied by increasing mixing speed. Similarly, higher dough densities would also increase the mixing temperature. The theory can also be applied during extrusion as the heat capacity will remain similar given that the powder matrix is kept constant. Mixing time ranged from 20-30 minutes for the Winkworth mixer and 40-60 minutes in the Werner and Pfleiderer mixer. For aqueous based dough, residue rested in the dead zones of the mixer. This was more difficult to re-distribute than solid lumps found in the dead zones of waxy based feedstock. Dough was mixed under vacuum to remove entrapped air. The vacuum levels obtained during mixing were higher with the Winkworth mixer (ranging from 20-25 mbar). The vacuum levels for the Werner and Pfleiderer mixer were not measureable although the Winkworth pump had a greater power output and mixer sealing rubbers were less worn. The Winkworth mixer temperature control was also more precise owing to separate chilling equipment as oppose to mains water cooling. The speed of the blade rotation was controlled in the Winkworth mixer on the directly driven blade. Torque required to rotate the mixing blades was measured directly from the motor drive. Mixes were prepared by increasing the WC-Co powder content incrementally up to and beyond the maximum solids loading for each different binder system. Small samples at each incremental increase in loading were removed in order to make density measurements.

3.7.5 Inverse Pressure Extrusion

Doughs described in sections 3.6.2, 3.6.3, 3.6.6 and 3.6.8 were extruded over a range of ram speeds with a 4 mm diameter square entry (90° entry angle) cylindrical die, 4 mm in length from a 23 mm diameter barrel, taking readings of pressure with time elapse. This allowed the quality of the extrudate to be examined. Extrusion of the doughs over a range of velocities at solids loadings either side of the critical value predicted by the torque curve derived from mixing was carried out. This provided the pressure data required to interpolate the maximum possible solids loading. The extrusion pressure was recorded for each dough as it was forced through a fixed geometry at a fixed rate. The inverse of the required extrusion pressure was plotted as a function of solids loading and a straight line extrapolated to the solids loading axis. This equates to the point where the powder voidage is just filled with liquid and therefore the maximum solids loading.

3.8 Pilot Scale Extrusion

A Loomis 70 tonne extrusion press allowed for the extrusion of solid rod products up to diameters of 20 mm in the sintered state. Sizes are quoted as the size that the product is machined to and is the WC-Co standard notation. The extruded size is significantly larger than this as the products are sold after drying, sintering, grinding and polishing. Tooling for 20 mm diameter sintered state rods with coolant holes had not yet been developed for the research and development press. Product and die diameters for the Loomis 70 tonne press are shown in Table 12.

Table 12 Product and tooling geometry

Product	Sintered Diameter (mm)	Tooling Diameter (mm)
Solid	6	8
Solid	14	19
Solid	20	27
Coolant	14	19.4

The extrusion process was the same for each product with the exception of ram speed adjustments for coolant hole geometries. Ram speed was adjusted for coolant hole geometries as extrusion flow was more complicated and an optimum speed needed to be determined. Before each trial run, extrusion feedstock was fed into the extrusion barrel and pre-compacted into a 12 Kg billet at a ram speed of 2 $mm.s^{-1}$ under vacuum. A vacuum was applied to the rear of the extrusion barrel and to the front of the die using an end cap and sealing ring surrounding the die land. It was necessary to vacuum the front section of the extrusion gun to insure that the whole extrusion press from barrel to die was kept under vacuum. All extrusion was carried out under vacuum to prevent the

compression of air pockets in the material and the potential sudden slip of material as pressure is released. Each rod was extruded onto graphite trays with low friction coatings ready for drying.

3.8.1 20 mm Solid Rod

20 mm solid rods were extruded in the Loomis 70 tonne press before production scale extrusion was attempted. Tooling consisted of components shown in Figure 9 with a 27 mm diameter die nozzle attached. The solid die geometries were polished and trumpet shaped at the die entrance. The barrel diameter was 80 mm, larger diameter dies would not generate high enough extrusion pressures to form dense rods as the reduction ratio would be too small. 20 mm rods were extruded using four of the newly developed binder systems described in sections 3.6.2, 3.6.3, 3.6.7 and 3.6.8. Rods were extruded at a ram speed of 0.07 $mm.s^{-1}$ for ease of handling. Faster speeds were not practical as rods had to be cut and moved in between each length of extrudate. This was a disadvantage as slower extrusion speeds gave stick slip behaviour.

3.8.2 6 mm Solid Rod (sintered diameter)

6 mm sintered diameter solid rods were manufactured for TRS testing of the methyl cellulose based feedstock. 8 mm diameter, 450 mm long rods were extruded. Extruding full length rods allowed for uninterrupted extrusion, reducing human induced defects from handling. Rods were cut in the green state which resulted in 15-20 mm curved rod ends which were later removed. Cutting in the as extruded state at shorter lengths often resulted in green state cracking. Therefore each rod was cut using diamond wheel slitting machines after drying and sintering. Sections of 145 mm long were cut for the TRS test rig.

3.8.3 14 mm Coolant Hole Rod

Following the 6 mm extrusion test and validation of materials from TRS testing, the manufacture of complex geometries at large diameter was evaluated. Only the methyl cellulose based formulations were evaluated with coolant hole geometries as other systems could not be dried at larger diameters. Formulations containing 8, 10, 15 and 16 mass % methyl cellulose in the binder pre-mix were included in the trials. Other variants of WC-Co solids loading (40.6, 41.6 and 42.6 volume %) were also evaluated for the 8% cellulose binder. 14 mm rods with coolant channels were extruded with a view to moving onto large scale production. Production trials were considered once the formulation had passed all of the standard tests for product quality. The holes are formed by the insertion of a core pin into the flow stream; this is shown in Figure 51.

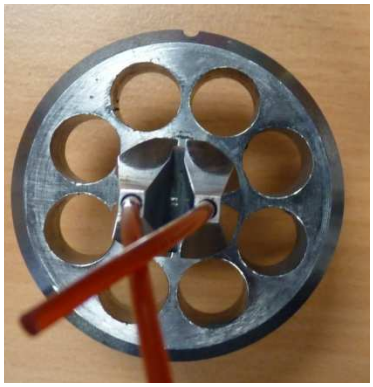

Figure 51 Sandvik Hard Materials extrusion core pin with filaments

A number of alternative core-pin and spider configurations were tested, as shown in section 3.12.1. Figure 51 shows the optimum design for the methyl cellulose formulation. An internally rifled die forced the material to twist around the core pin and coolant hole filaments, forming spiralled coolant holes in the product. A range of extrusion ram speeds from 0.07 $mm.s^{-1}$ to 0.5 $mm.s^{-1}$ were tested. Increased ram speed aided accurate die filling without causing stick slip behaviour. Slower ram speeds resulted in the splitting of material around the core-pin and incomplete die filling which was investigated further with improved tooling design. Properties such as pitch (Figure 60), pitch circle diameter (PCD) (Figure 57) and concentricity (Figure 58) were recorded for the coolant hole rods as measures of tolerance. Details of these quality measures are described in section 3.12.

3.9 Drying

Samples were dried in the standard drying cycle used for SHM extruded products in a standard drying oven regardless of extrudate diameter. The drying cycle used was 4 days long with a steady ramp up to 100 °C and a long hold time followed by a steady ramp down. No inert atmosphere or vacuum was applied although extraction was used to remove vapours. Only low volatility components such as water, ethanol or MPG were driven off in the drying cycle. Rods were initially inspected visually under magnification to evaluate surface defects.

3.10 Sintering

All samples were sintered using ALD sinter HIP furnaces at SHM for which the sintering cycle is shown in figure 187. A de-bind cycle was run in the sinter HIP furnace to remove organics up to 400-800 °C. Solid state sintering began at approximately 900 °C as described in section 2.8.1. Liquid state sintering occurred at approximately 1100 °C and beyond and is described in section 2.8.2. The sinter HIP cycle lasts 3 days and occurs in an inert argon and hydrogen atmosphere with high pressure gas applied in the liquid state stage. High pressure was used to remove process and binder induced pores commonly found in extruded products.

3.11 Drying and De-binding Analysis (TGA, DSC and DTA working principles)

The drying and de-binding cycles were analysed using thermal gravimetric analysis, differential thermal analysis and differential scanning calorimetry. Similar working principles apply to each of the heating methods and drying or de-binding cycles can be run on a small scale in order to determine binder removal rates, temperatures and burn off products. TGA essentially measures the change in mass in relation to changes in temperature. The measured weight loss curve provides information on changes in sample composition, thermal stability and kinetic parameters for chemical reactions. DTA however can be used to determine the point at which weight loss is most apparent. As a rule of thumb, TGA relates to mass, DTA relates to temperature difference and DSC relates to heat difference. There are several phenomena that give rise to changes in mass and typically these are split into physical and chemical categories for TGA (table 13) [157].

Table 13 Mass changes as a result of physical and chemical phenomena

Physical	Chemical
Gas adsorption	Decomposition
Gas desorption	Break down reactions
Phase transitions • Vaporisation • Sublimation	Chemisorption • Adsorption by means of chemical interactions

DTA is slightly different in that the sample in question is heated simultaneously with an inert reference sample. Both the sample and reference are connected to thermocouples and the difference in voltage between the thermocouples is recorded. The voltage difference corresponds to differences in temperature. DTA is shown schematically in figure 52.

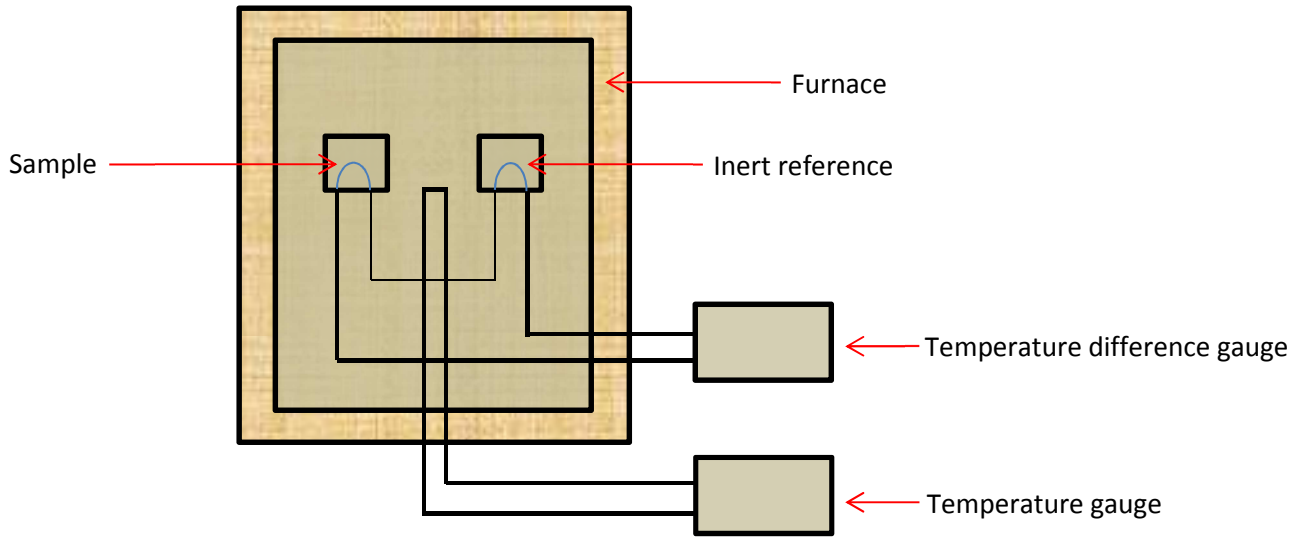

Figure 52 DTA equipment schematic

Depending on the manufacturer of the equipment, peaks in and troughs in the differential temperature then represent crystallisation (exothermic reaction) or melting (endothermic reaction) of the sample. For DTA, the observed phenomena can also be split into physical and chemical categories (table 14) [157].

Table 14 DTA physical and chemical phenomena

Physical	Chemical
Adsorption	Oxidation (exothermic)
Desorption	Reduction (endothermic)
Crystallisation (exothermic)	Chemisorption (exothermic)
Melting (endothermic)	Solid state reactions
Vaporisation (endothermic)	
Sublimation (endothermic)	

In both cases of TGA and DTA, during heating the sample receives energy and as a consequence the sample may change its state. As a result, either a phase transition occurs or the internal energy changes. Differential scanning calorimetry (DSC) differs from the above methods in that it is the difference in heating energy between the sample and reference that is measured rather than temperature. DSC measures the temperatures and the heat flows caused by transitions in materials due to temperature changes with time. In essence, DSC is a thermal analysis method that examines how a materials heat capacity changes with temperature. Typically, DSC is used to measure glass transitions, melting and boiling temperatures and crystallinity, which are a result of changes in the

heat capacity. In running the test, the most useful plot is heat flow against temperature and from this plot the glass transition, crystallisation, melting, cross-linking and oxidation points can be determined (figure 53).

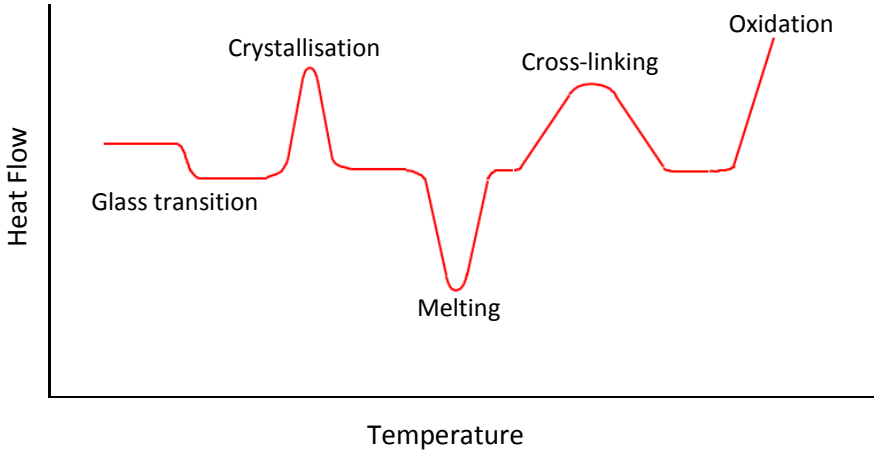

Figure 53 TGA heat flow plot, key points

In an endothermic process which is true for most phase transitions, the heat energy is absorbed and bonds are broken in the sample. Consequently, heat flow to the sample is higher than it is to the reference and therefore the change in heat flow is positive. In an exothermic process, such as crystallisation and cross linking, bonds are formed and the heat flow is negative. Using the above theories and figures, vital information relating to drying and de-binding processes for extrusion binders can be gleaned.

3.12 Production Scale up

3.13 Production Scale Extrusion Equipment

The production scale extrusion equipment is similar to the pilot scale set up shown in figure 9. The internal tooling is the same with the exception of barrel diameter (200 mm) and a series of reducers rather than a single reducer. There are also intricate handling systems situated directly after the gun to allow for automation.

3.13.1 Tooling (spider shear plate configurations)

Figure 54 Production scale experimental spider designs

Each of the spider designs had the same external geometry as the spider blank shown in figure 9. The idea behind using the intricate designs in figure 54 was to improve the flexibility of the tooling set up. The design shown in 51 is limited as only a single core pin PCD is achievable and a new core pin would be required for different products. In each of the designs shown in figure 54, multiple holes can be drilled giving the opportunity to manufacture several products with one set up. Whilst each of the experimental tooling designs were promising for flexibility, the formation of concentric coolant holes was not possible.

3.13.2 Extrusion Die Designs

16, 18 and 20 mm product dies are shown in figure 55 so that the scale of extrusion dies used in the production environment can be appreciated. The serrations present on the inner diameter of the die force the material to rotate around the internal core-pin thus giving a helical coolant holes pattern.

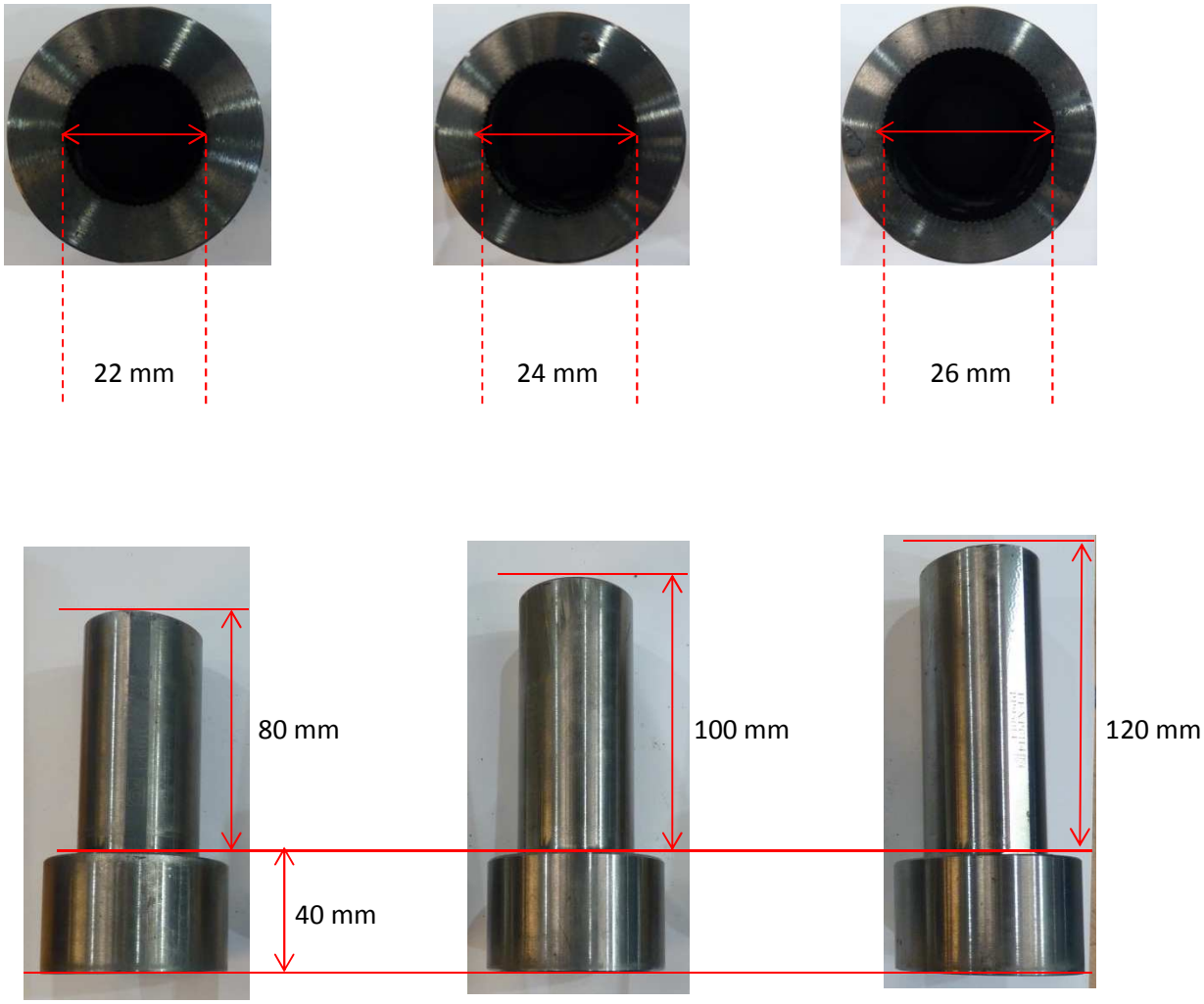

Figure 55 16, 18 and 20 mm product nozzle geometries

The most promising materials were evaluated on production equipment up to 14 mm sintered product diameter with future work focussed on larger scales. The selected system was based on a methyl cellulose formulation. Initially the 8 wt% methyl cellulose formulation was evaluated. This was adjusted to the 10 wt% to increase stiffness which proved necessary in the production environment. Production scale mixing and extrusion is described in Appendix I.

3.14 Quality Inspection

Rods were inspected on pilot and production scale for the properties detailed in Table 15.

Table 15 Quality Check Points

Extruded Rod	Dried Rod	Sintered Rod
Extrusion pressure	Weight loss	Hardness
Extrudate speed	Visual inspection	Density
Concentricity (figure 58)	Microscope inspection	Transverse Rupture Strength (TRS)
Coolant hole size		Porosity (Microscopy)
Outer diameter		Carbon balance
Pitch Circle Diameter (PCD) (figure 57)		Scanning Electron Microscopy (SEM) analysis
Pitch (figure 60)		Linear Shrinkage
		Cross-sectional shrinkage
		Concentricity
		Hole size
		Diameter
		Pitch Circle Diameter (PCD)
		Pitch
		Grain size distribution

Concentricity was a measure of how centralised the two coolant holes were with the outer diameter of the rod. Figure 58 shows a schematic of a rod that is within and out of specification. Figure 59 (left) shows a sintered sample with a concentricity of 0.2 which is within specification. Figure 59 (right) shows a sample from the same rod with a concentricity of 0.58 which is outside of the specification. There was a tendency for the concentricity to drift within specification. A separate study was evaluated to determine the cause of the drifting although it was believed to be a product of material and filament stability. The concentricity was determined from the radial distance between the centre of the PCD line and the rod centre. (Figure 58). PCD was a measure of distance between the two coolant holes from centre to centre (Figure 57). Concentricity, pitch, PCD, diameter and hole size (coolant hole diameter) were all measured using a shadowgraph. Each sample to be measured was placed on the shadowgraph stage and had bright light shone onto the front surface which projected a large image of extrudate cross-section. 12 data points corresponding to 4 points per each respective circle of 2 coolant holes and the outer diameter of the projected cross-section were logged (figure 56). The diameters, cross-section centre and relative position of coolant holes were determined from the logged data points (figure 56). The centre of the cross-section is determined from chord mid-points which are obtained from points 9, 10, 11 and 12 in figure 56 on the cross-section outer diameter. In a similar way, the coolant hole centres are determined from

points 1 through to 8 (figure 56). Knowing the hole centres and cross-section centre is vital for determining all other measurements.

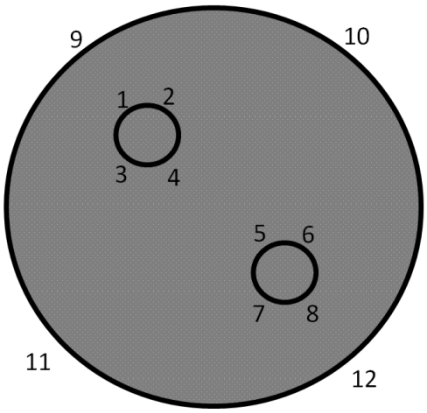

Figure 56 Hole centre determination

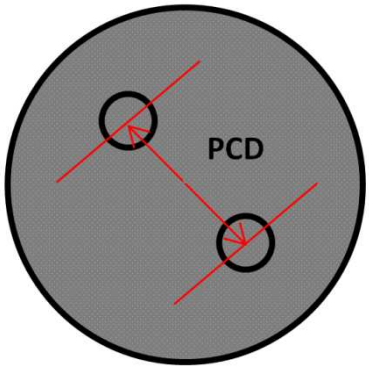

Figure 57 PCD measurements

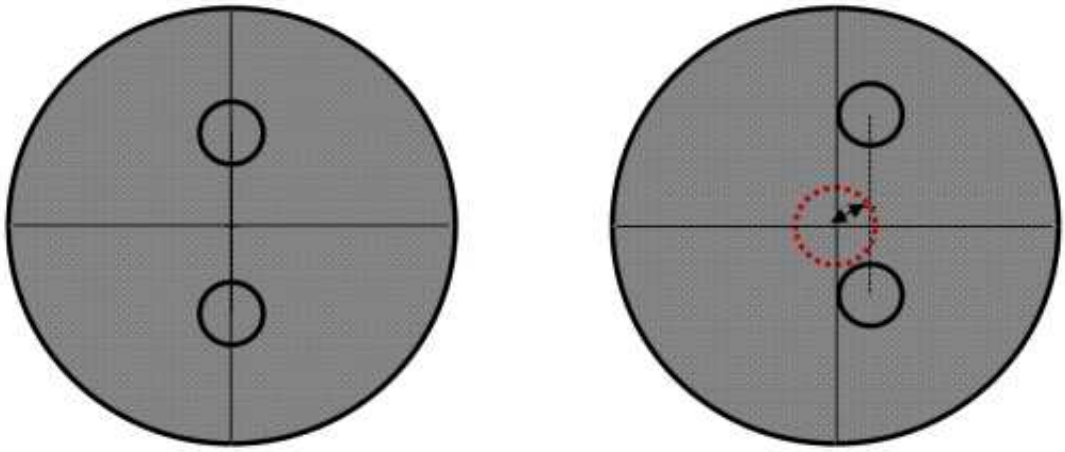

Figure 58 Cross-section of rod with coolant holes showing perfect and poor concentricity (left and right respectively)

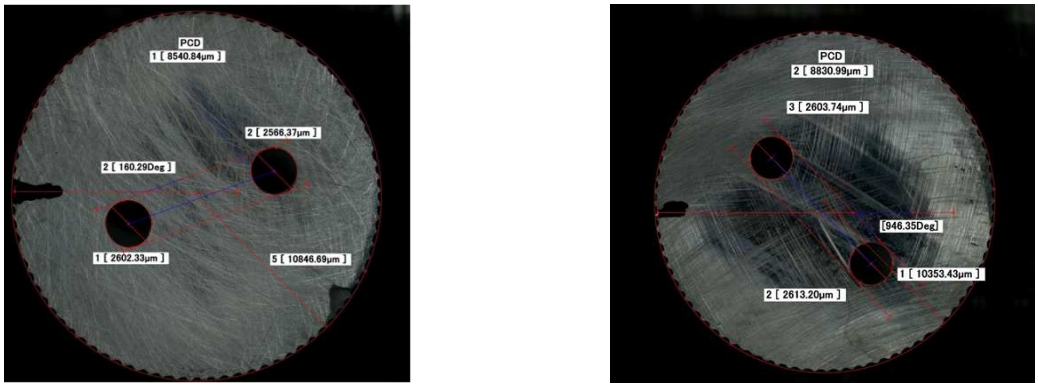

Figure 59 Good concentricity (left) poor concentricity (right), sintered WC-Co sample

The coolant holes were also measured to determine filament wear that occurred during extrusion. Wear caused filament diameter reduction and hence smaller diameter coolant hole formation. Many of the properties were measured in both the extruded and sintered states and had specifications assigned based on the demands of the customer. If extruded properties were outside of specification then extrusion conditions and tooling were adjusted accordingly before batches were sintered. TRS testing and Hardness testing are described in sections 7.4.1 and 7.4.2 respectively.

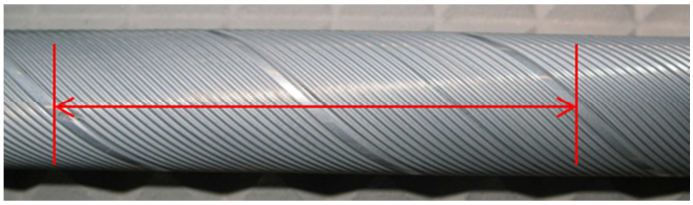

Figure 60 Helical pitch measurement distance, extruded WC-Co sample

The pitch length measurement was taken between a full rotation of the helix (Figure 60). Pitch measurements on production trials were more reliable as more data could be analysed than on a pilot scale. Pitch measurements were only taken for the methyl cellulose based dough as other materials were not extruded with rifles. The pitch was an important quality measure because it defines the finished product and how the flutes are machined into the rod to form drills. Therefore pitch was measured both for consistency and length. Consistent pitch was vital as a varying pitches caused incorrect coolant hole position. Position of coolant holes is important as they need to be in the centre of the drill flutes in the finished product. In extreme cases, the coolant holes could protrude through the flutes. PCD and concentricity measurements were destructive measurements as the rod had to be sectioned carefully in the extruded state in order to analyse the internal dimensions. As well as analysing the physical dimensions of the samples, optical and scanning electron microscopy was used to qualify material. Sintered SEM samples were used to determine the grain size distribution using the linear intercepts method. Micrographs were divided by five lines and intersections of those lines by WC grains were counted and marked using image analysis software.

The size of the intersecting WC grain was then recorded for each of the five lines on display to give an average grain size. Whilst this was a subjective process, it was used to give a comparative method of determining the grain size of sintered samples.

Chapter 4 Extrusion Binder Rheological Analysis and Selection

A series of experiments were designed to characterise the binder materials in terms of viscosity and viscoelasticity using controlled stress rheometry and dynamic oscillatory rheometry respectively. Initially, the selected binder systems were analysed with the compositions given in Table 10. Following evaluation without PEG the binders were further tested to simulate the interaction with the PEG contained in the WC-Co feed powder.

4.0 Binder Requirements

Extrudate was required to have a similar stability, green strength and extrusion flow properties to the SHM commercial PEG system whilst being able yield products greater than 12 mm finished diameter. The extrudate properties were related closely to binder behaviour and therefore binder flow properties have been compared against the SHM standard system. Binder materials detailed in Table 10 were selected based on the literature survey reported in Chapter 2 and the required properties detailed in section 3.2.1. Many variants of the binder systems in Table 10 were generated as a result of fine tuning. Fine tuning such as increasing binder stiffness and hence dough stiffness was required in the production environment. Increased dough stiffness was also achieved by increasing the WC-Co solids loading.

4.1 Binder Rheological Analysis

4.1.1 Shear Stress Analysis

Binder shear viscosity was analysed with shear stress sweeps as described in section 3.5.1. Figure 61 shows the flow curves of binder materials from Table 16 and Table 17 in which shear rate is given as a function of shear stress. Binder names and descriptions have been given in Table 10.

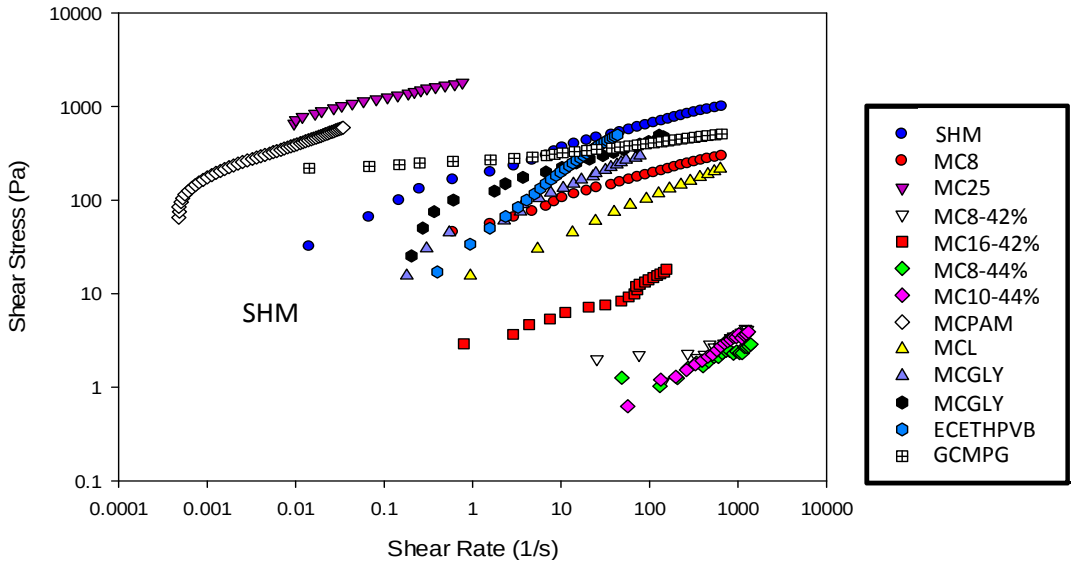

Figure 61 Binder shear stress vs shear rate, shown as a ln/ln plot to allow for material comparison

The Binder materials exhibited a range of shear viscosities for any given shear rate either side of the SHM binder system. Whilst a log plot of all binders is useful for comparative measures it does not show details of flow properties. Each binder system was measured in a shear stress ramp test and each ramp was repeated three times. The shear stress and shear rate responses were averaged at the same point in time for each experiment. The standard deviation range of the shear rate response is given in Table 16. The range of standard deviation shows a greater error in measurement at higher shear stresses. The maximum shear rate response is also given.

Table 16 Shear rate response standard deviation

Binder	MIN Standard Deviation	MAX Standard Deviation	Max shear rate response (1/s)
SHM	0.01	141	325
MC8	0.47	446	943
MC25	0.00050	0.49	1.34
MC8-42	10.6	51.90	1281.3
MC16-42	0.51	21.95	155
MC8-44	0.2	17.50	1397
MC10-44	3.10	69.01	1312
MCPAM	0.00005	0.003	0.03
MCM	0.42	282.25	1195
MCL	0.021	0.90	78
MCGLY	0.0040	30.80	128
ECETHPVB	0.00067	0.05	3.155
GCMPG	0.00014	0.015	0.12

A shear stress sweep showing standard deviation for the SHM binder is given in Figure 62.

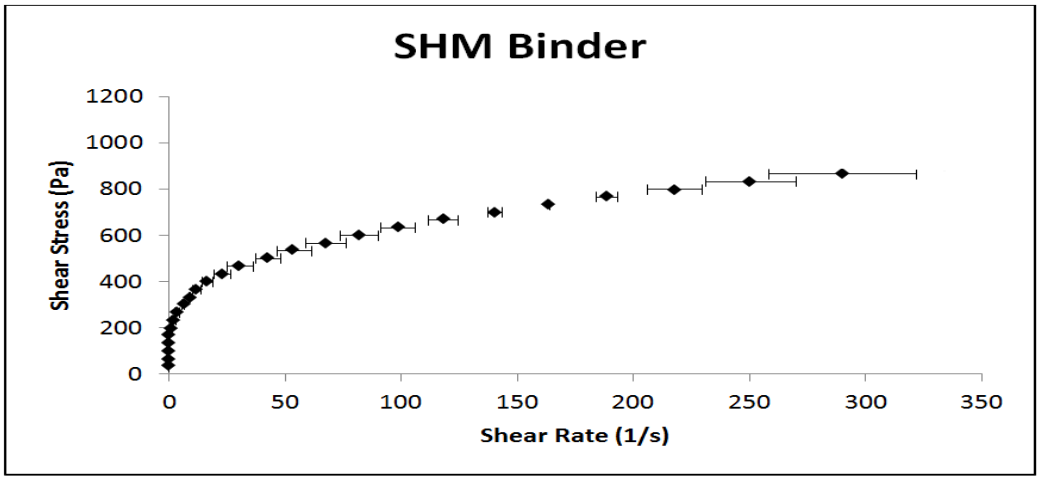

Figure 62 SHM binder shear rate as a function of applied shear stress, showing standard deviation

Figure 62 shows that the maximum standard deviation occurred at higher shear stresses. This trend was observed for each binder system tested. The standard deviation was often large due to sample loading and therefore for each binder system analysis an example has been given in which the three repeated tests are shown rather than the standard deviation. Standard deviations tabulated have been used as a guide of test accuracy combined with the repeated test figures. A high standard deviation at the maximum shear rate is due to greater test variation at higher rotational speeds, as indicated in Figure 63.

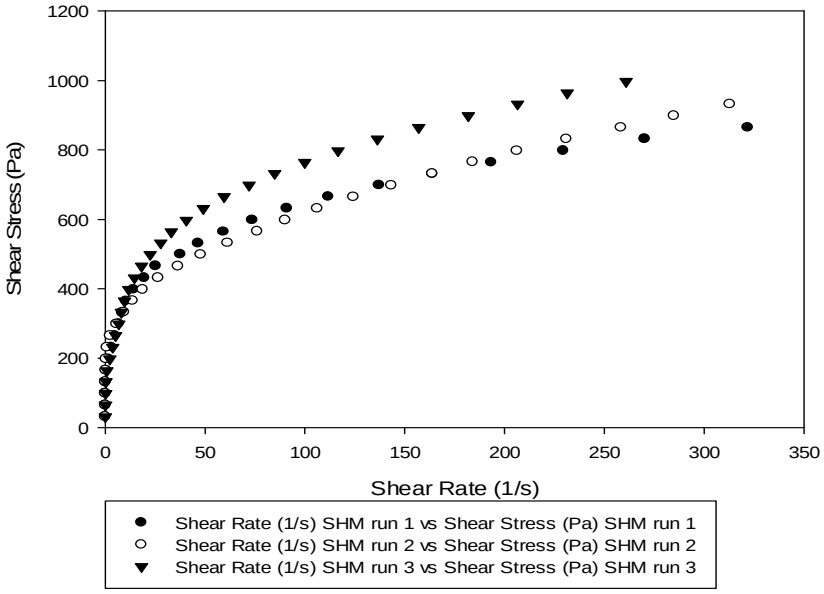

Figure 63 SHM binder repeated shear rate as a function of applied shear stress

Variations of methyl cellulose formulations were examined to obtain rheological properties desired. The ratio of cellulose to water in the binder system was increased in order to vary binder shear viscosity. Glycerol was added to the methyl cellulose binder system with the aim of increasing dough

green strength and stability as it is a known viscosity modifier for methyl cellulose. The binder systems have been separated into the groups in Table 17.

Table 17 Binder Groups

Group 1	Group 2	Group 3	Group 4
SHM Standard	MC, Water 8%	MCGLY1	MC8PEG40
MC, Water 8%	MC, Water 10%	MCM	MC8PEG42
MC, Water, Polyacrylamide	MC, Water 11%	MCL	MC8PEG44
Ethyl Cellulose, Ethanol	MC, Water 12%	MCMPG	MC10PEG40
Ethyl Cellulose, Ethanol, PVB	MC, Water 13%		MC10PEG42
Gelucire 50/13, MPG	MC, Water 14%		MC10PEG44
	MC, Water 16%		MC12PEG42
	MC, Water 18%		MC15PEG42
	MC, Water 20%		MC16PEG42
	MC, Water 22%		
	MC, Water 25%		

Group 1 binders were the starting formulations of this research based on the selection process outlined in section 3.2.1. Group 2 binders were extensions of the initial methyl cellulose formulation (MC8) as that binder showed the most promise from group 1. Group 3 binders were modified variants of the same MC8 binder and were developed in parallel with group 2 binders. Group 4 binders are based on the binders from group 2. They contain the added PEG to represent the binder that would be formulated when the PEG in the powder feed becomes solubilised on mixing with MC solutions. Compositions and descriptions of the binders in Table 17 have been given in Table 10.

4.1.1.1 Group 1 Binders Shear Stress Sweep data

Each of the binders was tested rheologically using the controlled stress rheometer with a cone and plate geometry (Figure 19). Flow curves were generated and the data fitted to the Herschel Bulkley equation represented by the solid black line. Data points (black) were averaged over three repeated tests and those within the confidence bands (blue) indicate whether or not the data was fitted to the model with 95 % accuracy. Data points exceeding the red plots were not within suitable accuracy to be predicted by the model. For all binders measured in this section, the model fit parameters are given in table 18 and figures 72 and 73.

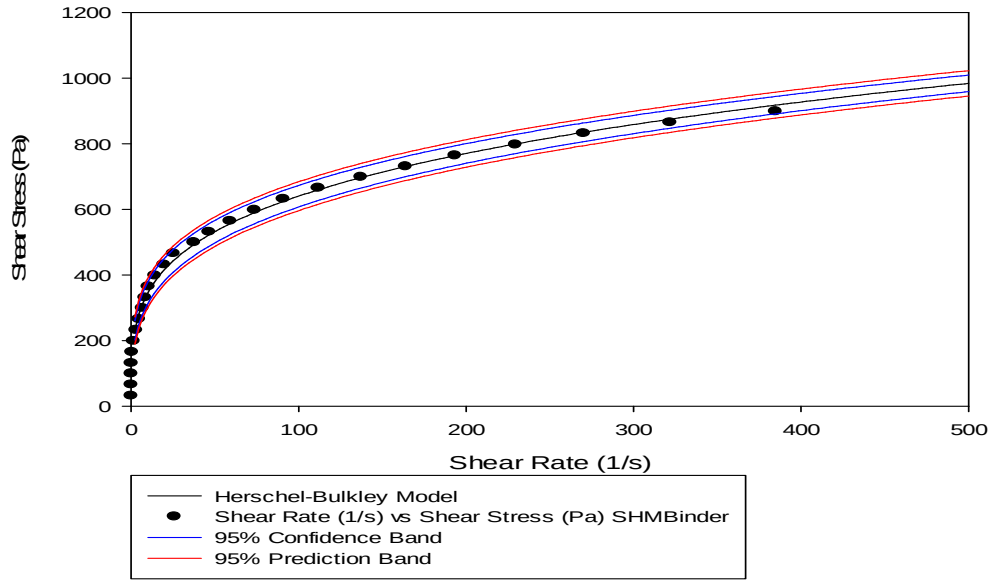

Figure 64 SHM binder, shear rate as a function of applied shear stress

Figure 64 shows the shear stress sweep of SHM production binder material made up of three grades of PEG and MPG. Figure 65 shows the methyl cellulose (MC) formulation in a ratio of 8 mass % MC to water.

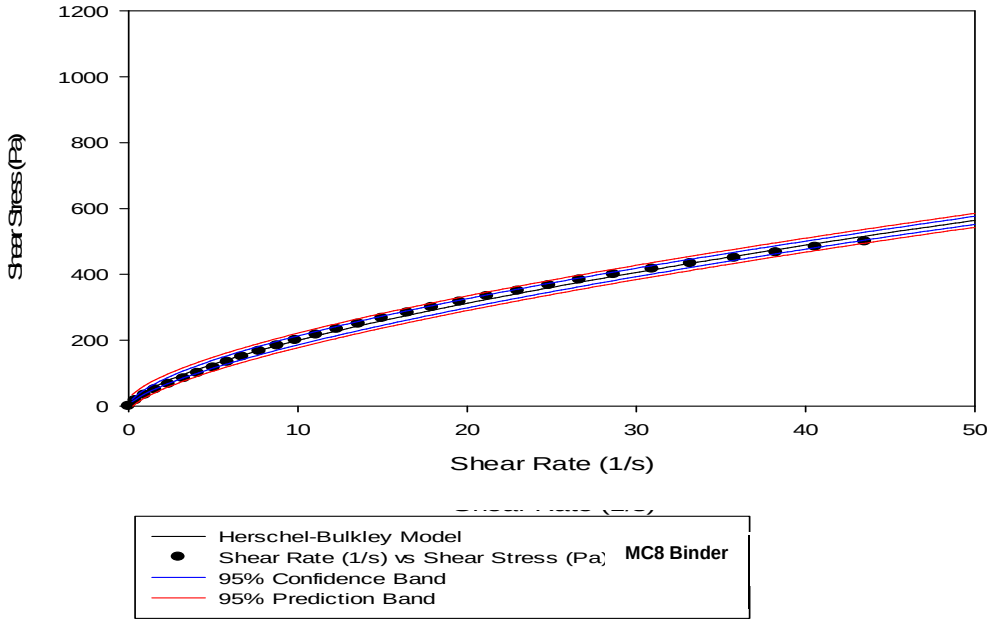

Figure 65 MC, and water binder (8%), shear rate as a function of applied shear stress

A direct comparison would show that methyl cellulose binder is much lower in shear viscosity for any given shear rate. For example, an applied shear stress of 200 caused the methyl cellulose based binder to give a shear rate response of 9.83 1/s. In contrast to this, the SHM binder had not begun to flow at this point. The shear rate response was different for many of the binders and hence required

different scaling in order to describe the binder flow properties individually. The shear stress had to be varied to obtain rheological information about specific binders thus giving different shear rate responses. The addition of polyacrylamide to the MC solution increased the apparent viscosity at a given shear rate. This is evident by comparing Figure 64 with Figure 65. The addition of polyacrylamide gave the formulation properties tending towards those of the SHM binder system such as an apparent increased yield stress. However, Figure 66 shows that the MCPAM binder flow curve is more accurately represented by a power law model which implies no yield stress. Although Figure 64 and Figure 66 show similar flow curves, the viscosities at any given shear rate are significantly different.

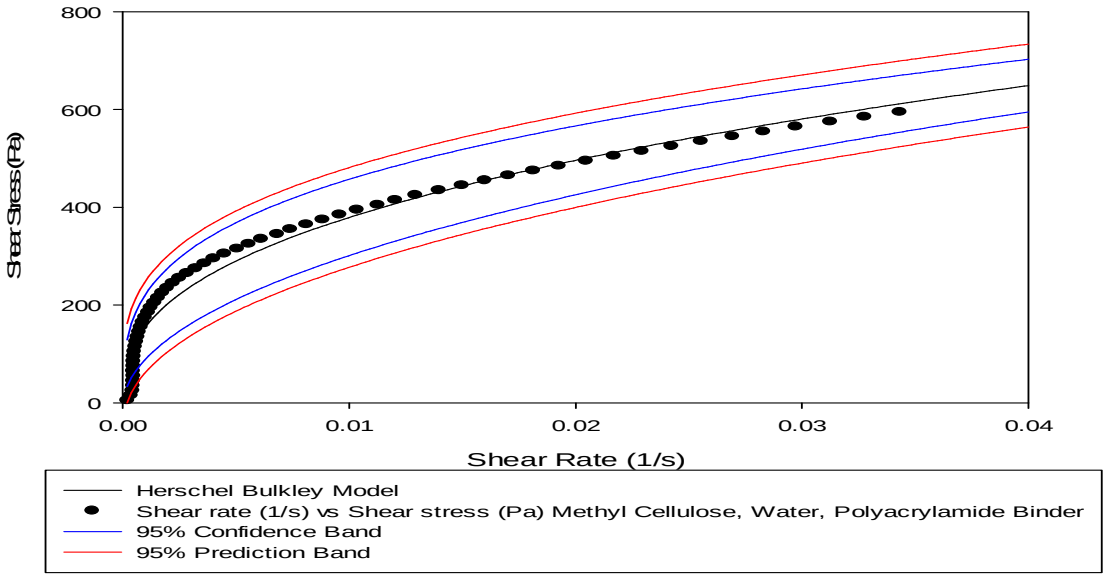

Figure 66 MC, water, PAM binder, shear rate as a function of applied shear stress (Herschel Bulkley)

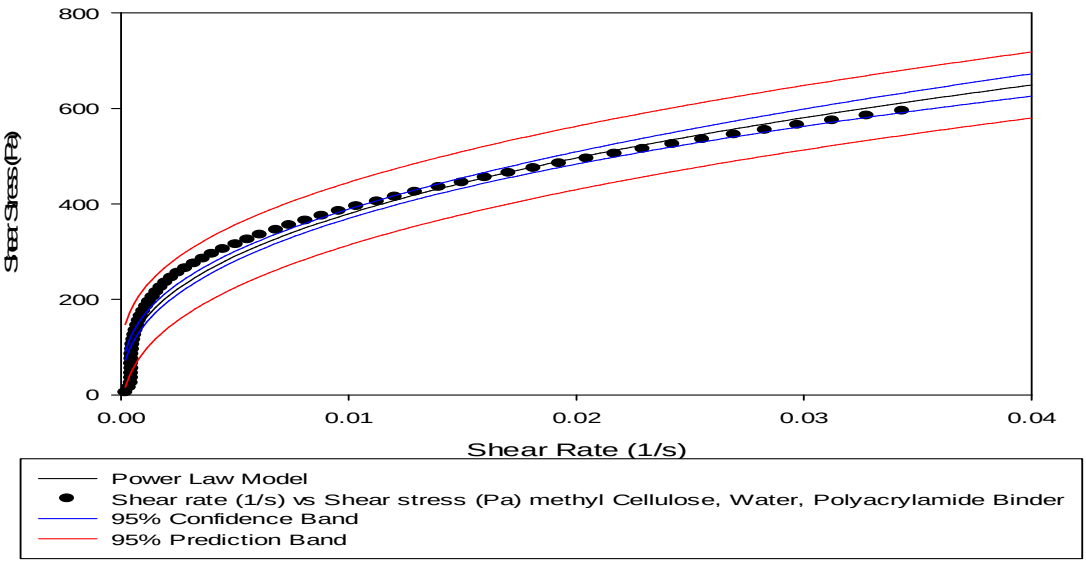

Figure 67 MC, water, PAM binder, shear rate as a function of applied shear stress (power law)

Figure 68 shows that ethyl cellulose when soluted in ethanol is effectively Newtonian. The addition of PVB gives a significant change to the flow properties. The fluid appears to become strongly shear thinning with a strongly developed yield stress. Figure 68 and Figure 69 show that the material is best fitted by a Herschel Bulkley model although statistically the best fit is the power law as indicated by the narrower confidence bands.

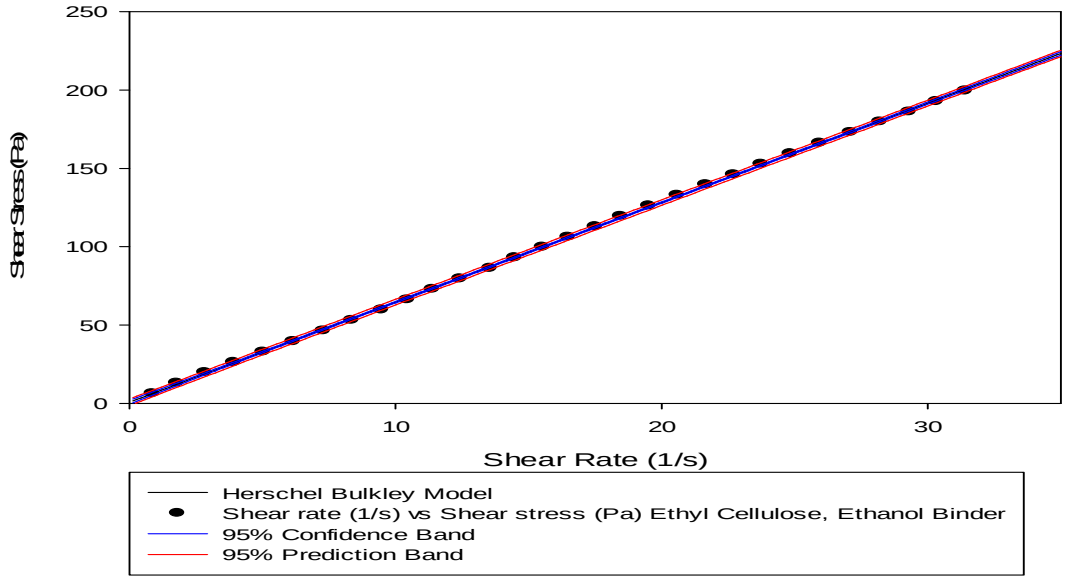

Figure 68 EC, ethanol binder, shear rate as a function of applied shear stress

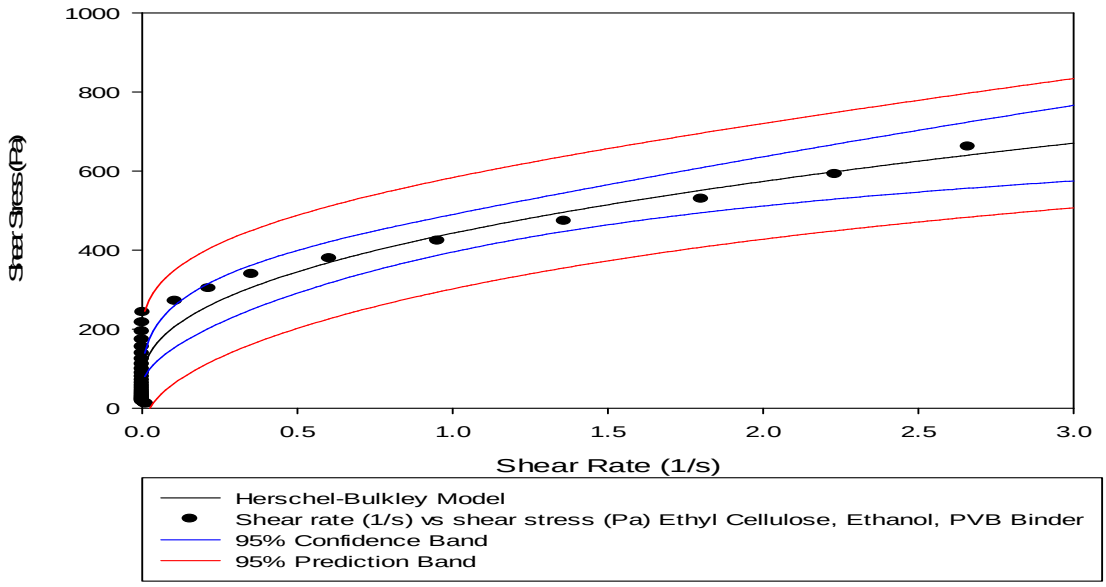

Figure 69 EC, ethanol, PVB binder, shear rate as a function of applied shear stress

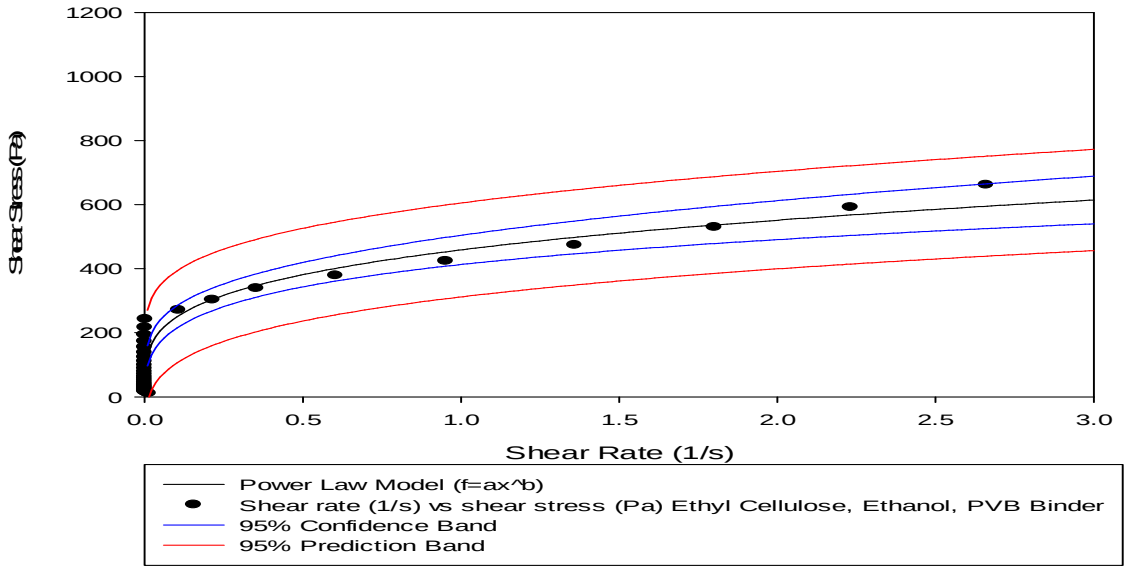

Figure 70 EC, ethanol, PVB binder, shear rate as a function of applied shear stress

Figure 70 shows the Gelucire 50/13-MPG based binder system. Whilst it was similar in preparation techniques and physical appearance to the SHM binder system, the flow properties were different owing to a lower shear viscosity for any given shear rate. The majority of the binders had flow curves allowing suitable predictions based on the Herschel Bulkley model.

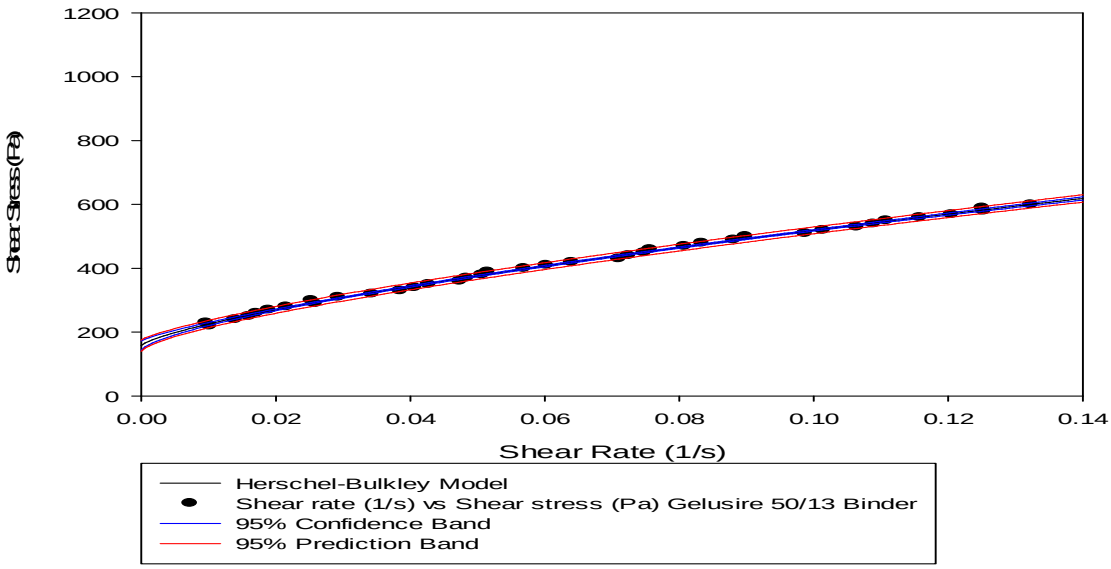

Figure 71 GC 50/13, MPG binder, shear rate as a function of applied shear stress

The parameters for group 1 binders based on the Herschel Bulkley model are given in Figures 72 and 73. The power law data for the Ethyl cellulose based binder containing PVB is also included. Each binder has been assigned a number (Table 18) for identification on each parameter plot.

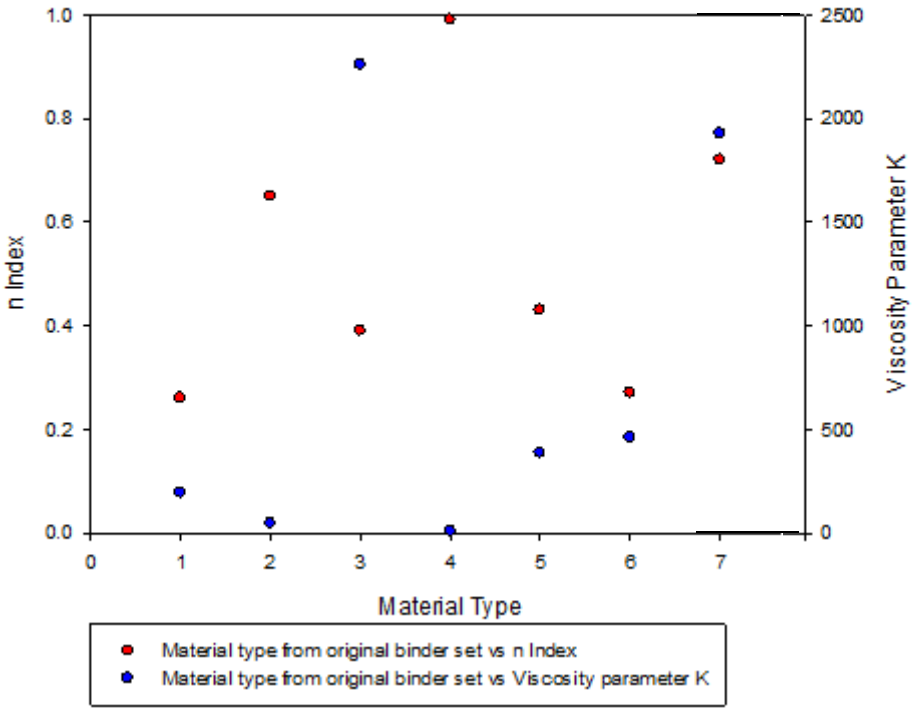

Figure 72 Herschel Bulkley Parameters Group 1 (see table 18 for binder description)

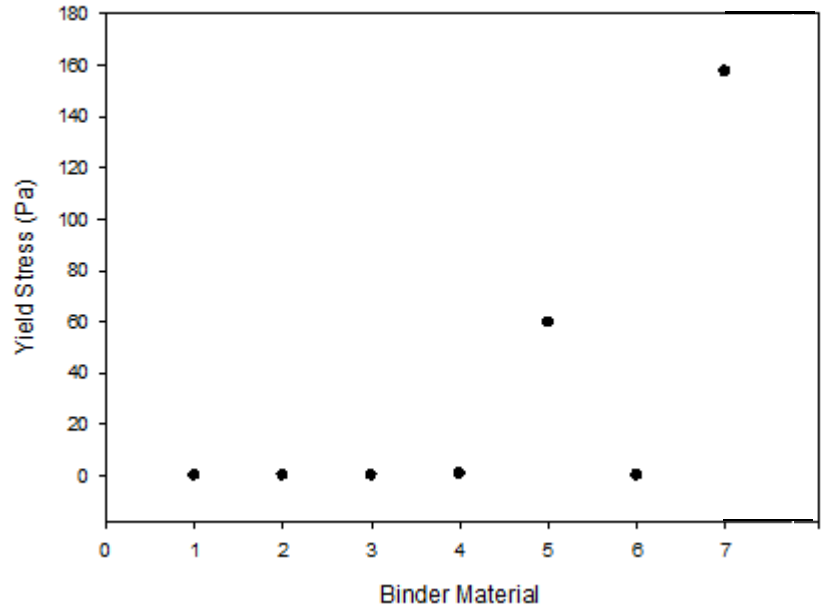

Figure 73 Binder group 1 yield stress values (see table 18 for binder description)

From Figure 72 the MC8 binder would be selected for further investigation as it has a similar viscosity parameter (K) to the SHM binder thus indicating similar flow behaviour. The ethyl cellulose based binder material also showed similar properties.

Table 18 Group 1 Binders Herschel Bulkley Parameters

Binder	Binder	WC-Co Solids Content (vol %)	T_Y (Pa)	K value (Pa.s^n)	n value	R squared
1	SHM Commercial	-	$2.5x10^{-14}$	193	0.26	0.997
2	MC8	41.6	$4.5x10^{-16}$	45	0.65	0.997
3	MCPAM	38	$4.1x10^{-14}$	2258	0.39	0.966
4	ECETH	45.8	0.67	6	0.99	0.999
5	ECETHPVB	45.8	59.62	383	0.43	0.860
6	ECETHPVB (Power Law)	45.8	0.0	460	0.27	0.870
7	GCMPG Binder	48.5	157.56	1930	0.72	0.998

Figure 73 shows that yield stresses predicted by the Herschel Bulkley model appear to be negligible although in practice that is not the case as there is a clear resistance to non-assisted flow.

4.1.1.2 Group 2 binder Shear Stress Sweep data

For group 2 binders, the mass ratio of cellulose to water in the binder ranged from 8 to 25%. For each of the samples measured in this section, the model fit parameters are given in table 20. Figure 74 shows how the shear rate response changed with cellulose concentration. Separate plots showing the Herschel Bulkley model fits are also presented for variants containing 8, 10 and 22 mass % methyl cellulose. Plots of K and n parameters and yield stress with increasing cellulose content are shown in Figures 80 and 82 respectively.

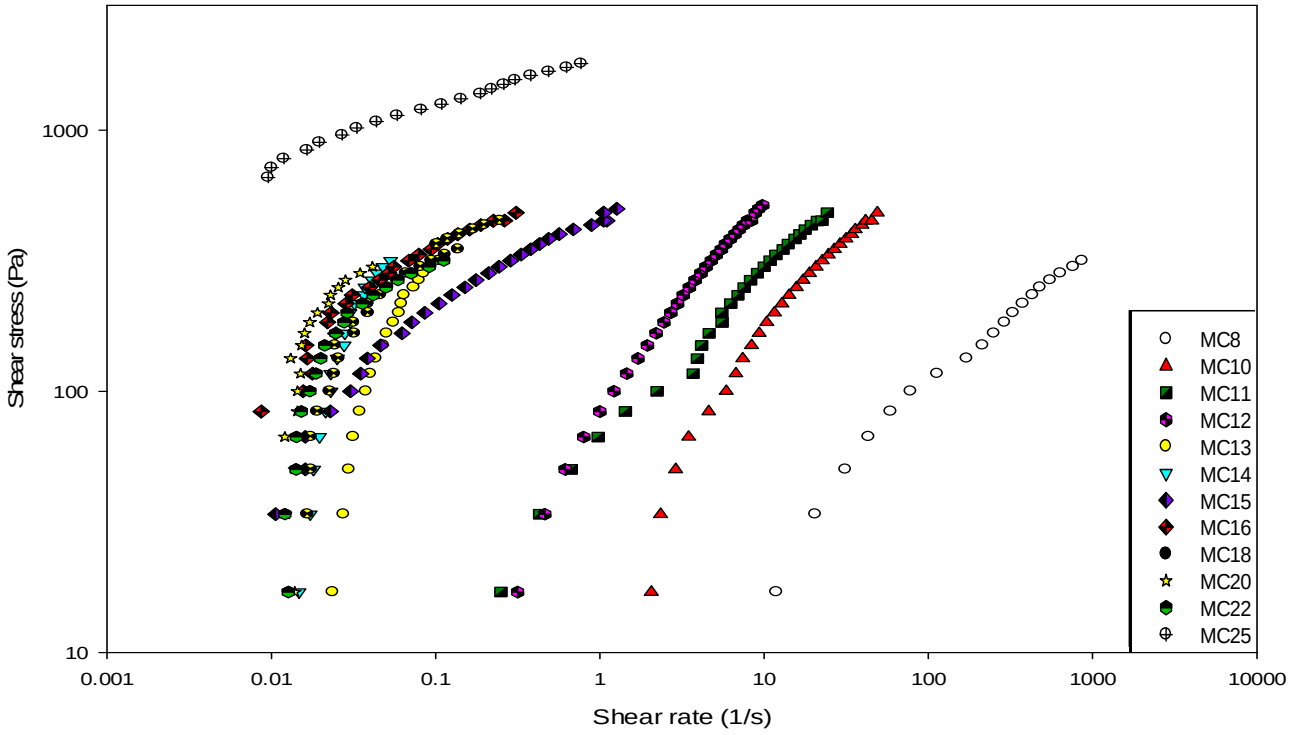

Figure 74 Group 2 binders, shear rate as a function of applied shear stress plot

A shift in shear rate towards the y axis with increasing cellulose content represents an increase in effective binder shear viscosity. Data plotted in Figure 74 becomes clustered beyond 14 mass % methyl cellulose. The standard deviation of repeated tests is low at high mass % cellulose content indicating good repeatability. However, the maximum shear rate response is low even at high shear stress which is indicative of wall slip. The presence of constant slip gave misleading data in the form of overlapping flow curves (Figure 74). The stress sweeps were therefore plotted from 8-14 mass % cellulose content where the maximum applied shear stress was restricted to less than 700 Pa (Figure 64).

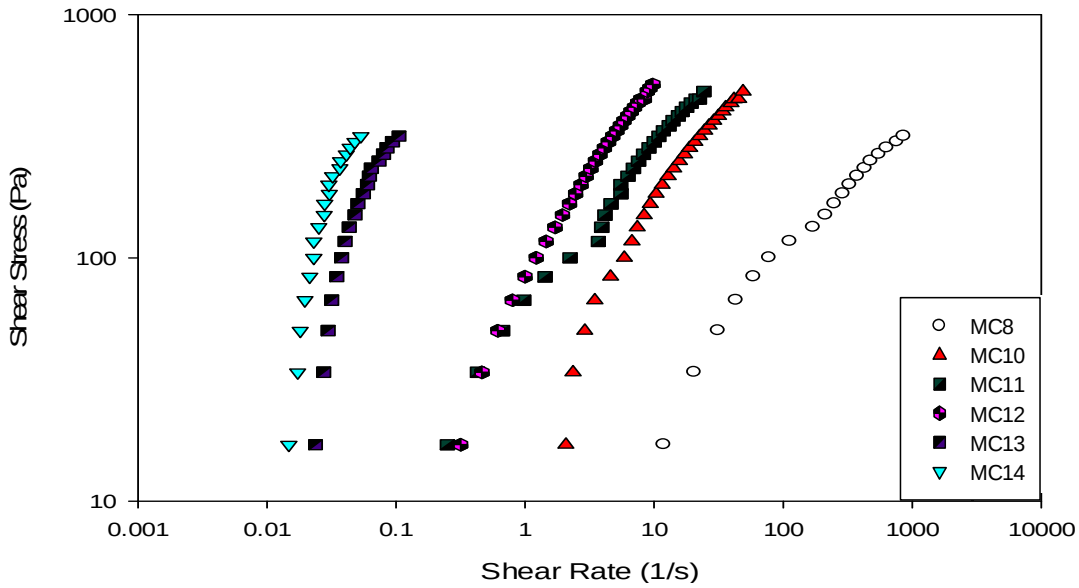

Figure 75 Group 2 binders, shear rate as a function of applied shear stress 8-14 mass % MC

Figure 75 shows that the binder shear viscosity increases with cellulose content for a given shear stress although not systematically. The unsystematic nature of this data is due to binder preparation, aging and rates of dissolution of the cellulose in water. 8 and 10 mass % cellulose plots (Figures 77 and 78) are of particular interest as these binders were mixed on a production scale. The binder prepared with 22 mass % methyl cellulose (Figure 68) has been plotted to show the inaccuracies observed at higher shear viscosities. The standard deviation of the repeated shear stress sweeps at the minimum and maximum shear rate and the maximum shear rate response are given in Table 19.

Table 19 Group 2 binder standard deviation

MC Variant	Standard Deviation at minimum shear rate	Standard deviation at maximum shear rate	Maximum shear rate response
8	+/- 0.235	+/- 223	943
10	+/- 0.01	+/- 1.335	51.6
11	+/- 0.005	+/- 0.36	25.0
12	+/- 0.005	+/- 0.045	9.8
13	+/- 0.005	+/- 0.005	4.25
14	+/- 0.005	+/- 0.005	2.16
15	+/- 0.005	+/- 0.1	1.52
16	+/- 0.02	+/- 0.075	0.50
18	+/- 0.02	+/- 0.025	0.25
20	+/- 0.005	+/- 0.005	0.05
22	+/- 0.015	+/- 0.045	0.25
25	+/- 0.005	+/- 0.245	1.34

Similarly to the group 1 binders, the standard deviation was found to be larger at the maximum shear rate. The Herschel Bulkley parameters are given in Table 20.

Table 20 Methyl Cellulose Variants Herschel Bulkley Parameters

MC Variant	T_y (Pa)	K value (Pa.s^n)	n value	HB model fit R squared value
8	$1.1x10^{-14}$	8.80	0.54	0.99
10	$2.8x10^{-15}$	48.5	0.61	0.99
11	$2.2x10^{-15}$	66.1	0.63	0.99
12	$1.2x10^{-15}$	104	0.70	0.99
13	$4.2x10^{-15}$	378	0.49	0.99
14	$3.2x10^{-15}$	388	0.46	0.99
15	$8.8x10^{-15}$	442	0.37	0.98
16	$8.8x10^{-15}$	841	0.37	0.96
18	$4.3x10^{-14}$	319	0.30	0.92
20	$8.6x10^{-16}$	525	0.19	0.79
22	$4.7x10^{-15}$	639	0.13	0.97
25	$2.4x10^{-15}$	1944	0.20	0.99

An example of the three repeated tests for the MC10 variant is given in Figure 76. An extension of Figure 76 would indicate that the data points intercept the shear rate axis which shows that the material is able to flow without an applied force and explains why the yield stress is zero in practical terms (Table 20).

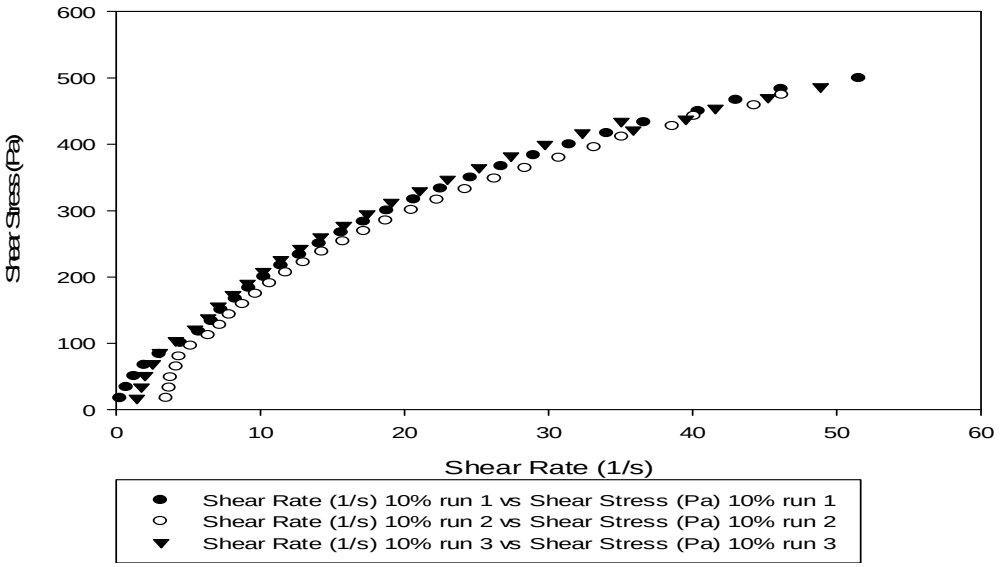

Figure 76 MC, Water 10% binder, shear rate as a function of applied shear stress, including repeated tests

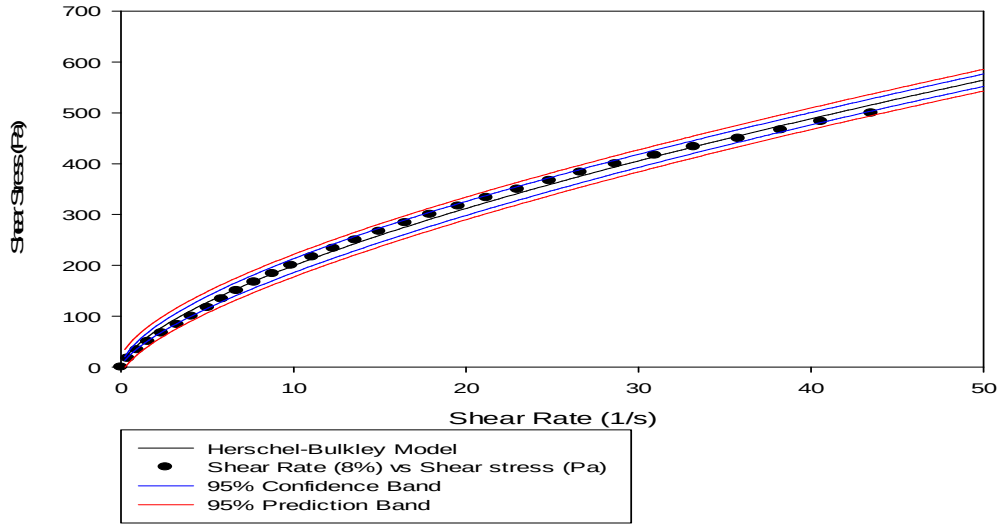

Figure 77 MC, Water 8% binder, shear rate as a function of applied shear stress

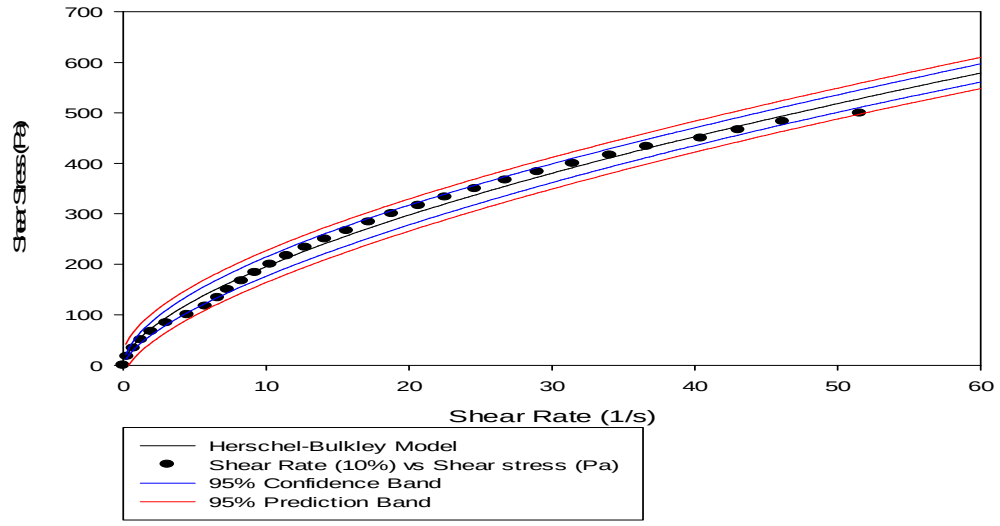

Figure 78 MC, Water 10% binder, shear rate as a function of applied shear stress

Shear stress/shear rate plots for the remaining binders in group 2 are given in appendix D. Kinks in data are shown in the flow curves for 13 and 14 mass % cellulose binders. This is procedure error rather than representative of the material behaviour. In some cases the accuracy of the Herschel Bulkley model is poor, particularly for higher shear stresses with more viscous binders. Figure 79 shows that as the shear stress increases (leading to a higher shear rate response) the accuracy of the model drops. In these cases material is slipping between the rheometer surfaces, thus giving a misrepresentation of material flow. This occurred for binders of high cellulose content, such data has been removed from Figure 74.

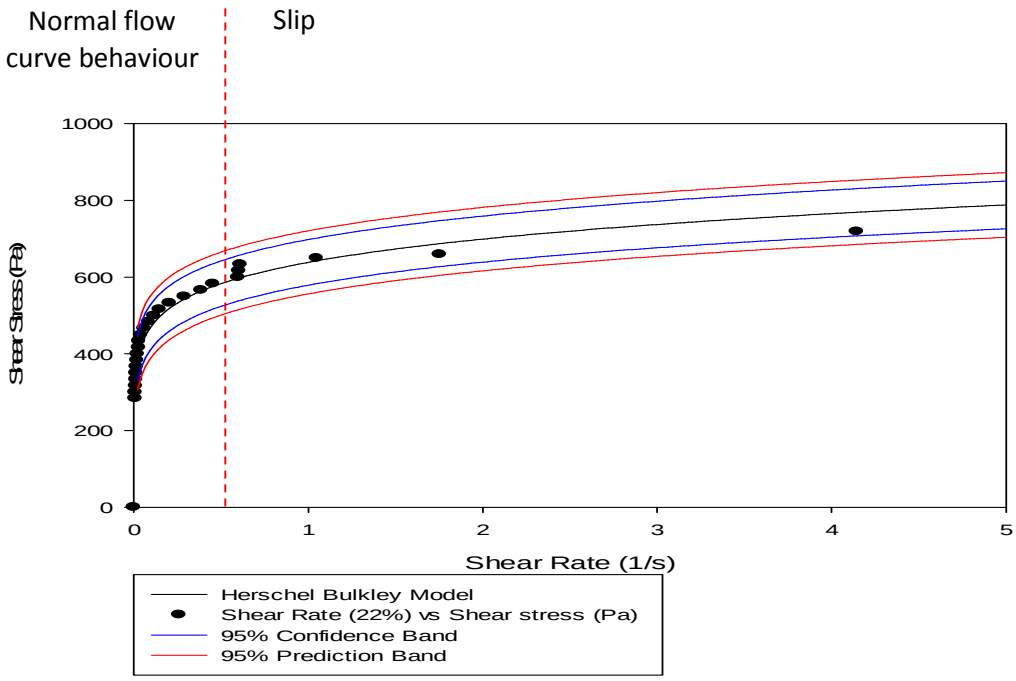

Figure 79 MC, Water 22% binder, shear rate as a function of applied shear stress

The Herschel Bulkley parameters have been plotted in Figure 80. Due to wall slip behaviour, data for methyl cellulose content above 14 mass % is not reliable. Data has been re-plotted omitting the higher cellulose contents in Figure 75.

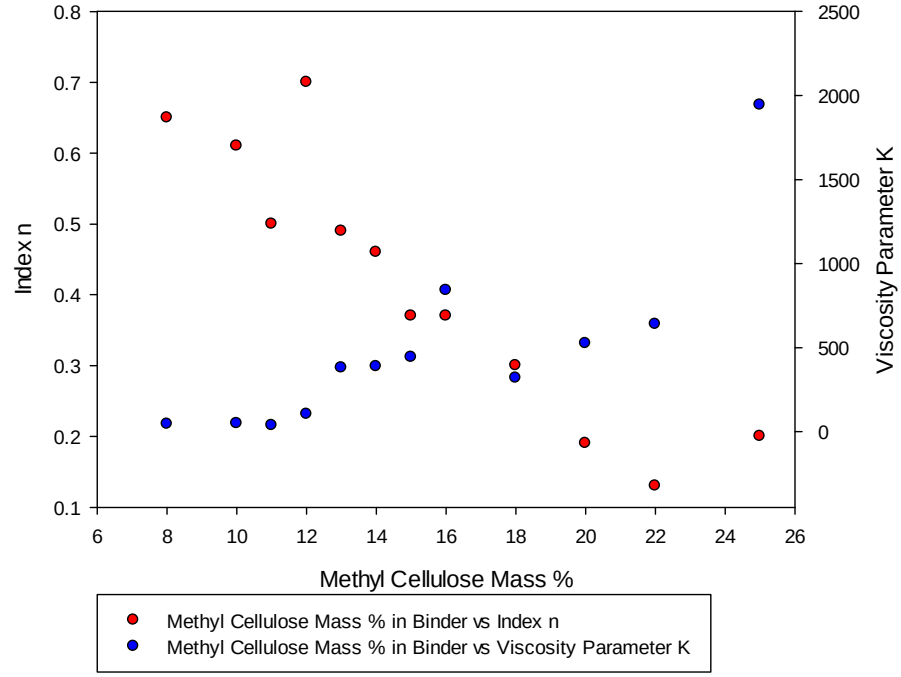

Figure 80 Group 2 binder, Herschel Bulkley Parameter vs MC Mass %

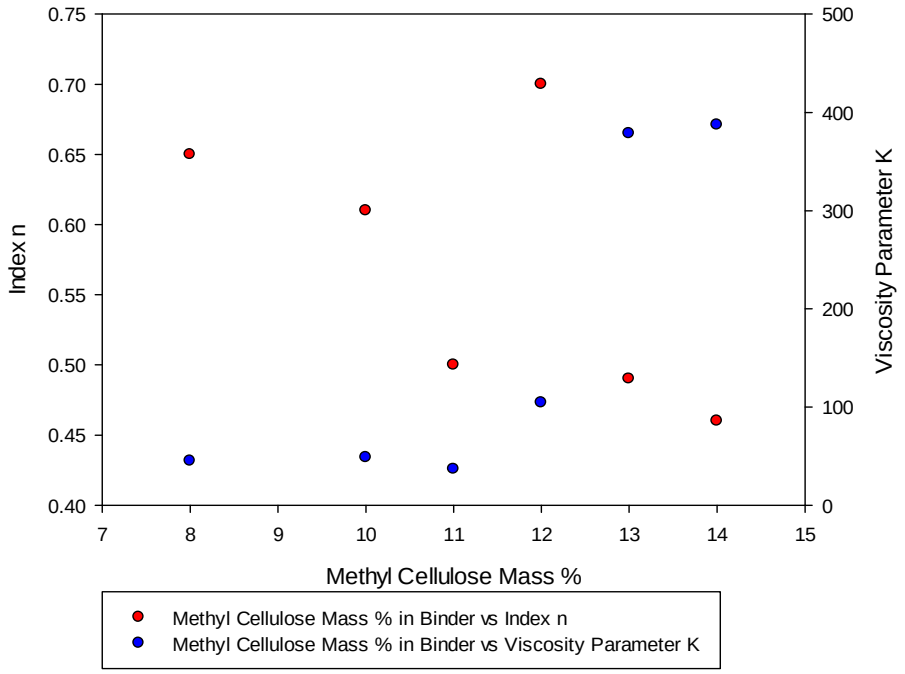

Figure 81 Group 2 binder, Herschel Bulkley parameter vs MC Mass % (MC8-MC14)

Figure 81 shows the yield stress calculated from the Herschel Bulkley model plotted against methyl cellulose content. A trend of decreasing n and increasing K with increasing cellulose content is observed although there is an outlier for n at 12 mass %. The yield stress does not increase significantly with large increases in cellulose content (Figure 82). The yield stress is low, to the point of being immeasurable although practically there was a clear resistance to flow.

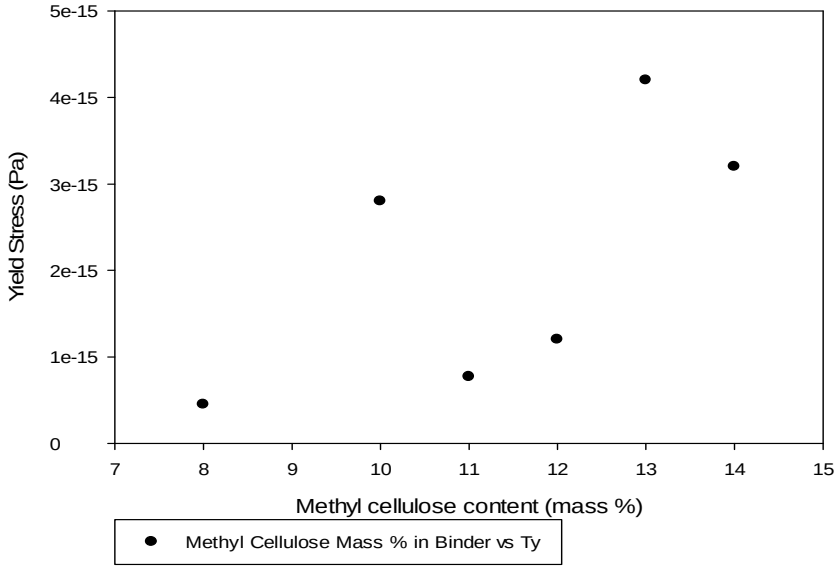

Figure 82 Group 2 binder, methyl cellulose content vs yield stress

4.1.1.3 Binder group 3 Shear Stress Sweep data

Rheological test results for group 3 binder systems are presented in Figures 83 to 90. The composition of group 3 binders is given in Table 21.

Table 21 Group 3 binders composition

Material Code	Material	Mass %	Supplier Code	Supplier
MCGLY1	Methyl cellulose	9.14	M0262	Sigma-Aldrich (MW 41000)
	Distilled water	84.60	-	SHM
	Glycerol	6.26		Sigma-Aldrich
MCGLY2	Methyl cellulose	8.22	M0262	Sigma-Aldrich (MW 41000)
	Distilled water	77.58	-	SHM
	Glycerol	14.19		Sigma-Aldrich
MCGLY4	Methyl cellulose	7.84	M0262	Sigma-Aldrich (MW 41000)
	Distilled water	52.50	-	SHM
	Glycerol	39.66		Sigma-Aldrich
MCGLY5	Methyl cellulose	7.14	M0262	Sigma-Aldrich (MW 41000)
	Distilled water	41.07	-	SHM
	Glycerol	51.79		Sigma-Aldrich
MC medium chain length (MCM)	Methyl cellulose	8.00	M0362	Sigma-Aldrich (MW 63000)
	Distilled water	92.00	-	SHM
MC long chain length (MCL)	Methyl cellulose	8.00	M0512	Sigma-Aldrich (MW 88000)
	Distilled water	92.00	-	SHM

The Herschel Bulkley model showed an accurate fit to the binder flow curves in this group and for each of the samples measured in this section, the model fit parameters are given in table 23. Flow curves for MCGLY2, MCGLY5 and mid and long chain length methyl cellulose formulations are shown in Appendix G. The compositions of group 3 binders are given in Table 21. The shear viscosity of binder MCGLY1 was too low for the controlled stress rheometer to measure accurately. The shear viscosity of binder MCGLY2 was also low as indicated by a high shear rate response to a low applied shear stress. Increasing the glycerol content in group 3 binders provided increased shear viscosity and yield stress.

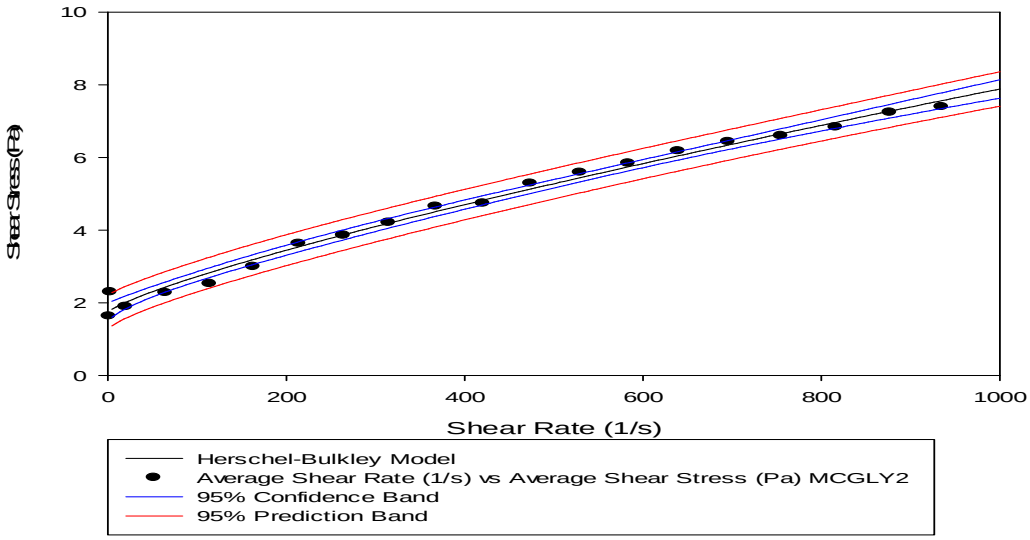

Figure 83 MCGLY 2 binder shear rate as a function of applied shear stress

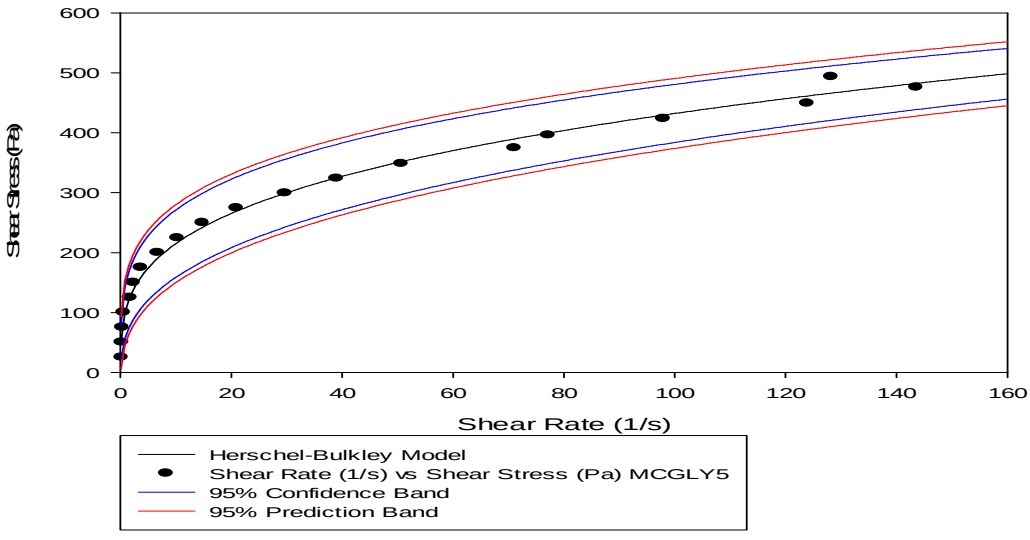

Figure 84 MCGLY 5 binder shear rate as a function of applied shear stress

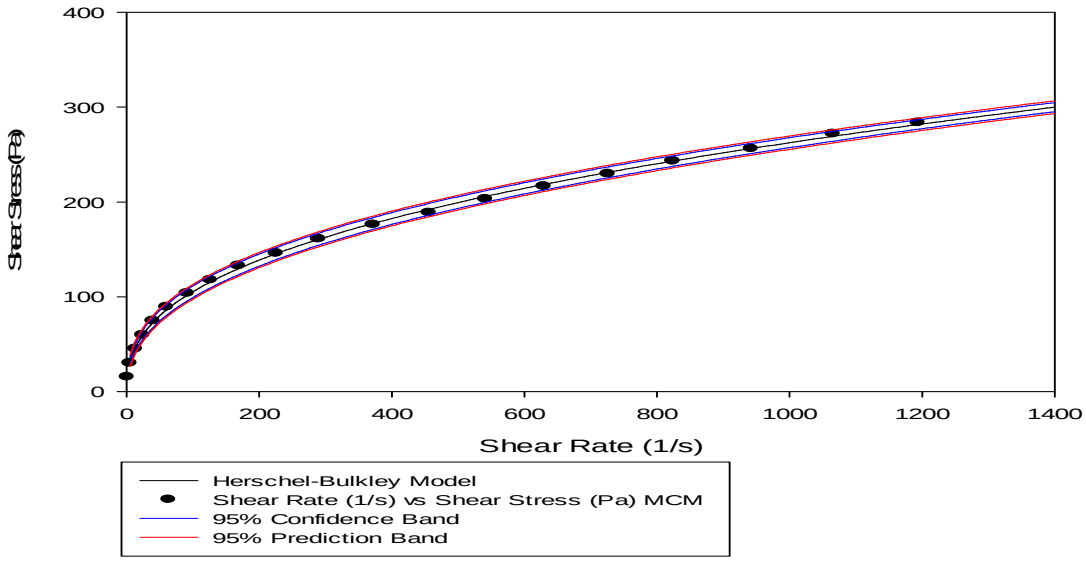

Figure 85 MCM Mid-range chain length binder shear rate as a function of applied shear stress

Figures 85 and 86 show binder stress sweeps for methyl cellulose with medium (MCM, MW 63000) and long (MCL, MW 88000) chain lengths respectively. The standard methyl cellulose used in other formulations had a molecular weight of 41000 (Table 10). High standard deviations indicate that wall slip occurred for the MCM and MCL binders, making results less accurate.

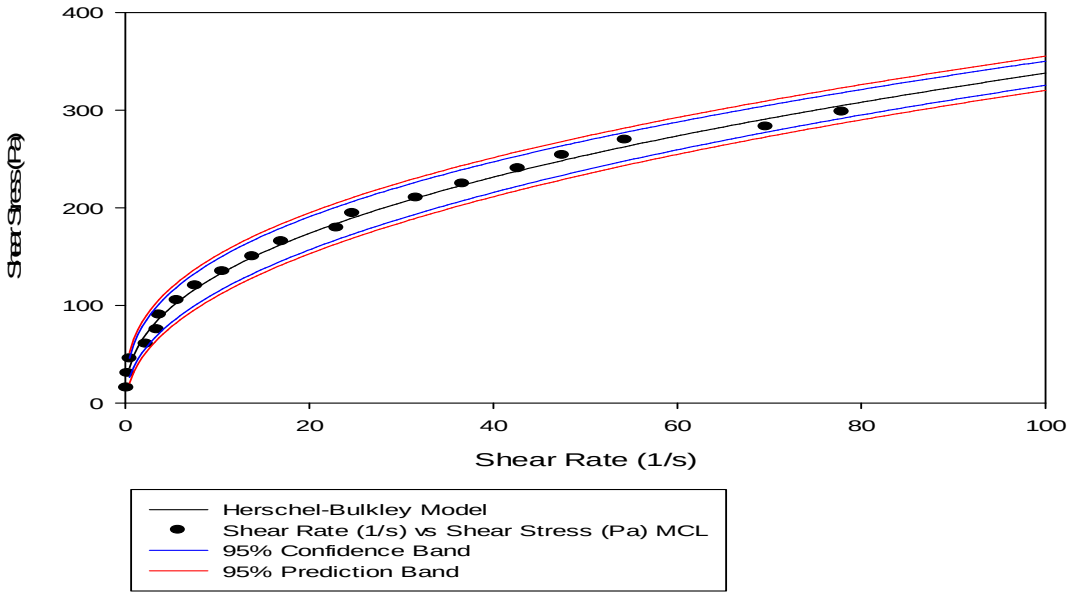

Figure 86 MCL Long chain length methyl cellulose shear rate as a function of applied shear stress

Each flow curve for the different molecular weights of cellulose have been plotted from 0 - 50 s^{-1} in Figure 87.

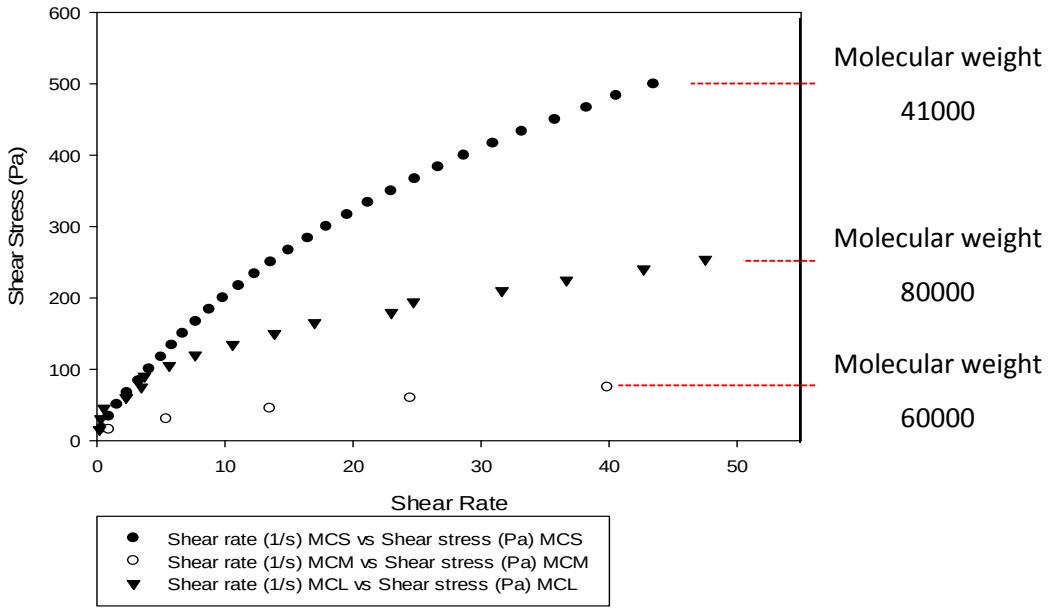

Figure 87 MC Chain length low shear rate test

Figure 87 shows that the MCL binder did not give the highest shear viscosity. In order to increase the dough shear viscosity, increasing the methyl cellulose chain length was therefore not viable. The standard deviation and maximum shear rate obtained are given in Table 22 and the Herschel Bulkley parameters are given in Table 23. To indicate test repeatability, three repeated shear stress sweeps of the MCGLY 2 binder are shown in Figure 88.

Table 22 Group 3 binders standard deviation

MC Variant	Standard deviation at minimum shear rate	Standard deviation at maximum shear rate	Maximum shear rate response
MCGLY1	-	-	-
MCGLY2	+/- 0.47	+/- 29	1102.2
MCGLY3	+/- 0.01	+/- 20.5	428.5
MCGLY4	+/- 0.005	+/- 25.15	313.2
MCGLY5	+/- 0.01	+/- 8.8	202.8
MCM	+/- 0.21	+/- 203.5	2096.0
MCL	+/- 3.625	+/- 67.5	295.6

Table 23 Methyl cellulose modified components Herschel Bulkley parameters

Binder	Binder Group 3	T_y (Pa)	K value (Pa.s^n)	n value	HB model fit R squared value
-	MCGLY1	n/a	n/a	n/a	-
7	MCGLY2	1.74	0.025	0.80	0.99
8	MCGLY3	$1.1x10^{-5}$	46.26	0.31	0.98
9	MCGLY4	$4.9x10^{-15}$	160.88	0.24	0.98
10	MCGLY5	$1.3x10^{-14}$	106.89	0.30	0.99
11	MCM	$6.7x10^{-16}$	16.98	0.40	0.99
12	MCL	$6.8x10^{-16}$	50.45	0.41	0.99

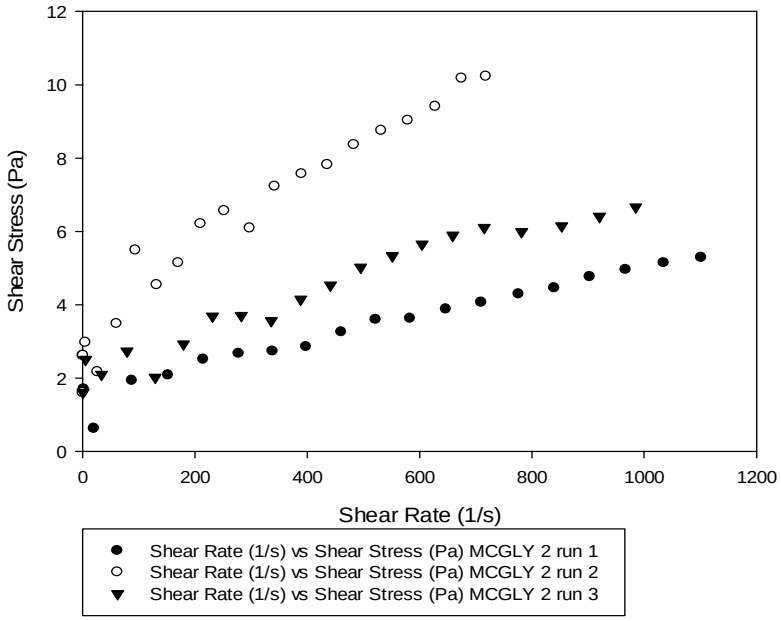

Figure 88 MCGLY 2 binder flow curve repeatability test

Figure 88 shows that the repeatability of shear stress sweep testing is poor for this binder. The Herschel Bulkley parameters in Table 23 have been plotted in Figure 89 for group 3 binders containing glycerol. An increase in K and therefore apparent shear viscosity with increasing glycerol content is observed. The standard deviation at the highest shear stress for MCGLY4 suggests an error in measurement and a likely outlier. Due to the high standard deviations for the MCM and MCL binders, Herschel Bulkley calculated parameters have not been plotted. Figure 87 also shows that the higher molecular weight binders exhibit lower apparent shear viscosities over most of the applied shear rate range. The highest molecular weight binder, however, gave an apparent viscosity greater than that of the 60000 molecular weight binder. A high standard deviation indicates that the data was not reliable. Material supply should also be questioned as Sigma-Aldrich are not the manufacturer.

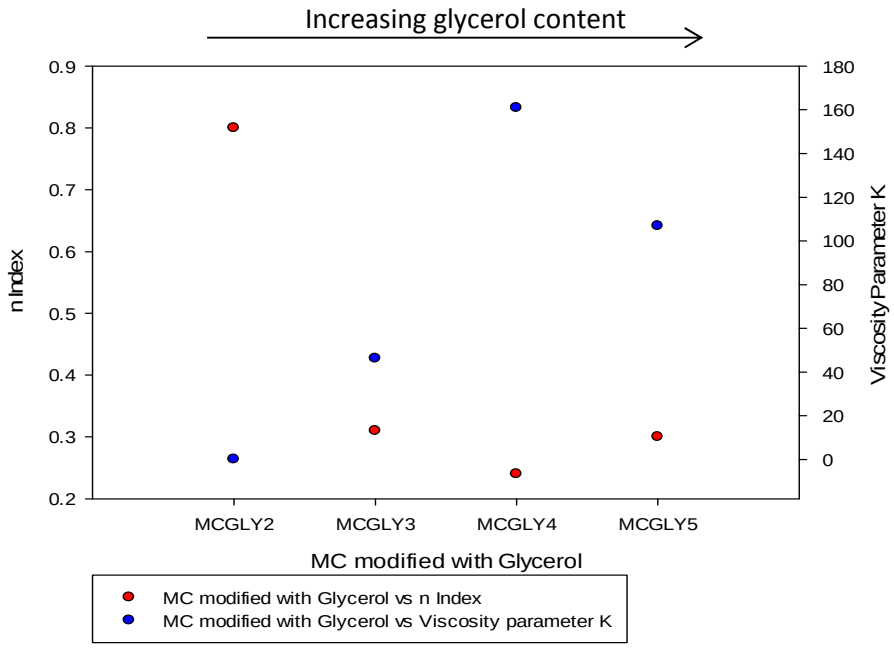

Figure 89 Group 3 binders Herschel Bulkley K and n parameters

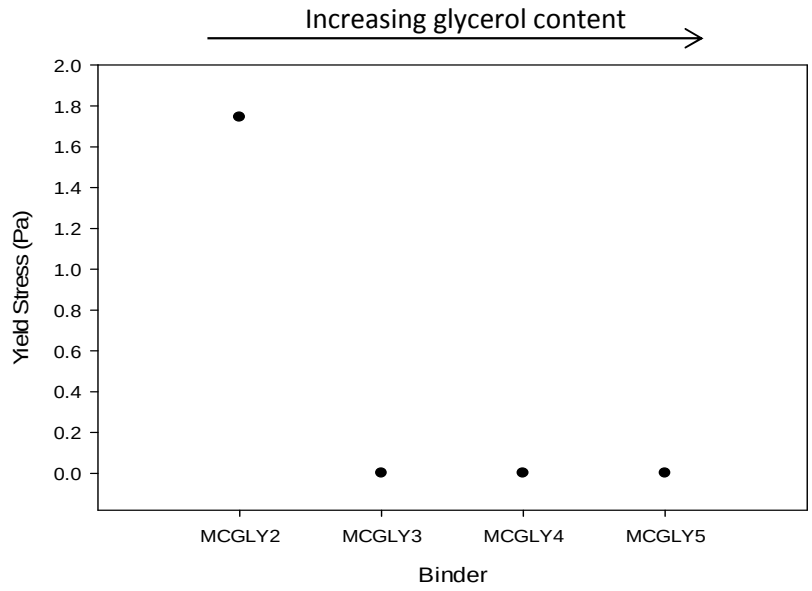

Figure 90 Group 3 binders yield stress values

The yield stress values calculated by the Herschel Bulkley model have been plotted in Figure 90. Binder MCGLY2 had a considerably higher yield stress than other binders in group 3. Figure 90 shows that the majority of group 3 binders had little to no yield stress from an engineering view point. Yield stresses are low enough for the binders to be equally well described by the power law model.

4.1.1.4 Group 4 binders Shear Stress Sweep data

Binder systems in group 4 consisted of methyl cellulose and distilled water with added PEG components. The mass % of each component in the binders is given in Table 24 along with the code used to identify the binder.

Table 24 Binder group 4 material composition

Binder	Methyl cellulose mass %	Distilled water mass %	PEG 300 mass %	PEG 1500 mass %	PEG 3400 mass %
MC8PEG40	6.59	75.8	1.76	1.76	14.1
MC8PEG42	6.46	74.0	1.92	1.92	15.4
MC8PEG44	6.03	69.4	2.46	2.46	19.7
MC10PEG40	7.93	71.4	2.07	2.07	16.6
MC10PEG42	8.08	72.8	1.92	1.92	15.3
MC10PEG44	7.91	71.2	2.09	2.09	16.7
MC12PEG42	9.71	71.2	1.91	1.91	15.3
MC15PEG42	12.2	68.9	1.90	1.90	15.2
MC16PEG42	13.0	68.1	1.90	1.90	15.1

8, 10, 12, 15 and 16% methyl cellulose formulations are plotted at a PEG content equivalent to 42 vol% WC-Co. For the 8 and 10% cellulose pre-mixes a range of PEG concentrations were also evaluated. Both groups of methyl cellulose binders containing PEG have been plotted in Figure 91. Figure 91 was sub-divided into its components to develop Figures 92 to 94 to observe effects of increasing either the methyl cellulose content or the PEG content in the binder pre-mix.

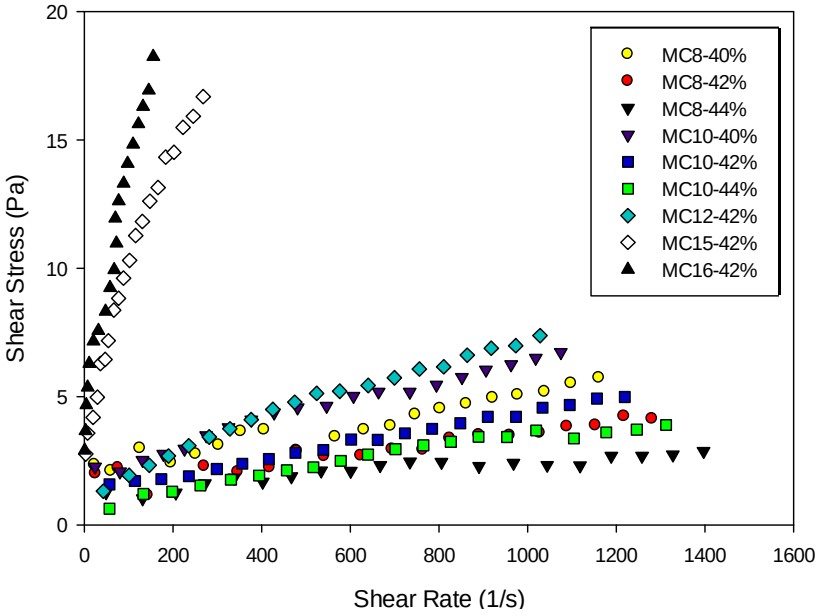

Figure 91 Group 4 binders (methyl cellulose with PEG additions) shear rate as a function of applied shear stress

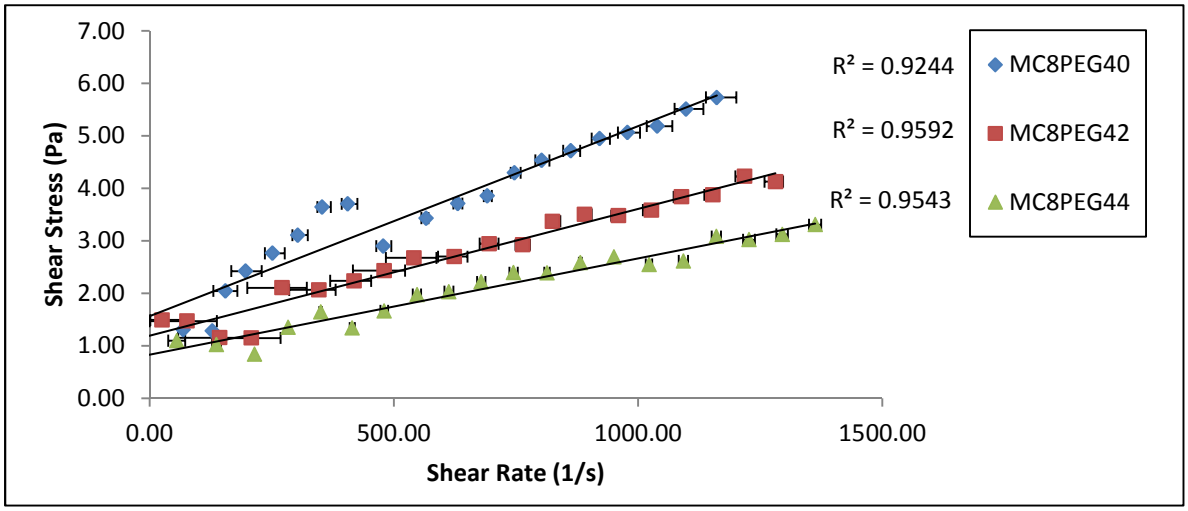

Figure 92 Group 4 binders, constant methyl cellulose content, increasing PEG content, shear rate as a function of applied shear stress

Figure 92 shows how increasing the PEG content at a constant methyl cellulose mass % decreases the binder shear viscosity. This is a significant result because if the solids loading of a dough is increased, the PEG content increases and therefore strongly influences the binder behaviour. Although the data is noisy, the error in shear rate response between repeated tests was small and the binder now appears near Newtonian although due to small yield stress is actually Bingham. Extrapolation of the linear trend line shows that the yield stress in each case is small yet significant and therefore behaviour is best represented by the Bingham relationship. Figure 93 shows similar trends to Figure 92 although the yield stress was slightly greater. The MC10PEG42 also has a significantly different gradient indicating a greater Bingham viscosity. Each flow profile was linear above a yield stress however indicating Bingham behaviour.

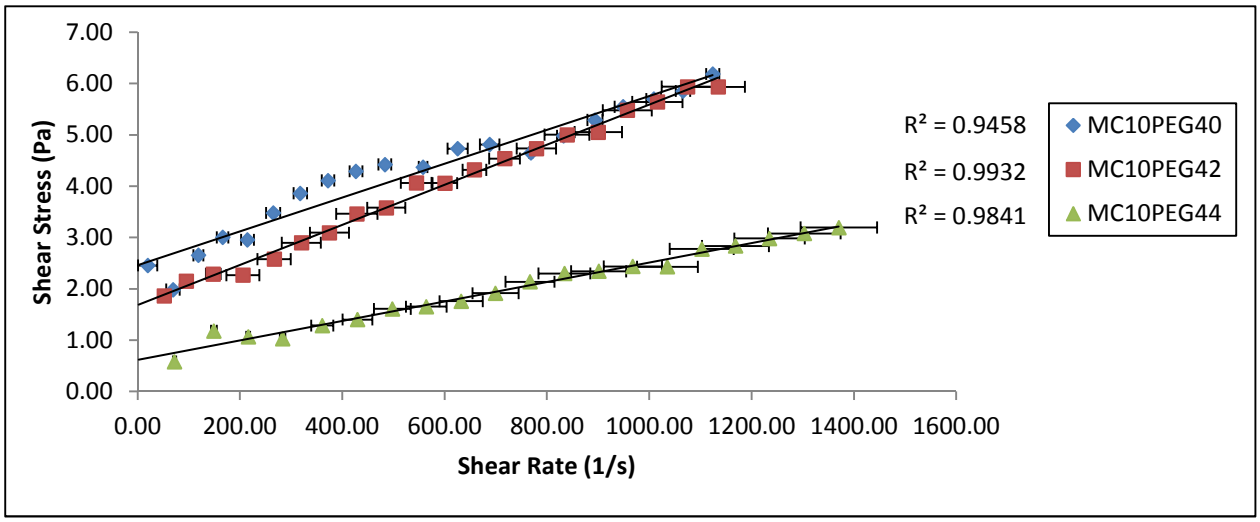

Figure 93 Constant methyl cellulose content (10% binder), increasing PEG content, shear rate as a function of applied shear stress

Figure 93 shows that increasing the MC content at constant PEG concentration systematically increases the apparent viscosity of the binder system. The materials can all be modelled using the Bingham equation. Although the desirable pseudoplastic behaviour has been lost compared to pure MC, apparent viscosity does fall with increasing shear rate.

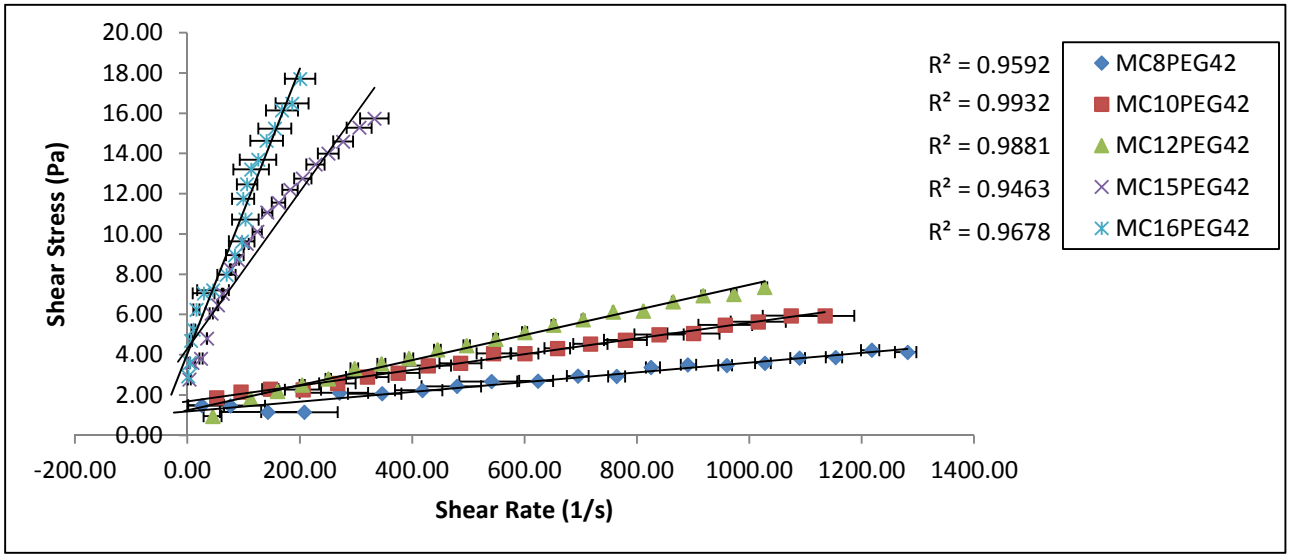

Figure 94 Constant PEG content, increasing methyl cellulose content, shear rate as a function of applied shear stress

Herschel Bulkey curves when fitted gave n values close to one and so Bingham models were more appropriate for the group 4 binders (Figure 91). Bingham viscosities (Figures 96 to 98) for each binder in this section were calculated from individual plots in which trend lines were applied. Yield stresses have been plotted in Figures 97 to 99. Standard deviations are reported in Figures 92 and 93, giving small error between similar tests.

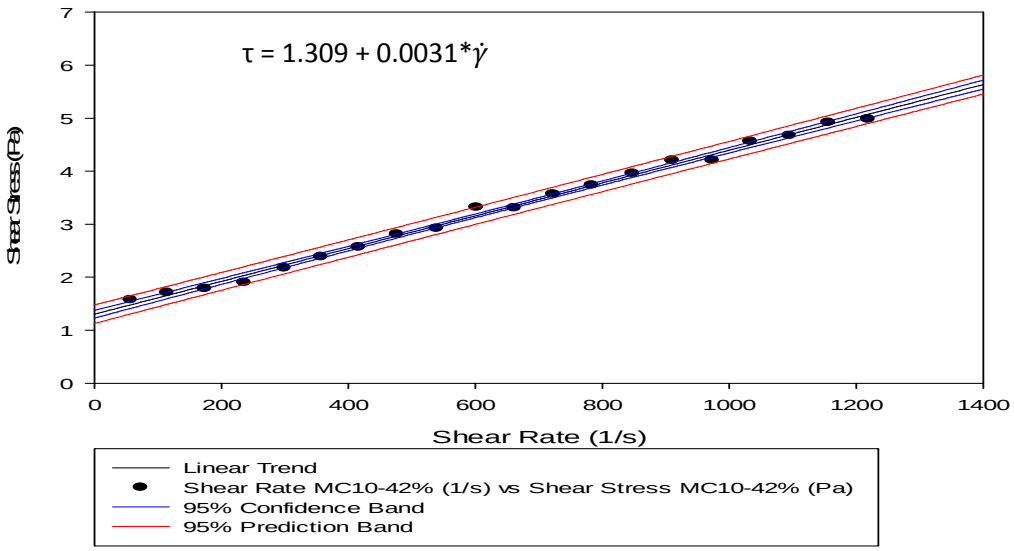

Figure 95 Linear viscosity plot MC10PEG42 binder

Figure 95 shows that the Bingham viscosity decreased linearly with increased PEG content, whilst methyl cellulose content was kept constant at 8 mass %.

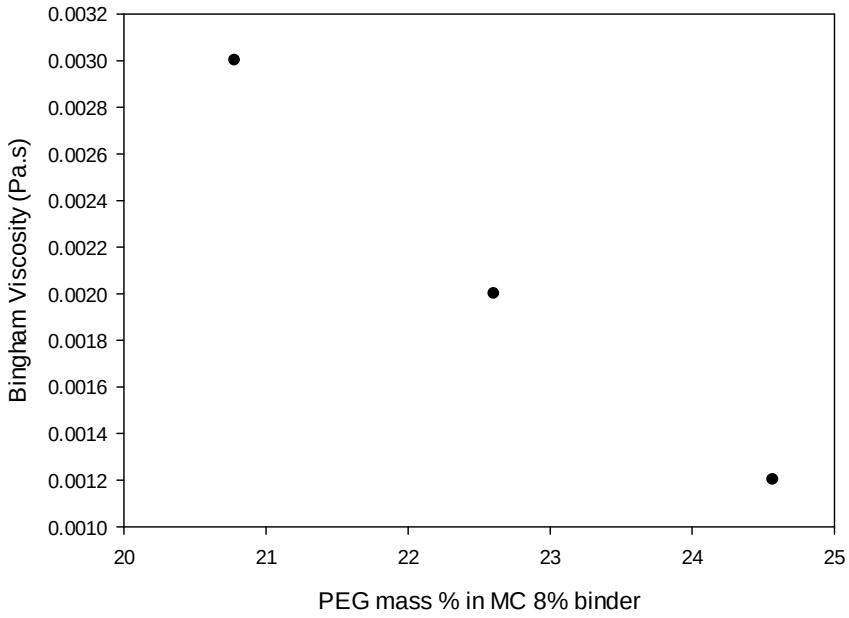

Figure 96 Bingham viscosity plot, MC 8% binder with increasing PEG content

Figure 96 shows that the Bingham viscosity also decreased with increasing PEG content at a constant methyl cellulose content (10 mass %).

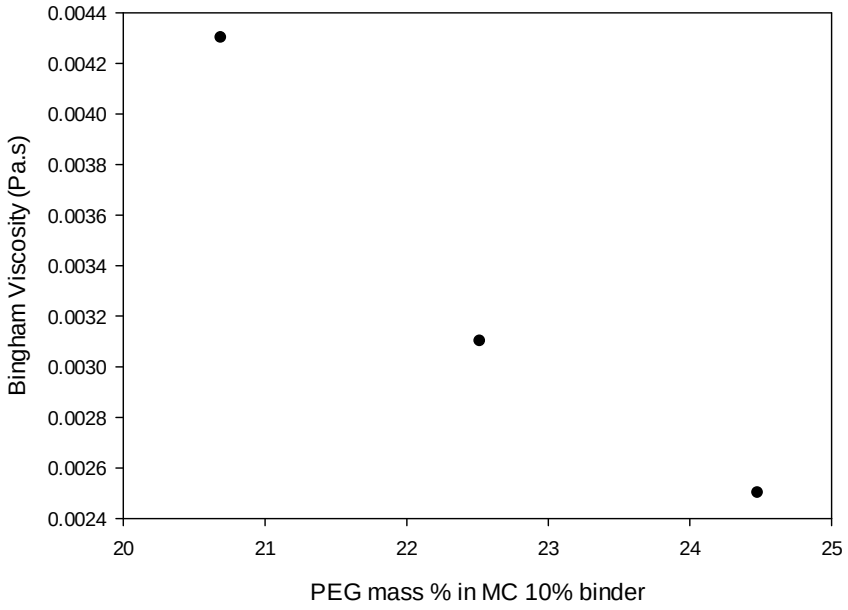

Figure 97 Bingham viscosity plot, MC 10% binder with increasing PEG content

Figure 97 shows how increasing the methyl cellulose content for a fixed PEG content in the binder influenced the Bingham viscosity. The PEG content in this instance was fixed at 21-22.5% as it was designed to equate to the amount of PEG present in the dough system.

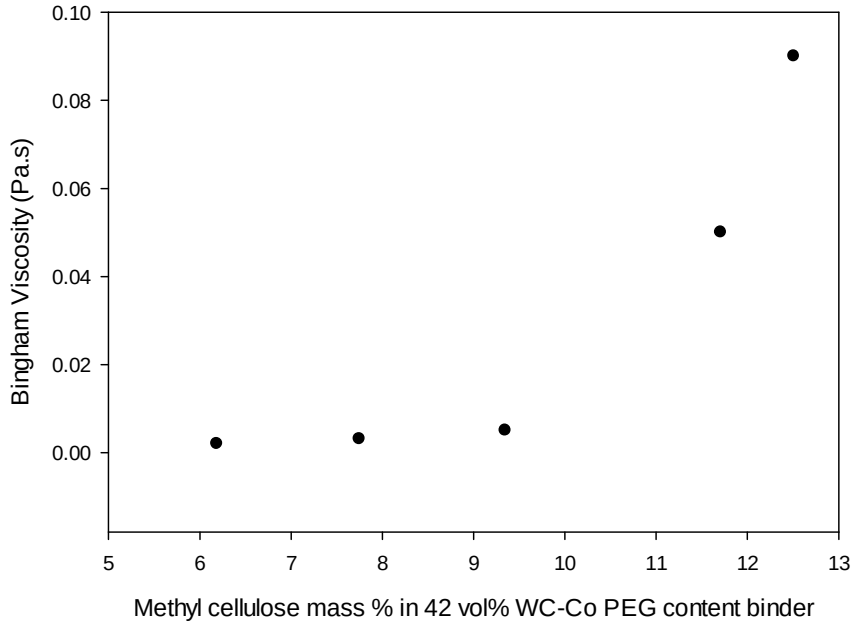

Figure 98 Bingham viscosity plot, constant PEG content with increasing methyl cellulose content

Figure 98 shows that increasing the methyl cellulose content had a greater effect on the binder system than increasing PEG content. The observed increase in Bingham viscosity as a result of increasing methyl cellulose content was non-linear. Figures 99 and 100 show how the yield stress

varied with increased PEG content for both the 8 and 10% methyl cellulose binders. Figure 90 shows how the yield stress increased with increased methyl cellulose content at fixed PEG content.

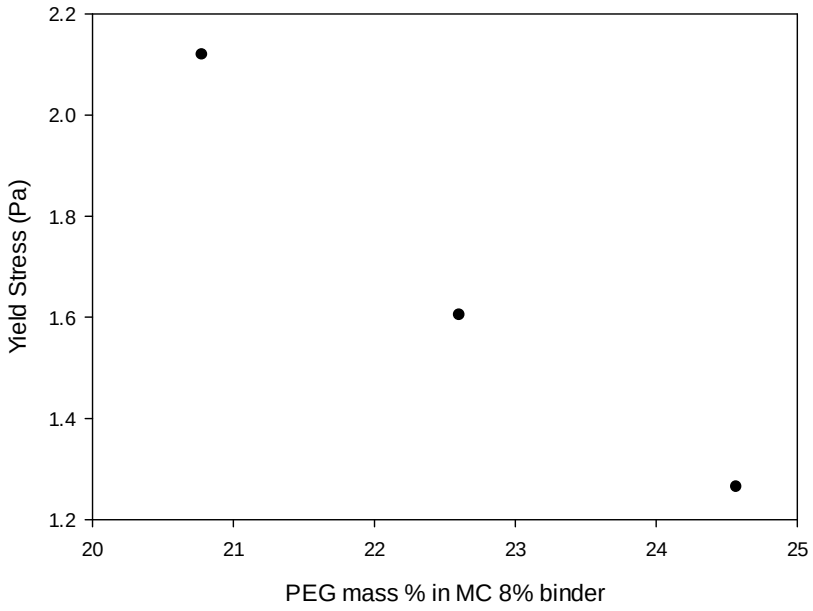

Figure 99 Yield stress vs PEG mass % in MC 8% plus PEG binder

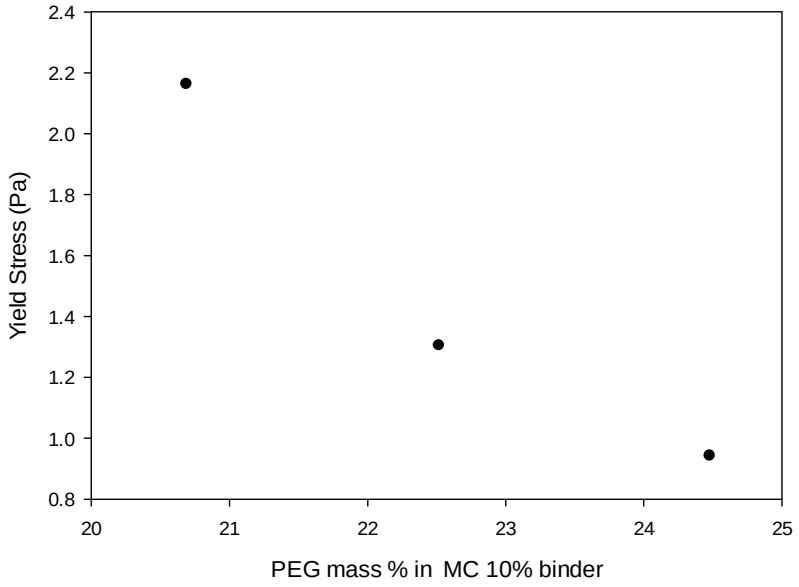

Figure 100 Yield stress vs PEG mass % in MC 10% plus PEG binder

Increases in PEG content gave predictable decreases in yield stress for the methyl cellulose binder systems containing 8 and 10 mass %.

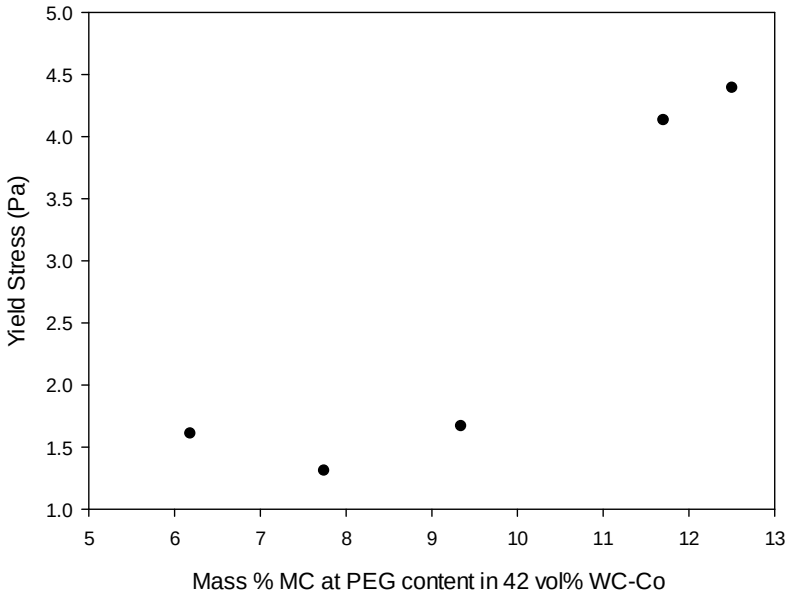

Figure 101 Yield stress vs MC content in (constant PEG content)

Similarly to the Bingham viscosity variability however, the yield stress increased non-linearly when increasing the methyl cellulose content in the binder at a fixed PEG content.

4.1.2 Oscillatory Rheometry

The technique of oscillatory rheometry is described in section 2.5.2.3, 3.5.2 and 3.5.3. The materials were separated into the same groups described in Table 17. For each organic binder, the first analysis determined the linear visco-elastic region (LVER), allowing for frequency sweep evaluation. The LVER for each binder is indicated with vertical green parallel lines in the figures. Frequency sweep data were recorded and hence the viscoelastic properties determined. The phase angle, tan delta was taken from the instrument software across the frequency range and was calculated from the elastic and viscous response data using equation 2-22 for each data point developed. Figures 102 to 113 show the LVER and frequency sweeps for group 1 binders. Figure 103 shows the phase angle of binders in group 1.

4.1.2.1 *Group 1 Binders LVER and Frequency Sweep data*

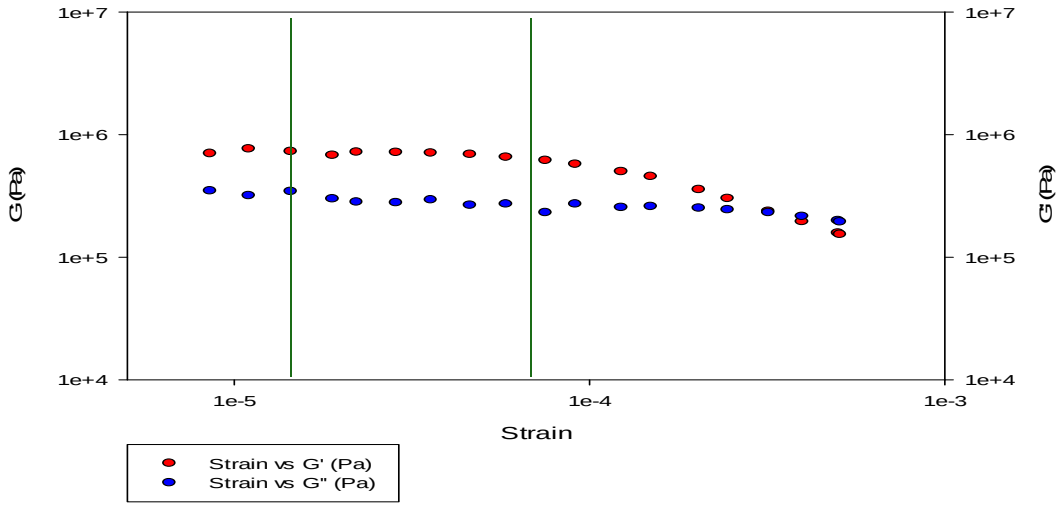

Figure 102 SHM binder LVER showing the elastic and viscous components as a function of strain

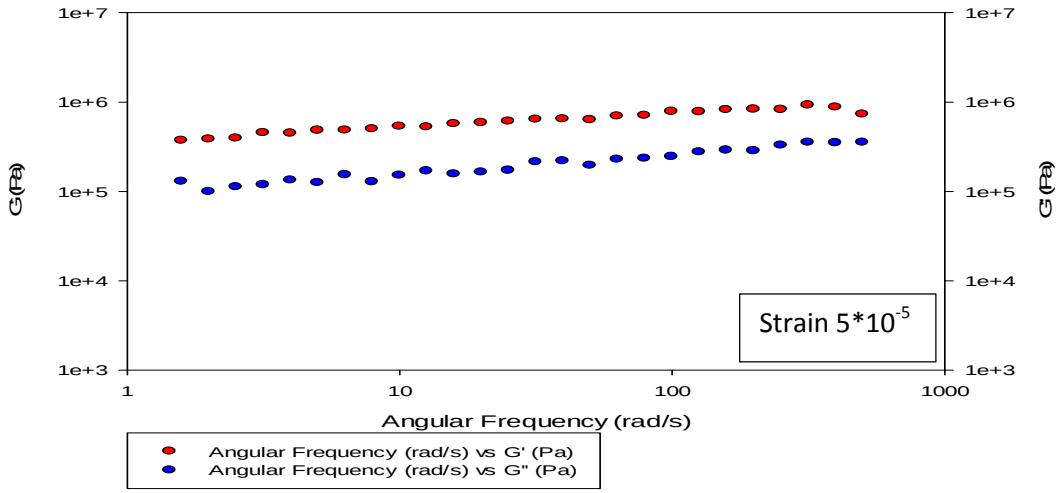

Figure 103 SHM binder, showing elastic and viscous components as a function of angular frequency

A longer LVER was taken to equate to greater stability, due to greater resistance to microstructural deterioration. This was crucial in a production environment as storage conditions can be harsh and stability is therefore important to shelf life. LVER lengths are given in Table 27.

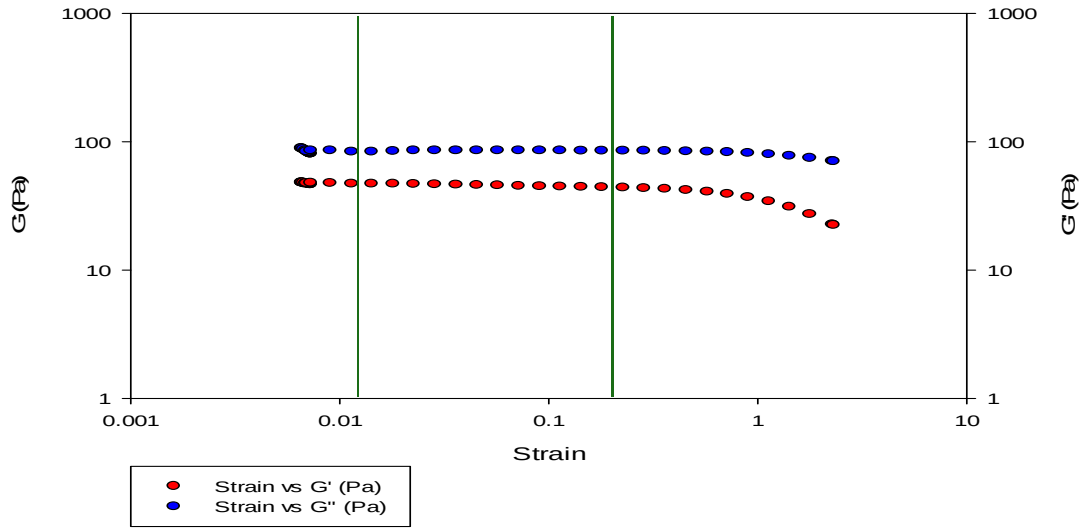

Figure 104 MC8 binder, LVER showing the elastic and viscous components as a function of strain

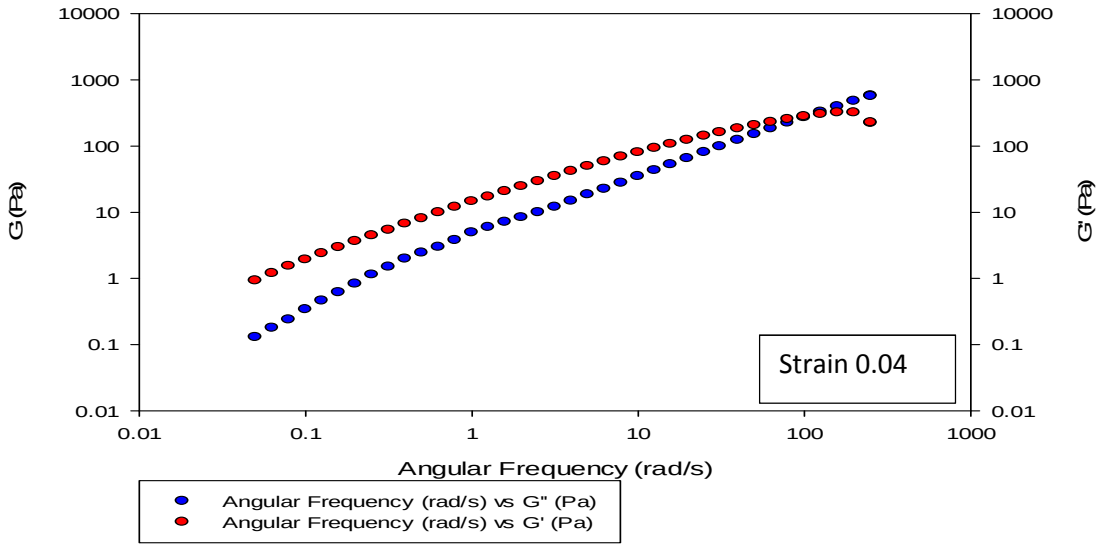

Figure 105 MC8 binder, showing elastic and viscous components as a function of angular frequency

In Figure 104, the LVER is indicated as short although there is no significant drop in G’ or G’’ although there is a significant change in behaviour (possibly slip) and so this has been interpreted as the LVER.

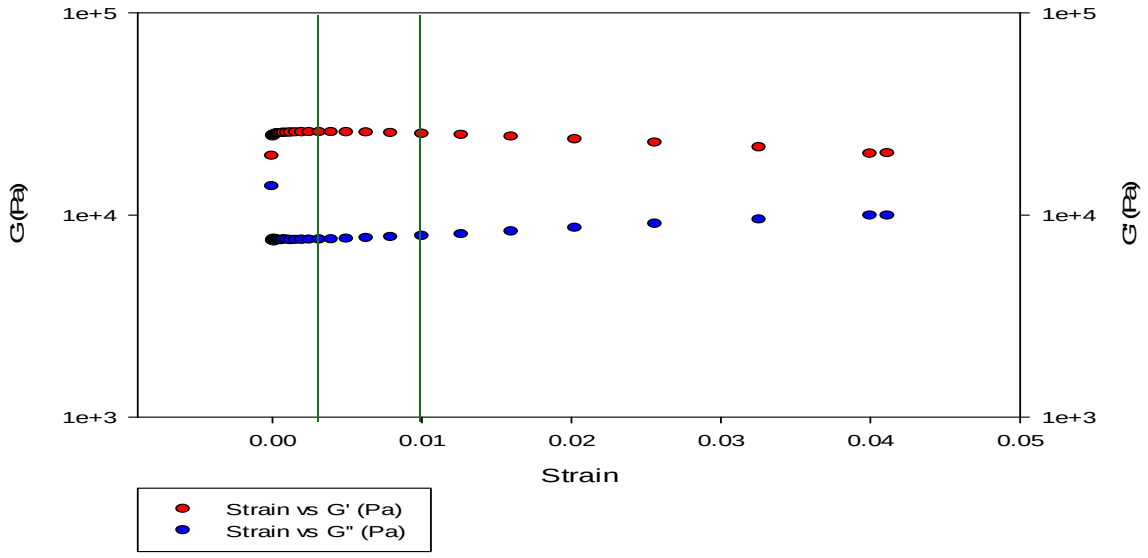

Figure 106 MCPAM binder, LVER showing the elastic and viscous components as a function of strain

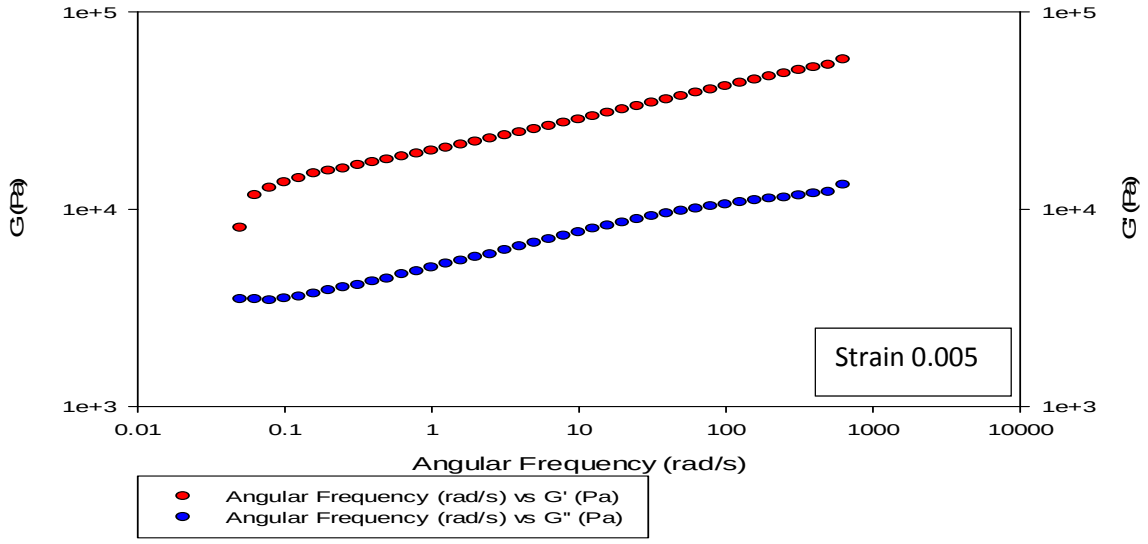

Figure 107 MCPAM binder, showing elastic and viscous components as a function of angular frequency

Many of the group 1 binders show a predominantly elastic behaviour, with G' being greater than G''. However, both binders formulated with ethyl cellulose (with and without PVB, Figures 107 and 108) exhibit a predominantly viscous response. When this is referred to the shear stress data there are however significant differences in the two binders. When PVB is added the shear viscosity rises significantly at a given shear rate while elasticity is not increased.

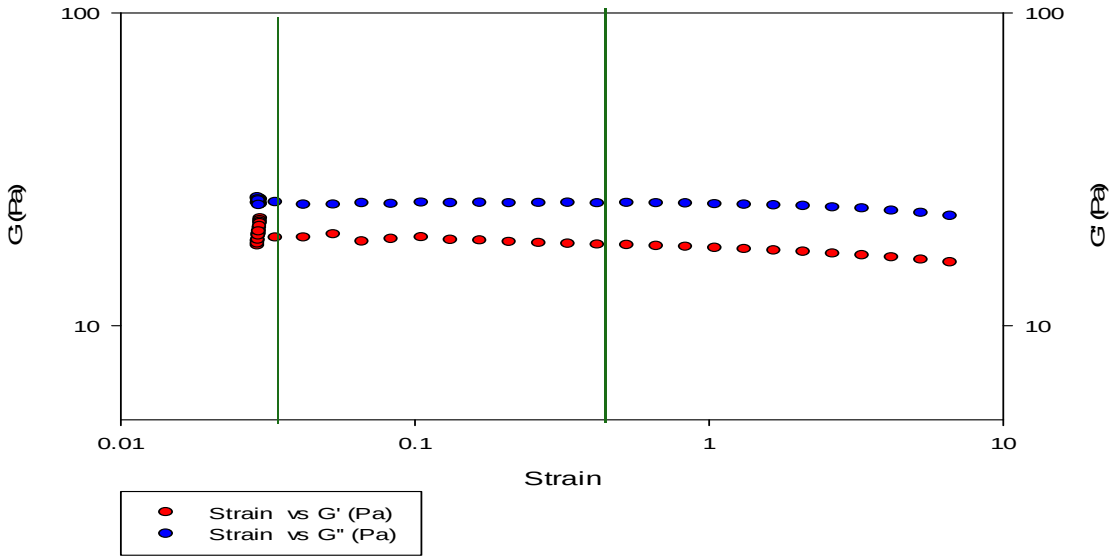

Figure 108 ECETH binder, LVER showing the elastic and viscous components as a function of strain

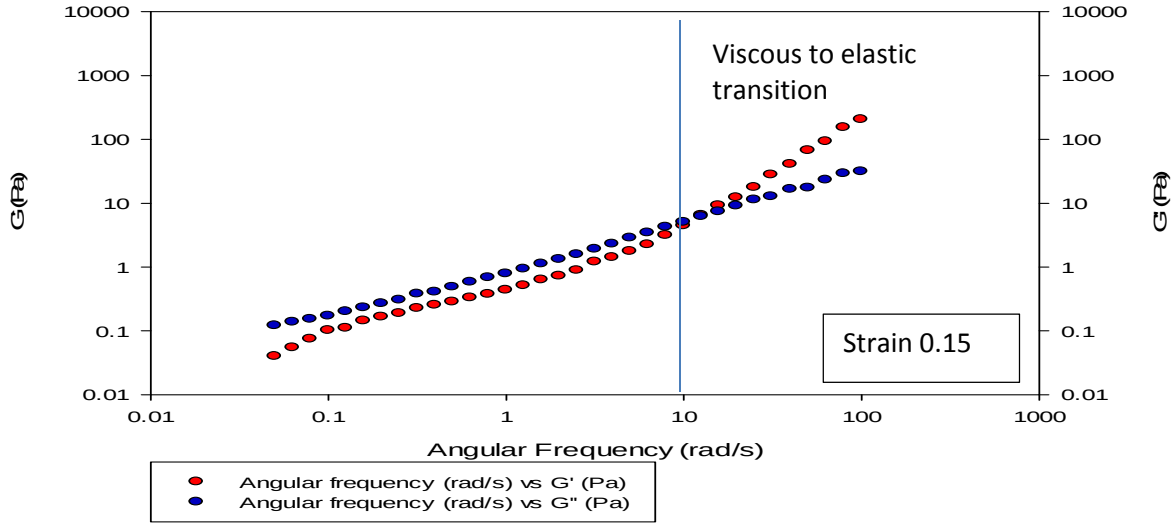

Figure 109 ECETH binder, showing elastic and viscous components as a function of angular frequency

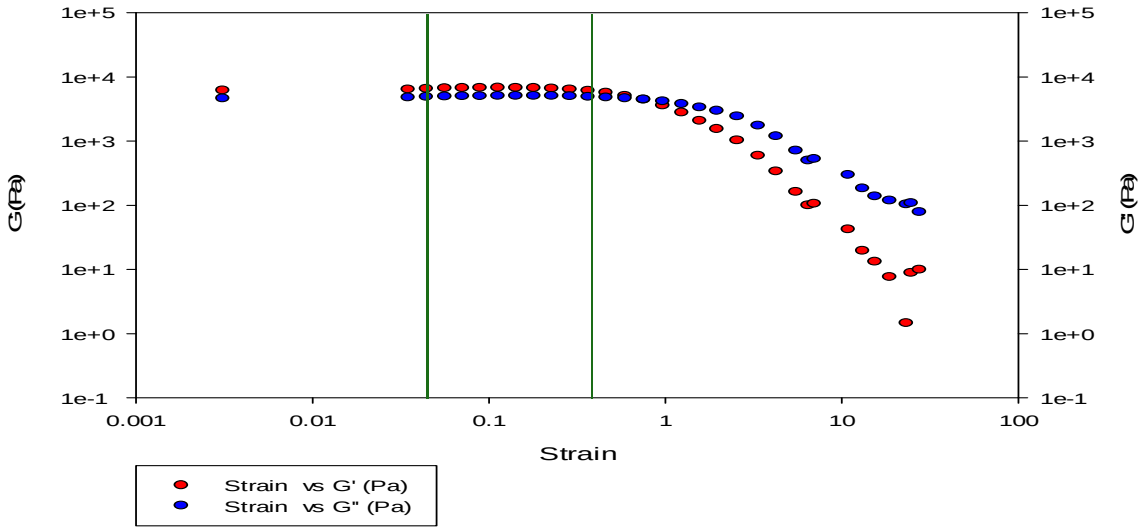

Figure 110 ECETHPVB binder, LVER showing the elastic and viscous components as a function of strain

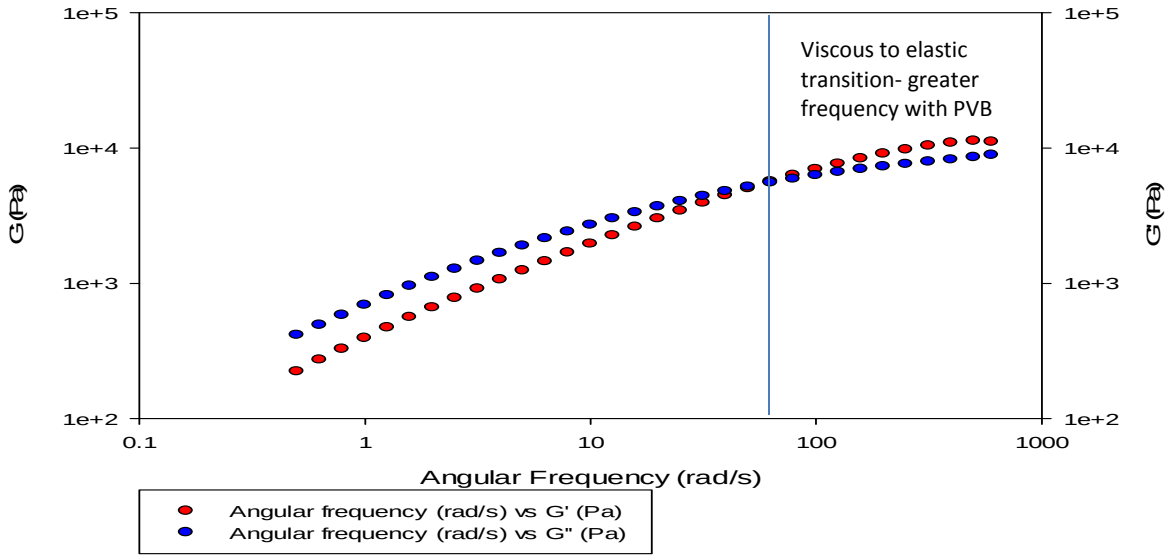

Figure 111 ECETHPVB binder, showing elastic and viscous components as a function of angular frequency

At higher angular frequency, 10 rad/s in Figure 109 and 98 rad/s in Figure 111, the ethyl cellulose based binders have a crossover point tending towards elastic behaviour. PVB has delayed this effect and simultaneously increased the elastic and viscous moduli and therefore complex viscosity. When compared with Figure 109, Figure 111 shows that the addition of PVB increases complex viscosity by four orders of magnitude at a similar angular frequency. Figure 112 shows that the LVER for the GCMPG binder appears to have two linear visco-elastic regions. It is likely however, that either the microstructure has been broken up at higher strain levels or that the LVER is across the whole plot. In order to prevent misleading data due to microstructural breakdown, the first region was used for frequency sweep analysis.

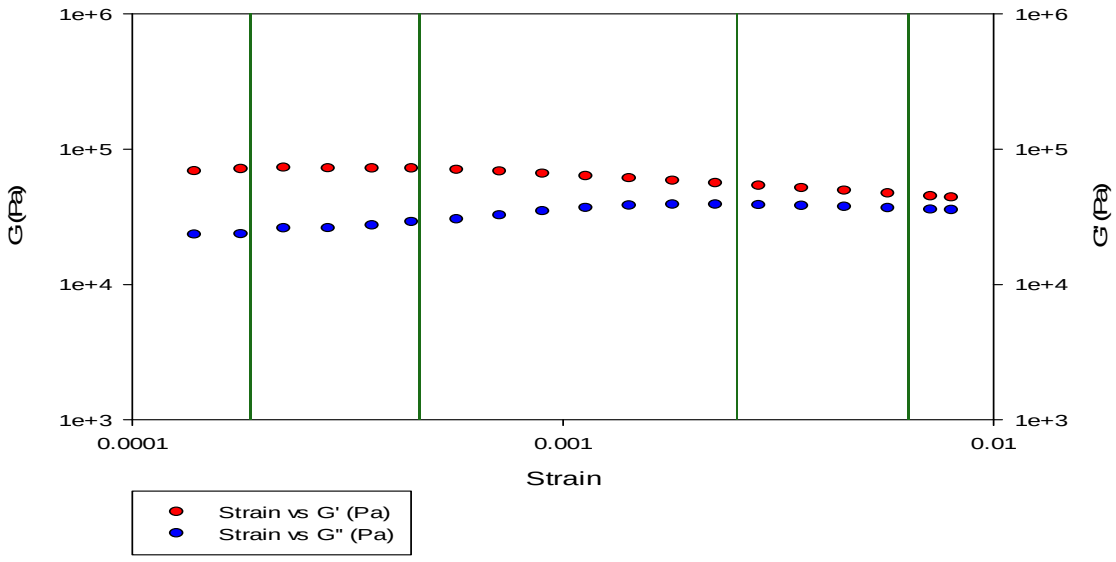

Figure 112 GCMPG binder, LVER showing the elastic and viscous components as a function of strain

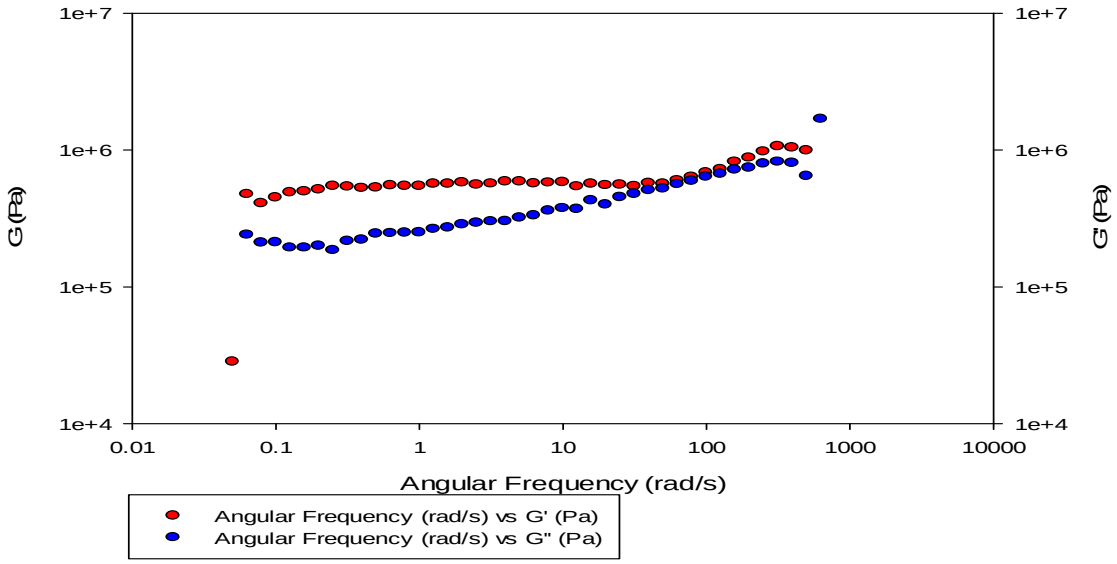

Figure 113 GCMPG binder, angular frequency sweep

Delta is plotted in Figure 114 to allow comparison of group one binder visco-elastic behaviour.

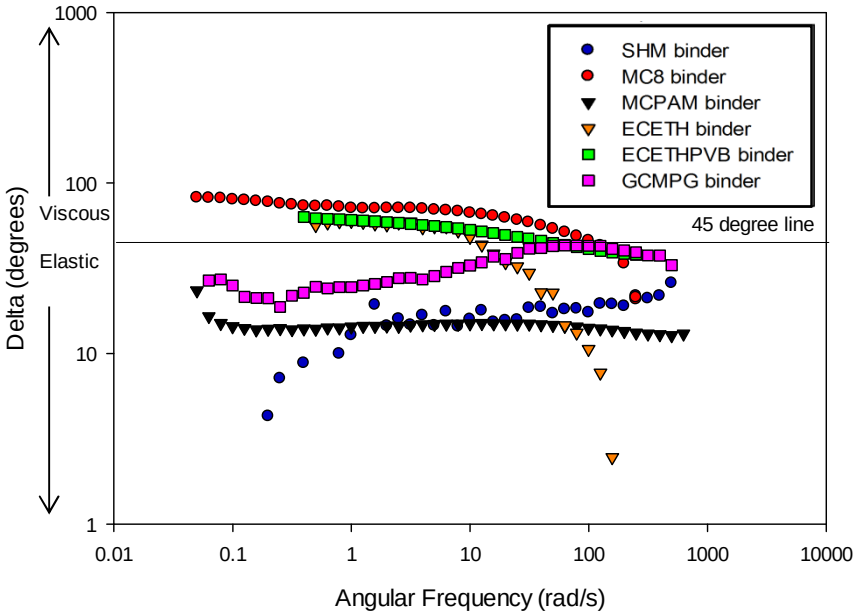

Figure 114 Delta as a function of angular frequency for Group 1 binders

Each frequency sweep test was repeated three times. The standard deviation for delta data did not vary significantly with angular frequency and so has been averaged across the angular frequency range in Table 25. The standard deviation for delta data for both the SHM and GCMPG binders is high indicating that the tests were not as repeatable for waxy solid binders.

Table 25 Binder group 1 delta standard deviation

Binder	Standard Deviation (degrees)
SHM	6.34
MC8	2.64
MCPAM	0.65
ECETH	2.17
ECETHPVB	0.84
GCMPG	6.49

4.1.2.2 Group 2 binders, LVER and frequency sweep data

Similar testing to the group 1 binders was applied to group 2 binders. The phase angle has been plotted for group 2 binders in Figure 121. As in section 4.1.1.2 binder formulations containing 8, 10 and 22 mass % methyl cellulose have been shown on individual plots (Figure 115 to Figure 120) in this section whilst remaining variants are shown in appendix F.

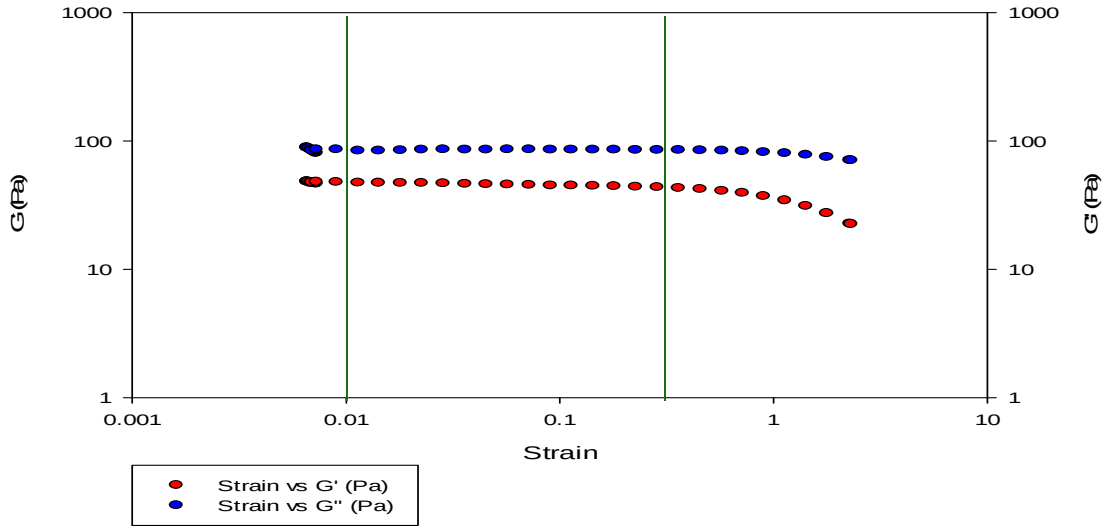

Figure 115 MC8 binder, LVER showing the elastic and viscous components as a function of strain

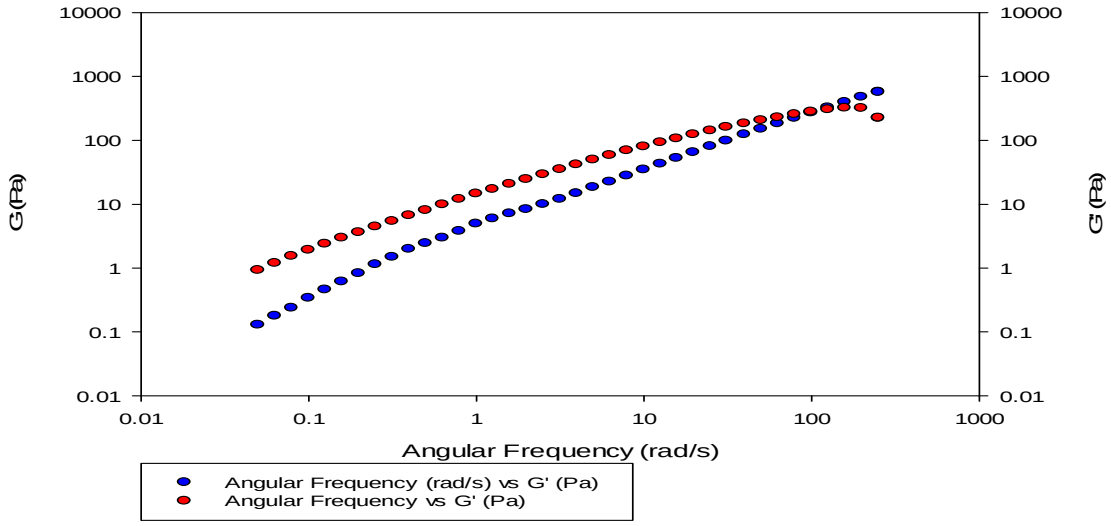

Figure 116 MC8 binder, showing elastic and viscous components as a function of angular frequency

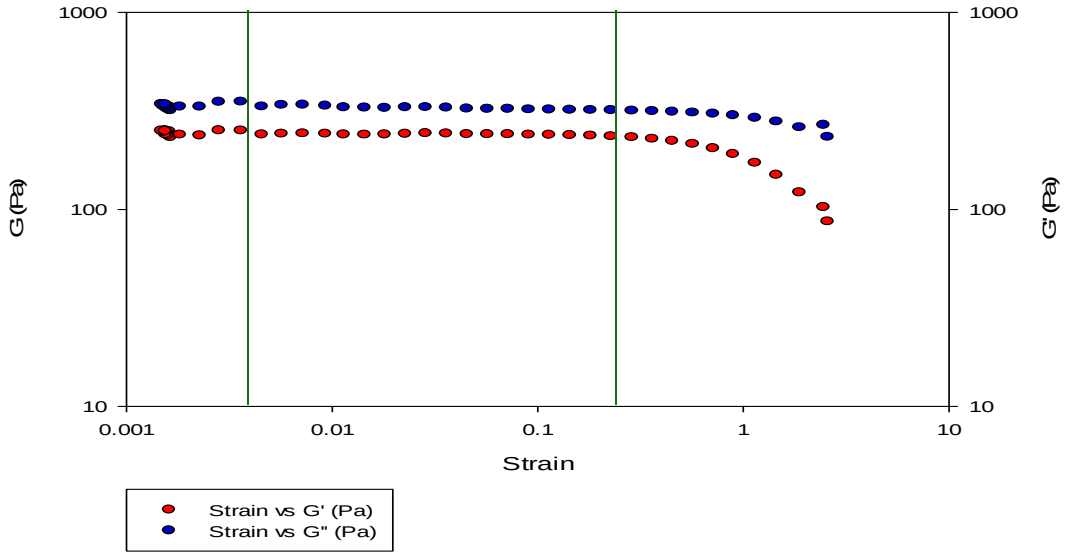

Figure 117 MC, water (10%) binder, LVER showing the elastic and viscous components as a function of strain

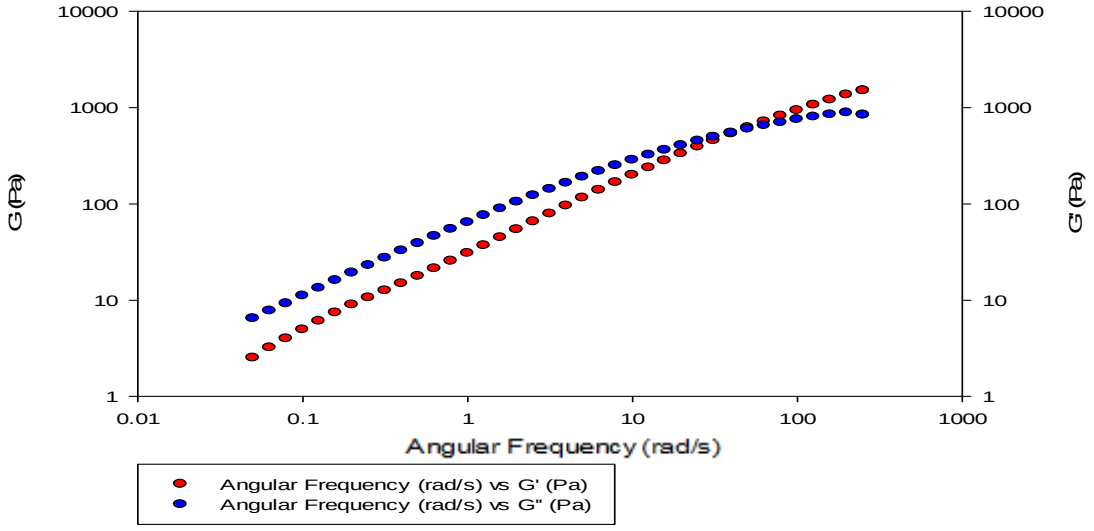

Figure 118 MC, water (10%) binder, showing elastic and viscous components as a function of angular frequency

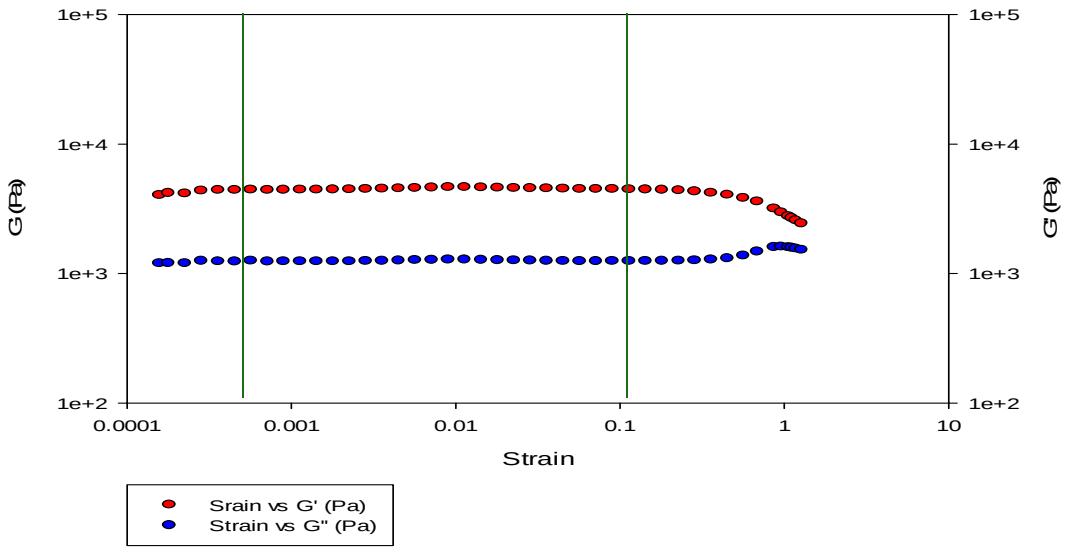

Figure 119 MC, water (22%) binder, LVER showing the elastic and viscous components as a function of strain

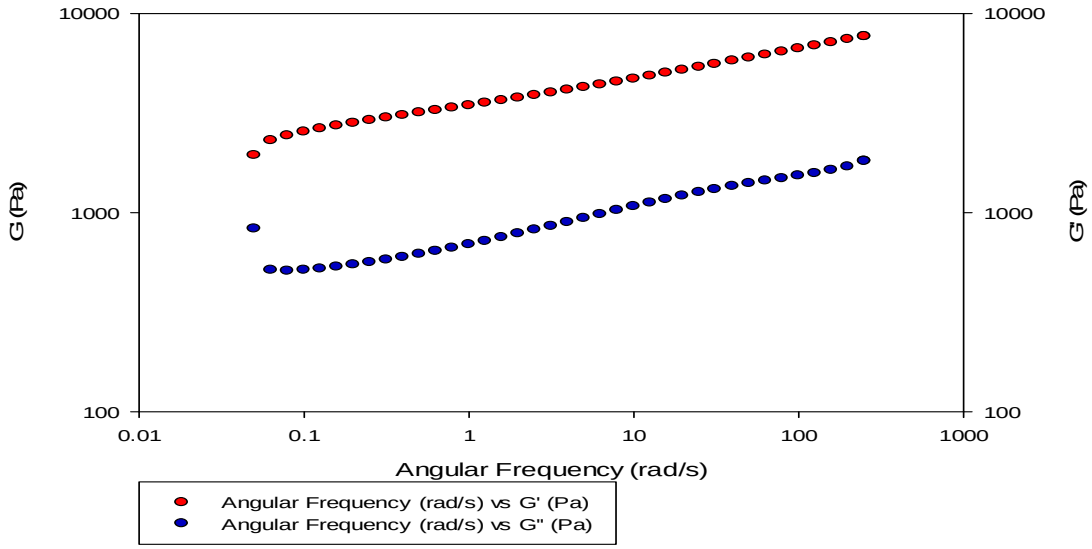

Figure 120 MC, water (22%) binder, showing elastic and viscous components as a function of angular frequency

A log plot of the phase angle delta (Figure 121) shows how the mass % of methyl cellulose in the binder pre-mix alters the visco-elastic behaviour.

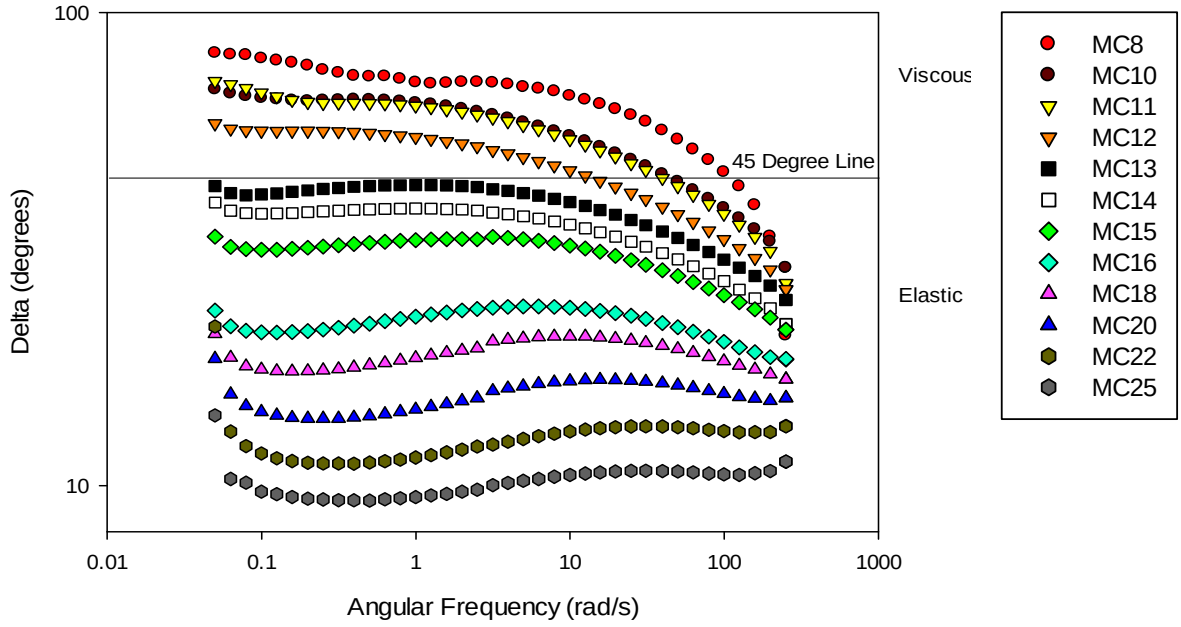

Figure 121 Group 2 binders, showing log delta as a function of angular frequency

As with group 1 binders, each frequency sweep test was repeated three times. The standard deviation has been averaged across the angular frequency range and is given in Table 26.

Table 26 Group 2 binders delta standard deviation

Binder	Standard Deviation (Pa)
MC8	2.64
MC10	0.99
MC11	0.55
MC12	20.33
MC13	6.17
MC14	3.06
MC15	3.00
MC16	0.77
MC18	0.67
MC20	0.50
MC22	1.01
MC25	0.29

4.1.2.3 Group 3 binders LVER and frequency sweep data

MCGLY1 had a very low viscosity and could not be measured which also resulted in unstable data in oscillation, the MCGLY2 binder data was also noisy in response to oscillation (Figure 122). Noise was reduced in the data presented for the MCGLY3 and MCGLY4 binder and MCGLY5 measurements are shown in Appendix G. Figures 122 and 123 show the LVER and frequency sweep of the MCGLY2 formulations respectively. Figure 123 shows that the MCGLY2 binder is equally viscous and elastic over the tested frequencies. Figure 122 also shows however, that the LVER is almost non-existent which can result in inaccurate frequency sweep data as a result of microstructural break down. This is apparent in Figure 123 as the frequency sweep data is also noisy.

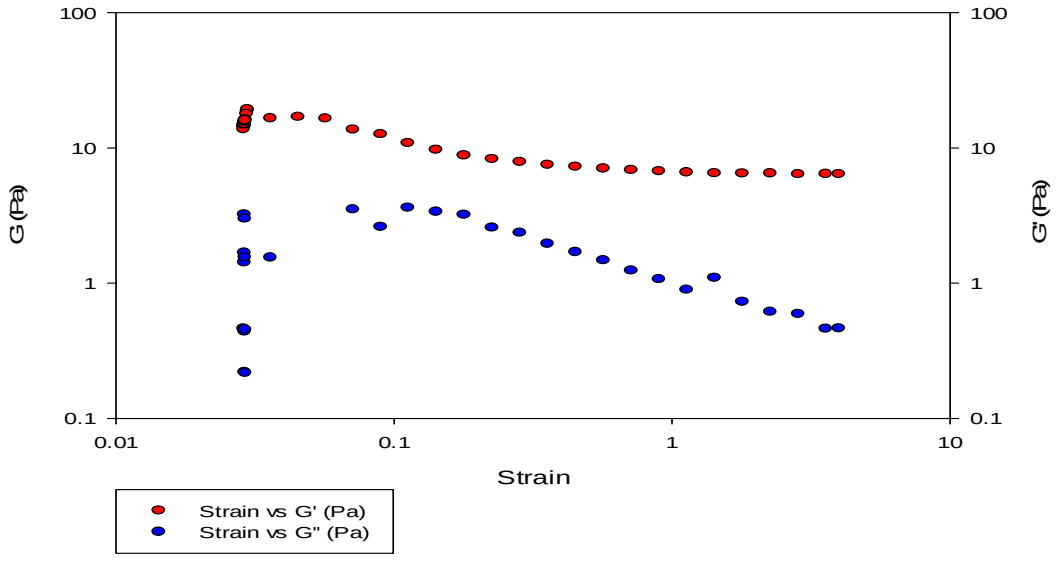

Figure 122 MCGLY2 binder, LVER showing the elastic and viscous components as a function of strain

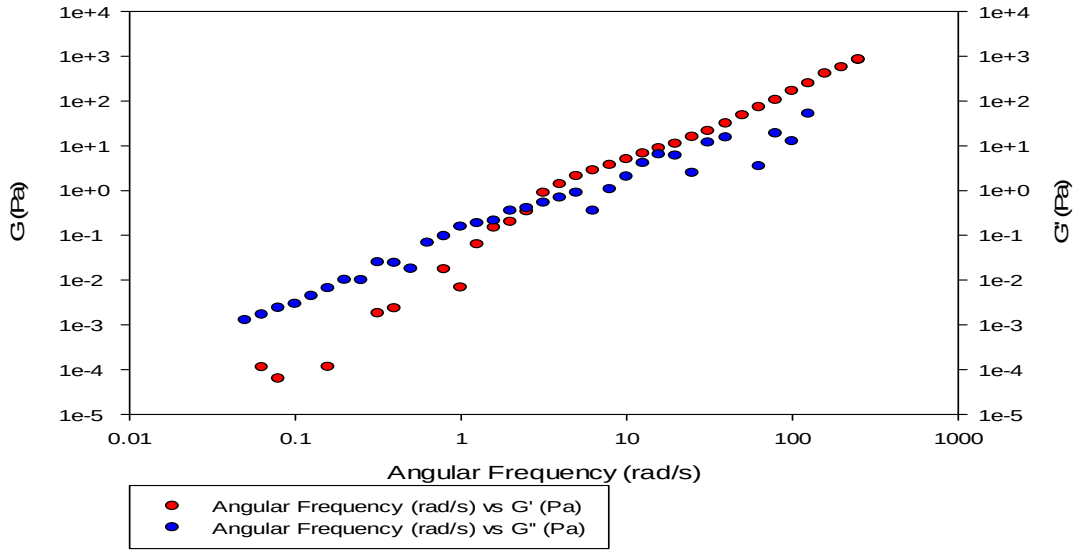

Figure 123 MCGLY2 binder, showing elastic and viscous components as a function of angular frequency

When the MCGLY2 formulation is compared to the standard MC formulation (Figure 115), the complex viscosity is lower at lower frequencies although is similar at higher frequencies. Increasing the glycerol content further (Figure 125) gives a similar behaviour to the original MC formulation.

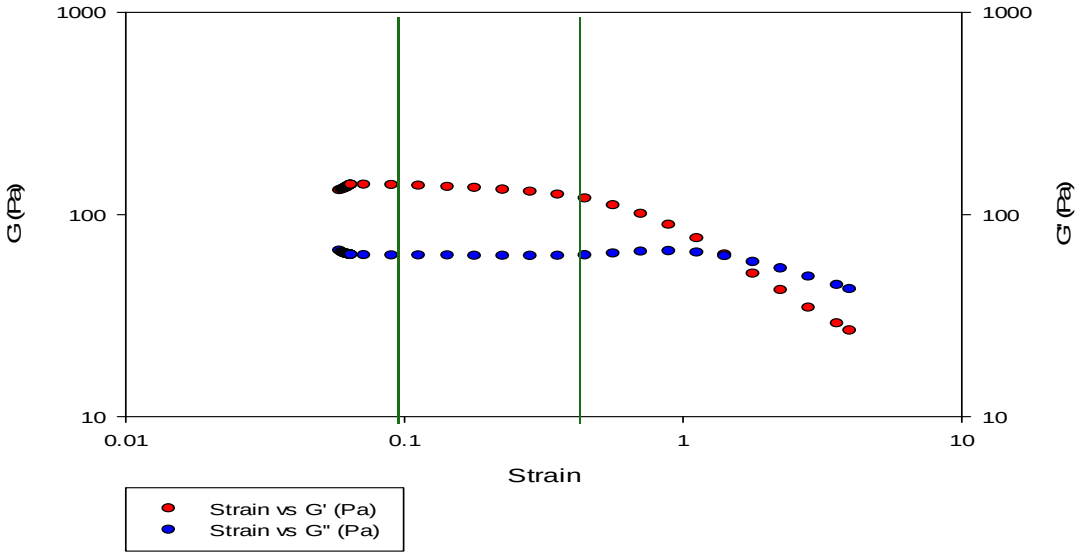

Figure 124 MCGLY3 binder, LVER showing the elastic and viscous components as a function of strain

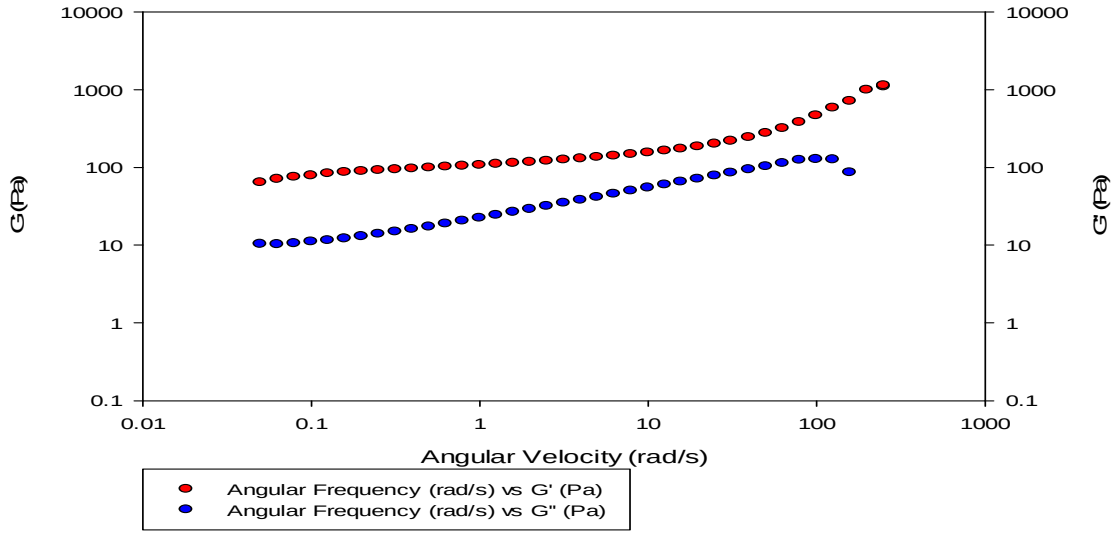

Figure 125 MCGLY3 binder, showing elastic and viscous components as a function of angular frequency

Higher glycerol content gave greater stability when comparing Figures 122 and 124. Figure 125 shows elastic behaviour similar to that of the original MC formulation.

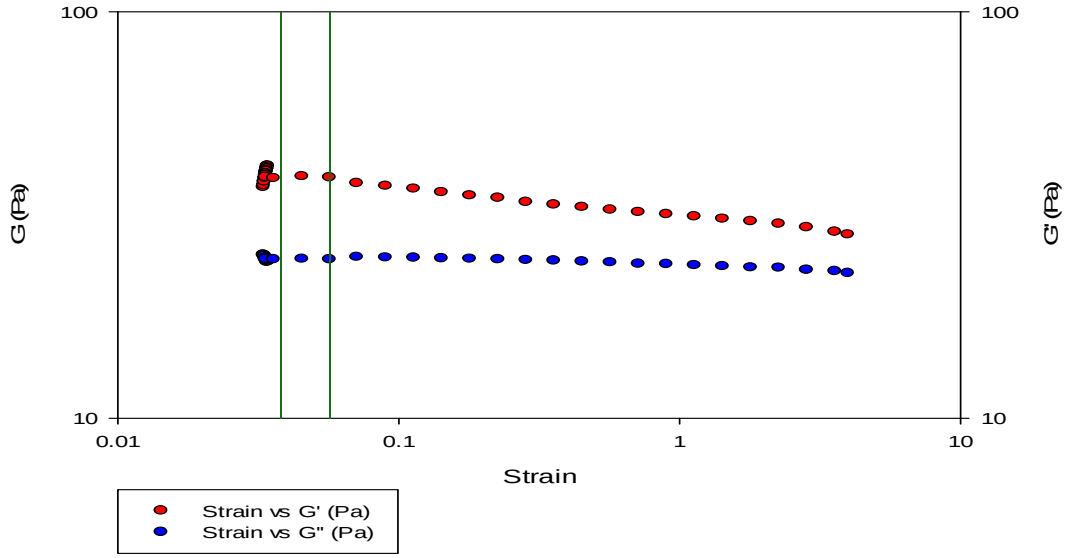

Figure 126 MC mid-range binder, LVER showing the elastic and viscous components as a function of strain

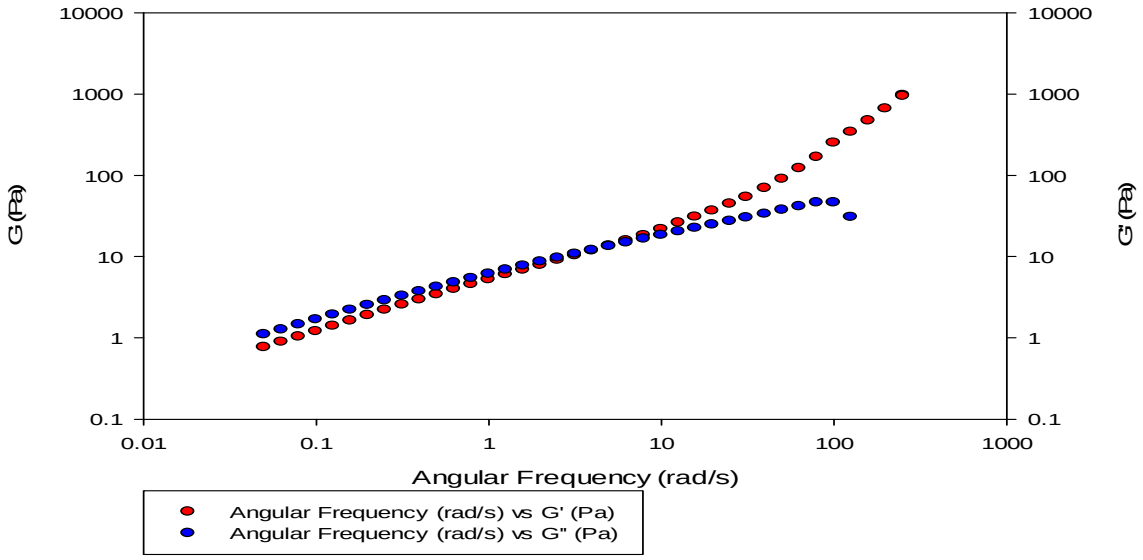

Figure 127 MC mid-range binder, showing elastic and viscous components as a function of angular frequency

Figures 126 to 129 show that as the methyl cellulose chain length increases, the structure becomes more stable and the material more elastic as the LVER becomes extended. At the viscous to elastic transition point the elastic and viscous moduli are greater for the long chain length cellulose than the mid chain length cellulose. However, Figure 115 shows that the lowest molecular weight cellulose is the most viscous at the transition point. The same trends were observed using viscosity measurement techniques in Figure 87.

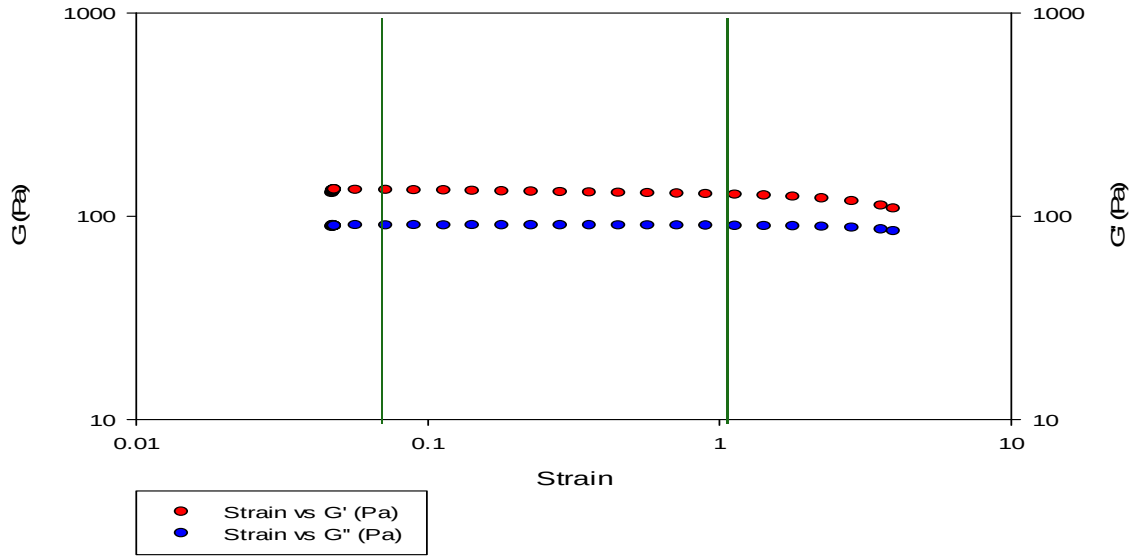

Figure 128 MC long-range binder, LVER showing the elastic and viscous components as a function of strain

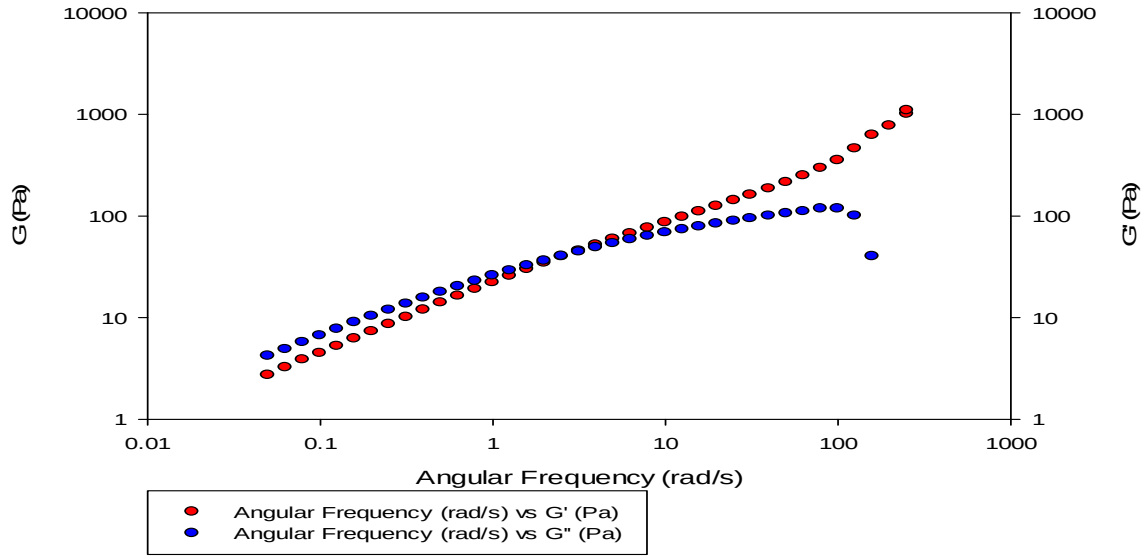

Figure 129 MC long-range binder, showing elastic and viscous components as a function of angular frequency

Similar results were observed in viscoelastic behavior from frequency sweeps in Figures 127 and 129 despite differences in the LVER. A phase angle plot is shown in Figure 130 for group 3 binders.

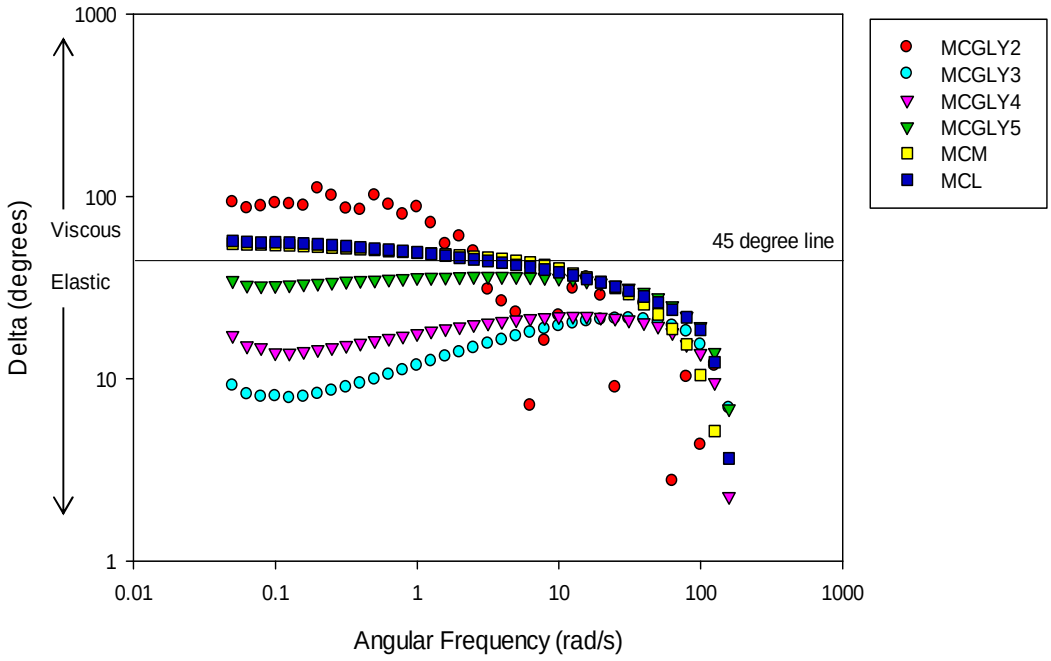

Figure 130 Group 3 binders showing delta as a function of frequency

As with group 1 and group 2 binders, each frequency sweep test was repeated three times and the standard deviation has been averaged across the angular frequency range in Table 27.

Table 27 Group 3 binders delta standard deviation

Binder	Standard Deviation (Pa)
MCGLY2	7.83
MCGLY3	2.68
MCGLY4	1.79
MCGLY5	3.54
MCM	2.36
MCL	3.12

The MC 8% materials with different chain lengths exhibit different delta behaviour and these are shown in Figure 131. In general, the greater the molecular weight, the greater the elasticity and the lower the frequency at which the transition from viscous to elastic behaviour occurs. The same general trend is observed with the complex viscosity.

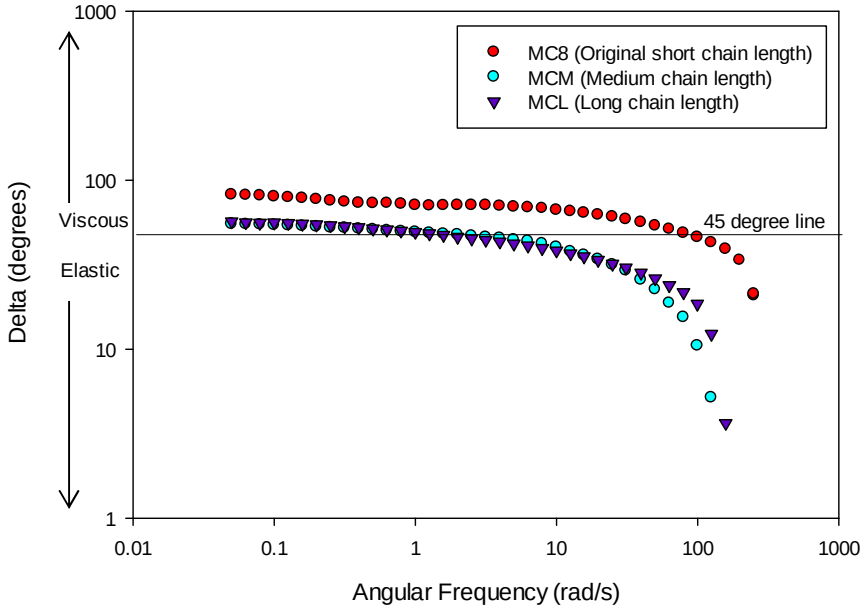

Figure 131 MC binder (short medium and long chain length) showing delta as a function of angular frequency

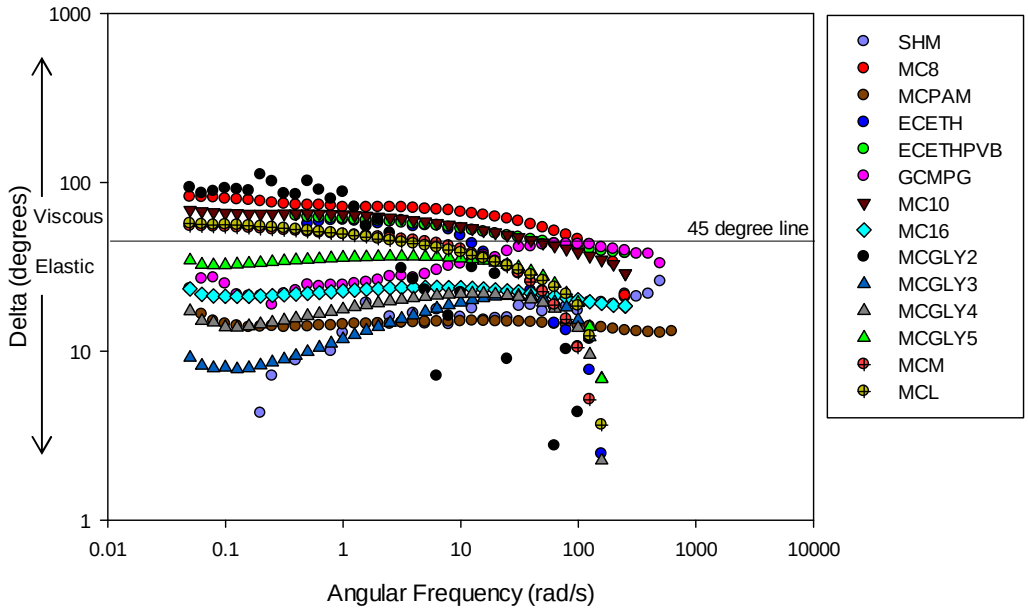

Figure 132 All binders, showing delta as a function of angular frequency plot

4.1.2.4 Group 4 binders LVER and frequency sweep data

LVER and frequency sweeps for MC8PEG42, MC10PEG42 MC16PEG42 have been plotted in this section. Figure 133 shows that the LVER for MCPEG binders was more difficult to determine, thus making frequency sweep data less accurate.

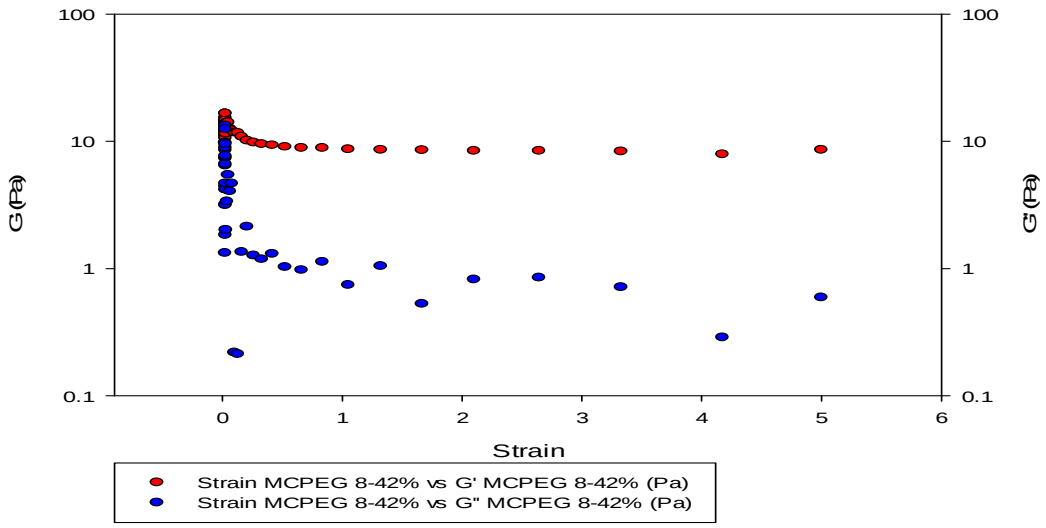

Figure 133 MC8PEG42 binder, LVER showing the elastic and viscous components as a function of strain

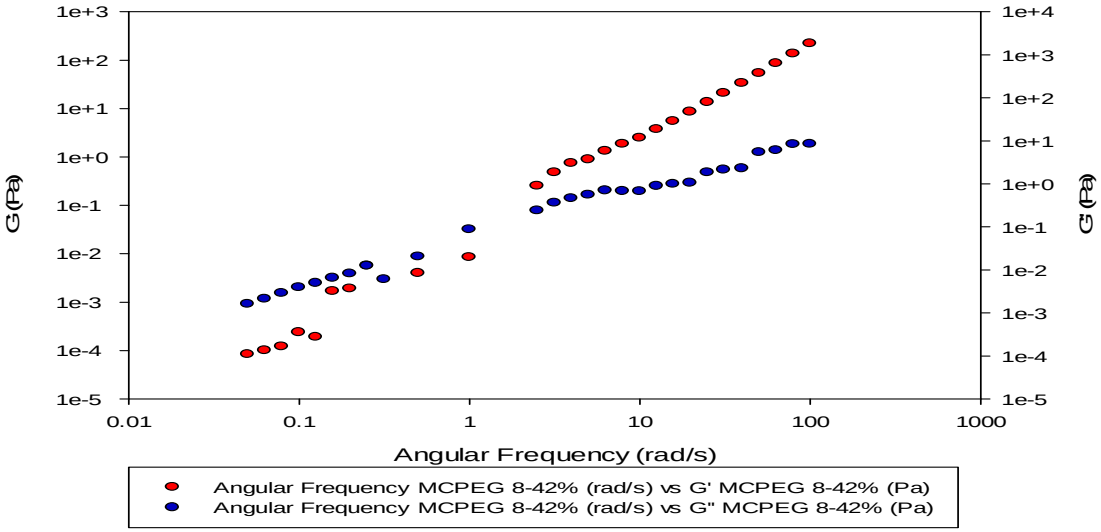

Figure 134 MC8PEG42 binder, showing elastic and viscous components as a function of angular frequency

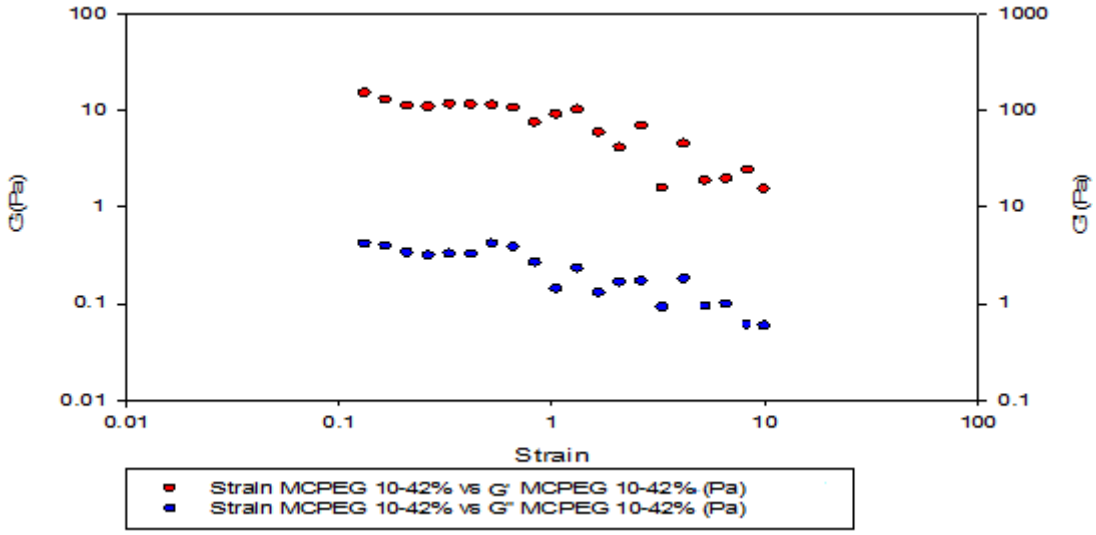

Figure 135 MC10PEG42 binder, LVER showing the elastic and viscous components as a function of strain

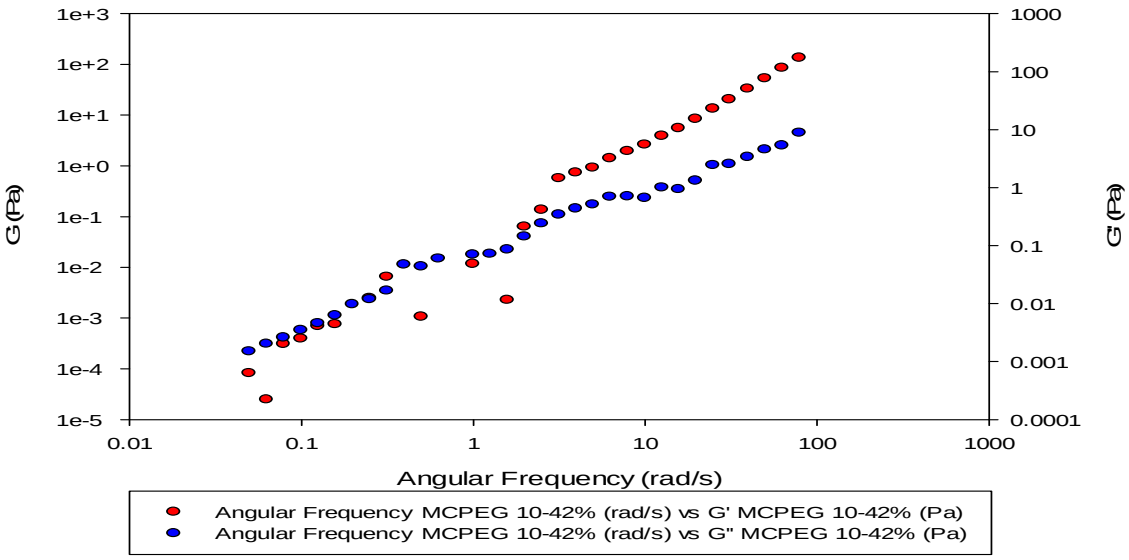

Figure 136 MC10PEG42 binder, showing elastic and viscous components as a function of angular frequency

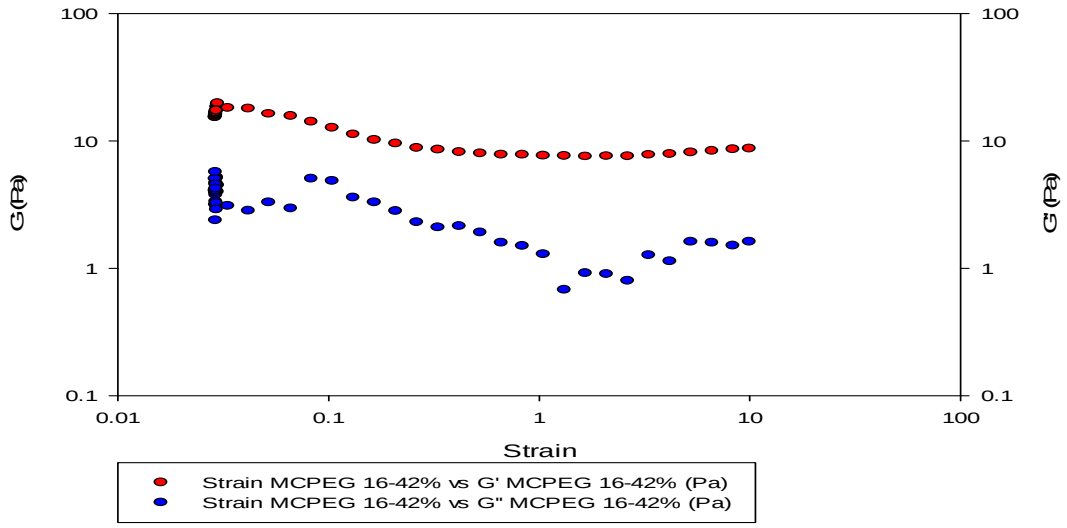

Figure 137 MC16PEG42 binder, LVER showing the elastic and viscous components as a function of strain

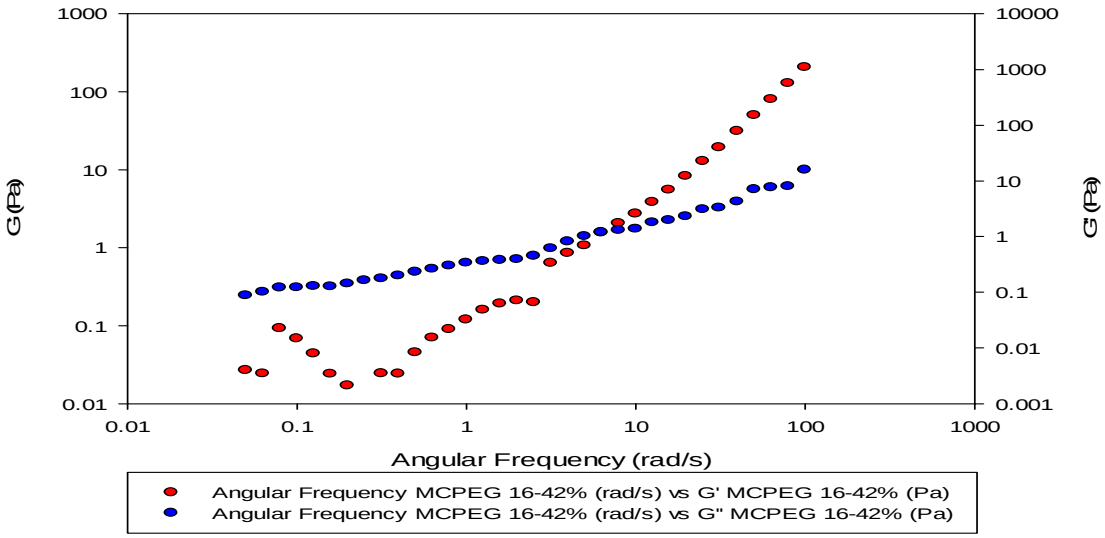

Figure 138 MC16PEG42 binder, showing elastic and viscous components as a function of angular frequency

Increasing the methyl cellulose content helped to resolve stability issues and as a result the LVER was more easily determined. Delta plots of the MCPEG binders in Figure 139 to Figure 141 show the influence that PEG has on the viscoelastic properties compared to binders containing no PEG components.

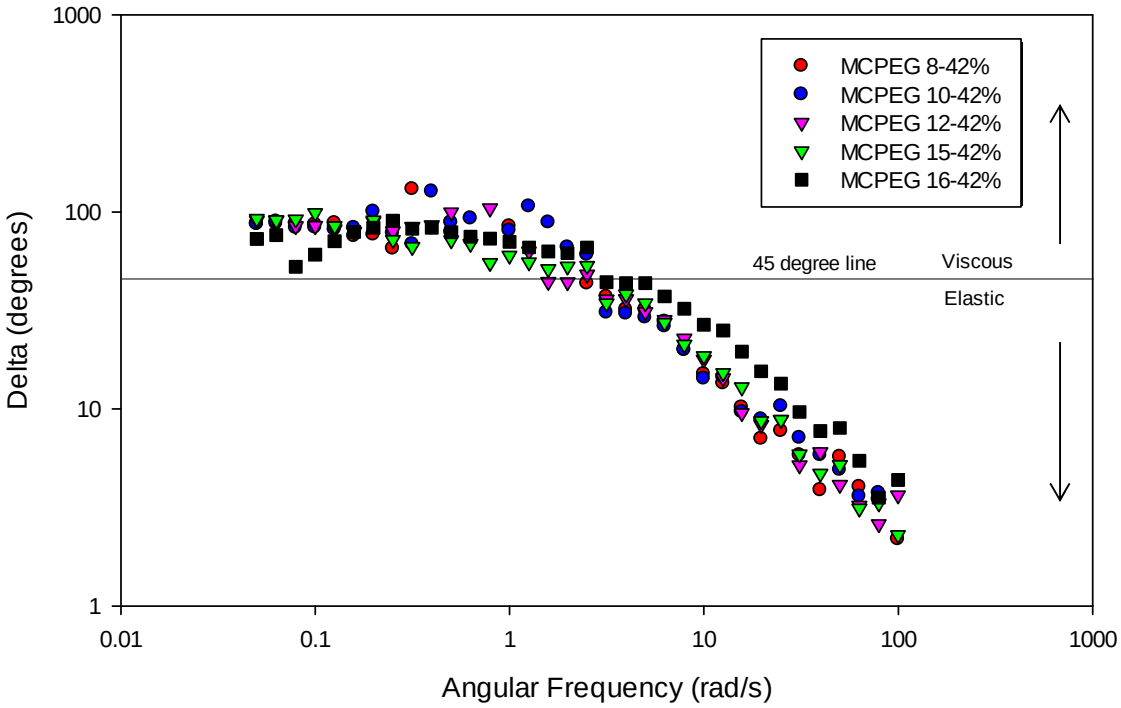

Figure 139 Delta as a function of frequency with increasing cellulose content

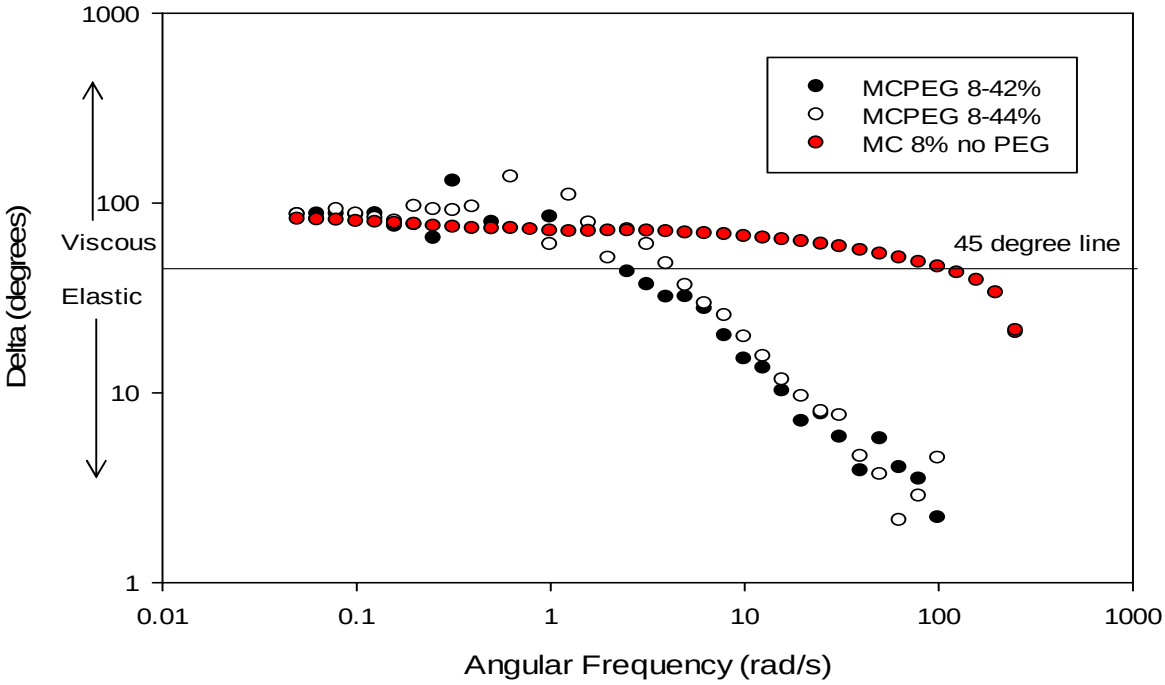

Figure 140 Delta as a function of frequency with increasing PEG content

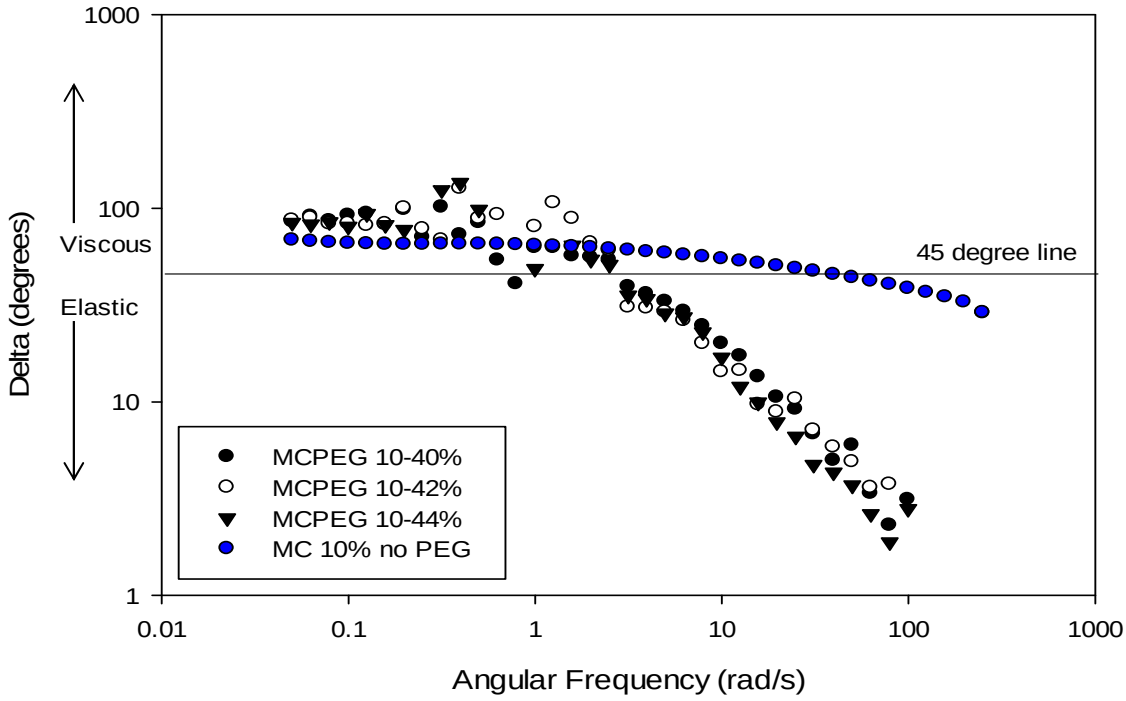

Figure 141 Delta as a function of frequency with increasing PEG content

As with other binder groups, each frequency sweep test was repeated three times. The standard deviation has been averaged across the angular frequency range in Table 28.

Table 28 Group 4 binders delta standard deviation

Binder	Standard Deviation (Pa)
MC842	2.32
MC1042	2.86
MC1242	2.53
MC1542	2.95
MC1642	2.62
MC844	3.91
MC1040	2.31
MC1042	1.42
MC1044	1.69

4.1.2.5 Binder Sytems LVER Lengths

The length of the linear visco-elastic region for each binder system tested has been given in Table 29. A longer LVER represents a greater stability. Group 4 binders showed a short LVER and so no range has been tabulated or plotted. Typically, binders with a significantly shorter LVER (SHM, MCPAM and ECETHPVB) have had a greater apparent viscosity.

Table 29 LVER lengths

Binder Material	Binder Group	LVER (Range of Strain)
SHM	1	0.00009
MC8		0.4
MCPAM		0.01
EC, ethanol		1.038
ECETHPVB		0.6
GCMPG		0.0003, 0.008
MC10	2	0.2
MC11		0.2
MC12		0.2
MC13		0.2
MC14		0.3
MC15		0.2
MC16		0.3
MC18		0.3
MC20		0.2
MC22		0.2
MC25		0.2
MCGLY2	3	-
MCGLY3		0.4
MCGLY4		1.9
MCGLY5		2.1
MCM		0.02
MCL		2.2

4.1.3 Rheology Testing Validation

In order to validate the results of both the oscillatory and stress sweep rheological testing, the Cox-Merz rule was applied [158] and states that:

$$\eta(\dot{\gamma}) = |\eta^*(\omega)| \qquad 4\text{-}1$$

where η and η^* are the steady shear and complex viscosities respectively. For the majority of the binder systems analysed, it was possible to plot the steady shear viscosity at 1 and 10 reciprocal seconds and the complex viscosity at an angular frequency of 10 rad.s^{-1} (Figures 141 to 145). Group 4 binders were evaluated at 150 and 800 reciprocal seconds as it was not possible to obtain data at lower shear rates. Although 150 and 800 reciprocal seconds were used it was not possible to obtain shear viscosity data at 150 reciprocal seconds in Figure 145.

4.1.3.1 *Group 1 Binders*

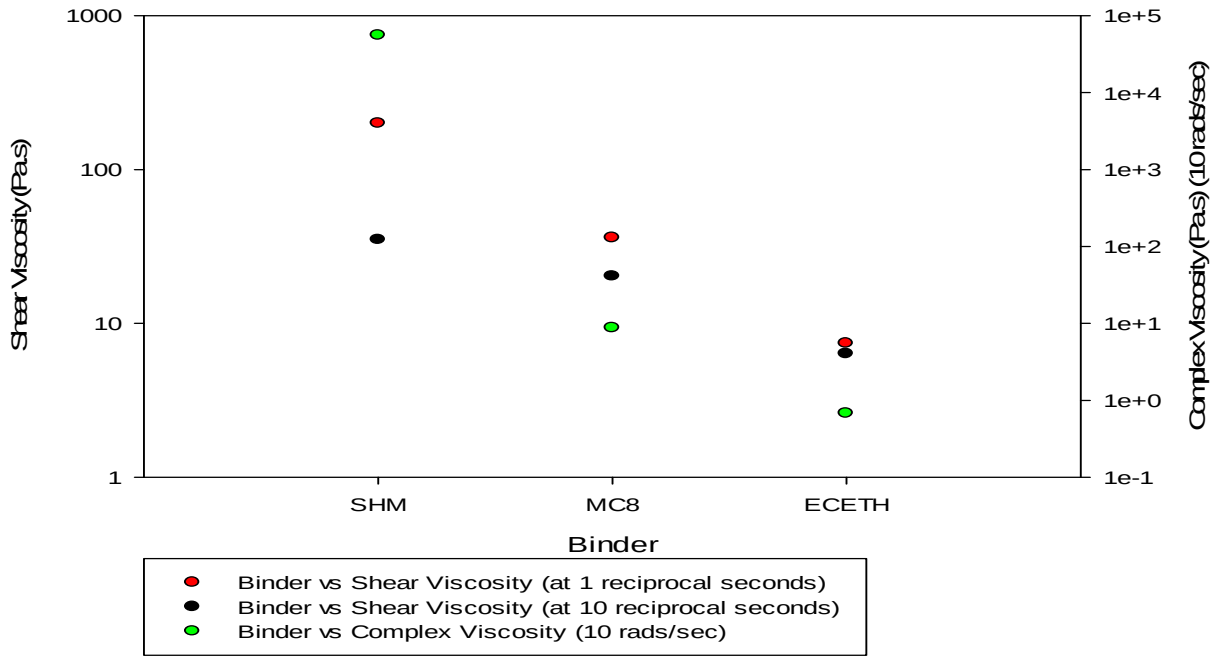

Figure 142 Group 1 binders shear and complex viscosity analysis

4.1.3.2 *Group 2 Binders*

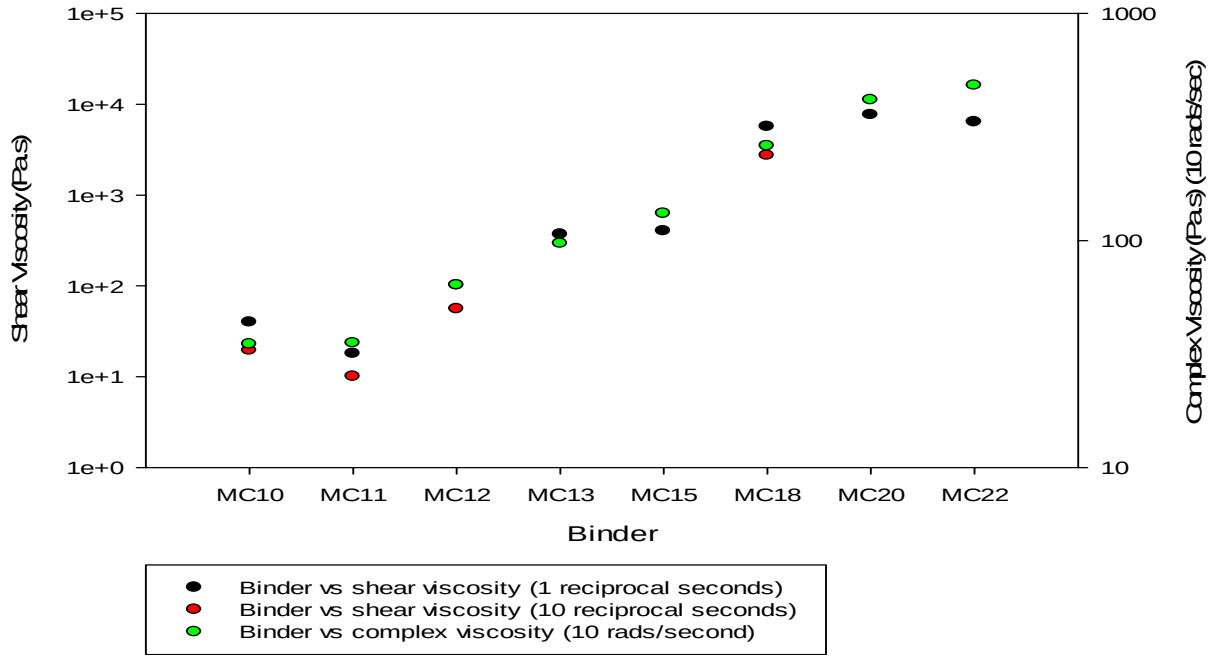

Figure 143 Group 2 binders shear and complex viscosity analysis

4.1.3.3 *Group 3 Binders*

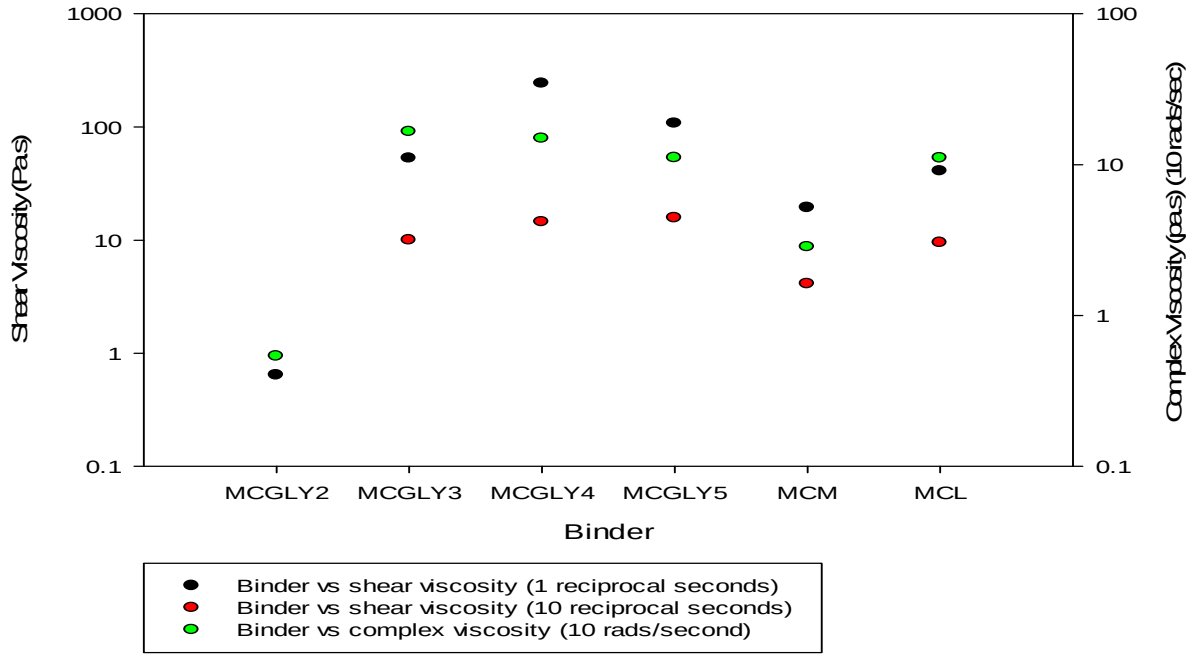

Figure 144 Group 3 binders shear and complex viscosity analysis

4.1.3.4 *Group 4 Binders*

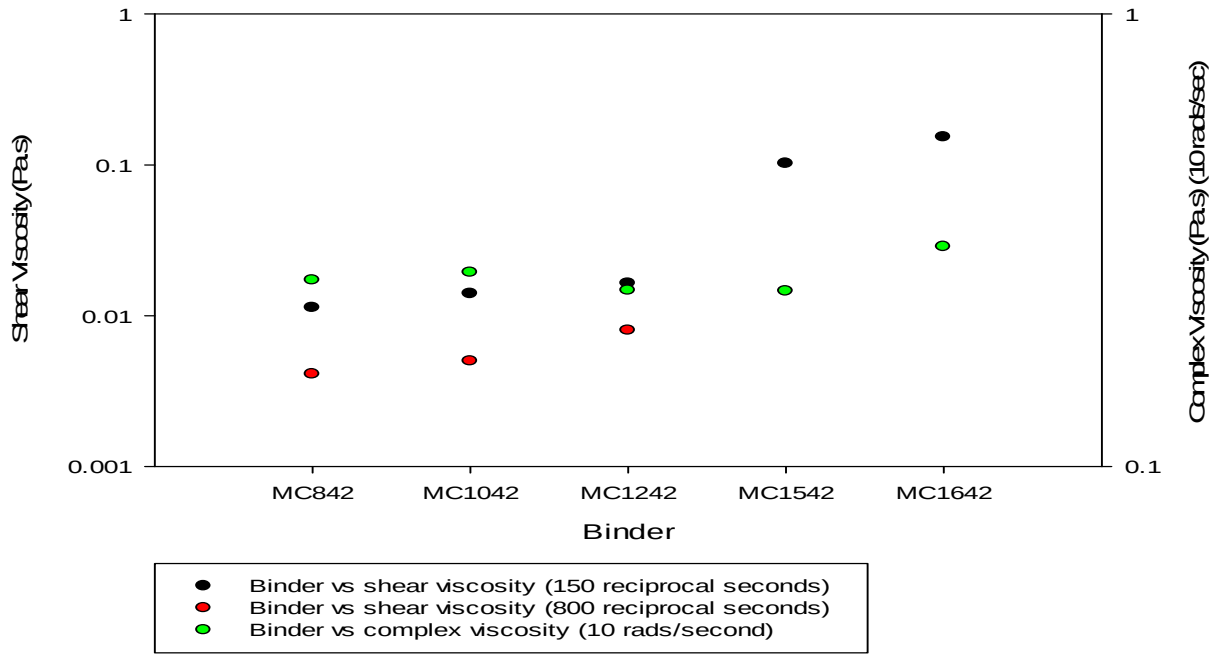

Figure 145 Group 4 binders shear and complex viscosity analysis

4.1.3.5 *Group 4 Binders Extended*

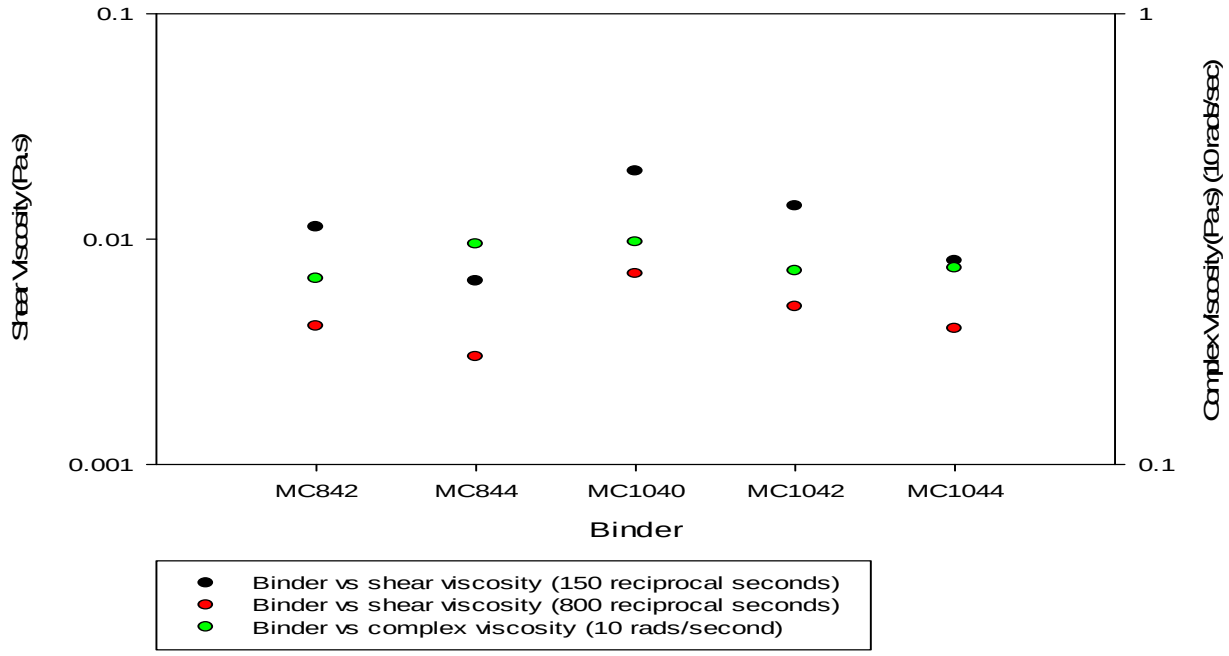

Figure 146 Group 4 binders extended shear and complex viscosity analysis

Although the viscosity data (shear and complex) is measured across different scales in the y axis, there are clear trends in the viscosity measurements for each binder system. However, due to the magnitude of the difference in complex and shear viscosity, the Cox-Merz rule cannot be said to be upheld for these materials.

4.2 Controlled Stress Rheometry Results and Discussion

In plotting the flow curves and combining results with the viscoelastic properties of each binder system, the appropriate binder was selected for further extrusion trials. A range of binders with a range of shear viscosities have been evaluated, each with different viscoelastic properties.

4.2.1 Shear stress sweep testing results and discussion

4.2.1.1 *Group 1 Binders*

The majority of binders were well fitted by the Herschel Bulkley model although the power law model was preferred when no or very low yield was reported. The majority of binders were shear thinning after a low yield stress had been overcome. Binders containing ethyl cellulose and Gelucire 5013 however had larger yield stresses. A low yield stress was observed with the SHM binder which suggests that the high pressures observed during extrusion are related more strongly to a high WC-Co solids loading rather than binder effects. From the Herschel Bulkley model higher K values represent greater shear viscosities for any given value of n. A K value similar to that of the SHM

binder was desirable to achieve a highly viscous binder. It was hypothesised that a highly viscous binder would provide stable extrusion flow similar to the SHM binder. A range of binders with shear viscosities either side of the SHM binder were proposed for extrusion trials as drying properties also needed to be considered. Those binders included the methyl cellulose and water binder, methyl cellulose, water and PAM binder, ethyl cellulose and ethanol binder and the Gelucire 5013-MPG binder. The Gelucire 5013-MPG binder had one of the highest K values of the binders evaluated and hence a high viscosity at a fixed n value. From group 1 binders it can also be seen in Figure 72 that additions of PAM to the methyl cellulose and water binder increased binder viscosity significantly.

4.2.1.2 Group 2 Binders (Increases in methyl cellulose content no PEG)

Increases in the methyl cellulose mass % in group 2 binders increased the K value (Figure 80) and therefore the Herschel Bulkley viscosity of the binder. Figure 82 shows that yield stress remained insignificant, despite increasing the mass % of methyl cellulose. It was expected that the yield stress would have increased with binder shear viscosity (and cellulose content) due to an increased resistance to flow. Group 2 binders with similar K and n values to the SHM binder contained 12-14% cellulose by mass. These binders were expected to behave in a similar way to the SHM binder when mixed into a feedstock and extruded. The shear thinning behaviour of methyl cellulose based binders has been described by Clasen et al. [60] and is caused by disentanglement of polymer coils and increased orientation of the coils in the direction of flow. Based on the findings of binder flow properties a range of methyl cellulose binders were evaluated under extrusion conditions (8-16 % by mass). Such variations in cellulose content allowed viscosity modifications to be made without varying WC-Co powder components or burnout quality.

4.2.1.3 Group 3 Binders Increases in glycerol content

In Figure 89 increasing the glycerol content in MCGLY binders increased the Herschel Bulkley K value and therefore Herschel Bulkley viscosity for given n. MCGLY3, MCGLY4 and MCGLY5 binders had similar K values to the SHM binder and therefore similar extrusion flow behaviour was expected. However when analysing LVER plots, this group of binders had poor stability due to poor miscibility of methyl cellulose with glycerol. Viscosity measurements were not possible with the MCGLY1 binder and therefore Herschel Bulkley parameters could not be defined. Similar issues presented themselves with the MCGLY2 binder although Figure 83 shows that the data was reasonably well fitted with the Herschel Bulkley model. Noisy and poorly fitted flow curves occurred more frequently with lower viscosity materials that had a tendency to separate out quickly.

4.2.1.4 *Group 4 Binders*

Binders containing methyl cellulose had insignificant yield stresses where PEG was not combined in the mix although adding PEG caused Bingham behaviour. The Bingham viscosities have been plotted in Figures 92 to 94 and show that group 4 binders have Bingham flow above the yield stress. From the flow curves presented in Figures 92 and 93, the Bingham viscosity decreases when PEG content is increased. Initially it was expected that added PEG would increase binder viscosity. However in agreement with work carried out by Turhan et al. [159] the PEG molecules reduce intermolecular interaction between cellulose molecules by forming hydrogen bonds giving increased flexibility and extensibility. In section 4.1.1.4 it was observed that increasing the PEG content lowered the Bingham viscosity of the binder. Conversely, Figure 94 indicates that when methyl cellulose content was increased, then the Bingham viscosity increased. Small increases in cellulose mass % from MC8-MC12 binders had little effect on Bingham viscosity. However, MC15 and MC16 binders had significantly greater Bingham viscosities. The increasing Bingham viscosity can be attributed to increased cross-linking. As with hydroxypropyl methyl cellulose and PEG mixtures [160], with a greater concentration of methyl cellulose, more interactions occur between the PEG and methyl cellulose chains forming a highly cross-linked structure.

4.3 Oscillatory rheometry testing results and discussion

Oscillatory rheometry testing was employed to investigate both stability and viscoelastic properties of binders. Linear viscoelastic regions for each binder system were determined so that frequency sweeps could be carried out.

4.3.1 Group 1 binders

Figures 102 to 113 show the LVER and frequency sweep plots of group 1 binders. The delta plot (Figure 114), describes the viscoelastic behaviour of each binder system with angular velocity. The methyl cellulose binders containing PEG are described separately due to their significantly different behaviour. The SHM binder is predominantly elastic although showing a tendency towards viscous behaviour with increased angular velocity. Opposite trends are shown for the methyl cellulose (8%) formulation and the ethyl cellulose and ethanol based binder containing PVB. Adding PAM to the methyl cellulose binder altered behaviour from viscous to elastic. This gave flow behaviour tending towards that of the SHM binder. The Gelucire 5013 MPG binder was also elastic in its behaviour with a slight tendency towards viscous behaviour at increased angular velocity.

4.3.2 Group 2 binders

Figure 121 shows that the phase angle delta decreased with increased cellulose concentration. The binder therefore became more elastic with increased cellulose content. Although elastic (solid) behaviour increased with increasing cellulose content, little effect was observed on the LVER. Elasticity was developed up to 13 mass % methyl cellulose and further increases in cellulose content increased the shear and the complex viscosity (Figure 143). Figure 143 shows that oscillatory analysis of complex viscosity followed the same trends of shear viscosity measured in the controlled stress sweeps for each binder in group 2. Although similar trends were observed, there was a large difference between the shear and complex viscosity. This indicated that the Cox-Merz rule could not be applied to methyl cellulose binder systems in this work. The MC8 binder used in group 1 was almost completely viscous in comparison to more highly loaded binder suspensions in group 2. Figure 121 showed that at higher angular velocities binders increase in elastic behaviour. Increased elasticity at a higher frequency of oscillation imparts binder stiffening. Therefore, during faster extrusion speeds increased work was expected to have a similar effect. Visco-elastic materials have been considered as a series of springs coupled with a series of viscous dashpots [161]. At lower frequencies of oscillation the springs can elongate whilst the dashpots have time to extend to greater lengths than the springs. The deformation of the springs eventually reaches equilibrium and no further deformation takes place [162]. The dashpots however deform continuously under oscillation. At this frequency, energy is dissipated and lost and hence the sample behaves more like a viscous liquid. At higher frequencies, the springs can elongate and contract, but the dashpots cannot react quickly enough. Energy is therefore stored in between each cycle of oscillation and the sample behaves as an elastic solid. The work completed on group 2 binders supports this theory with each increase in cellulose content.

4.3.3 Group 3 binders

Increasing glycerol content in methyl cellulose based binders increased the elastic component (Figure 130). Table 29 also shows that increases in glycerol content increased the length of the LVER and therefore binder stability. Binder MCGLY2 behaves as a viscous liquid at low angular frequency and elastically at higher angular frequencies. This is likely to be an effect of binder instability as the movement from viscous to elastic behaviour is sudden and data is scattered. Similarly, longer chain length methyl cellulose based binders behave more elastically than the shorter chain length binder. Figure 144 shows that the complex viscosity increased with increasing chain length from 60000-80000 molecular weight which supports this result although the shortest chain length (41000) had a higher complex viscosity. A large increase in chain length (41000-80000 MW) is required in order to observe noticeable changes in elastic behaviour. The MCM binder (61000 MW) has a short LVER in

comparison to the MCL binder (80000 MW) although the frequency sweep curve is similar. Clasen has carried out similar work with Hydroxypropyl methyl cellulose in which the molecular weight was increased and frequency sweeps were run. He suggested that at low frequency the viscous modulus was greater than the storage modulus because deformation takes place so slowly that the majority of energy is dissipated by viscous flow [60]. At this stage, cellulose chains have time to avoid the imposed deformation by relaxing to a more favourable state. Relaxation occurs by slippage of entanglement points of intertwined polymer. He reports that as frequency increases, relaxation has little time to take place and polymer chains can no longer slip past one another and so entanglement points act more as a solid network enabling a greater ability to store energy. Therefore at higher frequencies there is a more established elastic behaviour [60]. Similar affects were seen in this work, as increased chain length resulted in a more rapidly increasing elastic component than viscous component at higher frequencies (Figure 127 and Figure 129). The point of intersection between viscous and elastic components was said to shift to lower frequencies with increasing chain length by Clasen et al. This work supports that theory although small shifts in the intersection point were observed with large changes in chain length (Figure 127 and Figure 129).

4.3.4 Group 4 Binders

Methyl cellulose binders containing PEG showed significantly different visco-elastic behaviour to the other binders. The binders in this group behaved with increasing elasticity with increased angular frequency. Changing concentrations of either PEG or methyl cellulose however, made little difference to the viscoelastic behaviour. Increases in elasticity were more abrupt with this binder group than with others (Figure 139 to Figure 141). A short LVER also suggested that the MCPEG binder formulations were lacking in stability. Whilst a cross-over between viscous and elastic behaviour is observed for each of the binders, it occurs more suddenly for group 4 materials. A more progressive cross-over would result in more predictable behaviour thus implementing a more easily controlled formulation. Complex viscosity analysis in Figure 146 shows that similar trends were observed between controlled shear stress and oscillatory measurements.

4.4 Binder Selection

The binder selection process aimed to determine which of the binders gave similar flow properties to those witnessed with the SHM binder. A high binder shear viscosity was desirable to deliver extrudate with high stability. Flow characteristics were the focus at this stage in order to limit the number of extrusion trials required. Binder materials from group 1 (Table 17) were automatically selected for dough feedstock preparation because of the range of properties observed either side of the SHM binder. Larger extrusion diameter performance encouraged investigation of the methyl

cellulose based formulations in further detail. The SHM, methyl cellulose containing polyacrylamide, and Gelucire 5013 binders were not suitable for large diameter products due to cracking during drying. Methyl cellulose binder systems containing PEG (from the WC-Co) were later shown to dry more successfully and hence binder selection was narrowed down to find the optimum PEG and methyl cellulose contents in the binder. Although higher MC contents increased Bingham viscosity and thus extrudate stability, increased PEG contents lowered Bingham viscosity. An increased PEG content was driven by increasing the WC-Co solids loading. The optimum WC-Co solids loading was required and so this determined the PEG content. The optimum solids loadings for methyl cellulose based binders was 41.6 vol%. Therefore the PEG content was fixed at 22.22 mass % for the MC8 binder. For higher MC content, the mass % of PEG was reduced (Table 10). Following the determination of the optimum solids loading (see Chapter 5), the binder system chosen was further modified. By increasing or decreasing the cellulose content it was determined that the Bingham viscosity of the binder could be easily varied. This had a direct effect on dough apparent viscosity and therefore extrudate stability and flow properties. In the preparation of doughs, the binder formulation changes as the PEG impregnating the dry powder is dissolved into the MC polymer solution. To analyse the rheological behaviour of the resulting liquid phase system, PEG was systematically added to the MC polymer solutions. The MC-PEG binder systems and others taken forward for dough manufacture and evaluation are given in Table 30. As various solids loadings were evaluated the ratio of MC8 to PEG varied as well and this is illustrated in Table 30.

Table 30 Binder selection

Binder System	Description
SHM	As Table 10
MC8	As Table 10
MC10	As Table 10
MC12	As Table 10
MC15	As Table 10
MC16	As Table 10
MCPAM	As Table 10
ECETHPVB	As Table 11
GCMPG	As Table 11
MCGLY5	As Table 10
MCM	As Table 10
MCL	As Table 10
MC8-41.7	MC8 binder as standard, feedstocks prepared with increasing WC-Co solids loading
MC8-41.8	
MC8-41.9	
MC8-42	
MC8-42.5	

Typically, a binder would be selected based on rheological properties that are well correlated to the quality of the final extruded product. Focussing on group 2 binders, from Chapter 5, it can be seen that the higher cellulose concentrations in the binder lead to higher dough viscosities in the extrudate (Figure 147). Ordinarily, the yield stress of the binder and extrudate would be a good starting point for material classification and the two properties should be well correlated. However as the yield stress of the binders in this group were very low even when PEG additions to the binder were considered, a better measurement is the K value obtained from the Herschel-Bulkley tests and shear stress measurements. Figure 147 is a plot of dough viscosity at constant shear rate (100 s^{-1}). At constant shear rate, figure 147 shows that dough viscosity increases with increasing cellulose content in the binder. The K values from the Herschel Bulkley experiments given in table 20 are also plotted in this figure. In the lower cellulose concentration region of 8-12 mass%, the material behaviour is much more predictable and the two properties are well correlated, as shown in figure 148.

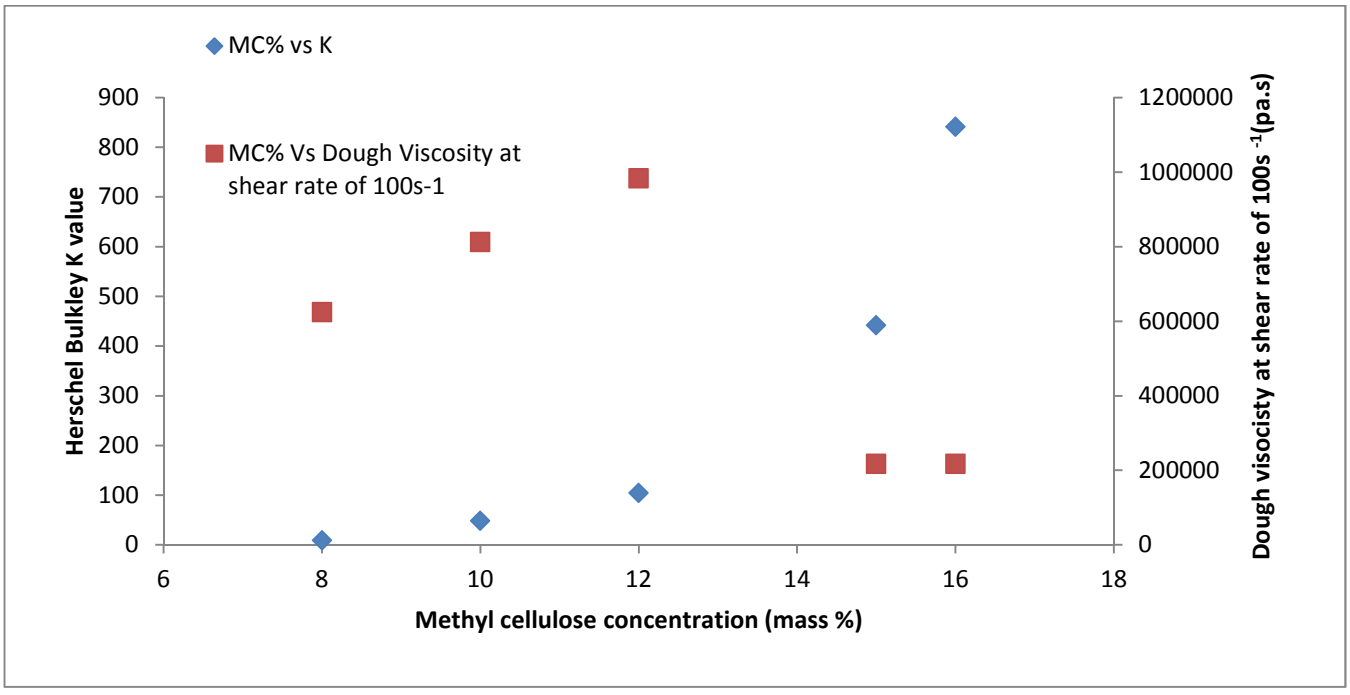

Figure 147 Herschel Bulkley binder K value vs dough viscosity at 100 s^{-1}

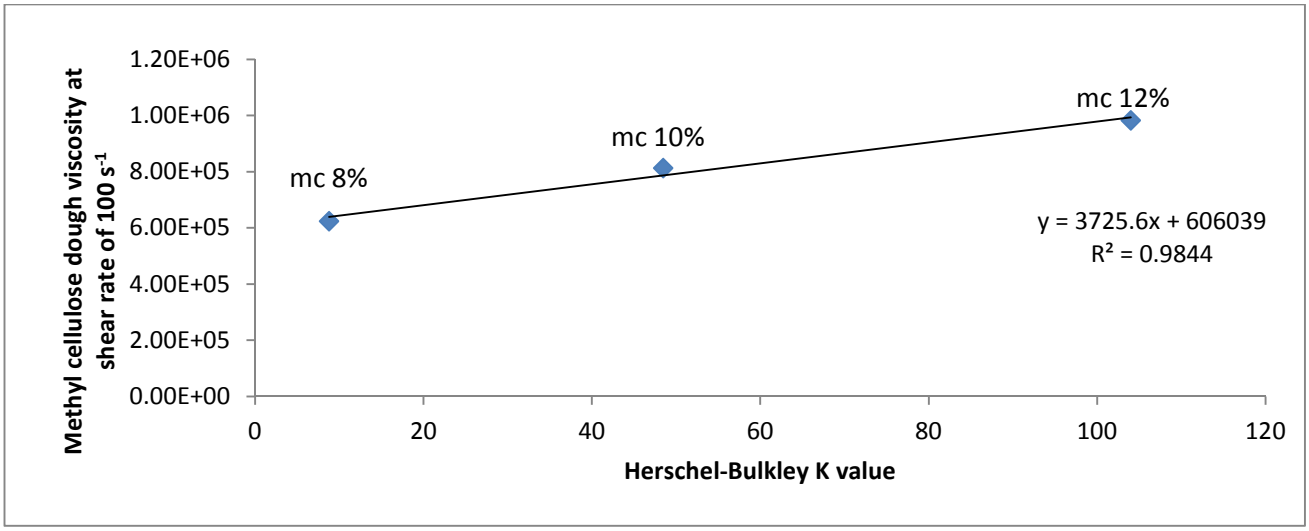

Figure 148 Methyl cellulose dough viscosity at 100 s^{-1} vs Herschel Bulkley binder K value

Assuming that the WC-Co solids loading remains constant throughout and that only low cellulose concentrations are considered, figure 147 can be used to predict dough viscosity at a shear rate of 100 s^{-1}. This is based on the binder K value which is controlled with cellulose concentration according equation 4-2.

$$\mu_{dough} = 3730K + 606040 \qquad 4\text{-}2$$

Equation 4-2 allows for the development of quality procedures in the binder preparations stages. As an example, dough viscosity in the range of 800000 – 1000000 Pa.s at a shear rate of 100s^{-1} based on practical extrusion work is desirable. Theoretically, if the binder K value is in the range of 50-105 then this is achievable. However, this is a large range to use as a quality control test and would bring large variation to the feedstock (for both binder and dough). A range of K from 50-70 for the binder would be also be achievable and this is a more suitable range as it encompasses the MC 10 binder formulation which gave the most positive extrusion results. Further quality tests could also be made in the binder preparation stage to insure that the correct formulation is obtained. As described in section 4.1.2.2, the elasticity of the binder increases with cellulose content. As the MC 10 formulation gave the most promising extrusion results, the viscous and elastic components should be considered for future material preparation. From figure 118, using a frequency range of 1-10 $rads^{-1}$ the elastic modulus should range from 50-260 Pa. In the same frequency range, the viscous modulus should range from 90- 400 Pa. This is a large range for a quality control test although there is an opportunity to reduce this range with further testing. Combining the above tests should provide adequate repeatability for extrusion dough behaviour that is related directly to the binder characteristics.

Chapter 5 Feedstock Mixing and Analysis

In this chapter the development of paste formulations from binders identified and characterised in Chapters 3 and 4 respectively is reported. Mixer Torque rheometry is applied to materials formulated with group 1 binders to evaluate mixing performance and optimum binder content. The maximum solids loading via stock extrusion and density via pycnometry are also reported to further assist in paste selection. The results of these approaches to mixing characterisation are reported and discussed.

5.0 Extrusion Feedstock Formulation and analysis

Figure 149 shows a schematic representation of a typical mixer torque rheometry (MTR) experiment. For the group 1 binders, MTR experiments were undertaken by working from high to low liquid content. For the first solids concentration there would be an initial torque rise up to a maximum which would fall back to a stable value (typically +/- 5% torque variation) as indicated by the first plateau in Figure 149. This was taken as the torque value for that solids loading. At the completion of mixing for each stage, a small sample of the paste was removed and density measured. WC-Co powder (containing PEG) was added in 1 vol % increments and mixed to stability with each addition before taking a torque reading (shown by the successive plateaus) and sampled for density. The process was repeated until a paste was no longer formed. It is these data points along with density that are plotted in the paste development plots.

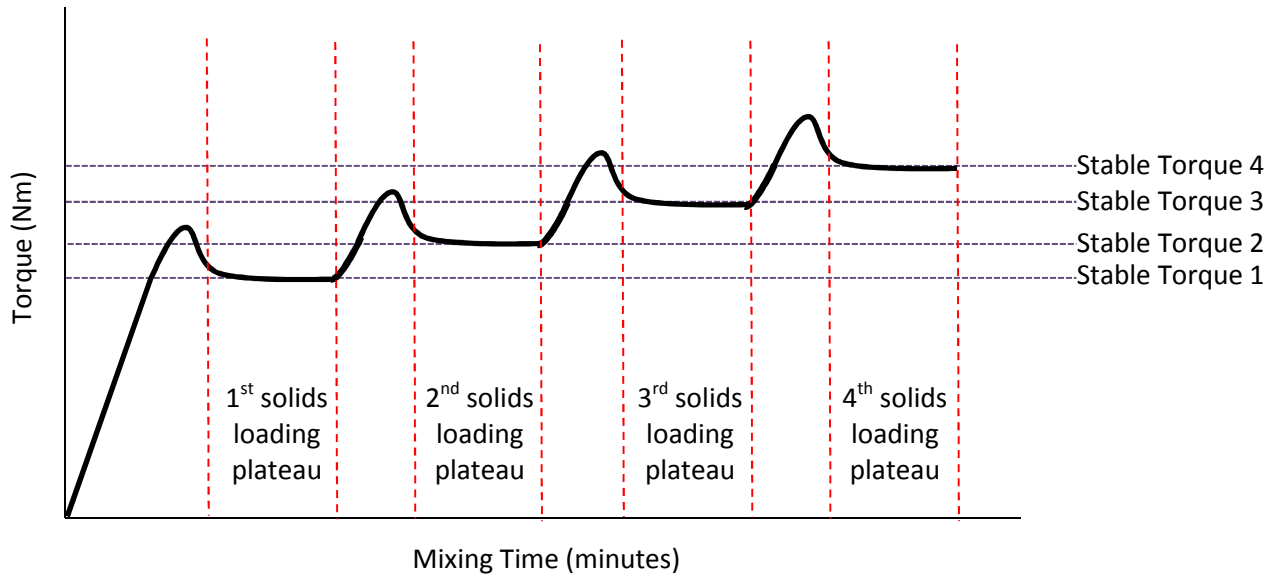

Figure 149 Schematic representation of mixer torque rheometry

Batches of paste were also mixed to completeness with increasing solids loadings in sufficient quantity to allow extrusion. Figure 159 shows the inverse of the recorded pressure drop through a fixed die geometry described in section 5.3.2 for these pastes. For all the other group 1 formulations, only the MTR procedure was carried out and the results are plotted in Figures 151, 153, 155 and 157. The Werner and Pfleiderer (WP) z-blade mixer was used to allow comparison of blade-bowl gap tolerances. The blade clearance for the Winkworth mixer was 0.6 mm between the blades and mixer bowl. The clearance between the two blades was 0.3 mm when in opposing positions. The WP mixer had a blade to blade clearance of 0.9 mm and a blade to bowl clearance of 1.2 mm. Feedstocks prepared in the Winkworth mixer had torque, temperature (mixer bowl) and density measured. Stable torque readings were taken after mixing each of the material additions to completeness (Table 31 and Figure 150). The Werner and Pfleiderer mixer did not have this capability.

Table 31 Stable Mixer Torque Readings

Dough Type	Binder Group	Mixer Stable Torque (Nm)	WC-Co Solids Loading (vol %)
MC8	1	6.6	41.6
MCPAM	1	3.6	38
ECETHPVB	1	3.9	45.8
GCMPG	1	6	48.5
MC10	2	2.4	41.6
MC12	2	1.6	41.6
MC15	2	2.2	41.6
MC16	2	2.5	41.6
MCS	3	6.6	41.6
MCM	3	6	41.6
MCGLY5	3	2.4	41.6
MCMPG	3	4.3	41.6

More highly loaded pastes in group 1 generated greater stable mixer torque with the exception of the MC8 dough, indicating that in this case the binder system is also contributing to mixer torque. Group 2 materials gave relatively constant stable torque readings despite increases in cellulose content. Table 31 shows that mixer torque decreased with increasing methyl cellulose chain length and decreased further with additions of MPG and glycerol. Decreased torque with increased chain length was unexpected due to binder rheological results in Chapter 4 (Figure 87) in which binder viscosity increased with chain length. However, a decrease in torque was expected with additions of MPG and glycerol as they are better lubricants to the cellulose than water alone.

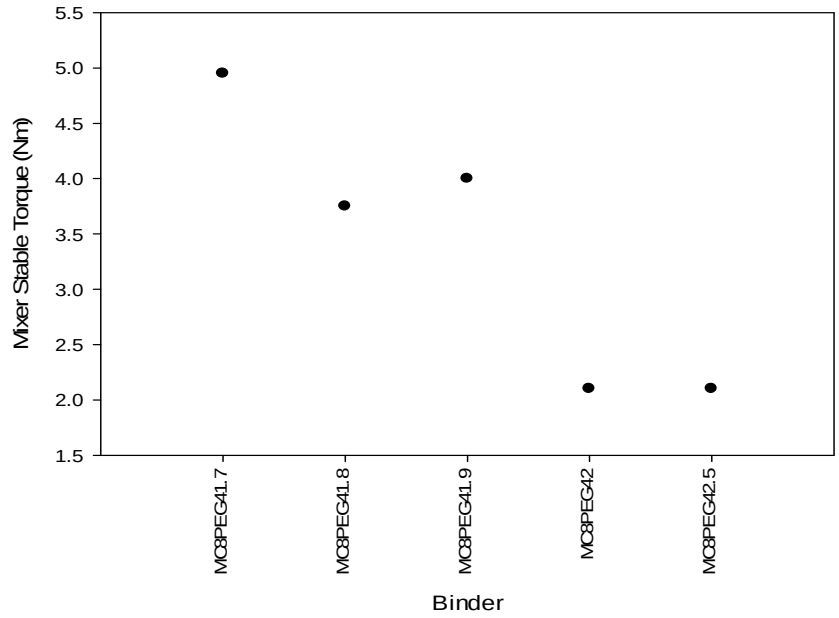

Figure 150 Stable mixing torque for dough prepared from group 4 binders

Figure 150 shows that mixer torque decreased with increased WC-Co solids loading.

5.1 Determination of Critical Solids Loading

Using MTR the critical solids loadings required to make a stable paste were determined for group 1 doughs and are reported in Table 17. The maximum packing fraction was determined using extrusion methods described in section 3.7.5 in order to confirm the accuracy of the mixer torque experiments. These observations were linked to density measurements, assuming that no porosity existed. Theoretical density was calculated from volume fractions and measured densities of individual components in the feedstock. The volume fraction was calculated from component density and mass of material added.

5.1.1 Mixer Torque Rheometry

Mixer torque rheometry methods were carried out following the protocol described in section 3.7.4. Figures 151, 153, 155 and 157 show how torque varies for group 1 feedstocks with increasing WC-Co content. The composition of pre-mixed binder materials for each mixer torque curve is given in Table 32.

Table 32 Mixer torque binder components

Binder	Components	Mass %
MC 8% (no PEG)	Methyl cellulose	8.00
	Distilled water	92.00
MCPAM	Methyl cellulose	17.64
	Distilled water	78.68
	Polyacrylamide	3.68
ECETHPVB	Ethyl cellulose	19.69
	Ethanol	64.98
	Polyvinyl butyral	15.33
GCMPG	Gelucire 5013	50.00
	Propylene glycol	50.00

For materials mixed in the Winkworth mixer, Figures 151, 153, 155 and 157, the peak torque is indicated as an aid to interpretation.

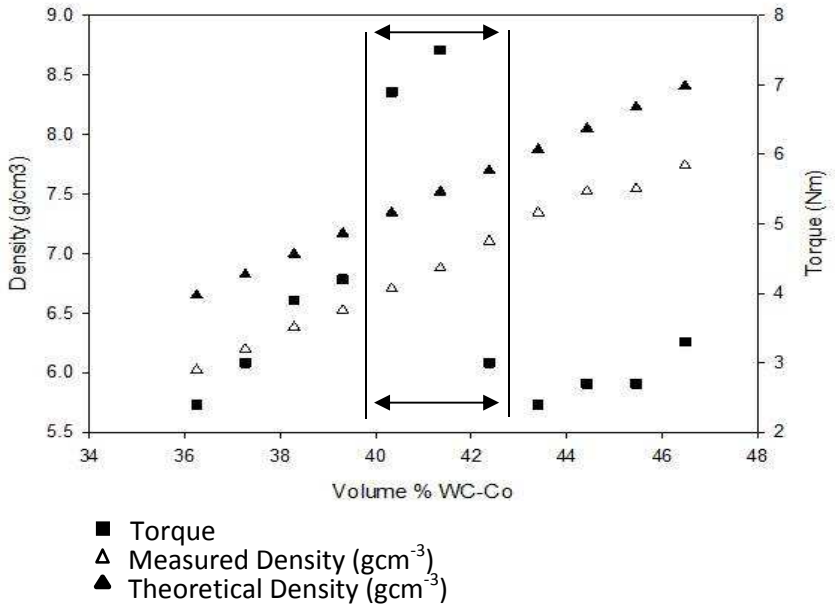

Figure 151 MC8 dough, torque and density measurements (Winkworth mixer)

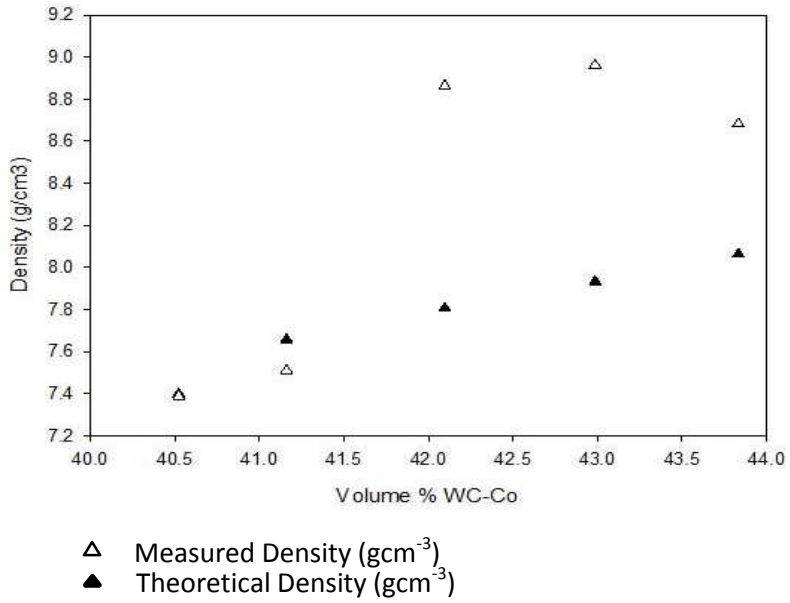

Figure 152 MC8 dough density plot (Werner and Pfleiderer mixer)

Figure 151 shows the MTR results for MC8 dough formulations. Figure 152 shows the same feedstock formulation, prepared in the Werner and Pfleiderer mixer described in section 3.7.4. Figure 153 shows the same set of experiments as Figure 151 with the PAM additions to the feedstock and a similar torque profile is observed.

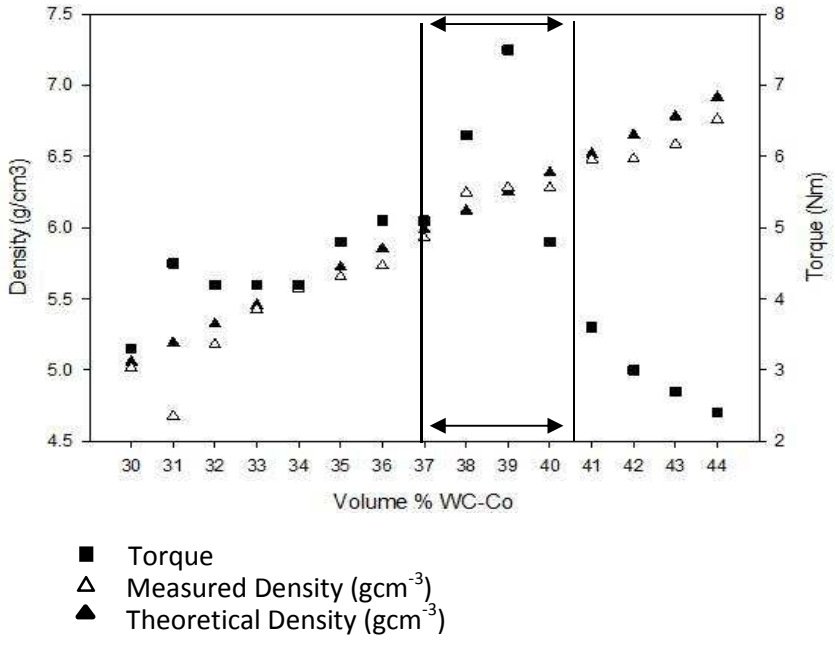

Figure 153 MCPAM dough, torque and density measurements (Winkworth mixer)

Figure 154 shows the theoretical and measured densities for the MCPAM dough mixed in the Werner and Pfleiderer mixer. Figure 142 shows the torque profile of the ethyl cellulose and ethanol dough.

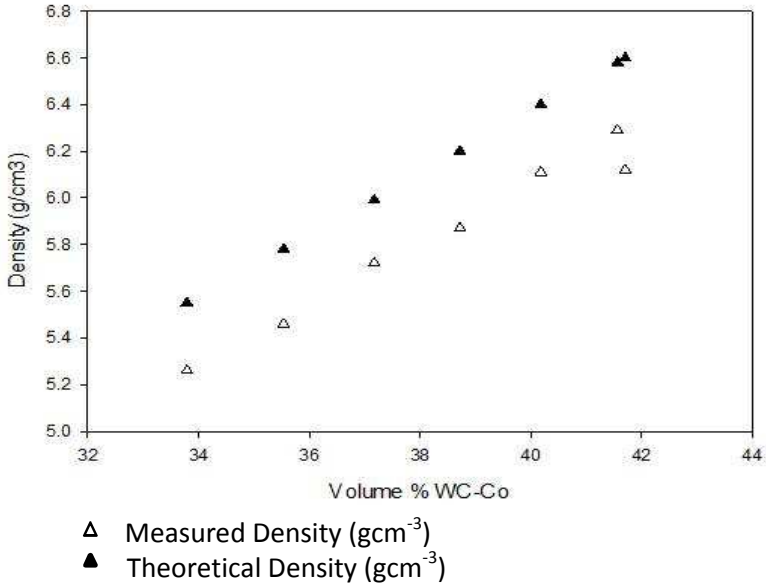

Figure 154 MCPAM dough density plot (Werner and Pfleiderer mixer)

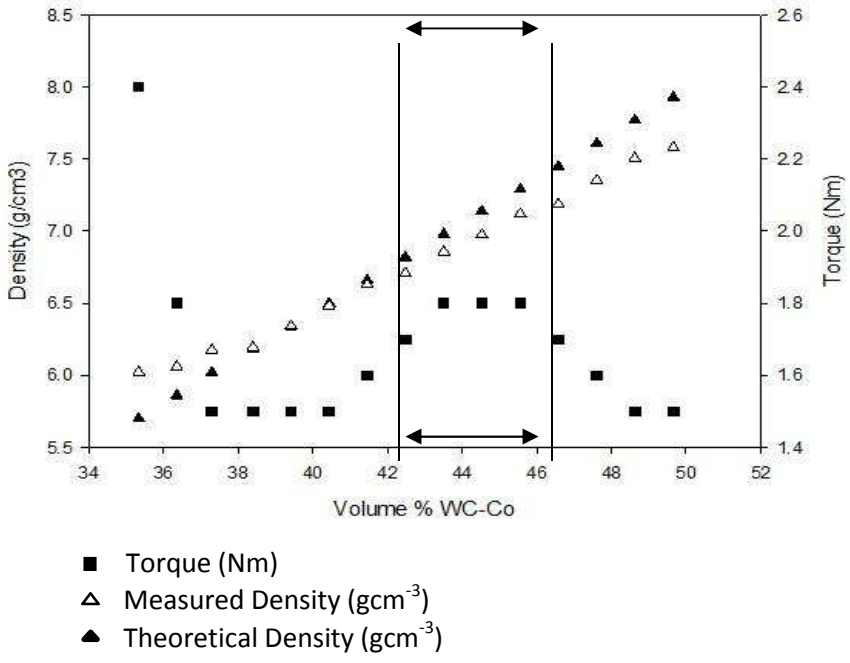

Figure 155 ECETHPVB dough, torque and density measurements (Winkworth mixer)

The torque profile is flatter than with other systems although a peak and fall of torque is still observed. Similarly, Figure 154 also shows a peak in density at higher solids loadings.

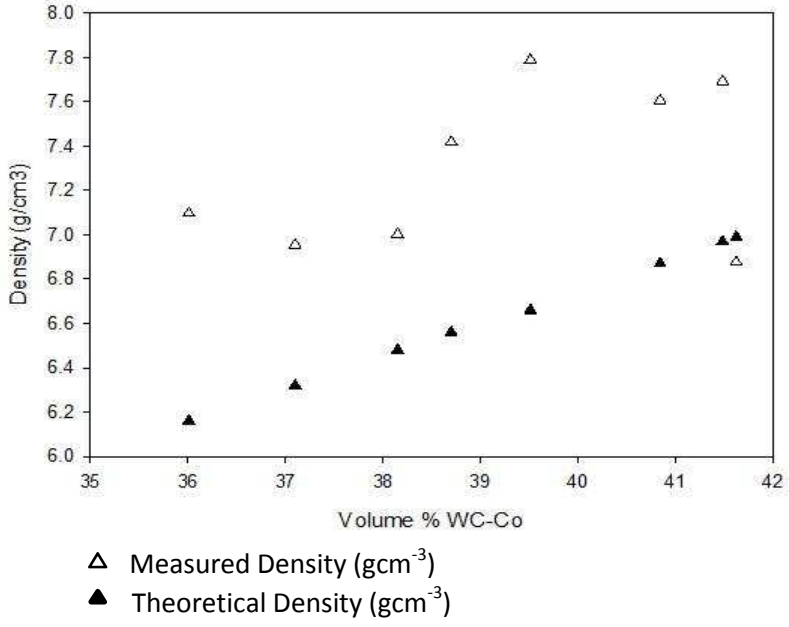

Figure 156 ECETHPVB dough density plot (Werner and Pfleiderer mixer)

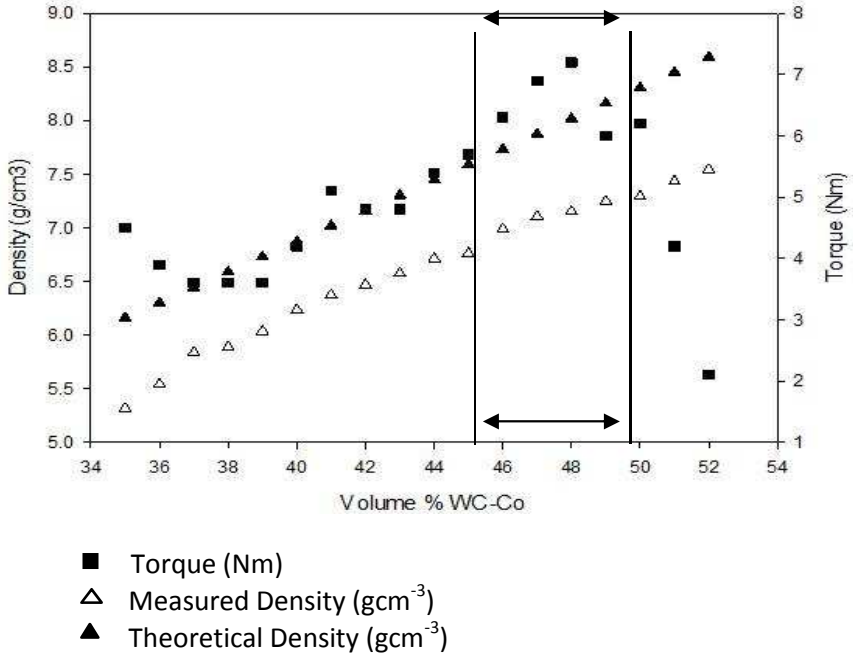

Figure 157 GCMPG dough, torque and density measurements (Winkworth mixer)

Figure 156 and Figure 157 show the torque profile and density measurements from the Winkworth and Werner and Pfleiderer mixers for the Gelucire 5013 and MPG dough feedstock respectively.

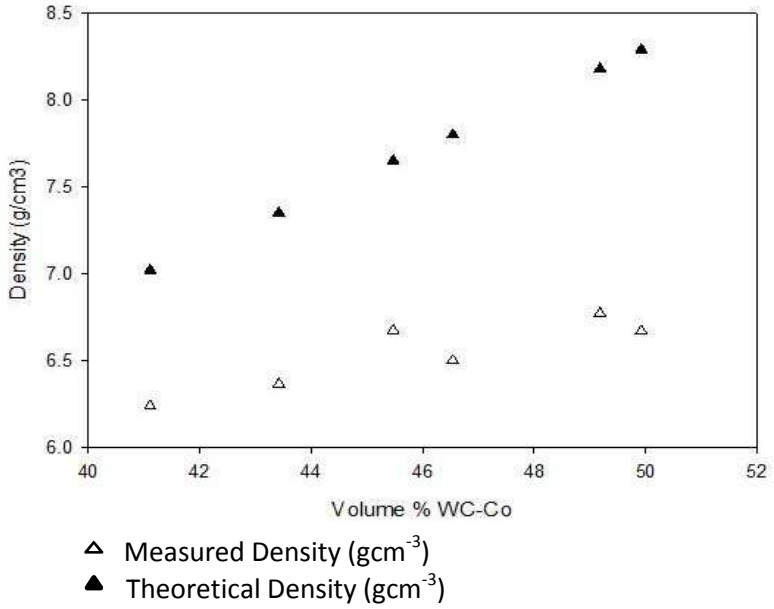

Figure 158 GCMPG dough density plot (Werner and Pfleiderer mixer)

Following mixer torque rheometry experiments, extrusion of the paste formulations was carried out to allow the inverse of extrusion pressure as a function of solids loading to be drawn for the methyl cellulose formulation (MC8), Figure 159.

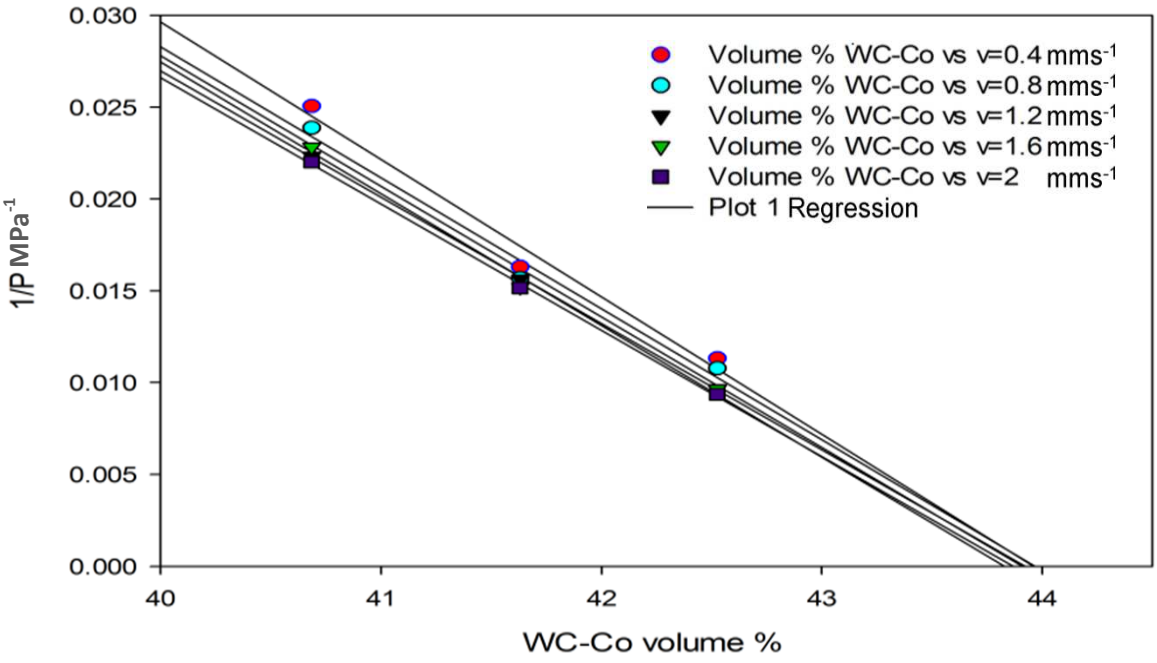

Figure 159 Inverse pressure data for extrusion feedstock prepared from the MC8 binder

Due to the inter-related properties caused by mixer temperature and torque respectively, mixing temperature investigations are also reported in Appendix H.

5.1.2 Dough Density Measurements

Dough densities at the optimum WC-Co content are given in Table 33. For the MC8 based feedstock, several WC-Co solids loadings were studied and in this case the densities are similar to those plotted in Figure 151. The SHM feedstock had a consistently high density as it could be prepared at a higher WC-Co content without granulating.

Table 33 Dough density measurements at fixed solids loadings

Dough Type	Binder Group	WC-Co Solids Loading (Vol%)	Density (g/cm^3)
SHM	1	43.6	7.50
MC8	1	41.7	6.76
MCPAM	1	38	6.18
ECETHPVB	1	44.2	7.24
GCMPG	1	47.5	6.91
MC10	2	41.7	6.82
MC12	2	41.7	6.71
MC15	2	41.7	6.73
MC16	2	41.7	6.75
MCGLY5	3	41.7	6.91
MCMPG	3	41.7	6.74
MCM	3	41.7	6.76
MC8	4	41.8	6.76
MC8	4	41.9	6.77
MC8	4	42.0	6.76
MC8	4	42.5	6.77

5.2 Mixing Results and Discussion

5.2.1 Mixer Torque Rheometry

For MC 8 dough shown in Figure 151, torque peaks at 41.5 volume % solids. At higher solids content the formulation granulates showing that the critical solids loading had been passed. WC-Co mass was increased incrementally for each binder system, increasing torque before reaching agglomeration. Johansson et al. however describe the rise in torque as a function of increasing binder concentration before a drop in torque caused by over wetting [85]. The measured density in Figure 151 increases steadily with increasing WC-Co content. There is however, no significant change in density at the critical solids loading as suggested in the literature [163, 164]. Higher theoretical density than the measured density is a common occurrence, suggesting air entrapment. Air entrapment would equate to lower volume % of WC-Co thus decreasing measured density, whereas theoretical density assumes no air entrapment and perfect packing. A lower measured density may also be a result of errors in density measurement and pycnometer accuracy. Peak torque was typically at 2.4 vol% less solid than the maximum packing of the solid calculated as a percentage of

solids maximum packing density as suggested by Figure 159. Figure 151 shows a similar torque profile to that shown in Figure 153. The additions of polyacrylamide to the methyl cellulose binder lowered peak torque. The maximum practical solids loading of the MCPAM bound dough was also lower at the peak torque. Figures 151 to 158 show a slight change in density above the critical solids loading. This can be attributed to the arrangement of the particles and finely dispersed closed cells of air (Figure 160). It is suggested that the binder began to incompletely fill the voidage of the powder as more solids were added. Figure 160 (a) shows a low volume per cent of WC-Co powder surrounded by the organic binder and Figure 160 (b) shows the maximum packing, or highest volume per cent of WC-Co powder. Figure 160 (c) shows the WC-Co powder particles interstitial included voids as there is now insufficient fluid to fill the space. This shows that the particles are not fully wetted by the binder material and that the space between has been occupied by closed voids that are not easily detected by the pycnometer, thus decreasing the density. However, further powder additions and increased voidage allows helium to penetrate through channels giving a higher density reading once more (Figure 160 (d)).

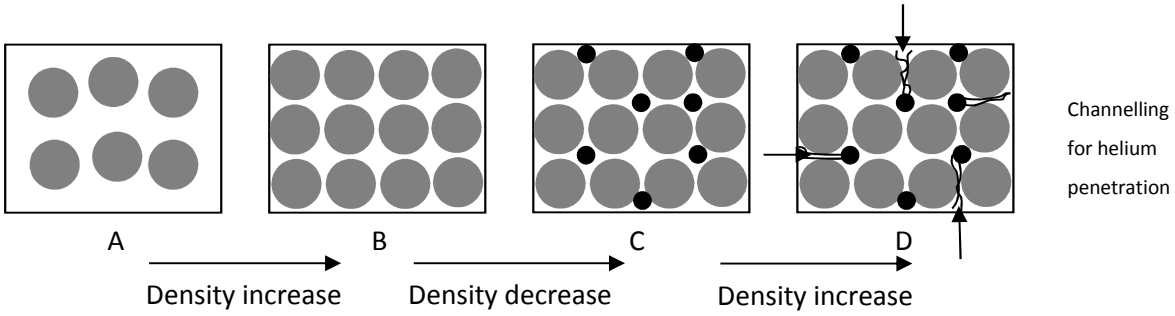

Figure 160 a-d particle packing where a is low vol % WC-Co, b is fully packed and c is beyond the critical loading with entrapped air

The work of Hay [82] suggests that for the density measurements to give a clear indication of critical solids loadings the formulation must be free from air. Materials prepared in the Werner and Pfleiderer mixer under no vacuum are shown in Figures 152, 154, 156 and 158. That data shows greater variation compared to the dough mixed in the Winkworth mixer. This is because the voidage developed by under wetting the powder in the mixer (WP) is not compensated for in all cases by the collapse of the structure when the vacuum is removed. When mixing with a vacuum the density does not decrease to the same extent and appears to be influenced by binder viscosity. Thus torque measurements provided greater accuracy for determining the critical solids loading. Figure 155 shows the critical solids loading predicted by the peak torque experiment. The critical solids loading is higher than that shown in Figure 151, indicating that the ethyl cellulose and ethanol based binder is more effective at wetting the powder particles. The critical loading differences indicate that the predicted maximum solids loading by rheological measurement is only an indication of packing and

is dependent on the interactions of the binder phases present. In the dough formulated with the ethyl cellulose binder there was an initial rapid decrease in torque as shown in Figure 155. This suggested that the yield stress of the binder had to first be overcome to allow for initial dispersion. Once that yield had been overcome the torque generated was comparatively low. At the critical solids loading the yield stress was no longer present whilst mixing. The lower torque before the critical solids loading was attributed to a better wetting of the WC-Co. Figure 156 shows a reduction in measured density before the critical solids loading was reached. The sharp rise in density in Figure 157 also occurred before the critical point indicating that the Werner and Pfleiderer mixer was ineffective at mixing dough systems at higher solids loadings. The measured density was greater than theoretical density for this binder in Figure 156. Therefore ethanol had evaporated during mixing, as theoretical density assumes perfect mixing and no air entrapment or solvent evaporation. Where the binder is a combination of Gelucire and MPG the density and torque curves followed similar trends to other dough formulations. The critical solids loading was higher for this formulation, ranging from 45-50 vol %. Figure 157 shows a drop in measured density close to the point of critical solids loading which was again not noticed when mixed in the Winkworth mixer. The peak torque levels are comparable to those shown for the MC8 dough in Figure 151. The high torque levels are associated with the melting characteristics of dough when a high shear was applied.

5.2.2 Inverse Extrusion Pressure

The reciprocal of mean extrusion pressure was plotted as a function of liquid phase content to yield Figure 159 for the MC8 dough formulation. This shows that the dough became infinitely ‘viscous’ at 43.9 volume % WC-Co. This is an adaptation of the method reported by Blackburn and Powell [164]. At 43.9 volume % the maximum solids volume or the volume of liquid which just filled the powder bed voidage was observed. It was assumed that no lubrication was provided at the particle contacts at infinitely high pressure as a result. The maximum packing behaviour was therefore a percentage of theoretical density of the solid phase. From practical experience stiff dough would result from adding 1 to 3 volume % liquid above that required to just fill the voids or 1-3 volume % solid below this value, a feature confirmed by mixer torque rheometry. However, the maximum packing evaluated via this method is binder dependent due to the fact that higher solids loading pastes could be prepared with alternative binders. Both ECETHPVB and GCMPG dough were prepared in excess of 46 vol% WC-Co.

5.2.3 Density Investigation

Table 33 shows greater methyl cellulose concentrations in the binder produced dough of higher density due to increased cross-linking. Cross-linking was a result of increased interactions between

cellulose molecules. The effects of increased WC-Co content were less noticeable than those observed by increasing cellulose content. This is because the PEG content is increased simultaneously with the WC-Co content. The increases in PEG content act against increases in density caused by the increased WC-Co mass. Longer chain cellulose binder formulations showed increased dough density whereas adding MPG to the binder system had the opposite effect and reduced the density. The ECETHPVB and GCMPG formulations gave a relatively high density due an ability to be mixed at significantly higher solids loadings. Conversely, MCPAM formulations could only be prepared at low WC-Co content thus giving low density, also exaggerated by porosity. The determination of the maximum practical solids loading via mixing, extrusion and density experiments, allowed further investigation into the extrusion of pastes to be investigated in Chapter 6.

Chapter 6 Extrusion

6.0 Extrusion

Rheological testing was carried out on a laboratory scale up to 8 mm extrudate diameter. For larger scale work however, extrusion sizes are described in the as sintered, non-ground state (Table 12). Neglecting any form of extrusion swell or shrinkage, the tooling geometry is equivalent to extrudate diameter. Pilot scale extrusion was used to manufacture 6, 14 and 20 mm solid geometries and 14 mm geometries with coolant holes. Production scale produced 14 mm and 20 mm diameter solid and coolant hole geometries. Extreme phase migration and incomplete die filling was noticed with MCMPG and MCGLY5 feedstocks and therefore further analysis beyond pilot scale was not required or undertaken.

6.1 Capillary Rheometry

A Rosand capillary rheometer (section 3.7) was used to evaluate shear viscosity for dough formulations. The Bagley correction described in section 2.5.3 was used on group 1 dough to correct for die entrance effects. The full Bagley plot for each extrudate velocity for SHM dough is shown in Figure 148. The corrected dough viscosities have been plotted in Figure 161.

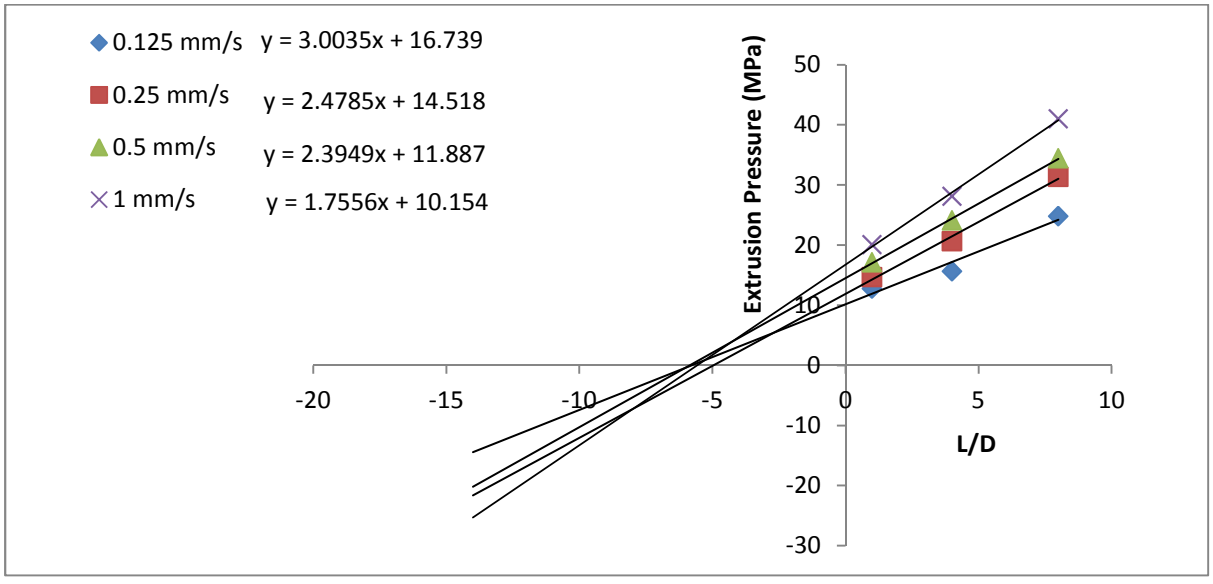

Figure 161 Bagley plot for SHM dough feedstock

The Bagley plots for each dough were used to develop log wall shear stress versus log apparent shear rate plots such as Figure 162, from which n' was determined for (in this case for the SHM dough). n' is the slope of $\ln(\tau)$ verses $\ln(\dot{\gamma}$ app) used in the Mooney-Rabinowitsch shear rate

correction described in section 2.5.3. n' stems from equation 2-29 whereas the viscosity is calculated from equation 2-30.

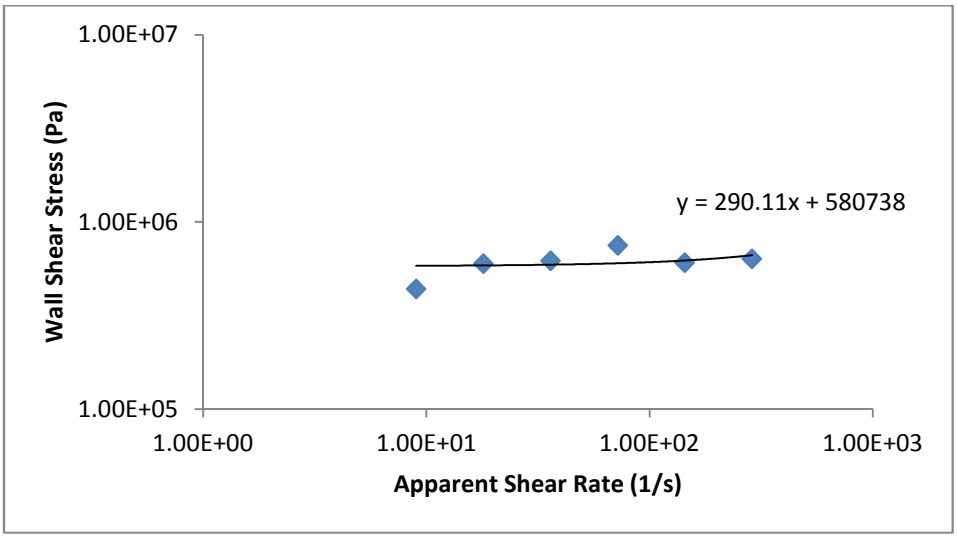

Figure 162 SHM dough shear stress as a function of apparent shear rate, log plot

Corrected dough viscosities are plotted for each of the group 1 feedstocks in Figure 163.

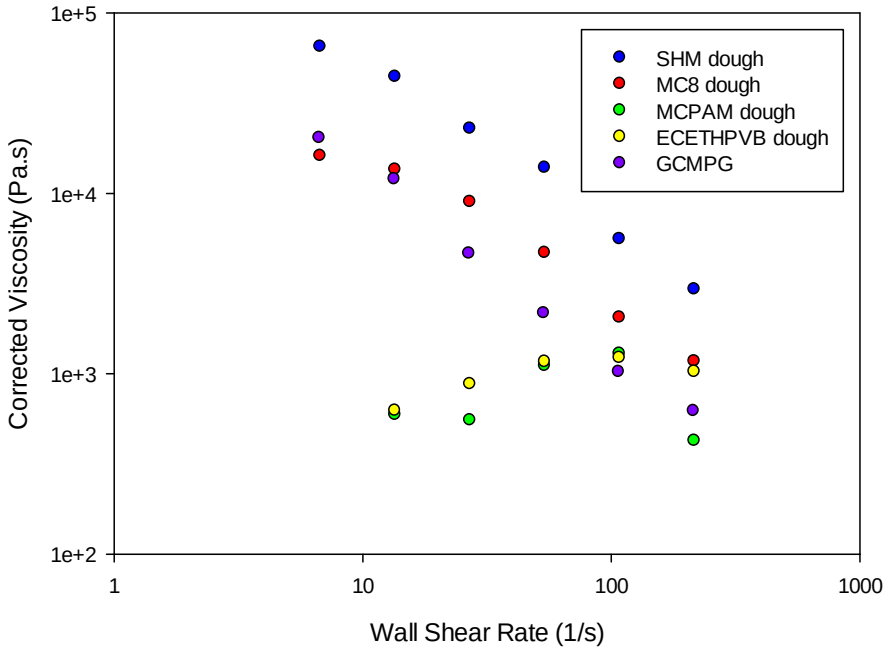

Figure 163 Corrected dough viscosities as a function of wall shear rate for dough prepared from group 1 binders

MCPAM and ECETHPVB dough formulations did not follow expected trends when corrected for Bagley viscosity. The MC8 dough corrected viscosity has also been plotted with the non-corrected MC8 dough viscosity in Figure 164. The differences in dough viscosities (approximately a decade

across a shear rate of 1000 s^{-1}) are a result of die entrance effects and linear plots allow for extrapolation to compare similar shear rates.

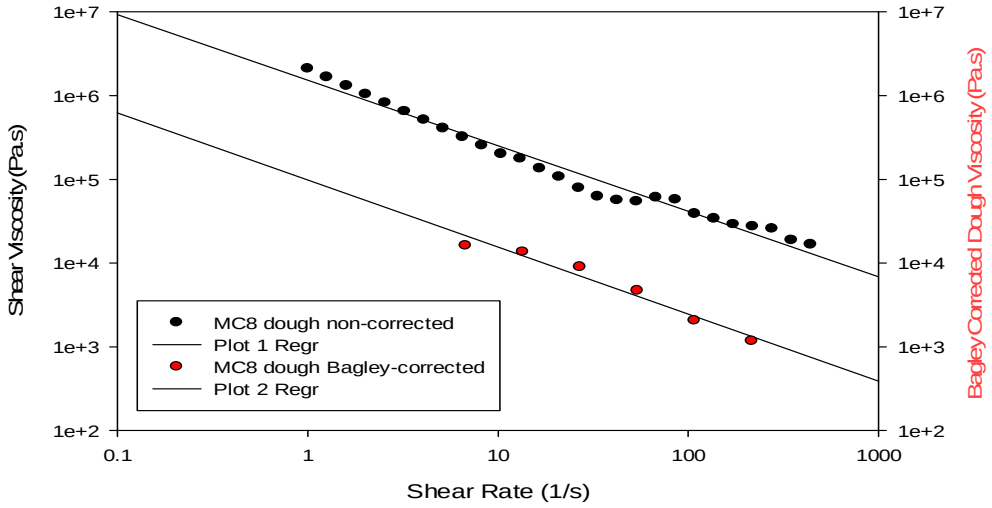

Figure 164 MC8 dough non-corrected dough shear viscosity (plot 1) and Bagley-corrected dough shear viscosity (plot 2)

6.1.1 Methyl Cellulose Variants

Non-corrected dough shear viscosities are plotted in Figure 165. The Bagley correction was not used for group 2 dough as it was only extruded through a 4 mm die and the same applies for group 4 dough at increased WC-Co content (Figure 153).

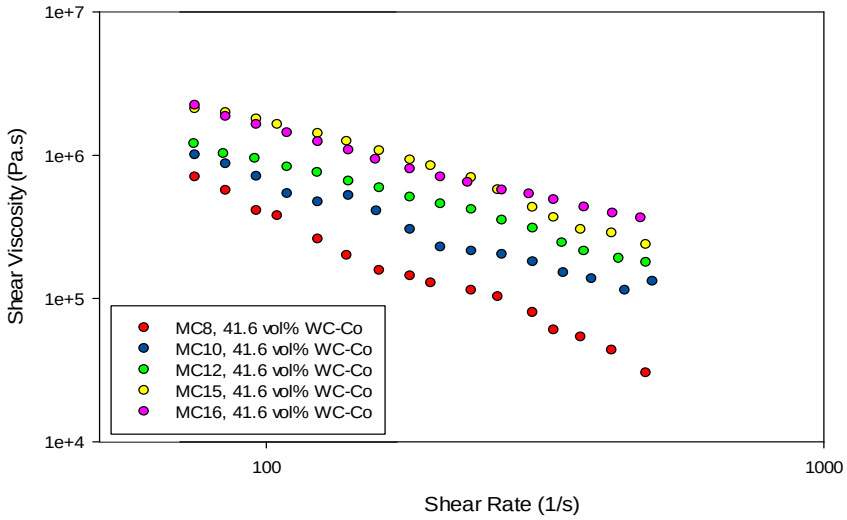

Figure 165 Increasing MC% dough shear viscosity as a function of shear rate plot

Group 4 dough non-corrected shear viscosity is plotted in Figure 166, the Bagley corrected dough viscosity (from Group 1 dough) has also been included as a point of reference. Increasing the cellulose content from 10-16 mass % in the binder (Figure 155) had a greater effect on shear viscosity than increasing the WC-Co content from 40.6-42.6 vol% (Figure 166). This was an

unexpected result due to the high density of WC-Co. Controlling dough stiffness with binder concentration is a useful attribute of the feedstock due to cost-effectiveness when comparing binder and WC-Co powder costs.

6.1.2 Methyl cellulose, water based dough increased WC-Co loading

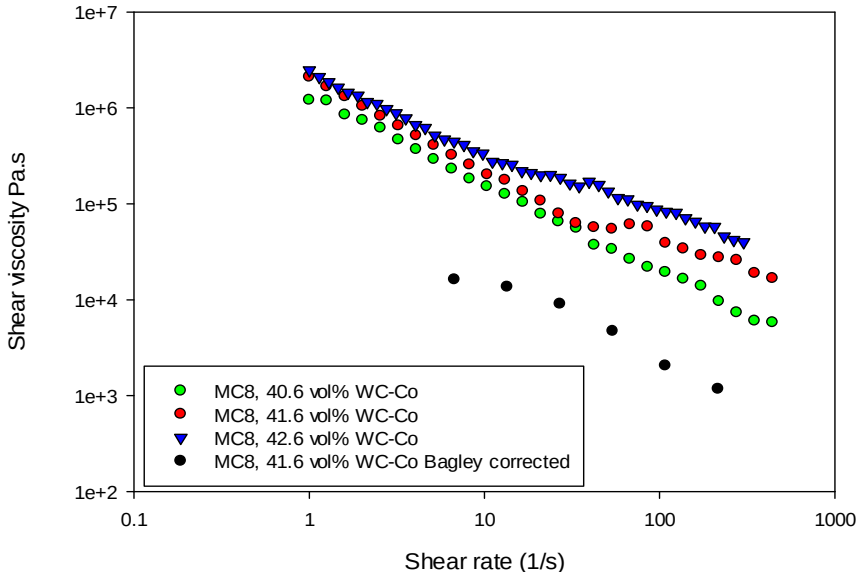

Figure 166 Increasing WC-Co loading dough shear viscosity as a function of shear rate plot

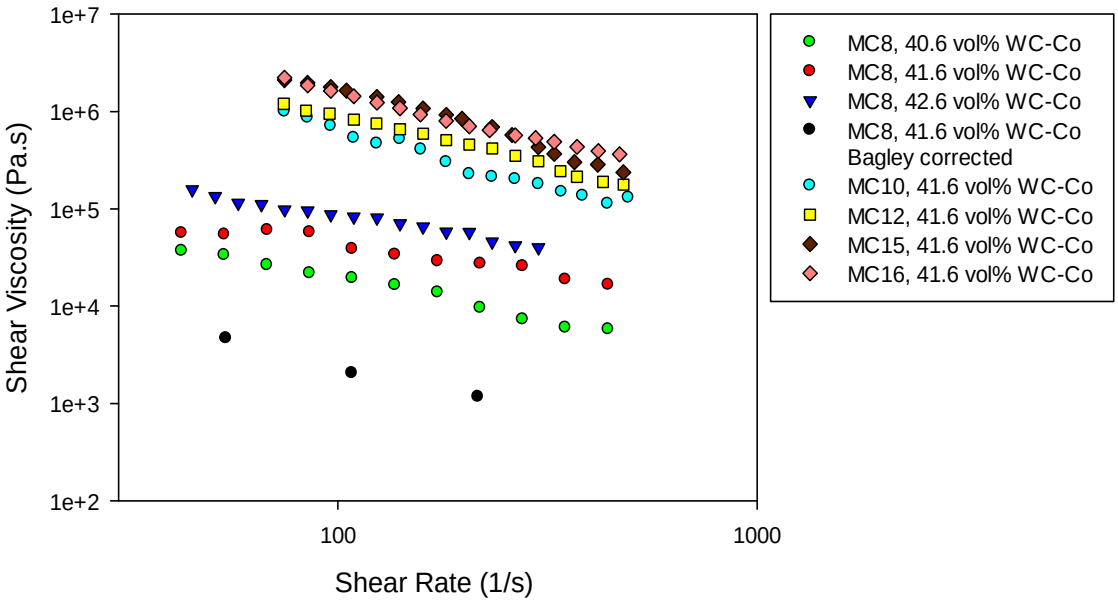

Figure 167 Combined methyl cellulose based dough shear viscosity as a function of shear rate plot

6.1.3 Methyl cellulose, water based dough aging tests

Aging was observed as discoloration of the extrudate surface which was associated with moisture loss from the binder phase. The MC10 binder and dough were rheologically tested at times corresponding to mixing and extruding to investigate the aging effect. Day 0 represents the day of

dough mixing, day 1 represents the day of 14 mm extrusion and day 2 represents the day of 20 mm extrusion due to days on which extrusion equipment was available for a given mix. Day 7 represents a week of aging of both binder and dough feedstock. No dough or binder aging was observed from day 0 to day 1 and hence the plots overlap in Figure 168 and cannot be seen.

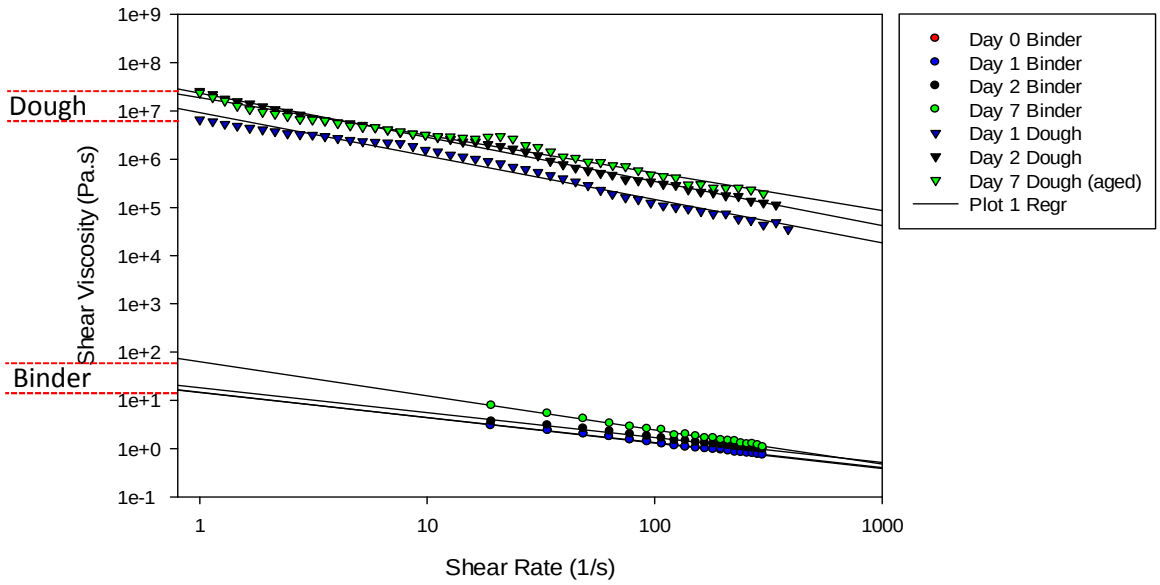

Figure 168 MC10 binder and dough age test (shear viscosity as a function of shear rate)

Figure 168 shows that both binder and dough viscosity increase with time after day 1. Figure 156 shows shear viscosity of the binder and dough for the MC10 dough for day 1 and day 7 on a linear scale. The dough shear viscosity was influenced more by aging than the binder shear viscosity, particularly at higher shear rates. From this observation it is likely that the PEG from the WC-Co powder is contributing to the aging effect of the dough. Figure 156 also shows that the dough becomes more shear thinning from day 1 to day 7.

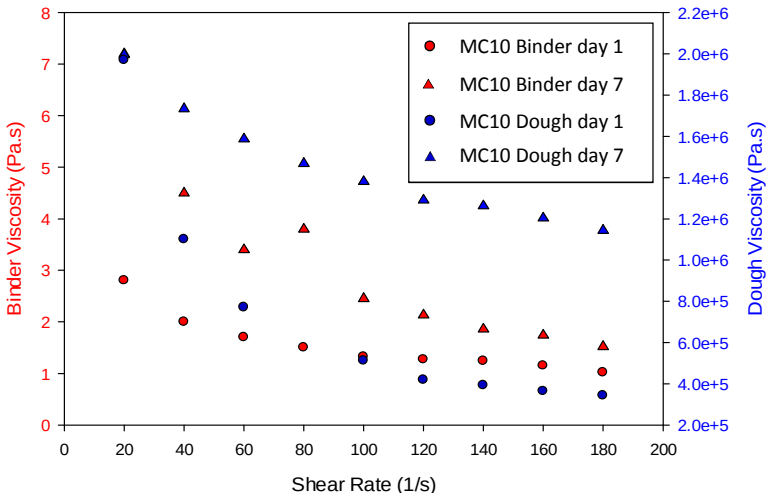

Figure 169 MC10 binder and dough shear viscosity as a function of shear rate plot

Figure 170 shows a plot of the difference between the viscosity of the binder and the dough after 1 and 7 days respectively for the MC10 based formulations. The difference between the viscosities was significantly reduced at higher shear rates.

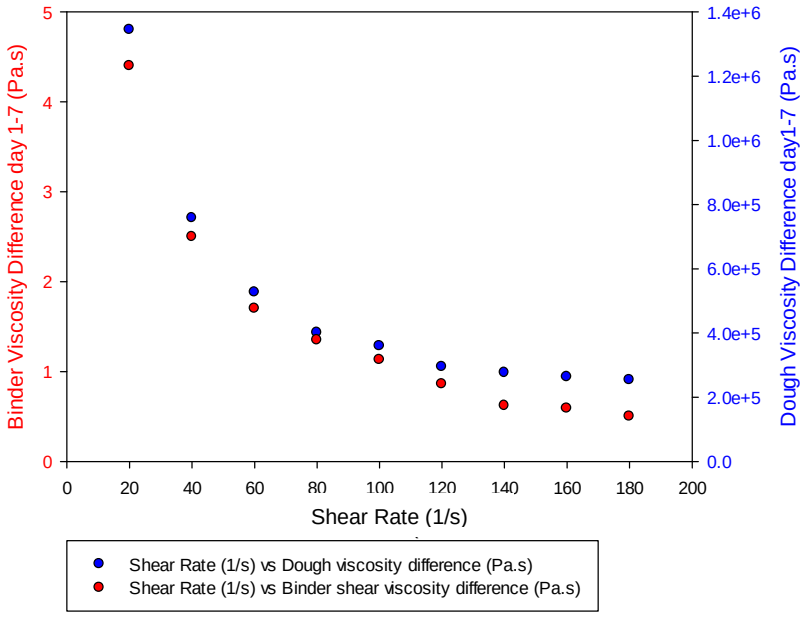

Figure 170 MC10 binder-dough shear viscosity difference plot

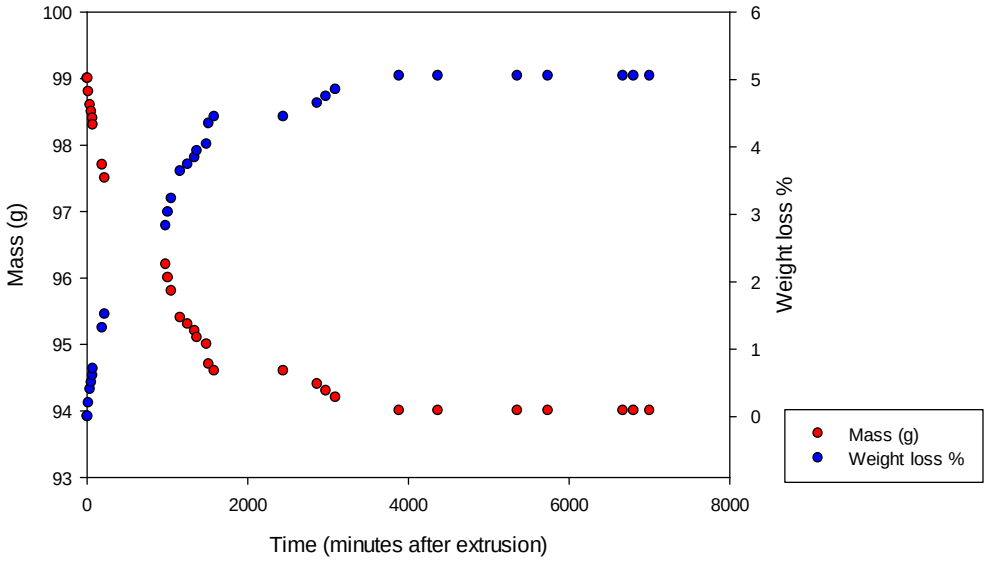

Figure 171 MC10 extrudate natural weight loss and weight % loss

MC10 extrudate was also examined for natural weight loss as there are at least two hours between the end of extrusion and drying processes due to equipment availability. MC10 extrudate was weighed periodically in a controlled laboratory atmosphere (22 °C and 38% humidity). Figure 158 shows that 5.21 mass % is lost as moisture from the extrudate over 133 hours which equates to the total water content in the sample from mixing.

6.2 Benbow-Bridgwater Analysis of WC-Co Dough

Group 1 doughs were analysed using the Benbow Bridgwater model. The ECETHPVB dough was omitted from the results because the model could not be accurately fitted. The data generated through this analysis was to be used to calculate the pressure drop in larger scale operations, section 6.2.3. The method of parameter fitting is described in section 2.5.3. Extrusion pressures were back-calculated at given extrudate velocities, allowing for comparison to the original measurements of pressure to give an indication of model accuracy and predictive capacity.

6.2.1 Benbow Bridgwater parameters

The Benbow Bridgwater parameters for group 1 dough systems have been plotted in Figure 172 using equation:

$$\Delta P = 2(\sigma_0 + \alpha V^m)\ln\left(\frac{D0}{D}\right) + 4(\tau_0 + \beta V^n)\left(\frac{L}{D}\right) \qquad 2\text{-}31$$

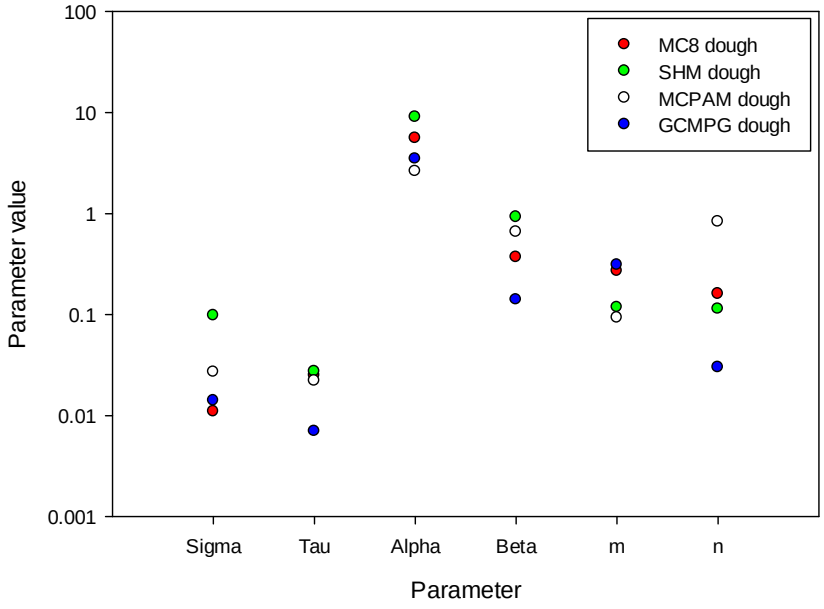

Figure 172 Benbow Bridgwater parameters for dough prepared from group 1 binders

Sigma refers to bulk yield stress of the material and the greater the value, then generally the stiffer the paste as high yield has to be overcome before extrusion occurs. For efficient material compaction and consequently good dimensional accuracy a high yield stress is desirable. Tau, refers to die wall shear stress. A high shear stress at the die wall implies that the feedstock has poor lubrication properties as there would be an implication of high friction at the die wall. Alpha and m are factors characterizing the effect of velocity on the die entry, whereas Beta and n are parameters characterizing the effect of velocity in the die land. The relatively high values for Alpha, Beta, m and

n are indicative of a paste that is highly velocity dependent. The SHM pilot scale extruder was analysed using the calculated Benbow Bridgwater parameters for a 6 mm die set as the experimental results gave greater accuracy than the 4 and 8 mm diameters experiments (Table 34). For the methyl cellulose dough a 3 dimensional plot has been created from which the Benbow Bridgwater parameters were derived (Figure 173). Predicted pressure calculated from the Benbow-Bridgwater model using parameters given in table 34 was plotted against the measured pressure for a die diameter of 6 mm in figures 161-163. For the range of velocities used on experimental data in figure 74, figure 175 and figure 176 the model equation has also been given. Plots were generated for each L/D ratio giving similar results although it is the L/D = 8 plot shown here. R squared values and parameter values for the Benbow Bridgwater model are given in Table 34. The remaining materials of group 1 were evaluated using the same approach.

Table 34 Benbow Bridgwater parameters (4 mm die unless stated otherwise)

Dough	σ_0 (MPa)	τ_0 (MPa)	α (MPa(m/s^{-m}))	β (MPa(m/s^{-n}))	m	n	R^2
SHM 4mm die	$9.80*10^{-2}$	$2.73*10^{-2}$	9.01	0.92	0.12	0.11	0.91
SHM 6 mm die	$4.44*10^{-2}$	$2.30*10^{-2}$	10.50	0.43	0.18	0.24	0.98
SHM 8 mm die	$1.61*10^{-2}$	$2.01*10^{-2}$	15.24	2.16	0.24	0.19	0.76
MC, water 8%	$1.10*10^{-2}$	$2.52*10^{-2}$	5.58	0.37	0.27	0.16	0.94
MC, water, Pam	$2.71*10^{-2}$	$2.22*10^{-2}$	2.63	2.63	0.09	0.83	0.83
Gelucire 50/13, MPG	$1.41*10^{-2}$	$7.00*10^{-3}$	3.47	3.47	0.31	0.03	0.93

The SHM 8 mm experiment and MCPAM feedstock showed a poor predicted pressure result when comparing the measured and model data. The R^2 value is calculated from the total experimental space and all L/D data sets may not be fitted with equal precision due to the interplay between model and experimental data. This is illustrated well when comparing Figure 175 and Figure 176 here the L/D 4 data fits the model with greater accuracy than L/D 8 fit even when the unified R^2 value is 0.98.

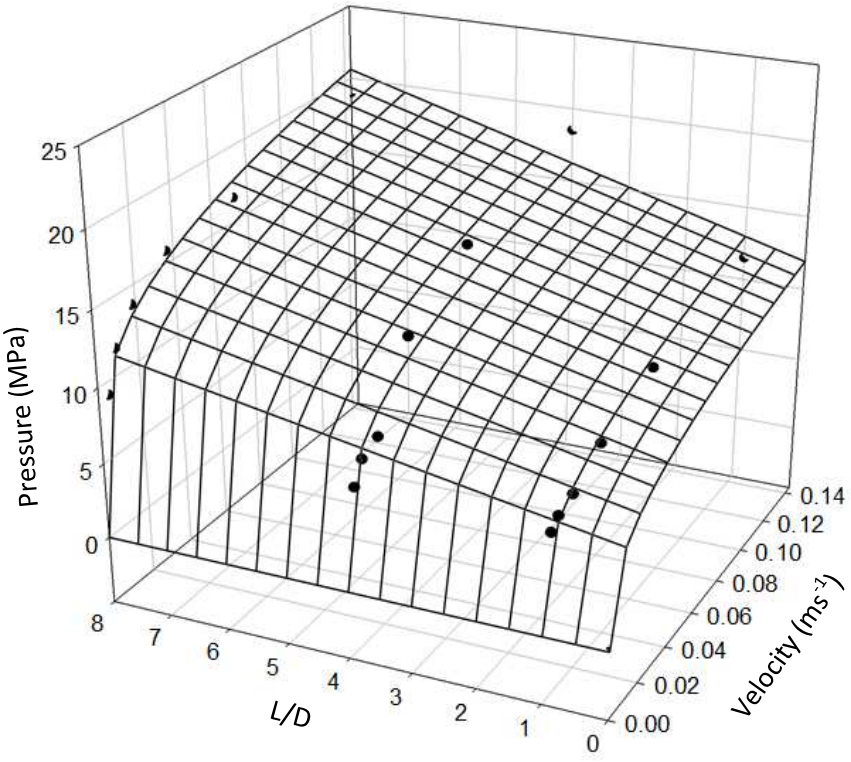

Figure 173 MC dough Pressure vs L/D vs extrudate velocity plot

$$\Delta P = 2.(0.04 + 10.50V^{0.18})\ln(3.83) + 4.(0.23 + 0.43V^{0.24})$$

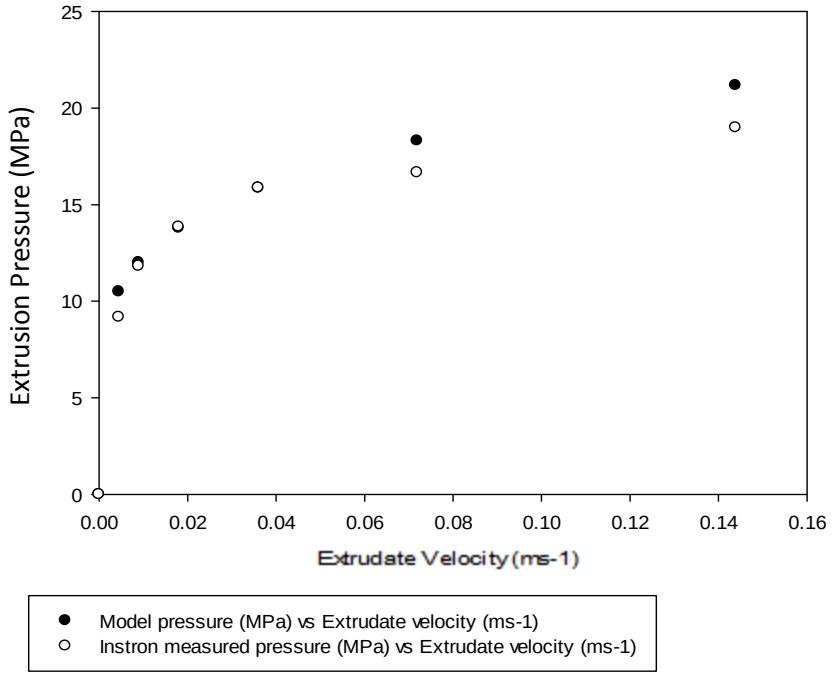

Figure 174 Measured and predicted pressure vs extrudate velocity (MC8 dough L/D = 1)

$$\Delta P = 2.(0.04 + 10.50V^{0.18})\ln(3.83) + 16.(0.23 + 0.43V^{0.24})$$

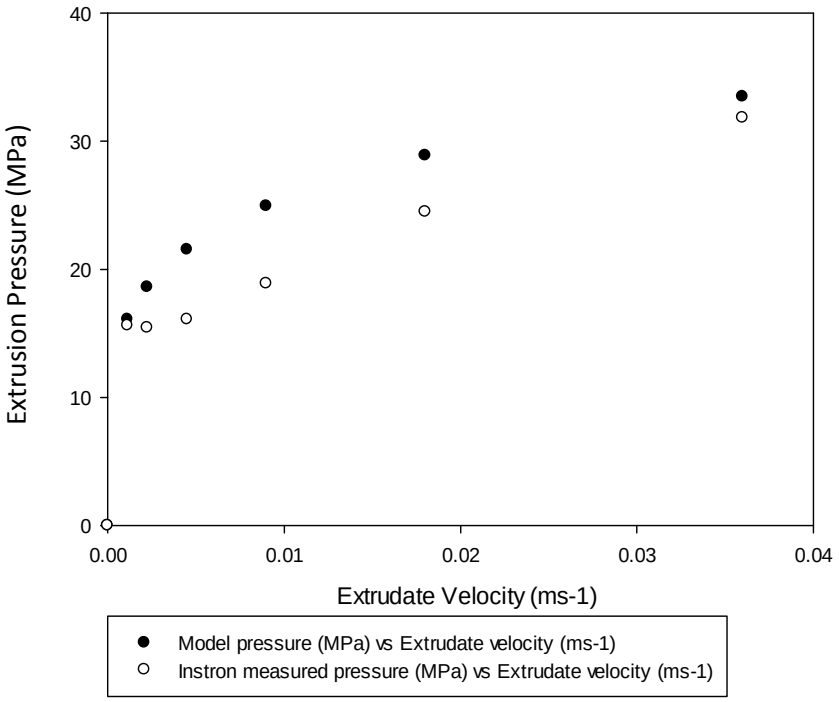

Figure 175 Measured and predicted pressure vs extrudate velocity (SHM dough L/D =4)

$$\Delta P = 2.(0.04 + 10.50V^{0.18})\ln(3.83) + 32.(0.23 + 0.43V^{0.24})$$

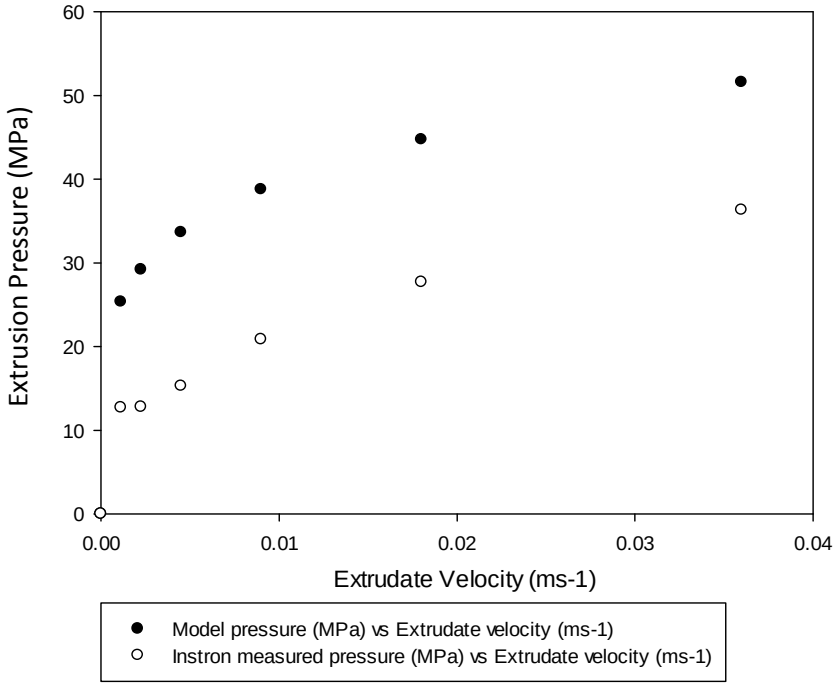

Figure 176 Measured and predicted pressure vs extrudate velocity (SHM dough L/D = 8)

6.2.2 SHM Laboratory Extrusion Press

Group 1 doughs were extruded using the pilot scale extrusion press described in section 3.8. Table 35 shows the different products that were extruded in the pilot scale extrusion press. Steady state back pressures for group 1 doughs (20 mm solid) are given in Table 36. Steady state back pressures for the SHM, MC8 and group 2 dough formulations are given in Figure 164. Ram pressure decreased with extrusion time due to reducing material volume and therefore pressure data was recorded at equal ram positions.

Table 35 Extruded product type

Feedstock Dough Material	Product Type
SHM	14 mm coolant
MC8	14 mm coolant & 20 mm solid
MC10	14 mm coolant
MC12	14 mm coolant
MC15	14 mm coolant
MC16	14 mm coolant
MCPAM	20 mm solid
ECETHPVB	20 mm solid
GCMPG	20 mm solid

Table 36 Group 1 dough steady state back pressure, 20 mm solid (MPa)

Feedstock Dough Material	Steady State Back Pressure (Mpa)
MC8	88.63
MCPAM	93.82
ECETHPVB	90.61
GCMPG	92.68

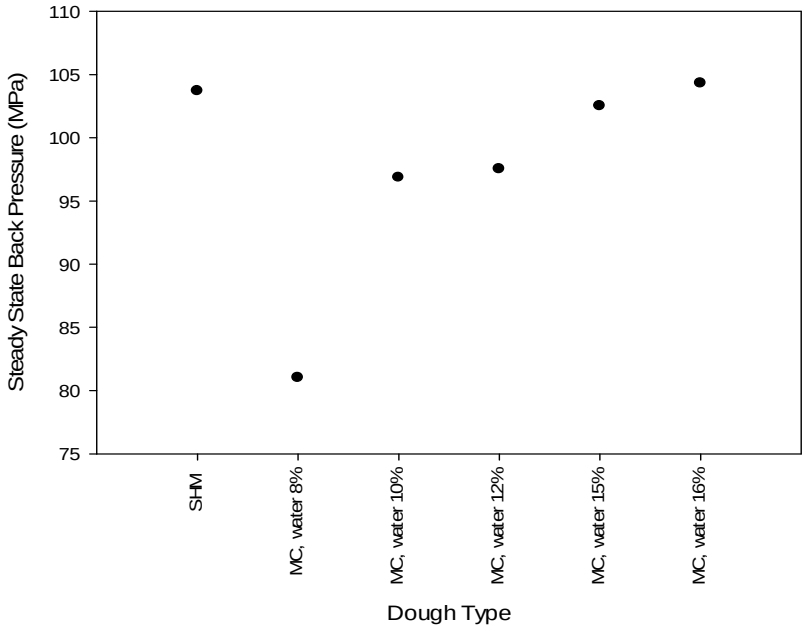

Figure 177 Group 2 dough steady state back pressure (14 mm coolant) vs dough type

The SHM feedstock is included in Figure 177 as a reference as this pressure was known to provide extrudate of high quality. The steady state back pressure for the 8% methyl cellulose sample is significantly lower than other methyl cellulose based formulations. The lower pressure is a result of sample preparation as the 8% formulation was measured at a different point in time to the remaining materials. Extruded rods prepared from MCPAM and ECETHPVB based dough were prone to cracking. Figure 178 shows how dry formulations (MCPAM) produced extrudate with a large population of defects. The dry cross-sectional fracture surface shows that the formulation could not bind and form high quality dense extrudate. The large crack and crumbling (Figure 178, left) occurred due to sample cutting. A blanking plate was evaluated up stream of the die to increase the ram pressure prior to extrusion in an attempt to improve the compaction of the binder/powder matrix. Little improvement resulted from the modified process and hence the MCPAM feedstock development was discontinued.

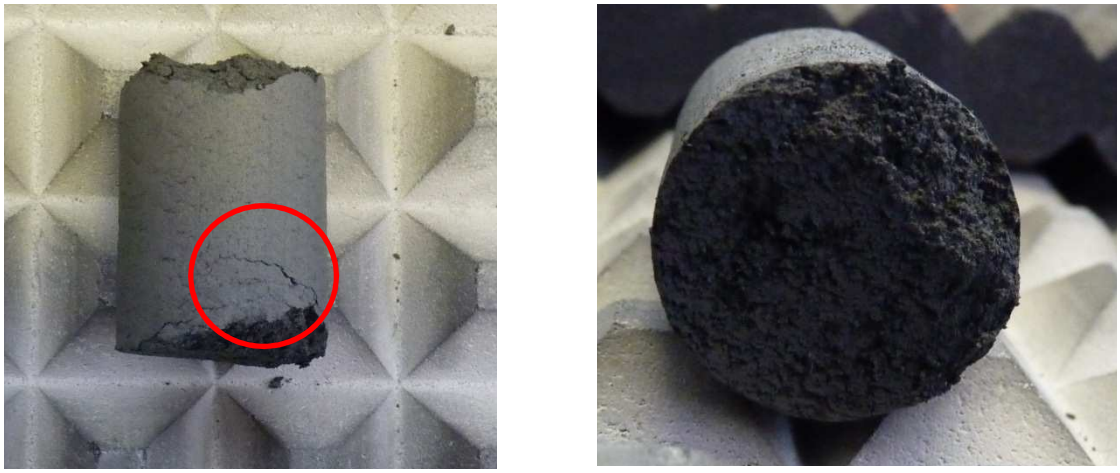

Figure 178 MCPAM 20 mm diameter solid extrudate

Extrudate prepared from the ECETHPVB dough is shown in Figure 179. The cross-sectional fracture surface is of poor quality although less voidage is observed compared to MCPAM. Whilst the internal surface after cutting was porous, the exterior rod surface was smooth and defect free with the exception of the indicated defect caused by contact with the tray.

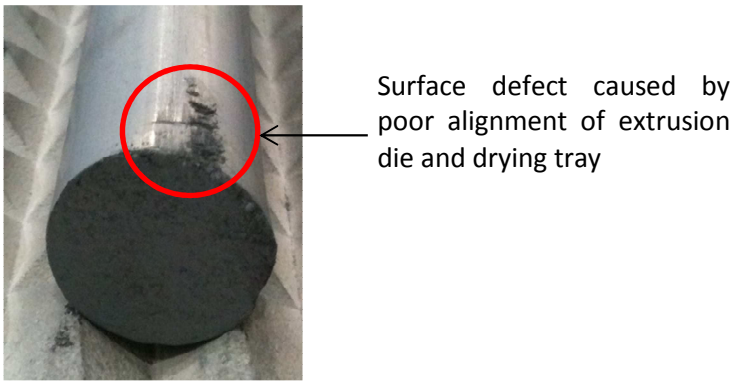

Figure 179 ECETHPVB cross-sectional surface with surface defect damage shown

6.2.3 Modelling of SHM Pilot Extrusion Press

SHM production dough was modelled at an extrusion ram speed of 0.07 mms^{-1}. This was the speed used for the majority of measurements and was also used in the production tests, scaled up for geometrical changes. The tooling used in the SHM laboratory extrusion press can be broken down into four principle components, the reducer, spider, die (trumpet shaped entrance) and die (parallel section towards exit). The reducer can be represented as a square entry die, the spider acts as a multi-holed die and the trumpet section can be approximated as a conical shaped die. Whilst the spider was included in the experiment, the model is only for solid rod extrusion and hence no core pin, filaments or rifled parallel sections were considered. Each approximation to the geometry has been previously modelled by Benbow and Bridgwater [32].

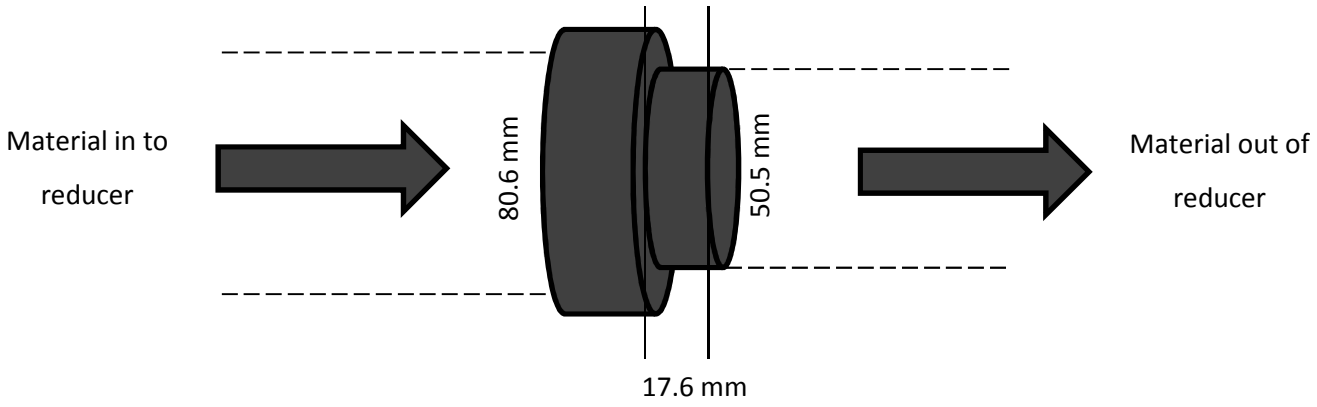

Figure 180 SHM tooling (reducer)

For the reducer (Figure 167), the standard Benbow Bridgwater equation (2-31) was used with the paste parameters derived from the 6 mm rod extrusion, Table 34. The pressure drop for the reducer is given in Table 37. Acting as a multi-holed die with 8 holes in total and substituting volumetric flowrate:

$$V = \frac{Q}{A} \tag{6-1}$$

into Equation 2-31, where A is the area of one hole multiplied by the number of holes (N), Q is volumetric flowrate and $V$is extrudate velocity obtains:

$$\mathrm{P}_s = \left[\left(\sigma_0 + \alpha\left(\frac{Q}{\frac{\pi D^2 N}{4}}\right)^{\mathrm{m}}\right)\ln\left(\frac{\frac{\pi D_0^2}{4}}{\frac{\pi N D^2}{4}}\right)\right] + 4\left[\left(\tau_0 + \beta_1\left(\frac{\mathrm{Q}}{\frac{\pi D^2 N}{4}}\right)^{\mathrm{n}}\right)\left(\frac{\mathrm{L}}{\mathrm{D}}\right)\right] \tag{6-2}$$

which can be further simplified to:

$$\mathrm{P}_s = \left[\left(\sigma_0 + \alpha\left(\frac{4Q}{\pi D^2 N}\right)^{\mathrm{m}}\right)\ln\left(\frac{\mathrm{D}_0}{\mathrm{D}\mathrm{N}^{1/2}}\right)\right] + 4\left[\left(\tau_0 + \beta_1\left(\frac{4\mathrm{Q}}{\pi D^2 N}\right)^{\mathrm{n}}\right)\left(\frac{\mathrm{L}}{\mathrm{D}}\right)\right] \tag{6-3}$$

The volumetric flowrate is calculated based on the speed of the material exiting the reducer and the total extrudate area leaving the spider. The dimensions for the spider are shown in Figure 181.

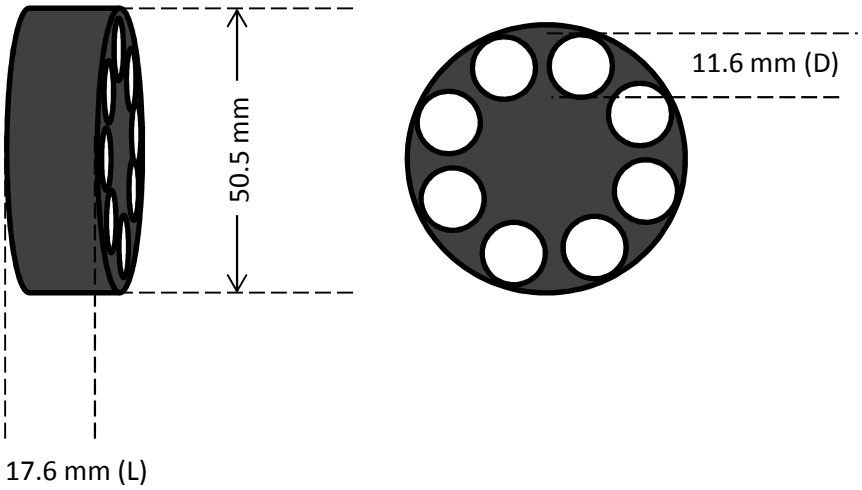

Figure 181 SHM tooling (spider dimensions)

The trumpet shaped section of the die was treated as a conical shape and is shown schematically in Figure 182.

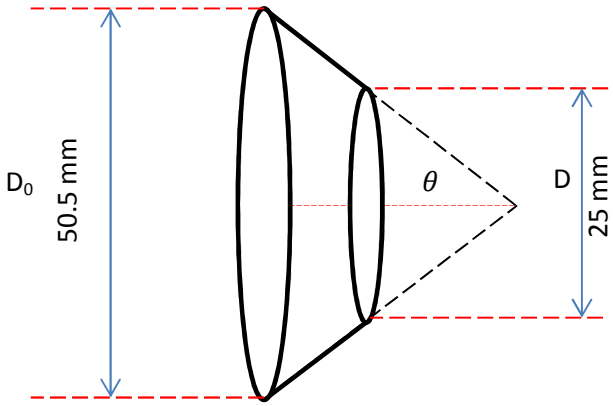

Figure 182 Conical die schematic

Conical dies have been modelled by Benbow and Bridgwater using equation 6-4 which is derived from taking a small slice from the conical section over which a shear stress is applied thus generating a force balance [32].

$$P_{c.d} = \left[2(\sigma_0 + \alpha V^m + \tau_0 cot\theta)\ln\left(\frac{D_0}{D}\right)\right] + \left[\left(\frac{\beta V^n}{n}\right)\left(1 - \left(\frac{D}{D_0}\right)^{2n}\right)cot\theta\right] \quad 6\text{-}4$$

where θ is the angle of the conical slope inside the die. As the die was trumpet shaped, a mould was taken and a shadow graph was used to make a plot of x verses y so that the angle θ could be determined. The trumpet shape was well approximated by a cone with an angle of 43.15°. The total pressure drop across the conical section using this method was 5.73 MPa. As a comparison to the

Benbow Bridgwater model of the conical die shape, the differential slice approach has also been analysed. In the differential slice approach, the pressure drop across several thin slices of the conical shape was considered, rather than using trigonometry and the angle of a cone. Using the Benbow Bridgwater parameters defined in Table 34 and Equation 2-31 the pressure drop was calculated across each slice of the conical shape. Pressure drop was calculated across D_{01} and D_1 for the first slice of the geometry through to D_{0n} and D_n for the nth slice. For the 1st slice, this was carried out as follows:

$$V = \left(\frac{4Q}{\pi {D_{01}}^2}\right) \tag{6-5}$$

substituting into equation 2-31 to obtain:

$$\Delta P = 2\left[\left(\sigma_0 + \alpha\left(\frac{4Q}{\pi {D_{01}}^2}\right)^m\right)\ln\left(\frac{D_0}{D_{01}}\right)\right] + 4\left[\left(\tau_0 + \beta\left(\frac{4Q}{\pi {D_{01}}^2}\right)^n\right)\left(\frac{L}{D_{01}}\right)\right] \tag{6-6}$$

The pressure drop can be calculated for each slice through to the nth slice. For each slice, the corresponding velocity was calculated from the volumetric flowrate and decrease in diameter over a slice length L of 0.005 m (Figure 183).

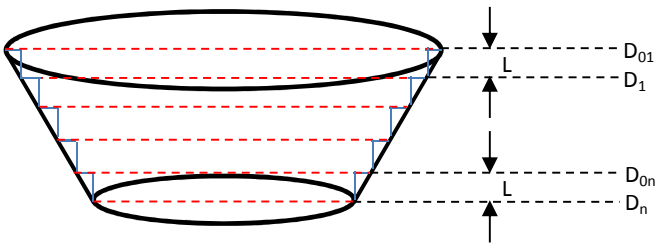

Figure 183 Differential slice method for conical geometry

The total pressure drop across the conical section using the differential slice method was 4.46 MPa.

A further more refined approach for calculating the pressure drop across the trumpet shaped section of the die is to use the Cartesian formula for an ellipse to represent the die shape (Figure 171). This more accurately defines the die shape as it allows for a smooth curved edge rather than the straight edge used in the conical representation (Figure 169 and Figure 170). Using the Cartesian coordinates for the elliptical curve:

$$\frac{X^2}{a^2} + \frac{y^2}{b^2} = 1 \tag{6-7}$$

and substituting values for a (exit radius) and b (length of trumpet section) provides the equation of the elliptical arc:

$$\frac{x^2}{0.0125^2} + \frac{y^2}{0.04^2} = 1 \qquad 6\text{-}8$$

Rearranged in terms of x gives:

$$x = \left[0.0125^2 - (0.0125^2)\left(\frac{y^2}{0.04^2}\right)\right] \qquad 6\text{-}9$$

Equation 6-9 allows for coordinates along the arc to be calculated for any value of y (b) which provides values for D_0 and D respectively. Therefore dimensions for thin slices of the trumpet section shown in Figure 184 can be calculated.

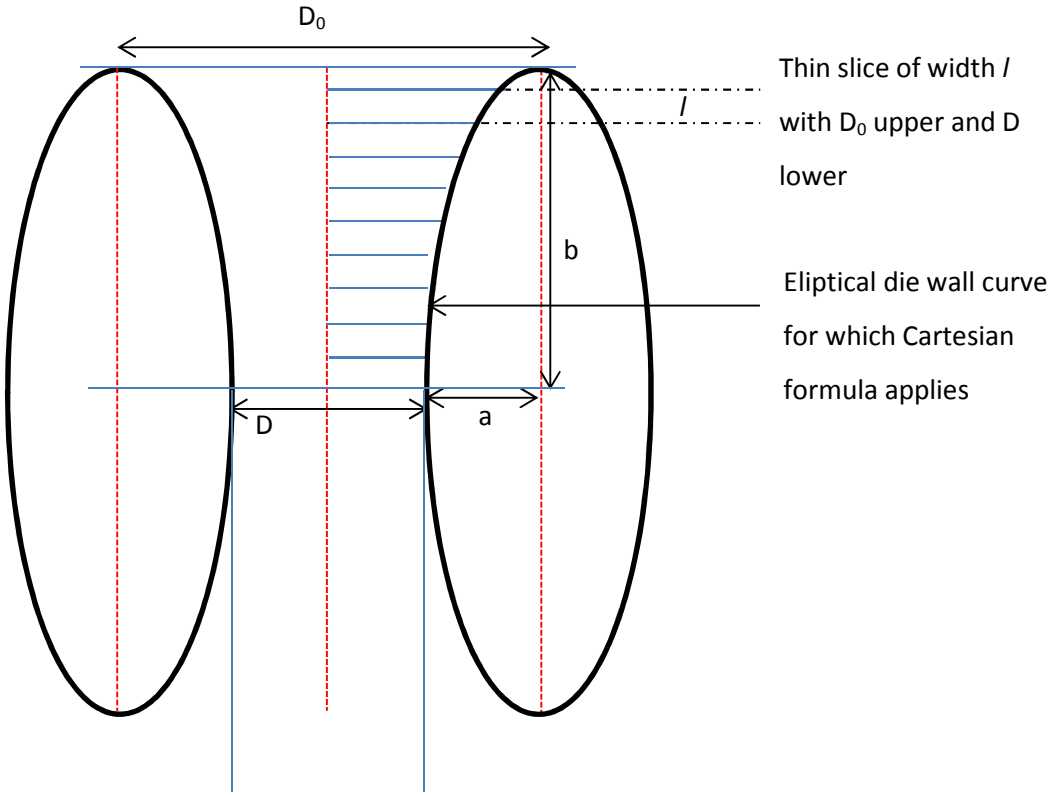

Figure 184 Elliptical representation of trumpet shape

Using the Benbow Bridgwater parameters defined in Table 34, and the dimensions derived from Equation 6-9, the pressure drop was calculated across thin sections 0.0005 m long in the trumpet shape for each incremental increase in extrudate velocity. The overall pressure drop across 78 slices was calculated to be 4.8 MPa whereas the conical shaped section provided a pressure drop of 5.73

MPa (Benbow Bridgwater approach) and 4.46 MPa (differential slice approach). Pressure drop is given in Table 37 and is represented by Figure 185 for each section, the dimensions of the tooling sections are provided in the individual schematics. The final section of the SHM extrusion press is the parallel part of the die. As the die entrance diameter was equal to the die exit, the die entrance pressure is zero. Therefore the pressure drop in this section is equal to 6-5.

$$P_p = (\tau_0 + \beta_1 V^n) 4 \left(\frac{L}{D}\right) \qquad 6\text{-}10$$

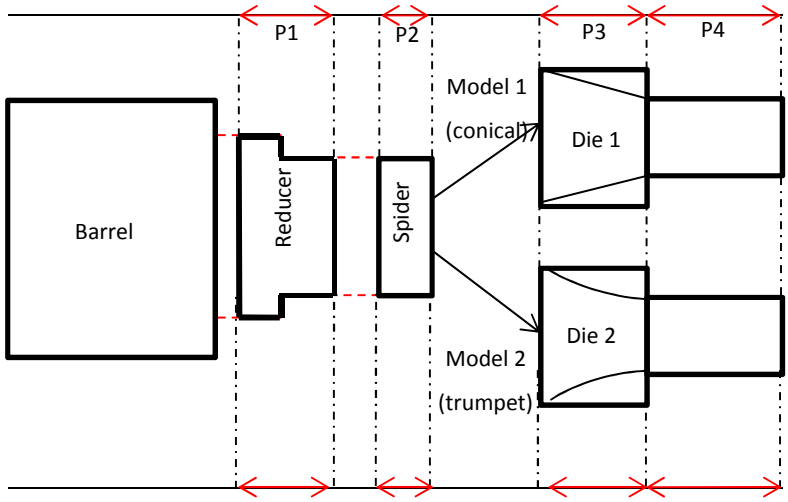

Figure 185 representation of pressure drop in pilot scale extrusion equipment

Table 37 Component pressure drops SHM extrusion press

Extruder Component	Presure drop	Pressure Drop (MPa)	Total Pressure Drop (MPa)
Reducer	P1	2.28	12.25 (Benbow Bridgwater approach) 10.98 (differential slice approach) 11.32 (differential slice of ellipse approach)
Spider	P2	3.35	
Conical die (Benbow Bridgwater approach)	P3	5.73	
Conical Die (differential slice approach)	P3	4.46	
Trumpet Die (differential slice of ellipse approach)	P3	4.80	
Parallel Section	P4	0.89	

The differential slice method shows that the conical shape gives a good approximation of pressure drop when compared with the trumpet shape. Reducing the step size and thus increasing the

number of slices taken over the die shapes did not give significant changes in pressure drop (Table 38).

Table 38 Increased number of slices in differential slice method

No. Slices (Conical)	Depth of Slice (m) (Conical)	Pressure Drop (ΔP MPa) (Conical)	No. Slices (Trumpet)	Depth of Slice (m) (Trumpet)	Pressure Drop (ΔP MPa) (Trumpet)
27	$5*10^{-4}$	4.46	78	$5*10^{-4}$	4.8
2490	$5*10^{-6}$	4.35	7980	$5*10^{-6}$	4.83

There was no device to measure pressure at the die in pilot scale equipment to give an indication of the overall pressure drop. Pressures could also not be back calculated based on ram pressure because the velocity control was not sufficient to generate a pressure-velocity profile.

6.3 Extrusion Results and Discussion

6.3.1 Capillary Rheometry

Capillary rheometry data was used to calculate die entrance effects with the Bagley correction. Die entrance effects have proved to be large for WC-Co feedstocks under stable extrusion flow conditions. Stable flow was determined by the pressure response from the pressure transducer and occurred at shear rates greater than 90 s^{-1}. The Bagley correction suggests that ECETHPVB and MCPAM dough systems had shear thickening behaviour. The Bagley corrected viscosity increased with shear rate for these systems (Figure 163). This result is unreliable as the materials were shear thinning according to the raw data from capillary rheometry. For the MC8 dough, Figure 164 shows that die entrance effects account for a viscosity reduction of a factor of 10 across the shear rate range. GCMPG dough had a Bagley corrected viscosity a factor of 1000 Pa.s below the capillary rheometer measured viscosity. Using the Bagley corrected viscosity; the methyl cellulose based dough has the closest match to the SHM dough for flow properties (Figure 164). Further to previous rheological measurements on the binder systems alone, it was the feedstock that was selected for further development. Further development (group 2 dough) showed that higher cellulose content gave greater dough shear viscosity at a given shear rate (Figure 165). Although Bagley corrected dough viscosities are not shown in Figure 165 it has been assumed that true dough viscosities are a factor of 10 lower across the shear rate range. Although increased cellulose content increased the dough shear viscosity, the effects were minimal at higher cellulose contents which was consistent with binder behaviour described in Chapter 4. MC15 and MC16 dough were more susceptible to incomplete wetting of the WC-Co powder. A compromise between wettability and increased dough viscosity was determined and 10% cellulose was selected for production scale investigation. The

second method for increasing the viscosity of the methyl cellulose based dough was to increase WC-Co powder solids loading. Results presented in Chapter 5 proved that dough with increased WC-Co content generated greater mixer torque values up to the critical solids loading due to increased shear viscosity, this has also been confirmed by capillary rheometry (Figure 166). The rise in dough viscosity as a result of increased WC-Co loading was less significant than that gained by altering the binder concentration in Figure 165. The optimum solids loading determined by extrusion was found to be 41.6 vol% WC-Co. Extrudate quality worsened above this solids loading giving brittle and dry extrudates. Lower solids loadings had good extrudate quality but higher shrinkage and therefore further development would be required with regards to tooling diameter. A solids loading of 41.6 vol% was also determined to be the maximum with the mixer torque rheometry experiments for this binder system.

6.3.2 Benbow Bridgwater analysis

The Benbow Bridgwater analysis was used to characterise dough materials prepared with group 1 binder materials. The parameters should have been independent of geometrical changes according to Benbow and Bridgwater [32]. SHM dough showed significant variations in α and β with increases in die diameter. This indicates that the extrusion pressure is dependent on the ratio of die diameter to velocity rather than just velocity. This observation has also been reported by Zheng et al. [109] and Martin [93]. Relatively high values of α and β for each material suggested that pastes were highly velocity dependent in the die entrance and die land. Although parameters did not remain constant at increased diameters the 6 mm model parameters were the most accurately fitted to experimental data. Experimental error may have caused discrepancies with data collected from 8 mm die configuration giving a low R^2. The yield stress and wall shear stress values for each dough system were low (Table 34) for pastes with a solids loading greater than 40 vol% and considering that WC-Co density is 11.4 gcm^{-3}. The stiffest dough (SHM feedstock) gave the highest values ($4.44x10^{-2}$ and $2.30x10^{-2}$ MPa with 6 mm tooling for yield stress and wall shear stress respectively. The majority of the dough feedstocks had similar die wall shear stress values indicating that lubrication properties were similar. However, the dough prepared using the Gelucire 5013-MPG binder had a significantly lower wall shear stress. The lower wall shear stress implies better lubrication and this was in line with the mixer torque rheometry studies for this material due to improved wettability of the powder phase. The model prediction shows a good correlation with back-calculated pressures as represented by Figure 174 for the MC dough. Back calculated pressures for other dough feedstocks were also highly representative of measured pressure data. Evaluation of the SHM pilot scale extrusion press showed that the greatest pressure drop occurred over the die which is shown by the greatest change in ΔP in the y-axis in figure 186. This is due to the application

of significant work to the material in the trumpet shaped construction and subsequent reduced cross sectional area. The trumpet model is the most representative of the actual die shape and should be used in future analysis of production scale equipment. The trumpet model gave a similar pressure drop estimation to the conical slice method whereas the Benbow Bridgwater model however gave an over estimate. The overestimate stems from the fact that the force balance used to generate equation 6-4 assumes that the normal stress exerted on the paste is independent of orientation. It is known from soil mechanics that this is not the case and therefore a degree of error is imparted on the pressure outcome. As the differential slice methods for both conical and elliptical geometries do not make this assumption and are based purely on pressure drops across many thin slices of reducing width, they are in better agreement with one another. It is believed that the differential slice approaches serve to give a more accurate representation of the actual die geometry and therefore give more reliable predictions to the pressure drop. High pressure drop was also observed across the spider. The pressure drops predicted by the Benbow Bridgwater model require validation in future work to enable the modelling of a full scale production extrusion press providing adequate process control is achievable. Due to the good fit of the Benbow Bridgwater model to the methyl cellulose dough, it was used to aid the design of tooling on a larger scale by increasing die land length and extrusion velocity. Figure 173 shows that with increases in velocity up to 0.14 ms^{-1} that the extrusion pressure increased. From this result, an equivalently scaled extrusion speed was used for the larger diameter extrusion which gave immediate improvements in the dough stability. Similarly, Figure 173 shows that longer die lands gave higher extrusion pressures. Knowing this, the production scale die land was increased in length by 25 mm as shown in Figure 187. A 25 mm increase in length was the maximum length that could be achieved due to limitations in the manufacturing process relating to the size of carbide starting block required.

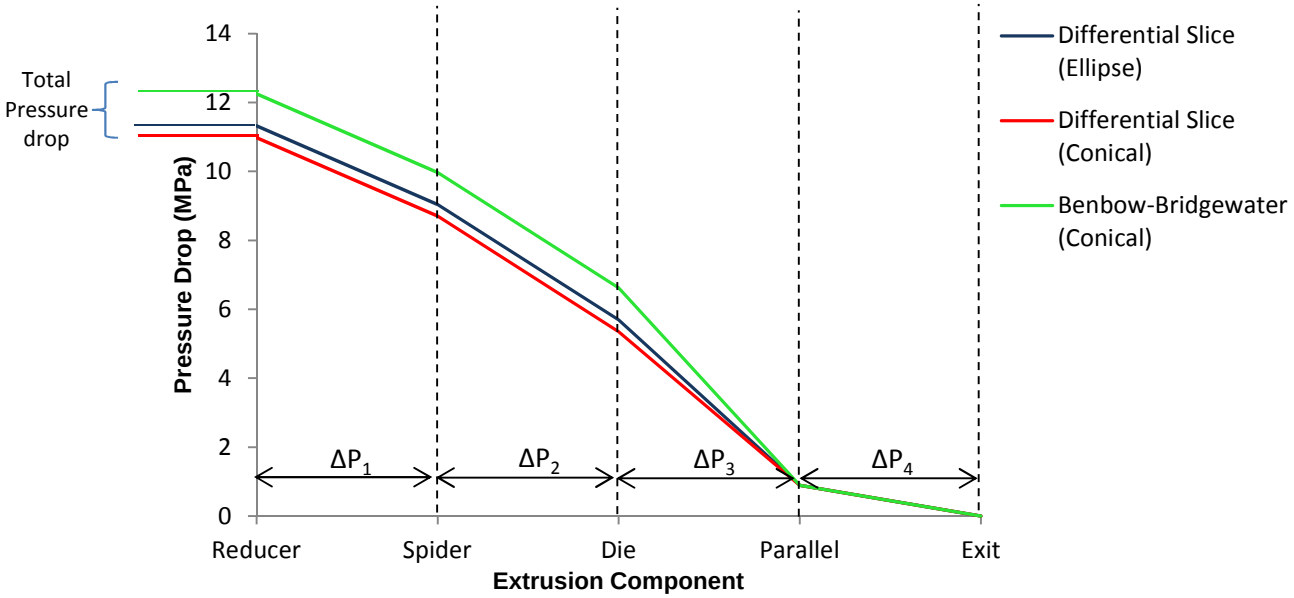

Figure 186 Pressure drop representation across each extruder component (from Benbow Bridgwater calculations)

Figure 187 Increased length of production tooling (extrusion die land)

Flow stability was improved with the longer die, giving better dimensional accuracy as the cork-screwing effect (Figure 289 and Figure 291) was removed. As well as improving the physical qualities of the extrudate, pitch variation was also reduced which is a sign of improved material flow. The reduced fluctuations in flow also aided improved internal dimensions such as coolant hole position and concentricity.

6.3.3 SHM Pilot Scale Extrusion Press

Larger diameters were extruded on a pilot scale press as insufficient force could be generated with smaller scale equipment. Initial testing produced 20 mm solid rods to validate the drying and sintering processes with simple geometry. If the rods survived drying and sintering at 20 mm diameter in the solid state, then 14 mm coolant holed rods were attempted. Steady state back pressure was recorded for each of the dough systems extruded in the pilot scale press (Figure 177). Increases in pressure with increased methyl cellulose content were observed on a pilot scale, as with capillary rheometry testing. Figure 177 shows that in order to achieve high extrusion pressures, higher cellulose contents were needed in group 2 systems (MC15 and MC16). MC8-MC14 dough was not able to provide extrusion pressures in the same region as SHM dough in the pilot scale press. This was not the case with capillary rheology experiments in which MC10-14 binders supplied the required pressures. The complex tooling design increased shear due to rifling and the presence of a spider and core pin. This had a greater shear thinning effect on the MC dough than the SHM dough. Therefore extrusion pressure was not increased proportionately across the extrusion equipment by increasing cellulose concentration. The dough extruded at 20 mm sintered diameter without a core pin had relatively low extrusion pressures due to the large die diameter. In the pilot scale press the ratio from barrel to diameter size was small. The small reduction had the effect of reducing extrusion pressure. Other binders from binder group 1 were also extruded in the pilot scale press. The quality of the Gelucire 5013 based extrudate was amongst the best in terms of product straightness and surface finish. Conversely, ECETHPVB and MCPAM dough were of a poor quality (Figure 178). This shows that the WC-Co powder and binder materials were not well mixed and indicates that the materials were not fully compatible. Although the surface finish and internal structure of both MCPAM and ECETHPVB extrudate was poor, rods were dried and sintered successfully whereas the GCMPG extrudate was not. It was later observed that porosity and low transverse rupture strength occurred with the MCPAM and ECETHPVB dough. Consequently, due to extrudate quality and burn out properties for the MCPAM, ECETHPVB and GCMPG dough respectively no further extrusion trials were carried out. From pilot scale extrusion it was determined that the only binder materials capable of drying and sintering large diameter products of good quality were the methyl cellulose formulations. The MC8 binder was investigated further leading to the development of all other binder groups. Group 2 feedstocks were formed into rods of complex geometry (coolant holes and rifling) at larger diameters (14 mm sintered diameter and above). From chapter 4, binder rheological analysis and chapter 5, mixing experiments, group 2 binders from MC8-MC16 were formulated and extruded. Figure 292 (appendix I) shows that up to the 16% MC formulation, the pitch length increased with methyl cellulose concentration. Stiffer

materials were initially expected to show less deformation and therefore shorter pitches. However, it is believed that the pitch is changing as a result of relaxation after extrusion. Tooling geometries remained constant throughout extrusion and therefore the pitch should remain the same regardless of the feedstock after taking material slip into account. During material movement up to the rifled die, polymer chains within the binders are forced to align and straighten out as a result of volume reduction. The volume reduction through the die causes material elongation and as the dough is twisted in an anti-clockwise direction in the rifled section of the die polymer chains straighten out further still. Once extrusion has finished, the rods store energy from the extrusion process and are left on trays to be examined before drying. As the external force from extrusion has now been removed and the rods are left to relax they can unwind in a clockwise direction as the polymer chains coil back up and tighten. Unwinding causes the pitch to lengthen and is dependent on the elasticity of the binder system (Figure 188 and Figure 189). Binders of greater elasticity (greater cellulose content) have the capability of storing more energy during the extrusion process. As more energy is stored, the rods unwind further upon relaxation and therefore a greater cellulose content gives a longer pitch (Figure 292). Long chained methyl cellulose also follows this trend of increased pitch. The MCL binder behaved elastically at high frequencies of oscillation (Figure 133).

Figure 188 tightly wound rod (immediately after extrusion)

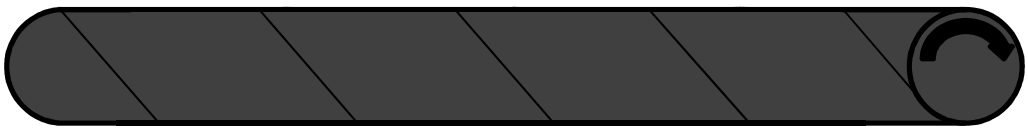

Figure 189 Relaxed rod (10 minutes after extrusion)

Extrusion quality control on both pilot and production scales is described in appendix I.

Chapter 7 Material Properties

7.0 Further product processing and material properties

After extrusion, samples were dried in conventional ovens and de-bound and sintered in a sinter-HIP furnace. Following sintering there are stages such as grinding, to remove rifling from the product and polishing to improve the surface finish and remove surface defects.

7.1 Drying

For large diameter products the most difficult procedures are drying and de-binding. Difficulty in drying increases with increasing cross section and material volume. During drying, liquid is forced through a porous network due to a pressure gradient. The pressure gradient causes deformation and expansion of the pores which allows for liquid transportation to the surface.

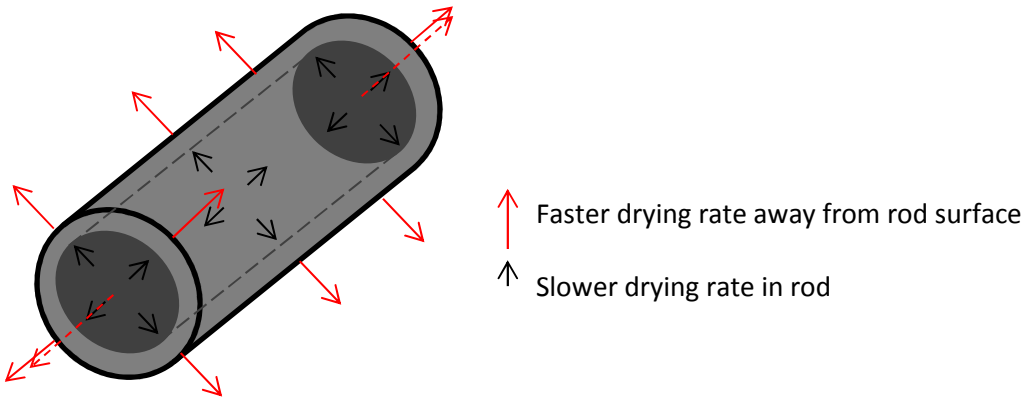

Figure 190 Drying rate from rod centre (black) and rod surface (red)

Figure 190 shows that during the drying and de-binding, binder materials at the surface are evaporated quickly. Liquid from the centre of the product cannot be transported through the porous network as quickly. This is due to a higher surface temperature than the temperature at the centre of the product in a conventional drying oven. Due to this temperature gradient, a difference in evaporation and transportation rates causes differential shrinkage. This results in greater tension at the surface and consequently cracking. Larger products have a greater temperature gradient from the centre to the surface and therefore develop greater stresses. A greater volume of material also has to be removed from a larger cross-section. Due to the increased stresses involved the drying rates cannot be increased to remove more material. Therefore larger products require significantly longer drying times and typically slower temperature ramp rates to cope with the stresses. Slower

ramp rates allow for equilibration between the diffusion and evaporative processes which aids minimisation of the temperature gradient. Experiments were carried out with the SHM feedstock which involved lengthening the drying times and reducing temperature ramp rates. The standard drying cycle used for diameters up to 12 mm sintered products by SHM is presented in Figure 191.

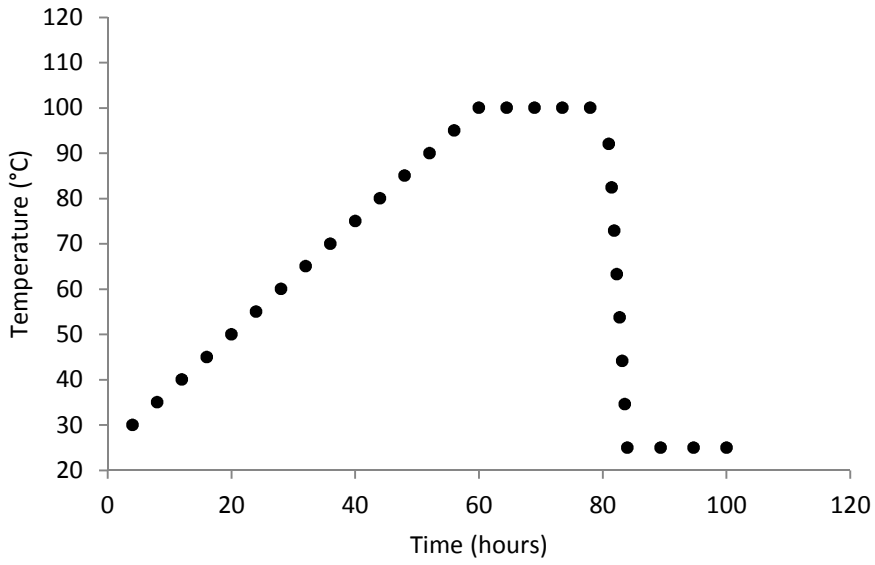

Figure 191 SHM standard production and laboratory drying cycle (temperature as a function of time)

This standard drying cycle was adopted for all material drying trials, including increased diameter and new binder formulations. This test was standardised as the SHM conventional extrudates could not survive if over 12 mm in diameter. If the new formulations could be processed under these conditions at larger size then they were considered potentials for industrialisation. Before undertaking this fixed regime the hold time was doubled and ramp up rate halved. The longer drying cycles showed success for 50% of samples at 14 mm sintered diameter with the standard SHM formulation. Figure 192 shows the typical failure type after sample drying. Similar drying failures were observed with the Gelucire 5013 plus MPG rods (Figure 193).

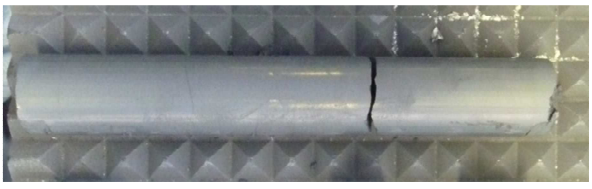

Figure 192 14 mm SHM cracked rod (drying at larger extrudate diameter)

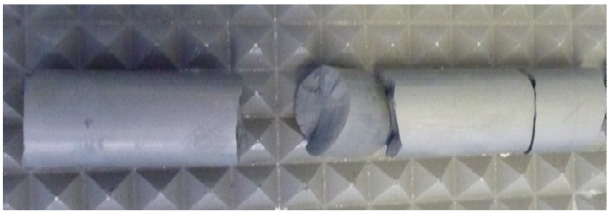

Figure 193 14 mm Gelucire 5013-MPG cracked rod (drying at larger extrudate diameter)

From the group 1 materials only the methyl cellulose based dough was capable of drying rods greater than 14 mm diameter whilst maintaining product quality. Dough feedstocks prepared with ECETHPVB and MCPAM binders were capable of drying up to 20 mm diameter solid products although product quality was low (Figure 178 and Figure 179). Products formed with coolant holes were more complicated to dry without cracking due to a lower green strength as a result of greater stress concentrators and surface rifling. Rifling increased the surface area of the product causing rapid drying at the surface when compared to solid rods. This imposed stresses and therefore the likelihood of cracking despite a lower material volume.

7.1.1 Weight Loss and Shrinkage Measurements

The mass of samples was recorded before and after the drying procedure, facilities were not in place to record weight loss during the drying cycle. Mass records gave an indication of whether or not the correct volume of material had been removed prior to using sintering furnaces. Linear and cross-sectional shrinkage was recorded across the whole process, before drying and after sintering. Shrinkage data was used in tooling design to manufacture precise diameter extrudate and minimise grinding and polishing waste. Due to a lower WC-Co solids loading than the SHM dough, higher shrinkage was expected for the MC based formulations. Linear shrinkage was also recorded so that a standard extrudate length could be determined to give the final correct product length. In the case of feedstock prepared from group 4 binders, only MC8 was evaluated for weight loss with an increasing WC-Co solids loading (Figure 196). For weight loss and shrinkage data it was important to consider the WC-Co solids loading of each individual feedstock as more highly loaded pastes would have a lower shrinkage and weight loss. The WC-Co solids loading for each dough formulation is given in Table 39.

Table 39 Dough feedstock WC-Co solids loading

Dough Name	WC-Co solids loading (vol%)
SHM	52.04
MC8	41.6
MCPAM	38
ECETHPVB	45.8
GCMPG	48.5
MC10-16	41.6
MCGLY	41.6
MCM	41.6
MCMPG	41.52

7.1.1.1 Group 1 Binder Feedstocks

Table 40 shows the weight loss and shrinkage of group 1 dough. As the binders were prepared from different materials with different melting and boiling points, a higher weight loss does not always correspond to a higher shrinkage. For example, the weight loss of the ECETHPVB dough is lower than the MC8 dough, yet the cross-sectional shrinkage is higher. In this isolated case, the weight loss is lower as the WC-Co solids loading was higher. Higher shrinkage is likely to be due to deformations in the rod surface. A higher solids loading should always give less cross-sectional shrinkage after sintering.

Table 40 Group 1 dough, weight loss and shrinkage

Sample Name	Weight Loss	Cross-sectional Shrinkage
SHM	5.45	22.45
MC8	5.47	23.78
MCMPG	5.51	28.32
ECETHPVB	5.16	25.8
GCMPG	3.76	22.47

7.1.1.2 Group 2 Binder Feedstocks

Figure 194 shows that the weight loss decreases with increasing cellulose content, with the exception of the MC16 formulation. Cross-sectional shrinkage also decreased with increasing cellulose content. The 8 % (MC8) variant in Figure 194 is for rifled samples whereas table 40 shows solid rod samples.

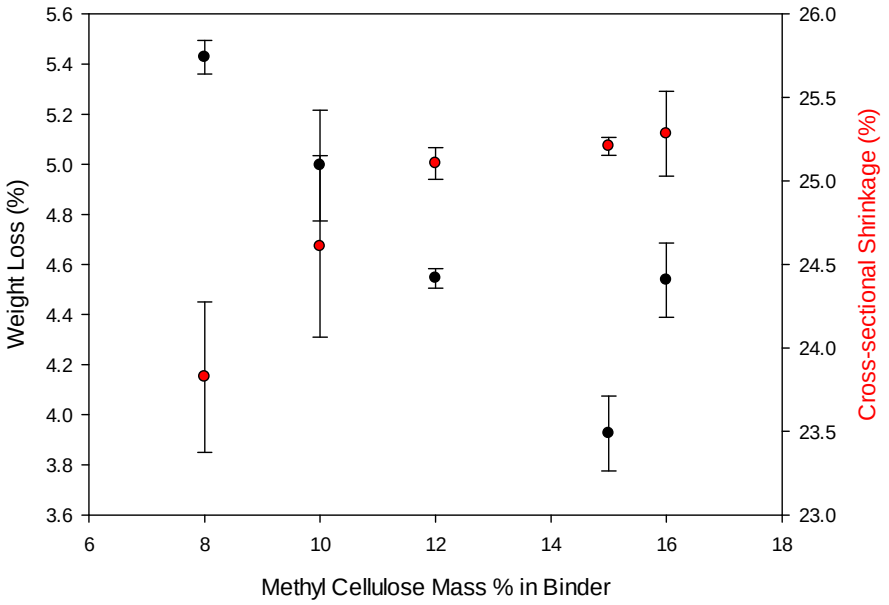

Figure 194 Group 2 binder based dough weight loss and shrinkage

Figure 194 shows that the weight loss for the MC16 based dough was greater than the MC15 based dough. The shrinkage remained relatively constant regardless of cellulose content with the exception of the MC8 dough which was prepared at an earlier stage in this work. Shrinkage and weight loss measurements had high error due to the procedure. Figure 195 shows the weight loss and shrinkage values for dough prepared with group 3 binders.

7.1.1.3 Group 3 Binder Feedstocks

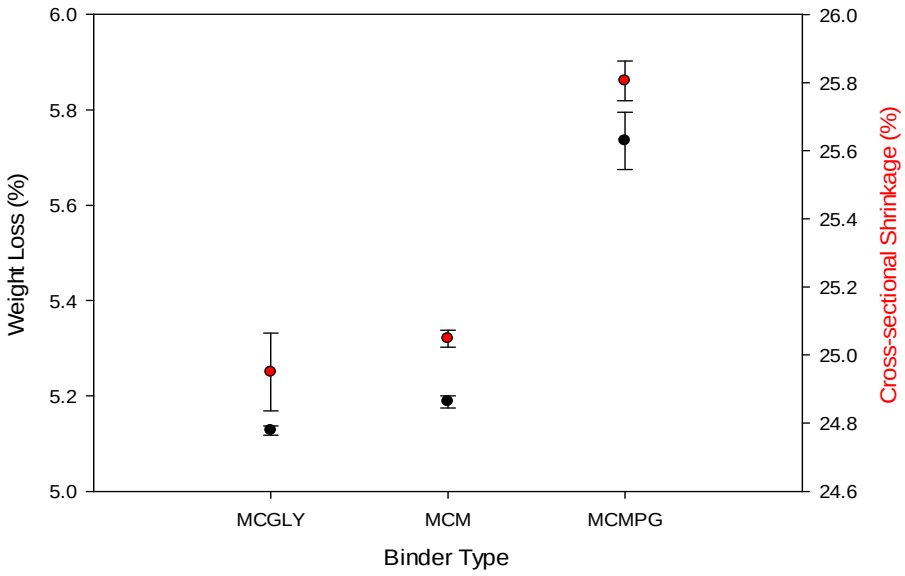

Figure 195 Group 3 binder based dough weight loss and shrinkage

The weight loss and shrinkage values were similar for MCGLY and MCM dough shown in Figure 195 as the WC-Co solids loading did not vary significantly. MCMPG dough had a solids loading of 41.52

vol% whereas MCGLY and MCM had solids loadings of 41.6. Due to high WC-Co density, small changes in the solids loading can affect shrinkage and weight loss significantly.

7.1.1.4 Group 4 Binder Feedstocks

Figure 196 shows how the weight loss changed with increasing WC-Co volume % for the 8% methyl cellulose based dough formulation. A trend of decreasing weight loss and shrinkage with increased WC-Co solids loading is observed as expected although there are large errors present in the data.

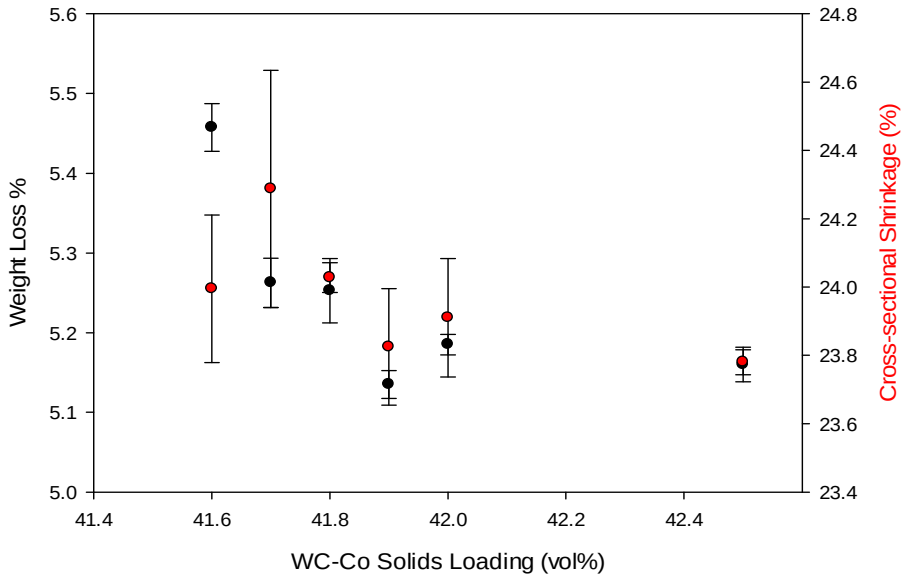

Figure 196 Weight loss and shrinkage data for increasing WC-Co vol% (MC8 dough)

Drying and de-binding conditions were analysed more thoroughly with thermal gravimetric analysis (TGA) and differential scanning calorimetry (DSC). TGA and DSC were used for group 1 formulations. Large errors in the shrinkage data are due to the use of Vernier callipers. For softer extrudate, the diameter could easily be reduced by closing the callipers too tightly.

7.1.2 Thermal Gravimetric Analysis (TGA)

TGA was used to determine the rate of mass loss of binder materials during the drying and de-binding process. The temperature ramp rates of the TGA equipment were therefore matched to the drying and de-binding stages used in production scale testing. Mass loss with temperature is shown in Figure 197 for group 1 feedstocks.

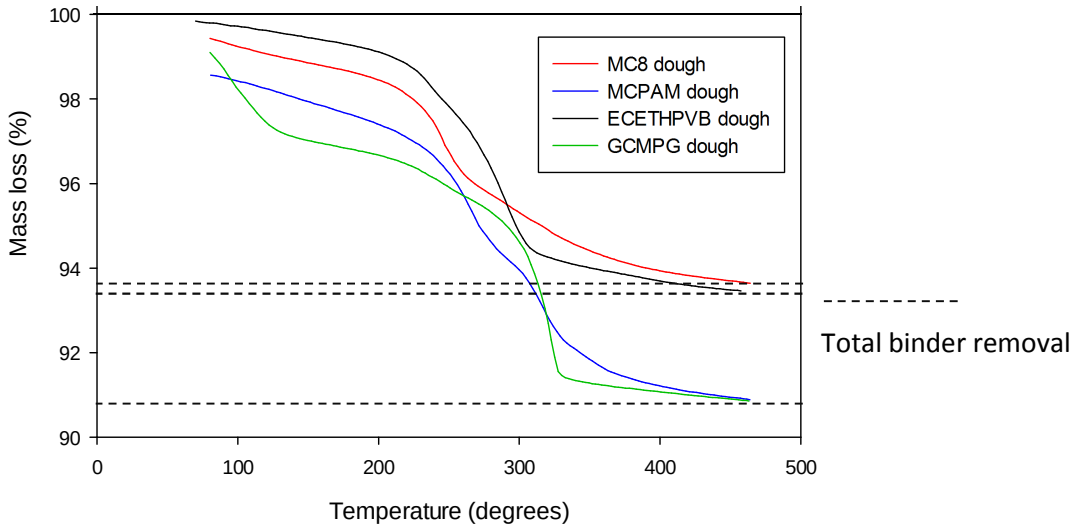

Figure 197 Mass loss as a function of temperature group 1 binder based feedstock

The MCPAM and GCMPG dough lost a greater proportion of their mass than other binders in the de-binding cycle. The MCPAM binder had a low WC-Co solids loading and hence a greater proportion of binder than other systems. For the GCMPG binder however, this was not the case. The GCMPG based dough had a low weight loss in the drying cycle (table 40). It can therefore be concluded that a high proportion of binder mass was retained after drying (22-100 °C). This gave a higher mass % lost in the de-bind cycle in which all of the binder is removed. A rate of mass loss plot for the materials in Figure 197 is given in Figure 198.

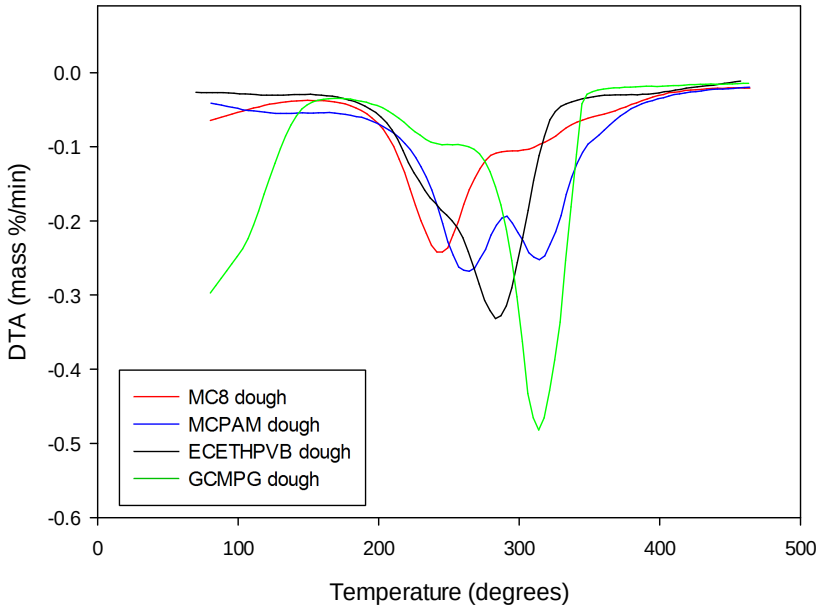

Figure 198 DTA as a function of temperature plot binder group 1 dough

The mass loss rates of extrusion dough given in Figure 197 show that there were significant differences in binder burnout temperatures. In the case of the MCPAM binder there is a decrease in

the rate of mass loss from 200-250 °C followed by an increase before 300 °C suggesting that two phases are present. Other dough systems show a stronger single peak with smaller deflections in data which may represent other phases. Peaks were expected as a result of PEG and in the WC-Co powder and other additional binder components. Broader peaks show that the burnout occurs over a wider temperature range. Narrow peaks suggest that the burnout occurs harshly and rapidly over a small temperature range, as with the GCMPG dough. Rapid mass loss rate of the GCMPG dough suggests that even if samples had survived the drying stages, de-binding without modification would have caused failure.

7.2 Sintering

The sinter HIP process used on all products in this work has been described in section 2.8. The sinter HIP cycle used did not vary from sample to sample and is shown in Figure 199.

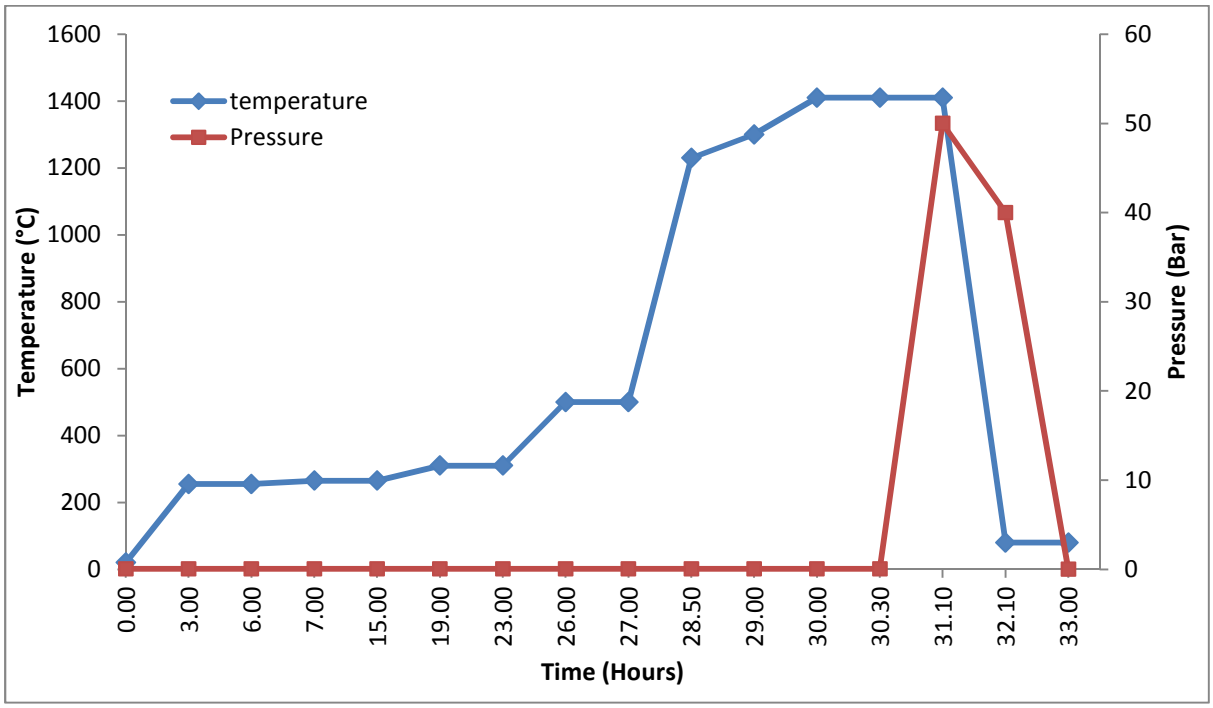

Figure 199 WC-Co extrusion sintering cycle, temperature, low pressure and high pressure as a function of time

The temperature ramp up to 500 °C occurred in stages in order to protect the extrudate from rapid expansion and sudden cracking. The ramp up in temperature was carried out under low pressure at 35 mBar although appears as zero due to the graph scaling. This aided binder removal at lower temperatures over a prolonged time period. The low pressure also insured that binder vapour was removed in a controlled environment. Pressure was increased to 50 mBar at the onset of sintering (high temperature). During the liquid state sintering stage the pressure was increased to 50 Bar (red)

ensuring pore closure brought into the sample during processing. Upon cooling, the high pressure was reduced.

7.3 Grinding and Polishing

Sintered pitch measurements are described in section 7.5.2. An extruded, sintered and polished rod is shown in Figure 200. Samples were ground after sintering to remove the rifling formed by the die geometry. Polishing to a surface finish of 0.8 µm insured a high quality surface finish with no surface defects.

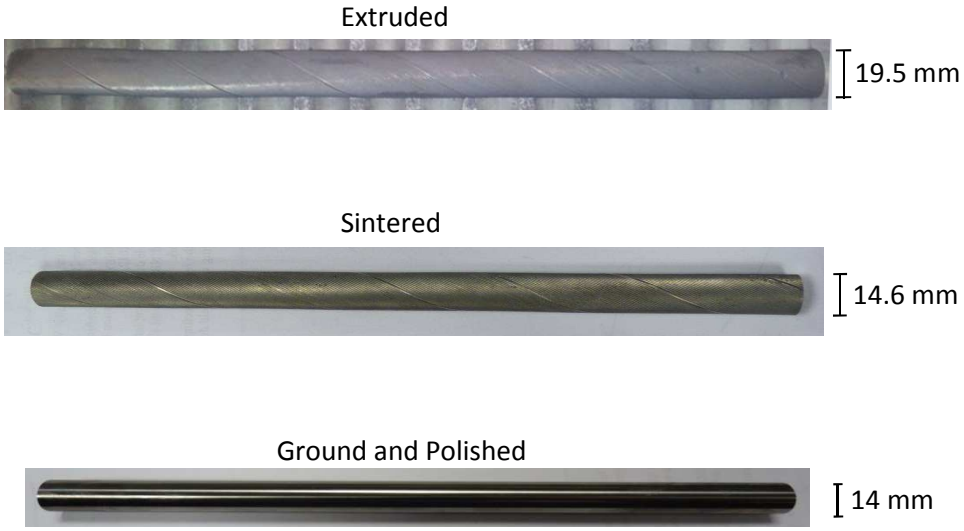

Figure 200 Extruded, sintered, ground and polished MC10 based WC-Co rod. Scale values represent the typical sizes expected.

7.4 Mechanical Testing

Mechanical testing of WC-Co products included Vickers hardness Hv testing and 4 point bend transverse rupture strength testing (TRS). TRS testing was carried out after production testing on the MC8 sintered product to validate material properties. Binder composition should not have affected the sintered properties unless defects were present. Defects commonly occur in the form of soft cracks (cracks formed in the green state) and extreme porosity.

7.4.1 Transverse Rupture Strength (TRS)

TRS testing using a 4 point bend test rig was configured for 6 mm diameter sintered solid rods. 4 point bend testing was applied as the aim was to test a large volume of material. Rods shatter at the break point, particularly with 4 point bend testing and this limited the test diameter to 6 mm for safety reasons. Solids loadings of 41.6, 41.9, 42.05 and 42.5 were evaluated to observe the effects of increased WC-Co content using test rig in Figure 201. 75 bars were tested for the 41.6 vol%, 45 for

41.9 vol%, 20 for 42.05 vol% and 20 for 42.05 vol%. For the highest solids loading, fewer bars were manufactured and available for testing due to extrusion handling issues.

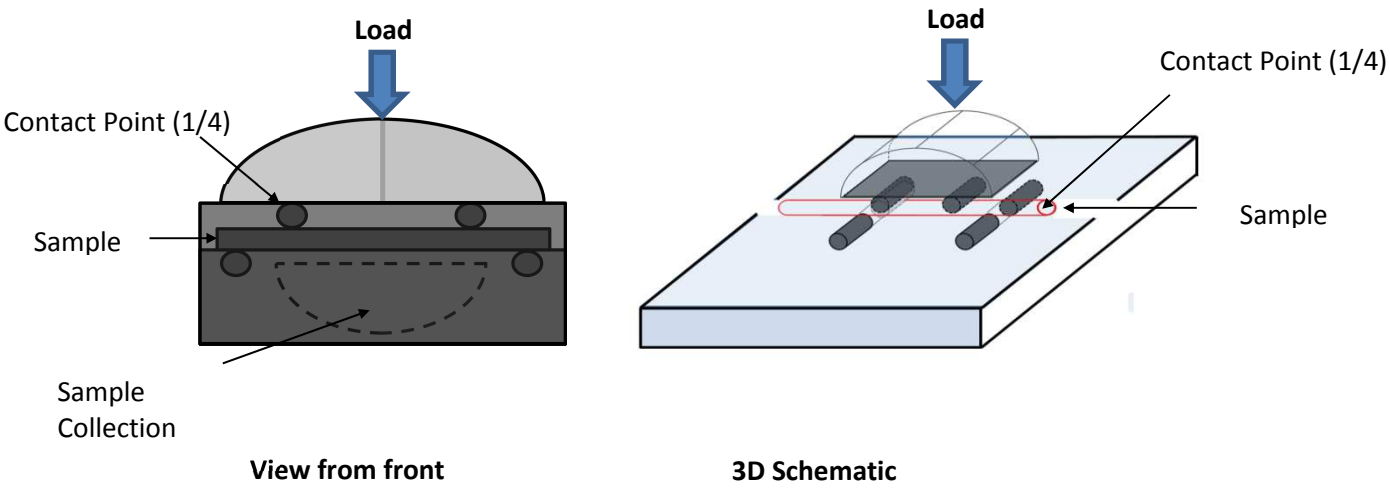

Figure 201 4 point bend test rig schematic used with load frame

Load was supplied to the test rig with a Mayes load frame. The sample indicated in the 3D schematic was placed in between the four cylindrical supports. The top half of the test rig was dome shaped in order to self-centre and supply even force across the rig. As samples were known to shatter, a collection chamber was machined into the test rig. A fixed loading rate of 0.05 mms^{-1} was applied until the sample fractured and the resultant load recorded to give the TRS test results shown in Figure 202.

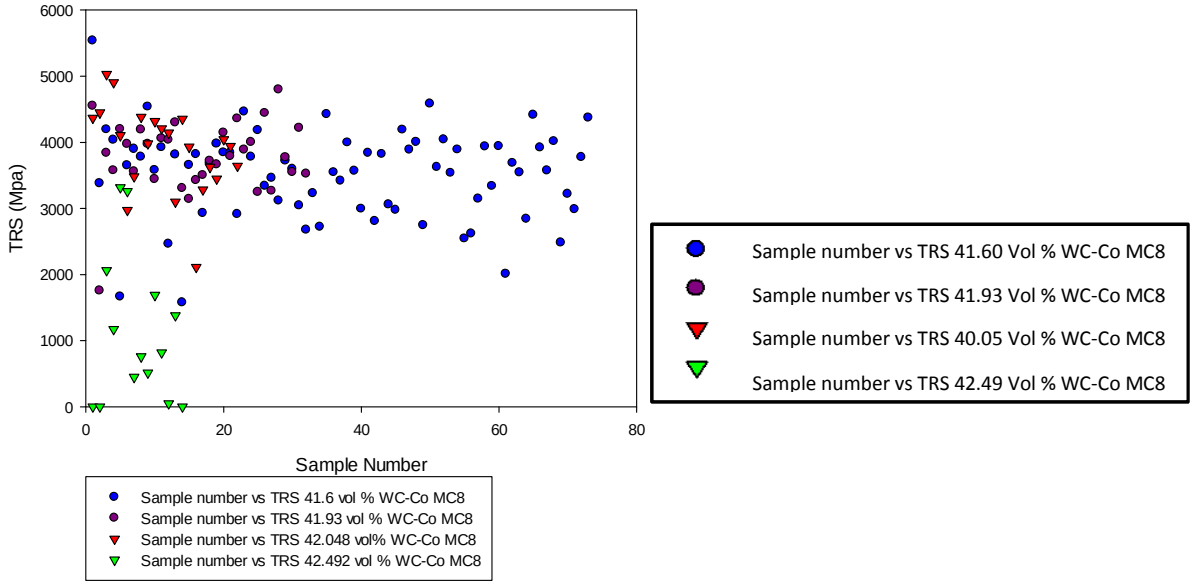

Figure 202 TRS data for sintered samples prepared from the MC8 binder

The scatter observed in Figure 202 is typical of brittle materials, such scatter often represents a large number of defects in a given sample and failure loads are therefore unpredictable. In order to better understand the probability of failure, a Weibull analysis was carried out. In the Weibull analysis it is assumed that the material is isotropic and statistically homogenous. It is also assumed that failure at the most critical flaw leads to total failure. The first assumption means that the probability of finding a critical flaw in a small volume of material is the same throughout. The second assumption is based on the weakest link of the chain concept whereby the failure of one link leads to total failure. The probability of failure is defined by the two parameter weibull distribution [165]. The two parameter Weibull distribution is described by equation 7-1 [166].

$$P_f = 1 - exp\left[-\left(\frac{\sigma}{\sigma_0}\right)^m\right] \; for \; \sigma > 0 \; and \; P_f = 0 \; for \; \sigma \leq 0 \qquad 7\text{-}1$$

where m is the Weibull modulus, σ is the stress at failure point and σ_0 is the stress at which the failure probability it approximately 63% [167].

P_f is the probability of failure at or below stress σ, calculated from the TRS data such as that in figure 202 using the ranking equation:

$$P_f = \frac{n - 0.5}{N} \qquad 7\text{-}2$$

where n is the ranked TRS strength number and *N* is the total number of samples tested. Equation 7-3 can be linearised using linear regression to give:

$$ln\left(\ln\left(\frac{1}{1-P_f}\right)\right) = mln\sigma - mln\sigma_0 \qquad 7\text{-}3$$

which can be further simplified to:

$$ln\left(ln\left(\frac{1}{P_f}\right)\right) = mln\sigma - k \qquad 7\text{-}4$$

The Weibull modulus is determined from the slope of the plot ln(ln(1/1-pf)) against lnσ (figure 203) and the scale parameter k can be deducted from the intercept term y [166].

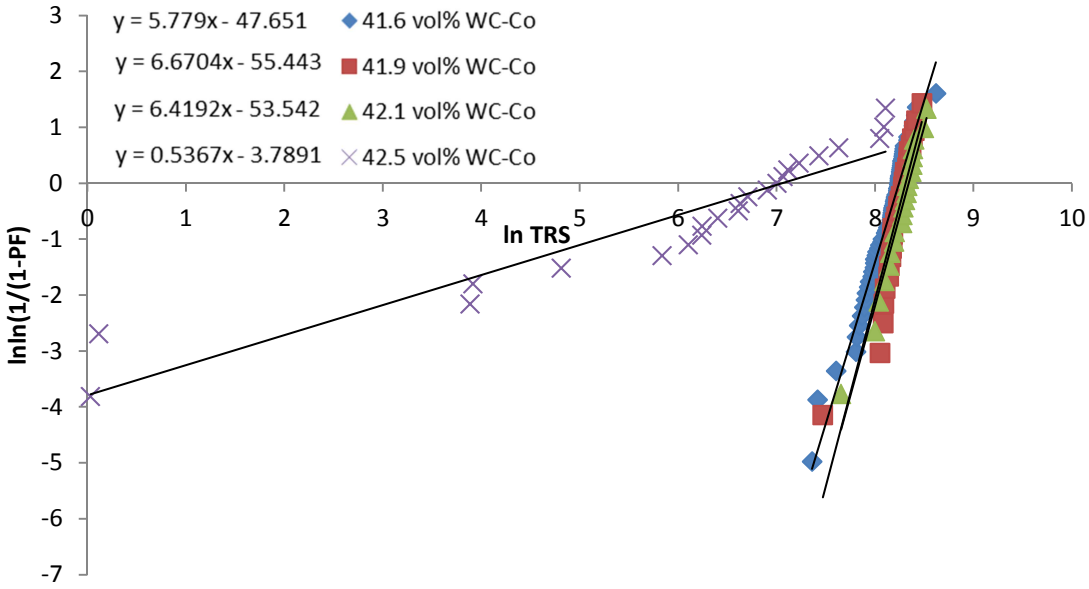

Figure 203 Weibull Moduli plot for increasing WC-Co solids loading

The results from figure 203 are given in table 41:

Table 41 WC-Co solids loading and Weibull number

WC-Co solids loading	Weibull number (m)
41.6	5.78
41.9	6.67
42.1	6.42
42.5	0.54

The m values are low when considering typical values for ceramics should be in the region of 10-20 and above. A batch of the standard SHM grade was examined to verify the typical values achieved at Sandvik and the results are given in table 42:

Table 42 SHM standard grade Weibull numbers

Batch	Weibull Modulus
1	12.98
2	6.608
3	10.91
4	14.68
5	8.15
6	16.89
7	12.66
8	18.01
9	11.97
10	14.92

It is clear that the Weibull analysis has revealed that the m values achieved from the methyl cellulose formulation are below the standard formulation. Low m values are indicative of a large scatter of strength values and thus defect sizes. Although the Weibull plot shows low values of m, Figure 203 shows that the Weibull modulus (slope) only varies significantly at the highest WC-Co solids loading in this work. The slope for the material prepared with 42.5 vol% WC-Co has two distinctive gradients (Figure 204). There is a less distinctive, steep third gradient in which the 3 points representing 3 samples indicated in Figure 204 could be interpreted as defect free (as with the lower WC-Co loadings).

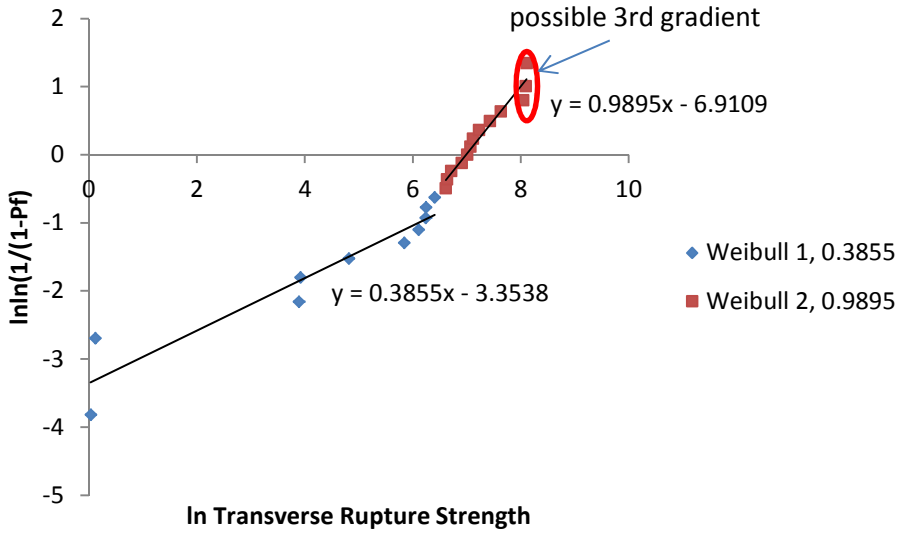

Figure 204 Extended Weibull plot for 42.5 vol% WC-Co

A low Weibull modulus, particularly with the shape of Figure 204 is indicative of a material with many defects of different sizes. Low and scattered TRS data is indicative of samples with large defects and hence this material is weak and unpredictable in the way that it fails. The most common form of defect were cracks in the green state known as soft cracks. An example of a soft crack is shown in Figure 205. Soft cracks were far more common in the materials prepared at a higher solids loading because the binders could not fully wet the powder as the maximum solids loading was approached. A lack of binding led to a dry and crumbly extrudate which was highly brittle and susceptible to stick slip flow. The constant stick slip behaviour at higher solids loadings formed internal cracks and once the product was sintered such cracks appeared as figure 205.

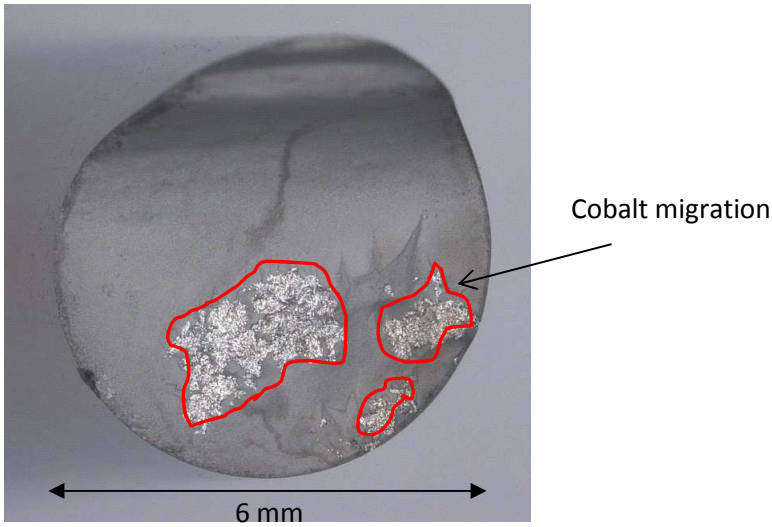

Figure 205 TRS tested rod showing cobalt migration (42.5 vol% WC-Co)

The reflective surfaces seen in Figure 205 were a result of cobalt migration. Cobalt migration occurred around exposed surfaces which were present due to internal cracking in the green state. Although the crack may have been small enough to be sealed in the sinter HIP process, the cobalt concentration would be high in this area giving a point of weakness. Soft cracks were problematic as they could easily go un-noticed in randomised sample testing. Hv30 Vickers hardness measurements were ineffective at detecting such defects. Hardness was tested over a section of the samples in random areas. As the diamond indentation was small, and the sample was ground and highly polished, the likelihood of indenting a defect was small. Soft cracks were only detected efficiently using TRS testing.

7.4.2 Hardness

Hv30 Vickers hardness testing was applied to each of the feedstocks sintered in this work. HV corresponds to the Vickers pyramid number which is determined by the load applied over the indentation area (30 Kg in this work). Hardness has been described in section 3.1.1. 3 µm polishing gave a mirrored finish to give true hardness values for the WC-Co material with no surface defects. The indent length was measured from corner to corner (3 indents per sample) as shown in Figure 206.

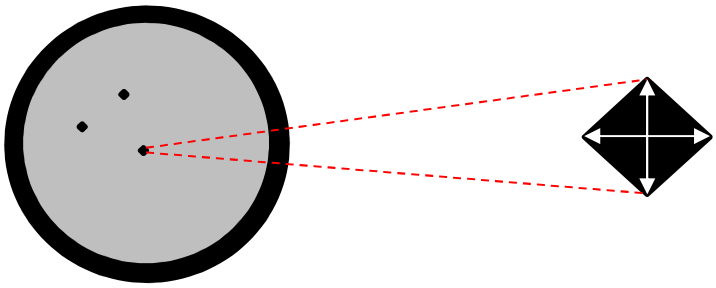

Figure 206 Mounted sampled and Hv30 hardness indentation

The target Hv30 hardness required was no less than that of the SHM extruded feedstock which had a specification range of 1550-1650 (Figure 207). This was the hardness range applied to all sinter HIP materials prepared with the same WC-Co (10 wt% cobalt) regardless of processing technique. The results of the hardness Hv30 test are shown in Figure 207 to Figure 210 for each group of dough formulations. Figure 207 shows that the hardness of the MCPAM material was significantly low, caused by excessive porosity also observed in Figure 225.

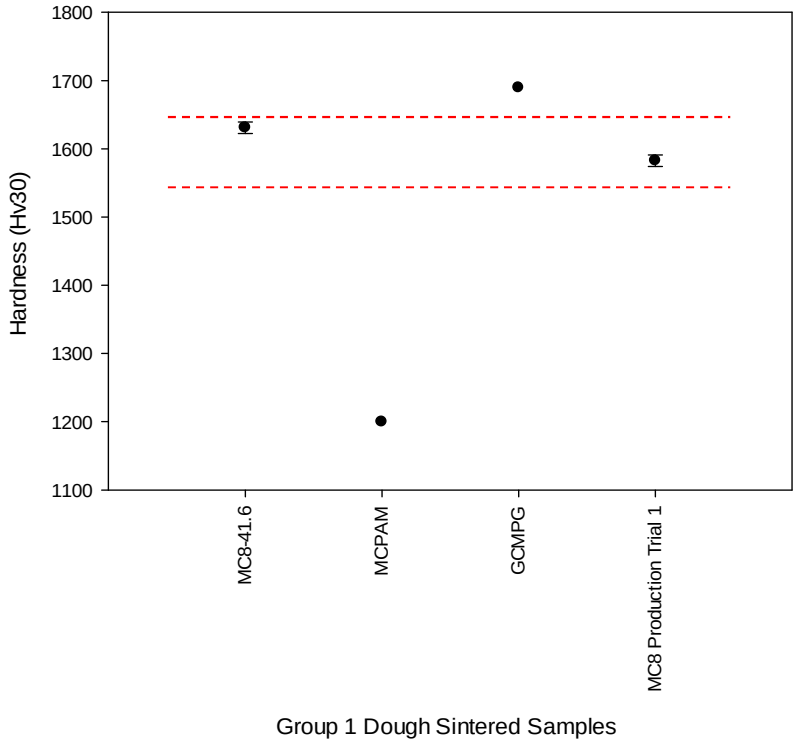

Figure 207 Group 1 dough sintered samples Hv30 hardness

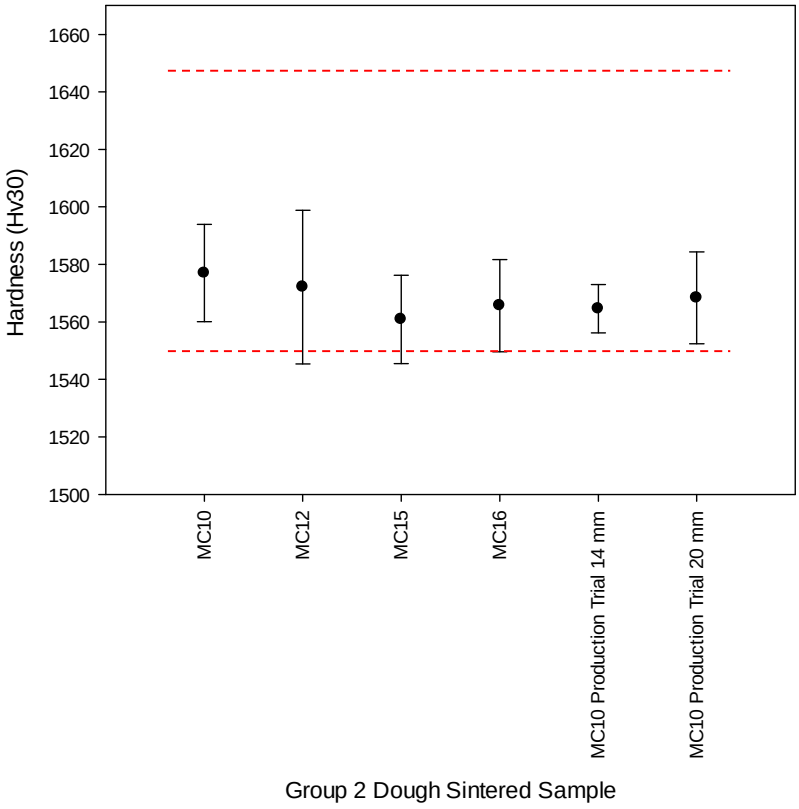

Figure 208 Group 2 dough sintered samples Hv30 hardness

Figure 208 suggests hardness was not affected by increasing cellulose concentration in the binder (MC10 and above) or by scaling up the mixing and extrusion process. The MC8 formulation from group 1 however was significantly harder.

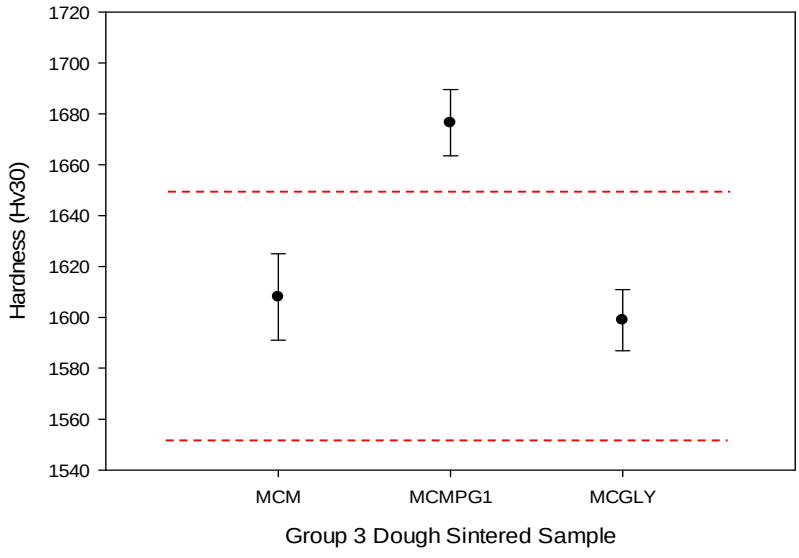

Figure 209 Group 3 dough sintered samples Hv30 hardness

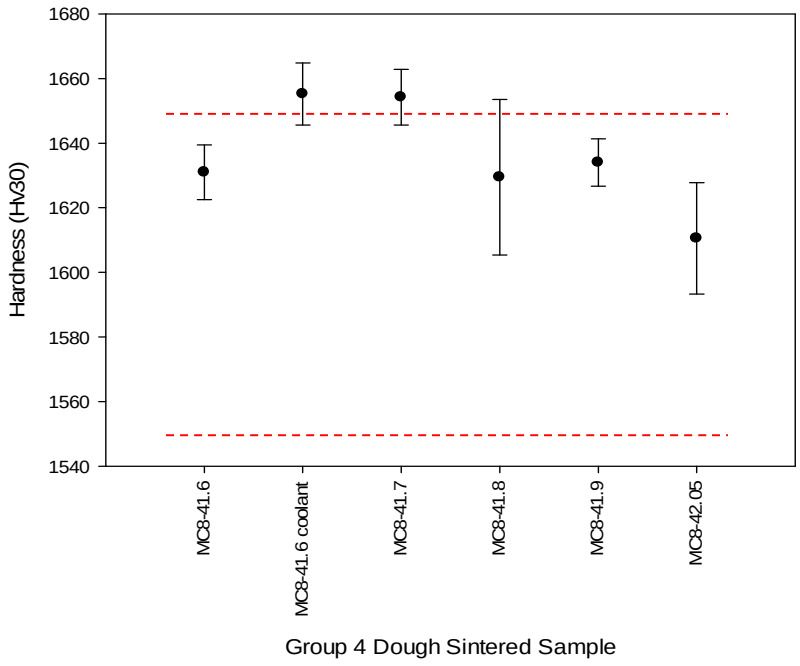

Figure 210 Group 4 dough sintered samples Hv30 hardness

Whilst a high hardness was desirable, hardness exceeding the range of 1550-1650 (HV30) is not ideal. Hardness greater than 1650 (HV30) implied that the sample was brittle and lacking in toughness. A brittle sample also implies that the carbon balance in the sintered sample was not correct due to the formation of eta-phase. The majority of the samples were within the desired range of hardness although the MCPAM sintered samples had a significantly lower hardness due to porosity. The data in this case is unreliable because it was difficult to indent the sample in between pores.

7.5 Other Sintered Properties

Measurements of density, pitch, concentricity and pitch circle diameter were measured in the sintered state as each is important for product quality.

7.5.1 Sintered Density

Sintered density was used as a measure of porosity against a standard for the grade of WC-Co. The standard sintered density was 14440-14600 $Kgm^{-3}$and lower values indicated porosity. The sintered density of each binder material formed into a product is shown in Figures 211 to 214. Many of the samples fell below the target density, although samples prepared on a production scale with group 2 binders and refined tooling were within specification. Sintered density measurements have given an indication that dough prepared with group 2 binders consistently outperforms other dough systems.

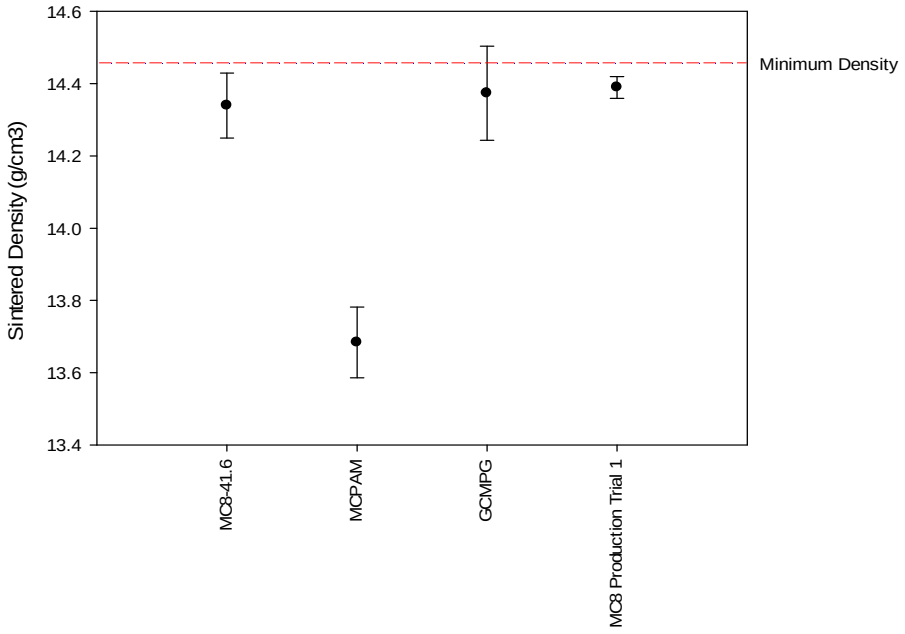

Group 1 Sintered Sample

Figure 211 Group 1 sintered density

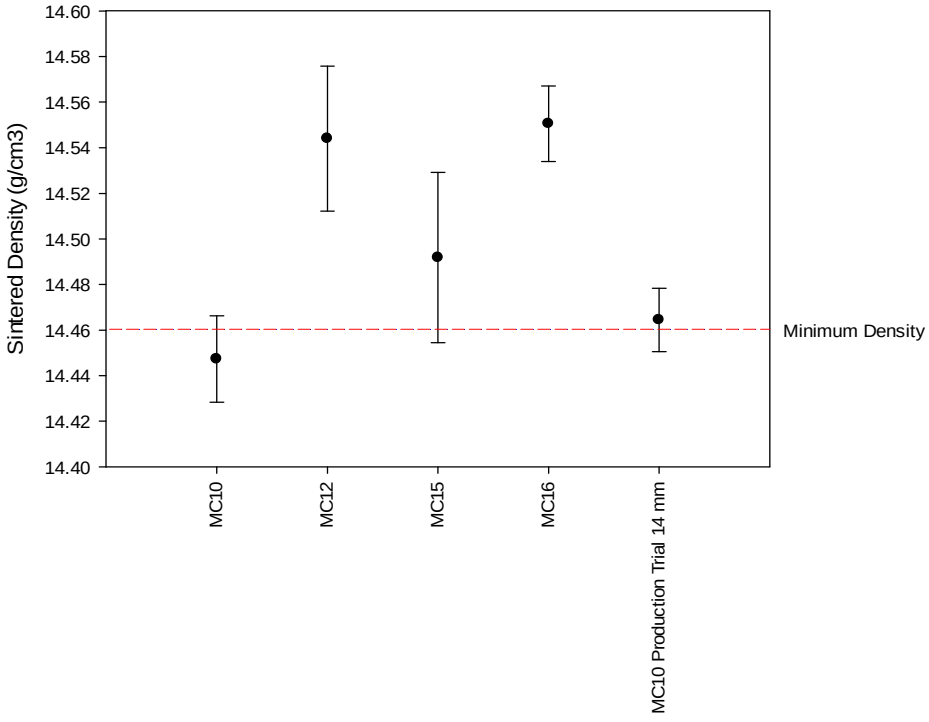

Group 2 Sintered Sample

Figure 212 Group 2 sintered density

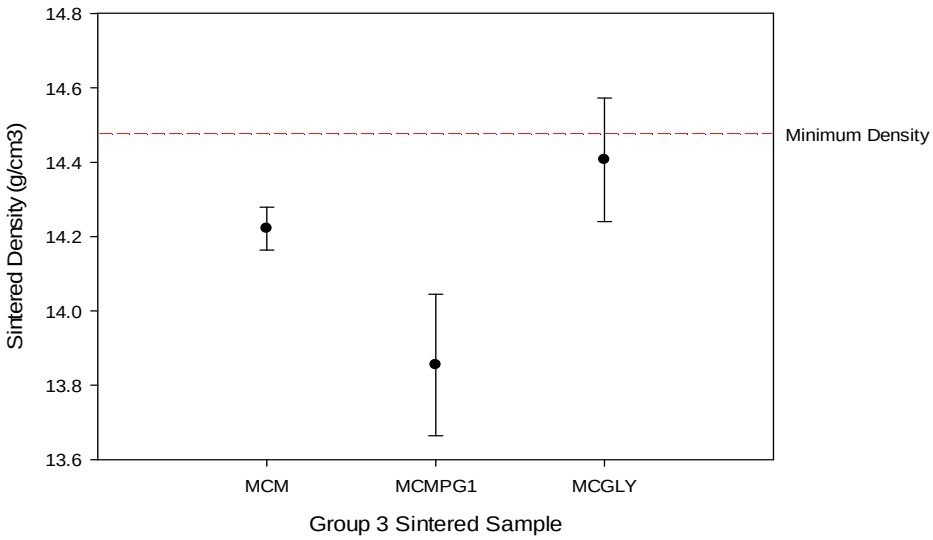

Figure 213 Group 3 sintered density

Figure 213 shows that sintered density was below specification for each of the dough systems measured in group 3 implying that porosity was present.

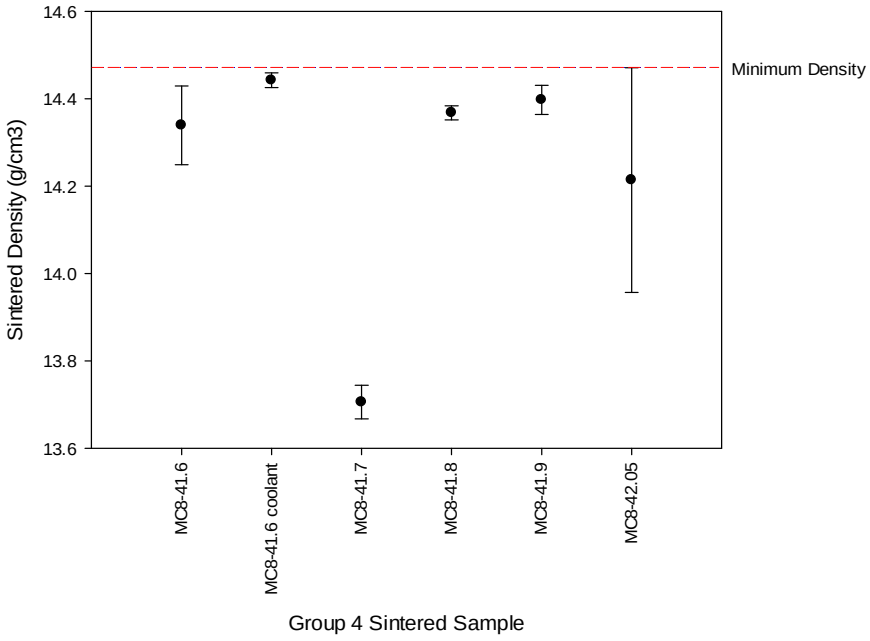

Figure 214 Group 4 sintered density

Figure 214 shows that increased WC-Co content for the MC8 sample did not increase sintered density significantly and that the presence of coolant holes also had no significant effect. The effect of coolant holes on the theoretical sintered density was not accounted for as it was the bulk material around the coolant holes that was considered important. As the sintered density was measured using the Archimedes principle, so long as bubbles did not form on the surfaces of the coolant holes, the density result was not affected. Agglomerated dough was formed during mixing at increased solids loadings and therefore porosity was expected and unpredictable (MC8-41.7). The sinter HIP process was not able to remove the porosity based on this evidence.

7.5.2 Sintered Pitch Measurements

Sintered pitch measurements for group 2 samples are shown in Figure 215. Significant differences between production testing highlight inconsistency in the formulation and or processing techniques.

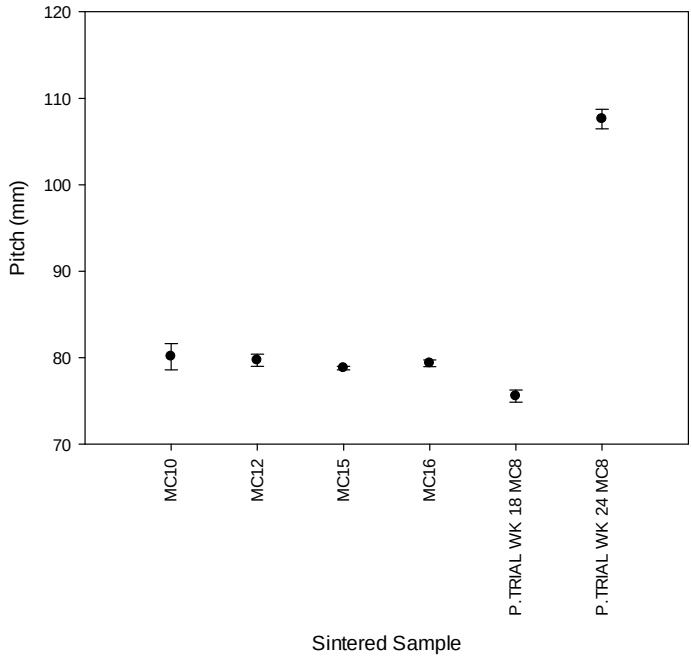

Figure 215 Sintered pitch data (14 mm sintered diameter)

Figure 216 shows a comparison plot of sintered and green state pitch measurements for samples prepared from group 2 dough.

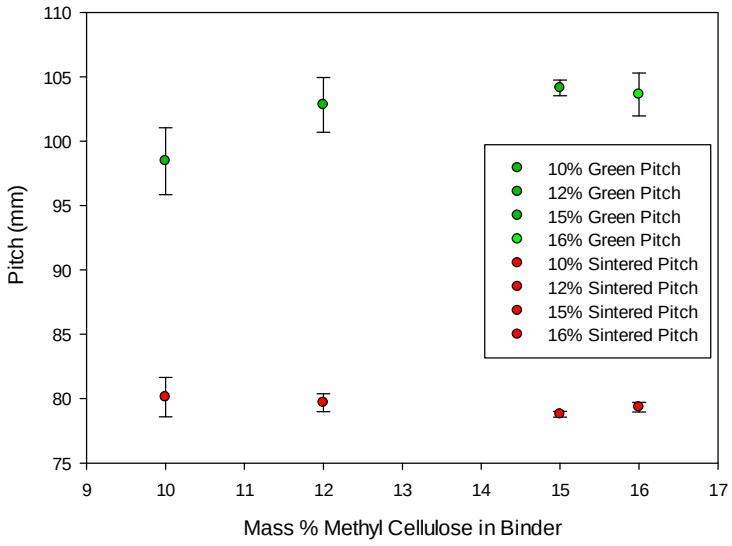

Figure 216 Green and sintered pitch comparison as a function of methyl cellulose content in extrusion binder

The sintered pitch did not vary significantly between batches of increased methyl cellulose content in the binder. Sintered pitch data was less scattered than green state pitch measurements due to relaxation as described in section 7.7.3.1 and distortion of material caused by the measurement. The

second production trial (indicated as week 24 2012) had an unexpected longer sintered pitch than previous experiments. As the second production scale trial indicated pitch variation, further care was taken in sample measurements. During the third set of production trials in week 37 (2012) tray by tray data was recorded to measure the variation in pitch throughout the production test. Sintered pitch data for the 14 and 20 mm samples prepared using the MC10 binder are shown in Figure 217 and Figure 218 respectively.

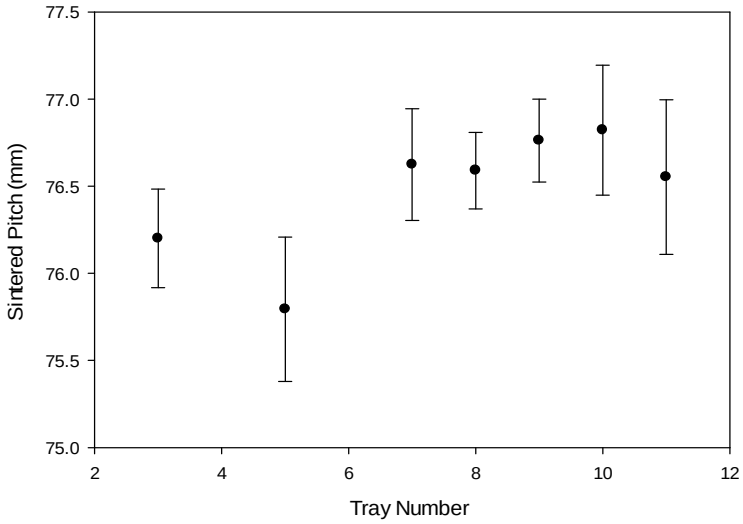

Figure 217 Tray number vs sintered pitch (14 mm coolant)

The blocking of handling equipment and misplacement of samples by the automatic picker device caused automatic extruder shutdown. Pitch measurements were only taken at tray 1, 5 and 10 in the as extruded state whereas sintered pitch measurements were taken from samples on each tray. If results from trays 3 and 11 were neglected as a result of an interruption to extrusion then there would be a trend of increasing pitch with extrusion progression. This projection of pitch results can be seen in Figure 218.

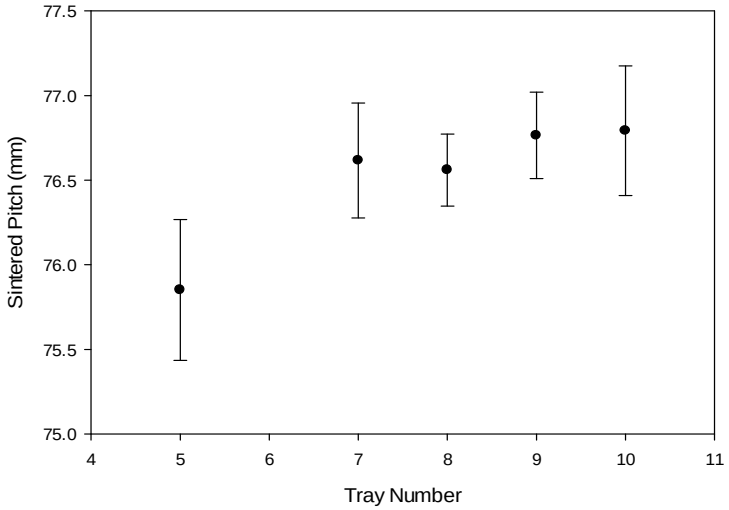

Figure 218 Tray number vs sintered pitch (14 mm coolant) tray 3 and 11 removed

The difference in sintered pitch measurements throughout a complete extrusion run in production was 1-2 mm in total from tray 5 to tray 10. This is a small variance given that up to 55-60 samples each 450 mm long were produced. The 20 mm production run had a greater pitch variance through the course of the test (3-4 mm) although a similar trend is shown at a longer pitch.

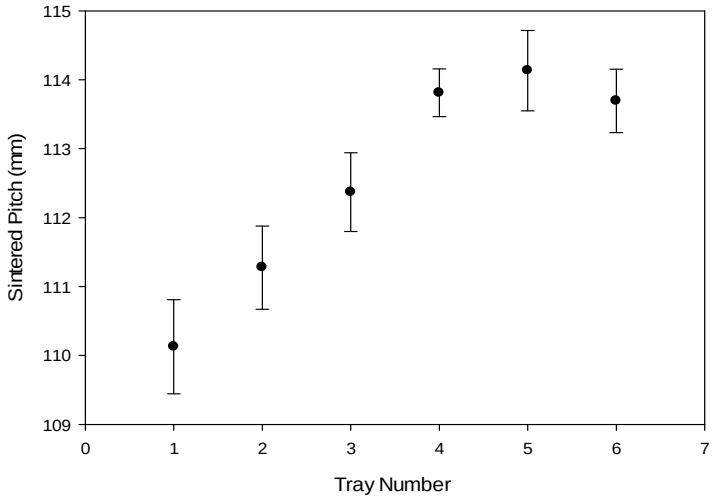

Figure 219 Tray number vs sintered pitch (20 mm coolant)

Figure 219 shows that the sintered pitch for 20 mm coolant products increased with the progression of the extrusion trial. The scattering of data is less than that observed in Figure 218 and so behaviour is more predictable. For the same trial, for a 20 mm sample, the PCD and concentricity were measured.

7.5.3 Sintered Concentricity and PCD Variance

A 20 mm diameter sample was sectioned every 30 mm from the leading end of the rod. This was carried out in an attempt to determine the cause of the variability in PCD and concentricity.

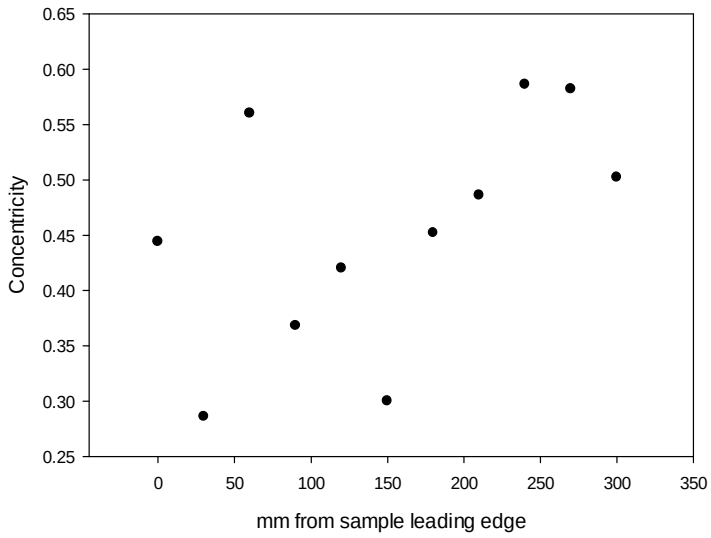

Figure 220 Concentricity variability in 20 mm rod as a function of rod length

Figure 220 shows that there is a slight increase in concentricity with rod length if the anomalies at 0, 50 and 150 mm are removed. This implies that the coolant holes are becoming less concentric with the outer diameter of the rod with rod length. Coolant holes are very rarely concentric with the outer diameter of the rod at the lead (0 mm) because the rod is distorted by the cutting system in the green state. Figure 221 shows that there is little correlation between PCD and rod length from the lead although the variation is small.

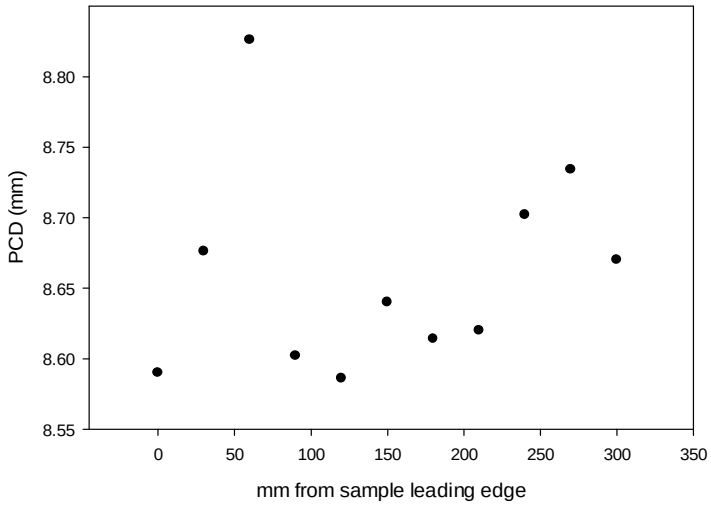

Figure 221 PCD variability in 20 mm rod as a function of rod length

The PCD has a maximum difference of 0.27 mm which is less significant than an increasing concentricity with rod length. This suggests that the distance between the coolant holes remained relatively constant for the 20 mm sample down its length. There was therefore an issue with tooling alignment in the extrusion set up rather than movement of internal coolant tooling (filaments). A schematic of the measurements made for the 20 mm samples has been shown in Figure 222. Concentricity was also measured as described in section 3.14.

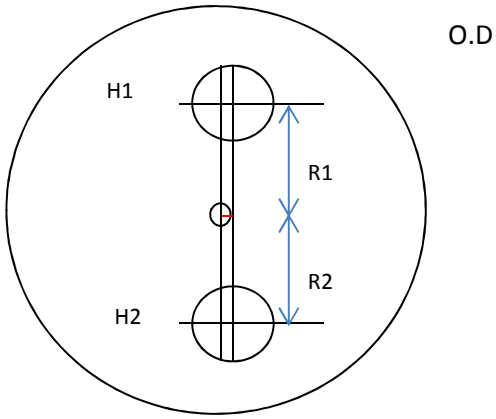

Figure 222 Measurements (20 mm coolant)

R1 + R2 is equal to the PCD, H1 and H2 are hole diameters and the red line indicates the distance of the rod centre to the centreline of the two coolant holes and this is the concentricity number. Figure 223 shows the measured sections of a 20 mm rod with coolant holes.

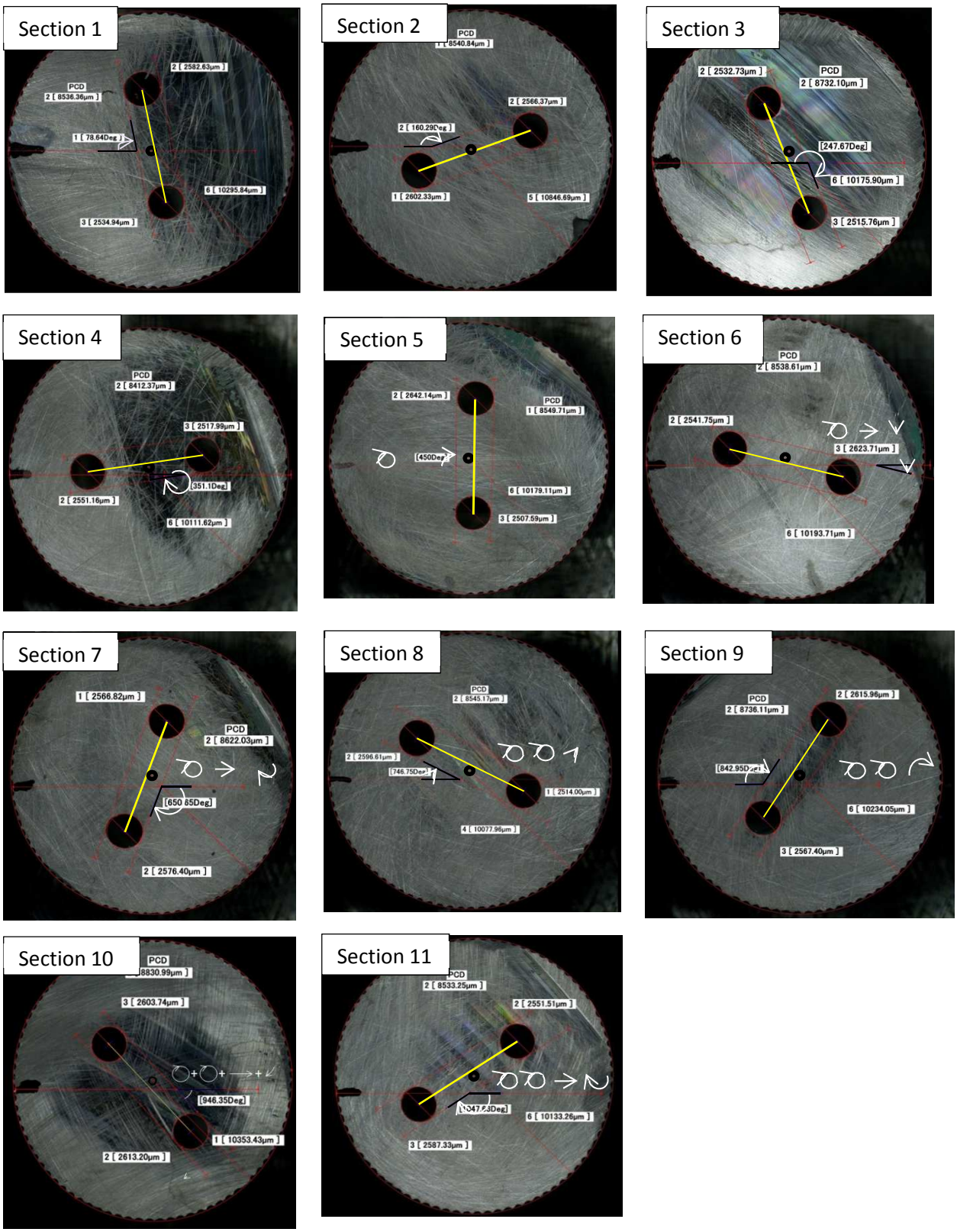

Figure 223 Sintered sections, 20 mm coolant hole rod

The angle of rotation of coolant holes was measured from the same reference point in each section from a line drawn against the outer diameter of each coolant hole, running parallel to the section centre line (Figure 222). The centre line shown in yellow moved independently from the rod centre. The rod centre in this case was determined by the Keyence software, by matching the red outer circle closely to the outer diameter of the rod section. The orthogonal distance of the mid-point of the yellow PCD line from the rod centre was then measured to scale. The PCD has been measured as R1 and R2 (Table 43) which showed whether or not the tooling was misaligned in the die set. R1 and R2 have been plotted in Figure 224.

Table 43 Sectioned rod measurements (20 mm coolant)

Section ID	H1 (mm)	H2 (mm)	PCD	Rod Diameter (mm)	Concentricity	Coolant hole Rotation (°)	R1 (mm)	R2 (mm)	X (mm)
0 (1)	2.6120	2.5780	8.59	20.65	0.4440	78.64	4.53	3.95	0.27
30 (2)	2.5920	2.5800	8.67	20.58	0.2860	160.29	4.44	4.10	0.14
60 (3)	2.6440	2.5760	8.82	20.57	0.5600	247.67	4.72	3.94	0.37
90 (4)	2.6360	2.5840	8.60	20.54	0.3680	351.10	4.40	4.01	0.32
120 (5)	2.6420	2.5820	8.58	20.49	0.4200	450.00	4.38	4.17	0.45
150 (6)	2.6580	2.5820	8.64	20.50	0.3000	553.80	4.40	4.07	0.32
180 (7)	2.6080	2.5540	8.61	20.50	0.4520	650.70	4.49	4.11	0.34
210 (8)	2.6300	2.5540	8.62	20.52	0.4860	746.80	4.41	4.08	0.39
240 (9)	2.6040	2.5320	8.70	20.55	0.5860	843.00	4.67	4.14	0.53
270 (10)	2.6140	2.5760	8.73	20.51	0.5820	946.35	4.69	4.12	0.51
300 (11)	2.5740	2.5400	8.67	20.58	0.5020	1047.63	4.46	4.03	0.41

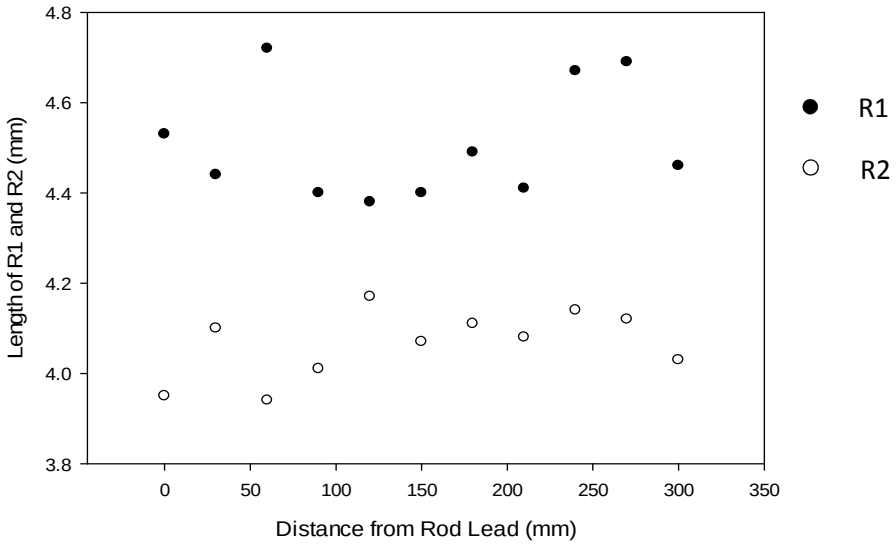

Figure 224 R1 and R2 length vs rod length

Figure 224 shows that whilst R1 and R2 were consistent with rod length, R1 was consistently greater than R2. As well as measuring R1 and R2 separately, the angle of coolant hole rotation was also

measured down the sample length. This was to determine the coolant hole rotation inside the rod with relation to the exterior pitch. The rotation of coolant holes has been plotted in Figure 225.

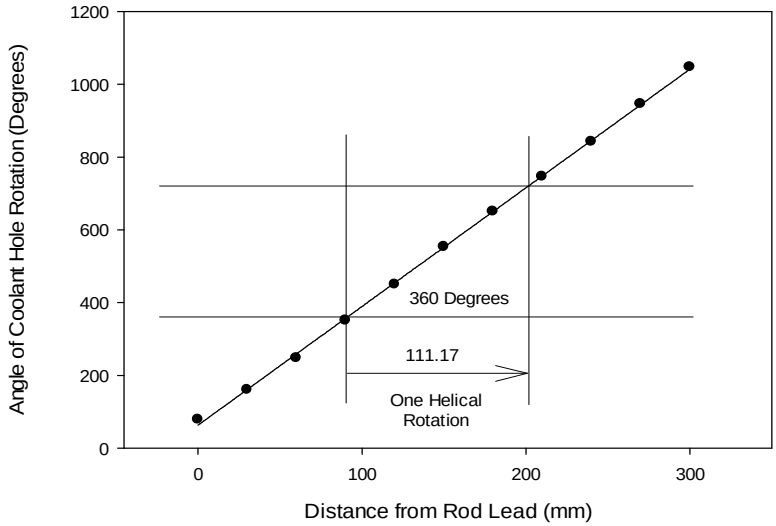

Figure 225 Rotation of coolant holes (20 mm coolant rod)

Figure 225 shows that a complete rotation of the coolant holes occurred in 111.7 mm of rod length which was similar to the exterior pitch length (Figure 219). In order to investigate the effects of concentricity and PCD, a tight pitch experiment was designed and is reported in Appendix J.

7.5.4 Internal Fracture Analysis

From production scale testing (week 37 2012), sintered rods were brittle and prone to failure in the grinding stage. Indentations were observed in the surfaces of each rod resulting in a failed batch of material (Figure 226 surrounded by the black hashed lines). The indentation was a crack perpendicular to the rifling. The crack was therefore perpendicular to the rotational flow of material rather than the bulk flow.

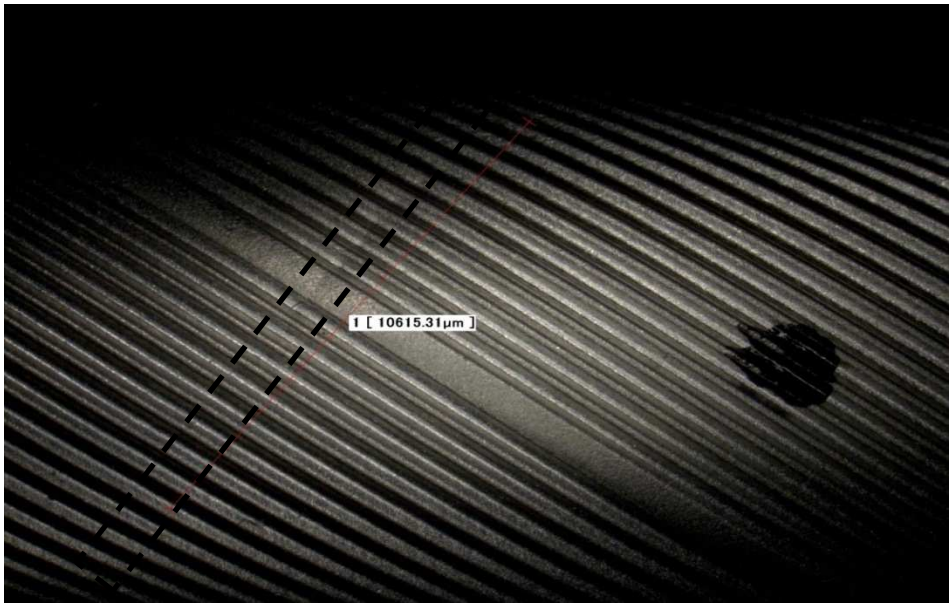

Figure 226 Perpendicular to flow crack in WC-Co sintered sample with rifling

The sample shown in Figure 226 was broken to observe the fracture surfaces. As expected the failure occurred at the indentation line in the surface (Figure 226).

Figure 227 WC-Co Sintered sample after fracture

A small piece was ejected from the sample during fracture and is shown in Figure 228 (rifled side down) and a coolant hole can be seen protruding into the piece.

Coolant hole protrusion

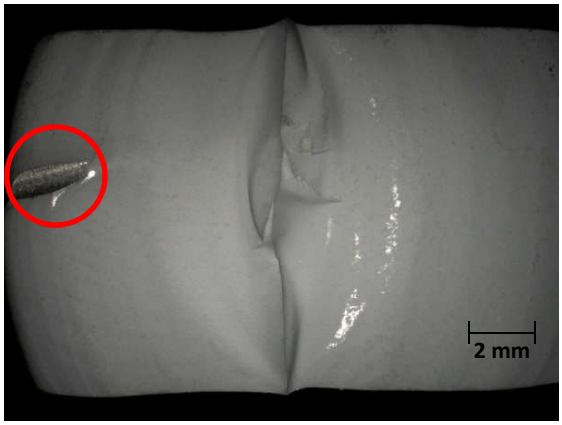

Figure 228 Underside of sintered piece ejected from fractured WC-Co sample

Other crack types observed from this production trial included cracks within the rifling (Figure 229 to Figure 230). Such cracks were noticeable in the green state on close inspection.

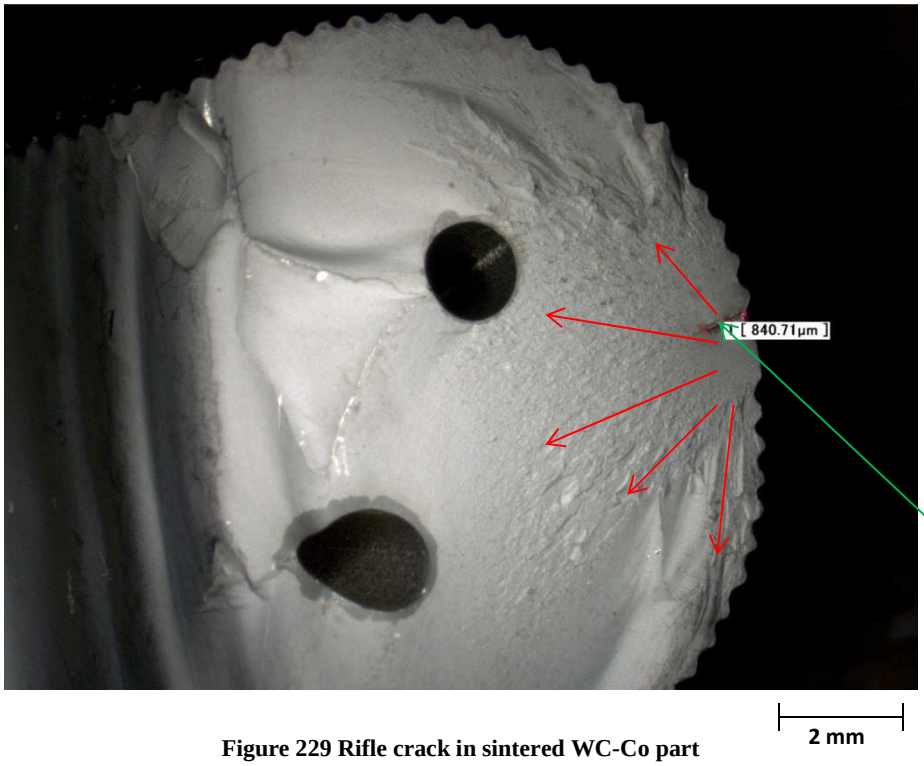

Figure 229 Rifle crack in sintered WC-Co part

The rifle crack in Figure 229 was the result of brittle fracture and emanates inwards towards the rod centre as shown by the surface pattern. The surface pattern is a result of speed of the fracture and stress travelling through the material. Rough surfaces represent a relatively slow fracture where the material is under tension before catastrophic failure at high speed. During the TRS test, one side of the material is under tension and the other under compression. Generally crack propagation is from the tension side up to the point in which the ultimate tensile strength is exceeded where the area of material left is too small to bear the applied load. The rough surface represents slow propagation whereby the material was under tension and the smooth represents rapid and total failure.

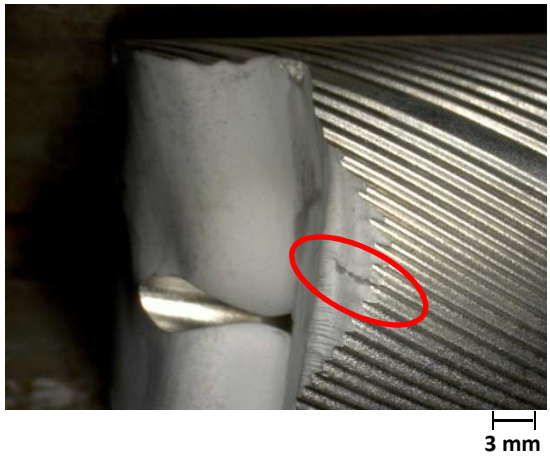

Figure 230 Rifle crack in WC-Co sintered part

Rifle cracks are normally formed in the green state and can be difficult to detect (Figure 230). An extreme case of rifle cracking (a form of tearing) is shown in Figure 231.

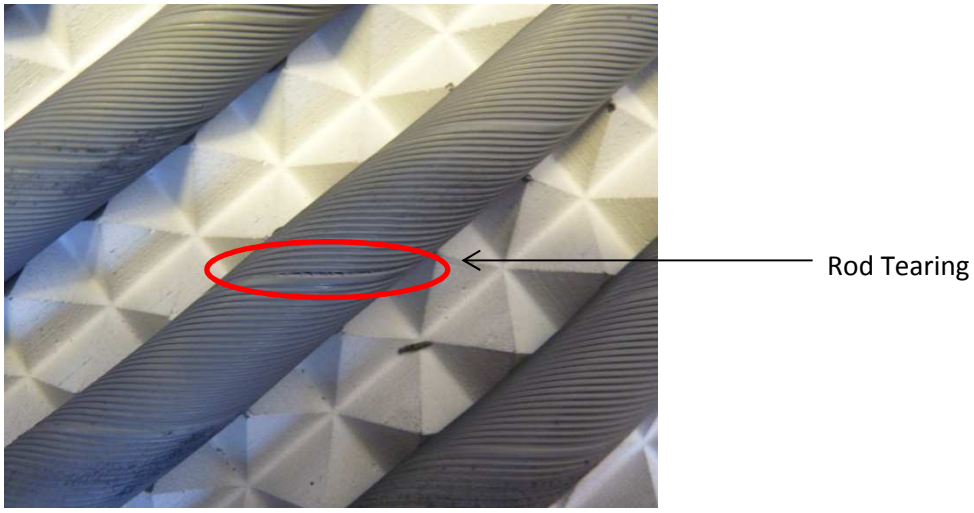

Figure 231 Rifle crack in extruded WC-Co part (rod tearing)

Figure 230 and Figure 231 are normally formed as a result of either incomplete die filling or surface roughness in the die. Incomplete die filling can occur if extrusion flow is uneven due to non-homogenous feedstock. Slight differences in localised velocity cause half of the feedstock to flow slightly faster thus causing separation.

7.6 Metallurgical Testing

Metallurgical testing for WC-Co sintered samples have been described in section 3.1.1, cobalt magnetic (Com) and coercivity (Hc) testing has been applied to all samples. The tests were used as methods to determine the cobalt % in the sample and the carbon balance. The two tests were also used to check that the sintering process had occurred under the correct conditions.

7.6.1 Com Testing

Results of the Cobalt magnetic testing are shown in Figure 232. Similar values of cobalt magnetic % (Com %) are shown for each material with the exception of higher percentage cellulose in the binder.

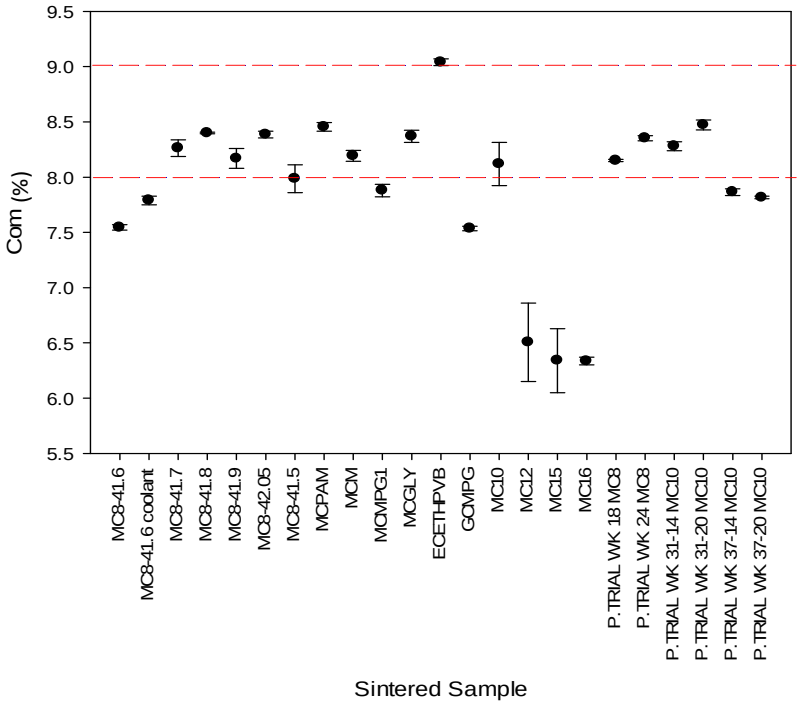

Figure 232 Com test of sintered WC-Co samples

The Com specifications imposed by SHM are shown by red dashed lines in Figure 232. The Com test measures the amount of cobalt present in the ferromagnetic form. η phase and other compounds of carbon are not ferromagnetic. Therefore, assuming that the correct composition has been mixed and milled in terms of tungsten, carbon and cobalt a different Com reading can be used to determine the carbon balance. For example, if the Com value is low, the ferromagnetic cobalt content is low, even though the actual cobalt content will be correct. This implies that η phase is present (Co_3W_3C) which is low in carbon content. η phase carbon is formed when sufficient tungsten metal or sub-stoichiometric carbide (W_2C) dissolves in the Co binder and is able to precipitate as the compound. Conversely, if the Com value is high then there is excess carbon present (free carbon). Free carbon is formed when WC powder is not fully reacted; this is more common with fine grain powder that is sintered for less time and at lower temperatures to avoid grain growth. Free carbon which is not reacted with W to form WC can precipitate as graphite which weakens the sample. The Com % limits are set low to account for dissolution of elements into Cobalt. There would be more Cobalt actually present in the sample that is not magnetically susceptible as it is alloyed with tungsten. A Com reading of 7-8% implies that the Cobalt content is close to 10%. Both η phase and

free carbon have undesirable effects on the properties of the WC-Co. Free carbon also contributes to the formation of η phase. O_x is present from the milling process and reacts with the free carbon and WC to form CO and CO_2. This removes carbon leaving free tungsten to dissolve in cobalt, thus forming eta phase with the remaining carbon. Due to a deficiency in carbon, η phase is inherently brittle [168]. Unlike the values determined for Com, the Hc test showed that each material tested was within specification. If the Com value is recorded as low and yet no η phase is detected using microscopy, then it can be assumed that the WC-Co recipe has been incorrectly prepared.

7.6.2 Hc Testing

The Hc test and specifications (shown in red) for all sintered samples tested is shown in Figure 233.

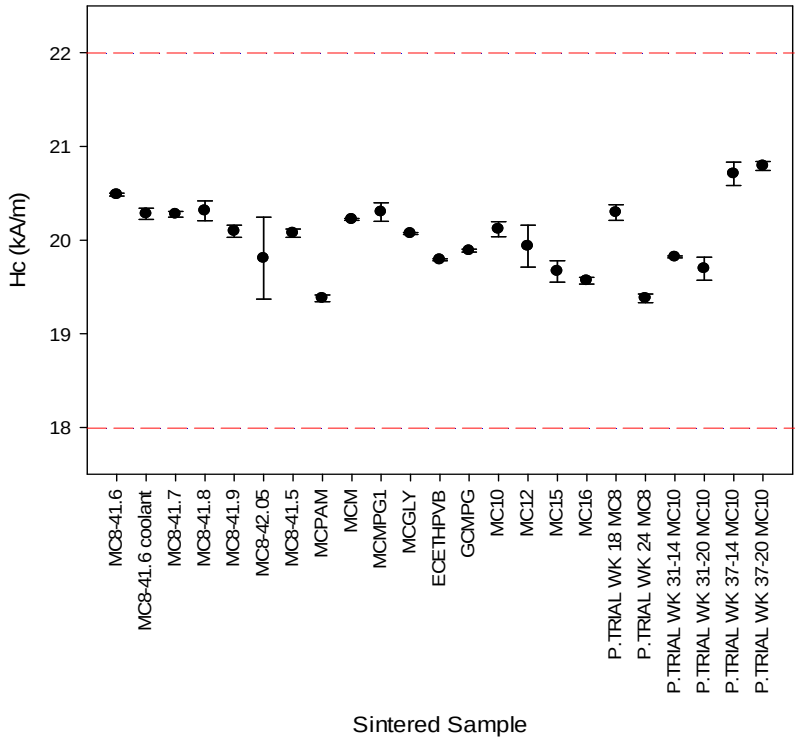

Figure 233 Hc test of sintered samples

The Hc test was used as an indication of grain size; higher Hc values represented finer grained samples (section 3.1.1).

7.7 Results and Discussion

7.7.1 Drying, De-binding and Sintering

From group 1 based dough, only the MC8, ECTHPVB and MCPAM dough systems were capable of drying and sintering solid products greater than 12 mm in diameter. Other samples from group 1 cracked in the drying stage at temperatures up to 100 °C. Samples that did not crack in the drying

cycle tended to sinter without failure. Of the three materials that did not crack in the drying stage, only the MC8 based dough sintered without issue. The MCPAM and ECETHPVB based feedstocks dried and sintered without rupturing although large voids and pores existed internally. The voids that developed are shown for the MCPAM and ECETHPVB samples in Figure 234 and Figure 235 respectively. Both of the samples were ground, polished and mounted before using optical microscopy following the procedure given in section 3.1.1.

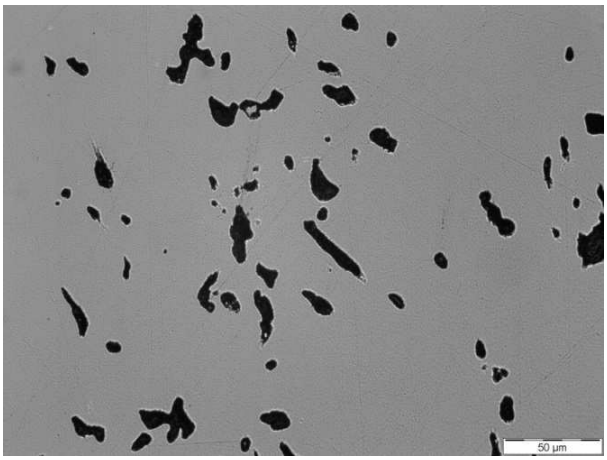

Figure 234 MCPAM based dough voids

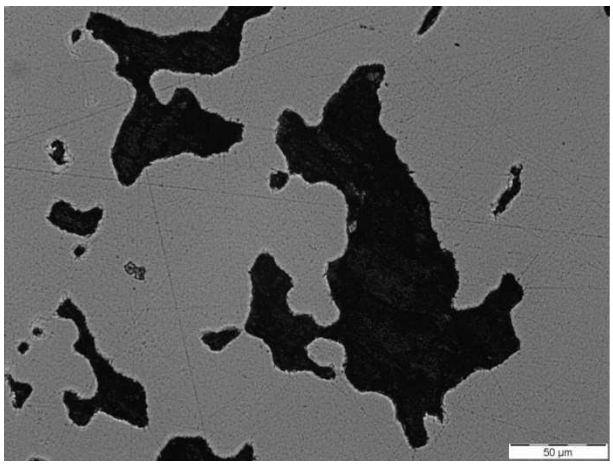

Figure 235 ECETHPVB based dough voids

The voidage in both cases was similar and was a consequence of poor binder removal in the de-binding stages. As a result of the voidage, neither dough systems could be used.

7.7.1.1 Weight Loss (TGA/DTA) and Shrinkage

The TGA plot in Figure 197 shows the mass loss profiles for group 1 materials. The GCMPG and MCPAM dough lost a greater proportion of their mass than the MC8 and ECETHPVB dough. As described in section 7.1.2 the MCPAM binder had a lower WC-Co solids loading and therefore more mass was lost in de-binding as a proportion of total mass. The GCMPG binder had a greater mass

loss in the de-binding because less mass was lost in the drying stage (20-100°C). All of the feedstocks showed a rapid drop in mass between 200-320°C. It is beneficial to flatten this section of the de-binding curve to allow for more progressive de-binding and gas release. The MC8 formulation has the smoothest mass removal curve and therefore is the most capable at large diameter de-binding. The DTA curve in Figure 198 shows the rate of mass loss for dough prepared with group 1 feedstocks. The GCMPG dough had a very narrow de-compositional reaction when compared to other systems and therefore most of the binder was removed quickly over a narrow temperature (300-350 °C) range. This caused rapid shrinkage and also the rapid release of gas and explains why drying and de-binding failure occurred. Abrupt mass loss often results in drying and de-binding cracks due to excessive stress caused by differential shrinkage. Stresses are also caused by relatively slow diffusion of vapours compared to the rapid release of decomposition gasses such as CO and CO_2. Rapid release of gases is undesirable as the pore vapour pressure rises more quickly than the pressure can be released by diffusional transport. A build-up of stress as a result of the gas release and rapid shrinkage caused rod rupture. A better drying performance was observed with the MC8 based dough. Whilst the curve in Figure 198 is initially steep, there is a gradual decrease in the mass loss rate at higher temperatures. At higher temperatures the feedstock was more sensitive to dimensional changes as it would have contained less binder and therefore been more brittle. As the ECETHPVB had a slightly steeper reduction in mass loss rate at higher temperatures, samples were more prone to failure in the drying and de-binding stages. The cross-sectional shrinkage was high and the weight loss low for the ECETHPVB dough (table 40) when compared with the MC8 feedstock. The surface of the ECETHPVB dough was of poor quality and therefore there were inaccuracies in cross-sectional measurements.

For the group 2 feedstocks weight loss reduced as cellulose content in the binder increased. The cross sectional shrinkage also decreased with decreasing cellulose content although the difference in shrinkage is only 0.7 % between MC10 and MC16 formulations. This is a small enough difference to be accounted for in measurement error. An exception to the weight loss and shrinkage trends in this group was the MC16 based dough. This system also cause discrepancies in other experiments such as capillary rheometry. It can therefore be concluded that this formulation had errors in the mixing and preparation procedures. Figure 195 shows the weight loss and shrinkage of the group 3 materials. Each weight loss and shrinkage measurement were as expected based on the WC-Co solids loading given in Table 18. Similarly, Figure 196 shows the weight loss and shrinkage measurements for the dough prepared from MC8 binder systems with increasing WC-Co solids loading. The more highly loaded feedstocks had less shrinkage and weight loss as expected.

7.7.2 Mechanical Testing

Vickers Hv30 hardness and transverse rupture strength (TRS) were used to insure that the addition of new binder systems had not introduced defects and sintering issues. A lower than specification hardness would give an initial indication that the product had not sintered to the correct grain size.

7.7.2.1 Vickers Hardness (Hv30) and Transverse Rupture Strength

The specifications for WC-Co Hv30 Vickers hardness and TRS testing were 1550-1650 (Hv30) and above 3000 MPa respectively. The TRS test is described in section 7.4.1 and the results are given in Figure 202 for the MC8 based dough feedstock. Figures 202 and 103 show how TRS data was scattered for the highest WC-Co solids loading. This was due to defect formation indicated in Figure 205. The work of Fang [169] has shown that there is a direct correlation between TRS and Vickers hardness for WC-Co composites. In his work it was reported that TRS increases with hardness up to a point before decreasing if porosity effects are neglected. In this work however hardness and TRS values remained relatively consistent when the highest solids loading sample was neglected. Fang also reported that an increased scattering of TRS data was due to the formation of excessive porosity, similar results were observed in this work. Hardness testing was less efficient than TRS testing at picking up defects due to the relatively small sample cross-section. The hardness was within specification with the exception of MCPAM and the production trial from week 31 (2012). MCPAM hardness was low because it was not possible to make an accurate measurement due to the voidage shown in Figure 234. Figure 207 also shows that the feedstocks containing MPG had a hardness exceeding the specification. Whilst high hardness is beneficial, the upper limit was in place to give an idea of when the sample was too brittle. Future work would include toughness measurements to confirm these observations.

7.7.3 Sintered Properties

Sintered properties such as pitch, PCD and concentricity were measured for each material prepared with coolant holes. Sintered density was also measured for all materials that were sintered as an initial investigation of pore formation.

7.7.3.1 Pitch, PCD, Concentricity and Density

Pitch, PCD and concentricity were difficult to control with the chosen MC8 and MC10 formulations. Each of the properties were variable throughout large scale trials and between large scale trials. Sintered pitch was consistent when small scale trials were conducted for feedstocks prepared with group 2 binders (Figure 215). During the extrusion of larger material volumes however, a degree of variation was observed for both 14 and 20 mm sintered diameter products. Figure 218 shows that during a production trial, once interruptions to the trial were removed, sintered pitch increased with

extrusion time. This was due to material changes as a result of equipment temperature and viscous heating. As the material was extruded, the material temperature increased up to a point as a result of wall friction and shearing at the die section. Increases in material temperature reduce shear viscosity as the PEG in the binder softens, it is hypothesised that the length of pitch increased as a result. The same trend was observed in Figure 219 for the 20 mm coolant extrusion trial. It was also observed that as the feedstock was left to rest after extrusion, the pitch tightened after relaxation. Upon relaxation, the pitch was unable to return fully to its original unworked state giving a progressive yet small increase in pitch with trial duration. Whilst the pitch showed clear trends, PCD and concentricity of the methyl cellulose based feedstock were more sporadic. The scattering of PCD and concentricity data was initially observed in the green state for both 14 and 20 mm diameter samples. Variation was observed for individual rods which implied material instability. Sections 7.5.3 and 7.5.4 show experiments designed to observe the concentricity and PCD variance in two separate rods. PCD and concentricity were more variable in 20 mm samples than in 14 mm samples due to the tooling used. For 20 mm tooling, a larger die volume, and straight (rather than spiralled) core-pin design were used. In Appendix J tighter pitch tooling was used in order to exaggerate the cork-screwing effect.

In Figures 220 and 221 an increase in concentricity and PCD was shown down the rod length for the 20 mm sample. This was in line with Figures 218 and 219 for increases with tray number. In order to analyse how the PCD and concentricity varied within the 20 mm samples, the sections were photographed under a microscope (Figure 223). Measurements including the rod centre and centreline between the two coolant holes show that the concentricity was never perfect. The centreline between coolant holes was consistently off line with respect to the rod centre, indicating that the core pin did not line up in the die accurately. Due to die dimensions, a small misalignment at the centre of the spider incurred a large deviation for the core pin tip from the centre of the die exit. This gave misaligned coolant holes and a subsequent poor concentricity. Added to this, the separate distances R1 and R2 were measured from the centre of each coolant hole to the rod centre. It was found that R1 was consistently longer than R2 throughout the length of the rod. This was either due to filament length, or inaccuracies in core pin manufacture. As the rod rotates during extrusion, a longer R1 or R2 would also offset the concentricity. R1 and R2 lengths have been plotted in Figure 224. The contributing factors to concentricity insured that for the 20 mm tooling set up, concentricity could not be within the tolerance specifications.

7.7.4 Fracture Analysis

Physical geometrical properties with the methyl cellulose based feedstocks have shown to be inconsistent and on occasion out of tolerance with regards to the concentricity. Material properties needed for material qualification have generally been within specifications set by SHM. The production test carried out in week 37 (2012) however, produced a number of samples that fractured during the grinding and polishing stages. This highlighted two issues with this test. Firstly the samples were significantly weaker than expected. Secondly, the rods were not straight, causing uneven stress down the rod length during centre less grinding. Complete (non-broken) samples were examined under microscopy and surface discoloration was observed in various locations perpendicular to rotational flow (Figure 226). The discoloration is attributed to perpendicular to flow (PTF). The PTF cracks were not detected until the grinding process although were a common occurrence and were often the failure point of the rods. Images of the cause of failure have been given in Figures 226 to 228. PTF cracks were caused either by misalignment of tooling and the handling air track or by uneven lifting of the samples by the picker. As the occurrence of the PTF cracks was frequent, it has been suggested that air track alignment issues were present. Rifle cracks shown in Figures 229 and 230 were a result of badly aligned tooling and a slightly dry material not binding suitably.

7.7.5 Com and Hc

Com and Hc values are shown in Figures 232 and 233 for sintered samples. Figure 232 shows that the majority of the cobalt magnetic values are within specification. However, higher quantities of methyl cellulose have given feedstocks with a low Com and therefore low cobalt content. The low Com value observed means that the samples measured were unable to retain magnetism following full saturation. This is due to a lower ferro-magnetic material content (cobalt). Low cobalt content gives issues such as low toughness due to subsequently higher carbon content by proportion. This would have caused brittleness in the sample. Each of the increased cellulose content feedstocks was prepared from the same powder batch (prior to cobalt addition) and so there was an issue in the cobalt addition phase of powder production. The lower Com requires adjusting in future work to insure that brittle products are not manufactured. Hc testing results given in Figure 233 show that all samples were within specification which indicated that the grain size was within tolerance (section 3.1.1). Samples within specification were produced on a production scale although not without issue. Material instability caused non-repeatable material properties. Although large diameter samples of adequate quality were produced, process and material improvements were still required in order to manufacture an acceptably repeatable product.

Chapter 8 Microscopy

Scanning electron microscopy (SEM) and reflective light optical microscopy have been used to analyse material structure and grain size distribution. SEM was used to observe the cobalt distribution within samples whilst optical microscopy was used to observe porosity.

8.1 Optical Microscopy

Each of the micrographs in Figures 236 to 237 was taken at 100 x magnification. Figure 236 also includes an HV30 Vickers hardness indentation with cracks indicative of low toughness. Such cracks can invalidate the hardness measurement and suggest that the force applied was too great. The indentation is also not completely square indicating either that the diamond tip was worn or the sample base was not flat.

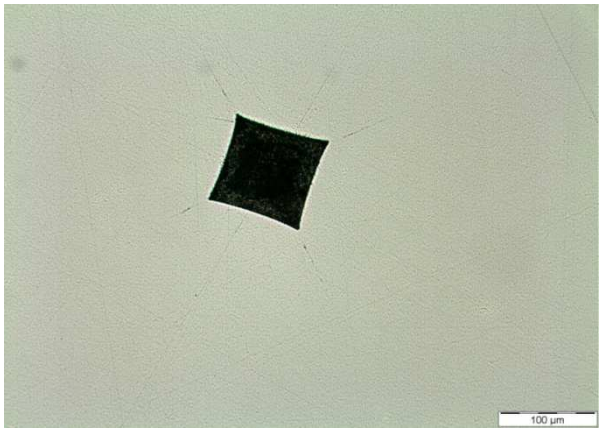

Figure 236 Sintered, ground and polished section prepared from MC8 feedstock micrograph (with Vickers indent)

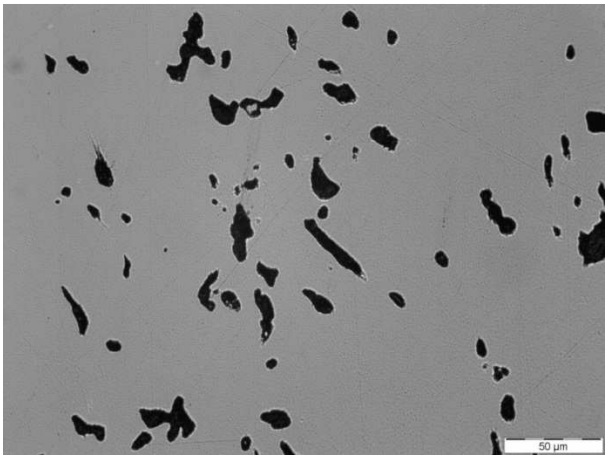

Figure 237 Sintered, ground and polished section prepared from MCPAM feedstock, micrograph showing voids and porosity

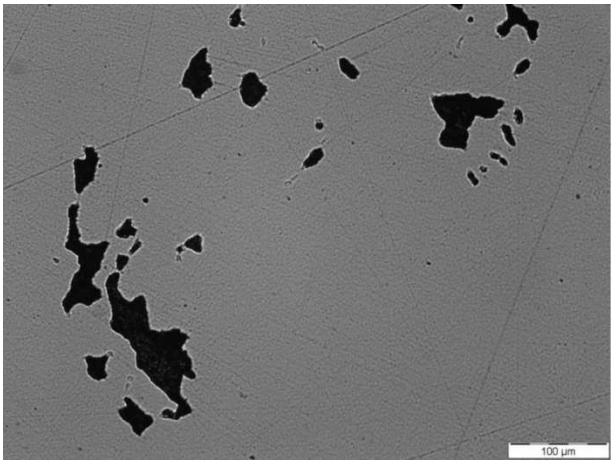

Figure 238 Sintered, ground and polished section prepared from ECETHPVB feedstock, micrograph showing voids and porosity

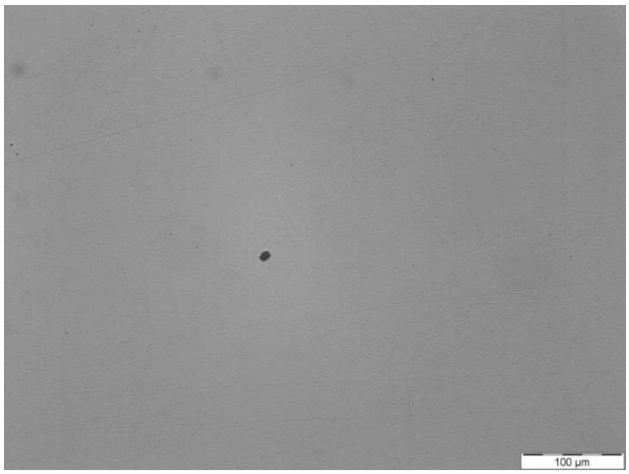

Figure 239 Sintered, ground and polished section prepared from GCMPG feedstock, micrograph showing low porosity

The material shown in Figure 236 gave acceptable levels of transverse rupture strength (TRS) due to little to no porosity being present in the sintered product. The high porosity levels shown in Figures 237 and 238 would have resulted in consistently low strength and therefore test bars were not formed from this material. Material shown in Figure 239 was not capable of producing large diameter products due to drying capability and therefore TRS test bars were not required.

8.1.1 Grain Size and Grain Size Distribution

Grain size distribution was evaluated using the linear intercepts method (section 3.14). A combination of SEM and optical microscopy were used. Initial micrographs were taken using SEM and optical microscopy and associated software were used to carry out linear intercept measurements. Histograms in Figures 240 to 242 show the sintered results of the different binder groups and the modal grain sizes for each of the dough feedstocks are given in Tables 44 to 46.

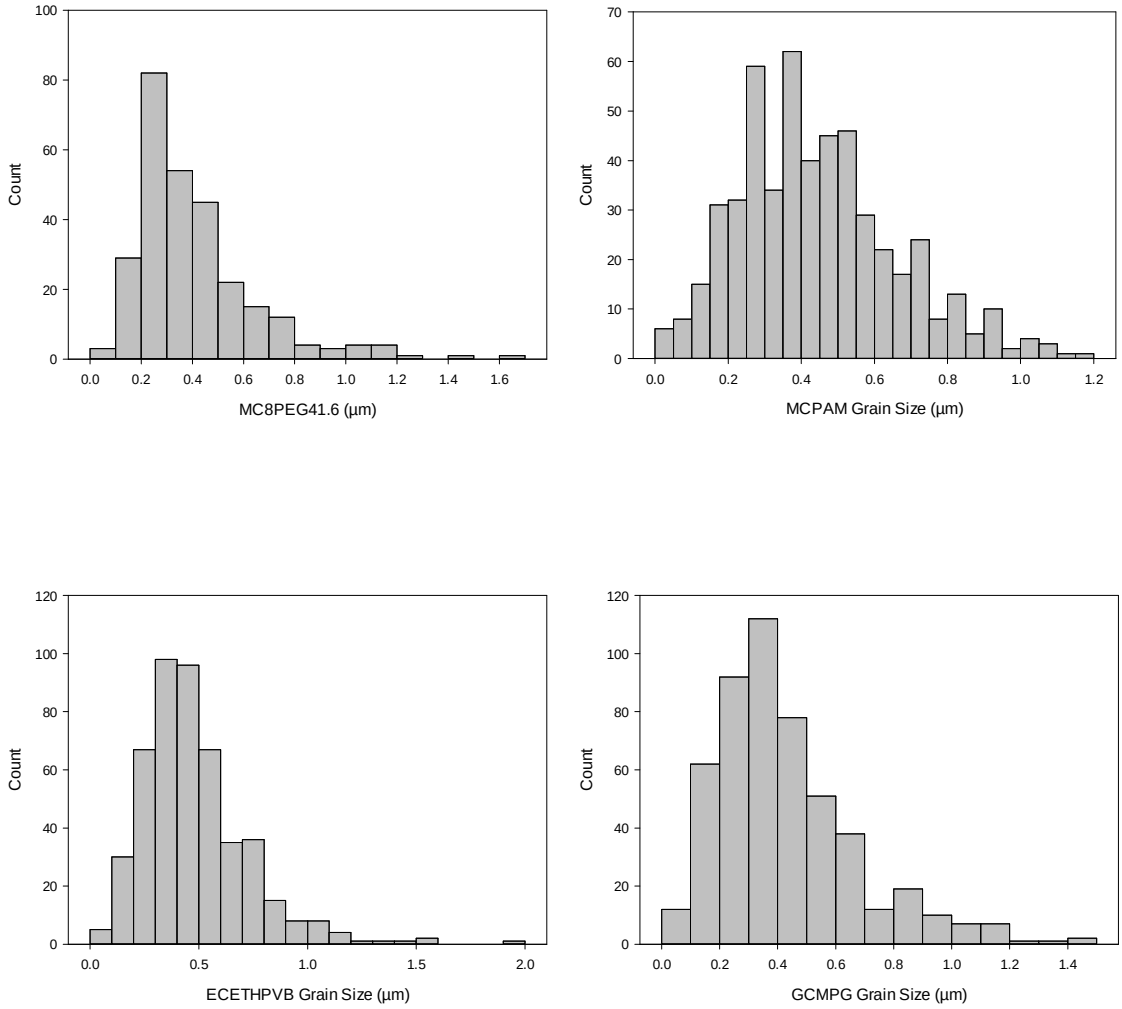

Figure 240 Group 1 based feedstock sintered sample grain size distributions

Table 44 Group 1 based dough modal grain size

Dough Feedstock	Modal Grain Size (µm)	Average Grain Size (µm)
MC8	0.26	0.41
MCPAM	0.27	0.44
ECETHPVB	0.43	0.48
GCMPG	0.37	0.43

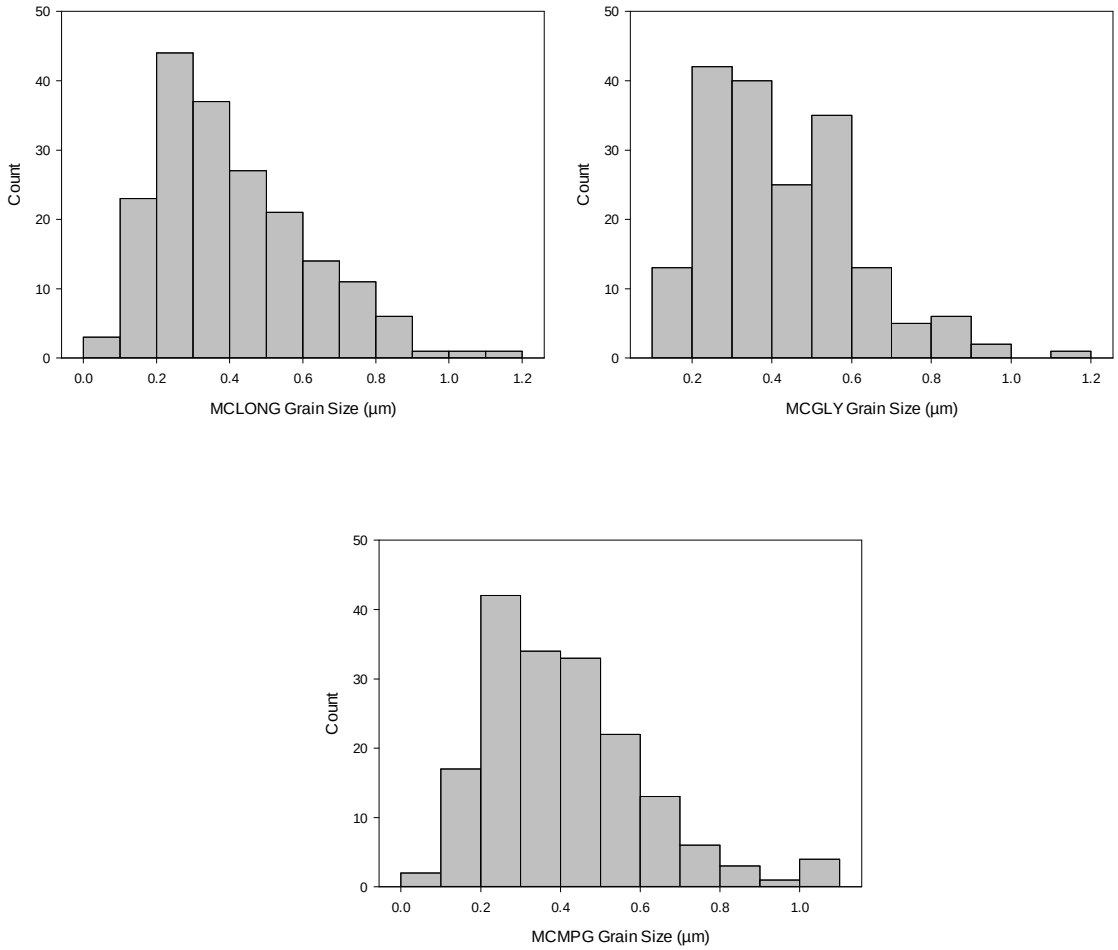

Figure 241 Group 3 based feedstock sintered sample grain size distributions

Table 45 Group 3 based dough modal grain size

Dough Feedstock	Modal Grain Size (µm)	Average Grain Size (µm)
MCM	0.21	0.41
MCGLY	0.25	0.43
MCMPG	0.33	0.41

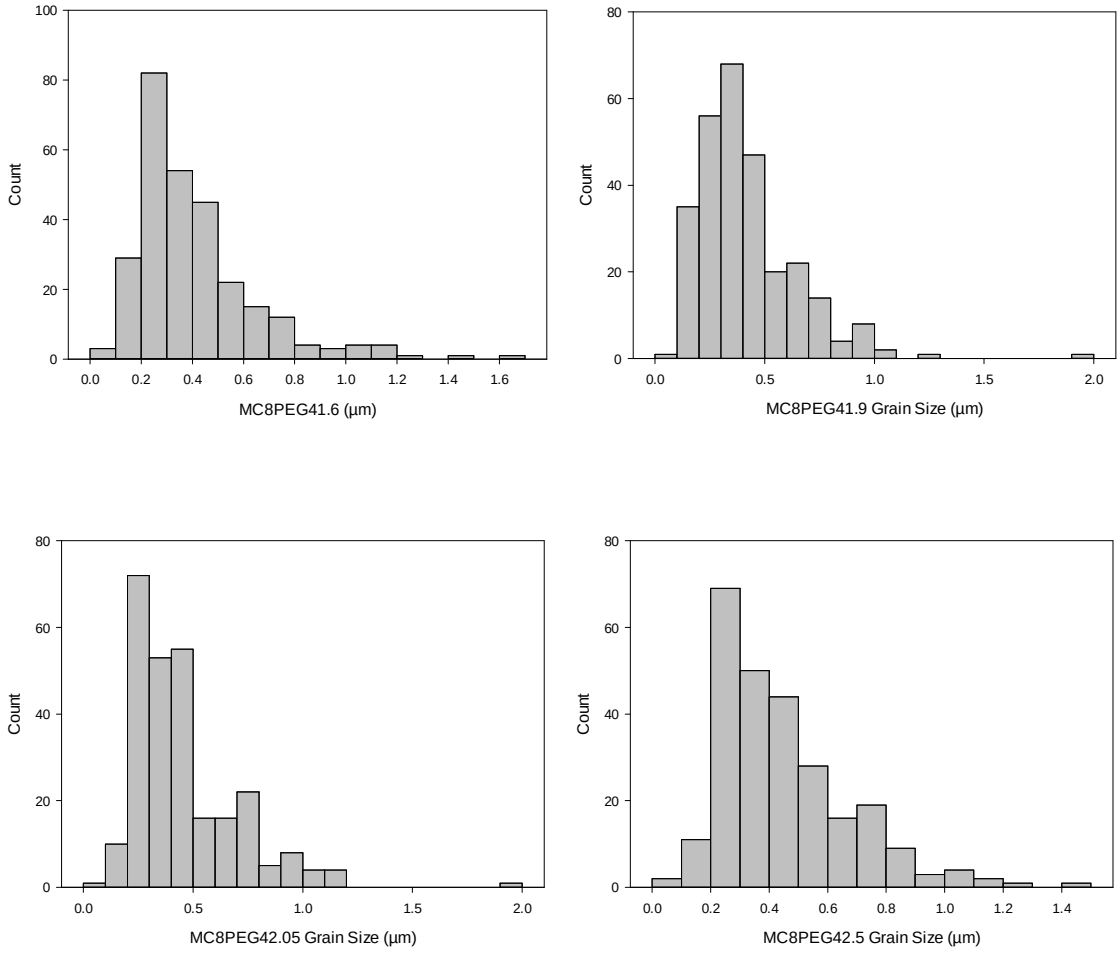

Figure 242 Group 4 based feedstock sintered sample grain size distribution

Table 46 Group 4 based dough modal grain size

Dough Feedstock	Modal Grain Size (µm)	Average Grain Size (µm)
MC8PEG41.6	0.26	0.41
MC8PEG41.9	0.38	0.42
MC8PEG42.05	0.26	0.44
MC8PEG42.5	0.26	0.45

Modal grain sizes have been plotted against Hc in Figure 243 in order to observe how accurate the Hc measurement was for determining grain size. Limitations in the linear intercept method also had to be considered when evaluating Hc measurements. The linear intercept method of determining grain size is a subjective process and therefore is operator dependent. In Figure 244 a plot of Hv30 Vickers hardness against modal grain size has been given.

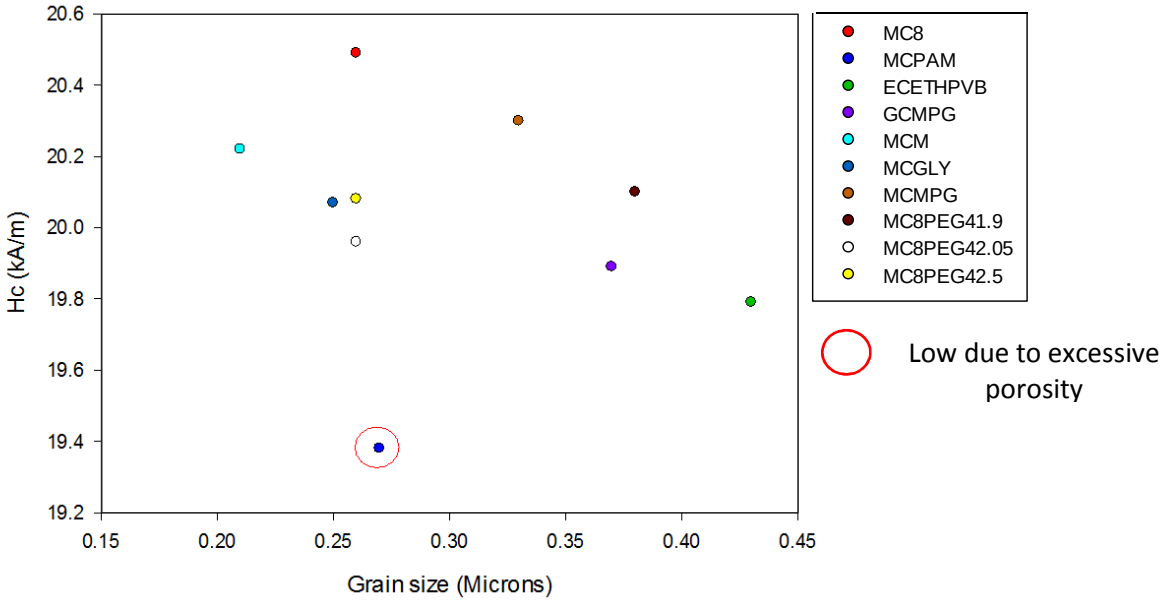

Figure 243 Hc (kA/m) as a function of modal grain size (microns)

Figure 243 shows that there is weak correlation between Hc and modal grain size. This confirms that Hc must be used with other methods to determine grain size.

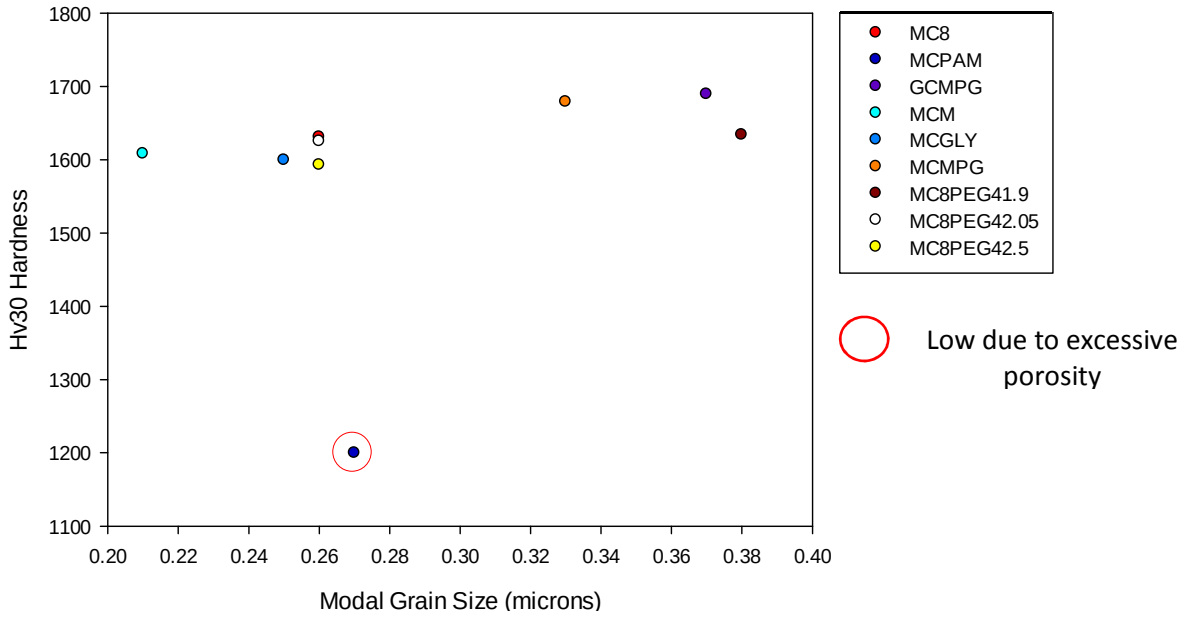

Figure 244 Hv30 hardness as a function of modal grain size (microns)

Figure 244 indicates that there is no appreciable change in hardness with modal grain size although the range of grain sizes measured was small. The MCPAM based feedstock provided a significantly low hardness due to poor sintered quality. There was a slight increase in hardness with increased grain size that was not expected.

As only a small sample area was measured, it was more representative of the material to use an average grain size measurement rather than the modal grain size measurement. The mean grain sizes were also a closer match for the grade of WC-Co used according to Figure 5. mean grain size has been plotted against Hc and Hv30 Vickers hardness in Figure 245 and 246 respectively.

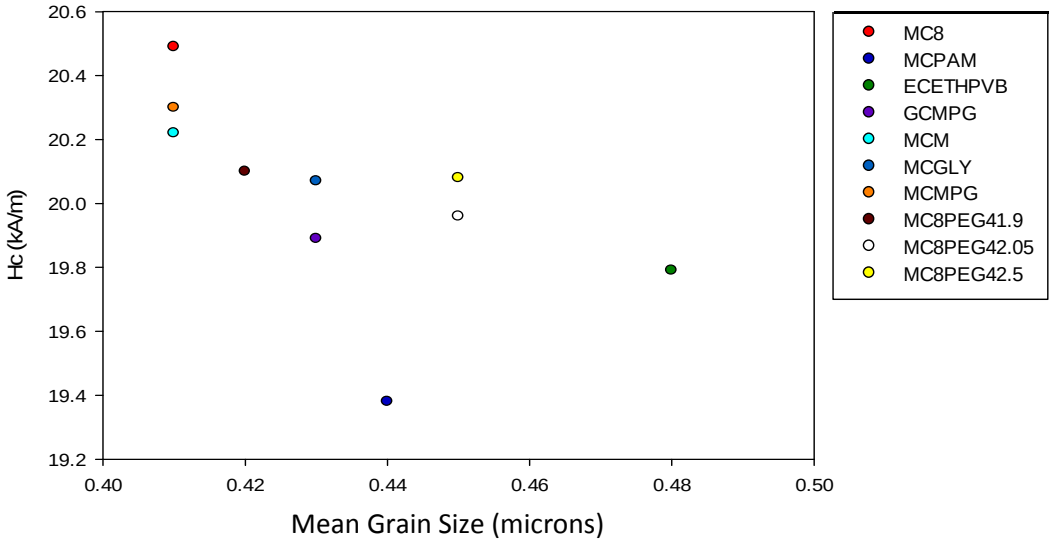

Figure 245 Hc (kA/m) as a function of average grain size (microns)

A clearer trend now emerges when using the average grain size rather than the modal grain size for a decreasing Hc with increasing grain size.

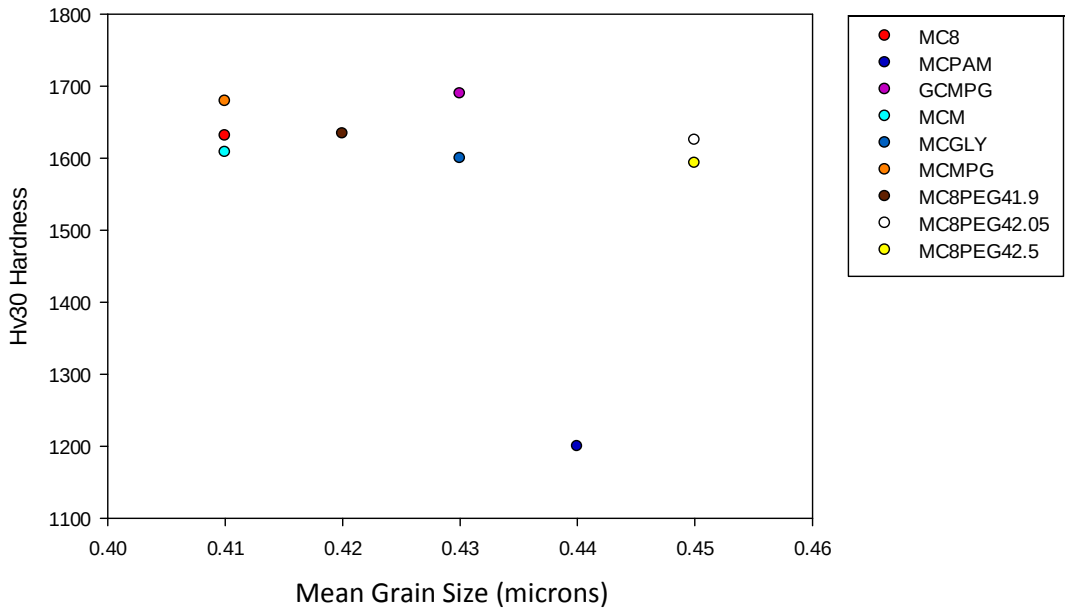

Figure 246 Hv30 Hardness as a function of average grain size (microns)

However, the Hv30 Vickers hardness remains fairly constant over the narrow range of grain sizes measured (Figure 246).

8.2 Scanning Electron Microscopy

8.2.1 Dough Feedstock

SEM was used to examine the microstructure of group 1 feedstocks. Figure 247 shows the MC8 feedstock in which a smooth dough mixture is illustrated (left). On closer examination (right) agglomerates of cellulose are observed, circled in red, which could lead to porosity.

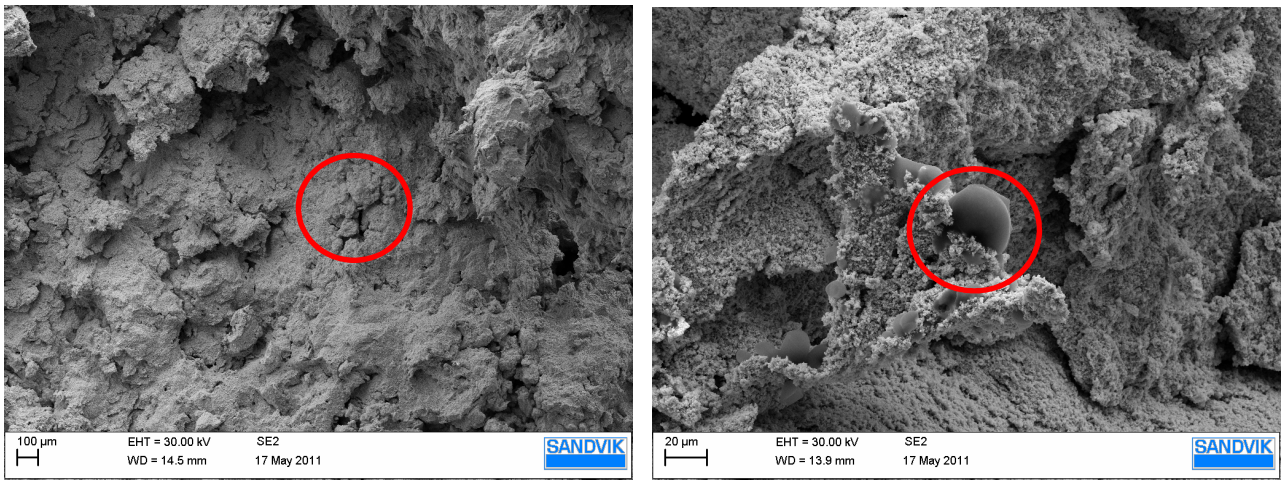

Figure 247 MC8 based dough feedstock SEM micrograpahs

Sphere shaped structures of 50 µm in diameter are also shown in Figure 247 (left) which are indicative of agglomerates from the spray-dried powder not broken down by mixing. Figure 248 shows micrographs of dough feedstocks prepared with the MCPAM binder.

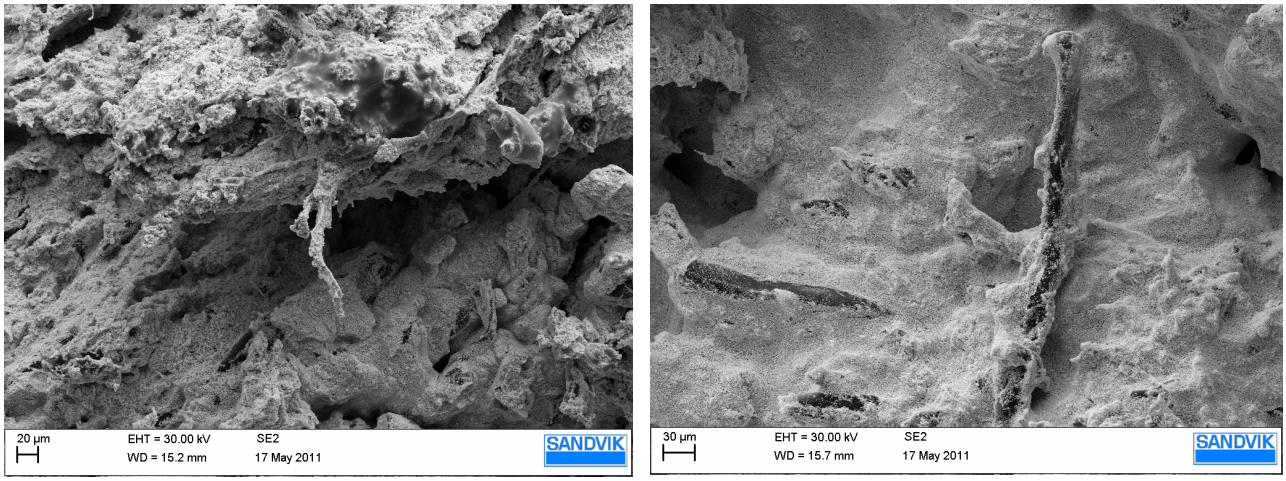

Figure 248 MCPAM based dough feedstock micrographs

String like structures were found in the microstructure of the MCPAM dough. These structures were substantial and frequent, and hence elongated pores were left in their place after the sinter HIP process (Figure 237). The dough also had rough surfaces when compared with the MC8 dough which are linked to poor mixing of the binder and powder phase. Micrographs of dough processed from the ECETHPVB binder are presented in Figure 249.

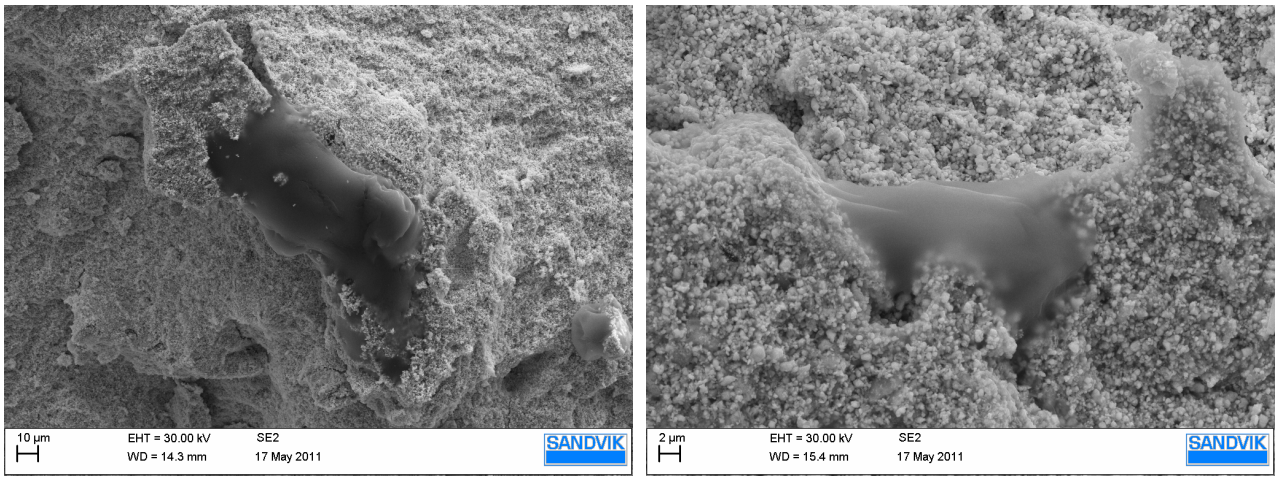

Figure 249 ECETHPVB based dough feedstock micrographs

Traces of un-mixed ethyl cellulose and ethanol binder were found in the ECETHPVB dough (Figure 238). Large voids formed between these extensive agglomerates and were not removed in the sinter HIP process. Figure 250 shows a micrograph of the dough feedstock prepared from the GCMPG binder.

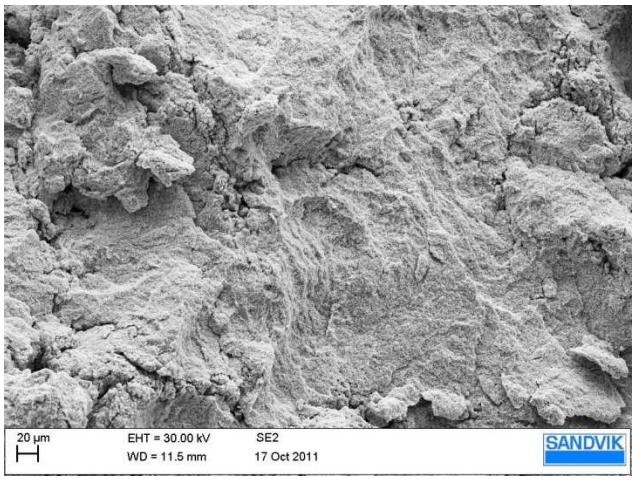

Figure 250 GCMPG based dough feedstock micrographs

The feedstock in Figure 250 was smooth and free from agglomerates which aided in the formation of a high quality extrudate.

8.2.2 Sintered Samples

Two micrographs of each sintered feedstock prepared from group 1 binders are presented, the first at 5000x magnification and the second at 15000x magnification. 5000x magnification micrograph allowed for a broader view of the sample, thus enabling examination of the cobalt distribution. In SEM micrographs, cobalt is shown as a darker grey region surrounding the WC grains. Cobalt lakes are attributed to pores or cracks in the sample formed initially in the green state, which can become sealed by sinter HIP processing. However, in the liquid state, cobalt migrates into the cracks and pores under pressure. Pilot scale trials of material manufactured from group 1 binders have been analysed in section 8.2.2.1. Sintered samples of the MC10 based dough feedstock (production scale) have been examined in section 8.2.2.2.

8.2.2.1 Pilot Scale

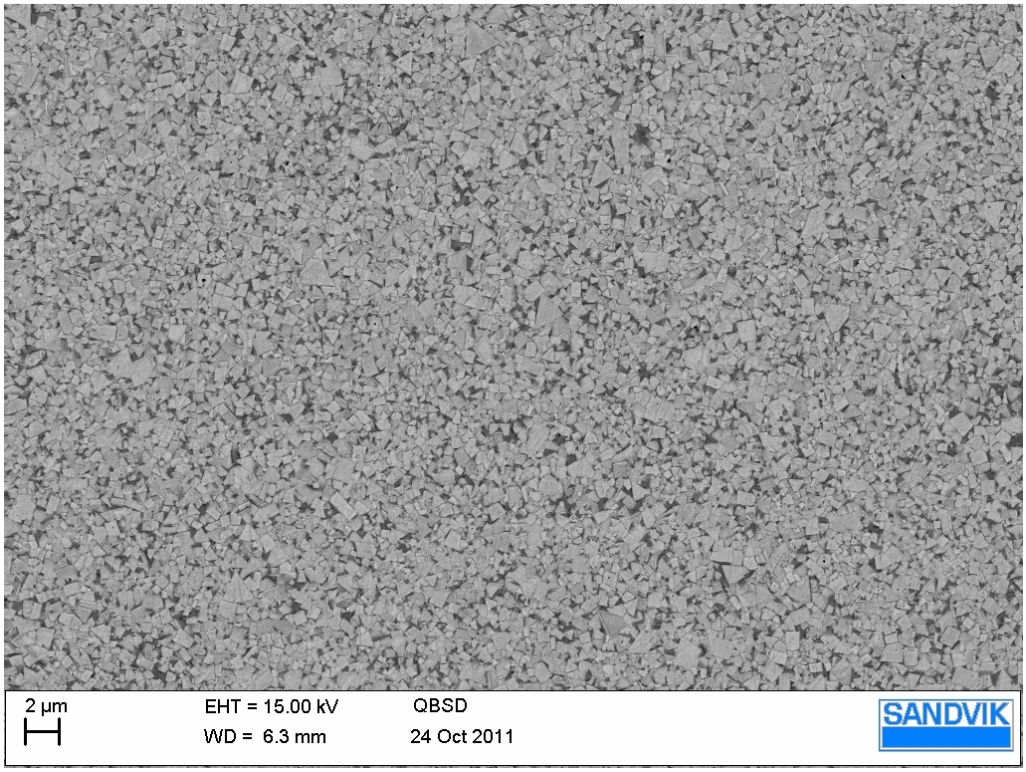

Figure 251 SEM micrograph, MC8 sintered sample 5000 x magnification

Figure 251 shows that the MC8 based feedstock sintered with a good cobalt distribution and even grain size. The micrograph is representative of the whole sample as the same distribution was observed in 20 fields of view of 2 samples per rod. Typically on a pilot scale, 10 rods were manufactured of which 2 sintered rods were examined using SEM.

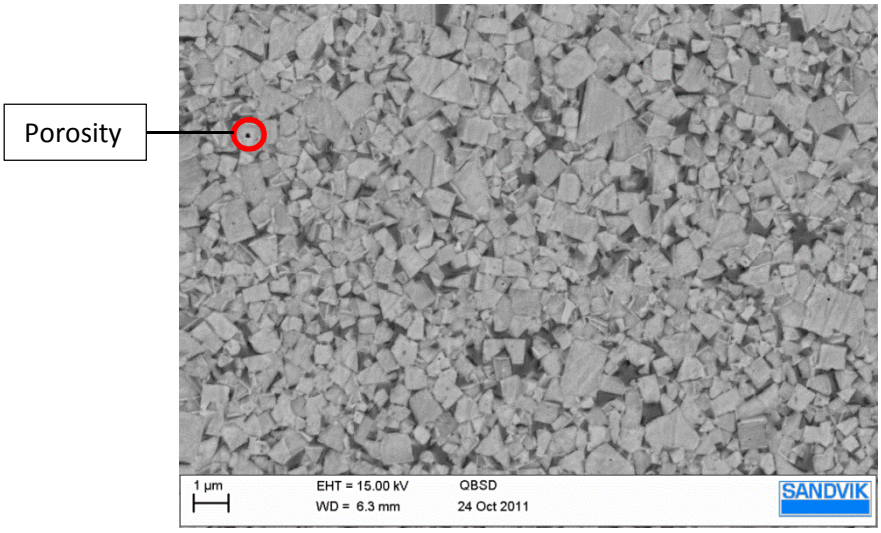

Figure 252 SEM micrograph, MC8 sintered sample, 1500 x magnification

The 1500 x magnification micrograph of the MC8 based feedstock shows that whilst the distribution of cobalt was evenly spread, porosity was present. These pores are infrequent and sufficiently small not to have a detrimental effect on material properties with regards to the specification. Such pores are often a result of the raw materials and are seen in the standard Sandvik sintered samples. Figure 241 shows a 5000 x magnification micrograph of the MCPAM based feedstock. In this case the cobalt distribution was poor and darker regions were observed in between the cobalt and WC grains. These darker regions were further analysed in Figure 254. The poor cobalt distribution for this sample was a result of porosity, voidage and subsequent cobalt migration.

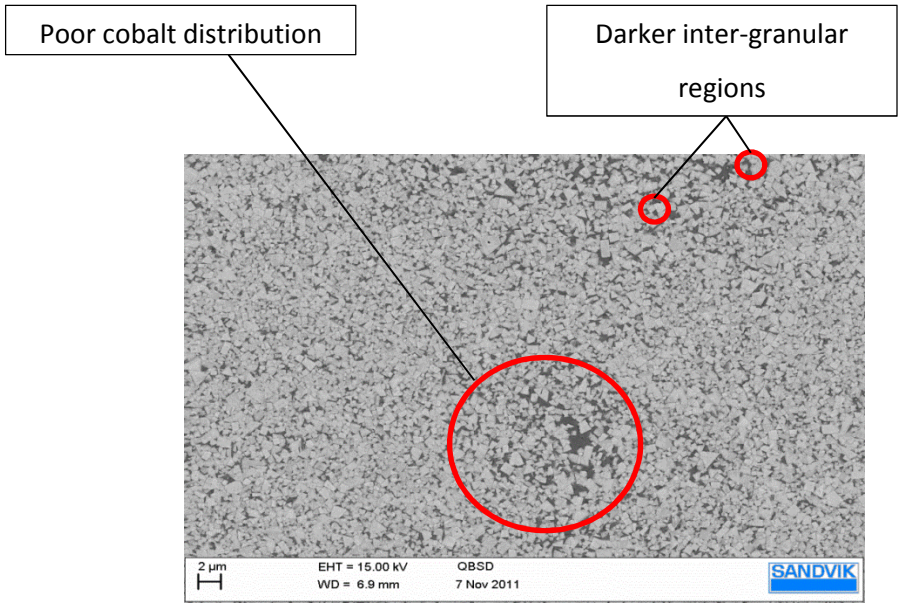

Figure 253 SEM micrograph showing uneven cobalt distribution in MCPAM sintered material, 5000 x magnification

In the top section of Figure 253 the darker regions have been expanded to form Figure 254. The darker regions in this section are due to inter-granular cracking.

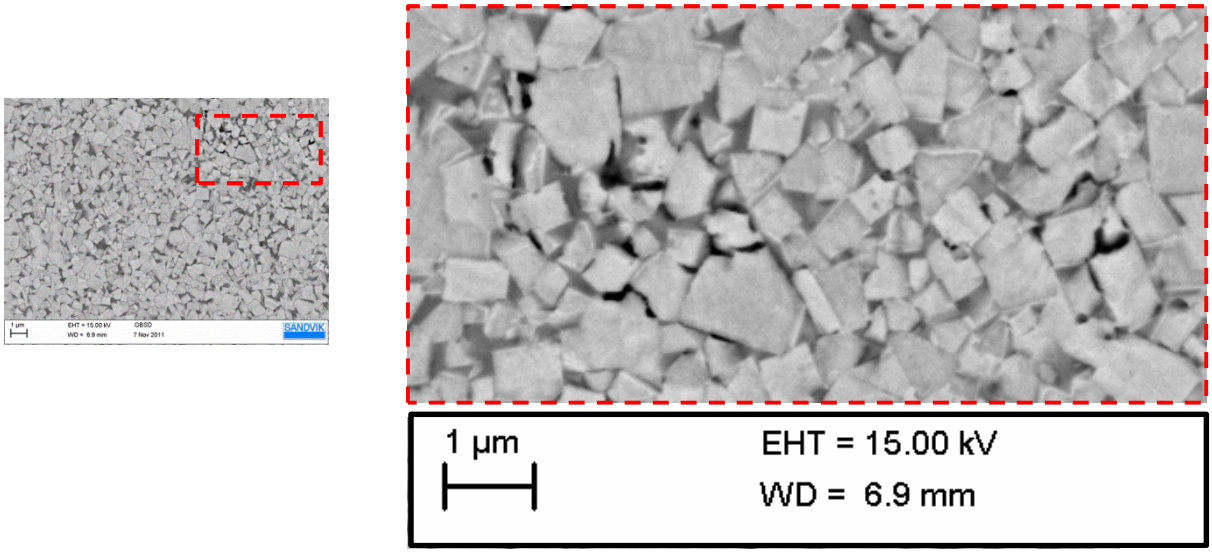

Figure 254 SEM micrograph showing MCPAM sintered material at 15000 x magnification with inter-granular cracking

As well as inter-granular cracking, material pull out was also observed for the MCPAM and ECETHPVB materials (Figure 237 and Figure 238). Due to large regions of cobalt building up in the sample as a result of green state porosity (circled in red, Figure 255), the sample structure is weakened. Large sections of material are then removed during grinding and polishing and appear as large pores or non-spherical voidage (Figure 255).

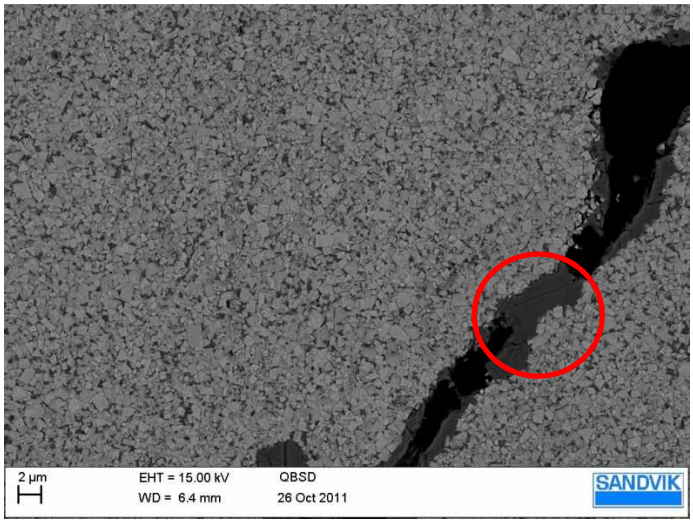

Figure 255 SEM micrograph of ECETHPVB sintered sample at 5000 x magnification

Porosity and large voids formed in the ECETHPVB based samples were less frequent than those observed with the MCPAM formulation. Although less frequent, they were equally detrimental to product performance as the voids were larger. Figure 256 shows that at 15000 x magnification, sections could be formed with good density and no cracks or voids.

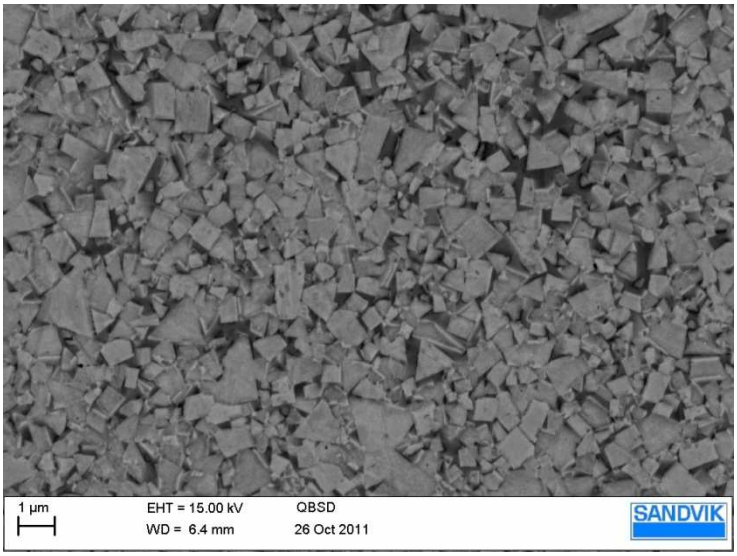

Figure 256 SEM micrograph of ECETHPVB sintered sample at 15000 x magnification

This highlights the fact that SEM is not suitable for detecting large voids without the combined use of mechanical testing and optical microscopy. Figure 257 shows the 5000x magnification SEM micrograph for the GCMPG based formulation. On initial inspection the distribution of cobalt and grain size distribution was satisfactory. Further analysis at 15000x magnification however revealed that porosity was present (Figure 258).

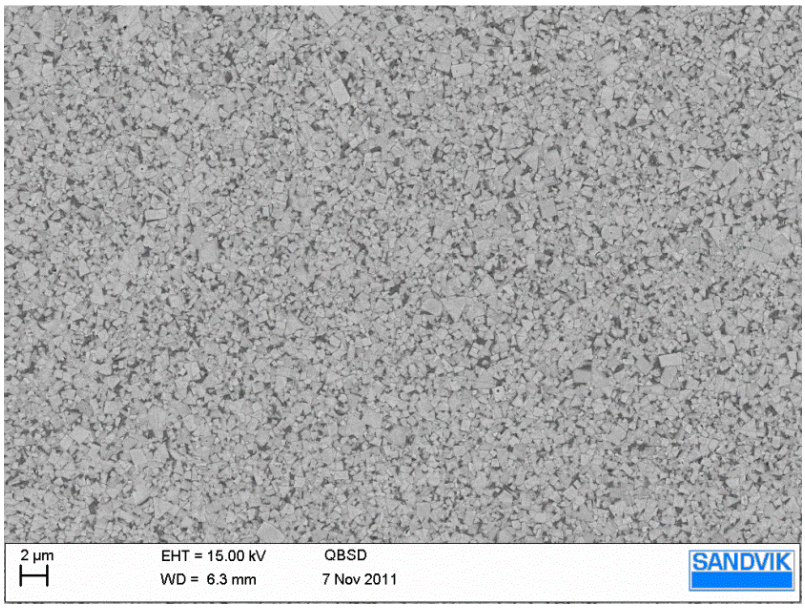

Figure 257 SEM micrograph of GCMPG sintered sample at 5000 x magnification

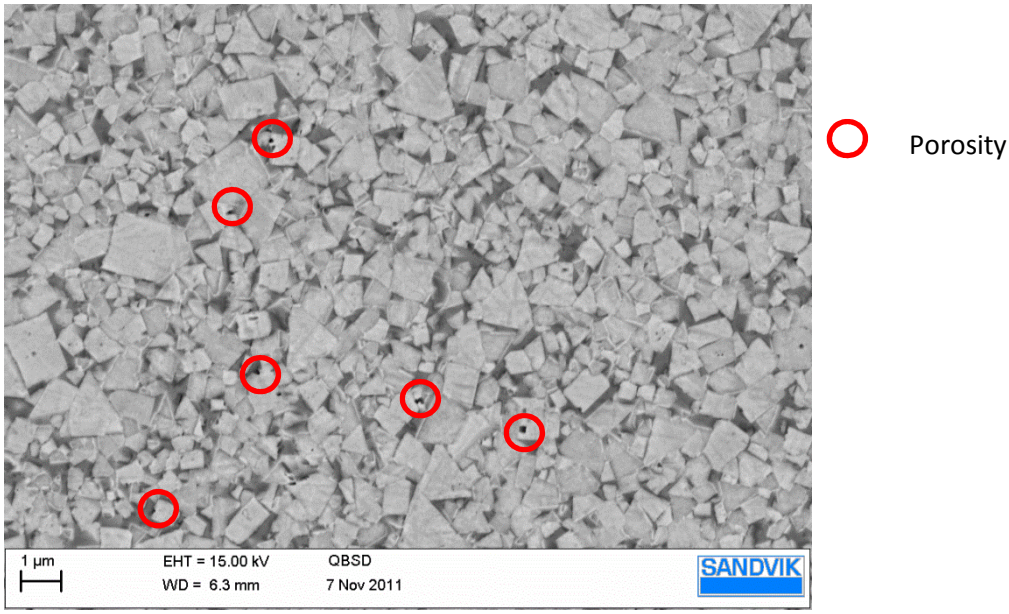

Figure 258 SEM micrograph of GCMPG sintered sample at 15000 x magnification

8.2.2.2 Production Scale

The MC10 based formulation was used in production scale testing. Examples of the SEM micrographs are given in Figures 259 and 260 at 5000x and 20000x magnification respectively. Figure 259 and Figure 260 both show that no porosity is present in the field of view and also that there is an even distribution of cobalt in the samples.

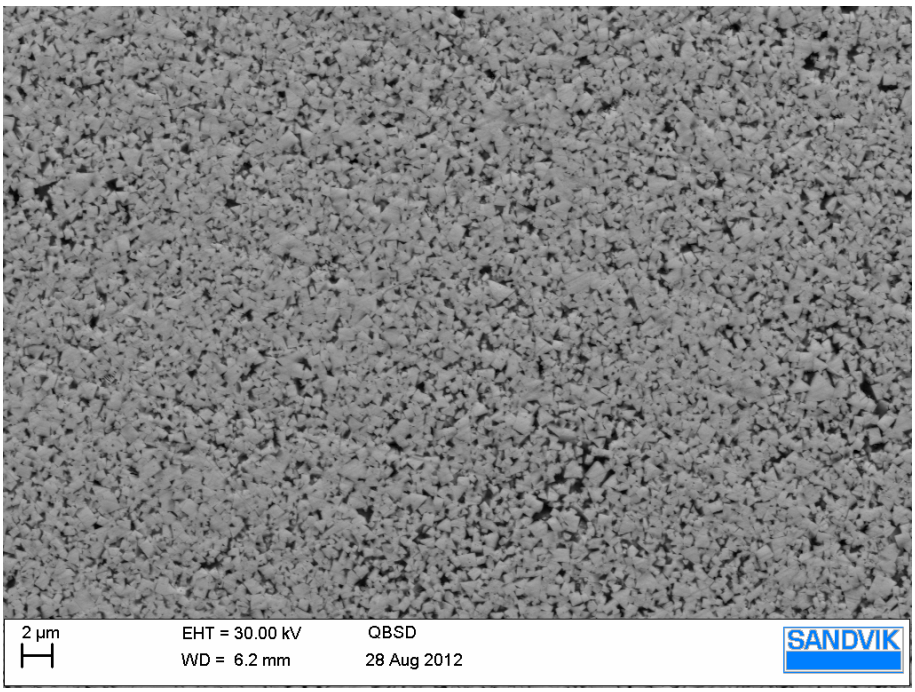

Figure 259 SEM micrograph of MC10 sintered sample at 5000 x magnification

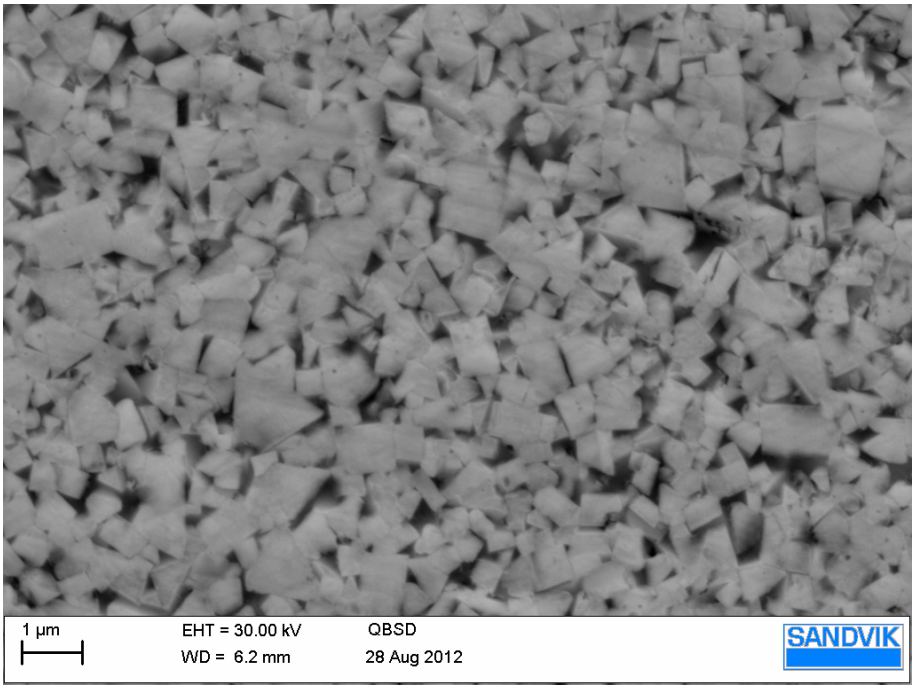

Figure 260 SEM micrograph of MC10 sintered sample at 20000 x magnification

8.3 Results and Discussion

8.3.1 Optical Microscopy

Optical microscopy shows that porosity is present in each of the group 1 based materials with the exception of the methyl cellulose sample. Figures 237 and 238 confirmed that the internal structure of these samples was weakly bonded shown by uneven material removal in the grinding and polishing stages. Poor material structure in the green state of the same materials (Figures 178 and 179) was not overcome in the sinter HIP process. The mechanical strength could not be quantified as test bars were not formed due to such poor structure. Figure 239 shows that isolated cases of porosity were present in the sintered samples prepared from GCMPG binders. Such porosity was caused by material inclusions (un-dissolved or poorly mixed binder) in the extrusion feedstock which led to catastrophic cracking in the drying stages at larger diameters. Although infrequent, the size of the pore was sufficient to cause unacceptable failures and was indicative of poor binder material removal.

8.3.2 Grain Size and Grain Size Distribution

The grain size distribution was measured in order to make comparisons with the non-destructive method of Hc testing described in section 3.1.1. Hc decreased with increasing average grain size for each material (Figure 245). This indicates that significantly low Hc values can be used to predict that samples have large average grain sizes according to section 3.1.1. Hc measurements however cannot

be used as a measure of exact grain size due to a lack of precision. There was also no strong correlation between Hc and modal grain size (Figure 243). Figures 244 and 246 show that Vickers hardness values did not change appreciably across the grain sizes that were measured.

8.3.3 Scanning Electron Microscopy

8.3.3.1 Dough Feedstock

In each of the dough systems, either agglomeration or material imperfections were observed with the exception of the Gelucire 5013 based formulation (Figure 250). Unmixed methyl cellulose and ethyl cellulose was present in the MC8 based material and the ECETHPVB formulations respectively due to a short mixing time. In the case of the MC8 feedstock, longer mixing time prevented any unmixed methyl cellulose remaining and subsequent porosity in the sintered product. Ethyl cellulose was less easily dissolved and increased mixing time did not make such improvements. The MCPAM based formulation (Figure 248) showed a more substantial mixing issue. String-like structures up to 60 µm in length were present in every field of view. The porosity left behind by these structures was not closed in the sinter HIP process and hence large areas of porosity and voids were present in the product. As this did not occur in the MC8 formulation, the structures were caused by the addition of polyacrylamide and or interactions between polyacrylamide and methyl cellulose. Polyacrylamide had the desired effect of increased dough viscosity although the sintered product formed was inherently weak. Figure 250 shows that a smooth dough was formed using a Gelucire 5013/MPG binder. An inability to dry samples at increased diameter however suggests that inclusions may have been present leaving porosity behind after sintering. Inclusions were not observed in the SEM images and therefore it is more likely that the binder system did not break down sufficiently during drying and de-binding. This was detrimental to the product as sufficiently large pores were not formed to allow binder removal in the de-binding stage, causing product rupture. SEM analysis was not capable of detecting whether a binder formulation was suitable for manufacture without other analytical techniques and practical investigation of drying cycles. SEM images of dough samples have however did provide an insight as to why dough systems created products with significant defects.

8.3.4 Sintered Samples

Sintered samples prepared from group 1 binder materials and the MC10 binder from group 2 were examined using SEM analysis (Figure 251 to Figure 260). SEM analysis allowed for the detection of porosity and poor cobalt distribution as well as giving an indication of the WC grain size. As with optical microscopy results, porosity was observed in each of the group 1 based sintered samples. Only the samples prepared with methyl cellulose gave acceptable levels of porosity (Figure 251). Figures 251 and 252 also show that methyl cellulose based samples had an even cobalt distribution,

which was essential for obtaining good toughness and hardness throughout products. An example of poor cobalt distribution is shown in Figure 253. The addition of polyacrylamide caused the formation of pores in the extrudate. Due to excessive porosity and voidage in this sample, cobalt was not homogenously distributed. During the liquid sintering phase in the sinter HIP process cobalt migrated towards and filled in the pores. Typically this would have given a low TRS and low bulk toughness (although not tested in this work). Further to a predicted low TRS, intra-granular cracking was encouraged due to localised cobalt deficiency (Figure 254). Such deficiency gave low binding strength and wetting as a result of increased cobalt concentration in pores. Pores were left behind by the string-like structures formed in the dough stage (Figure 248). A similar level of porosity was observed in the sintered sample prepared from ethyl cellulose based dough. The porosity in this case was caused by poor dissolution of the ethyl cellulose in ethanol in the binder pre-mix preparation stage. Agglomerates of ethyl cellulose were not sufficiently broken down during dough mixing and left large pores behind after sintering (Figure 255). Grinding and polishing for SEM analysis caused material to break away from the surface in samples with porosity and poor cobalt distribution. Porosity was also observed in the GCMPG based material using SEM analysis (Figure 258). Whilst an even cobalt distribution was shown in this sample, large diameters could not be dried or sintered without failure. The binder system was not suitable for large diameter production as it was not capable of being removed without rupturing samples using the desired drying and de-binding processes. Figure 259 and Figure 260 show that the methyl cellulose based material used in a production environment produced samples with little to no porosity with an even cobalt distribution.

Chapter 9

9.1 Conclusions and Future Work

The work presented was designed to develop an extrusion binder system and production process for the manufacture of large diameter tungsten carbide drill blanks. Larger diameters were required as the current production process at SHM had reached a maximum of 12 mm sintered diameter. The production of larger diameters would secure a greater customer base for the future operations. Using binder development as the cornerstone for this work, processes could be more easily implemented within the production environment without the need for designing new equipment and operations. Binder system development was centred on the behaviour of the existing SHM binder system due to its high extrusion stability. However, major development was carried out in terms of drying and sintering up to larger diameters. In order to carry out such development the main body of this work consists of rheological analysis of both binder and dough formulations. Rheological analysis of materials combined with drying and sintering investigations aided the selection of an appropriate binder material. In developing the new formulation for larger diameters, stabilisation activities relating to internal geometrical properties were also investigated.

9.1.1 Binder Selection and Rheological Analysis

Rheological analysis was used to determine binder properties over a range of shear rates. Binder viscosity was closely monitored as highly viscous binders provide greater extrudate stability due to a greater resistance to phase migration. The SHM binder had a high shear viscosity and exhibited good extrusion stability. Fitting the Herschel Bulkley parameters to binder system flow curves allowed for viscosity comparison against the SHM binder. Systems with similar viscosity parameters were selected for further investigation. From the first binders (group 1) only the methyl cellulose based binder system was capable of producing high quality extrudate at increased diameters. However, the methyl cellulose and water binder system had lower viscosity parameters than the SHM binder, particularly in the presence of other additives. Whilst additions of polyacrylamide to this system increased the shear viscosity sufficiently, the additions proved detrimental to product quality. Binders prepared with methyl cellulose had their shear viscosity successfully increased by increasing the methyl cellulose concentration (group 2 binders). This allowed for easy binder shear viscosity adjustments and had no adverse effects on drying and sintering properties. Oscillatory rheometry was used to measure viscoelastic behaviour and make comparisons with earlier shear stress analysis work. Complex viscosity and shear viscosity measurements showed that the same general trends were followed for each binder system. Although trends were similar, complex and shear viscosity

could not be directly related via the Cox-Merz rule. Although dough viscosity was increased with methyl cellulose content, the extrudate was still relatively soft in comparison with the SHM feedstock. This caused unstable extrusion flow and a weaker structure. Further increases in methyl cellulose content increased dough shear viscosity although introduced other failings such as extrudate cracking due to increased fragility. Other binder additives such as MPG and glycerol were investigated in order to increase dough shear viscosity. These tests formed the third set of binders, binder group 3 although each additive tested produced poorly performing dough feedstocks. Methyl cellulose binder systems were therefore not modified in further experiments. The fourth group of experiments, were all based on the MC8 formulation from group 1 only with increased WC-Co solids loading. The WC-Co solids loading was increased in order to improve extrusion stability by increasing extrudate stiffness. Cracks were observed in the extrudate prepared at higher WC-Co solids loadings due to poor wetting of the powder matrix. The maximum solids loading achievable with the methyl cellulose binder system was therefore investigated.

9.1.2 Maximum WC-Co solids loading

Mixer torque rheometry showed that the maximum WC-Co solids loading achievable with the methyl cellulose and water based binder system was 41.6 volume %. Further analysis using extrusion showed that the theoretical maximum packing fraction was 3-4 vol% higher than this. The mixer torque rheometry technique was able to validate the extrusion tests discussed in section 5.1. The extrusion experiments however, suggest that with better wetting of the powder matrix, higher practical solids loadings could have been achieved. Mixer torque rheometry also showed that beyond the maximum solids loading in the feedstock mix a reduction in mixing torque occurred due to agglomeration. Mixer torque rheometry measurements were combined with density measurements using helium pycnometry. Helium pycnometry was used to compare densities of feedstocks prepared with alternative mixing equipment. Mixing equipment showing greater wear in produced feedstocks in which density fluctuations were observed around the critical solids loading. These feedstocks were also lower in density and therefore mixer tolerances and maintenance were essential for product quality.

9.1.3 Extrusion

Each of the group 1 binder systems were mixed to formulate extrusion feedstocks. The feedstocks were then analysed using the Benbow Bridgewater technique. The model was well fitted to experimental extrusion data which allowed for estimations of extrusion pressure based on die lengths and diameters. The Benbow Bridgwater analysis was also used to model the SHM pilot scale extrusion equipment which utilised a more complicated tooling set up. The analysis was useful in

aiding the tooling re-design process. Whilst the model was used to predict pressures across simple tool set ups for each of the group 1 feedstocks, it could not be used effectively to accurately determine the optimum binder system. Pilot scale extrusion however, confirmed the optimum binder system to be methyl cellulose and water. Initially an 8 mass % cellulose to water binder was tested although this proved unstable in a production testing environment. A scale up to 150 Kg of WC-Co powder was evaluated and found to be unsuitable due to extrudate softness which promoted unstable extrusion flow. After further pilot scale development, the 10% methyl cellulose and water formulation was tested with 150 Kg of WC-Co powder. The selected binder allowed for the extrusion of a suitably stiff formulation that could be dried and sintered under the current SHM conditions. Extrusion stability was much improved and larger diameter extrudate was successfully produced. Further extrusion trials were made on the 10% formulation with tooling modifications. Tooling developments were a result of the Benbow Bridgwater pilot scale experiments and longer die lands were manufactured to suit the formulation. It was proved that a longer die lands and increased extrudate velocity would increase extrusion pressure and improve material stability in flow and dimensional tolerance.

9.1.4 Drying, Sintering and sintered properties

Drying experiments showed that only cellulose variants were capable of drying larger diameter tungsten carbide products without failure in this work. Only methyl cellulose feedstocks without additives produced samples of an acceptable standard. Nevertheless, many of the other feedstocks were sintered and the properties were examined prior to large diameter investigation. Scanning electron microscopy and optical microscopy showed that the majority of samples contained large pores. The effects of the porosity were greater at larger diameters due to the size of the pores and hence little to no porosity in the extruded body was essential. Extrudate prepared from ethyl cellulose and ethanol and methyl cellulose, water and polyacrylamide appeared to dry and sinter successfully. However, detailed examination showed porosity was present. Only the methyl cellulose and water based formulation provided dried and sintered products with sufficiently low levels of porosity. Initial levels of porosity in sintered samples were evaluated using sintered density measurements. A low sintered density measurement indicated that porosity was present although more detailed analysis was required in order to determine the frequency and size of pores. Although porosity was evident in many samples, Hv30 Vickers hardness was measured in order to qualify whether or not the sample had sintered correctly. Low hardness indicated that there were fundamental issues in the material grade of WC-Co such as incorrect grain size. During this work however, only a small range of grain sizes were used as the powder matrix was not changed throughout. Therefore there were only small variations in hardness other than in the case of

material prepared using methyl cellulose, water and polyacrylamide as a binder. The significant drop in hardness in this instance was due to excessive porosity. Grain size was also evaluated using Hc measurements described in section 3.1.1 whilst Cobalt magnetic measurements gave an indication of carbon content. It was determined that Hc could not be used accurately to measure grain size without combining with other techniques such as linear intercept measurements. The linear intercept method was used in conjunction with scanning electron microscopy and optical microscopy. This method showed that the average grain size distribution did not vary significantly for each of the materials tested. Scanning electron microscopy was also used to give an overview of quality of both sintered and non-sintered samples. During the observation of non-sintered samples it was determined that ethyl and methyl cellulose based formulations did not dissolve completely in the dough mixtures. Small agglomerates of cellulose were left in the mix and later left pores behind in sintered samples. Large string shaped structures were observed in the formulation containing polyacrylamide. SEM analysis also showed that cobalt distribution was not always homogenous in the sintered samples. This was most evident in materials prepared using methyl cellulose, water and polyacrylamide. Conversely, the cobalt distribution was homogenous for samples prepared using methyl cellulose and water.

9.1.5 Future work

The future work of this project centres on improving material quality and range from the methyl cellulose based extrusion feedstock. Material quality can be improved in a number of ways and requires significant development of the formulation and formulation process. Material stability is the key area of development that is required so that extrusion can be spread over a wider time frame and so that dough feedstocks can be made in advance and put into storage. This would be of particular benefit to the production environment. As well as a resistance to aging, the aqueous feedstock would also benefit from greater extrusion flow stability. The theory behind the formulation suggests that if a greater solids loading could be used with the methyl cellulose formulation then feedstock stiffness and therefore extrusion stability would be improved. In this instance work is required to improve the wettability of the powder by the organic binder system. Powder wettability is measured using tensiometers which work according to the Washburn theory. Surface wettability is generally determined by the contact angle of a liquid on a solid surface (figure 261). When a small droplet is placed on a solid substrate it assumes a shape that minimises the free energy of the system (wettability of mineral and metallic powders, applicability and limitations of sessile drop method and washburns technique page 68). Large contact angles correspond to a lack of spreading of the liquid on the solid and therefore a low degree of wettability (figure 261 right).

Figure 261 Droplet formation and contact angle on a flat surface

To improve the wettability of the powder by the binder, the contact angle must be reduced. Common methods for reducing the contact angle include reducing the surface tension of the liquid (binder) and increasing the surface energy of the solid (powder). In order to measure the contact angle for powders, the Washburn capillary rise (WCR) method is most commonly applied. In this method, a liquid is drawn through the powder to be measured in a capillary using attractive forces between the liquid and solid surfaces. The rate of the capillary rise of the liquid or the height of the capillary rise is used to determine the contact angle which is then used to classify wettability (applicability of washburn capillary rise for determining contact angles of powders/porous materials (page 169). Both the particle size of the powder and binder viscosity play a role in optimising the wettability of the powder by the binder and each should be investigated further to determine how to improve wettability. In addition to developing the formulation, there is also a requirement to analyse future materials more thoroughly with regards to equipment scale up. Scale up calculations and analysis would result in less of a need to run production scale experiments early on in material development. Modelling and simulation of the extrusion process, tooling and material would be the cornerstone to such scale up calculations. As well as the application of modelling work, factorial experimental design (FED) would also be useful in this work. Due to the fact that the product quality is dependant not only on a single factor, FED could be used to improve product quality and yield with a minimum number of experiments. Factorial experimental design (FED) allows the study of joint effects of the process or design parameters on a given aspect or response of the product. There are many potential factors that could be considered to influence the final product throughout the processes used. As there are so many factors, they have been sub-divided into the groups of powder, organic binder and dough. Whilst many factors are known to have big influences on the responses (product properties), the combined effects are not known and this, crucially is where factorial design could aid this project. The known influential factors and responses to measure are given in table 47:

Table 47 Factorial experimental design-factors and responses

	Factors	Responses	
	WC-Co BET	**Extruded Properties**	**Sintered Properties**
Powder (WC-Co)	Cobalt Fisher Subsize	Pitch	Pitch
	Cobalt particle shape (spherical or filamental)	PCD	PCD
	WC-Co density	Extrusion Pressure	Extrusion Pressure
	Moisture content	Concentricity	Concentricity
Organic Binder	Methyl Cellulose density	Diameter	Hc (see section…)
	Processed binder density (MC plus water)	Scrap rate	Com
	Processed binder pH (MC plus water)		Hardness
	Processed binder viscosity (MC plus water)		TRS
	Processed binder yield stress (MC plus water)		Porosity
Extrusion Feedstock	Density		Grain size
	Mixer torque		Surface Cracks
	Mixer temperature		Shrinkage
	Viscosity		Scrap rate
	Yield stress		
	Moisture content		

Further to improving the stability of the formulation and process, there is also future demand for a greater range of products including tighter helix angles of the coolant holes and greater than 30 mm diameter product. The first step in reaching such goals would be to determine the maximum diameter that the current methyl cellulose formulation can achieve before working towards more complex geometries. A demand for increased diameter extrudate is a common theme and issue across many extrusion industries due the customer demands and limitations of the drying and sintering processes respectively.

References

1. **Brookes, K.J.A. Hardmetals and other hard materials. 2nd ed. 1992, East Barnet: International Carbide Data. p. 5-100.**

2. **Kurlov. A.S. and Gusev. A.I. Tungsten Carbides Structure, properties and application in hardmetals, Springer international publishing, Switzerland. 2013. p.1-50.**

3. **Upadhyaya G.S. Cemented tungsten carbides. Production, properties and testing. 1999. p.7.**

4. **Hazell. P.J., Roberson. C.J. and Moutinho. M. The design of mosaic armour: the influence of tile size on ballistic performance 2008. p. 1498.**

5. **Klement. R., Rolc. S., Mikulikova. and Krestan. J. Transparent armour materials, Journal of the European ceramic society. 2008 28(5): p. 1091.**

6. **Urriolgoitia-Calderon. G. et al. Mechanical design and manufacture by powder technology of a new mandrel tool for the fabrication of assault rifle barrels, Powder technology. 2012 (224):p. 76.**

7. **Schuchard. A. and Watkins. E.C. Cutting effectiveness of tungsten carbide burs and diamond points at ultra-high rotational speeds. The journal of prosthetic dentistry. 1967 18(1) p. 58.**

8. **www.allaboutcementedcarbide.com. 23.11.2009.**

9. **van Put, J.W., Zegers, T.W, and Liu, H. Hydrogen reduction of ammonium paratungstate into tungsten blue oxide—Part II: Experimental. International Journal of Refractory Metals and Hard Materials, 1991. 10(3): p. 123-131.**

10. **Lackner, A., Filzwieser, A. and Paschen, P. On the Reduction of Tungsten Blue Oxide in a Stream of Hydrogen. International Journal of Refractory Metals and Hard Materials, 1996. 14(5): p. 383-391.**

11. **Marashi, M.S., Vahdati, J., Khaki, and Zebarjad, S.M. Comparing thermal and mechanochemical decomposition of ammonium paratungstate (APT). International Journal of Refractory Metals and Hard Materials, 2012. 30(1): p. 177-179.**

12. **http://www.itia.info/tungsten-oxides-acid.html. 2013.**

13. **Schubert, W.D. and Lassner, E. Production and Characterization of Hydrogen-Reduced Submicron Tungsten Powders. International Journal of Refractory Metals and Hard Materials, 1991. 10: p. 171-183.**

14. **Zhang, Z., Zhang, Y. and Mamoun, M. The reduction of cobalt doped ammonium paratungstate to nanostuctured W-Co Powder International Journal of Refractory Metals and Hard Materials, 2002. 20(3): p. 227-233.**

15. **de Medeiros, F.F.P., da Silva, A.G.P., de Souza, C.P. and Gomes, U.U. Carburization of ammonium paratungstate by methane: The influence of reaction parameters. International Journal of Refractory Metals and Hard Materials, 2009. 27(1): p. 43-47.**

16. **Levy, R.B. and Boudart, M. Platinum-Like Behavior of Tungsten Carbide in Surface Catalysis. Science, 1973. 181(4099): p. 547-549.**

17. **Zeiler, B. The potential of conventional tungsten carbide. powder manufacturing 14th International Plansee Seminar '97 Austria. 1997. Vol 4 p. 265-276.**

18. **Li, T., Li, Q., Fuh, J.Y.H., Yu, P.C. and Wu, C.C. Effects of lower cobalt binder concentrations in sintering of tungsten carbide. Materials Science and Engineering: A, 2006. 430(1–2): p. 113-119.**

19. **Zhang, F.L., Wang, C.Y. and Zhu, M. Nanostructured WC/Co composite powder prepared by high energy ball milling. Scripta Materialia, 2003. 49(11): p. 1123-1128.**

20. **Hewitt, S.A., Laoui, T. and Kibble, K.K. Effect of milling temperature on the synthesis and consolidation of nanocomposite WC–10Co powders. International Journal of Refractory Metals and Hard Materials, 2009. 27(1): p. 66-73.**

21. **Parti, M. and Palancz, B. Mathematical Model for Spray Drying. Chemical Engineering Science, 1974. 29: p. 355-362.**

22. **Armor, J.N., Fanelli, A.J., Marsh, G.M. and Zambri, P.M. Nonaqueous Spray-Drying as a Route to Ultrafine Ceramic Powders. Journal of the American Ceramic Society, 1988. 71(11): p. 938-942.**

23. **Duffie, J.A. and Marshall, W.A. Factors influencing the properties of spray dried products. 1953(49): p. 480-486.**

24. **Crosby, E.J. and Marshal, W.R. Effects of drying conditions on the properties of spray-dried particles. Chemical Engineering programme 54, 1958: p. 56-63.**

25. **Shinohara. N. et al. Formation mechanisms of processing defects and their relevance to the strength in alumina ceramics made by powder compaction process. Journal of materials science. 1999 34(17): p. 5384.**

26. **Mahdjoub. H. et al The effect of slurry formulation upon the morphology of spray-dried yttria stabilised zirconia particles. Journal of the European ceramic society. 2003 23(10): p. 1639.**

27. Bertrand .B. and Roy. P. Spray dried ceramic powders: A quantitative correlation between slurry characteristics and shapes of the granules. Chemical engineering science. 60(1) 2005:p. 96-101.

28. Weihua L. et al Agglomeration on drying of yttria stabilised zirconia slurry on a metal substrate. Journal of the European ceramic society. 2006 26(16):p. 3599

29. Walker. J. et al Influence of slurry parameters on the characteristics of spray dried granules. Journal of the American ceramic society. 1999 82(7):p. 1711-1719.

30. Fang, Z.Z. and Eso, O.O. Liquid phase sintering of functionally graded WC–Co composites. Scripta Materialia, 2005. 52(8): p. 785-791.

31. Wu, X. and Guo, J. Electric-discharge compaction of graded WC–Co composites. International Journal of Refractory Metals and Hard Materials, 2008. 26(1): p. 28-32.

32. Benbow, J. and Bridgwater, J. Paste flow and Extrusion. School of Chemical Engineering and inter-disciplinary Research Centre in Materials for High Performance Applications 1993, University of Birmingham. p.

33. Pradip, S. Aluminium Extrusion Technology, ASM International, the materials information society. 2000. p. 200-250.

34. Bardesley, M.A. and Bridgwater, J. Evaluation of Liquid Phase Migration in Pastes and Gels. Industrial & Engineering Chemistry Research, 2011. 51(4): p. 1774-1781.

35. www.mech.uwa.edu.au/.../hot_cold_working/ 2009.

36. Rough, S.L., Bridgwater, J. and Wilson, D.I. Effects of liquid phase migration on extrusion of microcrystalline cellulose pastes. International Journal of Pharmaceutics, 2000. 204(1–2): p. 117-126.

37. Yaras, P., Kalyon, D.M. and Yilmazer, U. Flow instabilities in capillary flow of concentrated suspensions. Rheologica Acta, 1994. 33(1): p. 48-59.

38. Fielden, K.E., Newton, J.M. and Rowe, R.C. The Effect of Lactose Particle Size on the Extrusion Properties of Microcrystalline Cellulose-Lactose Mixtures. Journal of Pharmacy and Pharmacology, 1989. 41(4): p. 217-221.

39. Morsi, K., Esawi, A.M.K., Lanka, S., Sayed, A. and Taher, M. Spark plasma extrusion (SPE) of ball-milled aluminum and carbon nanotube reinforced aluminum composite powders. Composites Part A: Applied Science and Manufacturing, 2010. 41(2): p. 322-326.

40. Zhou, J., Huang, B. and Wu, E. Extrusion moulding of hard-metal powder using a novel binder system. Journal of Materials Processing Technology, 2003. 137(1–3): p. 21-24.

41. Qu, X., Gao, J., Qin, M. and Lei, C. Application of a wax-based binder in PIM of WC–TiC–Co cemented carbides. International Journal of Refractory Metals and Hard Materials, 2005. 23(4–6): p. 273-277.

42. Ferstl, H., Barbist, R., Rough, S.L. and Wilson, D.I. Influence of visco-elastic binder properties on ram extrusion of a hardmetal paste. journal of materials science, 2012. 47(19): p. 6835-6848.

43. Sunil, B.R., Sivaprahasam, D and Subasri, R. Microwave sintering of nanocrystalline WC–12Co: Challenges and perspectives. International Journal of Refractory Metals and Hard Materials, 2010. 28(2): p. 180-186.

44. Martyn, M.T. and James, P.J. The processing of hardmetal components by powder injection moulding. International Journal of Refractory Metals and Hard Materials, 1993. 12(2): p. 61-69.

45. Bayer, R. and Knarr, M. Thermal precipitation or gelling behaviour of dissolved methylcellulose (MC) derivatives—Behaviour in water and influence on the extrusion of ceramic pastes. Part 1: Fundamentals of MC-derivatives. Journal of the European Ceramic Society, 2012. 32(5): p. 1007-1018.

46. Ananthakumar, S., Manohar, P. and Warrier, K.G.K. Effect of boehmite and organic binders on extrusion of alumina. Ceramics International, 2004. 30(6): p. 837-842.

47. Nath Das, R., Madhusoodana, C.D. and Okada, K.D. Rheological studies on cordierite honeycomb extrusion. Journal of the European Ceramic Society, 2002. 22(16): p. 2893-2900.

48. Draper, O., Blackburn, S., Dolman, G., Smalley, K. and Griffiths, A. A comparison of paste rheology and extrudate strength with respect to binder formulation and forming technique. Journal of Materials Processing Technology, 1999. 92–93(0): p. 141-146.

49. Huzzard, R.J. and Blackburn, S. A water-based system for ceramic injection moulding. Journal of the European Ceramic Society, 1997. 17(2–3): p. 211-216.

50. Forzatti, P., Ballardini, D. and Sighicelli, L. Preparation and characterization of extruded monolithic ceramic catalysts. Catalysis Today, 1998. 41(1–3): p. 87-94.

51. Sato, K., Hotta, Y., Yilmaz, H., Sato, K. and Watari, K. Fluidity of methyl cellulose-contained suspensions and pastes prepared from differently milled Al2O3 powder. Journal of Colloid and Interface Science, 2009. 331(1): p. 221-226.

52. Aranzabal, A., Iturbe, D., Romero-Saez, M., Gonzalez-Velasco, M.P., Gonzalez-Velasco. J.T. and Gonzalez-Marcos, J.A. Optimization of process parameters on the extrusion of honeycomb shaped monolith of H-ZSM-5 zeolite. Chemical Engineering Journal, 2010. 162(1): p. 415-423.

53. **Burbidge, A.S. and Bridgwater, J. The single screw extrusion of pastes. Chemical Engineering Science, 1995. 50(16): p. 2531-2543.**

54. **Zhu, S., Shen, Y., Wang, J., Zhang, Y. and Liu, Y. Preparation and Performance of Al2 TiO5 - TiO2 -SiO2 Honeycomb Ceramics by Doping Rare Earth. Journal of Rare Earths, 2007. 25(4): p. 457-461.**

55. **Navarro, A., Alcock, J.R. and Whatmore, R.W. Aqueous colloidal processing and green sheet properties of lead zirconate titanate (PZT) ceramics made by tape casting. Journal of the European Ceramic Society, 2004. 24(6): p. 1073-1076.**

56. **Heymann, E. Studies on sol-gel transformations. I. The inverse sol-gel transformation of methylcellulose in water. Transactions of the Faraday society, 1935. 31(0): p. 846-864.**

57. **Haque, A. and Morris, E.R. Thermogelation of methylcellulose. Part I: molecular structures and processes. Carbohydrate Polymers, 1993. 22(3): p. 161-173.**

58. **Sarkar, N. Kinetics of thermal gelation of methylcellulose and hydroxypropylmethylcellulose in aqueous solutions. Carbohydrate Polymers, 1995. 26(3): p. 195-203.**

59. **Heymann, E. Studies on sol-gel transformations. 1. The inverse sol-gel transformation of methylcellulose in water. Transactions of the Faraday society, 1935. 31: p. 846-864.**

60. **Clasen, C. and Kulicke, W.M. Determination of viscoelastic and rheo-optical material functions of water-soluble cellulose derivatives. Progress in Polymer Science, 2001. 26(9): p. 1839-1919.**

61. **Castro-Guerrero, C., Morales-Cepeda, A., Kharissova, O., Koschella, A. and Heinze, T. Mesophases in a Gel from Hydroxypropyl Cellulose/Polyacrylamide. Macromolecular Symposia, 2010. 294(2): p. 58-63.**

62. **Dey, R.K., Tiwary, G.S., Patnaik, T. and Jha, U. Controlled release of 5-aminosalicylic acid from a new pH responsive polymer derived from tamarind seed polysaccharide, acrylic acid, and polyamidoamine. Polymer Bulletin, 2011. 66(5): p. 583-598.**

63. **Das, R., Panda, A.B. and Pal, S. Synthesis and characterization of a novel polymeric hydrogel based on hydroxypropyl methyl cellulose grafted with polyacrylamide. Cellulose, 2012. 19(3): p. 933-945.**

64. **Crowley, M.M., Schroeder, B., Fredersdorf, A., Obara, S., Talarico, M., Kucera, S. and McGinity, J.W. Physicochemical properties and mechanism of drug release from ethyl cellulose matrix tablets prepared by direct compression and hot-melt extrusion. International Journal of Pharmaceutics, 2004. 269(2): p. 509-522.**

65. Kim, C-J., Kim, K-B., Kuk, I-H., Hong, G-W., Park, S-D., Yang, S-W. and Shin, H-S. Fabrication and properties of YBa2Cu3O7-δAg composite superconducting wires by plastic extrusion technique. journal of materials science, 1997. 32(19): p. 5233-5242.

66. Khan, A.U., Briscoe, B.J. and Luckham, P.F. Evaluation of slip in capillary extrusion of ceramic pastes. Journal of the European Ceramic Society, 2001. 21(4): p. 483-491.

67. Gandhi, R., Kaul, C. and Panchagnula, R. Extrusion and spheronization in the development of oral controlled-release dosage forms. Pharmaceutical Science & Technology Today, 1999. 2(4): p. 160-170.

68. Mehuys, E., Vervaet, C. and Remon, J.P. Hot-melt extruded ethylcellulose cylinders containing a HPMC–Gelucire® core for sustained drug delivery. Journal of Controlled Release, 2004. 94(2–3): p. 273-280.

69. Zaky, M.T., Soliman, F.S and Farag, A.S. Influence of paraffin wax characteristics on the formulation of wax-based binders and their debinding from green molded parts using two comparative techniques. Journal of Materials Processing Technology, 2009. 209(18–19): p. 5981-5989.

70. Tanguy, P.A. and La Fuente, E.B.D. Non-newtonian mixing with helical ribbon impellers and planetary mixers, in Rheology Series, D.D.K. D.A. Siginer and R.P. Chhabra, Editors. 1999, Elsevier. p. 301-330.

71. Chesterton, A.K.S., Moggridge, G.D., Sadd, P.A. and Wilson, D.I. Modelling of shear rate distribution in two planetary mixtures for studying development of cake batter structure. Journal of Food Engineering, 2011. 105(2): p. 343-350.

72. Grida, I. and Evans, J.R.G. Extrusion freeforming of ceramics through fine nozzles. Journal of the European Ceramic Society, 2003. 23(5): p. 629-635.

73. Song, J.H., Edirisinghe, M.G. and Evans, J.R.G. Formulation and Multilayer Jet Printing of Ceramic Inks. Journal of the American Ceramic Society, 1999. 82(12): p. 3374-3380.

74. Edirisinghe, M.J. and Evans, J.R.G. Review: Fabrication of engineering ceramics by injection moulding. II. Techniques. International Journal of High Technology Ceramics, 1986. 2(4): p. 249-278.

75. Handle, F. Extrusion in Ceramics (Engineering and Processes) 2009. p.150-280

76. www.mixer.co.uk. 2013.

77. Lindley, J.A. Mixing processes for agricultural and food materials: Part 2, highly viscous liquids and cohesive materials. Journal of Agricultural Engineering Research, 1991. 48(0): p. 229-247.

78. Haraszi, R., Larroque, O.R., Butow, B.J. Gale, K.R. and Bekes, F. Differential mixing action effects on functional properties and polymeric protein size distribution of wheat dough. Journal of Cereal Science, 2008. 47(1): p. 41-51.

79. Blackburn, S. and Bohm, H. Effect of mixing procedure on fine alumina paste extrusion. British Ceramic Transactions 1994. 93(5): p. 169-177.

80. Matchett, A.J., Teoh, H.A and Bland, B. Fluid mixing II. Institute of Chemical Engineers, 1984: p. 29-48.

81. Prabhakaran, K., Ananthakumar, S. and Pavithran, C. Preparation of extrudable alumina paste by coagulation of electrosterically stabilized aqueous slurries. Journal of the European Ceramic Society, 2002. 22(2): p. 153-158.

82. Hay, T.K. Reaching an objective in oil absorption measurements. journal of paint technology, 1974. 46: p. 44-50.

83. Lowell, S. and Shields, J.E. Powder Surface Area and Porosity 1991. p. 228-240.

84. Liu, F.-J. and Chou, K.S. Determining critical ceramic powder volume concentration from viscosity measurements. Ceramics International, 2000. 26(2): p. 159-164.

85. Johansen, A., Schæfer, T. and Kristensen, H. Evaluation of melt agglomeration properties of polyethylene glycols using a mixer torque rheometer. International Journal of Pharmaceutics, 1999. 183(2): p. 155-164.

86. Chatlapalli, R. and Rohera, B.D. Rheological characterization of diltiazem HCl/cellulose wet masses using a mixer torque rheometer. International Journal of Pharmaceutics, 1998. 175(1): p. 47-59.

87. Hancock, B.C., York, P. and Rowe, R.C. An assessment of substrate-binder interactions in model wet masses. 1: Mixer torque rheometry. International Journal of Pharmaceutics, 1994. 102(1–3): p. 167-176.

88. Chatlapalli, R. and Rohera, B.D. Study of effect of excipient source variation on rheological behavior of diltiazem HCl-HPMC wet masses using a mixer torque rheometer. International Journal of Pharmaceutics, 2002. 238(1–2): p. 139-151.

89. Zepnik S. et al. Cellulose Acetate for Thermoplastic Foam Extrusion. Agricultural and biological sciences. 2013. p. 56.

90. Powell, J., The Development of a Process for the Manufacture of Multilayered Ceramic Micro-tubes. Ph.D. Thesis, 2009. The University of Birmingham.

91. Aydin, I., Biglari, F.R., Briscoe, B.J., Lawrence, C.J. and Adams, M.J. Physical and numerical modelling of ram extrusion of paste materials: conical die entry case. Computational Materials Science. 2000. 18(2): p. 141-155.

92. **Horrobin, D.J. Theoretical aspects of paste extrusion. Ph.D. Thesis. 1999. University of Cambridge.**

93. **Martin, P. Mechanics of paste flow in radial screen extruders. Doctorial Dissertation. 2002. Department of Engineering, University of Cambridge.**

94. **Young, D.F., Okiishi, T.H., Huebsch, W.W. and Munson, B.R. Fundamentals of Fluid Mechanics 2006: John Wiley & Sons. p.58-73**

95. **Barnes, H.A., Hutton, J.F. and Walters, K. An Introduction to Rheology 1989. p. 20-51.**

96. **Malkin. A. and Isayev.A Rheology: Concepts, methods and applications. Chemtec publishing. 2006. p 132.**

97 **Otsubo. Y. Size effects of the shear thickening behaviour of suspensions flocculated by polymer bridging. Journal of rheology. 1993 37(799):p 800**

98. **Cross, M.M., Rheology of non-Newtonian fluids: A new flow equation for pseudoplastic systems. Journal of Colloid Science, 1965. 20(5): p. 417-437.**

99. **Huilgol, R.R. and You, Z. Application of the augmented Lagrangian method to steady pipe flows of Bingham, Casson and Herschel–Bulkley fluids. Journal of Non-Newtonian Fluid Mechanics, 2005. 128(2–3): p. 126-143.**

100. **Whorelow, R.W., Rheological Techniques. 1992. p. 15-70**

101. **Cheung, T., Turpin, M. and Rand, B. Controlled stress, oscillatory rheometry of mesophase-pitches. Carbon, 1995. 33(12): p. 1673-1679.**

102. **Liu. J. and Seright. R.S. Rheology of gels used for conformance control in fractures new Mexico petroleum recovery research centre. Society of petroleum engineers. 2001. P.121.**

103. **Murata. H. Rheology-theory and application to biomaterials. Department of prosthetic dentistry. 2012. p.100-120.**

104. **Franklin. A.G. and Krizek. J. Complex viscosity of a kaolin clay. Clays and minerals. 1969 volume 17. p. 101-110.**

106. **Lin, X., Li, Y., Chen, Z., Zhang, C., Luo, X., Du, X. and Huang, Y. Synthesis, characterization and electrospinning of new thermoplastic carboxymethyl cellulose (TCMC). Chemical Engineering Journal, 2013. 215–216(0): p. 709-720.**

106. **Maru, S.M., de Matas, M., Kelly, A. and Paradkar, A. Characterization of thermal and rheological properties of zidovidine, lamivudine and plasticizer blends with ethyl cellulose to assess their suitability for hot melt extrusion. European Journal of Pharmaceutical Sciences, 2011. 44(4): p. 471-478.**

107. Aho. J. and Syrjala. S. Determination of the entrance pressure drop in capillary rheometry using Bagley correction and zero length capillary. Annual transactions of the Nordic rheology society. 2006. vol 14. p. 1-5.

108. Hatzikiriakos S.G. and Mitsoulis. E. Excess pressure losses in the capillary flow of molten polymers. 1996. vol. 35. p.545-555.

109. Zheng, J., Carlson, W.B. and Reed, J.S. Flow Mechanics on Extrusion through a Square-Entry Die. Journal of the American Ceramic Society, 1992. 75(11): p. 3011-3016.

110. Cendrowicz, A. The characterisation of wax injection moulding and de-wax processes in investment casting. Ph.D Thesis. 2003. Department of Chemical Engineering, The University of Birmingham.

111. Scherer, G.W. The Theory of Drying. Journal of American Ceramic Society 1990. 73(1): p. 3-14.

112. Sherwood, T.K. The Drying of Solids-II. Industrial Engineering Chemistry 1929. 21: p. 976-980.

113. Kim, S.W., Lee, H.W. and Song, H. Effect of minor binder on capillary structure evolution during wicking. Ceramics International, 1999. 25(7): p. 671-676.

114. Mujumdar. A.S. Handbook of industrial drying. 2006. p. 349.

115. Shaw, H.M., Hutton, T.J. and Edirisinghe, M.J. On the formation of porosity during removal of organic vehicle from injection-moulded ceramic bodies. Journal of Materials Science Letters, 1992. 11(15): p. 1075-1077.

116. Calvert, P. and Cima, M. Theoretical Models for Binder Burnout. Journal of the American Ceramic Society, 1990. 73(3): p. 575-579.

117. Chen, G., Cao, P., Wen, G. and Edmonds, N. Debinding behaviour of a water soluble PEG/PMMA binder for Ti metal injection moulding. Materials Chemistry and Physics, 2013. 139(2–3): p. 557-565.

118. Crank. J. The mathematics of diffusion. 1975. p.1-100.

119. Robinson, S.K. and Paul, M.R. Debinding and sintering solutions for metals and ceramics. Metal Powder Report, 2001. 56(6): p. 24-29.

120. Kennedy, S.W. Vacuum furnace techniques for metal injection moulded part debinding and sintering. Metal Powder Report, 1990. 45(9): p. 597-599.

121. Markoulides, D., Koursaris, A. and Rafferty, M. Important factors which affect the removal of organic residues during the presintering of WC-Co. International Journal of Refractory Metals and Hard Materials, 1997. 15(1–3): p. 123-131.

122. **Shengjie, Y., Lam, Y.C., Yu, S.C.M. and Tam, K.C. Two-dimensional simulation of mass transport in polymer removal from a powder injection molding compact by thermal debinding. Journal of Materials Research, 2001. 16(08): p. 2436-2451.**

123. **Krauss, V.A., Oliveira, A.A.M., Klein, A.N., Al-Qureshi, H.A. and Fredel, M.C. A model for PEG removal from alumina injection moulded parts by solvent debinding. Journal of Materials Processing Technology, 2007. 182(1–3): p. 268-273.**

124. **Waldron, M.B. and Daniell, B.L. Sintering. Heyden. 1978. p. 1-80.**

125. **Xiaoping, X., Peizen, L. and German, R.M. Densification and strength evolution in solid-state sintering. journal of materials science 2002. 37: p. 117-1267.**

126. **Randall. M. Sintering with external pressure, Sintering from empirical observations to scientific principles. 2014. p. 305-354.**

127. **Kim, H.C., Shon, I.J., Jeong, I.K., Ko, I.Y., Yoon, J.K. and Doh, J.M. Rapid sintering of ultra fine WC and WC-Co hard materials by high-frequency induction heated sintering and their mechanical properties. Metals and Materials International, 2007. 13(1): p. 39-45.**

128. **Breval, E., Cheng, J.P., Agrawal, D.K., Gigl, P., Dennis, M., Roy, R. and Papworth, A.J. Comparison between microwave and conventional sintering of WC/Co composites. Materials Science and Engineering: A, 2005. 391(1–2): p. 285-295.**

129. **Liu, X., Song, X., Zhang, J. and Zhao, S. Temperature distribution and neck formation of WC–Co combined particles during spark plasma sintering. Materials Science and Engineering: A, 2008. 488(1–2): p. 1-7.**

130. **Keown, E. Personal communication, Sandvik Hard Materials 2013.**

131. **Rahaman, M.N., Sintering of Ceramics. 2007. p. 1-365.**

132. **German, R.M., Liquid Phase Sintering. 1985. p. 1-100.**

133. **Kim. H. et al Rapid sintering process and mechanical properties of binderless ultra-fine tungsten carbide. Materials science and engineering. 2006.vol 435-436. p. 718.**

134. **Raman. R. Microwave sintering of pure metal powders- a review. 2014. 4(3) page 315-322.**

135. **Vaidhyanathan. B. et al. Microwave sintering of multilayer integrated passive devices. Journal of the American ceramic society. 2010. 93(8). p. 2274-2280.**

136. **Agrawal. D.K. Microwave processing of ceramics. Solid state and material science. 1998. vol 3. p. 480.**

137. Erikkson. M. et al. Spark plasma sintering of WC, cemented carbide and functional graded materials. International journal of refractory metals and hard materials. 2013. vol 36. p. 34.

138. Yang, M.J. and German, R.M. Nanophase and superfine cemented carbides processed by powder injection molding. International Journal of Refractory Metals and Hard Materials, 1998. 16(2): p. 107-117.

139. Bayfield, M., Haggett, J.A., Williamson, M.J., Wilson, D.I. and Zargar, A. Liquid Phase Migration in the Extrusion of Icing Sugar Pastes. Food and Bioproducts Processing, 1998. 76(1): p. 39-46.

140. http://www.chemspider.com/Search.aspx?q=monopropylene+glycol. 2013.

141. Petrenko, V.I., Avdeev, M.V., Almasy, L., Bulavin, L.A., Aksenov, V.L., Rosta, L. and Garamus, V.M. Interaction of mono-carboxylic acids in benzene studied by small-angle neutron scattering. Colloids and Surfaces A: Physicochemical and Engineering Aspects, 2009. 337(1–3): p. 91-95.

142. Zhulina, E.B., Borisov, O.V. and Priamitsyn, V.A. Theory of steric stabilization of colloid dispersions by grafted polymers. Journal of Colloid and Interface Science, 1990. 137(2): p. 495-511.

143. Tseng, W.J., Liu, D.M. and Hsu, C.K. Influence of stearic acid on suspension structure and green microstructure of injection-molded zirconia ceramics. Ceramics International, 1999. 25(2): p. 191-195.

144. Wright, J.K., Zhang, J.G., Julian, R.G. and Edirisinghe, M.J. Particle Packing in Ceramic Injection Molding. Journal of the American Ceramic Society, 1990. 73(9): p. 2653-2658.

145. Housecroft, C.E. and Constable, E.C. Chemistry, an introduction to Organic, Inorganic and Physical Chemistry. 2006. p.1081

146. Yang, W.W., Yang, K.Y. and Hon, M.H. Effects of PEG molecular weights on rheological behavior of alumina injection molding feedstocks. Materials Chemistry and Physics, 2003. 78(2): p. 416-424.

147. NTP-CERHR Expert Panel report on the reproductive and developmental toxicity of propylene glycol. Reproductive Toxicology, 2004. 18(4): p. 533-579.

148. Bologna, L.S., Andrawes F.F. and Barvenik, F.W. Analysis of Residual Acrylamide In Field Crops. Journal of Chromatographic Science. 1999. 37(7): p. 240-244.

149. http://www.sigmaaldrich.com/catalog/product/sigma/92560?lang=en&region=GB, 2013.

150. Larsson, M., Hjartstam, J., Berndtsson, J., Stading, M. and Larrson, A. Effect of ethanol on the water permeability of controlled release films composed of ethyl cellulose and

hydroxypropyl cellulose. European Journal of Pharmaceutics and Biopharmaceutics, 2010. 76(3): p. 428-432.

151. Kim, D.H., Lim, K.Y., Paik, U. and Jung, Y.G. Effects of chemical structure and molecular weight of plasticizer on physical properties of green tape in BaTiO3/PVB system. Journal of the European Ceramic Society, 2004. 24(5): p. 733-738.

152. Mostafa, D.S. Personal Communication 2013.

153. Davidson, R.L. Handbook of Water-Soluble Gums and Resins 1980: McGraw-Hill. p. 200.

154. Morrison, F. http://www.chem.mtu.edu/~fmorriso/cm4655/lecture_2_cm4655.pdf. 2013

155. Denn, M.M., Extrusion instabilities and wall slip. Annual Review of Fluid Mechanics, 2001. 33(1): p. 265-287.

156. Russo. G. and Phillips. T.N. Numerical simulation of steady planar die swell for A Newtonian fluid using the spectral element method. Computers and fluids. 2010. 39(5) p. 780-790.

157. Froberg. L. Thermal Analysis TGA / DTA. Abo AKADEMI University. 2014. Lecture slides 1-35.

158. Ianniruberto, G. and Marrucci, G. On compatibility of the Cox-Merz rule with the model of Doi and Edwards. Journal of Non-Newtonian Fluid Mechanics, 1996. 65(2–3): p. 241-246.

159. Turhan, K.N., Sahbaz, F. and Güner, A. A Spectrophotometric Study of Hydrogen Bonding in Methylcellulose-based Edible Films Plasticized by Polyethylene Glycol. Journal of Food Science, 2001. 66(1): p. 59-62.

160. Sudharsan Reddy, K., Prabhakar, M.N., Kumara Babu, P., Venkatesulu, G., Sajan, U., Rao, K., Cowdoji, K. and Subha, M.C.S. Miscibility Studies of Hydroxypropyl Cellulose/Poly(Ethylene Glycol) in Dilute Solutions and Solid State. International Journal of Carbohydrate Chemistry, 2012. 2012: p. 9.

161. Barry, B.W. and M.C. Meyer, The rheological properties of carbopol gels II. Oscillatory properties of carbopol gels. International Journal of Pharmaceutics, 1979. 2(1): p. 27-40.

162. Kundu, M., Mallapragada, S., Larock, R.C. and Kundu, P.P. Rheological properties of methylcellulose aqueous gels under dynamic compression: Frequency sweep and validity of scaling law. Journal of Applied Polymer Science, 2010. 117(4): p. 2436-2443.

163. Warren, J. and German, R.M. The effect of powder characteristics on binder incorporation for injection moulding feedstock. Modern developments in powder metallurgy 1988. 18: p. 391-402.

164. Powell, J. and Blackburn, S. The unification of paste rheologies for the co-extrusion of solid oxide fuel cells. Journal of the European Ceramic Society, 2009. 29(5): p. 893-897.

165. Jayatilaka, A. de. S. Fracture of engineering brittle materials. Applied science publishers. 1979. p. 122.

166. Cias, A., and Czarsk, A. The use of weibull statistics to quantify property variability in Fe-3Mn-0.8C sinter-hardened structurally inhomogenous steels. Archives of Metallurgy and Materials. 2013. 58(4). p.1046.

167. Torres, B.R., et al. Analysis on the mechanical strength of WC-Co cemented carbides under uniaxial and biaxial bending. Materials and Design. 2014 vol.55. p. 851-856.

169. Li, C.J., Ohmori, A. and Harada, Y. Effect of powder structure on the structure of thermally sprayed WC-Co coatings. journal of materials science, 1996. 31(3): p. 785-794.

170. Fang, Z.Z. Correlation of transverse rupture strength of WC–Co with hardness. International Journal of Refractory Metals and Hard Materials, 2005. 23(2): p. 119-127.

171. Tadmor, Z. and Klein, I. Engineering Principles of Plasticating Extrusion 1978: Krieger Publishing Company. p.100-150.

172. Schneider, L., Pressing powder flow types, PowerPoint presentation, Sandvik Hard Materials, Coventry 2010.

173. Wu, C.Y., Dihoru, L. and Cocks, A.C.F. The flow of powder into simple and stepped dies. Powder Technology, 2003. 134(1–2): p. 24-39.

174. Mills, L.A. and Sinka, I.C. Effect of particle size and density on the die fill of powders. European Journal of Pharmaceutics and Biopharmaceutics, 2013 p. 642-652.

175. Bewlay, B.P., Consolidation dynamics of tungsten powder during dry bag cold isostatic pressing. International Journal of Refractory Metals and Hard Materials, 1992. 11(3): p. 165-174.

176. Egeland, G.W., Zuck, L.D., Cannon, W.R., Lessing, P.A. and Medvedev P.G. Dry bag isostatic pressing for improved green strength of surrogate nuclear fuel pellets. Journal of Nuclear Materials, 2010. 406(2): p. 205-211.

177. Baklouti, S., Chartier, T and Baumard, J.F. Mechanical Properties of Dry-Pressed Ceramic Green Products: The Effect of the Binder. Journal of the American Ceramic Society, 1997. 80(8): p. 1992-1996.

178. Uppalapati, M. and Green, D.J. Effect of Relative Humidity on the Viscoelastic and Mechanical Properties of Spray-Dried Powder Compacts. Journal of the American Ceramic Society, 2006. 89(4): p. 1212-1217.

179. Baklouti, S., Chartier, T., Gault, G. and Baumard, J.F. Young's Modulus of Dry-pressed Ceramics: The Effect of the Binder. Journal of the European Ceramic Society, 1999. 19(8): p. 1569-1574.

180. Tanaka, S., Chia-Pin, C., Kato, Z. and Uematsu K. Effect of internal binder on microstructure in compacts made from granules. Journal of the European Ceramic Society, 2007. 27(2–3): p. 873-877.

181. Wu, R.Y. and Wei, W.C.J. Torque evolution and effects on alumina feedstocks prepared by various kneading sequences. Journal of the European Ceramic Society, 2000. 20(1): p. 67-75.

Appendices

Appendix A – Extended Literature Review for Alternative Processing Techniques

Screw Extrusion

Three types of screw extruder exist [75]:

- Extruders without de-airing.
- De-airing extruders with vacuum device incorporated in the extruder barrel.
- Combined de-airing extrusion units consisting of extruder, vacuum chamber and mixer.

There are four zones to consider in the screw extruder with additional sub-zones within the four zones. Screw performance is dependent on all four of these zones working efficiently [170]. There are three zones in the barrel and the fourth zone is the die itself. Zone one is the feed zone, zone two is the compression zone and zone three is the metering zone. The four zones are shown in Figure 262.

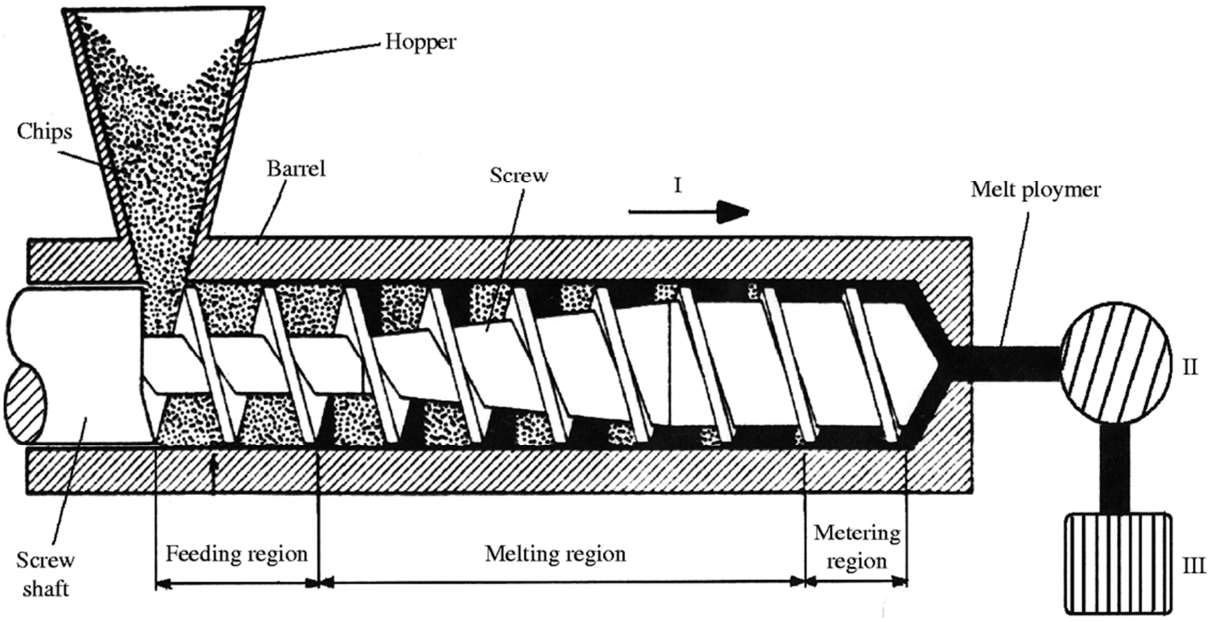

Figure 262 Single screw extruder zones [170]

The feed zone transports material from the feed hopper to the compression zone (melting region in many extruders). Screw depth is constant in the feed zone to enable constant pressure and feed rate. The compression zone is also known as the transition, melting and densifying zone as a number of functions can be performed. The material is compacted in this zone because of the decreasing channel depth of the screw. Following compaction, the material passes into the metering zone. The material is already compacted and homogeneous which makes it ready to pass through the die. The pressure and temperature at this stage are constant depending on the resistance of the die. Zone 4 is the die where material is shaped. Handle [75] suggests that extruders are classified with the following categories:

1. By the range of application of the extruder.
2. By the product to be extruded within the product range.
3. By the arrangement of the auger shaft and the direction of column exit.
4. By the diameter of the extruder barrel.
5. By the number of auger shafts.
6. By the consistency of the body to be processed.
7. By the design of the extruder barrel.
8. By the design and mounting of the augers.
9. By special extrusion methods
10. By the type of de-airing device employed
11. By the design of the extruder.
12. By the design of the de-airing mixer.
13. By the design of the combined de-airing extrusion unit.

The application for this work is to produce large diameter WC-Co drill blanks of low volume. As projected production volumes are low and high value, only a batch process is required. This allows for simple manufacture using ram extrusion rather than screw extrusion. Batch processes also allow for more consistent control of material properties as there are fewer variables to consider during the extrusion process. The implementation costs and complexity of screw extrusion processes outweighed the benefits of ram extrusion in the time frame of this project.

Pressing

Die filling is the first step of pressing. The process of filling for the pressing of hard metal powders is dependent on the following parameters [171]:

- Shoe Design
- Dies and their orientation
- Shoe kinematics (shaking)
- Quantity of powder
- Environment (vacuum or not)

- Tool kinematics (gravity or suction)

Wu, Dihoru and Cocks have shown that the faster the speed of the shoe, the greater the filling density [172]. Filling density increases when vibratory filling is used although higher frequencies cause fluidisation and a lack of filling [172]. Figure 263 shows powder flow types when pressing.

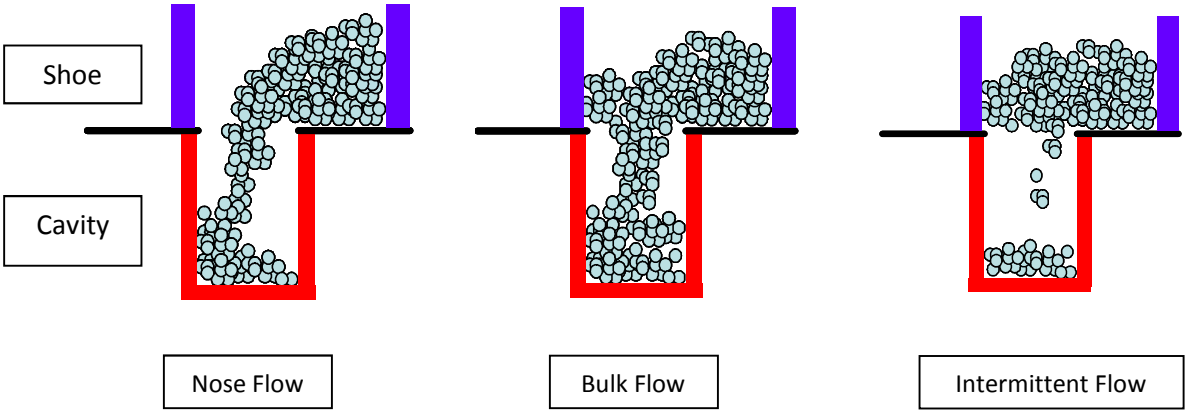

Figure 263 Die cavity flow types in powder pressing [172]

Nose flow is flow under gravity and is the landslide of the front region of the powder. The nose is destabilised as it moves over the die cavity. The first layer of grains can detach and fall into the die with relative ease [172]. Bulk flow occurs after nose flow as the tip of the nose moves across the die cavity. Nose flow dominates the filling process, although at higher speeds bulk flow can dominate [172]. Intermittent flow is the flow of sections of the powder that are held together by inter-particle attraction forces. During intermittent flow, blocks of powder detach from the shoe and fall into the cavity and can result in incomplete filling of the cavity [173]. Various presses exist; typically they can have a fixed base and a moving top or bottom plate, moving top and bottom plates or a hydraulic squeezing motion all around the surface of the powder as in isostatic pressing. Isostatic pressing involves the uniform application of pressure in all directions simultaneously to all external surfaces of a powder body which is sealed in a shaped flexible mould [174]. The pressure is applied by immersing the sealed mould in a fluid in a pressure vessel which is capable of withstanding pressures typically in the range of 14-211 MPa [174]. There are two types of isostatic compaction, wet bag and dry bag isostatic pressing. In dry bag pressing the mould is retained in the pressure vessel during the entire pressing cycle. Dry bag pressing is a form of gas isostatic pressing. In dry bag pressing the powder is pressed inside a polyurethane bag which is hydrostatically pressed through a master bag in a high pressure vessel [175]. This allows for rapid die filling as the hydraulic fluid is not in direct contact with the pressing mould which aids process automation. In wet bag pressing however, the mould is removed from the pressure vessel after each cycle due to being in contact with the fluid

[174]. The end closures are normally steel meaning that they are rigid whilst the bag or mould structure is either rubber or urethane as shown in Figure 264 [174].

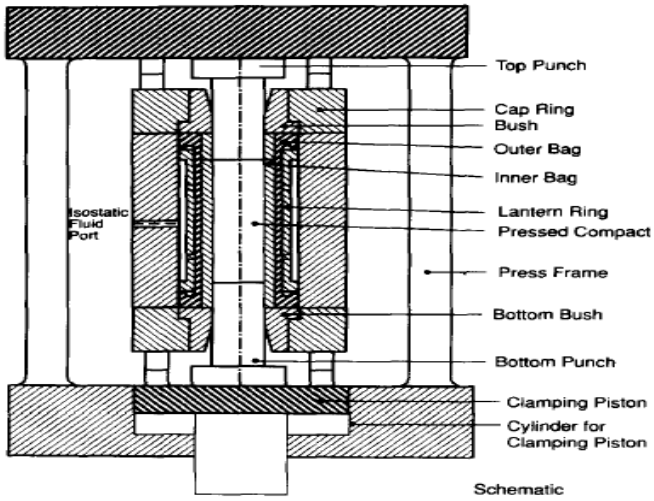

Figure 264 Dry bag press [174]

The choice of press is generally determined by product geometry. Isostatic pressing produces uniform density products more consistently than non-isostatic pressing (Uni-axial) pressing. Uniaxial pressing is more appropriate for flat surface shapes and gives higher reproducibility than isostatic pressing. However, axial pressure can be less than lateral pressure due to load transfer issues [174]. Isostatic pressing also tends to be less able to produce net-shaped products than uniaxial pressing. External axial pistons can be used to regulate the loading and the process then becomes triaxial pressing. Triaxial pressing increases green strength and compact density. It is possible to reach axial pressures of 1200 MPa with a triaxial press, with radial stresses reaching 700 MPa due to the pressure of the oil surrounding the sample [174]. There are three stages of hard material compaction; particle rearrangement, local plastic deformation and plastic deformation. Stage one is dominated by interparticle friction. However, stages two and three are dominated by yield strength, fracture strength and strain-hardening properties [174]. A disadvantage of pressing with WC-Co powder is the relaxation that can occur after decompression. Plastic deformation can cause elastic compression which can cause the material to form centerline cracks upon release of pressure. Hence presses are fitted with damping to prevent the rapid release of pressure from the sample. The relaxation of material is represented by Figure 265, and can be problematic to the point of causing product rupture.

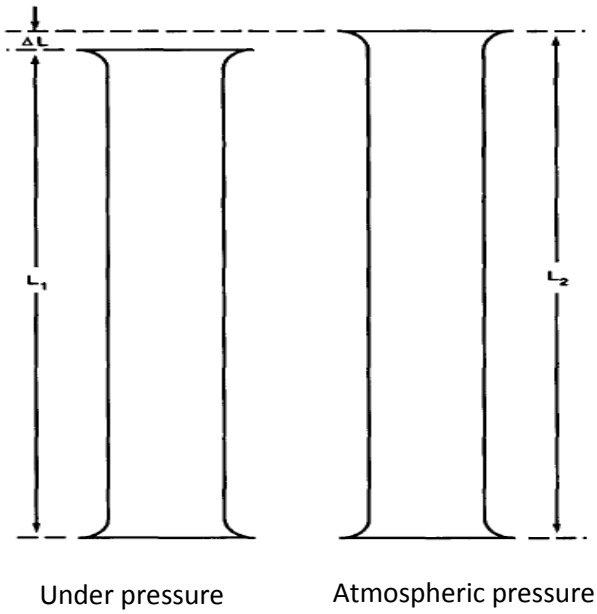

Figure 265 Pressed product, relaxation and elephants foot [174]

At Sandvik Coventry, the same powder production process is used for both pressing and extrusion feedstocks because the ready to press powder (RTP) is used for extrusion. Significant differences between the pressing and extrusion feedstocks only begin at the z-blade mixing stage for the extrusion process. A process flow diagram from the RTP stage onwards for the process of pressing and extrusion is provided in figure 266 and figure 267 respectively:

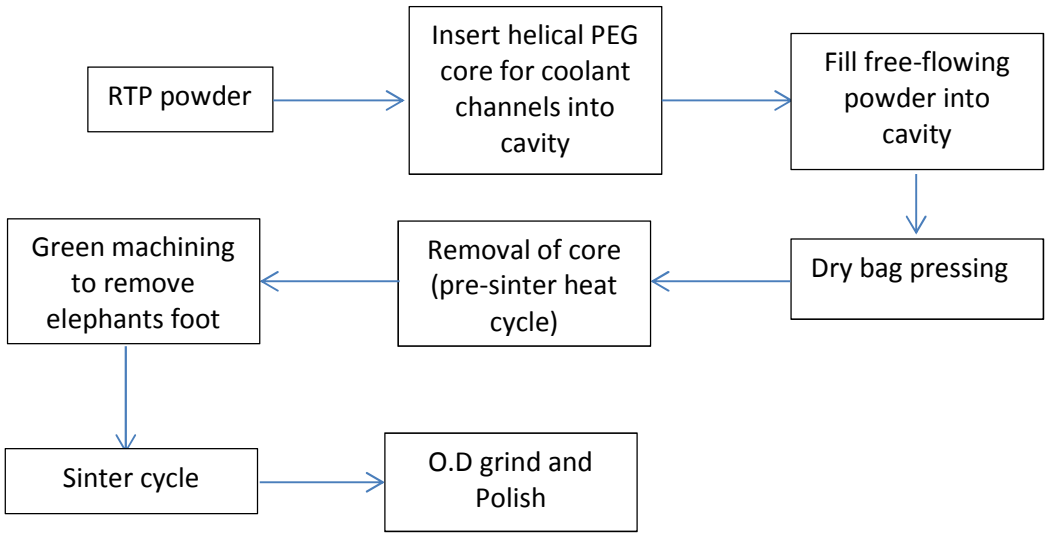

Figure 266 Pressing process flow diagram

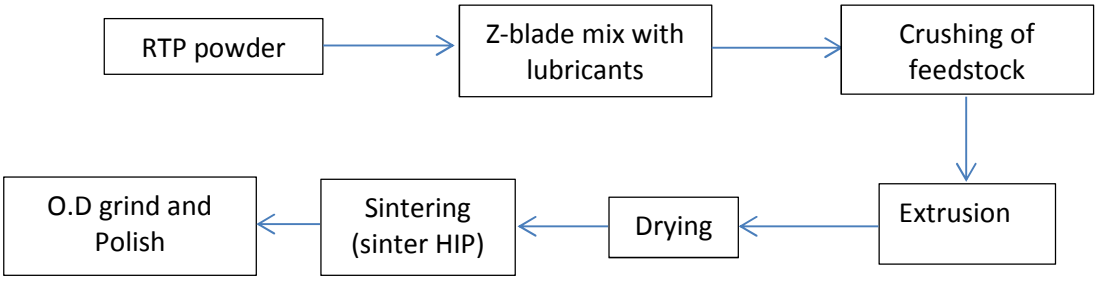

Figure 267 Extrusion process flow diagram

The process flow diagrams help to justify the decision to work with extrusion rather than pressing at Sandvik Coventry. Whilst extrusion is a more intricate and complex process to control, the benefits from the process flow diagrams are clear. Aside from being a more continuous process, there is no internal core to remove from the part and no green machining. Added to these benefits, it is much simpler to achieve completely round coolant holes, which is not possible in the pressing process as the holes become deformed under high pressure. A tight tolerance on coolant hole roundness exists in the production environment as it is a demand from the customer. Similarly there is no deformation of the extrusion tooling as there is with pressing cavities, thus enabling the formation of constant cross-section parts with no green machining much more easily.

Appendix B - Pressing Binders

Ceramic bodies are often made according to a powder processing method that involves spray-drying of a slurry followed by dry pressing of granules [176]. The green strength of the powder is increased by the addition of organics. This also allows for handling and machining of the part after pressing. Without the organics in the formulation the powder would break up after pressing and not maintain structural integrity. Polyethylene glycol (PEG) and polyvinyl alcohol are common binder additives for pressing and can be used in combinations with each other. The organic binders present in ceramic compacts also have influences on material properties such as creep, relaxation and elastic strain [177]. Baklouti [178] concluded that the presence of organic binders in pressing compacts improved both mechanical strength and Young's modulus in the green state.

Pressing Polyethylene Glycol Binder for Pressing

Polyethylene glycol (PEG), a commonly used binder for uniaxially pressed alumina compacts was initially used to increase the green strength. Baklouti et al. observed that the green strength of alumina-PEG samples increased linearly with pressing pressure before plateau was reached. The mechanical strength of compacts containing PEG was consistently greater than alumina powder with no binder. The plateau is a result of removing inter-granular porosity when the surface contact between granules reaches a maximum at higher pressures. Although mechanical strength increases, the distribution of binder around the powder particles is in-homogenous [176]. Fracture surfaces of the PEG based alumina compacts showed intra-granular fractures. Cracks propagated through the granules rather than inter-granular fractures observed with samples containing polyvinyl alcohol binders. PEG is hygroscopic; the intake of water makes PEG binders sensitive to environmental changes. Due to water solubility, PEG can also migrate to the granule surface during spray-drying which promotes a non-homogenous PEG distribution. This creates non-uniform behaviour throughout the part as the PEG concentration following pressing is greater at the sample surface [179].

Polyvinyl Alcohol Binder for Pressing

In the case of pressed alumina parts, PVA binders gave greater mechanical strength than PEG binders although this required higher pressures to achieve such strength. Due to inter-granular fracture (cracks propagating through deformed granules) the samples were also more brittle [175]. As with PEG binders, PVA is also sensitive to humidity and as a result pressing performance can suffer because PVA is plasticised by water. Tanaka [179] also found that PVA binders tended to segregate on the surface of granules. This caused the formation of defects in green and also de-bound and

sintered compacts. It was observed that hard elastic granules (formed from PVA) produced large flaws in green compacts.

Appendix C –De-binding Summary

Table 48 WC-Co wax binder de-binding summary

Debinding method	Materials	Binder	Removal technique	Advantages	Disadvantages
Vacuum Dewax	WC	Paraffin wax	13.3 Pa partial pressure during debinding	Low cost equipment	Longer clean up time due to wax build up in chamber. Shorter hot zone and insulation life. Less carbon control due to cracking of wax during debinding
Sweepgas (WC)	WC	Paraffin wax	133-1333 Pa partial pressure with argon sweepgas flowthrough	Less furnace maintenance. Increased hot zone insulation and element life. Removes wax from hot zone before contact with elements. Ensures constant vacuum level.	Could require change in customers formulation due to removal of more carbon during debinding. Expense of additional equipment including vacuum sensors, gauges, valves. Uses small quantities of inert gas during binder removal.

Table 49 Ceramic de-binding summary

De-binding method	Materials	Binder	Removal techniques	Advantages	Disadvantages
Positive pressure debinding (inert gas/hydrogen)	WC, MIM, powdered metals, Ceramics	PEG, PVA, PVOH, Acrawax, Stearates, Phenolics.	Positive pressure flow through (Ar, N_2 or H_2)	Reducing atmosphere gives complete combustion of organics. Positive pressure bathes parts in inert gas for better uniformity. No cold spots.	Not 100% effective for tarry binders requiring longer residence time. Expensive H_2 system. Expensive incinerator.
Continuous furnace thermal debinding	SiC, Si_3N_4, AIN, Electronic ceramics	Methyl- Cellulose Phenolics Epoxies PVA/PVOH	Atmospheric de-bind	Capability of handling tarry, sticky binders in high volume.	Routine maintenance required.

Table 50 Tool steel de-binding summary

De-binding method	Materials	Binder	Removal technique	Advantages	Disadvantages
Sweepgas (MIM/CIM)	Carbonyl iron Tool steels Ti super alloys	Wax/PP,PE Polymer Agar Polyacetal Various	1333-500 Pa partial pressure with sweep gas flow through or positive pressure inert gas/H_2 flow through	Precise gas flow over each individual tray and part ensures complete binder removal. Allows partial pressure or positive pressure binder removal with Ar, N_2, and H_2 gases. Higher partial pressures provide better heat transfer mechanism than pure vacuum environment for de-binding.	Expensive furnace design, and longer debind time.
Injectavac (MIM)	Carbonyl iron Tool steels Ti super alloys	Wax/PP,PE Polymer Agar Polyacetal Various	0.133 Pa wax diffusion pump de-binding & 1333-66660 Pa. sweep gas polymer removal	Inexpensive design, low operating costs. Capable of sintering most steels. Efficient binder removal.	Cannot be used for some special alloys due to carbon control.

Appendix D -Binder Flow Curves

Binder Group 2

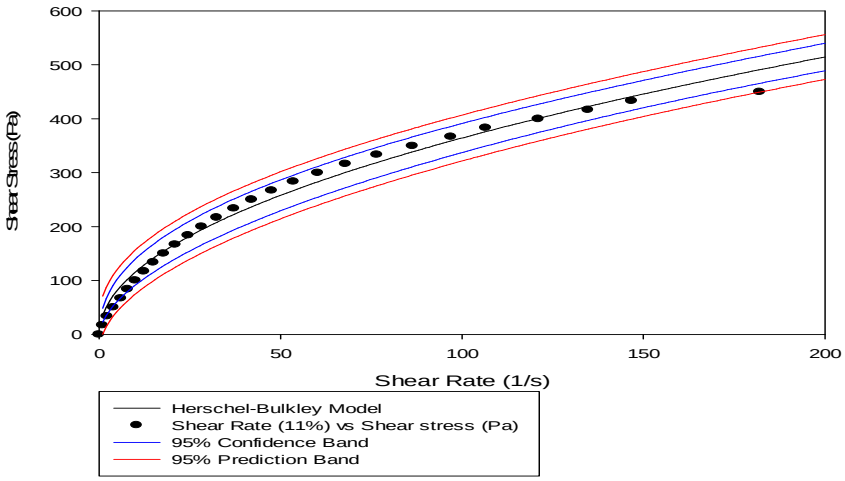

Figure 268 MC, Water 11% shear stress as a function of shear rate

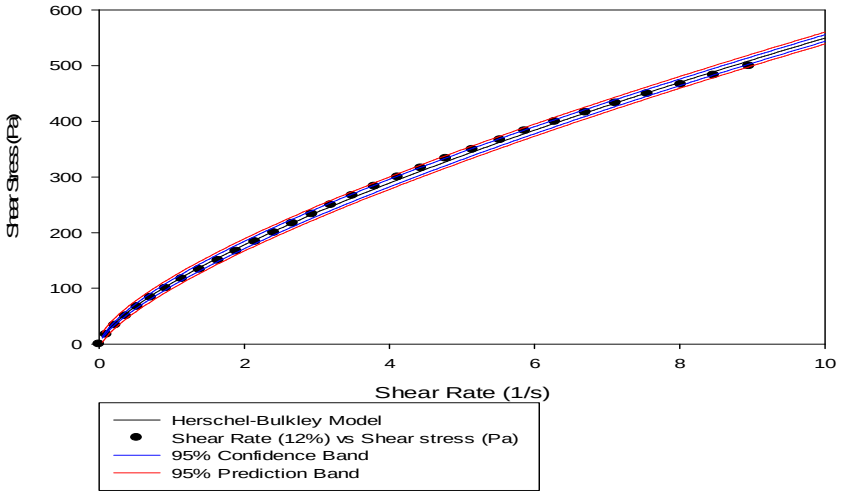

Figure 269 MC, Water 12% shear stress as a function of shear rate

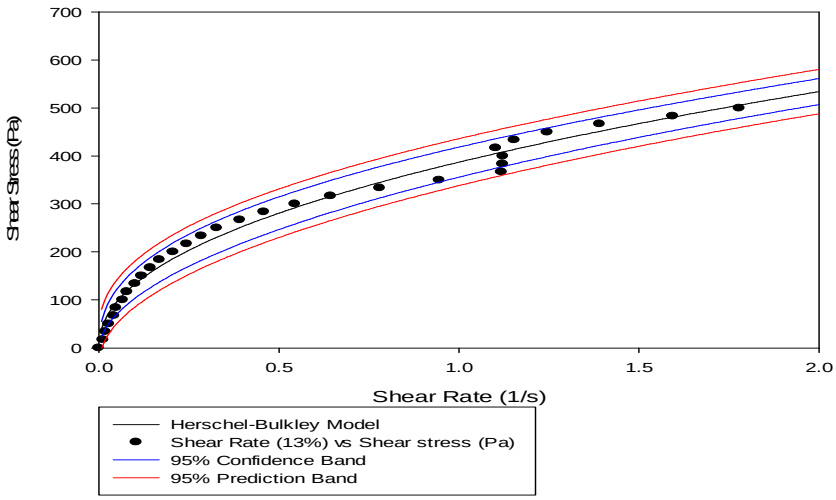

Figure 270 MC, Water 13% shear stress as a function of shear rate

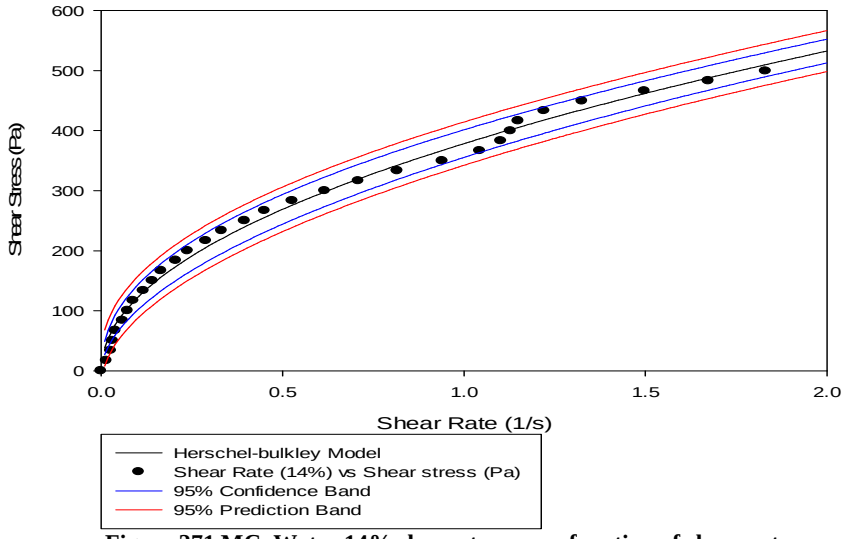

Figure 271 MC, Water 14% shear stress as a function of shear rate

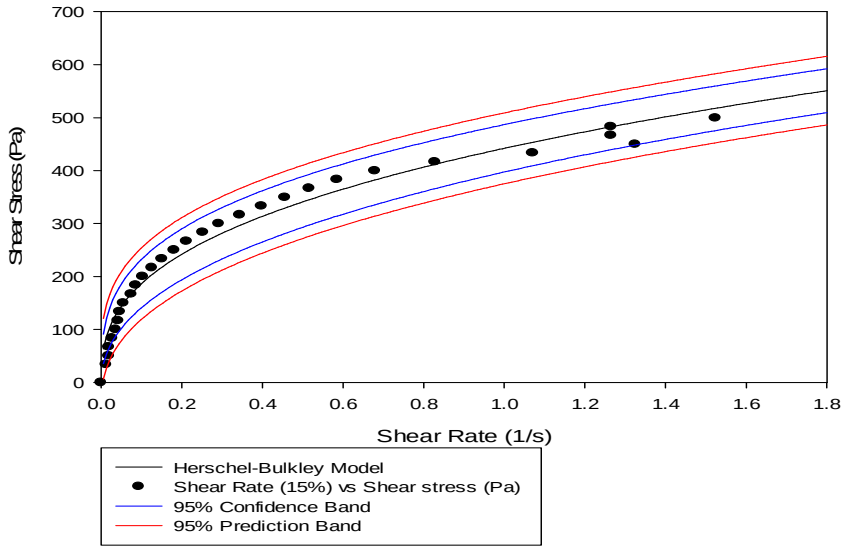

Figure 272 MC, Water 15% stress sweep

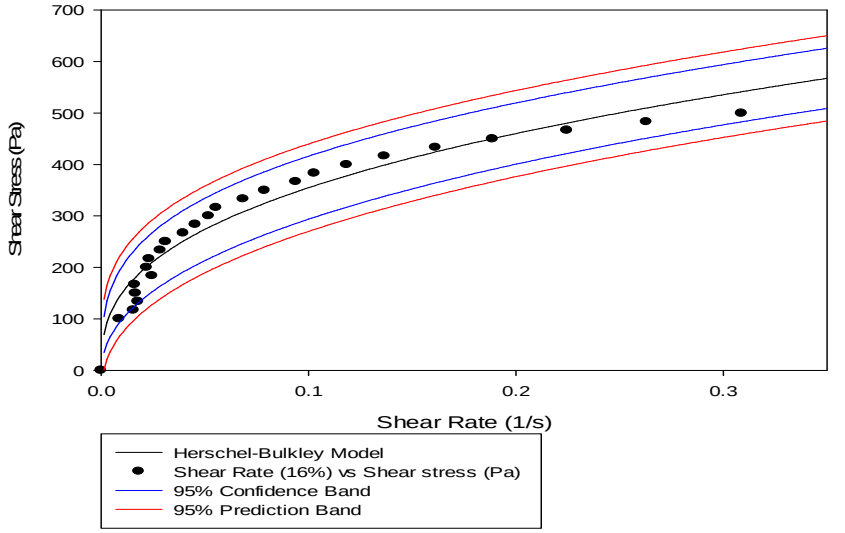

Figure 273 MC, Water 16% shear stress as a function of shear rate

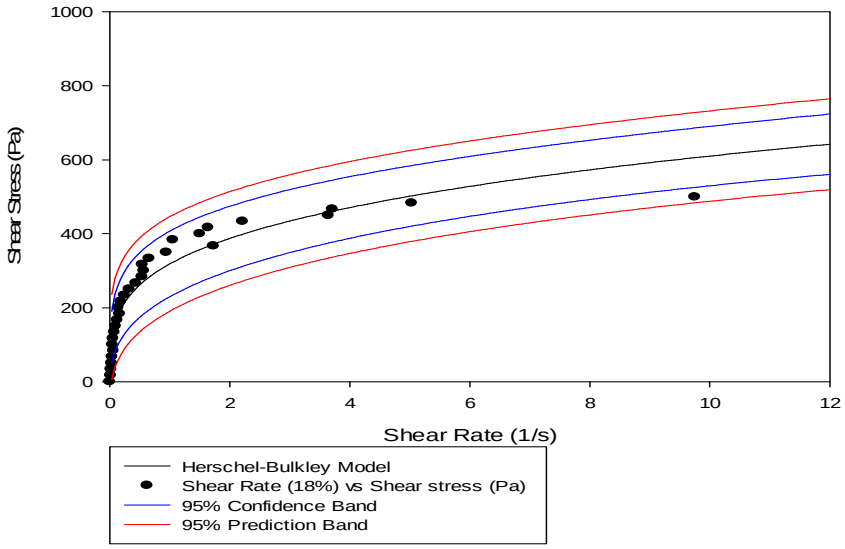

Figure 274 MC, Water 18% shear stress as a function of shear rate

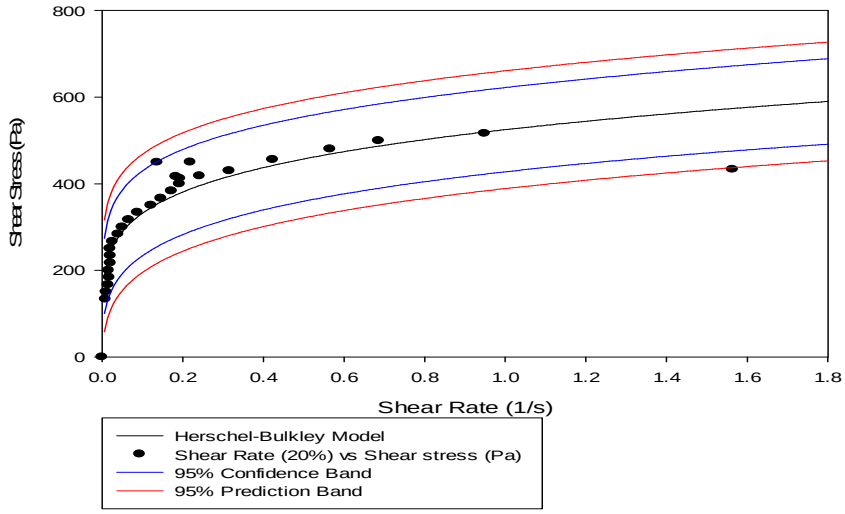

Figure 275 MC, Water 20% shear stress as a function of shear rate

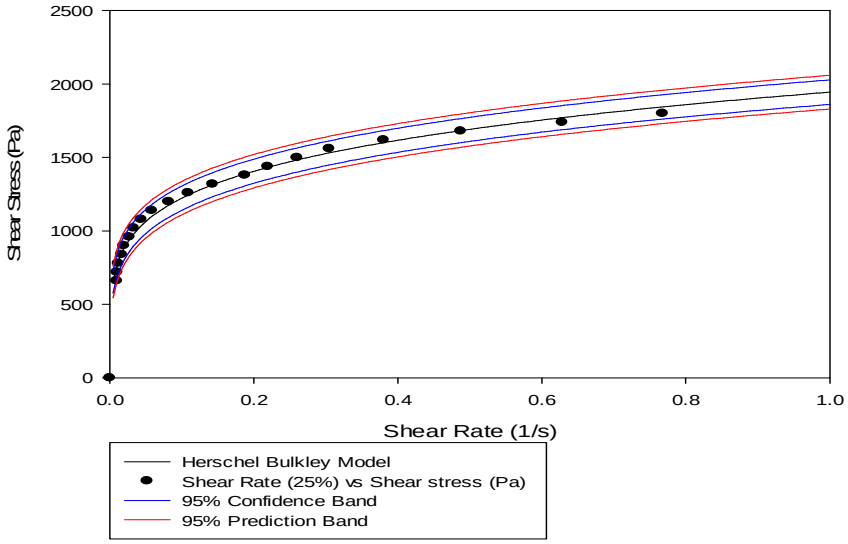

Figure 276 MC, Water 25% shear stress as a function of shear rate

Appendix E -Binder Flow Curves

Binder Group 3

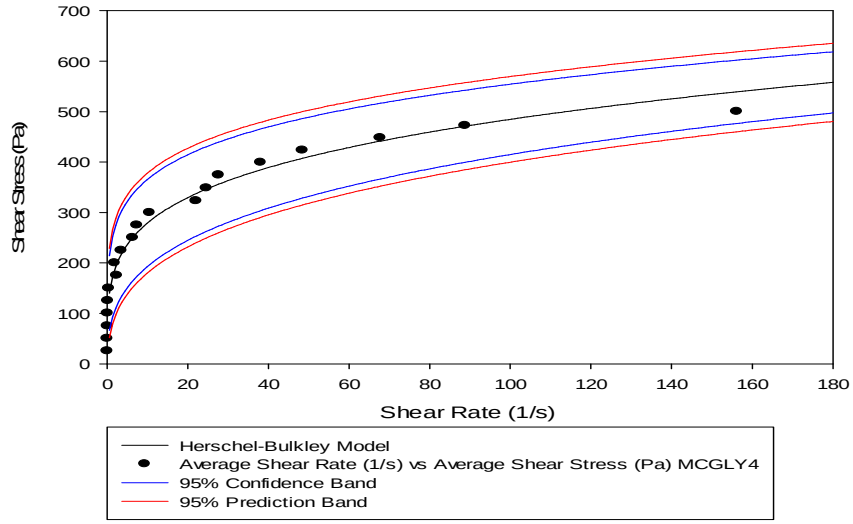

Figure 277 MCGLY3 shear stress as a function of shear rate

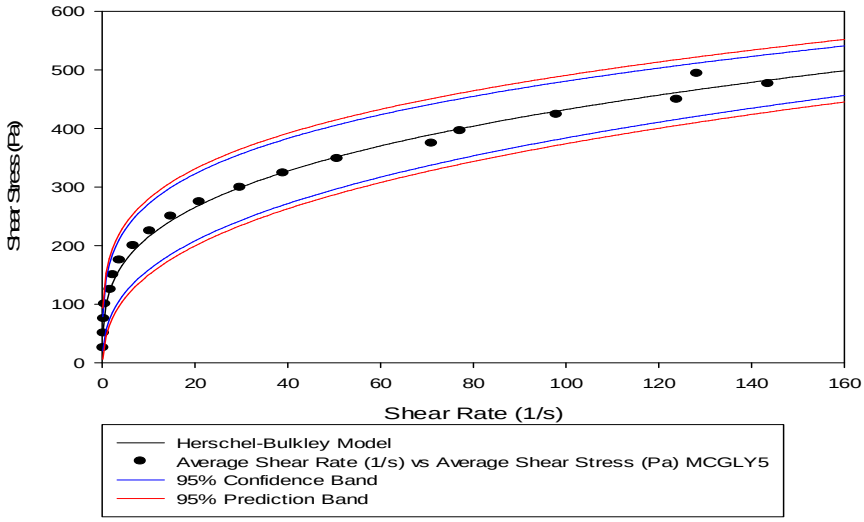

Figure 278 MCGLY4 shear stress as a function of shear rate

Appendix F-Binder Flow Curves (Oscillatory Rheometry)

Binder Group 2

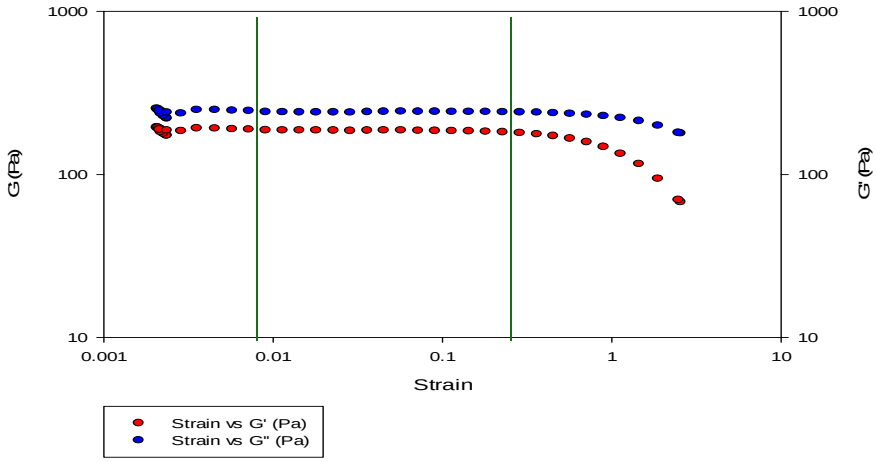

Figure 279 MC, water (11%) LVER, showing elastic and viscous components as a function of strain

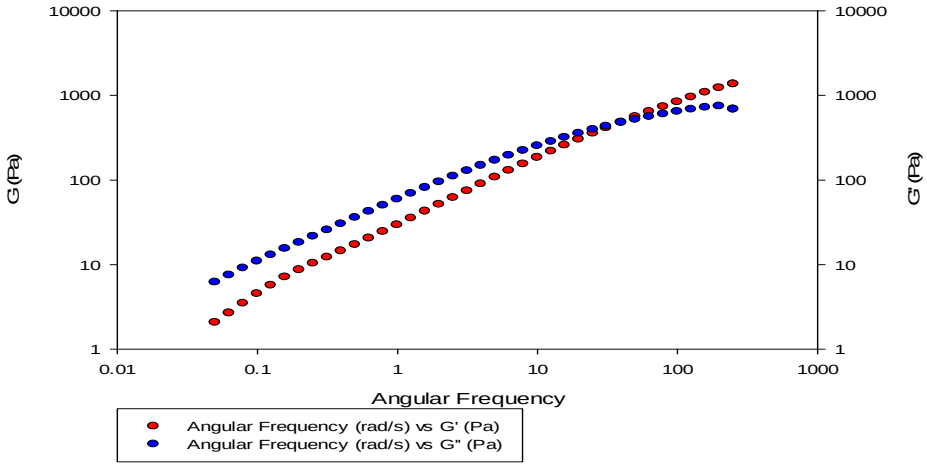

Figure 280 MC, water (11%), showing elastic and viscous components as a function of frequency

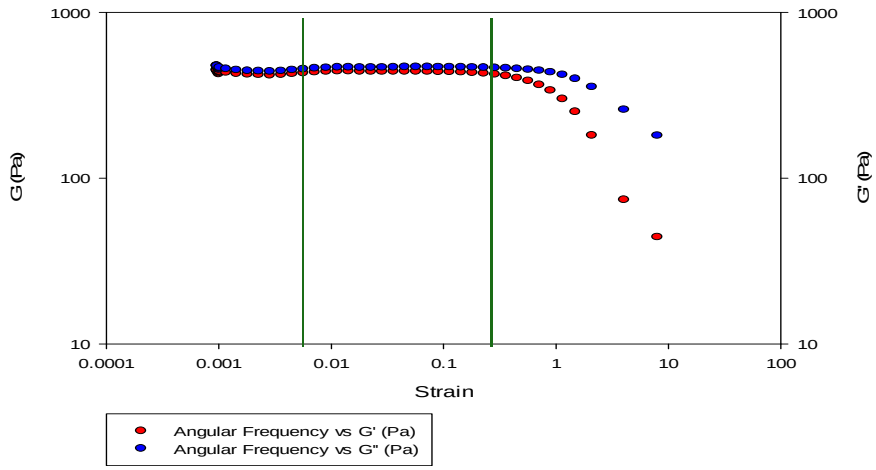

Figure 281 MC, water, (12%) LVER, showing elastic and viscous components as a function of strain

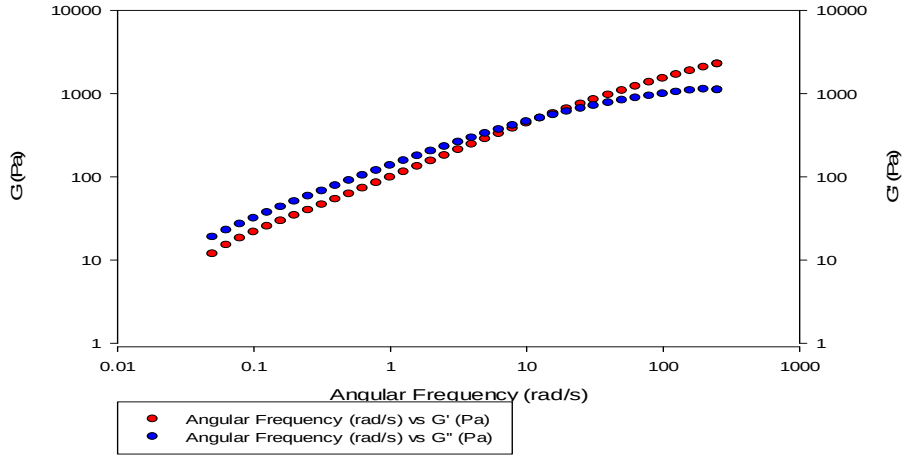

Figure 282 MC, water (12%), showing elastic and viscous components as a function of frequency

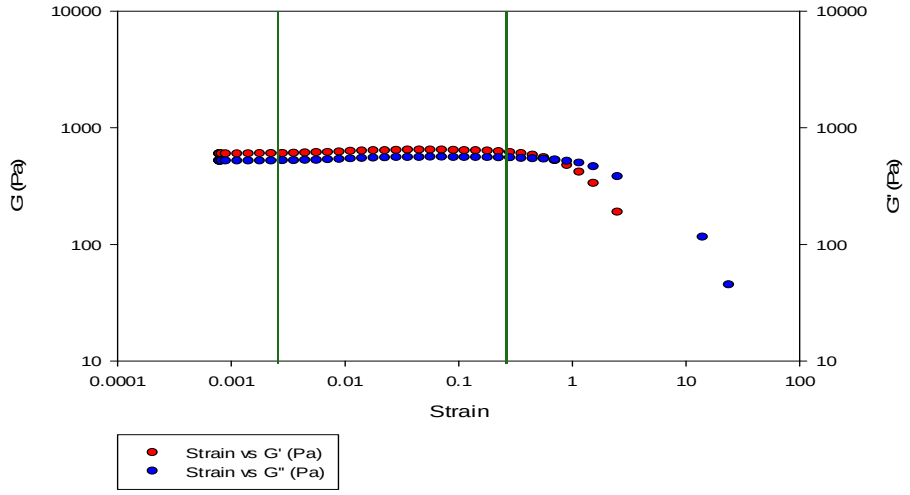

Figure 283 MC, water (13%) LVER, showing elastic and viscous components as a function of strain

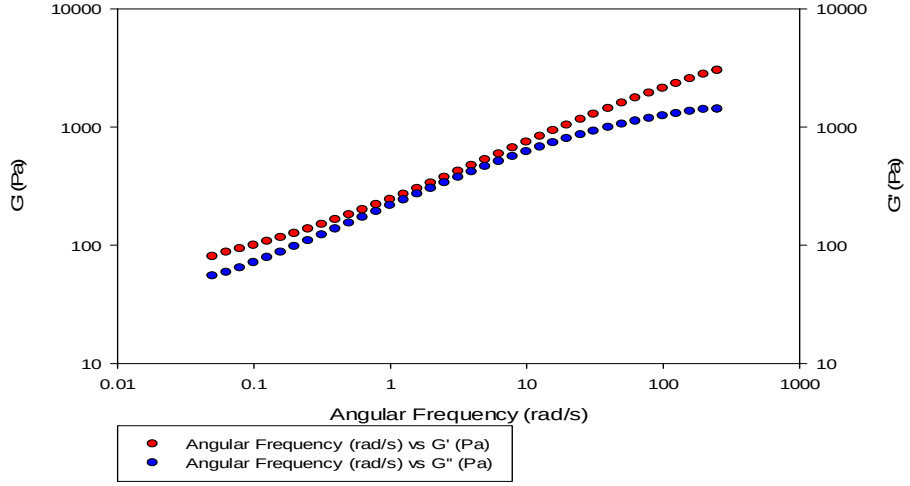

Figure 284 MC, water (13%), showing elastic and viscous components as a function of frequency

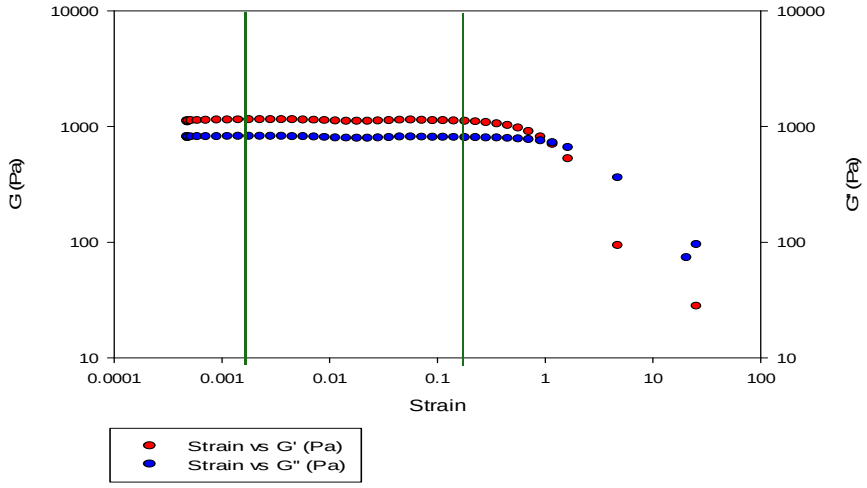

Figure 285 MC, water (14%) LVER, showing elastic and viscous components as a function of strain

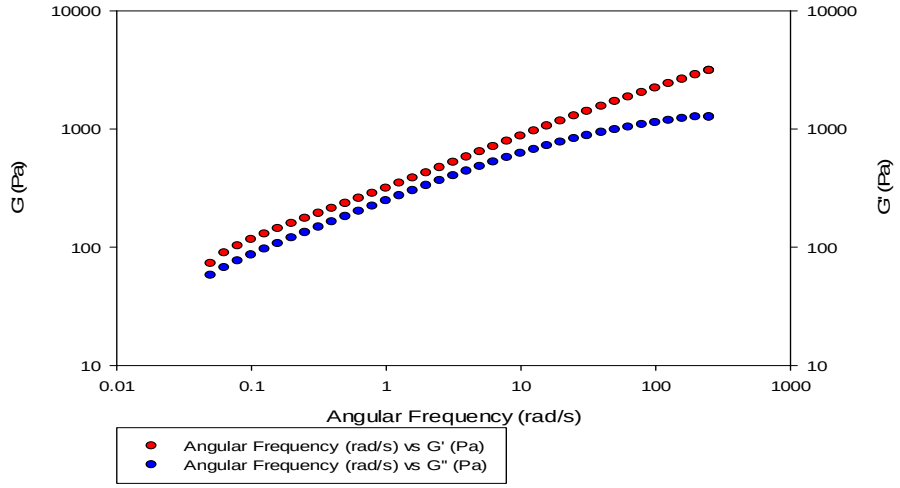

Figure 286 MC, water (14%), showing elastic and viscous components as a function of frequency

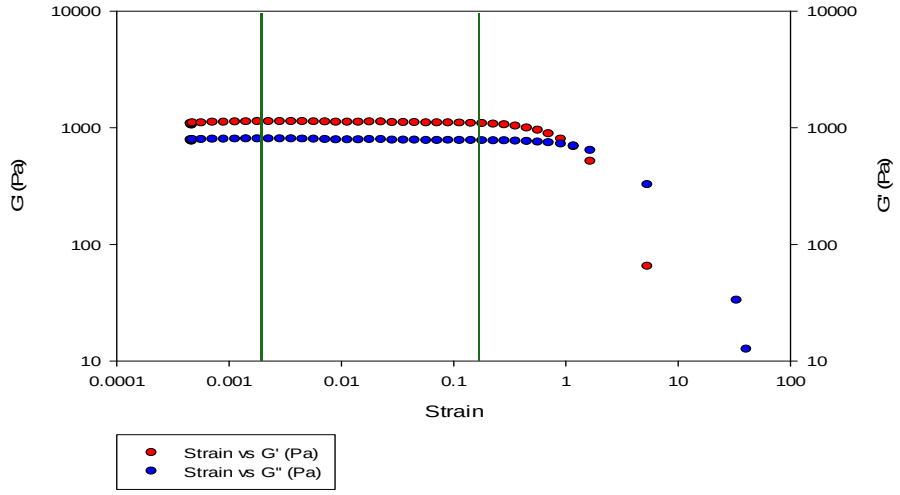

Figure 287 MC, water (15%) LVER, showing elastic and viscous components as a function of strain

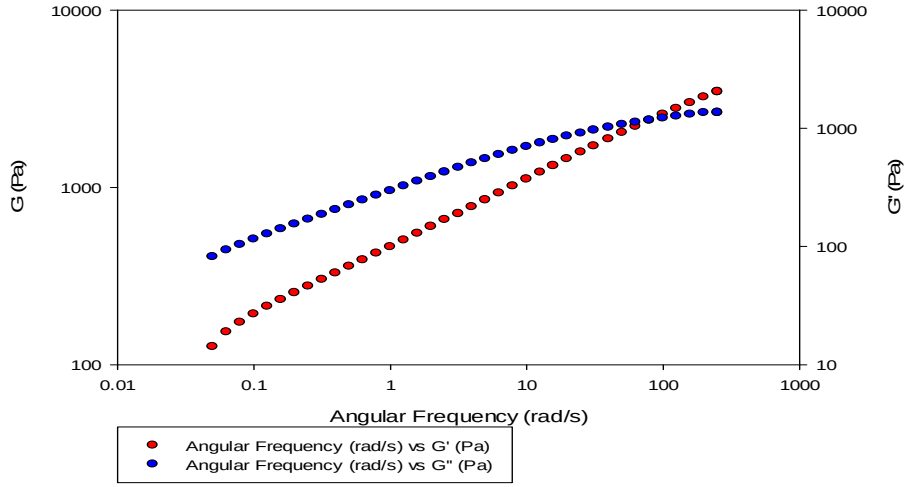

Figure 288 MC, water (15%), showing elastic and viscous components as a function of frequency

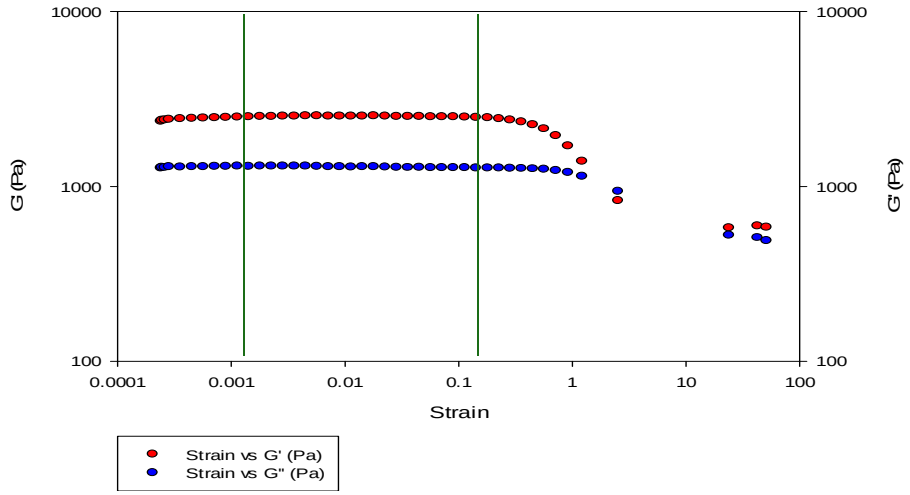

Figure 289 MC, water (16%) LVER, showing elastic and viscous components as a function of strain

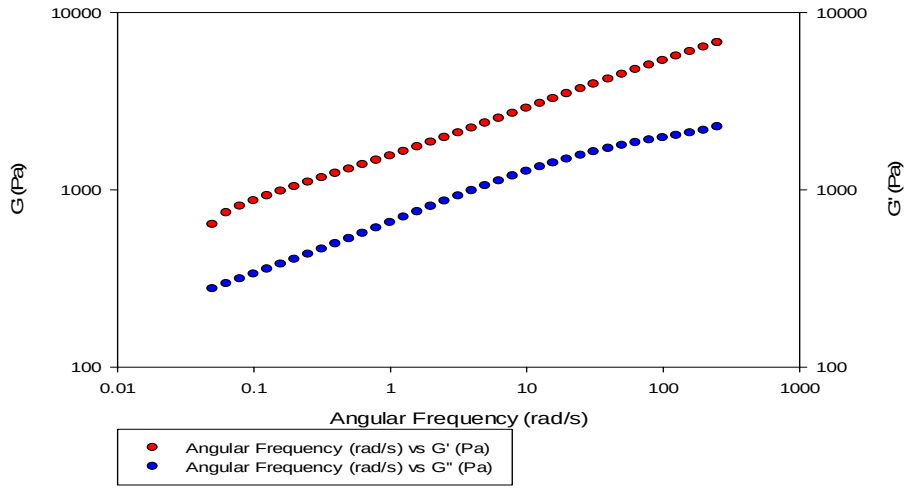

Figure 290 MC, water (16%), showing elastic and viscous components as a function of frequency

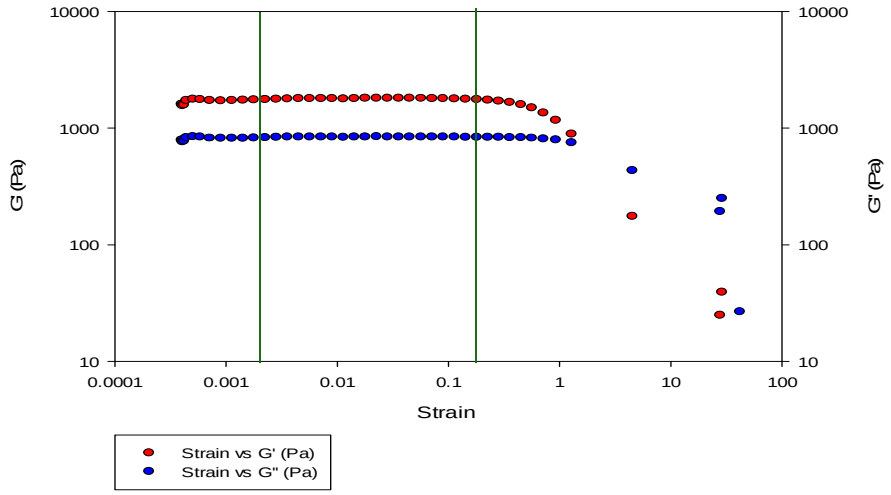

Figure 291 MC, water (18%) LVER, showing elastic and viscous components as a function of strain

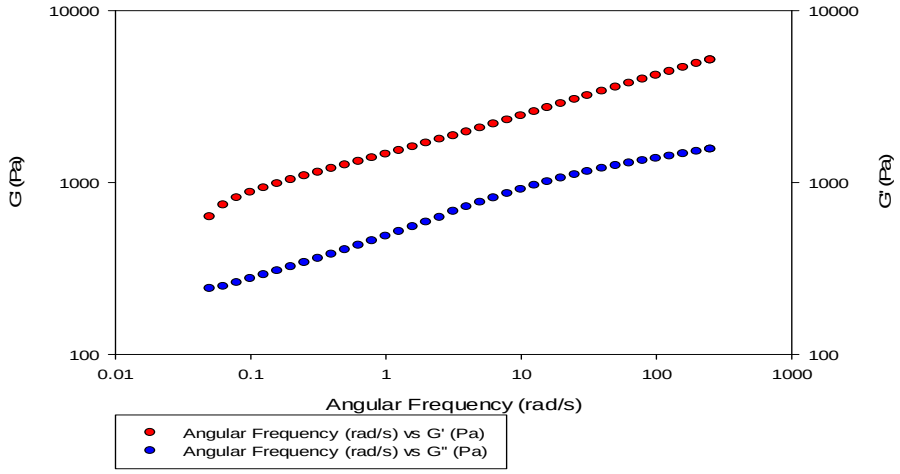

Figure 292 MC, water (18%), showing elastic and viscous components as a function of frequency

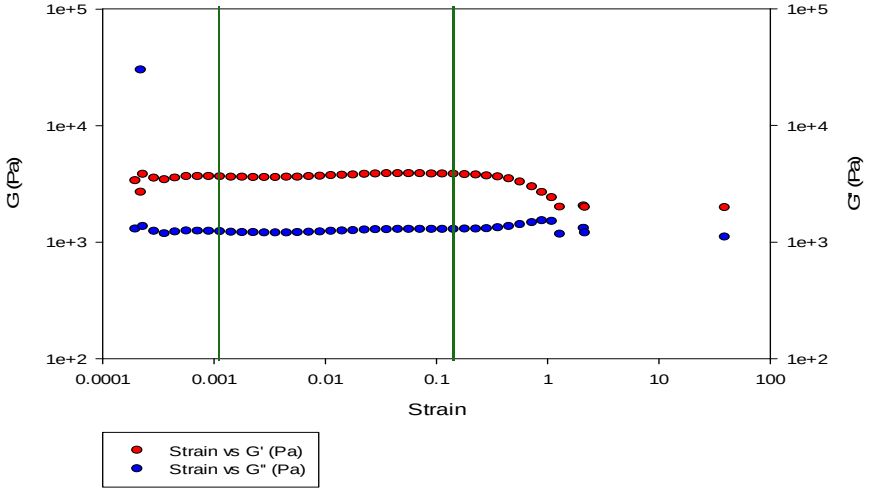

Figure 293 MC, water (20%) LVER, showing elastic and viscous components as a function of strain

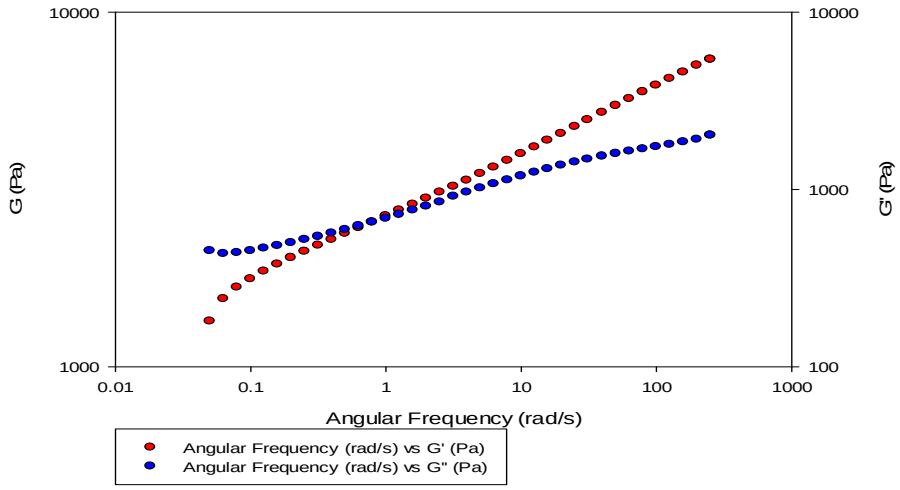

Figure 294 MC, water (20%), showing elastic and viscous components as a function of frequency

Appendix G-Binder Flow Curves (Oscillatory Rheometry)

Binder Group 3

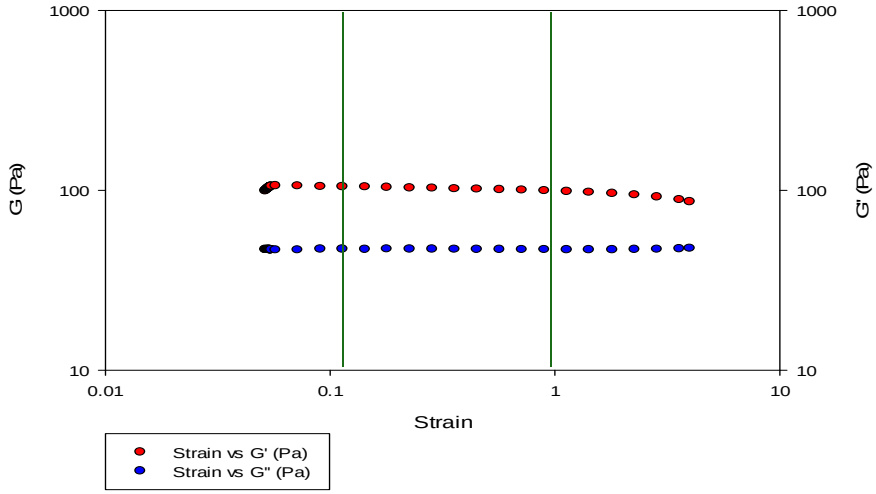

Figure 295 MCGLY4 LVER, showing elastic and viscous components as a function of strain

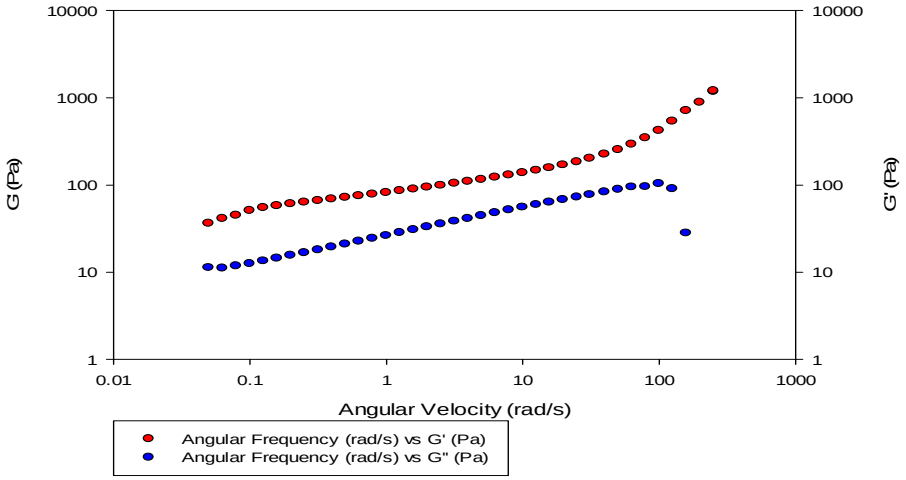

Figure 296 MCGLY4, showing elastic and viscous components as a function of frequency

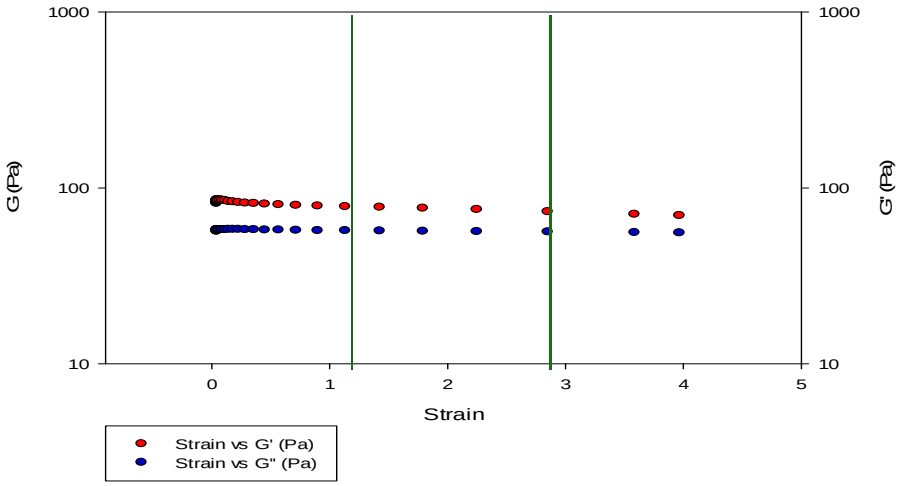

Figure 297 MCGLY5 LVER, showing elastic and viscous components as a function of strain

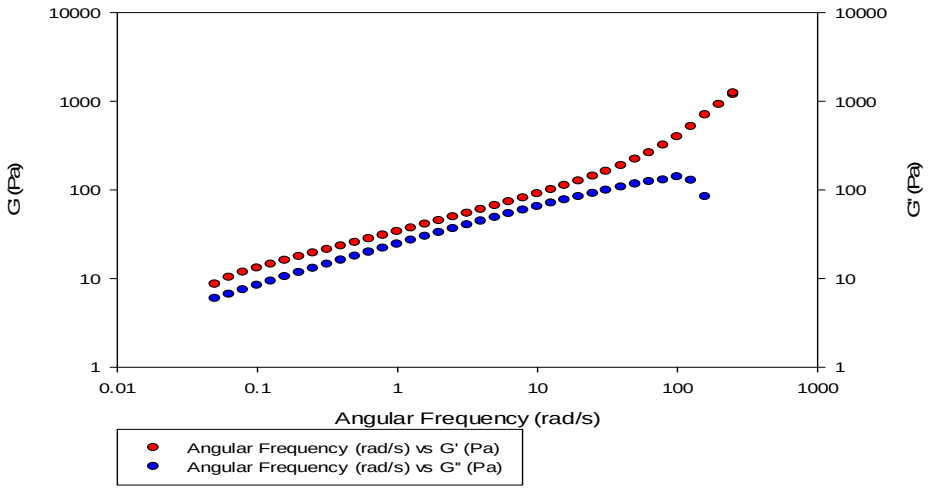

Figure 298 MCGLY5, showing elastic and viscous components as a function of frequency

Appendix H -Dough Temperature Measurements and Investigation

Mixer temperature was recorded with mixing time for each of the feedstocks prepared while mixing temperature was restricted by external cooling. Temperature was taken in the mixer bowl although localised dough temperatures closer to mixer blades were higher .Mixing temperatures for group 1 feedstocks have been plotted in Figure 299. Trends have been investigated for the MC dough formulations and have been plotted in Figure 300. Mixing was completed in under 30 minutes although doughs prepared with MCM MW 61000 and MCGLY5 required 40 minutes to achieve homogeneity. The completion of mixing was realised once a stable torque reading could be taken. Wu et al. [180] report that a wide scattering of torque during mixing implies that either inhomogeneous solid content or a distribution of temperature exists. This was observed during the early stages of mixing as the WC-Co was not well distributed throughout the batch. Although mixing temperature increased with mixing time, it was assumed to be uniform throughout the mix once stable torque was reached. The mixing temperature of GCMPG dough was initially higher than the mixer temperature of other feedstocks. Conversely, the mixing temperature of the ECETHPVB feedstock was lower. This is due to dough viscosity and viscous heating, described in section 3.7.4. The MCPAM dough however generated the lowest stable torque (Table 31) associated with low shear viscosity and had a high mixing temperature (Figure 299). Therefore viscous heating could not be systematically identified for group 1 dough. Figure 299 has been used to show how the mixing temperature of each system increases during mixing. The rate of temperature increase is similar for each feedstock despite significantly different WC-Co content. As the water cooling system is fixed and assuming that the water at the inlet, flow rate and cooling surfaces are constant, the rise in temperature indicates viscous heating (work). The heat transfer is insufficient to remove all of the generated heat. As a similar slope exists for each material in group 1, viscous heating is reasonably consistent between binders.

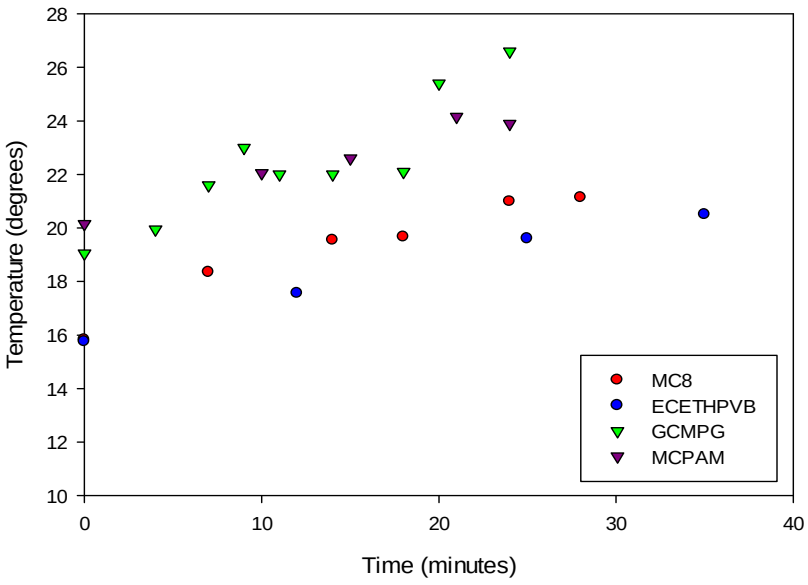

Figure 299 Group 1 binders dough temperature as a function of mixing time

Mixing time is plotted against temperature for group 2 doughs in Figure 301. Mixing temperature increases with increasing cellulose content up to MC15 dough. Temperature increased in this way due to viscous heating. Dough viscosity increased with cellulose content and therefore more work was required to mix dough systems with higher cellulose content. MC16 dough is an exception as this system was tending towards granulation. Granulated systems typically come into contact with thermocouples less effectively than well wetted formulations and therefore the temperature is recorded as a lower value. Figure 300 resembles the schematic torque plot in Figure 151. Torque however did not increase so systematically (Table 31). Spikes in temperature are unusual as the sensor would not normally respond so quickly to changes. Added to increased torque as a result of a stiffer binder at increased cellulose content, the temperature profile in Figure 300 also rises and plateaus. At the onset of mixing, the binder is stiffer which causes a rise in temperature, due to heating the binder thins and therefore temperature reduces to a steady state providing that gelation of the cellulose isn't reached (40 °C).

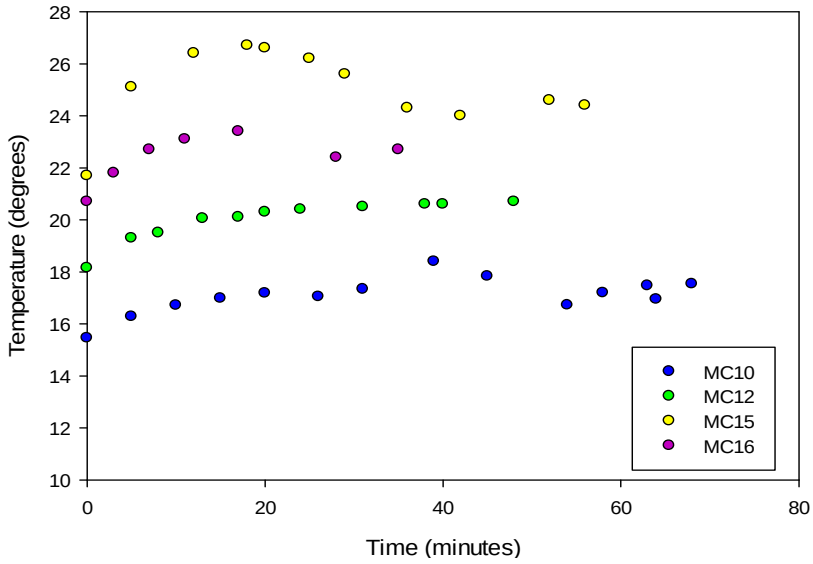

Figure 300 MC variants dough temperature as a function of mixing time

Figure 301 shows mixing temperature against mixing time for MC8 dough (group 4). WC-Co solids loading was systematically increased by 0.1 volume % in stages although significant changes in mixing temperature were not observed.

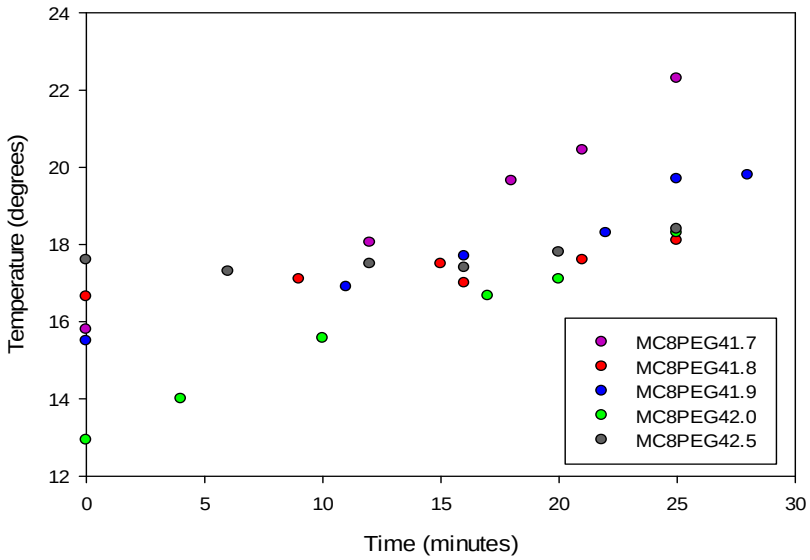

Figure 301 MCPEG dough temperature as a function of mixing time

Mixer Temperature Investigation

Mixer temperature increased due to friction between blades, material and bowl surfaces and work done on the material. Higher temperatures were generated for the GCMPG and MCPAM dough systems (Figure 299). This was expected because a higher torque was generated with these dough systems than with the ECETHPVB dough. The higher torque was associated with greater dough shear viscosity and therefore greater frictional forces. The MC8 dough formulation also generated high

torques during mixing yet had a relatively low mixing temperature. After mixer bowl examination, the surfaces were wetter for this material indicating that some phase migration had occurred. This promoted accelerated heat transfer and explains the lower mixing temperatures at the bowl surface where the temperature sensor was positioned. Figure 300 shows that with the exception of the MC16 formulation, mixer temperature increased with increasing cellulose content due to an increasing viscosity and subsequently mixing torque despite having controlled (and fixed) external cooling. This increases the energy and heat that was transferred to the material according to the viscous heating equation reported in 3.7.4. The effects on mixing temperature due to increased WC-Co solids loading were less noticeable as observed in Figure 301. Lab scale extrusion, extrudate drying and sintering contributed to the decision that initially the methyl cellulose dough formulation at 8% cellulose concentration would be evaluated on a production scale.

Appendix I -Production Scale Activities

Pre-mixes were prepared as described in section 3.3.3. Extra batches were prepared to account for 150 Kg WC-Co which is a pre-determined powder mass for the size of mixer. Large scale mixing was carried out in Winkworth Z-blade mixers. Large scale Z-blade mixers had an Archimedes screw in the bowl base for material removal. The screw rotates during operation to promote better mixing by re-circulating material that has fallen beneath the blade rotation. Temperature was not easily controlled as cooling water was only available from a mains water supply and was not chilled. In contrast to laboratory scale, mixing temperatures varied from 20-30 °C rather than 10-20 °C. Torque was measured as a percentage of the maximum achievable torque which was an unknown quantity for the large scale mixers. On a production scale, the tolerances were also more relaxed and mixing was therefore less efficient for a given volume of material. Following production scale mixing, the extrusion feedstock was passed through a mesh size of 5 mm^2. Crushing provided a more uniformly sized feedstock. Thus other than temperature differences and dough crushing, mixing proceeded as described in section 3.6.2.

Production Scale Extrusion

Production scale up to 14 mm sintered diameter used the same tooling as used pilot scale extruder. Each of the presses is manufactured by Loomis and hence the majority of tools are interchangeable. The barrel diameter however was considerably larger giving a reduction ratio of 1/4 down to the spider (rather than 1/1.5). Both the 8 and 10% methyl cellulose variants of dough feedstock were evaluated on production scale. Extrudate travelled onto an air track to reduce drag induced stresses on the product. Air track conditions were modified from the standard production settings to reduce blow drying which was not ideal for the aqueous systems. The air track was required to allow rods to move freely once extruded. This was particularly important for the twisting of the rods during coolant hole formation. Magnetic Lifting and mechanical moving of rods was automated, allowing for consistent production of rods at a rapid extrusion rate. Pressure data from extrusion trials for the 8 and 10% methyl cellulose dough feedstocks is given in Table 51. A pressure range from start to finish of the extrusion run has been given.

Table 51 Production trials extrusion running conditions

Date of Trial	Binder	Product	Ram Speed (mm/s)	Paste Pressure range (MPa)
2012 week 24	8%	14 mm coolant	0.25	14.34-13.938
2012 week 31*	10%	14 mm coolant	0.25	28.89-27.47

*Tooling set up changed to include improved core pin design and longer die land in the nozzle section.

On a production scale 10 Kg's of dough was first pre-compacted under vacuum before loading the full batch. This insured that the front section of the gun including tooling could be held under vacuum before loading. The press was held under vacuum for 60 seconds when fully loaded. An initial ram speed of 0.07 $mm.s^{-1}$ was use to fully compact the dough and reach stable conditions of pressure before extruding at 0.25 $mm.s^{-1}$ for 14 mm product. 20 mm product was extruded at 0.5 $mm.s^{-1}$ ram speed to give an equivalent extrudate speed of 1 rod per 18 seconds. Each rod was 450 mm long. Handling was automated for 14 mm diameter product, producing 65-70 rods per batch. Tooling was modified over a series of tests to achieve the best processing conditions. 20 mm rods were manually handled initially due to their weight overcoming the magnetic picking system. Although extrusion on a small scale was successful with the MC8 binder, larger scale and more demanding processing conditions in a production environment required a stiffer formulation. Whilst handling conditions were less demanding due to automation, the process of extrusion was significantly different. Due to barrel size, 150 Kg of material could be used in one batch thus improving consistency, although extrusion processing had a significantly longer time frame. Typically, extrusion runs took 3 to 4 hours to complete rather than half an hour on a pilot scale. Longer processing times coupled with higher equipment temperatures encouraged moisture loss from the binder formulation. Phase migration was also accelerated with the larger volume of material and increased die pressures due to greater barrel to die size reduction (Figure 302).

Figure 302 Evidence of liquid phase migration onto extrusion tooling surfaces

Residue coated the tooling surfaces after a complete production trial, showing that there has been preferential flow of the liquid phase. This would result in changing properties of the extrudate as the ratio of solid to liquid phase would increase in favour of the solid during extrusion. Other issues associated with production extrusion that had not been encountered in the small scale testing was a phenomenon termed cork-screwing. Filaments are shown in Figure 51 and were initially designed to be passive and follow the flow of material through the rifled die. However, extrusion flow was disrupted due to filament resistance. With SHM dough, filaments were forced into the path of the extrudate and therefore followed the helical pattern caused by rifling in the die nozzle. Filaments have a small resistance to extrusion flow and softer feedstocks are more susceptible to disruption caused by this resistance. Disruption to extrusion flow can result in bending or corkscrewing of product as shown in Figure 303.

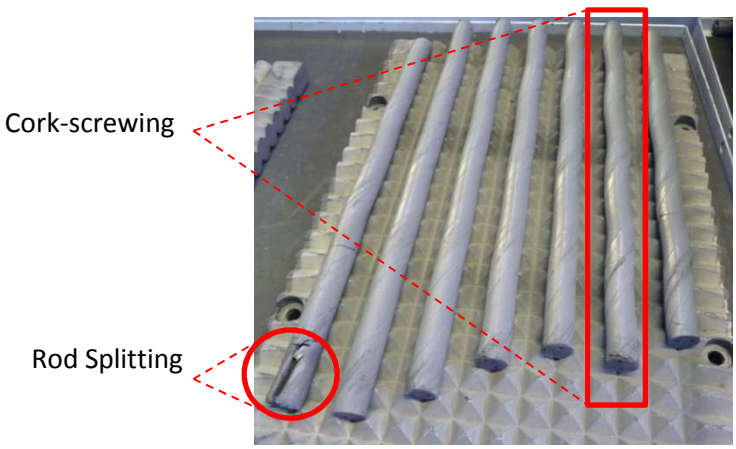

Figure 303 Extrudate corkscrewing behaviour

The bend shown in Figure 303 follows the pitch of the rifling in the extrusion die and this is mild cork-screwing. Rod splitting however was caused by the movement of filaments. Filament

movement physically blocked extrudate flow against the inner wall of the extrusion die by pinning material in place (Figure 304). This caused incomplete die filling (Figure 305). Faster ram speeds prevented the blockage of extrusion flow by keeping filaments in the correct position. However a dough of higher shear viscosity (MC10) was a more effective method of solving the issue.

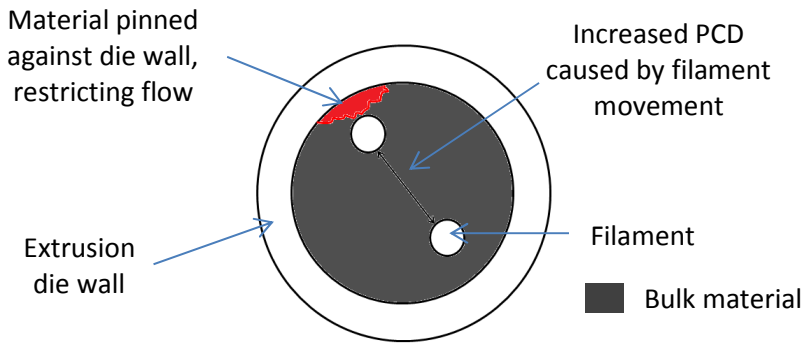

Figure 304 Filament movement causing trapped material against extrusion die inner wall

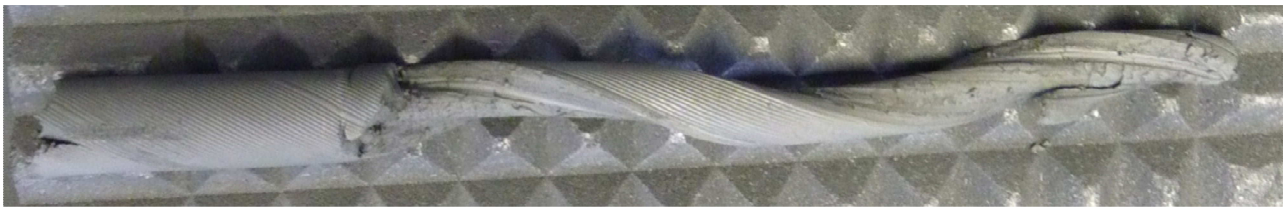

Figure 305 Extreme cork-screwing behaviour of extrudate

The MC10 based extrusion feedstock doubled extrusion pressures achieved from the early 8% trials (Table 51). The increased pressure was a result of increased dough shear viscosity which gave added extrusion stability. Cork-screwing behaviour was much less frequent with the 10% formulation. The MC10 formulation, a long die land and increased extrusion velocity (up to 18 seconds per 450 mm long rod) removed cork-screwing behaviour. Variation in pitch and concentricity was still present and so filament development work would be required.

Production Scale Extrusion Optimisation of Tooling set up and Process Conditions (Production Scale)

Tooling changes were based on the Benbow Bridgwater experiment described in chapter 6 from which longer die lengths were known to give increased extrusion pressures. The aim of increasing pressure was to increase dough flow stability to mimic the stiffer SHM dough. A longer nozzle with an extended rifled section was therefore designed with improved core pin design. The core pin (used to hold filaments in place for coolant holes) was altered to promote dough rotation before entering the lengthened parallel section. The core pin was grooved with a decreasing diameter towards the

rifled section. In doing this the core pin also reduced the volume of space within the trumped shaped section of the die thus increasing back pressure. Using a higher extrusion speed of 0.25 mm^{-s} was also beneficial for extrusion flow stability by increasing pressure. Faster extrudate speeds of 18 seconds per rod were not achievable on pilot scale equipment because the rods could not be manually cut and handled quickly enough.

Extrusion Quality Control

Quality was examined for rifled rods that contained coolant holes as data could be collected and compared to product specifications. The pitch of the rods was measured using a shadow graph as a measure of flow consistency and material stability (Figure 60). Change in pitch was measured for group 2 material a result of increasing cellulose content in the binder. Pitch, pitch circle diameter and concentricity measurements presented in this section were taken in the as extruded state. Due to excessive handling it was not ideal to measure every rod from a small batch of material on a pilot scale. Data from production trials was more reliable as a greater number of samples could be analysed after extrusion under stable pressure conditions. Pitch data from the pilot scale experiments for group 2 binder based dough is shown in Figure 306. Pitch measurements of Group 3 dough showed that longer chain methyl cellulose binders produced extrudate with a longer pitch. A stiffer dough was not expected to elongate as much as softer dough in the rifled section. However there is also a trend of increased pitch with cellulose content with the exception of the 16% methyl cellulose binder (Figure 306).

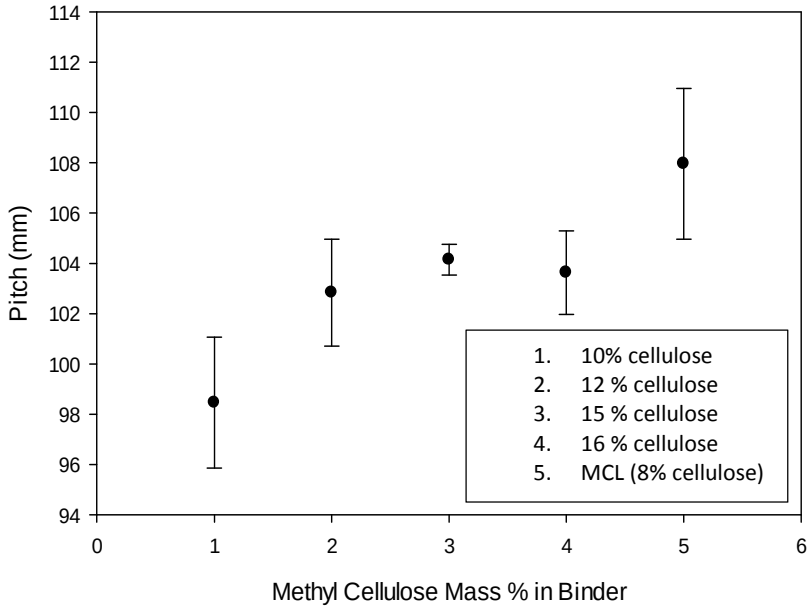

Figure 306 Pitch variation with MC mass %

Based on extrudate speed in a production environment, the equivalent extrudate speed from the capillary rheometry experiments was calculated and the shear viscosity at that ram speed determined in Figure 307.

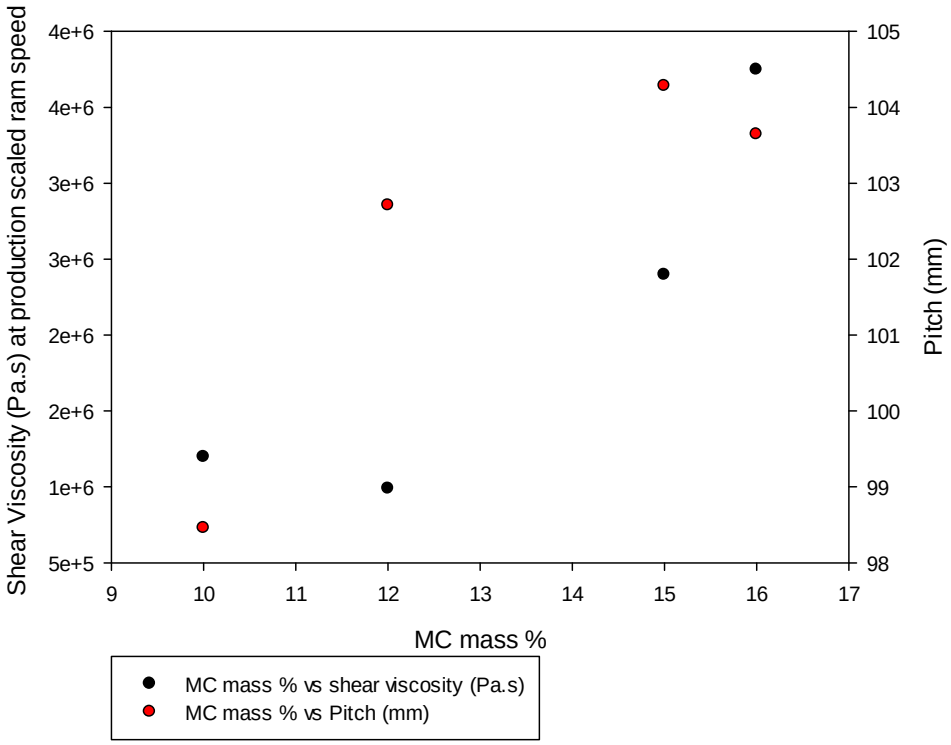

Figure 307 Pitch and dough shear viscosity variance as a function of methyl cellulose content

Production trial data for the MC10 formulation has been presented in Figure 308 to Figure 310. The tray number (x axis) represents an order of time depending on stoppages from the start of the extrusion run. 7 rods were placed on each graphite tray, in Figure 308 tray 1 was the start of extrusion (first 7 rods) and tray 10 represents the end of extrusion.

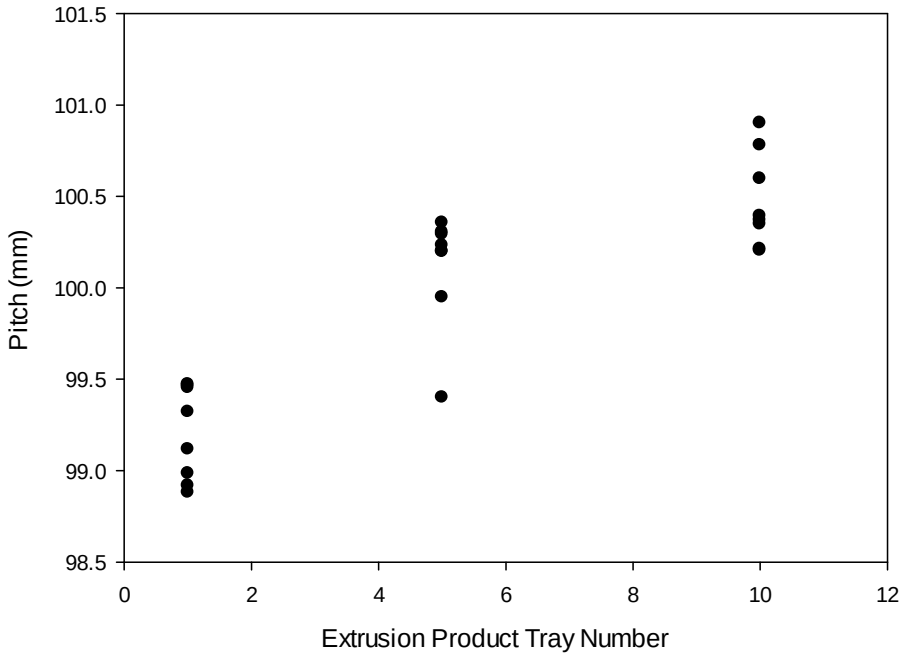

Figure 308 Production trial 1 pitch length extension with test duration

Rods were extruded onto trays capable of accepting up to 13 samples. Ideally, more samples would have been measured but excessive handling of the product was damaging. Fewer PCD and concentricity readings were made in each production trial as these measurement techniques are destructive (section 3.11.3). PCD and concentricity measurements for the same production trial have been plotted in Figure 309. The first production trial revealed that PCD and concentricity values were scattered and consequently that a more systematic approach was required to evaluate the parameters. Improved labelling was required so that the leading edge of the rod could be identified. This allowed for measurements to be taken with rod length to observe inter-rod variability (Figure 310).

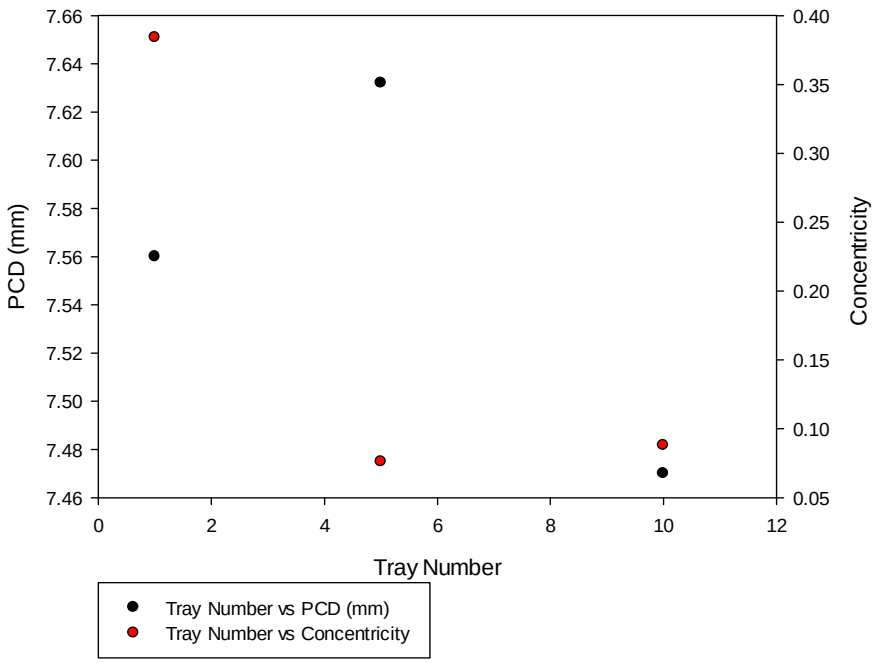

Figure 309 Production trial 1 PCD & concentricity measurements with test duration

For later testing in production on the same material, pitch measurements were tested more thoroughly to observe batch consistency. Figure 310 shows pitch results for the second production test.

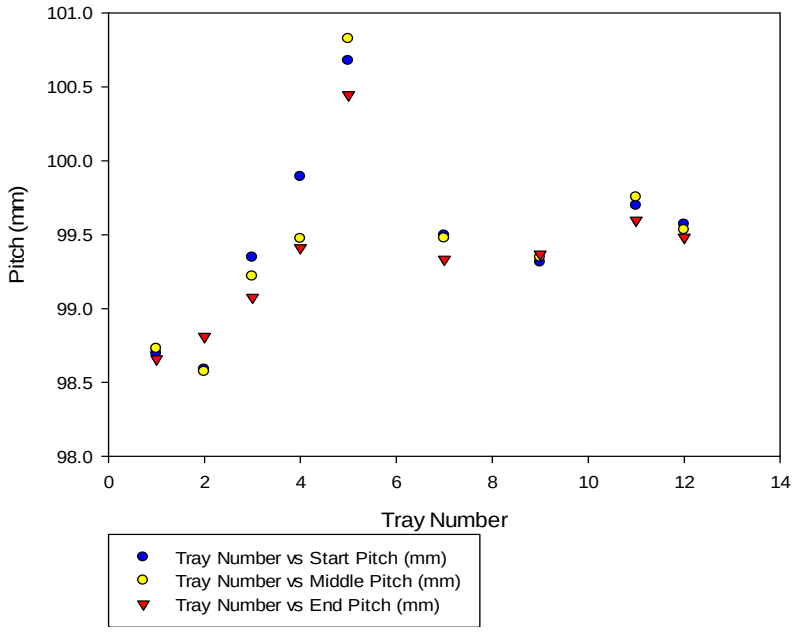

Figure 310 Production trial 2 pitch variation with test duration

An increase in pitch measurements followed by a sharp decrease (after tray 5) represents an event during the extrusion trial. In this instance the automatic handling system became blocked and

consequently the extrusion process shut down. The concentricity and PCD measurements for the test carried out in the second production trial have been plotted in Figure 311.

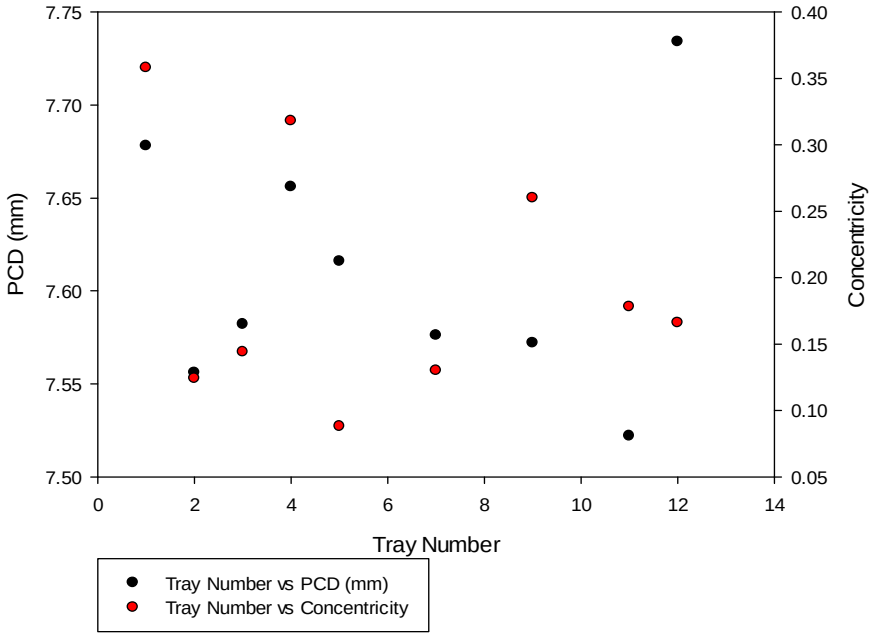

Figure 311 Production trial 2 PCD & concentricity measurements with test duration

Figure 311 shows a large scattering of PCD and concentricity data throughout the production trial. Although the data is scattered, the scale is small for PCD and is within specification, concentricity was more of an issue in this case as it was fluctuating out of specification.

Extrusion Quality Control Production Scale Extrusion, Quality Control

Pitch, concentricity and PCD varied throughout a production trial for MC10 feedstock and therefore flow stability was not optimised. Pitch increased up to tray number 6 and then dropped before progressively increasing (Figure 310). The drop in pitch coincided with a stop in production at that point. With SHM dough, pitch generally increased with extrusion running time due to a number of factors associated with tooling and material changes. During a production test, filaments would elongate by up to 5 mm and material would heat up through viscous heating. Heating the SHM material would reduce shear viscosity due to softening of the thermoplastic PEG binder. This also happened with the MC10 formulation, temperatures above 40 °C were not reached (which would cause gelation of the methyl cellulose). However, shear and temperatures above 25 °C and caused the PEG contained in the WC-Co to soften. The die land does not change its structure significantly with temperature as it is manufactured from WC-Co. Therefore the pitch of the extrudate is the

inverse pattern of the die assuming that complete die filling has occurred with no material slip. However, filaments influence the extrudate pitch and therefore the internally formed helix pattern of coolant holes. During an extrusion test, the filaments can elongate due to plastic deformation and heating. This causes a longer internal helix pattern which allowed the extrudate to unwind more as it relaxed thus lengthening the pitch further. The increased temperature also contributed to this effect as softer dough unwinds more easily. As the temperature of extrudate and length of filaments increased with extrusion running time, so did the pitch. For the data shown in Figure 310 after tray 6 the extrusion process was shut down for 2 hours, allowing material and equipment to cool down and relax. As a result of relaxation, pitch was shortened in the initial re-start up period. Faster ram speeds also encouraged the same behaviour with this particular dough due to increased shear thinning with increased shear rate. The increasing pitch however did not appear to have an effect on the concentricity and PCD. Concentricity and PCD vary randomly as seen in Figure 311. However, the variation was not out of specification in every case. Further tests were designed to investigate the concentricity and PCD are described in chapter 7.

Appendix J -Influence of Tight Pitch on Concentricity and PCD

For the tighter pitch experiment, sections were taken in the green state and measured using a shadowgraph. Coolant hole rotation was not monitored in the tighter pitch experiment as it was designed to observe the PCD and concentricity only. Rods were extruded through a nozzle with a tighter helix angle and therefore a tighter pitch, at an extrudate diameter of 12 mm. Tighter pitches were known to exaggerate the cork-screwing behaviour. Corkscrewing (Figure 312) was thought to be either the cause of poor concentricity, or caused by tooling misalignment giving rise to poor concentricity. Smaller diameter material has to twist at a faster rate for a given pitch length thus causing higher stresses. The tight pitch experiment showed that there were no similarities between the variance in PCD and concentricity to the 20 mm sintered sample tests. Figure 313 shows that the PCD decreased with sample length from the leading edge, whilst the concentricity was more random. From this data it could be concluded that the behaviour of filaments was vital to obtain the correct specifications with regards to coolant holes. Filaments were 1.5 mm in diameter and significantly less stiff than those used in other extrusion trials. The lack of stiffness shows that filaments were more prone to fluctuating movements, hence giving randomised concentricity measurements. As the PCD was decreasing however, it is likely that the randomised concentricity was occurring alongside movement of both filaments (for each coolant hole). In Figure 313 pitch lengths have been included. Sections were taken at random lengths and a trend for concentricity has been observed based on the cyclic rotation of the sample. With every full pitch length, the concentricity shows a cyclic trend of a decrease followed by an increase. This indicates that with every helical rotation during extrusion, concentricity drifts in and out of the required tolerance. Drifting concentricity values were caused by material cork-screwing which itself was caused by asymmetric tooling. Tooling was asymmetric as two coolant holes were formed in every sample and therefore the core-pin could not be symmetrically manufactured. The drifting of concentricity and cork-screwing were observed at all sizes. Sections were taken at random so that data could not be synchronised with corkscrewing behaviour. In the 20 mm extrudate, there was a chance that the first section could have been taken at a point where properties were well within specification. Subsequent equally spaced sections would also have fallen within the good band of the specification as a result. Taking sections at random removed this unlikely coincidence. The examined rod and indicated sections have been shown in the green state in Figure 312.

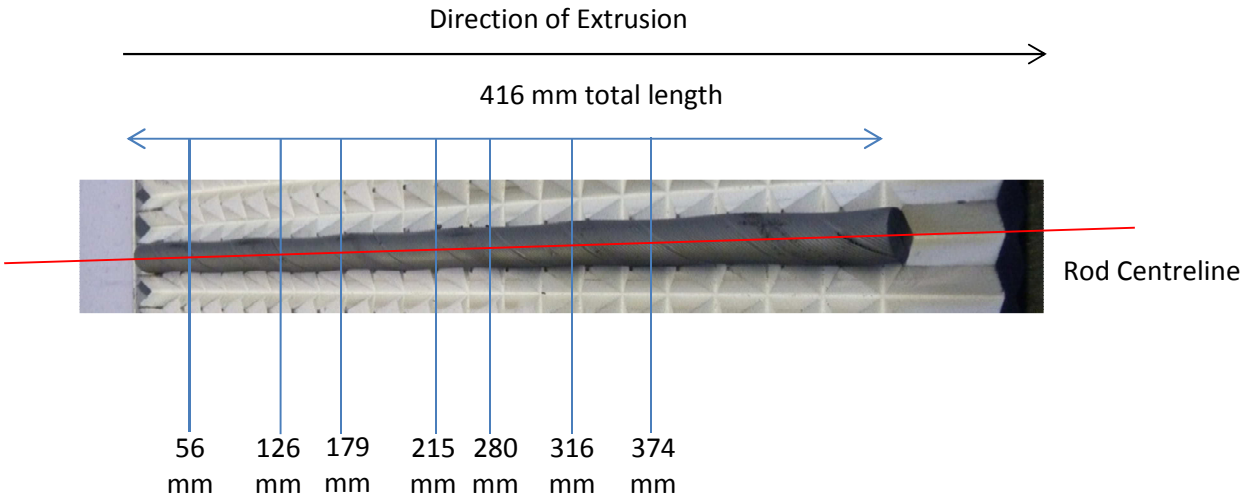

Figure 312 Tight pitch sectioning (12 mm coolant)

The excessive corkscrewing can be seen in Figure 298 whilst Table 52 shows the measured properties.

Table 52 Tight pitch section measurements

Rod I.D	PCD	Concentricity	Hole 1 (mm)	Hole 2 (mm)	Rod Diameter (mm)
1 (56)	4.774	0.512	1.45	1.29	17.012
1 (126)	4.746	0.43	1.416	1.388	16.884
1 (179)	4.68	0.604	1.322	1.432	16.878
1 (215)	4.682	0.636	1.436	1.420	16.756
1 (280)	4.640	0.452	1.288	1.522	16.798
1 (316)	4.658	0.504	1.426	1.328	16.752
1 (374)	4.524	0.7	1.582	1.290	16.796

Concentricity and PCD measurements for the tight pitch experiment are given in Figure 313.

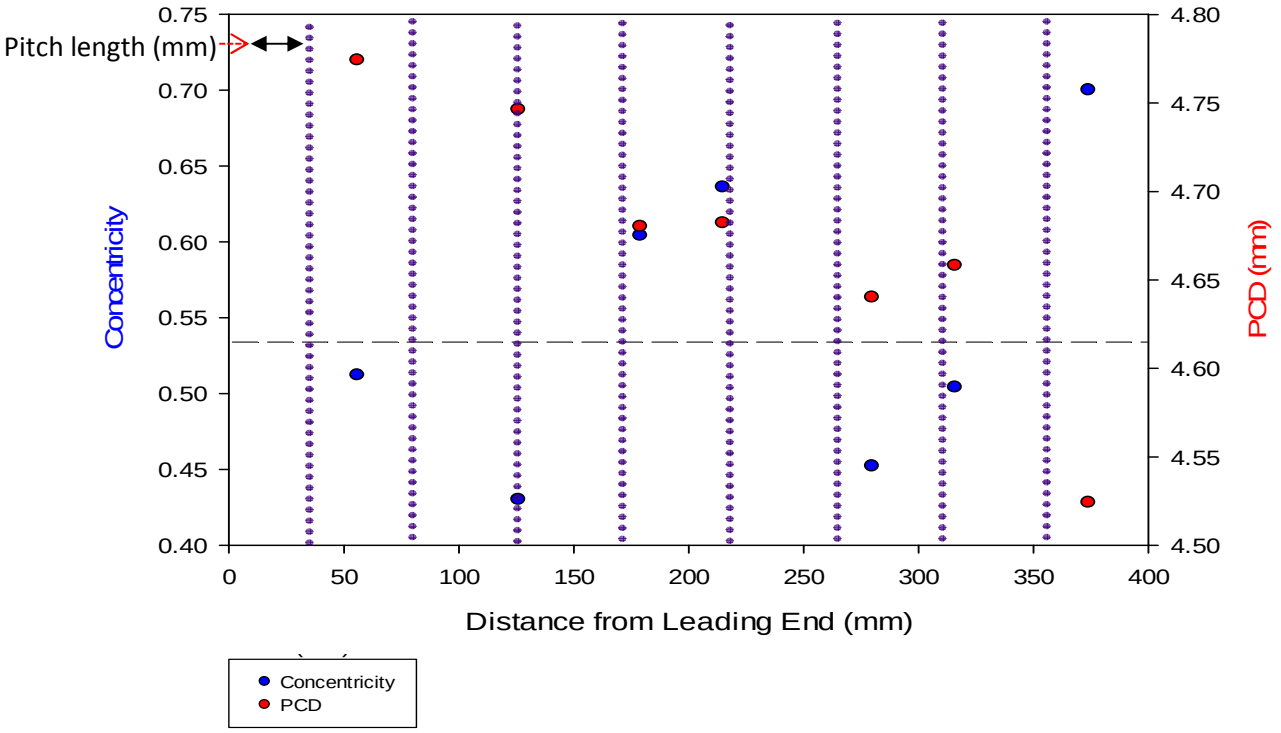

Figure 313 Tight pitch section measurements in the green state (concentricity and PCD as a function of rod length)

Different behaviour, particularly with the PCD was observed when compared to the 20 mm sintered properties. PCD decreased significantly with rod length whereas concentricity was more scattered. A cyclic trend was observed with the concentricity, suggesting that it was following the rotation of the sample during extrusion. Gridlines in Figure 313 represent pitch length (45-47 mm) for the 12 mm product. For every second pitch in the sample, there was a drop or rise in the concentricity although perfect synchronisation is not observed. Perfect synchronisation of the pitch and varying concentricity would suggest that the extrusion die was not centred correctly with the rest of the extrusion tooling. As the concentricity is not completely synchronised with rod rotation, it is likely that the formulation suffers from instability as well as tooling being misaligned. Regularly sectioned sintered parts of a tight pitch sample have also been analysed and photographed using optical microscopy in Figure 314 to Figure 320.

Tight Pitch Experiment (Sintered Regular Sections)

The sintered sections are shown in Figure 314 to Figure 320.

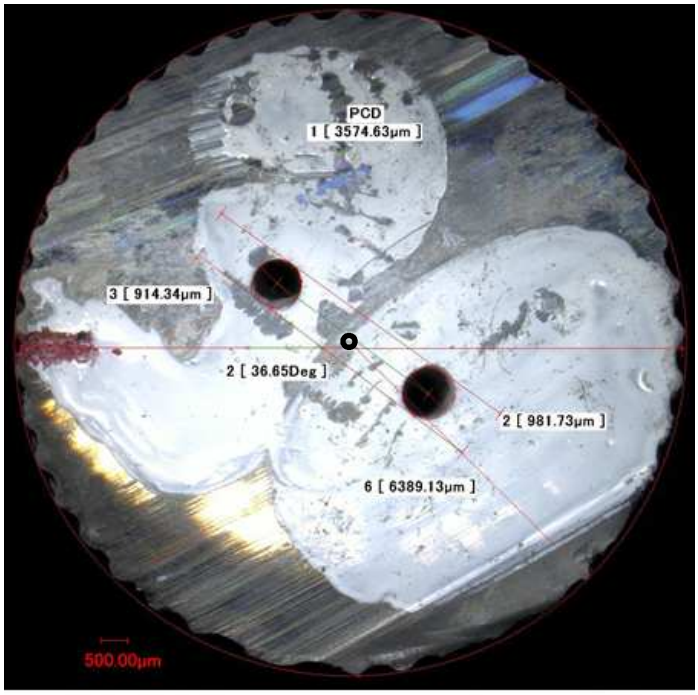

Figure 314 30 mm tight pitch sintered section

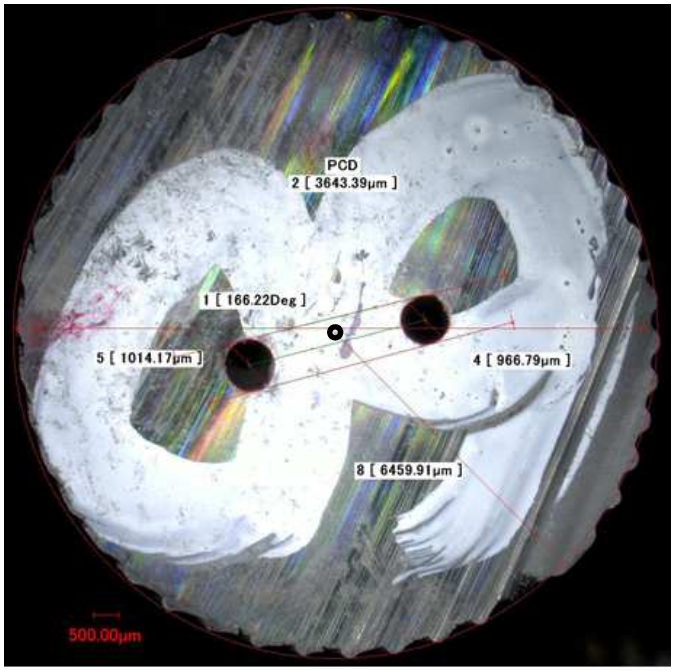

Figure 315 60 mm tight pitch sintered section

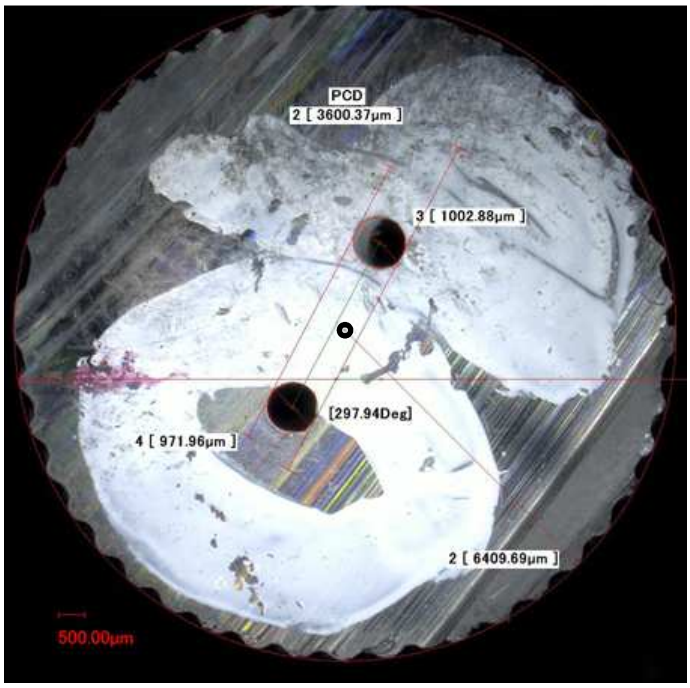

Figure 316 90 mm tight pitch sintered section

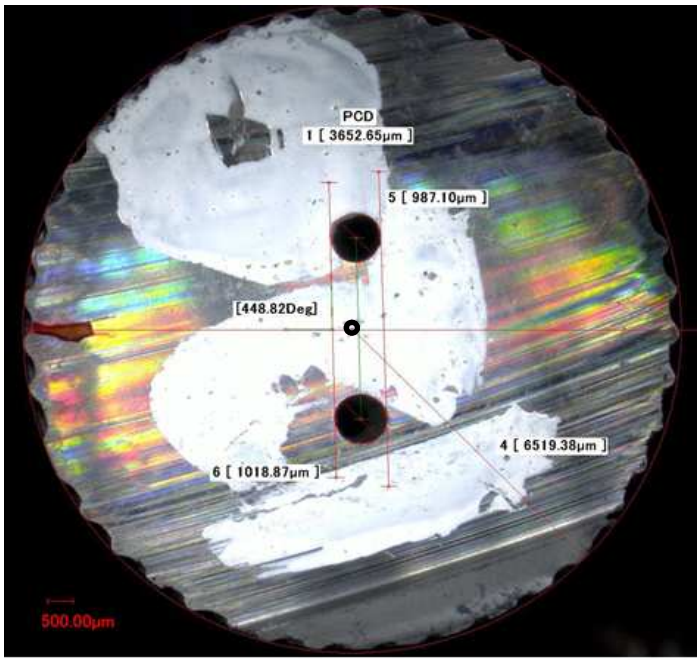

Figure 317 120 mm tight pitch sintered section

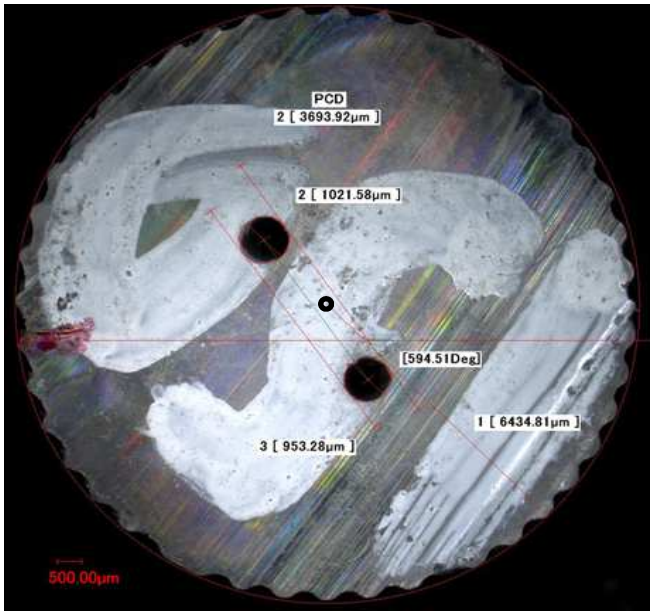

Figure 318 150 mm tight pitch sintered section

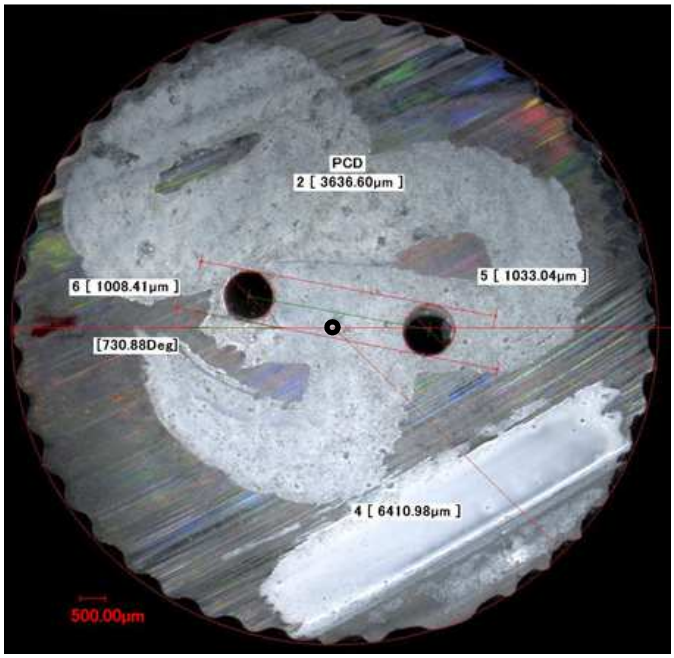

Figure 319 180 mm tight pitch sintered section

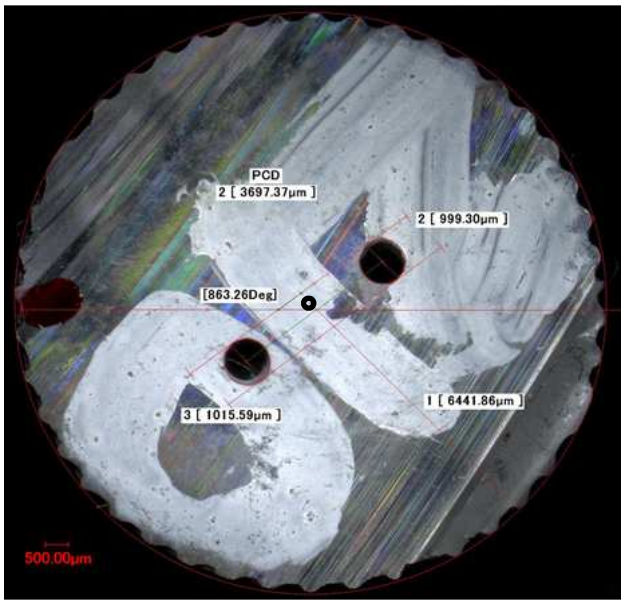

Figure 320 210 mm tight pitch sintered section

Figure 315 shows that the PCD centreline passes directly through the rod centre, as it should do. Although the concentricity is within specifications initially, by the final section of the rod it has drifted out of specification. Figure 319 shows the worst concentricity which indicates that the concentricity is fluctuating with corkscrewing behaviour as well as becoming worse with extrusion duration.